FIBER SPINNING AND RHEOLOGY OF LIQUID-CRYSTALLINE POLYMERS

by

SURESH RAMALINGAM

B.Tech, Chemical Engineering
Indian Institute of Technology, Madras
(1987)

M.S. Chemical Engineering Practice
Massachusetts Institute of Technology
(1990)

Submitted to the Department of Chemical Engineering
in partial fulfillment of the requirements
for the degree of

DOCTOR OF PHILOSOPHY

at the

MASSACHUSETTS INSTITUTE OF TECHNOLOGY

May, 1994

Author .....
Department of Chemical Engineering
March 10, 1994

Certified by .....
Robert C. Armstrong
Professor of Chemical Engineering
Thesis Supervisor

Accepted by .....
Robert E. Cohen
Chairman, Committee for Graduate Students

Fiber Spinning and Rheology of Liquid-Crystalline Polymers

by

Suresh Ramalingam

Submitted to the Department of Chemical Engineering
on March 10, 1994, in partial fulfillment of the requirements for the
degree of Doctor of Philosophy in Chemical Engineering

Abstract

The invention, development and commercialization of fibers such as Kevlar®, which possess unique mechanical and chemical properties, from processing liquid-crystalline polymer melts and solutions is of tremendous technological importance. Liquid-crystalline polymers are distinguished by strong molecular alignment which results in the unique properties that closely resemble a crystalline solid. It has been established that the tensile modulus of these fibers shows a strong dependence on the molecular orientation with respect to the fiber axis (Yang, 1993). Since substantial orientation is achieved during the fiber spinning flow, a model that would relate the development of microstructure in this flow to the macroscopic properties would be a very useful process design tool in predicting and controlling the product properties, optimizing product properties, and minimizing production costs. The aim of this research is to contribute to the development of such a design tool.

Achieving this goal involves 1) identifying a realistic constitutive equation for liquid-crystalline polymers and 2) using the constitutive equation to develop a finite element model for the complex fiber spinning flow. Four stages can be identified in the fiber spinning flow a) spinneret flow which involves flow through a contraction, b) die swell experienced by the polymer solution as it comes out of the spinneret, c) fiber drawing which involves extensional stretching of the polymer solution and d) solidification or coagulation where the solvent is extracted from the polymer solution and the microstructure is frozen in the resultant solid. The solidification issue is not addressed in this thesis.

The recently developed Bhave *et al.* (1993) constitutive equation, which is a molecular model, gives physically meaningful viscosity predictions that compare very well with experimental data for a wide variety of liquid-crystalline polymer systems as opposed to the Leslie, Ericksen and Parodi (LEP) model (1970, 1976 and 1979) and the Doi (1981) model which are widely discussed in literature. Consequently, the Bhave *et al.* constitutive equation is used to model the fiber spinning process.

A one-dimensional model was developed for the fiber drawing region by using the lubrication approximation. The Bhave *et al.* model uses a closure approximation to get a closed form of the constitutive equation. When the closure approximation is used, molecular tumbling (Larson and Ottinger, 1991) in simple shear flows are not predicted. The fiber drawing analysis was therefore carried out using the Bhave *et al.* constitutive equation and by directly solving the probability distribution function for the molecular orientation to test the effect of closure. The results indicate that the closure approximation is valid at moderate and high Deborah number (De) in this extensionally dominated flow. The technique used to solve directly for the distribution function also indicates a path for solving other complex flow problems with molecular models where approximations of uncertain validity must be used to obtain a closed-form constitutive equation. The fiber drawing model predictions clearly show the sensitivity of the velocity, stress and structure development to the initial microstructure. The final order predicted for an initial microstructure which would exist in a simple uniaxial elongational flow is always slightly higher than that predicted with an initial equilibrium microstructure; the corresponding tension required for

achieving the same drawdown in the fiber radius is 20% higher. The sensitivity to the initial condition is contrary to that observed in the modeling with isotropic viscoelastic constitutive equations (Fisher and Denn, 1976 for example), where the downstream velocity and stress profiles are found to be insensitive to the choice of the initial stress condition. Sensitivity of the liquid-crystalline polymer fiber drawing model to the initial microstructural condition requires 2-D calculations that couple to the upstream spinneret flow. The 2-D calculations are also necessary to assess the assumption of radial homogenity used in the one-dimensional fiber drawing model. Model predictions of steady state fiber drawing data (Prilutski, 1984) are good. However, the data are for extremely small flow rates and the order hardly changes from the equilibrium value. Consequently, the model predictions with the equilibrium initial microstructure and the initial microstructure predicted in a simple uniaxial elongational flow are the same.

Two-dimensional finite element calculations based on the EVSS-G formulation developed by Brown *et al.* (1993) were carried out for the flow through the spinneret. Flow through 2:1 and 4:1 contractions with cubic and conical boundary shapes were examined. The response in the molecular orientation is described in terms of the average orientation angle with respect to the spinneret axis (χ) and the degree of order (S). With increasing De, near the exit, the average molecular alignment with the spinneret axis improves across the entire spinneret cross section (χ increases from negative values to zero) and the degree of order also increases. The homogenity in S and χ at high De is much better for dies designed with short downstream tube lengths. To maximize and homogenize S and χ the 4:1 conical contraction geometry was found to be best among the geometric configurations examined. The pressure drop per unit volumetric flow rate is also least in the 4:1 conical contraction. No recirculation regions were observed for the spinneret geomtries and range of De examined. Spinneret calculations at moderate and high concentrations revealed no qualitative difference in the development of order. Dieswell for liquid-crystalline polymers is small; in fact it is comparable to a Newtonian dieswell (Prilutski, 1984). Consequently, the molecular deorientation is expected to be small and the initial microstructure and radial homogenity assumptions in the one-dimensional fiber drawing model can be assessed from the spinneret calculations. The spinneret calculations show that the microstructure is homogenous for short land lengths in the limit of which the radial homogenity assumption in the one-dimensional fiber drawing model is expected to be valid.

An important processing issue in fiber spinning is the appearance of periodic oscillations along the length of the fiber beyond a certain drawdown in the fiber radius (known as the critical draw ratio) which leads to the formation of an undesirable nonuniform fiber. This phenomenon is known as draw resonance. A linear stability analysis of the fiber drawing equations was carried out to predict the onset of draw resonance instabilitites. A strong correlation between an apparent fiber drawing elongational viscosity and the critical draw ratio is predicted by the analysis. Agreement with linear stability data (Prilutski, 1984) is found to be qualitative.

Future work must be directed to the development of an integrated model for the fiber spinning process. An outstanding issue that must be resolved to develop such a model is the numerical difficulty associated with a sudden change in the boundary data at the die exit (Apelian, 1987; Crochet and Keunings, 1982) which is crucial in polymeric systems due to memory effects. Determination of the singularity, known as the die swell singularity, through analytical means would help address the numerical difficulty through the incorporation of the singular behavior in the finite element algorithm via singular finite elements. The liquid-crystal model exhibits a singularity in the stress at the die exit that is Newtonian. However, the singular behavior is not well understood even for a Newtonian model. An analysis based on an expansion scheme for the free surface height is presented in this thesis from which the singular behavior in the stress can be determined and incorporated into the numerical algorithm. No experimental data on the development of order during the fiber spinning process exists in literature to rigorously test the model predictions. Future work must also address this important issue.

This thesis is dedicated to four people I cherish above all:

my wife, ***Shanthi***

my parents, ***Padmavati*** *and* ***Ramalingam***

and my brother, ***Shyam***

Acknowledgements

I would like to thank my thesis advisor Professor R.C. Armstrong for his support and guidance over this thesis. I would like to thank Prof. R.A. Brown for his useful suggestions and ideas at times when things seemed hopeless. I would like to thank my other thesis committee members, Professor T.A. Hatton and Professor W.M. Deen for their input to this research and willingness to accommodate me within their tight schedules even at short notice.

I would like to thank my wife, Shanthi, for her love, encouragement and the immense inspiration and support she provided me during very difficult and trying times.

Words are also not sufficient to describe the support and encouragement my parents have provided me. Truly, I do not know where I would be without their sacrifices. This thesis would not have been possible without them standing by me.

Shyam, thank you for those humorous letters and repartee's which always made me see the brighter side of life. The grit, determination and even humor that you showed in pulling through the accident last year has left an indelible mark on me.

I am indebted to Raghu Menon, my research colleague, and apartment mate for a few years for some of the happiest moments of my stay at M.I.T. and for being a true friend over the times. I am also indebted to Nandini Menon for the excellent food she served many a time and for being a pillar of support on numerous occasions.

For several exciting and thought provoking discussions and support over the years I would like to thank Sudhakar Puvadda. I would also like to thank other friends Ganesh Venkatraman, Vivek Mohindra, Ramprasad Narayanan, Ramakrishnan, Rajesh Panchanathan, Vishak Sanakaran and Godavarthi Varadarajan for all their help and support over the years.

I would like to thank my research colleagues Todd Tsalamon and Alparslan Oztekin for being good friends and extending their support on many many occasions. I would also like to thank several of my other research colleagues including John Lee, Lidia Quinzani, Angelos Kyrlidis, Howard Covert, Reza Mehrabi, Dilip Rajagopalan, Paul Coates, Aparna Bhave, Talid Sinno, Mike Szady, Christine Weigand and David Lee for their help and support on numerous occasions. Special thanks to David Bornside for his help with the finite element code for the axisymmetric contraction problem.

I would like to take this opportunity to thank Arline, Nancy and other staff in the Chemical Engineering Department for their immense help and cooperation during my stay here.

This research was funded by E.I. Dupont and Nemours. Most of the intensive numerical calculations in this thesis were performed on the M.I.T. Cray.

Table of Contents

Chapter One

Introduction 30

1.1 Importance of Fiber Spinning of Liquid-crystalline polymers 30

1.2 Outline of Thesis 35

1.2.1 Constitutive Modeling of Liquid-Crystalline Polymers 35

1.2.2 Modeling of the Fiber Spinning Process 38

Chapter Two

Background on Fiber Spinning 45

2.1 Experimental Observations 48

2.1.1 Draw Resonance 48

2.1.2 Sensitivity and Spinnability 50

2.2 Theoretical investigations 51

2.2.1 Inelastic flow modeling-viscous and power-law models ... 51

2.2.2 Viscoelastic Flow Modeling 54

Chapter Three

Liquid-Crystal Flow Modeling 61

3.1 Experimental observations 65

3.2 Liquid-Crystal Constitutive Equations 69

3.2.1 Leslie-Ericksen-Parodi and Doi constitutive equations 69

3.2.2 Bhave *et al.* constitutive equation 70

Chapter Four

Analysis of Isothermal Spinning of Liquid-crystalline Polymers 89

4.1 Orientation States for the Nematic Director in a Steady, Simple Elongational Flow 90

4.2 Steady Simple Elongational Flow 95

4.3 Steady-State Fiber Spinning Model 102

4.3.1 Bhave *et al.* Constitutive Equation 103

4.3.2 Direct Solution of Diffusion Equation 106

4.3.3 Results and Discussion 110

4.3.4 An Aside - Is the Fiber Spinning Model Developed with Doi's Constitutive Equation "Viscous" in Nature? 121

4.4 Linear Stability Analysis 123

4.4.1 Governing Equations and Boundary Conditions 124

4.4.2 Results and Discussion 127

4.5 Conclusions from Fiber Spinning Analysis 135

4.6 Direct Solution of Diffusion Equation: A Comparison of Legendre Polynomial Expansion Technique (LPET) with the Double Lagrangian Method (DLM) of Szeri and Leal 137

Chapter Five

Two-dimensional Flow Problems 142

5.1 Mathematical Type of Equations Governing LCP Flow 147

5.1.1 Classification of a System of Quasilinear, First-Order, Partial Differential Equations 148

5.1.2 Classification of System of Equations Governing LCP Flow 150

5.2 Description of Contraction Flow Problem 152

5.2.1 Flow Geometry for Contraction Flow 153

5.2.2 Governing Equations and Boundary Conditions 160

5.3 The FEM Method 165

5.3.1 The Method 166

5.3.2 FEM Formulation for LCP Flow 177

5.3.3 Solution of the Discretized Equation Set 187

Chapter Six

Tube and Axisymmetric Contraction Flows of LCP's 193

6.1 Flow through Tube Test Problem 193

6.2 Flow through Contraction 214

6.2.1 Moderate Concentration; N=4.0 214

6.2.1.1 Effect of Downstream Tube Length 215

6.2.1.2 Convergence with Mesh Refinement 222

6.2.1.3 Effect of De; De=0.1, 1.0 and 5.0 227

6.2.2 High Concentration; N=7.0 259

6.2.2.1 Effect of De; De=0.1, 1.0 and 5.0 260

6.2.2.2 Effect of Concentration 282

6.2.3 Effect of Contraction Ratio, Λ 289

6.2.4 Effect of Change in Geometry; Conical Contraction with Rounded Corners 315

6.2.5 Couette Correction for Λ = 2 and 4 346

Chapter Seven

Conclusions 351

7.1 Conclusions from Fiber Drawing Analysis 352

7.2 Conclusions from Spinneret Calculations 355

7.3 Conclusions from Die Swell Singularity Analysis 362

References 365

Appendix A

Die Swell Singularity Analysis for a Newtonian Fluid 375

Appendix B

Fiber Drawing Analysis for Liquid-Crystalline Polymers Using Doi's Reptation Time Constant 398

List of Figures

1.1 Structural backbone in PPD-T is illustrated. The long chain PPD-T molecules are oriented by the flow with the fiber axis 31

1.2 The tensile modulus of Kevlar® as a function of molecular orientation with respect to the fiber axis is illustrated for an as-spun fiber and a heat treated fiber. The modulus is in grams-per-denier which is roughly 1/8 of a Giga-Pascal (reproduced from Yang, 1993) 34

1.3 Global approach to predict process induced microstructure 36

1.4 Schematic diagram of fiber spinning process. The spinneret, die swell, fiber drawing and solidification regions are indicated 40

2.1 Critical draw ratio as a function of De for the White-Metzner model. n is the power-law viscosity index (reproduced from Fisher and Denn, 1976) . 56

3.1 Schematic diagram of isotropic and liquid-crystalline rods and disks 62

3.2 Classification of liquid-crystalline phases based on structural order; (a) Nematic, (b) Cholesteric and (c) Smectic 64

3.3 A schematic diagram of the fiber spinning apparatus used by Prilutski (reproduced from Prilutski, 1984) 67

3.4 Rigid dumbbell model of a liquid-crystalline polymer molecule 72

3.5 Liquid-crystal polymer solution is modeled as a solution of rigid dumbbells in a Newtonian solvent. The forces acting on each dumbbell are shown . 74

3.6 Equilibrium phase diagram for the Bhave *et al.* model. The solid curves

represent stable phases and dashed curves unstable phases 81

3.7 Comparison of the viscosity predictions of the Bhave *et al.* model with the data of (a) Doraiswamy and Metzner (1986) for 40 wt% HPC in acetic acid, and (b) Picken *et al.* (1990) for 20 wt% DABT in H_2SO_4 83

3.7c Comparison of the viscosity predictions of the Bhave *et al.* model with the unpublished data of Ramalingam and Armstrong for a 19.8 wt % PPTA in H_2SO_4 (Kevlar® spin dope) liquid-crystalline polymer solution 84

3.8 Elongational viscosity, $\bar{\eta}$, predictions of the Bhave *et al.* model for N=4.0, σ=0.1, 0.25, 0.5 and 1.0. Results are shown for $\lambda=\lambda_0$ and $\lambda=\lambda_0(1-S^2)^2$ 87

4.1 Schematic diagram of (a) a simple shear flow where the xy-plane is the plane-of-shear, and (b) a simple uniaxial elongational flow where the z-axis is the axis of symmetry 91

4.2 Equilibrium phase diagram (a) with closure and (b) without closure. The shift in critical concentration and order at onset of nematic phase is indicated 99

4.3 Effect of closure on the variation of (a) order parameter S and (b) elongational viscosity $\bar{\eta}$ with elongation rate $\dot{\epsilon}$ in a simple steady elongational flow. The concentration N is chosen so that $N/N_c = 4/3$ for both models 101

4.4 Test of convergence of the Legendre polynomial expansion for the distribution function f to the exact solution as a function of the number of

even Legendre polynomials for (a) $\dot{\varepsilon}\lambda/\sigma$=0.01 and (b) $\dot{\varepsilon}\lambda/\sigma$=100.0 in simple elongational flow 108

4.5 Variation of (a) velocity ϕ, (b) order parameter S, and (c) dimensionless normal stress difference $-(\tau_{zz}-\tau_{rr})/nkT$ with distance ζ down the threadline for N/N_c=4/3, σ=0.1, D_R=3.0, and De=0.01, 1.0 and 10. The initial condition for the microstructure is $S(0)=S_\epsilon$. Results with and without the closure approximation are shown. Velocity profiles for De=0.01 and 10.0 are indistinguishable 112

4.6 Variation of (a) velocity ϕ, (b) order parameter S, and (c) dimensionless normal stress difference $-(\tau_{zz}-\tau_{rr})/nkT$ with distance ζ down the threadline for N/N_c=4/3, σ=0.1, D_R=3.0, and De=0.01, 1.0 and 10. The initial condition for the microstructure is $S(0)=S_{eq}$. Results with and without the closure approximation are shown 113

4.7 Effect of draw ratio on the apparent elongational viscosity $\bar{\eta}_a$ for N=4.0 and σ=0.1 and 1.0 and for the two different initial conditions (a) $S(0)=S_\epsilon$ and (b) $S(0)=S_{eq}$. Results are shown for D_R=3.0 and 20.0. The true elongational viscosity $\bar{\eta}$ for the model of Bhave *et al.* and $\bar{\eta}_{a,origin}$ are shown for comparison 117

4.8 Comparison of model predictions with the velocity data of Prilutski (1984) for a hydroxypropyl cellulose solution in acetic acid with N=4.0, D_R=3.63, η_s=0.0012 Pa·s, De=7.63×10^{-3}, σ=0.95 and $S(0)=S_\epsilon$ and S_{eq}: (a) velocity and (b) normal stress difference. The prediction obtained without

including gravity and surface tension is shown for comparison with $S(0)=S_\epsilon$ and $\sigma=0.75$ 119

4.9 Variation of $D_{R,crit}$ with De for N=4.0 and σ=0.1 and 1.0. Results are shown for both $S(0)=S_\epsilon$ and S_{eq} 128

4.10 Variation of $D_{R,crit}$ with Re, Re/Fr and Re/We for N=4.0, σ=1.0, and De=0.01, 1.0, and 1000. The Newtonian neutral stability curves are shown for comparison. For the liquid-crystal results $S(0)=S_\epsilon$ 131

4.11 Comparison of model predictions for (a) fixed length, L=0.0341 m and (b) fixed flow rate, $Q=1.99\times10^{-8}$ m^3/s with the critical draw ratio data of Prilutski (1984) for a hydroxypropyl cellulose solution in acetic acid. Parameter values are N=4.0, σ=0.95 and η_s=0.0012 Pa·s. The initial condition is $S(0)=S_\epsilon$. Best fit values of σ and λ are shown for comparison 133

5.1a The smooth, cubic contraction geometry 154

5.1b The smooth, conical contraction geometry with rounded corners 155

5.1c Geometric construction to determine the endpoints of the internal common tangent 156

5.2 Effect of sharp corner on molecular orientation 159

5.3 Isoparametric transformation used to map an element in (z,r) space onto fixed parent element. (·) is the node number 168

5.4 Local refinement of quadrilateral mesh showing one-to-two element transition from element e_3 to elements e_1 and e_2 (reproduced from

Tsiveriotis and Brown, 1992) 170

5.5 Sample meshes for 2:1 and 4:1 contractions. The numbers along the mesh borders are dimensionless coordinates scaled by R_2 186

6.1a Contour plots of streamlines in the flow through a tube for N=4.0, σ=1.0, β=1.6x10^{-5} and De=0.1, 1.0 and 5.0 195

6.1b Contour plots of radial velocity in the flow through a tube for N=4.0, σ=1.0, β=1.6x10^{-5} and De=0.1, 1.0 and 5.0 196

6.1c Contour plots of axial velocity in the flow through a tube for N=4.0, σ=1.0, β=1.6x10^{-5} and De=0.1, 1.0 and 5.0 197

6.1d Contour plots of pressure in the flow through a tube for N=4.0, σ=1.0, β=1.6x10^{-5} and De=0.1, 1.0 and 5.0 198

6.1e Contour plots of S_{rr} in the flow through a tube for N=4.0, σ=1.0, β=1.6x10^{-5} and De=0.1, 1.0 and 5.0 199

6.1f Contour plots of S_{zz} in the flow through a tube for N=4.0, σ=1.0, β=1.6x10^{-5} and De=0.1, 1.0 and 5.0 200

6.1g Contour plots of S_{rz} in the flow through a tube for N=4.0, σ=1.0, β=1.6x10^{-5} and De=0.1, 1.0 and 5.0 201

6.1h Contour plots of Deτ_{rr} in the flow through a tube for N=4.0, σ=1.0, β=1.6x10^{-5} and De=0.1, 1.0 and 5.0 202

6.1i Contour plots of Deτ_{zz} in the flow through a tube for N=4.0, σ=1.0, β=1.6x10^{-5} and De=0.1, 1.0 and 5.0 203

6.1j Contour plots of De$\tau_{\theta\theta}$ in the flow through a tube for N=4.0, σ=1.0,

$\beta=1.6\times10^{-5}$ and De=0.1, 1.0 and 5.0 204

6.1k Contour plots of $De\tau_{rz}$ in the flow through a tube for N=4.0, σ=1.0, $\beta=1.6\times10^{-5}$ and De=0.1, 1.0 and 5.0 205

6.1l Contour plots of G_{rr} in the flow through a tube for N=4.0, σ=1.0, $\beta=1.6\times10^{-5}$ and De=0.1, 1.0 and 5.0 206

6.1m Contour plots of G_{zz} in the flow through a tube for N=4.0, σ=1.0, $\beta=1.6\times10^{-5}$ and De=0.1, 1.0 and 5.0 207

6.1n Contour plots of G_{rz} in the flow through a tube for N=4.0, σ=1.0, $\beta=1.6\times10^{-5}$ and De=0.1, 1.0 and 5.0 208

6.1o Contour plots of G_{zr} in the flow through a tube for N=4.0, σ=1.0, $\beta=1.6\times10^{-5}$ and De=0.1, 1.0 and 5.0 209

6.2 Eigenvectors associated with the structure tensor in the flow through a tube and contraction geometries. z is along the axis of the tube and the contraction geometries. The nematic director is indicated by $\mathbf{n}$. $\mathbf{e}_2$ is perpendicular to $\mathbf{n}$ in the xz-plane and $\mathbf{e}_3$ is perpendicular to the xz-plane. χ is shown in degrees in subsequent figures 211

6.3 Radial variation in (a) the axial velocity v_z, (b) the degree of order S, and (c) the director orientation χ in the flow through a tube for De=0.1, 1.0 and 5.0 212

6.4 Effect of downstream tube length on the radial variation in (a) v_z, (b) S, and (c) χ at the downstream exit in a 2:1 contraction for N=4.0, σ=1.0, $\beta=1.6\times10^{-5}$, De=5.0 and downstream tube length L=2.5, 5.0, 7.5, 10.0, 60.0

and 225.0 217

6.4 Variation in (d) centerline S and (e) centerline χ at the downstream exit with downstream tube length in a 2:1 contraction for N=4.0, σ=1.0, β=1.6x10^{-5} and De=5.0 219

6.5 Comparison of the radial variation in (a) v_z, (b) S, and (c) χ at z = 30 and 40 for downstream tube lengths of 10.0 and 225.0 in a 2:1 contraction for N=4.0, σ=1.0, β=1.6x10^{-5} and De=5.0 220

6.5 Comparison of the variation in (d) centerline S and (e) centerline χ upto z = 40 for downstream tube lengths of 10.0 and 225.0 in a 2:1 contraction for N=4.0, σ=1.0, β=1.6x10^{-5} and De=5.0 221

6.6 Variation in the L_2-norm of the solution field with number of elements in a 2:1 contraction for N=4.0, σ=1.0, β=1.6x10^{-5} and De=5.0 224

6.7 Effect of number of elements on the radial variations in (a) S and (b) χ at z=0, 30 and 40 in a 2:1 contraction for N=4.0, σ=1.0, β=1.6x10^{-5} and De=5.0 225

6.7 Effect of number of elements on the variation in (c) centerline S and (d) centerline χ in a 2:1 contraction for N=4.0, σ=1.0, β=1.6x10^{-5} and De=5.0 226

6.8a Contour plots of streamlines in the flow through a 2:1 contraction for N=4.0, σ=1.0, β=1.6x10^{-5} and De=0.1, 1.0 and 5.0 228

6.8b Contour plots of radial velocity in the flow through a 2:1 contraction for N=4.0, σ=1.0, β=1.6x10^{-5} and De=0.1, 1.0 and 5.0. Radial velocity is

made dimensionless with the average velocity in the downstream tube $V_{2,avg}$ 229

6.8c Contour plots of axial velocity in the flow through a 2:1 contraction for N=4.0, σ=1.0, β=1.6x10^{-5} and De=0.1, 1.0 and 5.0. The axial velocity is made dimensionless with the average velocity in the downstream tube $V_{2,avg}$ 230

6.8d Contour plots of pressure in the flow through a 2:1 contraction for N=4.0, σ=1.0, β=1.6x10^{-5} and De=0.1, 1.0 and 5.0 231

6.8e Contour plots of S_{rr} in the flow through a 2:1 contraction for N=4.0, σ=1.0, β=1.6x10^{-5} and De=0.1, 1.0 and 5.0 232

6.8f Contour plots of S_{zz} in the flow through a 2:1 contraction for N=4.0, σ=1.0, β=1.6x10^{-5} and De=0.1, 1.0 and 5.0 233

6.8g Contour plots of S_{rz} in the flow through a 2:1 contraction for N=4.0, σ=1.0, β=1.6x10^{-5} and De=0.1, 1.0 and 5.0 234

6.8h Contour plots of Deτ_{rr} in the flow through a 2:1 contraction for N=4.0, σ=1.0, β=1.6x10^{-5} and De=0.1, 1.0 and 5.0 235

6.8i Contour plots of Deτ_{zz} in the flow through a 2:1 contraction for N=4.0, σ=1.0, β=1.6x10^{-5} and De=0.1, 1.0 and 5.0 236

6.8j Contour plots of De$\tau_{\theta\theta}$ in the flow through a 2:1 contraction for N=4.0, σ=1.0, β=1.6x10^{-5} and De=0.1, 1.0 and 5.0 237

6.8k Contour plots of Deτ_{rz} in the flow through a 2:1 contraction for N=4.0, σ=1.0, β=1.6x10^{-5} and De=0.1, 1.0 and 5.0 238

6.8l Contour plots of G_{rr} in the flow through a 2:1 contraction for N=4.0, σ=1.0, β=1.6x10^{-5} and De=0.1, 1.0 and 5.0 239

6.8m Contour plots of G_{zz} in the flow through a 2:1 contraction for N=4.0, σ=1.0, β=1.6x10^{-5} and De=0.1, 1.0 and 5.0 240

6.8n Contour plots of G_{rz} in the flow through a 2:1 contraction for N=4.0, σ=1.0, β=1.6x10^{-5} and De=0.1, 1.0 and 5.0 241

6.8o Contour plots of G_{zr} in the flow through a 2:1 contraction for N=4.0, σ=1.0, β=1.6x10^{-5} and De=0.1, 1.0 and 5.0 242

6.8p Effect of De on S in a 2:1 contraction for N=4.0, σ=1.0, β=1.6×10^{-5} and De=0.1, 1.0 and 5.0. S=0.683 is the equilibrium value for N=4.0 and S=1.0 corresponds to perfect order 243

6.8q Effect of De on χ in a 2:1 contraction for N=4.0, σ=1.0, β=1.6×10^{-5} and De=0.1, 1.0 and 5.0. χ=-20.1 degrees is the zero-shear-rate limit for N=4.0. For χ=0 the director is aligned with the die axis 244

6.9 Effect of De on the radial variation in (a) v_z, (b) S, and (c) χ at z=0, 30 and 40 in a 2:1 contraction for N=4.0, σ=1.0, β=1.6x10^{-5} and De=0.1, 1.0 and 5.0. The fully developed downstream exit velocity profile for a power-law model with the same shear thinning behavior as the viscosity for the liquid-crystal model is shown for comparison 245

6.9 Effect of De on the variation in (d) centerline axial velocity gradient $\dot{\varepsilon}$, (e) centerline S, and (f) centerline χ in a 2:1 contraction for N=4.0, σ=1.0, β=1.6x10^{-5} and De=0.1, 1.0 and 5.0. $\dot{\varepsilon}$ is made dimensionless with

$V_{2,avg}/R_2$. The response in S and χ to $\dot{\epsilon}$ is also illustrated 246

6.10 Effect of De on the response of χ to startup and relaxation after cessation of steady elongational flow along the centerline in a 2:1 contraction for N=4.0, σ=1.0, β=1.6x10^{-5} and De=0.1, 1.0 and 5.0. De$\dot{\epsilon}/\lambda$ is in s^{-1} 255

6.11a Contour plots of streamlines in the flow through a 2:1 contraction for N=7.0, σ=1.0, β=1.6x10^{-5} and De=0.1, 1.0 and 5.0 261

6.11b Contour plots of radial velocity in the flow through a 2:1 contraction for N=7.0, σ=1.0, β=1.6x10^{-5} and De=0.1, 1.0 and 5.0 262

6.11c Contour plots of axial velocity in the flow through a 2:1 contraction for N=7.0, σ=1.0, β=1.6x10^{-5} and De=0.1, 1.0 and 5.0 263

6.11d Contour plots of pressure in the flow through a 2:1 contraction for N=7.0, σ=1.0, β=1.6x10^{-5} and De=0.1, 1.0 and 5.0 264

6.11e Contour plots of S_{rr} in the flow through a 2:1 contraction for N=7.0, σ=1.0, β=1.6x10^{-5} and De=0.1, 1.0 and 5.0 265

6.11f Contour plots of S_{zz} in the flow through a 2:1 contraction for N=7.0, σ=1.0, β=1.6x10^{-5} and De=0.1, 1.0 and 5.0 266

6.11g Contour plots of S_{rz} in the flow through a 2:1 contraction for N=7.0, σ=1.0, β=1.6x10^{-5} and De=0.1, 1.0 and 5.0 267

6.11h Contour plots of Deτ_{rr} in the flow through a 2:1 contraction for N=7.0, σ=1.0, β=1.6x10^{-5} and De=0.1, 1.0 and 5.0 268

6.11i Contour plots of Deτ_{zz} in the flow through a 2:1 contraction for N=7.0, σ=1.0, β=1.6x10^{-5} and De=0.1, 1.0 and 5.0 269

6.11j Contour plots of $De\tau_{\theta\theta}$ in the flow through a 2:1 contraction for N=7.0, σ=1.0, β=1.6x10^{-5} and De=0.1, 1.0 and 5.0 270

6.11k Contour plots of $De\tau_{rz}$ in the flow through a 2:1 contraction for N=7.0, σ=1.0, β=1.6x10^{-5} and De=0.1, 1.0 and 5.0 271

6.11l Contour plots of G_{rr} in the flow through a 2:1 contraction for N=7.0, σ=1.0, β=1.6x10^{-5} and De=0.1, 1.0 and 5.0 272

6.11m Contour plots of G_{zz} in the flow through a 2:1 contraction for N=7.0, σ=1.0, β=1.6x10^{-5} and De=0.1, 1.0 and 5.0 273

6.11n Contour plots of G_{rz} in the flow through a 2:1 contraction for N=7.0, σ=1.0, β=1.6x10^{-5} and De=0.1, 1.0 and 5.0 274

6.11o Contour plots of G_{zr} in the flow through a 2:1 contraction for N=7.0, σ=1.0, β=1.6x10^{-5} and De=0.1, 1.0 and 5.0 275

6.11p Effect of De on S in a 2:1 contraction for N=7.0, σ=1.0, β=1.6×10^{-5} and De=0.1, 1.0 and 5.0. S=0.840 is the equilibrium value for N=7.0 and S=1.0 corresponds to perfect order 276

6.11q Effect of De on χ in a 2:1 contraction for N=7.0, σ=1.0, β=1.6×10^{-5} and De=0.1, 1.0 and 5.0. χ=-13.7 degrees is the zero-shear-rate limit for N=7.0. For χ=0 the director is aligned with the die axis 277

6.12 Effect of De on the radial variation in (a) v_z, (b) S, and (c) χ at z=0, 30 and 40 in a 2:1 contraction for N=7.0, σ=1.0, β=1.6x10^{-5} and De=0.1, 1.0 and 5.0. The fully developed downstream exit velocity profile for a power-law model with the same shear thinning behavior as the viscosity

for the liquid-crystal model is shown for comparison 278

6.13 Effect of concentration on the radial variation in (a) v_z, (b) S, and (c) χ at z=0, 30 and 40 in a 2:1 contraction for De=1.0, σ=1.0, β=1.6x10^{-5} and N=4.0 and 7.0. The fully developed downstream exit velocity profile for a power-law model with the same shear thinning behavior as the viscosity for the liquid-crystal model is shown for comparison 283

6.13 Effect of concentration on the centerline variation in (d) $\dot{\varepsilon}$, (e) S, and (f) χ in a 2:1 contraction for σ=1.0, β=1.6x10^{-5}, N=4.0 and 7.0 and De=0.1, 1.0 and 5.0 284

6.14 Effect of concentration on the dimensionless viscosity for σ=1.0, β=1.6x10^{-5} and N=4.0 and 7.0 285

6.15a Contour plots of streamlines in the flow through a 4:1 contraction for N=4.0, σ=1.0, β=1.6x10^{-5} and De=0.1, 1.0 and 5.0 290

6.15b Contour plots of radial velocity in the flow through a 4:1 contraction for N=4.0, σ=1.0, β=1.6x10^{-5} and De=0.1, 1.0 and 5.0 291

6.15c Contour plots of axial velocity in the flow through a 4:1 contraction for N=4.0, σ=1.0, β=1.6x10^{-5} and De=0.1, 1.0 and 5.0 292

6.15d Contour plots of pressure in the flow through a 4:1 contraction for N=4.0, σ=1.0, β=1.6x10^{-5} and De=0.1, 1.0 and 5.0 293

6.15e Contour plots of S_{rr} in the flow through a 4:1 contraction for N=4.0, σ=1.0, β=1.6x10^{-5} and De=0.1, 1.0 and 5.0 294

6.15f Contour plots of S_{zz} in the flow through a 4:1 contraction for N=4.0,

σ=1.0, β=1.6x10^{-5} and De=0.1, 1.0 and 5.0 295

6.15g Contour plots of S_{rz} in the flow through a 4:1 contraction for N=4.0, σ=1.0, β=1.6x10^{-5} and De=0.1, 1.0 and 5.0 296

6.15h Contour plots of $De\tau_{rr}$ in the flow through a 4:1 contraction for N=4.0, σ=1.0, β=1.6x10^{-5} and De=0.1, 1.0 and 5.0 297

6.15i Contour plots of $De\tau_{zz}$ in the flow through a 4:1 contraction for N=4.0, σ=1.0, β=1.6x10^{-5} and De=0.1, 1.0 and 5.0 298

6.15j Contour plots of $De\tau_{\theta\theta}$ in the flow through a 4:1 contraction for N=4.0, σ=1.0, β=1.6x10^{-5} and De=0.1, 1.0 and 5.0 299

6.15k Contour plots of $De\tau_{rz}$ in the flow through a 4:1 contraction for N=4.0, σ=1.0, β=1.6x10^{-5} and De=0.1, 1.0 and 5.0 300

6.15l Contour plots of G_{rr} in the flow through a 4:1 contraction for N=4.0, σ=1.0, β=1.6x10^{-5} and De=0.1, 1.0 and 5.0 301

6.15m Contour plots of G_{zz} in the flow through a 4:1 contraction for N=4.0, σ=1.0, β=1.6x10^{-5} and De=0.1, 1.0 and 5.0 302

6.15n Contour plots of G_{rz} in the flow through a 4:1 contraction for N=4.0, σ=1.0, β=1.6x10^{-5} and De=0.1, 1.0 and 5.0 303

6.15o Contour plots of G_{zr} in the flow through a 4:1 contraction for N=4.0, σ=1.0, β=1.6x10^{-5} and De=0.1, 1.0 and 5.0 304

6.15p Effect of De on S in a 4:1 contraction for N=4.0, σ=1.0, β=1.6x10^{-5} and De=0.1, 1.0 and 5.0. S=0.683 is the equilibrium value for N=4.0 and S=1.0 corresponds to perfect order 305

6.15q Effect of De on χ in a 4:1 contraction for N=4.0, σ=1.0, β=1.6×10^{-5} and De=0.1, 1.0 and 5.0. χ=-20.1 degrees is the zero-shear-rate limit for N=4.0. For χ=0 the director is aligned with the die axis 306

6.16a Effect of contraction ratio on the radial variation in v_z at z=0, 30 and 40 for N=4.0, σ=1.0, β=1.6x10^{-5}, De=0.1, 1.0 and 5.0 and Λ=2 and 4. The fully developed Newtonian velocity profiles in the respective upstream tubes and the fully developed velocity profile in the downstream tube for a power-law model with an index n=1/3 are shown for comparison. For z=40 the 2:1 and 4:1 results are indistinguishable 307

6.16b Effect of contraction ratio on the radial variation in S at z=0, 30 and 40 for N=4.0, σ=1.0, β=1.6x10^{-5}, De=0.1, 1.0 and 5.0 and Λ=2 and 4. For z=40, the 2:1 and 4:1 results are indistinguishable 308

6.16c Effect of contraction ratio on the radial variation in χ' at z=0, 30 and 40 for N=4.0, σ=1.0, β=1.6x10^{-5}, De=0.1, 1.0 and 5.0 and Λ=2 and 4. χ is in degrees 309

6.16 Effect of contraction ratio on the centerline variation in (d) $\dot{\epsilon}$, (e) S, and (f) χ for N=4.0, σ=1.0, β=1.6x10^{-5}, De=0.1, 1.0 and 5.0 and Λ=2 and 4 310

6.17 Geometric difference between the 4:1 cubic and conical contractions ... 316

6.18 Effect of $\Re$ on the perturbation parameter $(x-x_0)/\Re = \sin\theta$ 317

6.19 Effect of $\Re$ and the number of terms in the perturbation expansion on the accuracy of y_1-y_{exact} and $y_1'-y_{exact}'$ 318

6.20 Variation in the pressure field along the 4:1 conical contraction boundary

with axial distance for N=4.0, σ=1.0, β=1.6x10^{-5}, De=5.0, $\Re$=10 and A=4 319

6.21a Contour plots of streamlines in the flow through a 4:1 conical contraction with rounded corners for N=4.0, σ=1.0, β=1.6x10^{-5} and De=0.1, 1.0 and 5.0 321

6.21b Contour plots of radial velocity in the flow through a 4:1 conical contraction with rounded corners for N=4.0, σ=1.0, β=1.6x10^{-5} and De=0.1, 1.0 and 5.0 322

6.21c Contour plots of axial velocity in the flow through a 4:1 conical contraction with rounded corners for N=4.0, σ=1.0, β=1.6x10^{-5} and De=0.1, 1.0 and 5.0 323

6.21d Contour plots of pressure in the flow through a 4:1 conical contraction with rounded corners for N=4.0, σ=1.0, β=1.6x10^{-5} and De=0.1, 1.0 and 5.0 324

6.21e Contour plots of S_{rr} in the flow through a 4:1 conical contraction with rounded corners for N=4.0, σ=1.0, β=1.6x10^{-5} and De=0.1, 1.0 and 5.0 . 325

6.21f Contour plots of S_{zz} in the flow through a 4:1 conical contraction with rounded corners for N=4.0, σ=1.0, β=1.6x10^{-5} and De=0.1, 1.0 and 5.0 . 326

6.21g Contour plots of S_{rz} in the flow through a 4:1 conical contraction with rounded corners for N=4.0, σ=1.0, β=1.6x10^{-5} and De=0.1, 1.0 and 5.0 . 327

6.21h Contour plots of Deτ_{rr} in the flow through a 4:1 conical contraction with rounded corners for N=4.0, σ=1.0, β=1.6x10^{-5} and De=0.1, 1.0 and 5.0 . 328

6.21i Contour plots of $De\tau_{zz}$ in the flow through a 4:1 conical contraction with rounded corners for N=4.0, σ=1.0, β=1.6x10^{-5} and De=0.1, 1.0 and 5.0 . 329

6.21j Contour plots of $De\tau_{\theta\theta}$ in the flow through a 4:1 conical contraction with rounded corners for N=4.0, σ=1.0, β=1.6x10^{-5} and De=0.1, 1.0 and 5.0 . 330

6.21k Contour plots of $De\tau_{rz}$ in the flow through a 4:1 conical contraction with rounded corners for N=4.0, σ=1.0, β=1.6x10^{-5} and De=0.1, 1.0 and 5.0 . 331

6.21l Contour plots of G_{rr} in the flow through a 4:1 conical contraction with rounded corners for N=4.0, σ=1.0, β=1.6x10^{-5} and De=0.1, 1.0 and 5.0 . 332

6.21m Contour plots of G_{zz} in the flow through a 4:1 conical contraction with rounded corners for N=4.0, σ=1.0, β=1.6x10^{-5} and De=0.1, 1.0 and 5.0 . 333

6.21n Contour plots of G_{rz} in the flow through a 4:1 conical contraction with rounded corners for N=4.0, σ=1.0, β=1.6x10^{-5} and De=0.1, 1.0 and 5.0 . 334

6.21o Contour plots of G_{zz} in the flow through a 4:1 conical contraction with rounded corners for N=4.0, σ=1.0, β=1.6x10^{-5} and De=0.1, 1.0 and 5.0 . 335

6.21p Effect of De on S in a 4:1 rounded corner contraction for N=4.0, σ=1.0, β=1.6x10^{-5} and De=0.1, 1.0 and 5.0. S=0.683 is the equilibrium value for N=4.0 and S=1.0 corresponds to perfect order 336

6.21q Effect of De on χ in a 4:1 rounded corner contraction for N=4.0, σ=1.0, β=1.6x10^{-5} and De=0.1, 1.0 and 5.0. χ=-20.1 degrees is the zero-shear-rate limit for N=4.0. For χ=0 the director is aligned with the die axis . . 337

6.22a Effect of contraction geometry on the axial velocity profiles at z=0, 30 and 40 for N=4.0, σ=1.0, β=1.6x10^{-5}, De=0.1, 1.0 and 5.0 and Λ=4. The fully

developed downstream exit velocity profile for a power-law model with the same shear thinning behavior as the viscosity for the liquid-crystal model is shown for comparison 338

6.22b Effect of contraction geometry on the degree of order profiles at z=0, 30 and 40 for N=4.0, σ=1.0, β=1.6x10^{-5}, De=0.1, 1.0 and 5.0 and Λ=4 ... 339

6.22c Effect of contraction geometry on the director orientation profiles at z=0, 30 and 40 for N=4.0, σ=1.0, β=1.6x10^{-5}, De=0.1, 1.0 and 5.0 and Λ=4 . 340

6.22 Effect of contraction geometry on the centerline variation in (d) $\dot{\varepsilon}$, (e) S, and (f) χ for N=4.0, σ=1.0, β=1.6x10^{-5}, De=0.1, 1.0 and 5.0 and Λ=4 .. 341

6.22g Effect of contraction geometry on the centerline response in the dimensionless normal stress difference for N=4.0, σ=1.0, β=1.6x10^{-5}, De=0.1, 1.0 and 5.0 and Λ=4 345

6.23 Variation in the dimensionless total pressure drop with De for N=4.0 and 7.0, σ=1.0, β=1.6x10^{-5}, and Λ=2 and 4 347

6.24 Variation in the Couette correction with De for N=4.0 and 7.0, σ=1.0, β=1.6x10^{-5}, and Λ=2 and 4 348

A.1 Planar die swell with the boundary conditions of interest to the local singularity analysis are shown. The free surface height h(x) and the free surface exit angle α are also indicated. The downstream fully developed velocity is V 376

A.2 Contours of (a) τ_{xx}, (b) τ_{yy} and (c) τ_{yx} for the planar die swell of a Newtonian fluid close to the singularity. Results are in the limit of zero

surface tension (reproduced from Apelian, 1987) 377

A.3 Contours of (a) pressure, (b) τ_{yx} and (c) τ_{xx} for the planar die swell of a UCM fluid close to the singularity. Results are shown for De=0.0 (Newtonian limit) and De=0.5. The finite element mesh and streamlines for De=0.5 are also shown (reproduced from Crochet and Keunings, 1980) 378

A.4 The effect of mesh refinement close to the singularity and De on the final swell ratio, h(x=∞), for the planar die swell of a MUCM fluid. The capillary number Ca=0.015 in these calculations. The smallest element size close to the singularity for meshes M4 and M5 are 0.01 and 0.005 respectively; mesh M6 has twice the discretization as mesh M5 in the x-direction close to the singularity (reproduced from Apelian, 1987) 380

A.5 The stick-slip problem with the boundary conditions of interest to the local singularity analysis are shown. The downstream fully developed velocity is V 386

B.1 Variation of (a) velocity ϕ, and (b) order parameter S with distance ζ down the threadline for N=4.0, σ=1.0, D_R=3.0 and De=10^{-1}, 10, 10^3, 10^5, 10^8 and 10^{12}. The initial condition for the microstructure is $S(0)=S_\epsilon$ and the time constant $\lambda=\lambda_0(1-S^2)^2$. Velocity profiles for De=10^{-1} and 10^{12} are indistinguishable 401

B.2 Variation of (a) the dimensionless final elongation rate $\dot{\epsilon}_L$ with De for σ=0.5 and σ=1.0, and (b) order parameter S with distance ζ down the

threadline for σ=0.5 and De=10^{-1}, 10, 10^3, 10^5, 10^8 and 10^{12}. The other model parameter values are N=4.0 and D_R=3.0. The initial condition for the microstructure is $S(0)=S_\epsilon$ and the time constant $\lambda=\lambda_0(1-S^2)^2$ 402

B.3 Variation of (a) velocity ϕ and (b) order parameter S with distance ζ down the threadline for N=1.0, σ=1.0, D_R=3.0 and De=10^{-1}, 10, 10^3, 10^5, 10^8 and 10^{12}. The initial condition for the microstructure is $S(0)=S_\epsilon$ and the time constant $\lambda=\lambda_0(1-S^2)^2$. Effect of N on (c) the variation of the dimensionless final elongation rate $\dot{\epsilon}_L$ with De is also illustrated 405

B.4 Variation of (a) velocity ϕ and (b) order parameter S with distance ζ down the threadline for N=4.0, σ=1.0, D_R=3.0 and De=10^{-1}, 1, 10 10^3, and 10^8. The initial condition for the microstructure is $S(0)=S_\epsilon$ and the time constant $\lambda=\lambda_0$. Variation of (c) the dimensionless final elongation rate $\dot{\epsilon}_L$ with De is also illustrated 406

B.5 Variation of (a) velocity ϕ and (b) order parameter S with distance ζ down the threadline for N=4.0, σ=1.0, D_R=3.0 and De=10^{-1}, 10^2, 10^3, 10^5 and 10^8. The initial condition for the microstructure is $S(0)=S_{eq}$ and the time constant $\lambda=\lambda_0(1-S^2)^2$ 407

B.6 Variation of (a) velocity ϕ and (b) order parameter S with distance ζ down the threadline for N=4.0, σ=1.0, D_R=3.0 and De=10^{-1}, 1, 10^2 and 10^8. The initial condition for the microstructure is $S(0)=S_{eq}$ and the time constant $\lambda=\lambda_0$ 409

B.7 Effect of draw ratio on the apparent elongational viscosity $\bar{\eta}_a$ for N=4.0,

σ=1.0 and the two different time constants (a) $\lambda=\lambda_0(1-S^2)^2$ and (b) $\lambda=\lambda_0$. The initial microstructural condition is $S(0)=S_\epsilon$. The true elongational viscosity $\bar{\eta}$ for the respective time constants are also shown for comparison 411

B.8 Effect of N, σ and $S(0)$ on (a) the apparent elongational viscosity $\bar{\eta}_a$ for $\lambda=\lambda_0(1-S^2)^2$. The effect of $S(0)$ on (b) the apparent elongational viscosity $\bar{\eta}_a$ for $\lambda=\lambda_0$ is also shown 412

B.9 Effect of draw ratio on the apparent elongational viscosity $\bar{\eta}_a$ for N=4.0, σ=1.0 and D_R=3.0, 5.0, 20.0 and 30.0. The initial microstructural condition and time constant are $S(0)=S_{eq}$ and $\lambda=\lambda_0(1-S^2)^2$ respectively .. 413

B.10 Comparison of model predictions with the data of Prilutski (1984) for a hydroxy propyl cellulose solution in acetic acid with N=2.3, D_R=7.89, η_s=0.012 Poise, De=7.84×10^{-3}, σ=0.87, $\lambda=\lambda_0(1-S^2)^2$ and $S(0)=S_\epsilon$ and S_{eq}: (a) velocity and (b) normal stress difference. The prediction obtained without including gravity and surface tension is shown for comparison with $S(0)=S_\epsilon$ 416

B.11 Comparison of model predictions with the data of Prilutski (1984) for a hydroxy propyl cellulose solution in acetic acid with N=2.3, D_R=7.89, η_s=0.012 Poise, De=7.84×10^{-3}, σ=0.87, $\lambda=\lambda_0$ and $S(0)=S_\epsilon$ and S_{eq}: (a) velocity and (b) normal stress difference. The prediction obtained without including gravity and surface tension is shown for comparison with $S(0)=S_\epsilon$ 417

B.12 Comparison of model predictions with the data of Prilutski (1984) for a hydroxy propyl cellulose solution in acetic acid with N=4.0, D_R=3.63, η_s=0.012 Poise, De=7.63×10^{-3}, σ=0.14, $\lambda=\lambda_0(1-S^2)^2$ and $S(0)=S_\varepsilon$: (a) velocity and (b) normal stress difference. The prediction obtained without including gravity and surface tension is shown for comparison 418

B.13 Variation of $D_{R,crit}$ with De for (a) N=1.0 and (b) N=4.0 and σ=1.0, $S(0)=S_\varepsilon$ and both choices of λ 421

B.14 Effect of (a) N and (b) σ on the variation of $D_{R,crit}$ with De. Results are shown for $\lambda=\lambda_0(1-S^2)^2$ and $S(0)=S_\varepsilon$ 422

B.15 Effect of initial condition $S(0)$ on the variation of $D_{R,crit}$ with De. Results are shown for N=4.0, σ=1.0 and $\lambda=\lambda_0(1-S^2)^2$ and λ_0 423

Chapter One

Introduction

1.1 Importance of Fiber Spinning of Liquid-crystalline polymers

The invention, development, and commercialization of fibers made by processing liquid-crystalline polymeric melts and solutions prepared from high-molecular weight organic compounds is of tremendous technological importance. Liquid-crystalline polymer solutions, such as PPD-T/sulfuric acid (Kevlar® is poly(p-phenylene terephthalamide)), phase separate due to the electrostatic and steric interactions that result from the rigidity of the polymer chain backbones at polymer concentrations as low as one to two percent by volume and form anisotropic phases with a high degree of molecular orientation even in the quiescent state. This orientational ordering is evidenced by the ability to exhibit birefringence under static conditions (Elliot and Ambrose, 1950; Meyer *et al.*, 1985). In polyaramid PPD-T (Fig. 1.1), for example, the π bonding electrons on either side of the planar phenylene rings and the conjugated double-bond character of the carbon-nitrogen and carbon-oxygen bonds lend structural rigidity to individual backbone moieties (Zero and Aharoni, 1987). During processing these molecules are aligned by the flow, yielding products with highly anisotropic properties.

The unique mechanical, electrical, chemical, and optical properties of liquid-crystalline polymers have been exploited industrially to produce specialty polymers

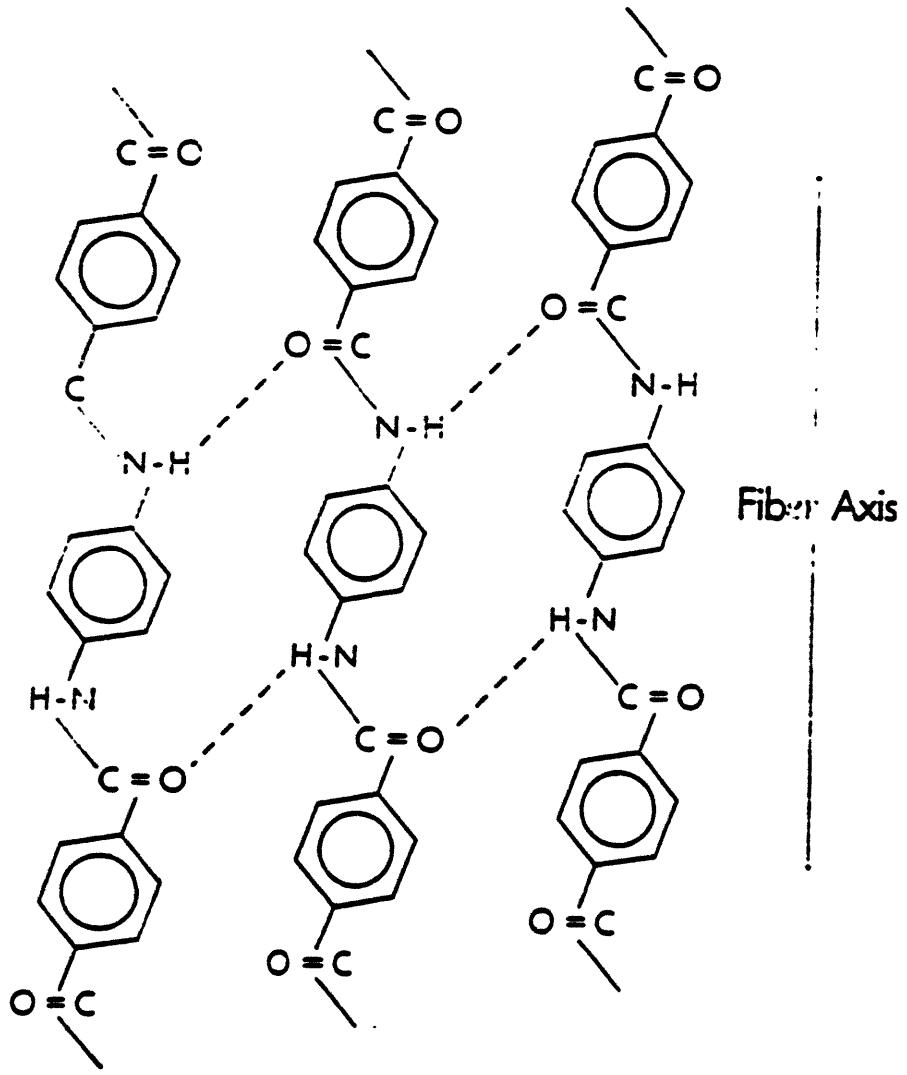

Figure 1.1: Structural backbone in PPD-T is illustrated. The long chain PPD-T molecules are oriented by the flow with the fiber axis.

(White and Fellers, 1978; Berry and Sroog, 1978; Cifferi and Ward, 1979; Samulski and Du Pre, 1979; Jenkins and Jenkins, 1983). Liquid-crystalline polymers such as Kevlar® have been used to make composites with ultra-high modulus and tensile strength and high strength-to-weight ratio which are exploited in a host of applications such as aircraft parts, satellites and automobiles, bullet proof vests, fiber optic and telecommunication cables and recreational equipment such as tennis racquets, skis and hulls of racing yachts. Kevlar® engineered short fibers offer excellent thermal stability, wear and chemical resistance, and non-abrasiveness which makes them ideally suited for friction products and gaskets; they are a key ingredient in brake and clutch linings and other industrial applications for an effective asbestos-free formulation. Other liquid-crystalline polymers besides Kevlar® manufactured commercially include para-linked aromatic polyamides, polyesters, polyazomethanes, polyacrylonitriles, polyphenylenebenzobisthiazoles for use in high performance aircraft (Samulski, 1985). Organic precursors to coke and manufactured graphite (petroleum and coal-tar pitches) when carbonized, undergo aromatic polymerization to yield large, flat, polynuclear aromatic molecules. As the molecular weight approaches 1500, usually near 450°C, the molecules condense to form a liquid-crystal which has been termed the carbanaceous mesophase or mesophase pitch. The mesophase pitch is of considerable technological importance in the spinning of high-modulus and high-strength carbon fibers. Besides the unique mechanical properties of interest in this thesis, liquid-crystalline polymers are also used in polymer dispersed films for light control applications and in optical information processing and display devices (Wissbrun, 1981).

The processing of highly anisotropic polymeric fluids is understandably very different from that of Newtonian or isotropic viscoelastic polymeric fluids. The development of the structural orientation of the polymeric molecules, the directions in which the molecules orient, the degree to which they orient, the interplay between the polymer rheology, fluid flow and development of order, and other processing parameters affect the final internal structure of the polymer product formed. Furthermore, the microstructure formed strongly affects the properties of the product. Figure 1.2 (reproduced from Yang, 1993) shows the strong dependence of the tensile moduli of an as-spun and a heat treated Kevlar® fiber on the molecular orientation angle with respect to the fiber axis determined from X-ray scattering measurements; the tensile moduli dependence is stronger for smaller orientation angles. Figure 1.2 also shows that the tensile modulus is slightly higher for the heat treated fiber. However, subsequent thermal treatment, for example by annealing (Rutledge, 1990) above 450°C, in order to produce a more favorable microstructure, *i.e.* an increase in the degree of crystallinity but not the molecular orientation itself, is expensive.

Therefore, in order to be able to predict and control the properties of the product, optimize product properties and minimize production costs, it is vitally important to understand the flow behavior of the anisotropic melts and solutions from which they are produced and the development of microstructure during processing. Since a high degree of molecular orientation is achieved during the fiber spinning process, a model that would relate the development of the microstructure in this flow to the macroscopic properties would be a very useful process design tool. The objective of this thesis, in short, is to

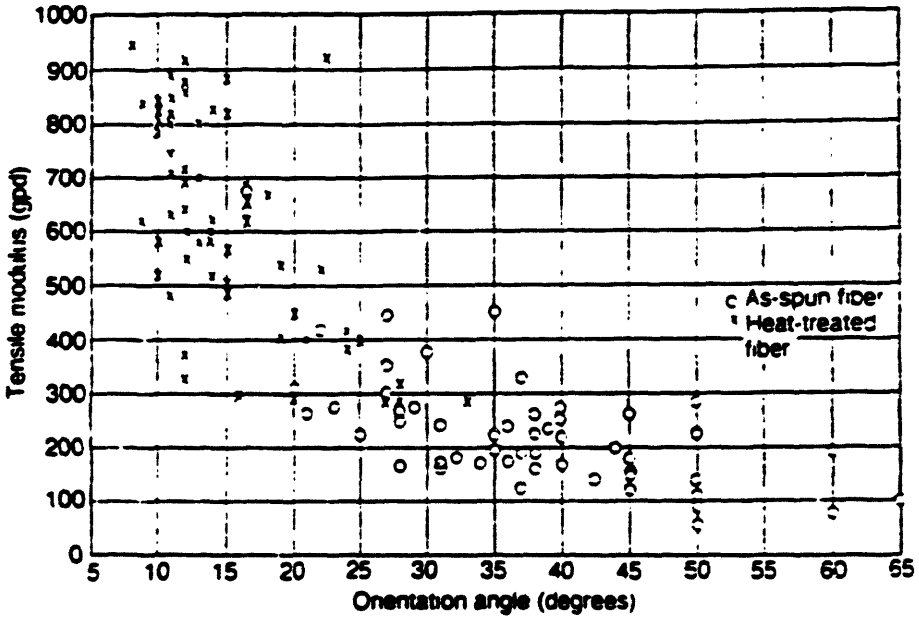

Figure 1.2: The tensile modulus of Kevlar® as a function of molecular orientation with respect to the fiber axis is illustrated for an as-spun fiber and a heat treated fiber. The modulus is in grams-per-denier which is roughly 1/8 of a Giga-Pascal (reproduced from Yang, 1993).

contribute to the development of such a process design tool. Figure 1.3 illustrates a typical global approach to process modeling. A constitutive equation that accurately predicts the experimental data in simple rheological flows is required before a realistic process model can be developed. Recognizing this aspect of the problem, the outline of this thesis is divided into two parts.

1.2 Outline of Thesis

Section 1.2 summarizes the work on developing appropriate constitutive models for liquid-crystalline polymers. Section 1.3 discusses issues related to developing a model for a complex flow such as the fiber spinning flow.

1.2.1 Constitutive Modeling of Liquid-Crystalline Polymers

Viscoelastic fluids in general exhibit nonlinear properties such as shear thinning and elasticity. Liquid-crystalline polymer melts and solutions, in addition to the above nonlinear properties, possess anisotropic properties which are associated with the microscopic structural order. A constitutive model that attempts to describe such systems must provide a detailed understanding of how the microstructure responds to the flow field and leads to anisotropic effects. In addition, it must be able to predict the equilibrium phase transitions observed in such systems.

The two most widely discussed models in literature are the Leslie, Ericksen and Parodi (LEP) model (1970, 1976, 1979) and the Doi model (1980). A discussion on the merits and failings of these models is presented in Chapter 3. A detailed description can

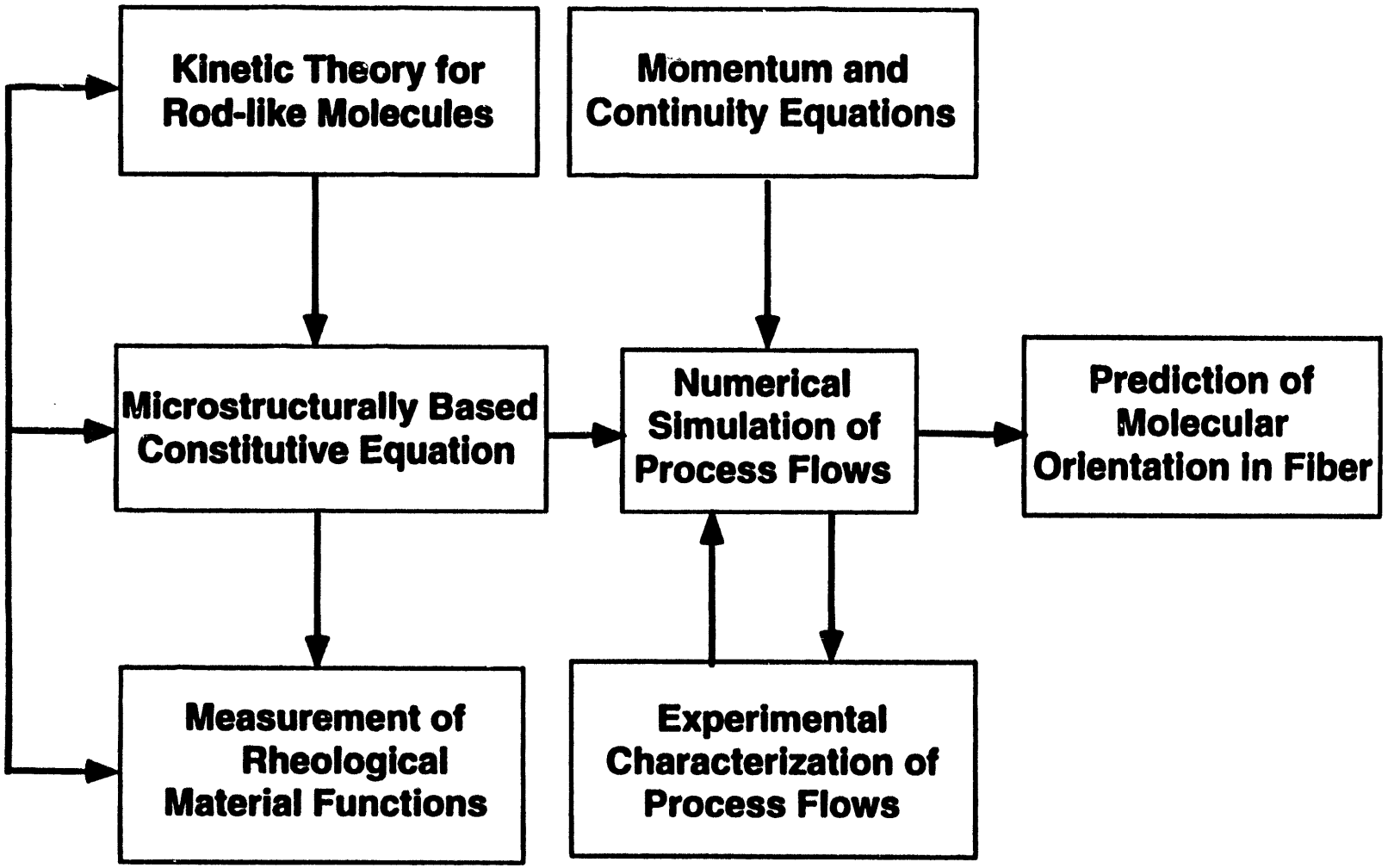

Fig. 1.3: Global approach to predict process induced microstructure.

be found in Menon (1990). A recent model due to Bhave *et al.* (1993) overcomes the serious shortcomings of the LEP and the Doi models. The Bhave *et al.* model is discussed in detail in Chapter 3. A brief discussion on the LEP, Doi and Bhave *et al.* model follows.

The LEP model is a continuum theory approach and extends Franks's (1958) theory of elasticity developed for liquid-crystals at rest to a dynamic situation to model polymeric liquid-crystals. The model provides no description of the presence of structural order at equilibrium and of phase transitions that take place in these solutions as the polymer concentration is increased. The model also does not predict nonlinear effects such as shear thinning in the viscosity. The molecular model due to Doi (1980) extends the Kirkwood and Auer (1951) diffusion equation for a dilute solution of rodlike molecules to the concentrated liquid-crystalline polymer solutions by using the reptation argument developed by Doi and Edwards (1978) to modify the rotational diffusivity and by introducing the Maier-Saupe (1958, 1959) approximation to Onsager's free energy expression for rod-rod interaction to account for intermolecular forces of interaction between the polymer molecules. The model is able to predict the concentration driven phase transition at equilibrium and also nonlinear effects such as shear thinning in the viscosity. However, the shear thinning predicted in the viscosity is aphysical due to the absence of a hydrodynamic contribution to the stress tensor.

The Bhave *et al.* (1993) model is also a molecular model developed from a kinetic theory framework. Similar to Doi's model, it incorporates the Maier-Saupe mean field potential to describe intermolecular forces of interaction between the polymer molecules.

The resulting evolution equation for the microstructure is similar to that obtained by Doi. Consequently, it predicts the same phase transition at equilibrium. However, the stress tensor includes hydrodynamic effects which leads to physically plausible shear thinning predictions in the viscosity. In fact, as demonstrated in Chapter 3, the model is able to predict shear thinning viscosity data accurately for a variety of liquid-crystalline polymer solutions. Hence, the Bhave *et al.* constitutive equation is chosen to develop a model for the fiber spinning process. The Bhave *et al.* model also has a shortcoming which is associated with the usage of a closure approximation. This aspect is discussed in brief in the following section and in detail in Chapters 3 and 4.

1.2.2 Modeling of the Fiber Spinning Process

Numerical simulations of liquid-crystalline polymer flows with realistic constitutive equations is very much a new field. Few simulations exist with realistic constitutive equations due to the nonlinear nature of the equations; abrupt changes in the molecular order close to the phase transition also increase the mathematical complexity of the equations. Hence, most of the simulations to date have been with the LEP model due to its relative mathematical simplicity. Menon (1990) provides a summary of the flow simulations that exist with the LEP model. Menon (1990) was the first to develop a finite element model using the Bhave *et al.* constitutive equation and a slightly modified version of the EVSS (Elastic-Viscous-Split-Stress) formulation, discussed in Chapter 5, for the flow between eccentric cylinders. Though a finite element method based on the EVSS formulation performs well under steady state conditions, Brown *et al.* (1993) demonstrate

that it can predict fictitious numerical instabilities in the linear stability of a planar Couette flow and they suggest a modified formulation, the EVSS-G formulation, that overcomes the problem. Hence, the finite element calculations in this thesis are with the EVSS-G formulation.

A schematic diagram of the fiber spinning process is shown in Fig. 1.4. Four primary regions can be identified in the fiber spinning flow: (1) the spinneret flow which involves the flow through a contraction, (2) die swell experienced by the polymer solution as it comes out of the spinneret, (3) fiber drawing which involves extensional stretching of the polymer solution and (4) solidification or coagulation where the solvent is extracted from the polymer solution and the microstructure is frozen in the resultant solid. The solidification issue is not addressed in this thesis.

Traditionally, in literature, fiber spinning is synonymous with the fiber drawing region. The fiber drawing region is also interchangeably addressed as the fiber spinning region in this thesis. A number of analyses of the fiber drawing flow with viscous and viscoelastic, but isotropic, constitutive equations exist in literature. An extensive account of the modeling efforts directed towards the fiber drawing region is provided in Chapter 2.

Kase and Matsuo (1965) followed by Matovich and Pearson (1969) were the first to derive one-dimensional fiber drawing equations for steady, axially symmetric, isothermal, viscous flows of Newtonian fluids. Most of the fiber drawing models to date use the slender body momentum equation derived by these authors. A number of steady state and linear stability analyses that predict draw resonance instabilities (periodic

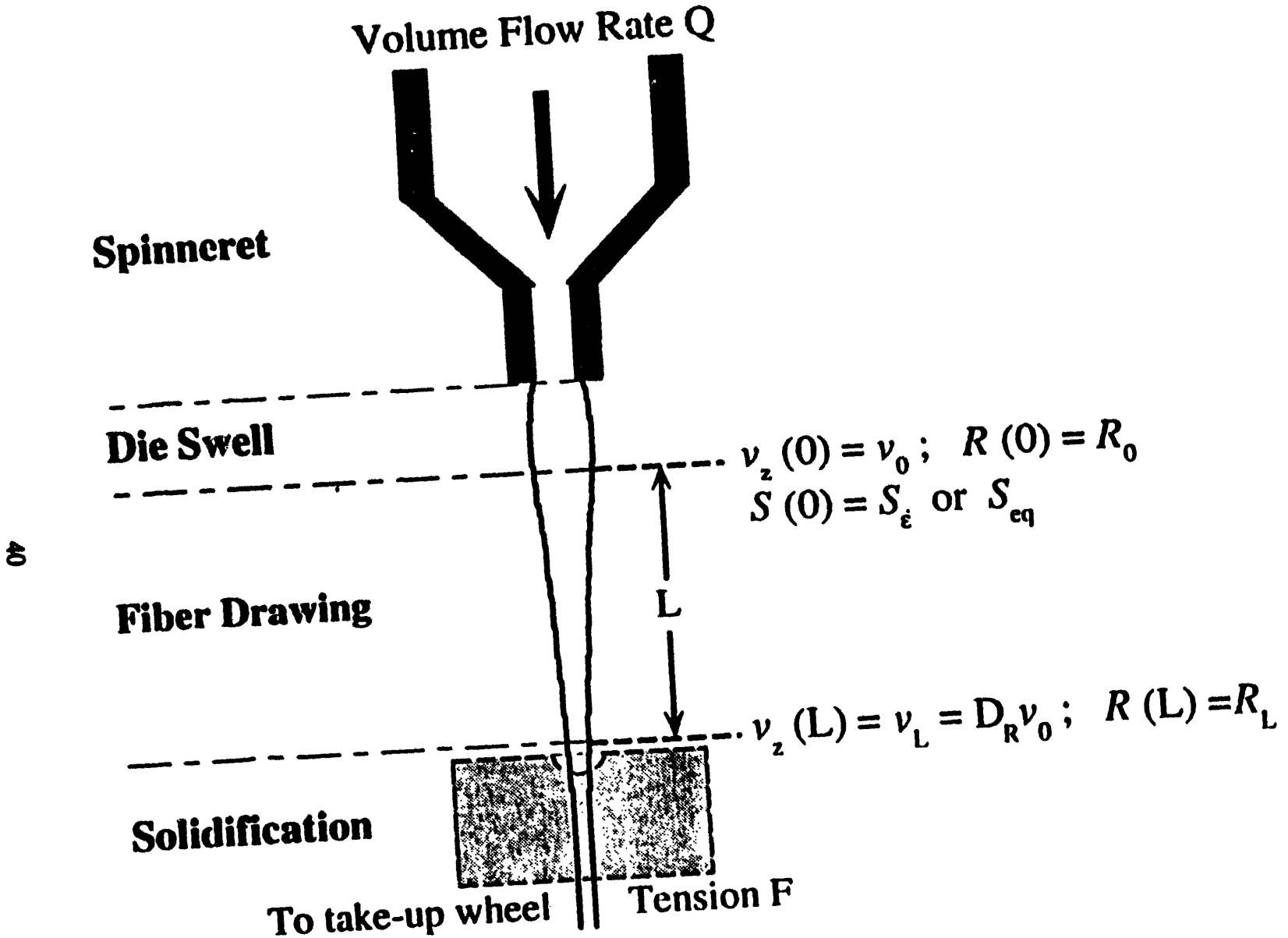

Figure 1.4: Schematic diagram of fiber spinning process. The spinneret, die swell, fiber drawing and solidification regions are indicated.

fluctuation in the take-up fiber cross-sectional area that occurs even at constant extrusion and take-up speeds) exist for viscous models. However, omission of fluid elasticity and memory are serious assumptions when modeling polymeric systems whose viscoelastic behavior is well established (Bird *et al.*, Vol. 1, 1987). Fisher and Denn (1976) were the first to develop a fiber drawing model with a viscoelastic constitutive equation. A key difference between the analysis with a viscoelastic model and a viscous model is the requirement of an initial stress specification at the inlet due to upstream memory effects. Since the initial stress is not known *a priori*, Fisher and Denn studied initial conditions ranging from a Newtonian limit to a purely elastic limit and found, surprisingly, that the development of the downstream velocity and stress profiles is insensitive to the choice of the initial stress condition. Equivalently, it is important to test the effect of different initial microstructural order on the development of downstream order in liquid-crystalline polymers; as already discussed in connection with Fig. 1.2, even a small change in the fiber orientation could lead to a large change in the tensile modulus. This issue is addressed in Chapter 4. Model predictions of the experimental data obtained by Prilutski (1984) for a 40 wt% hydroxy propyl cellulose in acetic acid solution and a linear stability analysis to predict the onset of draw resonance instabilities are also presented in Chapter 4.

A drawback with molecular models is the usage of a closure approximation to tackle complex flow problems, since solving the original diffusion equation for the molecular orientation distribution function is computationally very involved. Recent work by Larson and Ottinger (1991) shows that the original diffusion equation predicts

molecular tumbling at low-to-intermediate shear rates in the start-up of a simple shear flow, which, as demonstrated by Bhave *et al.* (1993), is not predicted with the closure approximation. A Legendre polynomial expansion technique commonly used in the solution of the diffusion equation in simple shear and extensional flows is extended to the fiber drawing flow to test the effect of the closure approximation. The results are discussed in Chapter 4. The expansion technique used in the fiber drawing analysis indicates a path for solving more complex flow problems with molecular models where approximations of uncertain validity must be used to obtain a closed-form constitutive equation.

The results discussed in Chapter 4 demonstrate the need to carry out two-dimensional finite element calculations going back into the spinneret to accurately predict the degree and homogenity of the initial orientation in the fiber drawing region. Development of stable and convergent finite element formulations for viscoelastic flow simulations has been the object of much study the last decade or so (King *et al.*, 1988; Rajagopalan *et al.*, 1990; Marchal and Crochet, 1987; for example). The equation set is of mixed type, *i.e.* elliptic momentum-continuity pair and hyperbolic constitutive equation (Joseph *et al.*, 1985 for the upper-convected Maxwell model; Joseph and Saut, 1986 for the Oldroyd-B model; Menon, 1990 for the liquid-crystal model), which requires mixed finite element formulations that respect the mathematical type of the equations. The merits and demerits of commonly used formulations such as the EEME and the EVSS formulation are discussed in detail in Chapter 5. A very recently developed formulation, the EVSS-G formulation, proves to be more robust than either the EEME or the EVSS

formulation (Brown *et al.*, 1993). Finite element results based on a slight variation of the EVSS-G formulation are presented in Chapter 6 for the liquid-crystalline polymer flow through the spinneret. The effect of Deborah number, polymer concentration, contraction ratio and die design on the development of molecular order and orientation is discussed in detail in Chapter 6. The implications of the spinneret calculations on processing and the regions of validity of the fiber drawing analysis in parameter space are also discussed in Chapter 6.

An integrated model for the spinneret and fiber drawing flows is required in order to fully optimize the spinneret and fiber drawing flows in creating a fiber with a high tensile modulus. Such an integrated model would have to include the die swell region as well. Apelian (1987), Crochet and Keunings (1982) and others have demonstrated numerical difficulties in die swell calculations of Newtonian and viscoelastic models which are associated with the die swell singularity; the die swell singularity arises from the singular behavior in the stress components at the die exit due to a sudden change in the boundary data from no slip along the die wall to shear free on the extrudate surface. The singular behavior at the die exit is not completely understood even for a Newtonian flow. Consequently, one of the aims of this thesis is to better understand the die swell singularity through analytical means which would aid in evaluating the numerical predictions close to the singularity; such an evaluation is essential in viscoelastic calculations due to the sensitivity of the final swell to the accuracy of the stress field close to the die exit (Apelian, 1987). An elaborate discussion of the regions of validity of the singularity analyses published in literature is presented in Appendix A. A

singularity analysis that is more general in scope than the analyses to date is also presented in Appendix A.

Chapter Two

Background on Fiber Spinning

Fiber spinning is a process in which a filament is extruded through a die, and drawn down in cross-sectional area by being taken up at a velocity greater than the extrusion velocity. A schematic diagram of the fiber spinning process was shown in Fig. 1.4. The filament is initially a melt or a solution; the point of solidification or coagulation is variable, and depends on the heat transfer or rate of solvent loss along the filament. The primary experimental variables are: the draw ratio, D_R, which is the ratio of the take-up velocity to extrusion velocity; the length of the draw zone, L; and the take-up or extrusion velocity, v_L.

There are at least two distinct instability phenomena of interest. Draw resonance is a long wavelength (of the order of the spinning length) periodic variation in take-up area, which sometimes occurs despite a constant extrusion rate and a constant take-up speed, persisting over a long period of time with well defined and unchanging period and amplitude. Another distinctly different instability is related to the problem of determining whether a liquid may be spun, or when a liquid filament will break, and is known as the problem of spinnability.

Tables 2.1 and 2.2 summarize the experimental and theoretical investigations that have been carried out in fiber spinning under isothermal and nonisothermal, steady state and draw resonance conditions.

		Inelastic		Viscoelastic	
		Newtonian	Power-law	No Shear thinning	Shear thinning
Steady State	Isothermal	Several workers e.g. Prilutski '84 - polybutene		Sridhar *et al.* '86 - Boger fluid; PIB in polybutene	Spearot & Metzner '72 - LDPE Zeichner '73 - HDPE, LDPE, polystyrene and polypropylene Tsou & Bogue '85 - polypropylenes
	Non-isothermal				
Draw Resonance	Isothermal	Weinberger *et al.* '75 - silicone oil Kase '74 - constant viscosity PET; $D_{R,crit}$=20	Han *et al.* '72 experiments with polypropylene with n=0.117. $D_{R,crit}$ could not be determined accurately		Ishihara & Kase '76 observed draw resonance at draw ratios of 48.6 and 50 for two shear thinning PET melts Chang & Denn '79 determined critical draw ratios for polyacrylamide in corn syrup Tsou & Bogue '85 determined critical draw ratios as a function of De for polypropylenes
	Non-isothermal	Kase '74 - PET			Ishihara & Kase '76 carried out experiments with PET in the unstable region

Table 2.1 Experimental investigations in fiber spinning

		Inelastic		Viscoelastic	
		Newtonian	Power-law	No Shear thinning	Shear thinning
Steady State	Isothermal	Matovich & Pearson '69	Shah & Pearson '72; Kase '85	Sridhar *et al.* '86 - Oldroyd B model. Good agreement with Sridhar *et al.* '86 data	Fisher & Denn '76 - White-Metzner model Phan-Thien '78 - PTT model. Reasonable agreement with data of Spearot & Metzner '72 and Zeichner '73
	Non-isothermal				Fisher & Denn '77 - Marrucci's '72 temperature dependent Maxwell model
Linear Stability	Isothermal	Matovich & Pearson '69; Gelder '71. $D_{R,crit}=20$	Shah & Pearson '72 - numerical Kase '85 - analytical $D_{R,crit} > 20$ for $n>1$ $D_{R,crit} < 20$ for $n<1$		Fisher & Denn '76 - White-Metzner model
	Non-isothermal	Shah & Pearson '72 Kase '74	Shah & Pearson '74		Fisher & Denn '77 - Marrucci's '72 temperature dependent Maxwell model. Qualitative prediction of Ishihara & Kase '76 data
Nonlinear Stability	Isothermal	Fisher & Denn '75; Ishihara & Kase '75	Ishihara & Kase '76		Fisher & Denn '76 - White-Metzner model. Reasonable agreement with Ishihara & Kase '76 data
	Non-isothermal				

Table 2.2 Theoretical investigations in fiber spinning

2.1 Experimental Observations

2.1.1 Draw Resonance

Draw Resonance is the name given to periodic fluctuations in the take-up area with constant extrusion and take-up speeds. The draw ratio when these fluctuations start to appear is known as the critical draw ratio, $D_{R,crit}$. The spinning process is usually stable for all draw ratios below $D_{R,crit}$. The draw resonance phenomenon seems to have been first described by Christensen (1962) in a discussion of extrusion coating with polypropylene. Three groups of experimenters have studied draw resonance under controlled conditions, where the spinning was carried out isothermally, followed by rapid quenching. Weinberger and co-workers (Donnelly and Weinberger, 1975; Cruz-Saenz et al, 1976), and Kase (1974) and Ishihara and Kase (1976) studied respectively, silicone oil and polyethylene terephthalate (PET), both of which have small relaxation times and viscosities which are nearly independent of deformation rate. The critical draw ratio $D_{R,crit}$ based on maximum diameter, is approximately 20 for silicone oil. The data of Kase (1974) is in the unstable region, but he too extrapolates to stability at a $D_{R,crit}$ slightly over 20. This value is relevant to the theoretical discussion to follow. The other polymers studied in isothermal spinning by these investigators and by Zeichner (1973); high density polyethylene (HDPE), low density polyethylene (LDPE), polypropylene are all shear thinning, though the LDPE and HDPE samples tested appear to be extension thickening and polypropylene appears to be extension thinning. In all cases $D_{R,crit}$ is less than 20, in some cases an order-of-magnitude less.

One series of isothermal experiments on two PET melts by Ishihara and Kase

(1976), deviates from the above description and provides an important check on theory. They spun at constant draw ratios of 48.6 and 50 over various lengths. They found that the magnitude of the ratio of maximum-to-minimum diameter in draw resonance, decreased with decreasing length of the melt zone. Draw resonance disappeared completely for one melt and nearly disappeared for the other at a spinning length of $5x10^{-3}$ m, the shortest distance which could be achieved experimentally. As regards constant viscosity PET, it can be concluded that draw resonance normally sets in at a draw ratio of 20, but there is an upper stable region at higher draw ratios for sufficiently short spinning lengths. A high draw ratio means that the same drawn filament diameter can be achieved with a larger spinneret diameter, hence, greater throughput and less pressure drop in the spinneret. Lamb (1967) also reports an upper stable region for polypropylene.

Chang and Denn (1979) carried out experiments with a 0.05 wt% polyacrylamide in corn syrup. The viscoelastic liquid has a nearly constant viscosity that is close to that of the Newtonian liquid (corn syrup). The spinline forces were observed to be one to two orders of magnitude greater than those in the Newtonian liquid. Filament breakup occured at a constant stress which was an order of magnitude greater than the breakup stress for the Newtonian solvent and three orders of magnitude greater than the shear modulus. A delay in the onset of draw resonance was observed for high throughputs, though the Deborah number De defined in Section 2.2.2 was in the same range for both low and high throughputs.

The effect of nonisothermal conditions on spinning cannot be completely defined

if the experiments are not carried out under controlled conditions. For long melt zones, where the Stanton number St (dimensionless heat transfer coefficient, proportional to length and inversely proportional to powers of flow rate and filament diameter) is high, Kase (1974) and Vassilatos (1975) find that, qualitatively, the draw resonance is damped with increasing length (increasing St). Lamb also observed stabilization (1967). Ishihara and Kase (1976) carried out well defined nonisothermal spinning experiments with PET. Reviews by Petrie and Denn (1976), Denn (1980), and White (1981) give extensive citation of experimental and theoretical literature on draw resonance.

2.1.2 Sensitivity and Spinnability

Sensitivity is more important than stability from a processing point of view. Sensitivity refers to the amplification of small input disturbances, resulting in a nonuniform product. Ziabicki (1976) shows data on product variations due to variations in cross-flow air. Sensitivity was first considered by Pearson and Matovich (1969). Denn (1980) cites more work in this area.

Spinnability refers to the ability to pull a melt out into a long thread. The practical limitation in commercial spinning is generally filament breakage, so that the prediction of spinnability is of considerable practical interest. It is usually not possible to draw either low or very high molecular weight melts into long filaments. Petrie and Denn (1976), and Ziabicki (1976) have given a good summary of the work in this area.

2.2 Theoretical investigations

A number of theoretical investigations (Kase & Matsuo, 1965; Kase, Matsuo & Yoshimoto, 1966; Matovich & Pearson, 1969; Pearson & Matovich, 1969; Shah & Pearson, 1972, 1974; Kase, 1974; Ishihara & Kase, 1975, 1976; Denn, Petrie, & Avenas, 1975; Fisher & Denn, 1976; Phan-Thien, 1978; Sridhar, Gupta, Boger, & Binnington, 1986) have been carried out to characterize the fiber spinning of isotropic polymers under isothermal, steady-state, and draw resonance conditions. In sections 2.2.1 and 2.2.2 the results from these investigations are discussed.

2.2.1 Inelastic flow modeling-viscous and power-law models

Kase and Matsuo (1965) were the first to formulate the melt spinning equations in the correct form. Matovich and Pearson (1969) also derived the one-dimensional fiber spinning equations for steady, axisymmetric, isothermal, viscous flows of Newtonian fluids by using a perturbation expansion with the slenderness ratio being the perturbation parameter. Most of the fiber spinning models to date use their version of the slender body momentum equation. Matovich and Pearson (1969) also derived fiber spinning equations for second order fluids which treat elastic effects as a perturbation of the Newtonian stress i.e. viscous forces are much more significant. They also discuss possible extensions to nonisothermal flows. A stability analysis of an isothermal Newtonian spinline was published first by Kase *et al.* (1966). Pearson and Matovich (1969) also studied the linear stability of the Newtonian model to infinitesimal disturbances. They obtain analytical results for the amplification factor in terms of the

frequency of the disturbance and the draw ratio for three sets of boundary conditions. They show that for certain draw ratios the lowest of which is 20.21, the small disturbance theory implies an infinite response to fluctuations in the input of a certain period. Gelder (1971), however, demonstrated by using an eigenvalue approach that the process is in fact unstable for all draw ratios greater than 20.21. The critical draw ratio of 20.21 is in good agreement with the isothermal spinning data for polysiloxane (Donnelly & Weinberger, 1975) and polyethylene terephthalate (PET) (Kase, 1974; Ishihara & Kase, 1975 also deduce the critical draw ratio of 20.21 for the Newtonian model) which have small relaxation times and viscosities that are nearly independent of deformation rate. Though Gelder derives this limit using a finite difference code, Pearson (1985) reports an analytical result that agrees well with the numerically determined critical draw ratio. We too obtained the same result by solving the set of differential equations analytically by decoupling them.

Shah and Pearson (1972) present a stability analysis for isothermal power-law fluids for the (i) purely viscous case, and (ii) the case of significant viscous and inertial forces. For the purely viscous case they have determined that the critical draw ratio $D_{R,crit}$ is > 20 for the power-law constant n >1, and <20 for n<1. In the presence of inertial and viscous forces they found that the critical draw ratio can be correlated to a quantity R_n=n-1+3·Re for n>1, where Re is the Reynolds number. For R_n>0.5 they obtain very high critical draw ratios. However, their computed effect of inertia is too large (Denn, 1980). Kase and Katsui (1985) have obtained analytical solutions to transients in melt spinning of isothermal power-law and Newtonian fluids by a transformation to

Lagrangian coordinates. Their results agree with the numerical results of Shah and Pearson (1972).

Shah and Pearson (1972) have also extended the stability results of Pearson and Matovich (1969) for Newtonian fluids to the non-isothermal case. They plot critical draw ratio $D_{R,crit}$ vs. $S = k \cdot St \cdot e^{-St}$, where St is the Stanton number (defined previously), and k is the dimensionless temperature viscosity coefficient defined by $\eta=\eta_a e^{-k\theta}$, where $\theta=(T-T_a)/(T_o-T_a)$ is the dimensionless temperature at any axial position along the filament. η_a is the viscosity at the ambient temperature T_a. T_o is the melt temperature at the point of exit from the spinneret. They show that for S>1.0, very large values of $D_{R,crit}$ are obtained. In a subsequent paper (Shah and Pearson (1972)) they present results for the general case where surface tension, gravity, and inertia are also important. When viscous and inertial forces alone are important they plot $D_{R,crit}^{1/2}$ *vs.* $S_r = kSte^{-St} + 4Ree^{ke^{-St}}$. For S_r>0.6 very large values of $D_{R,crit}$ are obtained. They also discuss stability of non-isothermal power-law fluids (Shah and Pearson, 1974). The relation between $D_{R,crit}$ and power-law index proves to be monotonic, whereas the effect of cooling seems to be far less important with shear thinning fluids than with Newtonian fluids. Kase (1974), who includes a term which allows the viscosity to become infinite when the temperature drops to the temperature of solidification, and Pearson et al. (1976) have solved the linear stability problem for an inelastic fluid which solidifies prior to take-up. They conclude that fiber spinning would be unconditionally stable provided solidification took place at a fixed temperature on the threadline and the solidified fiber was completely rigid.

$D_{R,crit}$ of 20 is in good agreement with isothermal spinning data for constant

viscosity melts as described above. The power-law results do not agree well with the data of Zeichner (1973) and Cruz-Saenz et al. (1976) for shear thinning melts. LDPE is extension thickening (n>1) so that $D_{R,crit} > 20$ predicted by theory does not agree with the data of Cruz-Saenz et al. For non-isothermal spinning, the prediction that flow is stabilized at high St is in qualitative agreement with experiments (Kase, 1974; Vassilatos, 1975; and Lamb, 1967). Solidification is shown to enhance stability greatly as indicated by experiments (Ziabicki and Kedzierska, 1960) which is consistent with theory. The power-law analyses do not include fluid elasticity, so that quantitative comparison is probably meaningless.

2.2.2 Viscoelastic Flow Modeling

As mentioned in section 2.2.1, most of the fiber spinning models to date use the slender body momentum equations derived by Matovich and Pearson (1969). Starting from the three-dimensional conservation laws and using the Oldroyd-B model, Bechtel *et al.* (1988) have derived approximate, one-dimensional equations for viscoelastic free jets; in doing so they use the classical velocity assumptions of von-Kármán and a slender-jet asymptotic scaling. Their model identifies the physical effects of gravity, inertia, viscoelasticity, and surface tension in terms of the slenderness ratio. They show by a reduction to axisymmetry and suppression to leading order of some of these effects that previous one-dimensional models do correspond to the lowest order equations in their asymptotic theory.

A linear stability analysis of spinning a viscoelastic liquid has been carried out by

Fisher and Denn (1976), following an earlier approximate analysis by Zeichner (1973), for a shear thinning generalization of the Maxwell fluid known as the White-Metzner model. The stress τ is related to the deformation gradient as follows:

$$\tau + \frac{\eta(\dot{\gamma})}{G}\tau_{(1)} = -\eta(\dot{\gamma})\gamma_{(1)} \tag{2.1}$$

where $\eta(\dot{\gamma}) = m\dot{\gamma}^{n-1}$ is the power-law viscosity and G is the constant shear modulus. $D_{R,crit}$ depends on "n" and the Deborah number defined as

$$De = \frac{\lambda_o v_o}{L} = \left(\frac{3^{\frac{n-1}{2}}}{G}\right)\left(\frac{v_o}{L}\right)^n \tag{2.2}$$

where v_o is the velocity at the maximum die swell and L is the length of the melt zone. The result for the stability analysis is shown in Fig. 2.1. For De→0, the results of Shah and Pearson are recovered. For $D_R De^{1/n} \sim 0.1$, where D_R is the $D_{R,crit}$ computed for an inelastic liquid, the critical draw ratio begins to increase, indicating a stabilizing effect of elasticity, and shortly thereafter the stability envelope turns on itself, indicating a region of stability at high draw ratios.

The results are in good agreement with the isothermal data of Zeichner (1973) on polystyrene, and Ishihara and Kase (1976) on PET, including a quantitative prediction of the value of L for which stabilization was achieved at a draw ratio of 50 in the latter experiments. The stabilization by decreasing L, corresponds to approaching the neutral stability curve at a fixed D_R by increasing De. However, the mean relaxation time (η/G), which for the nearly shear-rate-independent-viscosity PET is determined by setting n = 1, required to match experimental velocity profiles and force measurements, is consistently 2-4 times those measured in shear flow (Denn et al. 1975, Fisher and Denn

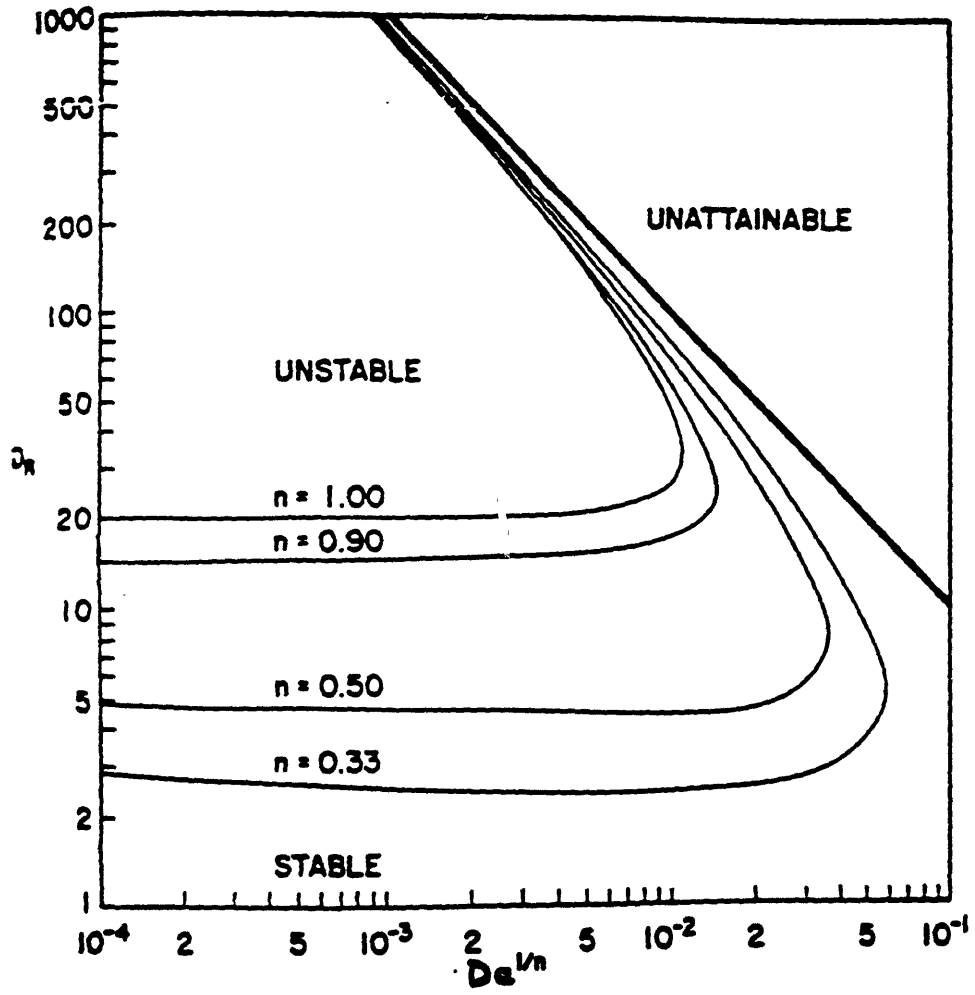

Figure 2.1: Critical draw ratio as a function of De for the White-Metzner model. n is the power-law viscosity index (reproduced from Fisher and Denn, 1976).

1977, Chang and Denn 1979). This is a consequence of multiple relaxation times resulting in strain hardening (Denn, 1980). Since extensional flow is stronger than shear flow longer relaxation times are more important as more molecular stretching occurs for the same deformation gradient, leading to more rapid diameter attenuation and higher forces than would be predicted for a fluid with the same mean properties but a single relaxation time (Denn and Marrucci, 1977).

Phan-Thien (1978) used the Phan-Thien and Tanner (PTT) model (derived from the Lodge-Yamomoto type of network theory) with multiple relaxation times and rheological properties measured in shear flow, to predict the behavior in a continuous drawing experiment. The comparisons with the polystyrene data of Zeichner (1973) and polyethylene data of Spearot and Metzner (1972) are good.

There have been two nonlinear analyses of the stability of isothermal spinning. Ishihara and Kase (1975, 1976) solved the transient nonlinear equations for Newtonian and inelastic power-law liquids by direct numerical simulation, whereas Fisher and Denn (1976) used the methods of nonlinear stability theory they described earlier for a Newtonian model (Fisher and Denn (1975)). The calculations of Fisher and Denn (1976) show that the system is stable to finite disturbances below the critical draw ratio computed from linear theory, and that for higher draw ratios there will be sustained oscillations with a period and amplitude close to that observed experimentally in draw resonance. The stable region at high draw ratios for the viscoelastic liquid is also stable to finite amplitude disturbances, and the calculations of diameter oscillations by Fisher and Denn (1975,1976) near this upper region are in reasonable agreement with the

diameter variations measured by Ishihara and Kase (1976). The isothermal spinning data of Chang and Denn (1979) are in accordance with the stability predictions of the Maxwell model with a single relaxation time and deformation rate dependant shear modulus at slow throughputs, but a delay in the onset of draw resonance at higher throughputs and the same range in De cannot be predicted possibly because the longer relaxation times become more important leading to greater elastic effects and consequently a higher critical draw ratio.

Fisher and Denn (1977) extend their analyses to include the effect of heat transfer between filament and surroundings. The analysis is restricted to a Maxwell model with a single relaxation time and deformation rate independent viscosity and modulus. The model appropriate for nonisothermal conditions is given by Marrucci (1972). The effect of cooling is to increase the initial rate of diameter attenuation of the viscoelastic filament. Cooling inhibits draw resonance, and the interaction of cooling and viscoelasticity results in a stabilization at high St which cannot exist for an inelastic liquid. Short spinlines (high De) will be stabilized by elasticity and long spinlines (high St) by cooling. General features of draw resonance data for PET (Ishihara and Kase, 1976) in the form of intensity of diameter fluctuations as a function of length of the melt zone are predicted by a linear stability analysis of the nonisothermal equations.

Denn et al. (1980) have studied profile development near the spinneret for low speed isothermal spinning of a Newtonian fluid using a finite element code developed by Nickell et al. (1974) to determine the validity of the thin filament approximation developed by Matovich and Pearson (1969). They find that the thin filament equations

used in most analyses, is valid within one spinneret diameter. The approach to the asymptotic uniform velocity profile is the same for all cases (gravity drawn free-jet, drawn jet with gravity, drawn jet without gravity, surface tension included), regardless of the magnitude of the imposed drawing force, or Froude number (Fr), or the ratio Re/Fr. They find that the magnitude of extrudate swell decreases with increasing force at the spinneret, and disappears for a sufficiently large force. Also free extrudate swell provides a reasonable estimate of the initial behavior only when the drawing force is very small relative to the product of the spinneret area and shear stress. Thus they conclude that spinneret conditions can be taken as initial conditions for the asymptotic equations with little error for a long spinline and are preferrable to free extrudate swell correlations. However their studies were performed under conditions not observed in commercial practice, and hence the validity of using spinneret conditions as initial conditions is open to question.

Keunings *et al.* (1983) have also carried out profile development simulations for Maxwell, PTT, and Oldroyd-B fluids. They reach spinline force levels where viscoelastic effects are significant. They find that thin filament equations are valid within two spinneret diameters, but downstream of the point of maximum extrudate swell which occurs within a spinneret diameter. They demonstrate that the use of the spinneret area and velocity as initial conditions for the thin filament equations is adequate and conclude that the uncertainty about the location of the origin of the thin filament equations will not be important in long spinlines. Also important in the solution of the thin filament equations derived using viscoelastic constitutive equations are the initial conditions on the

axial and transverse stress components, τ_{zz} and τ_{rr}. However, the initial conditions on τ_{zz} and τ_{rr} are related, and once an initial condition is specified on τ_{rr}, the initial condition on τ_{zz} can be determined from the thin filament momentum equation. The calculations of Keunings *et al.* (1983) support the practice of taking the transverse stress τ_{rr} to be zero for integration of the thin filament equations.

The isothermal spinning flow of isotropic polymeric liquids thus appears well understood. As discussed in Chapter 1, the anisotropic liquid-crystalline fibers such as Kevlar® are also of significant technological importance. The liquid-crystalline fibers possess unique tensile properties that derive from the high degree of molecular orientation with the fiber axis during the spinning process. However, the only investigation that has appeared in the literature on the fiber spinning of anisotropic liquid-crystalline polymeric solutions is due to Prilutski and Metzner (1986); as will be discussed in Chapter 3, these experimental results for a 40 wt % solution of hydroxy propyl cellulose in acetic acid are inadequate since they are limited to very small extension rates and they do not attempt to determine the molecular orientation during the fiber spinning process which is of considerable importance. Thus, no investigation, experimental or theoretical, has appeared in the literature that has attempted to characterize the molecular orientation dynamics during the spinning process. As already discussed in Chapter 1, the aim of this thesis is to develop a model for the fiber spinning process that would predict the evolution of the molecular orientation during the spinning process and study the effect of various process and design parameters on the molecular orientation dynamics.

Chapter Three

Liquid-Crystal Flow Modeling

Liquid-crystals are materials which possess properties of both liquids and crystals (de Gennes, 1974). In liquids, the centers of gravity of the molecules have no long range order. In crystals, the centers of gravity of the molecules are located on a three-dimensional lattice. Liquid-crystals are ordered liquids. They possess either oriented molecules or a regular spacing between two-dimensional liquid layers. Molecules which can be oriented to form liquid-crystals are generally either long rods or flat disks. Schematic diagrams of liquid-crystals formed from rods and disks are shown in Fig. 3.1.

Liquid-crystals are usually lyotropic or thermotropic (de Gennes, 1974). Lyotropic liquid-crystals are formed from a solution of rigid rods dissolved in a non-mesogenic solvent (Wissbrun, 1981). A lyotropic liquid-crystalline phase can be formed from an isotropic solution of rods by increasing the concentration of rods. Thermotropic liquid-crystals are formed from small, pure organic molecules such as PAA (p-azoxyanisole). Phase transitions in such systems are most naturally induced by a change in temperature. Depending on the type of symmetry in the order these liquid-crystalline phases are classified as nematic, cholesteric or smectic (Freidel, 1922). A brief description of the primary features of these phases follows. A detailed description is provided by de Gennes (1974).

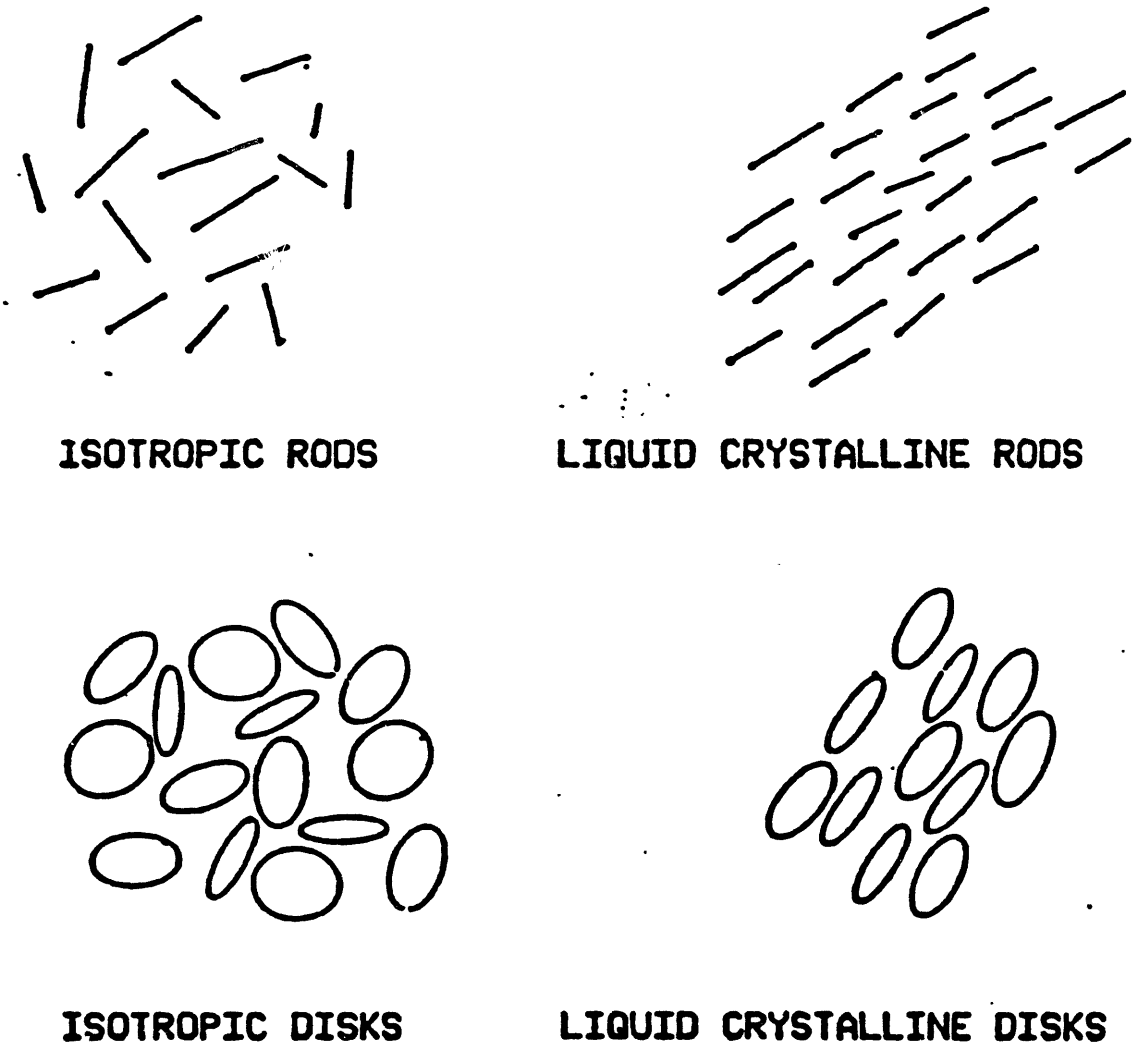

Figure 3.1: Schematic diagram of isotropic and liquid-crystalline rods and disks.

Nematic phases

Liquid-crystalline polymers most commonly form nematic phases. Lyotropic liquid-crystalline polymers processed commercially are almost exclusively nematic. In these phases the molecules possess long-range orientational order, but there is no long-range positional order (Fig. 3.2a). The preferred direction of orientation is commonly referred to as the "nematic director". The molecules are not all oriented along the director but are distributed at angles with respect to the director orientation. The degree of order for nematic liquid-crystals has been traditionally characterized by a scalar order parameter S, defined as

$$S = \frac{1}{2}(3\langle\cos^2\theta\rangle - 1) \tag{3.1}$$

where θ is defined as the angle between the molecular axis and the director, and <> denotes an average with respect to the orientation distribution function (Hermans and Platzek, 1939; Born and Green, 1949). S can take on values in the range $-0.5 \leq S \leq 1$. S=0 corresponds to a state of random, isotropic order; and S=1 to perfect orientational order with the molecular axes aligned parallel to the director vector. Maier and Saupe (1958) derived an approximation to the mean field intermolecular potential for rod-rod interaction obtained by Onsager (1949), that predicts a first-order phase transition with concentration from an isotropic to a nematic state for rod-like molecules. McMillan (1971) used a modified form of this potential to model the corresponding phase transitions for disc-like molecules.

Cholesteric phases

Cholesteric phases, in addition to the long range orientational order present in nematics,

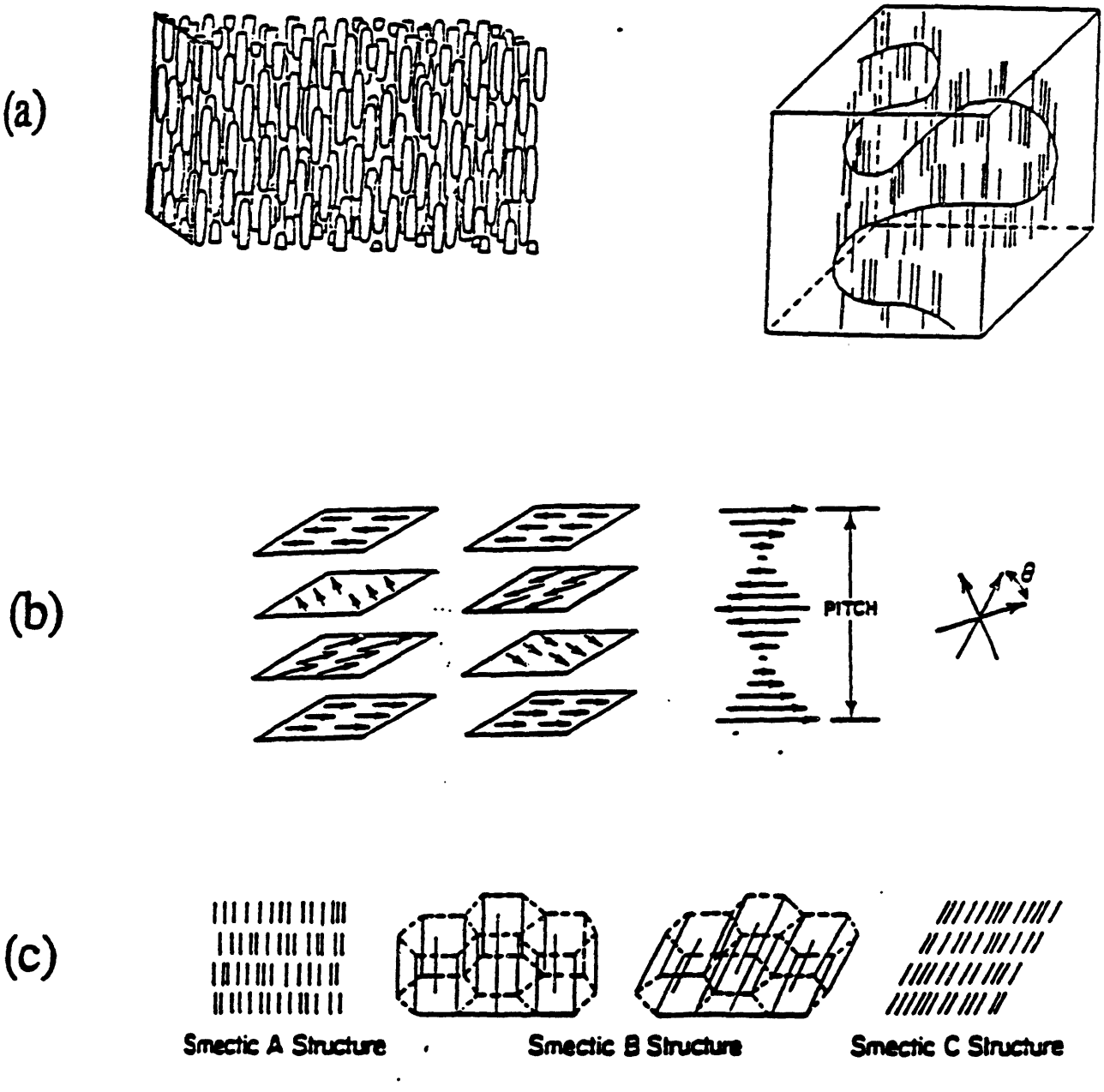

Figure 3.2: Classification of liquid-crystalline phases based on structural order; (a) Nematic, (b) Cholesteric and (c) Smectic.

possess a director that varies helically in space along an axis perpendicular to the plane of the director (Fig. 3.2b). They are also addressed as helical phases or chiral nematics. Polymers with flexible backbones and rigid side-chains like DNA and polypeptides tend to form cholesteric liquid-crystals. The helical pitch is often comparable to the wavelength of light and this results in the materials being highly colored. This property is exploited in watch display devices. The helical pitch is very sensitive to temperature changes which is used in accurate temperature detection.

Smectic phases

Smectic phases possess long range orientational and positional order. The molecules are arranged in well defined layers with long range orientational order in each layer and long range positional order in the dimension perpendicular to the layer plane (Fig. 3.2c). Therefore, like crystalline solids, smectic phases have X-ray patterns showing sharp Bragg diffraction lines. When the organic precursors to coke and manufactured graphite (petroleum and coal-tar pitches) are carbonized, carbonaceous mesophases composed of disc-like molecules are formed that tend to be either nematic or smectic.

3.1 Experimental observations

The majority of the rheological work with polymeric liquid-crystals (PLCs) has been in simple shear flow. Prilutski (1984) cites a number of references in this area. More recent work in simple shear and oscillatory flows of lyotropic liquid-crystals are due to Doraiswamy and Metzner (1986), Suto *et al.* (1989), Grizzuti *et al.* (1990), Picken *et al.* (1990) and Moldenaers *et al.* (1991). However, extensional flows dominate the flow field

used for fiber formation. Prior to Prilutski, the only extensional flow data which gave stretch rate as a function of location on the spinline are those of Onogi et al. (1980) for the hydroxy propyl cellulose (HPC)/water system. They report that the material deforms uniformly until about halfway down the spinline, at which point it stops stretching and maintains a constant velocity. Later it became known that with the concentration and solvent they used, HPC has an yield stress (Prilutski, 1984). A material with a yield stress will exhibit draw resonance at low stretch rates. So, their data cannot be used for comparative purposes.

Prilutski carried out his experiments with an HPC/acetic acid system which forms a mesophase at 30 wt% HPC. Prilutski performed his fiber spinning experiments at two concentrations, 23 wt% (isotropic phase) and 40 wt% HPC (anisotropic phase). Several runs were carried out at different draw ratios and flow rates, and velocity and axial stress profiles were generated. Gravity spinning experiments were also performed to test the importance of gravity in extensional flow. Metzner and Prilutski (1986) have reported the axial stress data as a function of the elongation rate for the 40 wt.% HPC solution in their paper on rheological properties of polymeric liquid-crystals.

A schematic diagram of the fiber spinning apparatus is reproduced from Prilutski's thesis in Fig. 3.3. The torsion bar is connected to a force measurement equipment which registers the force resulting from the torque exerted by the stretching filament. Once the force exerted by the polymer solution at the spinneret is known, the axial stresses in the stretching filament are determined as a function of axial position by solving the thin filament momentum equation, Eq. 4.21 presented in Chapter 4. A displacement or

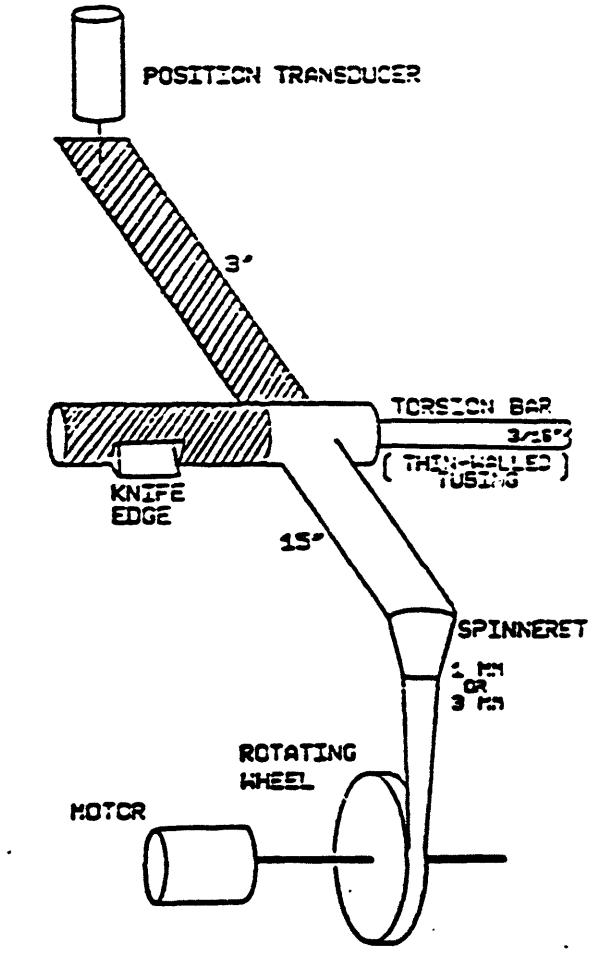

Figure 3.3: A schematic diagram of the fiber spinning apparatus used by Prilutski (reproduced from Prilutski, 1984).

position transducer is used for calibrating the alignment of the torsion bar with the knife edge. Without proper alignment the spinneret could support forces of 10 dynes without appreciable movement. The knife edge also supports a thin walled tubing through which the liquid-crystal polymer solution flows from a reservoir into the spinneret via a spinneret tube that is connected at right angles to the torsion bar. A detailed description of the materials of construction and the operating procedure is provided by Prilutski (1984). All experiments were performed at low flow rates to minimize the pressure offset resulting from spinneret tubing distortions, which causes an offset of the force reading at the spinneret resulting in erroneous computed values of the axial stresses in the filament. The pressure offset problem is really serious for high viscosity fluids. More recent work by Khagram et al. (1985) suggests that fiber spinning can be carried out at much higher flow rates by replacing the take-up wheel with capillary suction. But the aqueous xanthum gum used in their spinning experiments has a very low viscosity for which case tubing distortions are minimal. The capillary suction device is most useful only for fluids that do not adhere to the take-up wheel.

For the small flow rates used by Prilutski, the velocity profiles match the Newtonian behavior closely. To make meaningful comparisons with the commercial production of PLCs, spinning data at high flow rates are required. Prilutski also observed draw resonance at three different final stretch rates and reported the values for the corresponding critical draw ratios.

3.2 Liquid-Crystal Constitutive Equations

As mentioned in Chapter 1, the constitutive equations most widely discussed and used for liquid-crystalline polymers are due to Leslie-Ericksen-Parodi and Doi. These models are discussed in Section 3.2.1. Due to the serious limitations of these models discussed in detail by Menon (1990), a better constitutive equation is necessary. The Bhave *et al.* (1993) constitutive equation overcomes these limitations and is discussed in Section 3.2.2.

3.2.1 Leslie-Ericksen-Parodi and Doi constitutive equations

Of the models for PLCs that have appeared in literature, the two most widely discussed models are due to Leslie-Ericksen-Parodi (1970,1976,1979) and Doi (1980,1981). The Leslie-Ericksen-Parodi (LEP) model is a continuum theory approach and extends Frank's (1958) theory of elasticity developed for liquid-crystals at rest to a dynamic situation to model PLCs. The model provides no description of the presence of structural order at equilibrium and of phase transitions that take place in these solutions as the concentration of polymer is increased. The model cannot distinguish between weak and strong velocity gradients. Any gradient is sufficient to perfectly orient the molecules along the director vector. As a result, the viscosity and elongational viscosity are deformation rate independent. Consequently, it cannot describe the non-linear effects like shear-thinning observed in PLCs (Wissbrun, 1981) at high deformation rates. Also the phenomenologically derived expression for the extra stress tensor involves five adjustable parameters which are difficult to determine experimentally.

Doi developed a molecular model for liquid-crystalline polymer solutions (1980)

by generalizing the Doi-Edwards theory for a semi-concentrated solution of rigid rod-like polymer molecules (1978). He develops a conservation equation for the orientational distribution function starting from the theory of Kirkwood and Auer (1951) and using the Maier-Saupe approximation (1958, 1959) to Onsager's expression for free-energy (1949) of a solution containing rod-like polymeric molecules to describe the intermolecular interaction between the rod-like molecules. Doi also develops an expression for the stress tensor from Onsager's expression for the free-energy of a solution of rod-like molecules. The derivation assumes that Onsager's expression for the equilibrium free-energy can be used to describe non-equilibrium states. Unlike the Leslie-Ericksen-Parodi theory, the model provides a description of the phase transitions that occur as the concentration of polymer is increased, and also predicts non-linear effects such as shear-thinning at high deformation rates. But an asymptotic analysis in the high shear rate limit yields a power-law index of -8/7 in the viscosity which predicts an aphysical shear stress maximum. The main flaw in the model is that it does not account for the effects of hydrodynamic drag in the stress tensor expression. For a more elaborate discussion of the limitations of this model refer to Menon (1990) or Bhave (1992).

3.2.2 Bhave *et al.* constitutive equation

This model is developed for a solution of rigid rod-like macromolecules by using the principles of non-equilibrium statistical mechanics. The polymer solution is modeled as a collection of rigid dumbbells, each of length L, suspended in a Newtonian solvent. This model accounts for the ability of polymer molecules to orient in flow fields and ignores

the less important stretching and bending motions which are of minor importance in determining the rheological properties of such solutions. A pictorial representation of the dumbbell, with the notation used to locate it in physical space is shown in Fig. 3.4. Each dumbbell consists of two equal mass beads connected by a massless rod. It is assumed that the interaction with the solvent takes place only at the beads. The two beads are denoted by $\nu = +1$ and -1. The position vector of the bead ν with respect to an arbitrary origin is $\mathbf{r}_\nu$, and $\mathbf{r}_c$ is the position vector of the center of mass of the dumbbell. The unit vector along the axis of the dumbbell is $\mathbf{u}$ which gives the orientation of the rod-like molecule. The coordinates of a dumbbell can be completely specified by $\mathbf{u}$ or the polar angles θ and ϕ since the length of the dumbbell is fixed.

The distribution function for the dumbbells in configuration space is given by $f(\mathbf{u},t)$ and $f(\mathbf{u},t)d\mathbf{u}$ is the fraction of dumbbells in the orientation range $\mathbf{u}$ to $\mathbf{u}+d\mathbf{u}$ where $d\mathbf{u}=\sin\theta d\theta d\phi$. To compare with any macroscopic experimental response an average value for the corresponding physical quantity must be obtained. If the property B depends only on the configuration coordinates the average value is given by

$$\langle B \rangle = \int B(u)\, f(u,t)\, du \tag{3.2}$$

S is an average property called the orientational order tensor or structure tensor, which is defined as follows:

$$S(t) = \left\langle uu - \frac{\delta}{3} \right\rangle = \int \left(uu - \frac{\delta}{3}\right) f(u,t)\, du \tag{3.3}$$

The nematic director is given by the eigenvector corresponding to the dominant eigenvalue of the structure tensor and the degree of order is given by the invariant of the

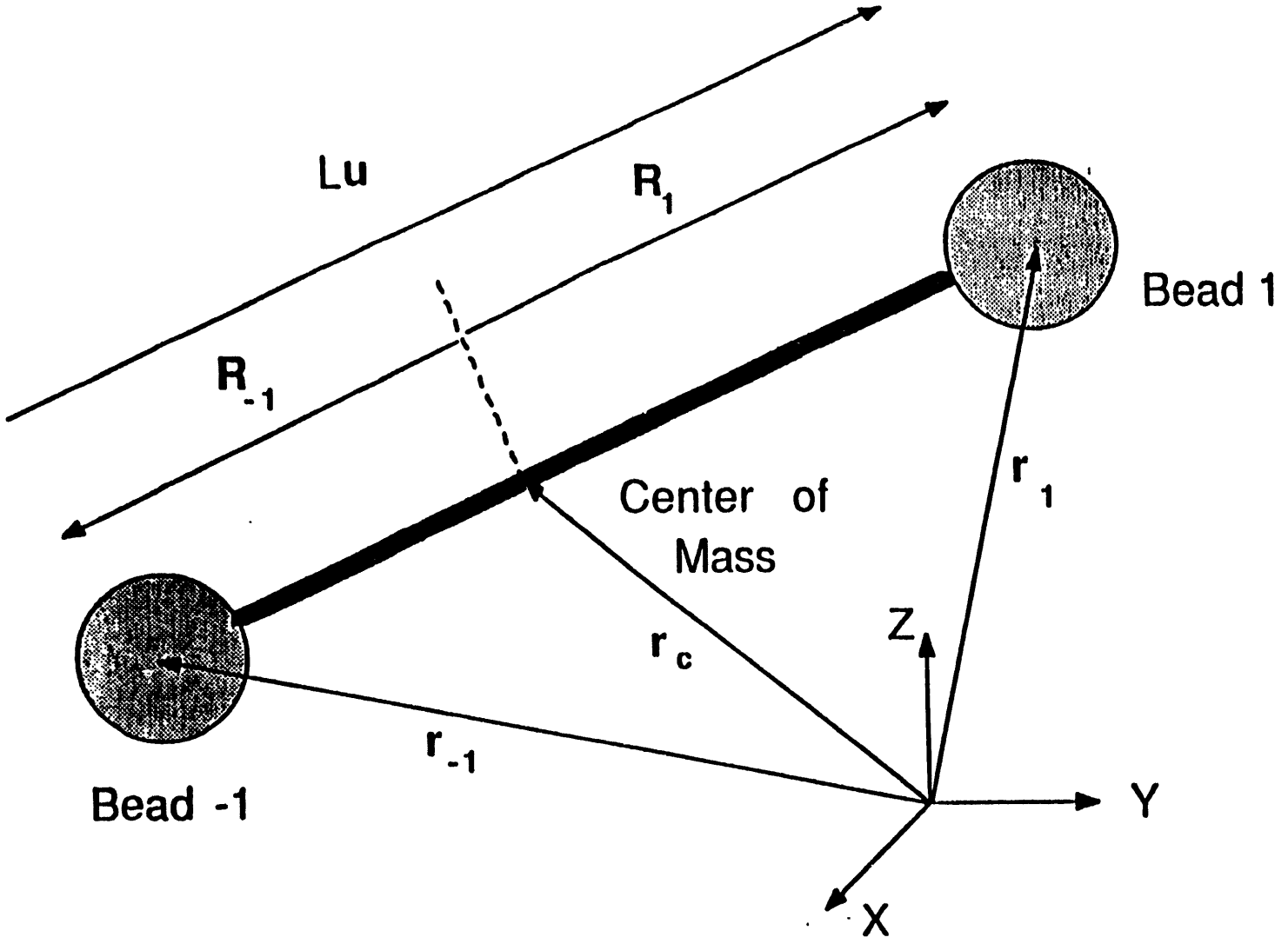

Figure 3.4: Rigid dumbbell model of a liquid-crystalline polymer molecule.

structure tensor $S = [(3/2)S:S]^{1/2}$. S takes on values between -1/2 and 1. A state of random order corresponds to S=0 and perfect order to S=1; S=-1/2 corresponds to random orientation in a plane perpendicular to the director.

The kinetic theory for the development of the constitutive equation involves two main parts: (i) derivation of an equation for the distribution function which determines the distribution of dumbbells in orientation space for a non-equilibrium situation and, (ii) derivation of a stress tensor expression which takes into account the various mechanisms by which the system of forces (Brownian, hydrodynamic, and polymer-polymer intermolecular interaction forces) shown in Fig. 3.5 are transmitted through the fluid. The physical meaning behind the forces considered relevant and the mathematical expressions used to account for them is described briefly in the ensuing paragraphs.

The thermal fluctuations in the solution cause the dumbbells to be bombarded constantly and jostled about in an irregular manner by the solvent molecules. The randomizing force is called the Brownian force. The time average of the rapidly fluctuating Brownian force on bead ν can be expressed in terms of the distribution function $f(\mathbf{u},t)$ as (Bird et al., vol 2 (1987)),

$$F_{\nu}^{(b)} = -\frac{\nu kT}{Lf}\frac{\partial}{\partial u}\cdot[\xi^{-1}f] \qquad (\nu = \pm 1) \tag{3.4}$$

where

$$\xi^{-1} = \beta\delta + (\alpha-\beta)uu \tag{3.5}$$

The above is an empiricism to account for anisotropy in the Brownian motion and is related to the notion of "reptation"; that is, when the polymer concentration increases the rotational motion of an individual polymer molecule becomes severely restricted by

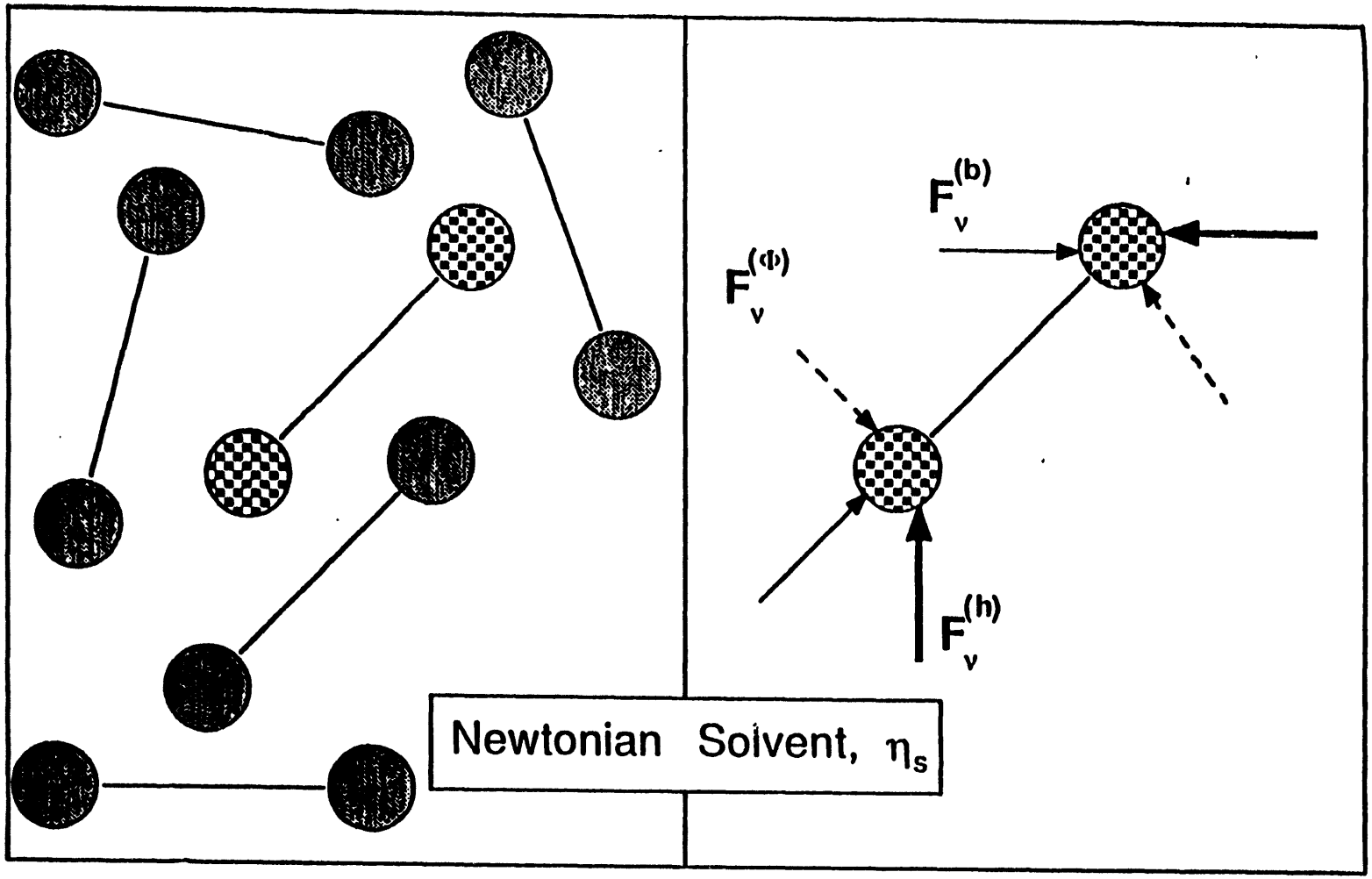

Figure 3.5: Liquid-crystal polymer solution is modeled as a solution of rigid dumbbells in a Newtonian solvent. The forces acting on each dumbbell are shown.

surrounding polymer molecules and the Brownian motion is restricted to the direction along the length of the rod-like polymer molecule. For isotropic Brownian motion, $\alpha=\beta=1$. This form was first used by Bird and DeAguiar (1983) in connection with an encapsulated elastic dumbbell model and is also described in Bird *et al.* (1987). Menon (1990) demonstrated that if the liquid-crystal constitutive equation is derived introducing anisotropy into the Brownian motion no qualitative change in the material functions are predicted. Consequently, for this thesis, Brownian motion is assumed to be isotropic, so that $\xi=\delta$.

As the dumbbell moves through the solution it experiences a drag force caused by the interaction between the solvent and polymer molecules. In a solution of dumbbells possessing some degree of orientational order the resistance to motion in the direction perpendicular to the dumbbell axis can be expected to be somewhat higher than that encountered along its axis. This resisting force called the hydrodynamic drag force is represented by a modified Stoke's law expression that has different friction coefficients in the directions of dumbbell rotation and axial translation (Bird et al., vol 2 (1987)).

$$\boldsymbol{F}_v^{(h)} = -\boldsymbol{\zeta}\cdot([[\dot{\boldsymbol{r}}_v]] - \boldsymbol{v}_v) \tag{3.6}$$

where,

$$\boldsymbol{\zeta} = \zeta[\boldsymbol{uu} + \frac{1}{\sigma}(\boldsymbol{\delta} - \boldsymbol{uu})] \tag{3.7}$$

The Stokes expression assumes that the force is proportional to the difference between the bead velocity averaged with respect to the velocity distribution $[[\dot{\mathbf{r}}_v]]$, and the velocity $\mathbf{v}_v$ of the solution at the bead. The fluid velocity field $\mathbf{v}$ is assumed to be homogeneous, so $\mathbf{v}_v = (\mathbf{v}_o + \boldsymbol{\kappa}\cdot\mathbf{r}_v)$, which implies a constant velocity gradient over the length scale of

the dumbbell. This is a very reasonable assumption (Bird *et al.*, 1987). ζ is called the friction tensor. The anisotropic drag coefficient σ lies in the range $0 \leq \sigma \leq 1$. When $\sigma=1$ the hydrodynamic drag is fully isotropic. Decreasing the value of σ corresponds to increasing the ratio of resistance encountered perpendicular to the dumbbell to that encountered along the axis.

In non-dilute liquid-crystalline polymer solutions the polymer molecules interact with each other. These forces cause the molecules to become aligned even in the absence of flow. As the polymer concentration is increased the intermolecular spacing decreases and the interaction forces become stronger. The degree of alignment of polymer molecules in such systems is also found to increase. The intermolecular interaction potential is modeled by means of the Maier-Saupe approximation to the mean-field potential for rod-rod interaction derived by Onsager (1949). The mean field potential which is supposed to act on the test rod by the surrounding rodlike molecules can be written as

$$\Phi = 2ndL^2kT\int f(u)\sin(u,u')\,du \tag{3.8a}$$

Expanding sin(**u**,**u**′) in terms of irreducible tensors (Bird *et al.*, 1987), and dropping the first term which is irrelevant to orientational ordering and higher order terms involving tensors of rank greater than two gives the Maier-Saupe approximation to the mean field potential in the form

$$\Phi = -\left(\frac{3}{2}\right)NkT(uu-\frac{\delta}{3}):\langle uu-\frac{\delta}{3}\rangle \tag{3.8b}$$

In Eq. 3.8b the dimensionless concentration N is $= c_1 ndL^2$, where n is the number density of the dumbbells, d and L are the diameter and length of the polymer molecule, and c_1

is a numerical factor of order unity. The interaction force is given by,

$$F_v^{(\Phi)} = -\left(\frac{v}{L}\right)\frac{\partial \Phi}{\partial u} \tag{3.9}$$

Combining the equation of motion for the entire molecular model and the configuration or orientation conservation equation for $f(\mathbf{u},t)$ which states that the dumbbells leaving one orientation must end up in another, Bhave *et al.* obtain a diffusion equation which describes the time evolution of the distribution function f in a homogenous flow. For a spatially inhomogenous flow in which translational diffusion of the macromolecules can be ignored the diffusion equation must be modified; the partial derivative of the distribution function with respect to time is replaced by the substantial derivative which gives the following equation for f

$$\frac{Df}{Dt} = \frac{\sigma}{6\lambda}\left(\frac{\partial}{\partial u}\cdot\frac{\partial f}{\partial u}\right) - \frac{\partial}{\partial u}\cdot\left([\kappa\cdot u - \kappa:uuu]f - \frac{\sigma}{6kT\lambda}\left(\frac{\partial \Phi}{\partial u}\right)f\right) \tag{3.10}$$

As mentioned previously, u is the unit vector along the axis of the rod-like macromolecule; $\kappa = \nabla v^{\dagger}$; σ is a parameter which describes the anisotropic drag that a molecule experiences as it moves relative to the solution ($\sigma = 1$ being isotropic and $\sigma = 0$ fully anisotropic, i.e., motion is allowed only along the axis of the molecule); and $\lambda=\zeta L^2/12kT$ is a time constant for the solution where ζ is the scalar factor which appears in the definition for the friction tensor given by Eq. 3.7. If, for example, the flow is spatially inhomogenous only in the z direction, the distribution function $f(u,z,t)$ is defined so that $f(u,z,t)du$ is the fraction of molecules at position z whose orientation is in a range du about u.

The extra stress is given by

$$\boldsymbol{\tau} = -\eta_s\dot{\boldsymbol{\gamma}} - 3nkT\left\langle \boldsymbol{uu} - \frac{1}{3}\boldsymbol{\delta}\right\rangle - 6nkT\lambda\kappa:\langle \boldsymbol{uuuu}\rangle - n\left\langle \boldsymbol{u}\frac{\partial\Phi}{\partial \boldsymbol{u}}\right\rangle \qquad (3.11)$$

where $\dot{\boldsymbol{\gamma}} = \nabla\mathbf{v} + \nabla\mathbf{v}^{\dagger}$ is the rate-of-strain tensor, and <·> denotes an average with respect to the distribution function. This is the same expression as is found for a dilute solution of rigid dumbbells in which the external force $\mathbf{F}_v^{(e)}$ is replaced by the intermolecular force $\mathbf{F}_v^{(\Phi)}$ (Bird *et al.*, 1987). It is clear that with the current formulation of Eqs. 3.3 and 3.11, and the definition for the average, <·>, given by Eq. 3.2, the orientational order tensor and the stress tensor can be evaluated only after the distribution function is determined by solving the diffusion equation, Eq. 3.10. However, solving for the distribution function even in a typical, steady state, two-dimensional, non-axisymmetric, spatially inhomogenous flows, say, using a finite-difference scheme, would be computationally very intensive because of the discretization required in several independent variables; θ and ϕ in orientation space, and x and y coordinates in physical space. The flow calculations would be greatly simplified if the averages that appear in Eqs. 3.3 and 3.11 can be evaluated without solving for the distribution function and a closed form constitutive equation for $\boldsymbol{S}$ and $\boldsymbol{\tau}$ that does not involve f is obtained.

Closed Form Constitutive Equation

It is possible to obtain a closed form of the constitutive equation which enables the stress tensor to be written solely in terms of the macroscopic structure tensor $\boldsymbol{S}$ given by Eq. 3.3. The ability to work in terms of $\boldsymbol{S}$ instead of the complete distribution function greatly simplifies the solution of flow problems. However, in order to write the constitutive equation solely in terms of $\boldsymbol{S}$ it is necessary to invoke a closure approximation (Hand, 1962) of the form $\boldsymbol{A}$:<uuuu> = $\boldsymbol{A}$:<uu><uu> for a symmetric

tensor Λ.

The final approximate constitutive equation obtained by Bhave *et al.* in this way is

$$\tau = -\eta_s\dot{\gamma} - 3nkT\left[(1-\frac{N}{3})S - N(S\cdot S) + N(S:S)(S+\frac{1}{3}\delta) + 2\lambda(\kappa:S)(S+\frac{1}{3}\delta)\right] \quad (3.12)$$

where the evolution of the structure tensor S is given by the equation set

$$S_{(1)} = \frac{D}{Dt}S - \kappa\cdot S - S\cdot\kappa^{\dagger} = F(S) + G(\kappa,S) \quad (3.13)$$

$$F = -\frac{\sigma}{\lambda}\left[(1-\frac{N}{3})S - N(S\cdot S) + N(S:S)(S+\frac{1}{3}\delta)\right] \quad (3.14)$$

$$G(\kappa,S) = \frac{1}{3}\dot{\gamma} - 2(\kappa:S)(S+\frac{1}{3}\delta) \quad (3.15)$$

The subscript $_{(1)}$ in the evolution equation denotes the convected time derivative (Bird *et al.*, Vol.1, 1987). As pointed out in the introduction, Marrucci (1991) and Larson and Öttinger (1991) show that use of the closure approximation results in the evolution equation's not describing molecular tumbling at low shear rates in steady shear flow. Although similar errors due to the closure approximation are not anticipated in elongationally dominated flows such as fiber spinning, its correctness has not been verified for elongationally dominated flows. The effect of the closure approximation on the order and the elongational viscosity in a simple elongational flow and a fiber spinning flow is discussed in Sections 4.2 and 4.3.

Consider the polymer contribution to the stress in Eq. 3.12. The first three terms involving nonlinear contributions from the structure tensor S represent the net of the randomizing effect of Brownian motion and the ordering effect of intermolecular forces.

The last term involving the deformation gradient κ arises from the hydrodynamic drag contribution. A comparison with Doi's model indicates that inclusion of the effects of the hydrodynamic drag force results in extra terms involving the deformation gradient κ in the stress tensor expression and the anisotropic drag coefficient σ in the evolution equation for the structure tensor.

Menon (1990) studied the predictions of the closed form of the constitutive equation for two choices of the time constant λ

$$\lambda = \begin{cases} \lambda_0 \\ \lambda_0(1 - S^2)^2 \end{cases} \tag{3.16}$$

The first choice follows directly from the kinetic theory model and is independent of the degree of order and equals a constant λ_0. The second expression is the same as that obtained by Doi and Edwards using reptation arguments for Brownian motion of concentrated solutions. This assumes that the rotation of a rod-like molecule in such a solution is hindered by the presence of other molecules and that the molecule moves by translating in a tube-like region about its axis. The order dependent time constant also implies that the diffusion coefficient which scales as $1/\lambda$ increases as the rod-like molecules beome aligned.

Like Doi's theory, the model provides a description of the equilibrium phase transitions by setting κ=0. The equilibrium phase diagram is shown in Fig. 3.6. The polymer solution is fully isotropic upto N=8/3, and is a mixture of isotropic and anisotropic phases until N=3.0. Beyond N=3.0 the polymer solution is completely anisotropic. Bhave *et al.* have studied the break-up of the phase diagram under shear,

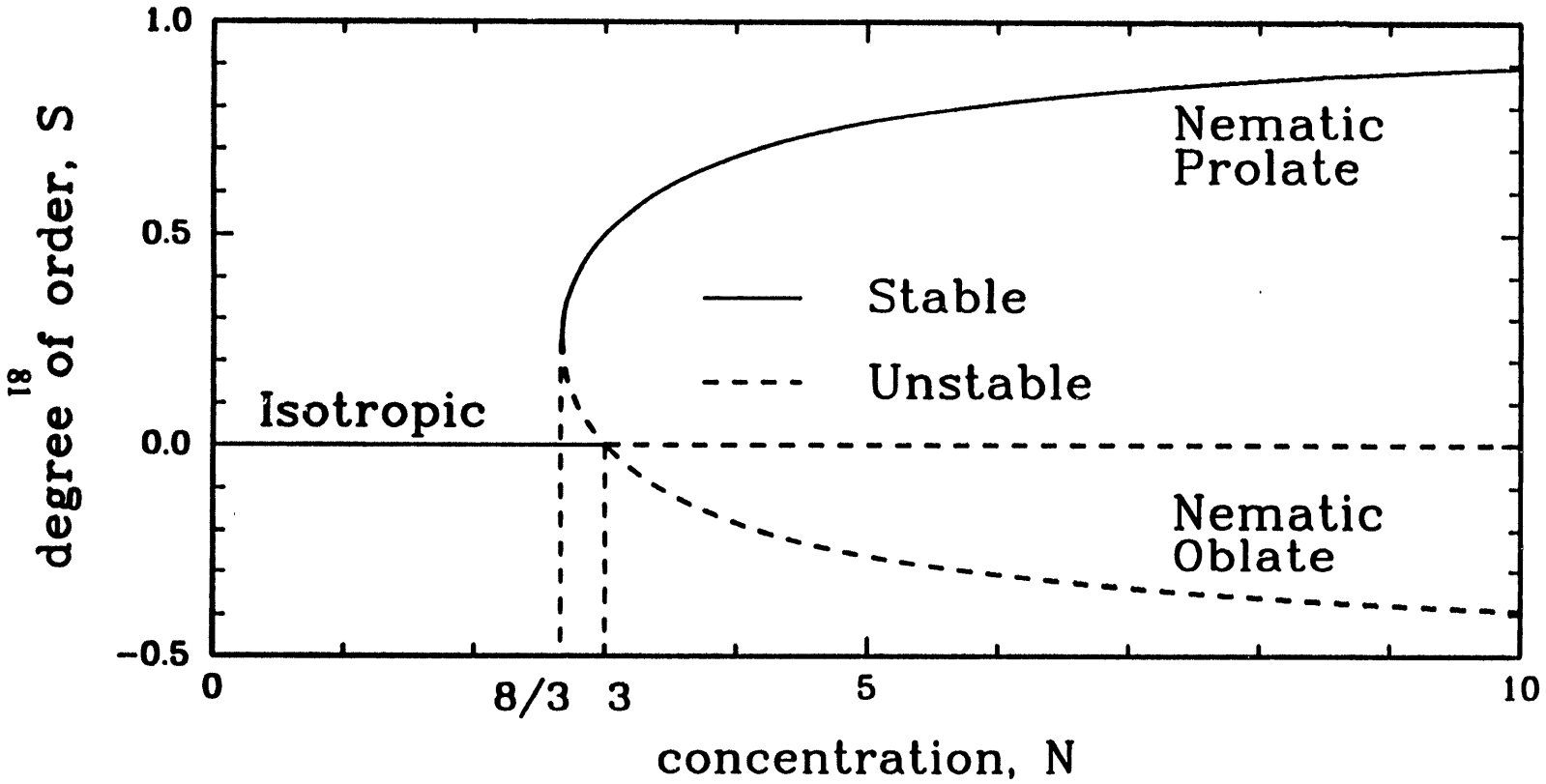

Figure 3.6: Equilibrium phase diagram for the Bhave *et al.* model. The solid curves represent stable phases and dashed curves unstable phases.

uniaxial, and biaxial extensional flows. At high shear rates, the viscosity predicted by Doi's theory and Bhave *et al.* model scale respectively like:

$$\begin{aligned} &(Doi) \qquad \eta \sim \dot{\gamma}^{-8/7} \\ &(Bhave) \quad \eta \sim \begin{cases} \dot{\gamma}^{-2/3} & (\lambda = \lambda_0) \\ \dot{\gamma}^{-6/7} & (\lambda = \lambda_0(1-S^2)^2) \end{cases} \end{aligned} \tag{3.17}$$

As can be seen, Doi's prediction implies that the shear stress passes through a maximum with increasing $\dot{\gamma}$, an aphysical prediction, whereas the Bhave *et al.* model predicts physically plausible shear stress for both λ's.

Bhave *et al.* have computed a variety of rheological properties for this constitutive equation. Predictions of the model and the experimental results for the shear-rate-dependent viscosity obtained by Doraiswamy and Metzner (1986) for 40 wt% HPC in acetic acid, Picken *et al.* (1990) for 20 wt% DABT in sulfuric acid, and the unpublished data of Ramalingam and Armstrong for Kevlar spin dope which is about 20 wt% PPTA in sulfuric acid shown in Fig. 3.7. are in good agreement. In fact, the experimental data show a shear thinning region with a slope close to -2/3. Thus, the Bhave *et al.* model seems better in viscosity predictions and also more physically plausible than Doi's model. It is also clear that the viscosity prediction of the Bhave *et al.* model with $\lambda=\lambda_0$ is better than the viscosity prediction with $\lambda=\lambda_0(1-S^2)^2$ which predicts more shear thinning in the viscosity than is indicated by the data. More details on the comparison with Doi's model are discussed by Menon (1990).

The 20 wt % PPTA in sulfuric acid is solid at room temperature. Consequently, viscosity measurements were carried out at 80°C the temperature at which the

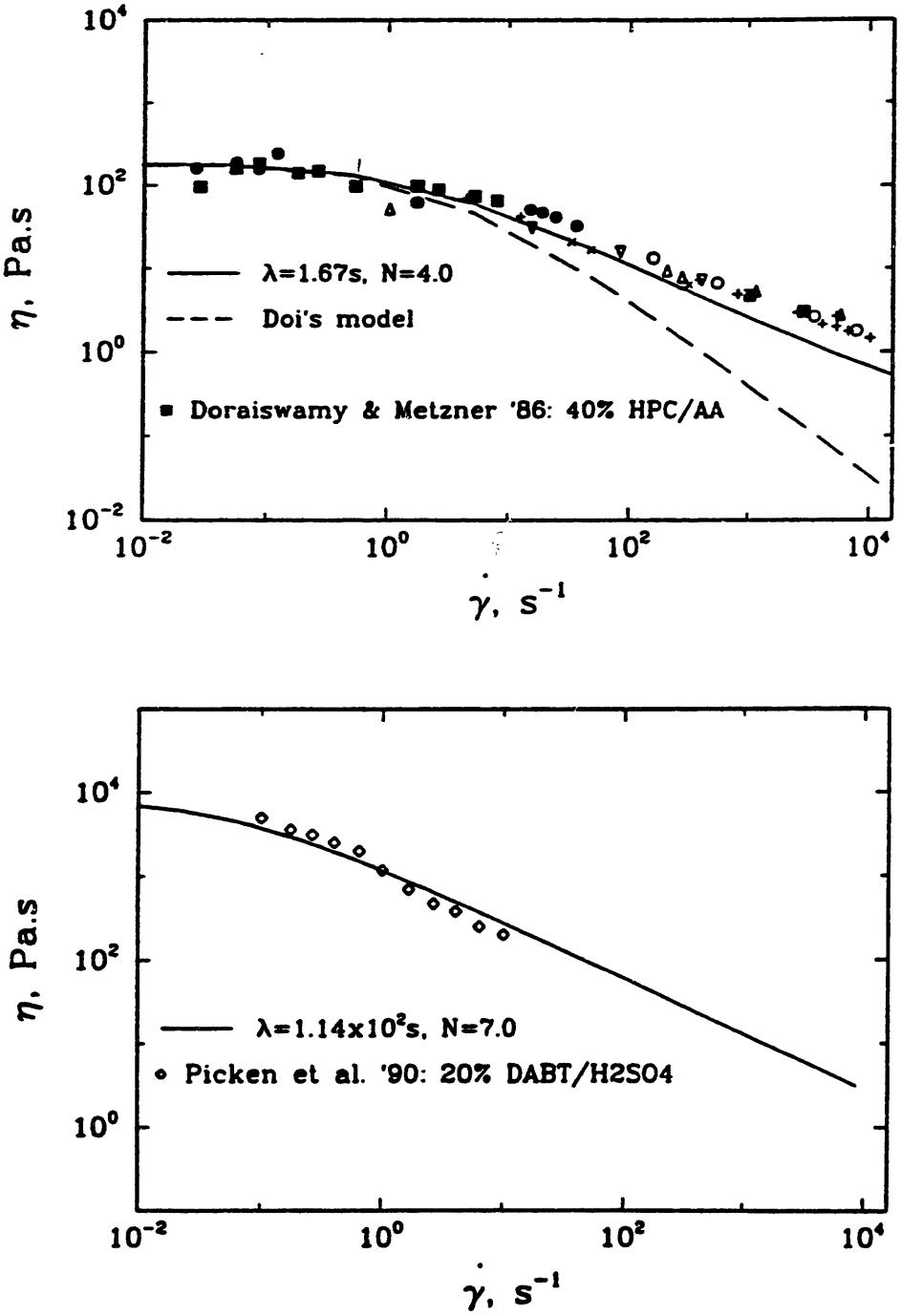

Figure 3.7: Comparison of the viscosity predictions of the Bhave *et al.* model with the data of (a) Doraiswamy and Metzner (1986) for 40 wt% HPC in acetic acid, and (b) Picken *et al.* (1990) for 20 wt% DABT in H_2SO_4.

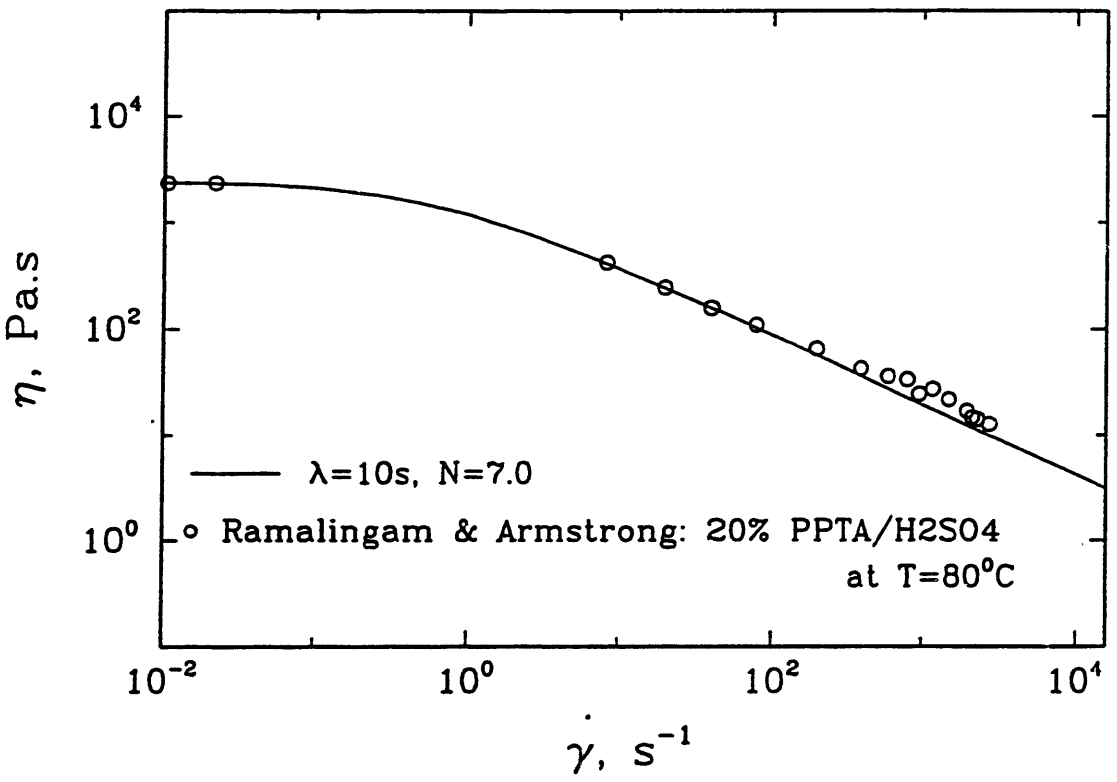

Figure 3.7c: Comparison of the viscosity predictions of the Bhave *et al.* model with the unpublished data of Ramalingam and Armstrong for a 20 wt % PPTA in H_2SO_4 (Kevlar® spin dope) liquid-crystalline solution.

liquid-crystalline polymer solution is typically processed. The molecular weight of the sample is about 40,000. The viscosity was determined by using a RMS-800 Mechanical Spectrometer and a Capillary Viscometer. In the Mechanical Spectrometer, 60 mm parallel plates with a gap of 1.25 mm between the plates were used to measure the viscosity. In the Capillary Viscometer, a 0.05 in capillary was used to measure the viscosity.

It is important to prevent exposure of the PPTA sample to moisture for more than 4-5 minutes since the sulfuric acid comes out of the polymer solution. The exposure to moisture was prevented in the Mechanical Spectrometer by carrying out the experiments inside a oven heated by Nitrogen. In carrying out viscosity measurements with the Capillary Viscometer, the air above the plunger in contact with the sample and the air below the sample were purged with Nitrogen every few minutes.

Viscosity measurements with the Mechanical Spectrometer were limited to the zero-shear-rate viscosity region due to the sample coming out of the gap between the parallel plates at intermediate and high shear rates. Viscosity at intermediate and high shear rates were determined by using the Capillary Viscometer.

Since the fiber drawing flow, which is examined in Chapter 4, is predominantly an extensional flow it is of interest to examine the elongational viscosity predictions of the Bhave *et al.* model in a simple uniaxial elongational flow; the elongational viscosity predictions can be used to judge the departure of the fiber drawing flow from a simple elongational flow and answer questions on the suitability of using the fiber drawing flow to determine the elongational viscosity of a liquid-crystalline polymer solution. The

elongational viscosity predictions of the Bhave *et al.* model are shown in Fig. 3.8 for N=4.0 and several values of σ. It is clear that for $\lambda=\lambda_0$ and $\lambda=\lambda_0(1-S^2)^2$ the elongational viscosity is constant at low elongation rates though the constant values are different for different values of σ. For $\lambda=\lambda_0$ and σ=1.0 (isotropic hydrodynamic drag), $\bar{\eta}$ is slightly extension thickening at intermediate elongation rates and asymptotes to a constant value at high elongation rates. With increase in the drag ($\sigma < 1$), $\bar{\eta}$ extension thins at intermediate elongation rates; however, $\bar{\eta}$ asymptotes to the same constant value predicted for σ=1.0 at high elongation rates. The elongational viscosity predictions are quite different with $\lambda=\lambda_0(1-S^2)^2$ at high elongation rates; $\bar{\eta}$ extension thins for all values of σ. In fact, Menon (1990) carried out an asymptotic analysis to determine the asymptotic behavior in the elongation viscosity at high elongation rates for the Doi model and the Bhave *et al.* model. The elongational viscosity predicted by Doi's theory and Bhave *et al.* model scale respectively like:

$$\begin{aligned} &(Doi) \qquad \bar{\eta} \sim \varepsilon^{-1} \\ &(Bhave) \quad \bar{\eta} \sim \begin{cases} \varepsilon^{0} & (\lambda = \lambda_0) \\ \varepsilon^{-2/3} & (\lambda = \lambda_0(1-S^2)^2) \end{cases} \end{aligned} \tag{3.18}$$

Since the elongational viscosity predictions are very different for the two choices of λ, it is important to ascertain which choice of λ is better for the elongational viscosity predictions of liquid-crystalline polymer solutions. As will be shown in Chapter 4, the only available elongational viscosity data due to Prilutski (1984) are at small elongation rates, and since the elongational viscosity predictions are qualitatively different only at intermediate and high elongation rates, it is not possible to conclude which choice of λ

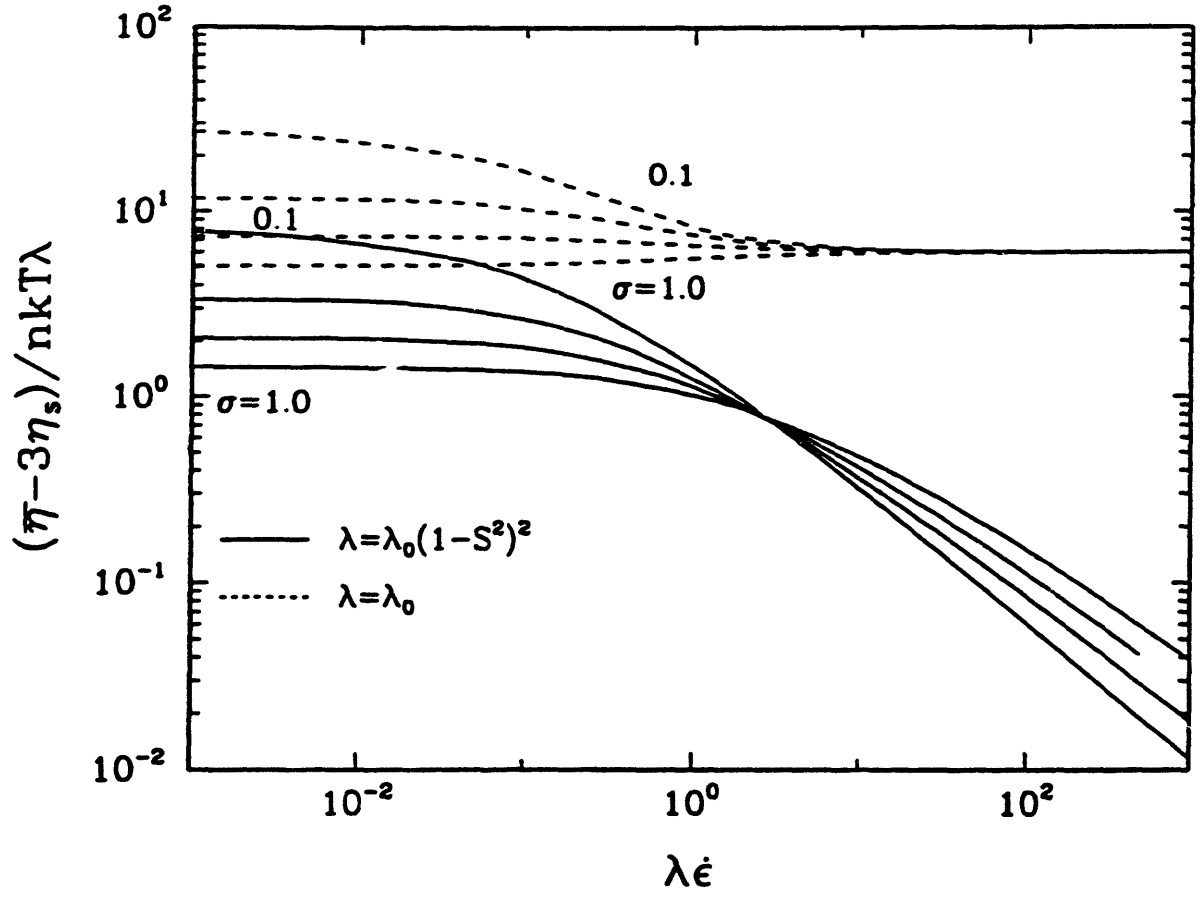

Figure 3.8: Elongational viscosity, $\bar{\eta}$, predictions of the Bhave *et al.* model for N=4.0, σ=0.1, 0.25, 0.5 and 1.0. Results are shown for $\lambda=\lambda_0$ and $\lambda=\lambda_0(1-S^2)^2$.

is better based on elongational viscosity data. However, since the predictions of the Bhave *et al.* model in a simple shear flow, for which data is available for a variety of liquid-crystalline polymer solutions, are much better with $\lambda=\lambda_0$, fiber spinning and finite element results discussed in Chapters 4 and 6 are presented only for this choice of time constant. The reader interested in the fiber spinning predictions with $\lambda=\lambda_0(1-S^2)^2$ can obtain more information from Appendix B.

Chapter Four

Analysis of Isothermal Spinning of Liquid-crystalline Polymers

The purpose of this chapter is to develop an isothermal fiber spinning model for nematic, rod-like, liquid-crystalline polymeric solutions in order to predict the molecular orientation induced along the spinline, as well as the velocity and axial stress. The fiber spinning model is developed from the constitutive equation of Bhave *et al.* (1993) which is an extension of the earlier kinetic theory of Doi (1980, 1981). Since the fiber spinning flow is an extensionally dominated flow it is expected that the orientation states, mathematically represented by the nematic director, that prevail in a steady, simple, uniaxial elongational flow would also prevail in the fiber spinning flow. A derivation is presented in Section 4.1 for the possible orientations that the nematic director could assume in a simple elongational flow. As discussed in Section 3.2.2, Bhave *et al.* invoke a closure approximation to obtain a closed form of the constitutive equation. Marrucci (1991) and Larson and Öttinger (1991) show that use of the closure approximation results in the evolution equation's not describing molecular tumbling at low shear rates in steady shear flow. Although similar errors due to the closure approximation are not anticipated in elongationally dominated flows such as fiber spinning, its correctness has not been verified for elongationally dominated flows. The effect of the closure approximation on the order and the elongational viscosity in a simple elongational flow is discussed in

Section 4.2. The development of the steady state fiber spinning model, the effect of closure approximation and different initial microstructural orientations, the predictions of available experimental data and the "viscous" nature of the fiber spinning model developed using Doi's constitutive equation are discussed in Section 4.3. A linear stability analysis of the fiber spinning model to predict the onset of draw resonance instabilities and the model predictions of the draw resonance data of Prilutski (1984) are discussed in Section 4.4.

4.1 Orientation States for the Nematic Director in a Steady, Simple Elongational Flow

In the nematic region, liquid-crystalline solutions are oriented preferentially about a concentration and flow dependent director vector, traditionally denoted by the symbol **n**. At equilibrium, however, the nematic director could be pointing in any direction. Doi (1981) demonstrated that the arbitrariness in the nematic director disappears in shear flow with the flow direction deciding the direction of spontaneous orientation much like the spontaneous orientation of a ferromagnet in a magnetic field. Doi, however, limited his analysis to finding the nematic director in the plane-of-shear (xy-plane in Fig. 4.1a). Bhave *et al.* show that the nematic director perpendicular to the plane-of-shear (also called the logrolling state) is another orientation allowed by the flow. In this section, the possible orientations for the nematic director in a simple, steady, uniaxial elongational flow are determined from a perturbation scheme for the structure tensor $\boldsymbol{S}$. These orientations for the nematic director are also expected to prevail in the extensionally

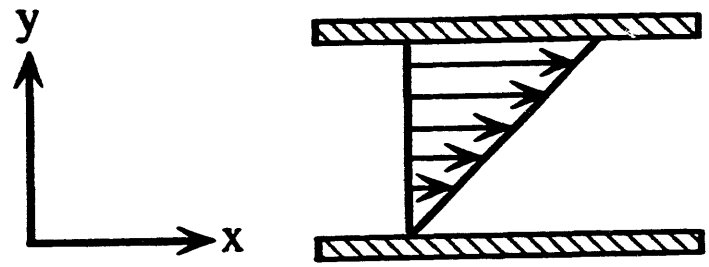

(a)

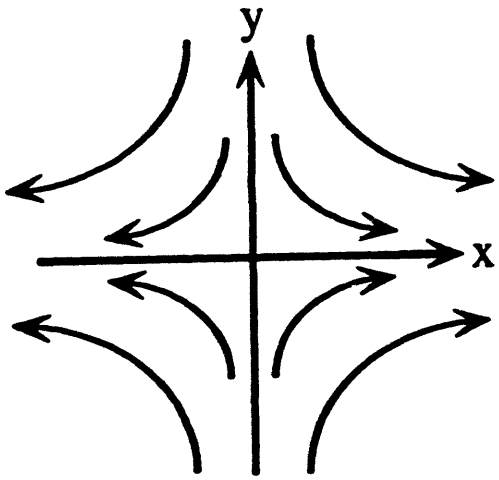

(b)

Figure 4.1: Schematic diagram of (a) a simple shear flow where the *xy*-plane is the plane-of-shear, and (b) a simple uniaxial elongational flow where the *z*-axis is the axis of symmetry.

dominated fiber spinning flow.

The steady state perturbation expansion for the structure tensor S

$$S = S_0 + \frac{\lambda\dot{\varepsilon}}{\sigma}S_1 + O\left(\left(\frac{\lambda\dot{\varepsilon}}{\sigma}\right)^2\right) \tag{4.1}$$

with the dimensionless elongation rate $\lambda\dot{\varepsilon}/\sigma$ as the perturbation parameter ($|\lambda\dot{\varepsilon}/\sigma| < 1$) is introduced into Eqs. 3.13-3.15 which describe the evolution of the structure tensor. At zeroth order in the perturbation parameter the following equation for the equilibrium structure S_0 is obtained

$$O(1): \qquad (1-\frac{N}{3})S_0 - N(S_0 \cdot S_0) + N(S_0 : S_0)(S_0 + \frac{1}{3}\delta) = 0 \tag{4.2}$$

We can check that the expression

$$S_0 = S_0(n_0 n_0 - \frac{1}{3}\delta) \tag{4.3}$$

satisfies Eq. 4.2 with the scalar quantity S_0 defined by the following equation

$$S_0\left[(1-\frac{N}{3}) - \frac{1}{3}NS_0 + \frac{2}{3}NS_0^2\right] = 0 \tag{4.4}$$

The range of S_0 is then $-1/2 \le S_0 \le 1$. Negative values of S_0 are obtained for the liquid-crystalline phase that exhibits oblate symmetry about the nematic director and positive values for prolate symmetry.

The nematic director n_0 compatible with the flow can be determined from the equation at $O(\lambda\dot{\varepsilon}/\sigma)$.

$$O(\frac{\lambda\dot{\varepsilon}}{\sigma}): \quad -\kappa\cdot S_0 - S_0\cdot\kappa^T = -\dot{\varepsilon}\left[(1-\frac{N}{3})S_1 - N(S_0\cdot S_1 + S_1\cdot S_0) + N(S_0:S_0)S_1 + 2N(S_0:S_1)(S_0+\frac{1}{3}\delta)\right] + \frac{1}{3}\dot{\gamma} - 2(\kappa:S_0)(S_0+\frac{1}{3}\delta) \tag{4.5}$$

In general, the nematic director in the limit of equilibrium is given by

$$n_0 = \sin\theta_0\cos\phi_0\delta_x + \sin\theta_0\sin\phi_0\delta_y + \cos\theta_0\delta_z \tag{4.6}$$

If the elongational flow is symmetric about the z direction (Fig. 4.1b), the transpose of the velocity gradient is given by the equation

$$\kappa = \begin{pmatrix} -\frac{1}{2}\dot{\varepsilon} & 0 & 0 \\ 0 & -\frac{1}{2}\dot{\varepsilon} & 0 \\ 0 & 0 & \dot{\varepsilon} \end{pmatrix} \tag{4.7}$$

Introducing Eqs. 4.3, 4.4, 4.6 and 4.7 into Eq. 4.5, and taking the dot product with n_0 from the right, the following component equations are obtained after much algebraic simplification

<u>x-direction</u>

$$\frac{1}{3}(1+S_0)\sin\theta_0\cos\phi_0 - S_0\left(\frac{1}{2}\cos^2\theta_0(1-4S_0)+\frac{2}{3}S_0\right)\sin\theta_0\cos\phi_0 = -\xi\sin\theta_0\cos\phi_0 \tag{4.8}$$

<u>y-direction</u>

$$\frac{1}{3}(1+S_0)\sin\theta_0\sin\phi_0 - S_0\left(\frac{1}{2}\cos^2\theta_0(1-4S_0)+\frac{2}{3}S_0\right)\sin\theta_0\sin\phi_0 = -\xi\sin\theta_0\sin\phi_0 \tag{4.9}$$

<u>z-direction</u>

$$\frac{2}{3}(1+S_0)\cos\theta_0 + S_0\left(\frac{1}{2}\cos^2\theta_0(1-4S_0)+\frac{2}{3}S_0-\frac{1}{2}\right)\cos\theta_0 = \xi\cos\theta_0 \tag{4.10}$$

ξ is a scalar function of the concentration N and the components of S_0 and S_1. Let us examine the possible solutions to Eqs. 4.8-4.10: (1) Assume that $\sin\theta_0$, $\cos\theta_0$, $\sin\phi_0$ and $\cos\phi_0$ are all non-zero. Cancelling the non zero terms $\cos\theta_0$ and $\sin\theta_0\sin\phi_0$ that multiply

Eqs. 4.9 and 4.10 respectively, and eliminating ξ between Eqs. 4.9 and 4.10 gives S_0=-2 which is impossible according to Eq. 4.4. Note that when the non zero terms $\sin\theta_0\cos\phi_0$ and $\sin\theta_0\sin\phi_0$ which multiply Eqs. 4.8 and 4.9 respectively are cancelled, Eqs. 4.8 and 4.9 are the same; (2) Assume that $\sin\theta_0 = 0$; that is, the nematic director is aligned with the flow direction (z-direction). Then Eqs. 4.8 and 4.9 are trivially satisfied. Setting $\cos\theta_0$=1, Eq. 4.10 reduces to $3\xi=2+2S_0-4S_0^2$ which is a valid equation for the components of S_1 in terms of S_0; (3) Assume that $\cos\theta_0 = 0$; that is, the nematic director is in the plane perpendicular to the flow direction (xy-plane). Then Eq. 4.10 is trivially satisfied. Equations 4.8 and 4.9 reduce to the same relation $3\xi=-1-S_0+2S_0^2$ which is a valid equation for the components of S_1 in terms of S_0; (4) Assume that either $\sin\phi_0$ or $\cos\phi_0 = 0$. In either case, combining Eqs. 4.8 and 4.10 or 4.9 and 4.10, S_0=-2 which is impossible according to Eq. 4.4. Note that in the solution choices (2) and (3), the equation set for the components of S_1 would be completed by taking the dot product of Eq. 4.5 with the unit vectors perpendicular to $\mathbf{n}_0$.

Thus, Eqs. 4.8-4.10 demonstrate that the nematic director can only be in the stretching direction (z-direction) or in the plane perpendicular to the stretching direction (xy-plane). However, the calculations of Bhave *et al.* show that only the nematic director along the stretching direction exists at moderate to large $\lambda\dot{\varepsilon}/\sigma$. Consequently, the fiber spinning analysis is restricted to this nematic director.

The analysis presented here employs a formal perturbation expansion whereas Doi's derivation in shear flow does not; the expansion also accounts properly for perturbations in the nematic director about the equilibrium limit $\mathbf{n}_0$ as opposed to Doi's

derivation. When employed in shear flow, the pertubation expansion technique yields the same expression obtained by Doi for the nematic director in the plane-of-shear; in addition, the analysis predicts the nematic director perpendicular to the plane-of-shear, which corresponds to the logrolling state studied by Bhave *et al.*

4.2 Steady Simple Elongational Flow

Bhave *et al.* show that the only observable phase for the liquid-crystalline solution in uniaxial elongational flow at moderate to large $\lambda\dot{\varepsilon}/\sigma$ is the phase which exhibits prolate, uniaxial symmetry about the direction of stretching. In particular, for the choice of N used in the fiber spinning calculations the prolate phase without uniaxial symmetry ceases to exist at $\lambda\dot{\varepsilon}/\sigma = 0.25$. For $\sigma = 0.1$ (which is chosen for the fiber spinning calculations) this corresponds to $\lambda\dot{\varepsilon} = 0.025$. Consequently the analysis of the kinetic theory equations presented in Section 3.2.2 is restricted to the prolate phase with uniaxial symmetry. In this section, analytical expressions are derived for the structure tensor and the elongational viscosity without and with closure to quantify the effect of closure on these quantitites.

Form of the Structure Tensor and the Elongational Viscosity

See *et al.* (1990) exploit the fact that the simple elongational flow is a potential flow and write the solution to the distribution function in terms of the Maier-Saupe potential and a potential for the flow. For a liquid-crystalline solution which exhibits prolate, uniaxial symmetry about the direction of stretching, $f = f(\theta,t)$, where θ is the angle subtended by the molecular axis and the direction of stretching, the z-axis. Consequently, only the xx, yy, and zz components of $\boldsymbol{S}$ are nonzero. In addition, the xx- and yy-components are

equal, and S is traceless. Hence,

$$S = S(\delta_z\delta_z - \frac{1}{3}\delta) \; ; \quad S = \left[\frac{3}{2}S:S\right]^{1/2} \tag{4.11a,b}$$

When this form for S is combined with Eq. 3.8 for the Maier-Saupe potential, the distribution function can be written as

$$f = \frac{1}{2\pi} \frac{e^{\frac{1}{2}[9\frac{\varepsilon\lambda}{\sigma}+3NS]\cos^2\theta}}{\int_0^{\pi} e^{\frac{1}{2}[9\frac{\varepsilon\lambda}{\sigma}+3NS]\cos^2\theta} \sin\theta \, d\theta} \tag{4.12}$$

where the conditions $df/d\theta = 0$ at $\theta = 0$ and π and the normalization requirement $\int f du = 1$ have been used. Note that this result is implicit since f is contained in S which appears in the integrand. A comparison with the distribution function reported by Bird *et al.* (Vol.2, 1987) for a dilute solution of rigid dumbells shows that inclusion of the Maier-Saupe intermolecular potential introduces an additional exponential term, and anisotropy in the drag produces the dimensionless group $\varepsilon\lambda/\sigma$ instead of $\varepsilon\lambda$. From Eq. 3.3 for the structure tensor S and Eq. 4.11b for S the equation

$$S = \frac{3}{2} \frac{\int_{-1}^{+1} t^2 e^{\frac{1}{2}[9\frac{\varepsilon\lambda}{\sigma}+3NS]t^2} dt}{\int_{-1}^{+1} e^{\frac{1}{2}[9\frac{\varepsilon\lambda}{\sigma}+3NS]t^2} dt} - \frac{1}{2} \tag{4.13}$$

is obtained which when substituted into Eq. 4.11a completely defines the structure tensor. An unoriented isotropic state corresponds to S=0, and it is expected that $0 < S \leq 1$ for prolate symmetry in the order in the presence of flow. Equation 4.13 is implicit in S and requires an iterative procedure to solve for S. From the expression for the stress in Eq.

3.11, the elongational viscosity is found to be

$$\frac{\bar{\eta}-3\eta_s}{nkT\lambda} = -3\left[\frac{(\sigma-1)}{\lambda\dot{\varepsilon}}-2\right]+\frac{9/2}{\int_{-1}^{+1} e^{\frac{1}{2}[9\frac{\dot{\varepsilon}\lambda}{\sigma}+3NS]t^2}dt}\left([\frac{(\sigma-1)}{\lambda\dot{\varepsilon}}-1]\int_{-1}^{+1}(1-t^2)e^{\frac{1}{2}[9\frac{\dot{\varepsilon}\lambda}{\sigma}+3NS]t^2}dt\right. \tag{4.14}$$

$$\left. + NS\frac{(\sigma-1)}{\lambda\dot{\varepsilon}}\int_{-1}^{+1}(1-t^2)t^2e^{\frac{1}{2}[9\frac{\dot{\varepsilon}\lambda}{\sigma}+3NS]t^2}dt\right)$$

Once S has been determined from Eq. 4.13, the elongational viscosity can be evaluated by means of this result.

Test of Closure Approximation

Next, results are obtained for S and $\bar{\eta}$ which are analogous to Eqs. 4.13 and 4.14 but which are based on the closure approximation. Equation 4.11a,b is used to represent the structure tensor for prolate, uniaxially symmetric order, and it is substituted into the evolution equation with the closure approximation given in Section 3.2.2 to get the following cubic equation for S

$$S^3 - \left(\frac{1}{2}-\frac{3}{N}\frac{\dot{\varepsilon}\lambda}{\sigma}\right)S^2 - \left(\frac{1}{2}-\frac{3}{2N}+\frac{3}{2N}\frac{\dot{\varepsilon}\lambda}{\sigma}\right)S - \frac{3}{2N}\frac{\dot{\varepsilon}\lambda}{\sigma} = 0 \tag{4.15}$$

The general solution to this cubic equation is

$$\begin{aligned} S_1 &= E + F + \frac{1}{2N}B \\ S_2 &= -\frac{1}{2}(E+F) + \frac{1}{2N}B + \frac{1}{2}i\sqrt{3}(E-F) \\ S_3 &= -\frac{1}{2}(E+F) + \frac{1}{2N}B - \frac{1}{2}i\sqrt{3}(E-F) \end{aligned} \tag{4.16}$$

where

$$B = \frac{1}{3}N - 2\frac{\varepsilon\lambda}{\sigma}$$

$$E = \left[\frac{3B}{8N^2}\left(\frac{\varepsilon\lambda}{\sigma}+\frac{N}{3}-1\right) + \frac{3}{4N}\frac{\varepsilon\lambda}{\sigma}+\frac{B^3}{8N^3}+\sqrt{D}\right]^{1/3} \tag{4.17}$$

$$F = \left[\frac{3B}{8N^2}\left(\frac{\varepsilon\lambda}{\sigma}+\frac{N}{3}-1\right) + \frac{3}{4N}\frac{\varepsilon\lambda}{\sigma}+\frac{B^3}{8N^3}-\sqrt{D}\right]^{1/3}$$

and D is the discriminant

$$\sqrt{D} = \frac{1}{24N^2}\left[-3N^4+\left[18\frac{\varepsilon\lambda}{\sigma}+26\right]N^3+\left[81\left(\frac{\varepsilon\lambda}{\sigma}\right)^2+18\left(\frac{\varepsilon\lambda}{\sigma}\right)-75\right]N^2+\right.$$
$$\left.\left[72-80\left(\frac{\varepsilon\lambda}{\sigma}\right)+864\left(\frac{\varepsilon\lambda}{\sigma}\right)^2-324\left(\frac{\varepsilon\lambda}{\sigma}\right)^3\right]N-108\left(\frac{\varepsilon\lambda}{\sigma}\right)^2+216\left(\frac{\varepsilon\lambda}{\sigma}\right)^3-972\left(\frac{\varepsilon\lambda}{\sigma}\right)^4\right]^{1/2} \tag{4.18}$$

Of the three solutions, solutions S_2 and S_3 are neglected since they do not possess prolate symmetry. Solution S_1 possesses prolate symmetry and exists for all values of the concentration and elongation rate. Combining Eqs. 4.16 and 3.12, and dropping the subscript 1 in S_1 gives the following result for the elongational viscosity

$$\frac{\bar{\eta}-3\eta_s}{nkT\lambda} = 6S^2 + \frac{3S}{\lambda\varepsilon}\left(1-\frac{N}{3}(2S+1)(1-S)\right) \tag{4.19}$$

The effects of the closure approximation on (a) the equilibrium phase transition and (b) the response of order and viscosity to an elongational flow are examined next. The equilibrium phase diagram (S vs. N) can be determined from the above equations by setting $\varepsilon\lambda/\sigma$ to zero; Fig. 4.2 shows the equilibrium phase diagrams with and without the closure approximation. Closure does not change the qualitative behavior of the phase transition, but there are quantitative differences in the critical concentration N_c for the isotropic-nematic phase transition (where the isotropic phase ceases to exist) and the order

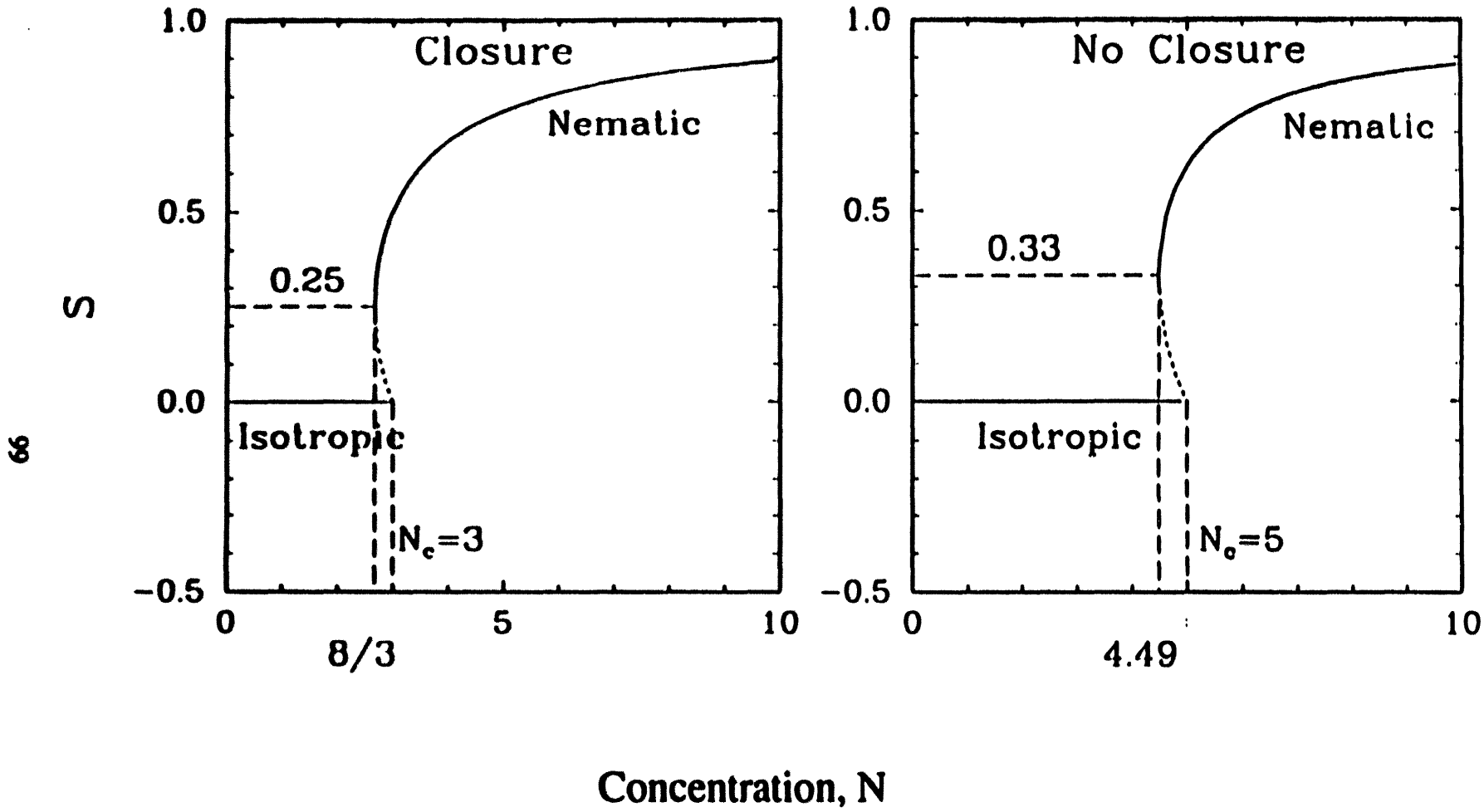

Figure 4.2: Equilibrium phase diagram (a) with closure and (b) without closure. The shift in critical concentration and order at onset of nematic phase is indicated.

S at the onset of the stable nematic phase. The critical concentrations with and without closure, N_c=3.6 and 5.0 respectively, agree with the reported values of several authors (Doi, 1980; See *et al.*, 1990; and Bhave *et al.*, 1993 with closure, and See *et al.* (1990); and Bhave, 1992 without closure). In fitting the model predictions to experimental data, the differences in N_c for the two approaches can be accounted for simply by normalizing concentrations by the phase transition concentration. For example, a 40 wt % solution of hydroxypropylcellulose in acetic acid has a critical concentration of 30 wt %; in either the closure or no closure model, the dimensionless concentration N is taken so that N/N_c = 4/3. However, compensating for the difference in the equilibrium order at $N = N_c$ is not easy. This difference leads to all the observed differences of the two approaches in describing a simple elongational flow and also the fiber spinning flow examined in detail in the next section. Note that since $S \rightarrow 1$ for $N/N_c \gg 1$ for either model, the differences in results for the two are expected to decrease as concentration increases.

In Fig. 4.3 the effect of closure on the order and the elongational viscosity in a steady elongational flow is examined for N/N_c = 4/3. The differences in the order at low and moderate elongation rates result from the equilibrium order's being much higher without closure. Differences in the elongational viscosity at these elongation rates, however, are well within a factor of 2. In spite of the quantitative differences, the closure model captures the essential trends in the order and the viscosity, which suggests that the closure model should be adequate for describing the physics of the prolate-ordered, uniaxially symmetric fiber spinning model. This hypothesis is tested in Section 4.3 where the fiber spinning equations without the closure approximation are solved by expanding

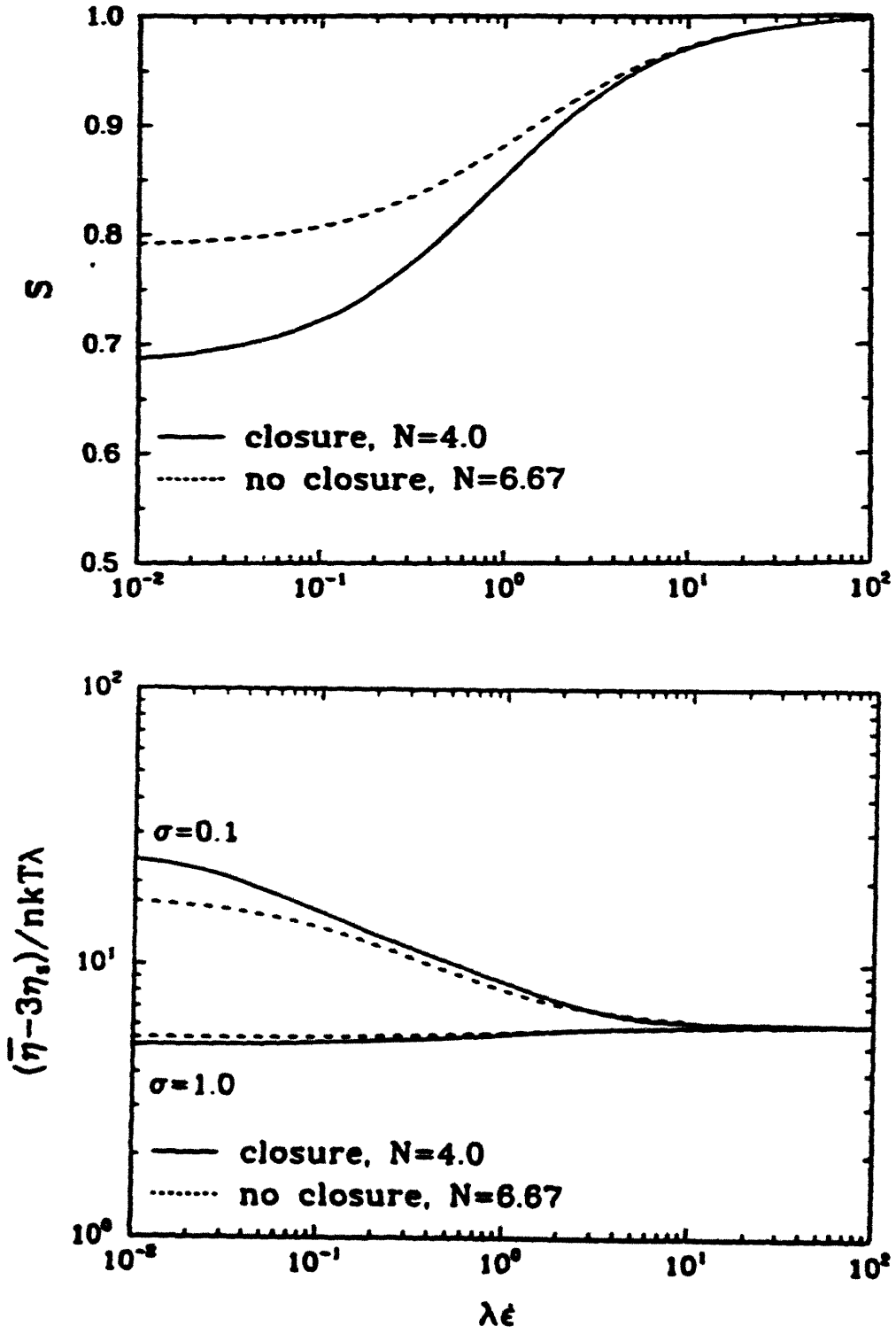

Figure 4.3: Effect of closure on the variation of (a) order parameter S and (b) elongational viscosity $\bar{\eta}$ with elongation rate $\dot{\epsilon}$ in a simple steady elongational flow. The concentration N is chosen so that $N/N_c = 4/3$ for both models.

the distribution function in terms of Legendre polynomials. The results, also discussed in Section 4.3, clearly demonstrate that the closure approximation affects the velocity and the stress profiles only at small elongation rates, and even then the quantitative differences are well within a factor of 2.

4.3 Steady-State Fiber Spinning Model

A liquid-crystalline polymeric solution is formed into a fiber by extruding it at volume flow rate Q through a spinneret and winding the resulting filament on a spool. A schematic diagram of the process was shown in Fig. 1.4. The velocity of the fiber at the wind-up spool is greater than the extrusion velocity, so that the fiber is under tension F. In addition to being stretched during the travel between the spinneret and the take-up spool, the polymer may pass through a solidification bath, be cooled, experience solvent evaporation, or be coagulated. The following analysis models the stretching of the polymer before it is solidified. To keep the analysis simple, only isothermal spinning is considered and the concentration is assumed to be uniform.

A cylindrical coordinate system is used with the origin at the position where the axial velocity profile can first be assumed independent of radial position and where the radius R of the fiber is not changing rapidly, that is, $|\partial R/\partial z| \ll 1$. This point should occur just downstream from the point of maximum extrudate swell. At $z = 0$ the velocity of the filament is v_0. In this problem, v_0 is not specified directly, but is fixed by specifying the take-up velocity v_L and the draw ratio D_R. At a distance L downstream from the origin the polymer solidifies. For $z > L$ the velocity of the filament is assumed

constant (no further stretching occurs), so that v_L is fixed by the speed at the wind-up spool.

For an incompressible liquid, the mass conservation equation is

$$\frac{d}{dz}(Av_z) = 0 \tag{4.20}$$

where A and v_z are the local cross-sectional area and axial velocity of the filament. A differential momentum balance results in the following expression for momentum conservation in the z-direction (Bird *et al.*, Vol. 1, 1987, pp. 51-52):

$$\rho v_z \frac{dv_z}{dz} = \left[-\frac{d}{dz}(\tau_{zz} - \tau_{rr}) + (\tau_{zz} - \tau_{rr})\frac{d\ln v_z}{dz} \right] - \frac{\sigma_s}{2}\sqrt{\frac{\pi}{A}}\frac{d\ln v_z}{dz} + \rho g \tag{4.21}$$

in which τ_{zz}-τ_{rr} is a normal stress difference, σ_s is the surface tension, and g is the acceleration due to gravity. It is useful to rewrite the momentum equation explicitly in terms of τ_{zz}-τ_{rr}. Multiplying Eq. 4.21 by πR^2 and rearranging the terms gives after one integration

$$\tau_{zz}-\tau_{rr} = -\frac{F}{Q}v_z + \sigma_s\sqrt{\frac{\pi v_z}{Q}}\left[1 - 2\sqrt{\frac{v_z}{v_0}}\right] + \rho v_z(v_0 - v_z) + \rho g v_z \int_0^z \frac{1}{v_z(s)}ds \tag{4.22}$$

The continuity equation has been used to eliminate A. The development so far is general to any constitutive equation. To proceed further, a constitutive relation for τ must be specified.

4.3.1 Bhave *et al.* Constitutive Equation

The liquid-crystal structure and stress tensor for this constitutive equation are given by Eqs. 3.12-3.15. For $|\partial R/\partial z| \ll 1$, to lowest order only the diagonal components of the

velocity gradient tensor $\kappa^{\dagger}$ are nonzero and $\{\nabla v\}_{rr}=\{\nabla v\}_{\theta\theta}$. Consequently, Eq. 4.11a,b is used for the structure tensor but S is allowed to vary with z; i.e. $S \equiv S(z)$. The evolution equation for the structure (in terms of S) and the stress tensor (in terms of the normal stress difference) are then given by

$$\frac{dS}{dz} = (1-S)(2S+1)\frac{d\ln v_z}{dz} - \frac{\sigma S}{v_z\lambda}\left(1-\frac{N}{3}(1-S)(2S+1)\right) \tag{4.23}$$

and

$$\tau_{zz}-\tau_{rr} = -3(\eta_s+2nkT\lambda S^2)\frac{dv_z}{dz} - 3nkTS\left(1-\frac{N}{3}(2S+1)(1-S)\right) \tag{4.24}$$

The next step is to introduce the dimensionless axial coordinate ζ, velocity ϕ, and stress components T_{ii}

$$\zeta = \frac{z}{L}\ ; \quad \phi = \frac{v_z}{v_L}\ ; \quad T_{ii} = \frac{\tau_{ii}}{(F/\pi R_L^2)} \tag{4.25}$$

In terms of these dimensionless variables, the governing equations for the spinning problem can be written as

<u>z-component of equation of motion</u>

$$T_{zz}-T_{rr} = -\phi + \frac{\beta}{(1-\beta)}\frac{De}{T}\left(\frac{1}{Ca}\phi^{1/2}(1-2(\phi D_R)^{1/2}) + Re\,\phi\left(\frac{1}{D_R}-\phi\right) + \frac{Re}{Fr}\phi I_1(\zeta)\right) \tag{4.26}$$

$$\frac{dI_1}{d\zeta} = \frac{1}{\phi} \tag{4.27}$$

<u>Stress tensor equation</u>

$$De\frac{d\phi}{d\zeta} = \left[\frac{\frac{-(T_{zz}-T_{rr})T}{3} - S\left(1-\frac{N}{3}(2S+1)(1-S)\right)}{\frac{\beta}{1-\beta}+2S^2}\right] \tag{4.28}$$

Evolution equation for the structure tensor

$$\frac{dS}{d\zeta} = (1-S)(2S+1)\frac{d\ln\phi}{d\zeta} - \frac{\sigma S}{\phi De}\left(1-\frac{N}{3}(1-S)(2S+1)\right) \tag{4.29}$$

where the Deborah number De, capillary number Ca, Reynolds number Re, Froude number Fr, dimensionless threadline tension T, and dimensionless solvent viscosity β arise and are defined by

$$\begin{aligned} De &= \frac{\lambda v_L}{L}\ ; \quad Ca = \frac{\eta_s v_L/L}{\sigma_s/R_L}\ ; \quad Re = \frac{\rho v_L L}{\eta_s} \\ Fr &= \frac{v_L^2}{gL}\ ; \quad T = \frac{F}{\pi nkTR_L^2}\ ; \quad \beta = \frac{\eta_s}{\eta_s + nkT\lambda} \end{aligned} \tag{4.30}$$

The parameter T is unknown *a priori*, but is determined once De and D_R are specified. The function I_1 is given by the integral in the last term of Eq. 4.22.

The three boundary conditions and one algebraic constraint needed to solve the system of equations, Eqs. 4.26-4.29, and also to determine the parameter T are

$$\begin{aligned} &\text{at } \zeta = 0, \\ &\qquad \phi = 1/D_R \\ &\qquad S = S_\epsilon \quad \text{or} \quad S = S_{eq} \\ &\qquad I_1 = 0 \\ &\text{at } \zeta = 1, \\ &\qquad \phi = 1 \end{aligned} \tag{4.31}$$

Since nothing is known about the flow inside the capillary and the spinneret, two values that bracket the range of possible initial values of S that the threadline might see are chosen arbitrarily. These are $S = S_\epsilon$, that is, S has the value it would have in a simple elongational flow for the same elongation rate $\dot{\epsilon}$ as exists at $\zeta = 0$, and $S = S_{eq}$, that is,

S has its equilibrium value (corresponding to the stable prolate order) at the concentration N. The value for S_ε is given by S_1 in Eq. 4.16. However, the elongation rate at the origin is not known *a priori* and the initial order must be determined along with the solution of the fiber spinning problem. The equilibrium order can be determined from Eq. 4.15 by setting $\dot{\varepsilon}\lambda/\sigma$ to zero. A shooting method (Press *et al.*, 1986) in conjunction with a stiff ordinary differential equation solver that uses a semi-implicit Runge-Kutta scheme (Press & Teukolsky, 1989) is used to solve the system of algebraic-differential equations.

4.3.2 Direct Solution of Diffusion Equation

Consistent with the small slope approximation and axisymmetry of the fiber spinning flow, the distribution function is taken as $f=f(\theta,z)$. The diffusion equation and the deviatoric stress for a spatially inhomogenous flow was presented in Section 3.2.2. Introducing the prolate, uniaxially symmetric form of the structure tensor and exploiting the fact that κ is diagonal with the small-slope approximation for the fiber spinning flow, allows the diffusion equation to be written in the dimensionless form

$$6\frac{De}{\sigma}\phi\frac{\partial f}{\partial \zeta} = \underline{\frac{1}{\sin\theta}\frac{\partial}{\partial\theta}\left(\sin\theta\frac{\partial f}{\partial\theta}\right)} + \left(9\frac{De}{\sigma}\frac{d\phi}{d\zeta}+3NS\right)\frac{1}{\sin\theta}\frac{\partial}{\partial\theta}\left(\sin^2\theta\cos\theta f\right) \qquad (4.32)$$

The presence of the underlined operator suggests a Legendre polynomial expansion for the distribution function (Bird *et al.*, Vol.2 1987). Introducing the expansion

$$f(\theta,\zeta) = \sum_{n=0}^{N} a_n(\zeta)P_n(\cos\theta) \qquad (4.33)$$

into Eq. 4.32 gives

$$\sum_{n=0}^{M} 6\frac{De}{\sigma}\phi\frac{da_n}{d\zeta}P_n = -\sum_{n=0}^{M} n(n+1)a_nP_n + (9\frac{De}{\sigma}\frac{d\phi}{d\zeta}+3NS)\sum_{n=0}^{M}\sum_{m=n-2}^{n+2} a_nc_{nm}P_m \quad (4.34)$$

where $P_n(\cos\theta)$ is the n^{th} Legendre polynomial and

$$\begin{aligned} c_{n,n-2} &= -\frac{n(n-1)(n-2)}{(2n+1)(2n-1)} \\ c_{n,n} &= 2 + \frac{n(n+1)^2-3(n+1)(n+2)}{(2n+1)(2n+3)} - \frac{n^2(n+1)+3n(n-1)}{(2n-1)(2n+1)} \\ c_{n,n+2} &= \frac{(n+1)(n+2)(n+3)}{(2n+1)(2n+3)} \end{aligned} \quad (4.35)$$

All other $c_{nm} = 0$

The orthogonality of the Legendre polynomials can then be exploited to obtain a system of M coupled ordinary differential equations for the coefficients $\{a_n(\zeta)\}$ from the above equation. Since the rodlike molecules have no polarity the distribution function must have reflection symmetry about the $\theta=\pi/2$ plane. Consequently, the expansion for *f* has only *even* Legendre polynomial terms, and this can be used in the computational scheme to include more terms in the expansion and improve the accuracy. Note also from Eq. 4.34 that $da_0/d\zeta=0$, so that a_0 is independent of ζ. Using the normalization condition for the distribution function, $\int f du = 1$ gives the value of a_0 as

$$a_0 = \frac{1}{4\pi} \quad (4.36)$$

which is the isotropic equilibrium contribution to the distribution function.

Since the exact form of the distribution function is known for a simple elongational flow, this flow is used to demonstrate the convergence of the corresponding Legendre polynomial expansion with increasing number of terms (see Fig. 4.4). It can

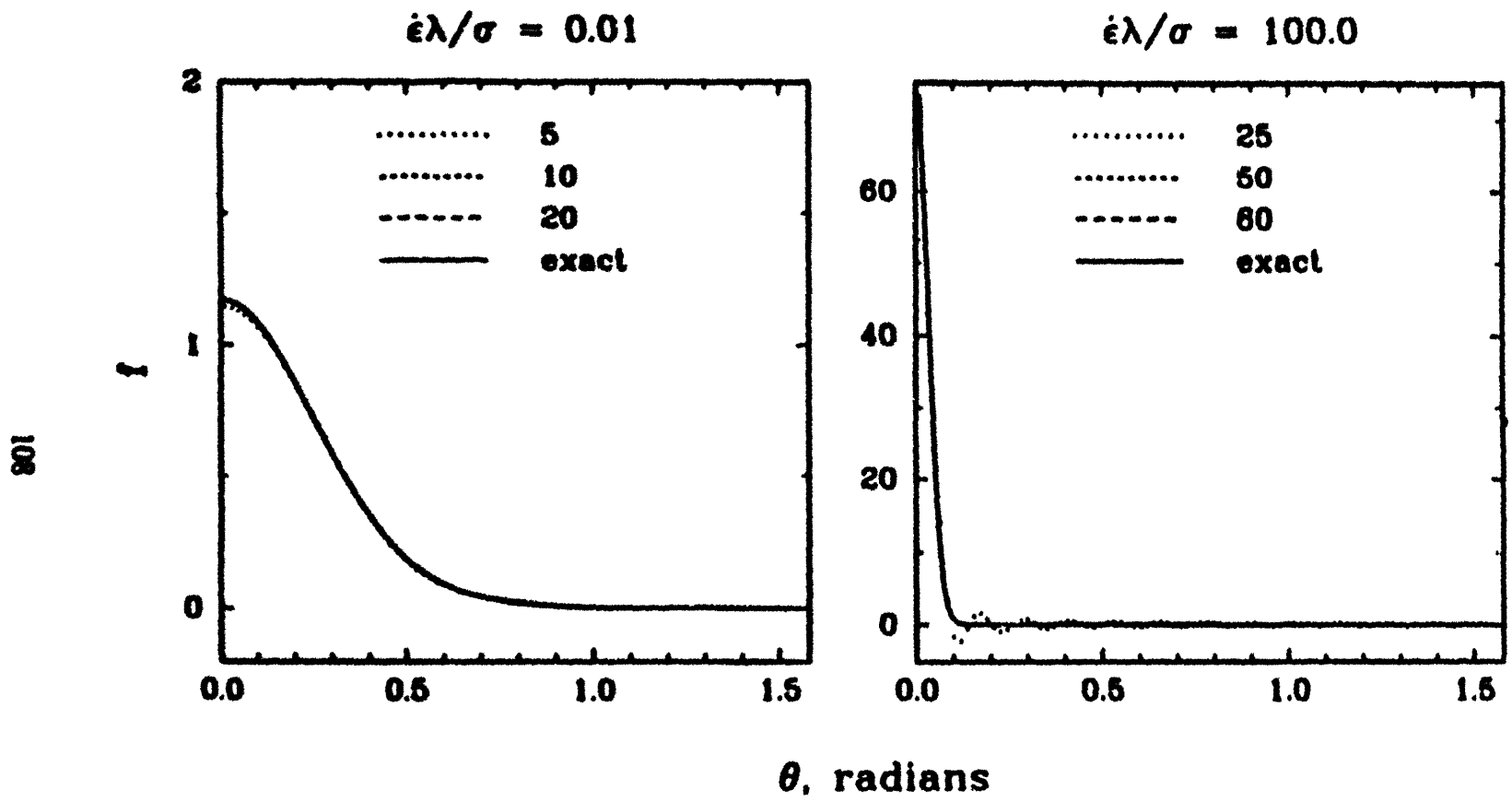

Figure 4.4: Test of convergence of the Legendre polynomial expansion for the distribution function f to the exact solution as a function of the number of even Legendre polynomials for (a) $\dot{\epsilon}\lambda/\sigma$=0.01 and (b) $\dot{\epsilon}\lambda/\sigma$=100.0 in a simple elongational flow.

be seen that for $\varepsilon\lambda/\sigma$=100.0, when f is close to a delta function, 50-60 even Legendre polynomial terms are required to obtain good agreement; it takes only a couple of seconds on a STARDENT minicomputer to determine this many terms.

In order to solve the fiber spinning problem without the closure approximation Eqs. 4.28 and 4.29 which have incorporated this approximation must be replaced. Equation 4.29, the evolution equation for the structure tensor, is replaced by the diffusion equation for the distribution function as given in Eqs. 4.34-4.35. Once the distribution function is known, the stress tensor is calculated from Eq. 3.11, rather than Eq. 3.12 which was used to obtain Eq. 4.28. In solving Eq. 4.34 and also evaluating Eq. 3.11 it is useful to write the order S in terms of the Legendre coefficients as

$$\begin{aligned} S &= 3\pi\sum_{n=0}^{M} a_n\int_0^{\pi}(\cos^2\theta-\frac{1}{3})P_n(\cos\theta)\sin\theta\,d\theta \\ &= 2\pi\sum_{n=0}^{M} a_n\int_0^{\pi}P_2(\cos\theta)P_n(\cos\theta)\sin\theta\,d\theta = \frac{4\pi}{5}a_2(\zeta) \end{aligned} \tag{4.37}$$

so that the range of a_2 is limited to $0 \le a_2(\zeta) \le 5/4\pi$. Similarly κ:<uuuu> and <u$\partial\Phi/\partial$u> are expressed in terms of a_n, the difference τ_{zz}-τ_{rr} is evaluated (cf. Eq. 3.11), and the resulting equation is solved for the dimensionless velocity gradient to give

$$De\frac{d\phi}{d\zeta} = \left[\frac{\dfrac{-(T_{zz}-T_{rr})T}{3} - S\left(1-\dfrac{N}{3}\left(-\dfrac{16\pi a_4}{35}+\dfrac{12\pi a_2}{35}+\dfrac{3}{5}\right)\right)}{\dfrac{\beta}{1-\beta}+2\left(\dfrac{8\pi a_4}{35}+\dfrac{8\pi a_2}{35}+\dfrac{1}{5}\right)}\right] \tag{4.38}$$

This result replaces Eq. 4.28 in the fiber spinning model.

Equations 4.26, 4.27, 4.34 and 4.38 are the governing equations for the fiber

spinning problem without the closure approximation. The boundary conditions used are those listed in Eq. 4.31. For $S(0)=S_\varepsilon$, the distribution function is given by Eq. 4.12. The same equation is used to determine the distribution function for the equilibrium condition by setting $\varepsilon\lambda/\sigma$ to zero. Once the distribution function is known at $\zeta = 0$, the initial values of the coefficients $\{a_n(0)\}$ are determined from the orthogonality of the Legendre polynomials. As with the analysis incorporating closure, for the initial condition $S(0)=S_\varepsilon$, the elongation rate at the origin is not known *a priori*, and the initial value of the Legendre coefficients must be solved along with the fiber spinning equations. A shooting method (Press *et al.*, 1986) in conjunction with an ordinary differential equation solver that uses a fourth order Runge-Kutta scheme is used to solve the system of algebraic-differential equations. For De=10, which is the maximum value of the Deborah number for which results are reported in this thesis, 61 even Legendre polynomial terms were used. This required solving a system of 62 coupled, nonlinear differential equations (1 (momentum)+ 1 (stress)+ 60 ($\{a_n(\zeta)\}$); a_0 is known) and one unknown algebraic parameter T which took less than 20 seconds on the STARDENT with a "good" initial guess for the algebraic parameter. Typically, convergence was obtained in 3-5 Newton's iterations for the algebraic parameter.

4.3.3 Results and Discussion

This section begins with a presentation of the steady-state results in which the effects of gravity, surface tension, and inertia are neglected. In addition results are presented only for $\sigma = 0.1$ for which the drag is highly anisotropic. Whereas σ has no effect on the

shape of the viscosity $\eta(\dot{\gamma})$, it has a qualitative effect on the shape of the elongational viscosity $\bar{\eta}(\dot{\varepsilon})$ as demonstrated by Bhave *et al.*. They show that $\bar{\tau}_{\cdot}$ is almost constant for isotropic hydrodynamic drag (corresponding to $\sigma = 1.0$) and is severely extension thinning when the drag is highly anisotropic ($\sigma = 0$ corresponds to fully anisotropic drag). As can be judged from the discussion to follow, the same qualitative behavior is observed in the fiber spinning flow. The nearly constant elongational viscosity for $\sigma = 1.0$ is associated with Newtonian-like velocity and stress profiles, and for this reason velocity, order, and stress profiles are presented only for $\sigma = 0.1$ in this Chapter. The reader interested in the fiber spinning predictions for $\sigma = 1.0$ is referred to Appendix B. Later in this section model comparisons with data for a 40 wt. % hydroxypropylcellulose solution which has a 30 wt.% critical concentration are presented, so a value for the dimensionless concentration that is 4/3 times the critical value is chosen in the ensuing calculations. Hence N=4.0 is taken for the closure model and N=20/3 for the exact model.

In Figs. 4.5a-c and 4.6a-c results are shown for the dimensionless axial velocity ϕ, the order parameter S, and the dimensionless normal stress difference as functions of the dimensionless axial distance ζ for the two initial conditions $S(0) = S_{\dot{\varepsilon}}$ and S_{eq}, respectively. For clarity results are presented only for 3 different values of De, but the range chosen is sufficient to highlight all the important trends. First the effect of the initial condition on these results for the closure model is examined, and then the importance of the closure approximation for the two different initial conditions is studied. In connection with these steady-state results the possibility of using fiber spinning to measure the elongational viscosity is noted. Finally the model predictions are compared with experimental data.

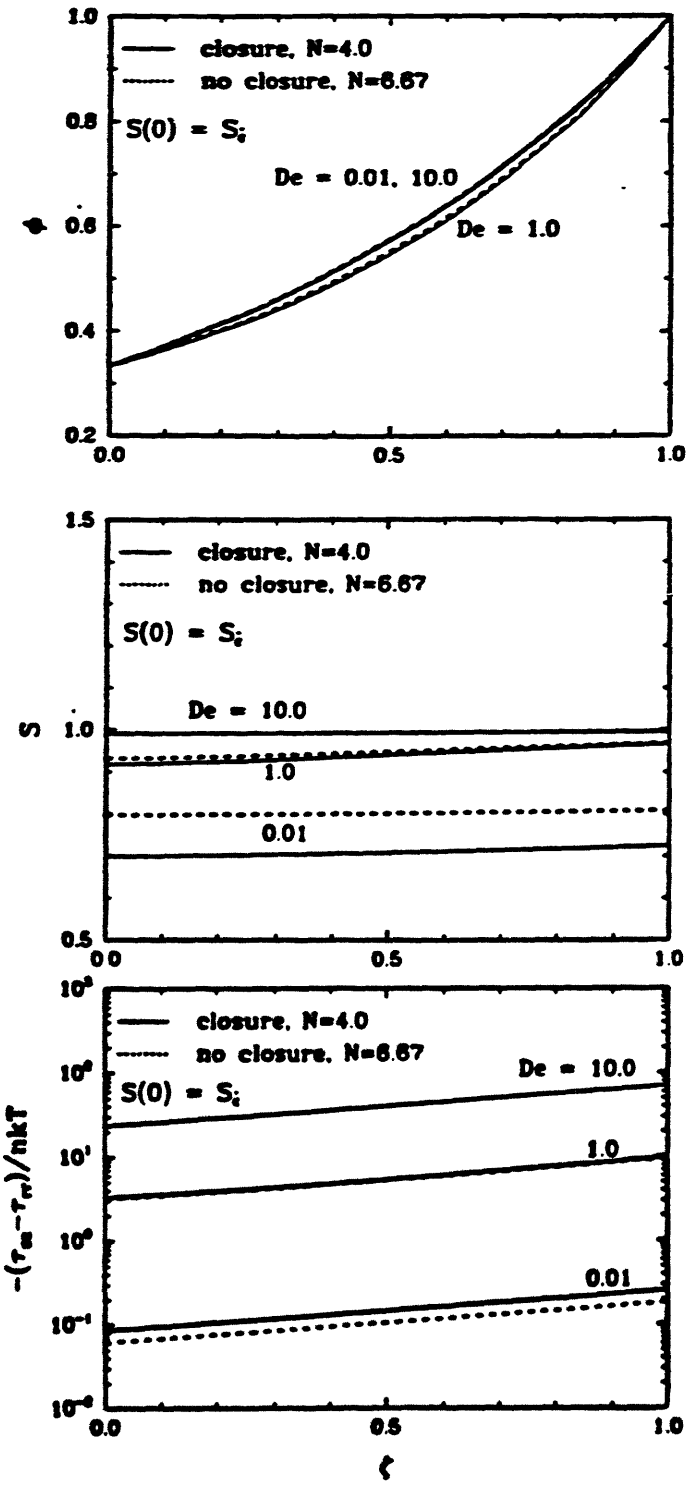

Figure 4.5: Variation of (a) velocity ϕ, (b) order parameter S, and (c) dimensionless normal stress difference $-(\tau_{zz}-\tau_{rr})/nkT$ with distance ζ down the threadline for N/N_c=4/3, σ=0.1, D_R=3.0, and De=0.01, 1.0 and 10. The initial condition for the microstructure is $S(0)=S_c$. Results with and without the closure approximation are shown. Velocity profiles for De=0.01 and 10.0 are indistinguishable.

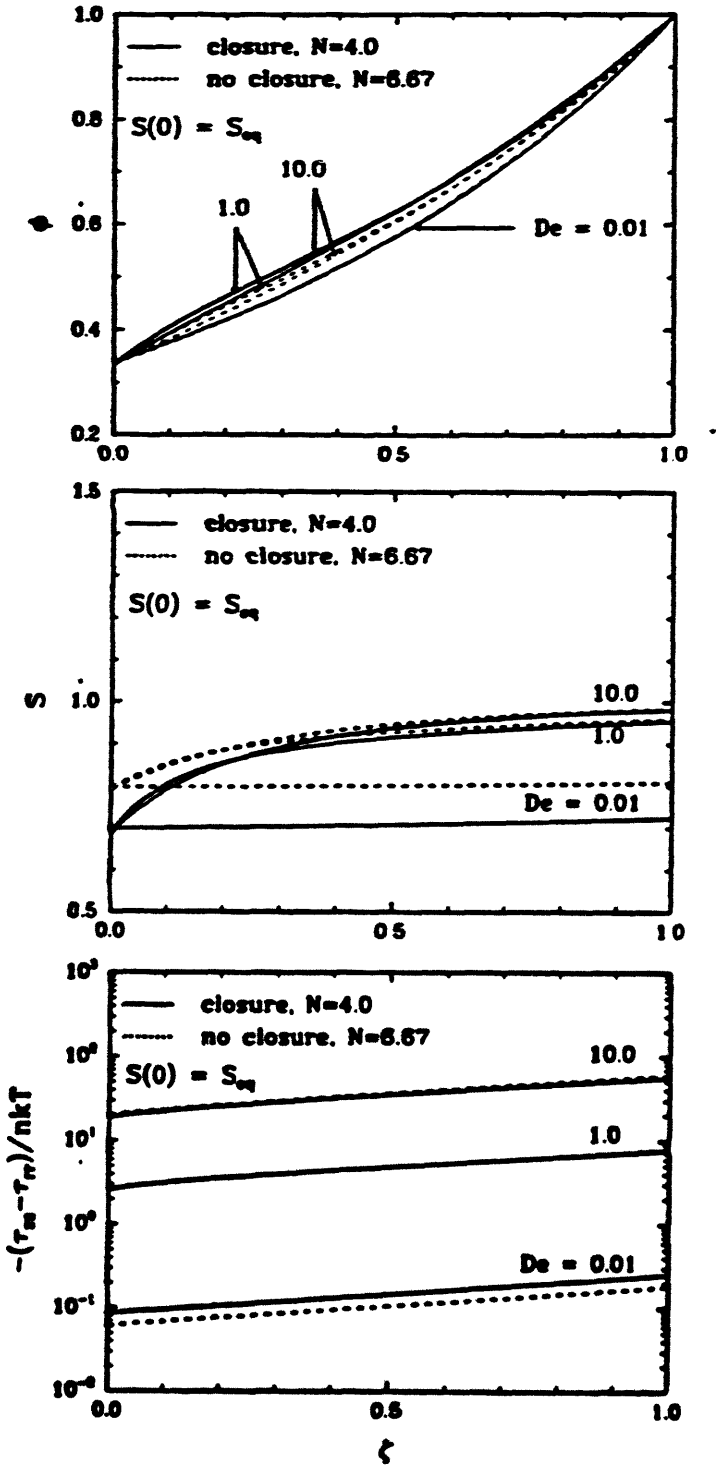

Figure 4.6: Variation of (a) velocity ϕ, (b) order parameter S, and (c) dimensionless normal stress difference $-(\tau_{zz}-\tau_{rr})/nkT$ with distance ζ down the threadline for N/N_c=4/3, σ=0.1, D_R=3.0, and De=0.01, 1.0 and 10. The initial condition for the microstructure is $S(0)=S_{eq}$. Results with and without the closure approximation are shown.

Fig. 4.5a demonstrates that as De increases the velocity profiles become more concave initially, but with further increase in De the profiles become less and less concave and finally become Newtonian. For all De > 10 the velocity profiles are Newtonian. The corresponding order increases with De from the equilibrium value to almost perfect order, and does not show much dependence on ζ. A comparison of Fig. 4.5a with 4.6a and 4.5b with 4.6b, reveals that a change in the initial condition alone affects both the velocity and structure development. For $S(0) = S_{eq}$ as De is increased from zero, the velocity profiles become less concave than the Newtonian limit and remain so for large De's in contrast to the initial condition $S(0) = S_{\varepsilon}$ where they become Newtonian for De $\gg$ 1. The structure development is affected in an obvious way by requiring $S(0) = S_{eq}$. It is interesting that the final order for the fiber with the initial alignment S_{ε}, is slightly higher than that for $S(0) = S_{eq}$, so that the higher degree of initial order in the $S(0) = S_{\varepsilon}$ problem is never fully compensated for in the spinning section of the $S(0) = S_{eq}$ problem. This result is universal for all De studied. Figure 1.1 shows that the tensile modulus is very sensitive to even small changes in the molecular order when the order is close to being perfect, *i.e.* the molecules are predominantly oriented with the fiber axis, whence, the small difference in the order at the end of the spinning section for the two different initial conditions could be significant. Comparing Fig. 4.5c with 4.6c shows that the force required to achieve the same drawdown is also higher for $S(0) = S_{\varepsilon}$. Though not immediately obvious, the force required is as much as 20% higher at large De's. A rigorous comparison of the required spinning forces requires an accurate accounting of the initial diameter of the fiber; in this analysis it is assumed that the initial

radius R_0 is the same, even though the upstream die swell will probably depend on the local order parameter S as well as the tension F itself. From these results it is concluded that the velocity and stress profiles are sensitive to the choice of the initial condition in contrast to results reported for fiber spinning models with isotropic, viscoelastic constitutive equations.

The effect of the closure approximation on the threadline behavior for the initial condition $S(0)=S_\epsilon$ is examined next. There is very little difference in the velocity profiles for all De. For small De, the order is much higher without closure as expected from the equilibrium phase diagram in Fig. 4.2. The higher equilibrium order results in a slightly lower normal stress difference, which is paralleled by the lower elongational viscosity when closure is not used as seen in Fig. 4.3b. For moderate and large De's there is almost no difference in the velocity, structure, and stress profiles.

For the equilibrium initial condition, the velocity profiles obtained with and without closure are in good agreement at low De and have only small quantitative differences at intermediate and high De. As with $S(0) = S_\epsilon$, the order as De $\rightarrow$ 0 is higher without closure. At moderate and high De, the order profiles do not match near $\zeta = 0$ since the equilibrium values are different, but approach one another as $\zeta \rightarrow 1$. Inspite of the lack of agreement in the order at the beginning of the spinning section, the stress profiles show very good agreement at moderate and high De throughout the spinline. The final value of the predicted order is also independent of the closure approximation at moderate and high De. The conclusion is that the closure approximation has only a small effect on the velocity and stress profiles, and hence, in the rest of the

analysis only the closure model is used.

An interesting aside of this study is that it suggests that the fiber spinning flow can be used to measure the elongational viscosity of a liquid-crystal polymer solution. A similar observation was previously made by Mackay and Petrie (1989) for flexible polymers. To see this an apparent elongational viscosity $\bar{\eta}_a$ is defined as the ratio of the normal stress difference to elongation rate at the end of the spinline

$$\bar{\eta}_a = -\frac{(\tau_{zz} - \tau_{rr})_L}{\dot{\varepsilon}_L} \tag{4.39}$$

In Fig. 4.7 the prediction of the constitutive equation for the elongational viscosity $\bar{\eta}$ is compared with the apparent elongational viscosity $\bar{\eta}_a$ defined this way. For draw ratios ranging from 3 to 20 the agreement between $\bar{\eta}$ and $\bar{\eta}_a$ for the two choices of σ is found to be nearly quantitative, independent of initial conditions, suggesting that fiber spinning flows can be used to determine $\bar{\eta}$ for a liquid-crystal polymer solution provided that the normal stress difference τ_{zz}-τ_{rr} can be measured. Note that very nearly the same $\bar{\eta}_a$ is obtained independent of draw ratio. The agreement between $\bar{\eta}_a$ and $\bar{\eta}$ for the rodlike molecules considered in this analysis is much better than that for flexible polymers. It is interesting that for σ = 1.0, $\bar{\eta}_a$ is only slightly extension thickening; and the corresponding threadline velocity profiles are Newtonian. For σ = 0.1, the elongational viscosity shows substantial thinning, but is constant at high and low elongation rates. The velocity profiles in Fig. 4.5a correspondingly show Newtonian behavior at high and low De, and at intermediate De the velocity shows the more concave shape typical of shear thinning, power-law liquids. These observations suggest that, at least qualitatively, the spinning results for the liquid crystal model of Bhave *et al.* can be understood with a

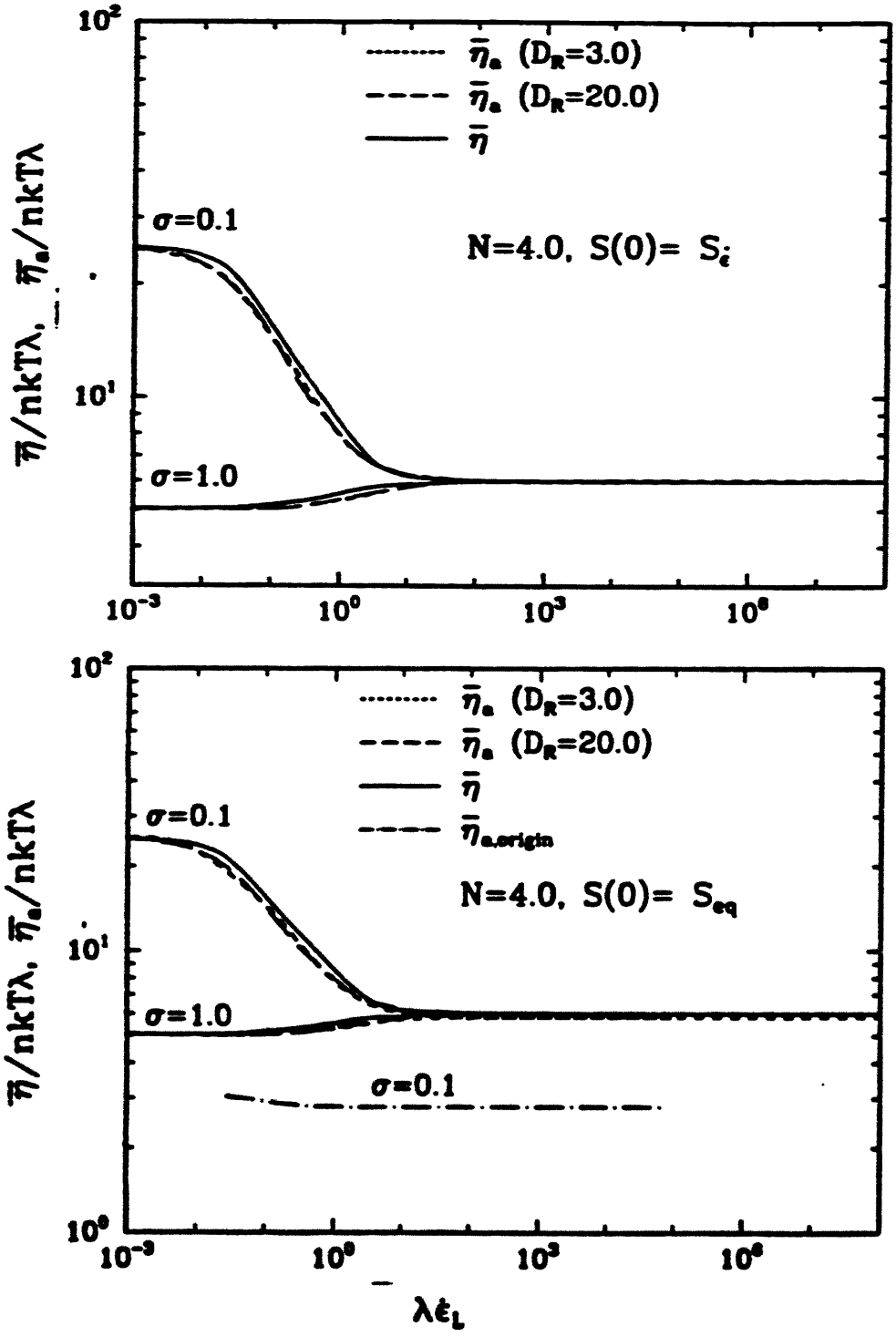

Figure 4.7: Effect of draw ratio on the apparent elongational viscosity $\bar{\eta}_e$ for N=4.0 and σ=0.1 and 1.0 and for the two different initial conditions (a) $S(0)=S_\epsilon$ and (b) $S(0)=S_{eq}$. Results are shown for D_R=3.0 and 20.0. The true elongational viscosity $\bar{\eta}$ for the model of Bhave *et al.* and $\bar{\eta}_{e,origin}$ are shown for comparison.

power-law model analysis in which the shear thinning index n is chosen to match that of $\bar{\eta}_a$ for $\dot{\varepsilon}_L$.

In the definition of $\bar{\eta}_a$ the choice of location for evaluating the normal stress difference and the strain rate is important for getting good agreement between $\bar{\eta}$ and $\bar{\eta}_a$ for the equilibrium initial condition. This sensitivity is illustrated in Fig. 4.7b by plotting $\bar{\eta}_{a,origin}$, which is the ratio of the normal stress difference to the elongation rate at the origin. As can be seen the agreement with $\bar{\eta}$ is very poor. The difference arises because, at the origin, the initial equilibrium order has not adjusted to the elongational nature of the flow. Even for the apparent elongational viscosity based on the exit conditions, there is some deviation from $\bar{\eta}$ at high elongation rates (high De), because the residence time is small and consequently the initial equilibrium order is convected further downstream before any substantial increase in the order occurs to satisfy the exit boundary conditions.

Model predictions of the velocity and normal stress are compared with data of Prilutski in Fig. 4.8 at the indicated concentration for both initial conditions in S. Only the data points downstream from the initial die swell (Prilutski reports a 15% die swell) are considered in order to be consistent with the assumptions in the model. Since the liquid-crystal model predicts an isotropic-nematic phase transition at a dimensionless concentration of $N = 3.0$, and the HPC/acetic acid system undergoes a phase transition at 30 wt.% HPC, a dimensionless concentration of 4.0 is used for the 40 wt. % HPC/acetic-acid solution. In order to calculate the dimensionless group β (Eq. 4.30), the number density n was estimated by using a number averaged molecular weight M_n of 1.67×10^4 and a solution density of 1.07 gm/cc reported by Prilutski. This results in

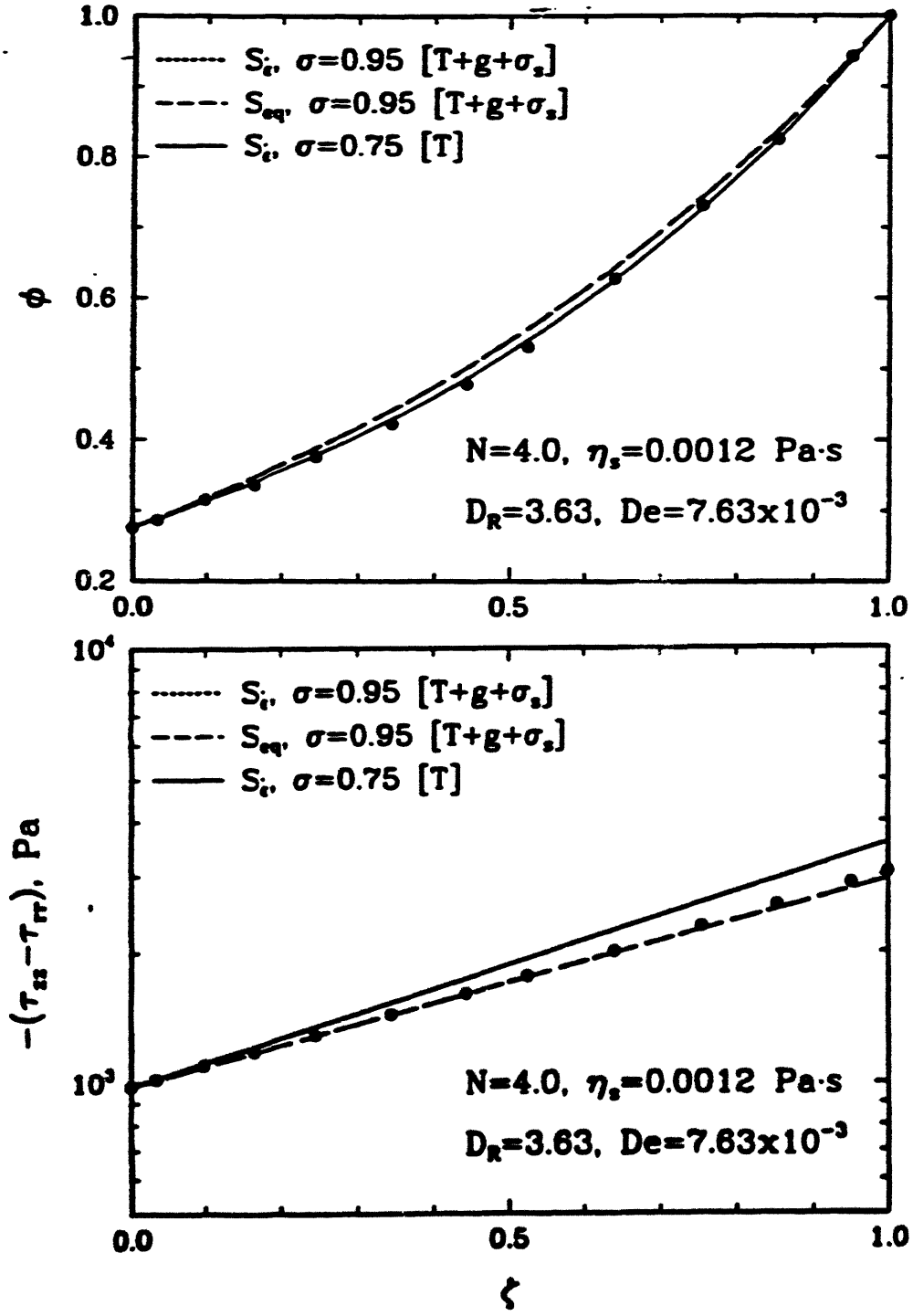

Figure 4.8: Comparison of model predictions with the velocity data of Prilutski (1984) for a hydroxypropyl cellulose solution in acetic acid with N=4.0, D_R=3.63, η_s=0.0012 Pa·s, De=7.63x10^{-3}, σ=0.95 and $S(0)=S_\varepsilon$ and S_{eq}: (a) velocity and (b) normal stress difference. The prediction obtained without including gravity and surface tension is shown for comparison with $S(0)=S_\varepsilon$ and σ=0.75.

nkT=6.28×10^4 Pa for the 40 wt.% solution. Prilutski computes a rotational diffusivity D_r^* of 5.7s^{-1} for Doi's model from his viscometric data, which gives λ of 0.003 s for the constitutive equation we use. Finally, β was found to be 6.4x10^{-6} for a solvent viscosity η_s of 0.0012 Pa-s. The Deborah number and draw ratio are calculated from the fiber spinning data. Since the anisotropic drag coefficient σ cannot be determined from viscosity data, σ is varied until the normal stress difference at the inlet is within the error bounds (±30 Pa) of the experimentally measured value.

Figure 4.8 shows that the model predicts the velocity distribution very well, but not the normal stress difference. Further consideration suggests that for small De, gravity and surface tension are probably important and that the momentum balance should also include these forces. Inclusion of these forces results in much better normal stress difference predictions. The particular choice of initial condition does not seem to alter either the velocity or normal stress predictions because De is very small. Thus available experimental data do not favor one initial condition over the other.

Though the model predictions compare well with the data, it should be kept in mind that all data are at very low De, due to the experimental limitations on the flow rate. Therefore in all of Prilutski's steady-state experiments the elongation rates attained are low enough that the viscosity hardly varies from the zero-elongation-rate-apparent-viscosity $\bar{\eta}_{a,0}$. Consequently a Newtonian model with viscosity $\mu = \bar{\eta}_{a,0}/3$ would fit the data well. Note, however, that a Newtonian model with the viscosity equal to the zero-shear-rate viscosity of the liquid-crystal solution would underpredict the spinline axial stress behavior because the liquid-crystal solution does not obey Trouton's ratio. Larger elongation rates are encountered in the commercial production of polymeric liquid-crystals

because of higher throughputs and shorter spinning lengths. Consequently, De will also be much higher. Data at higher De are needed for a rigorous test of the model.

4.3.4 An Aside - Is the Fiber Spinning Model Developed with Doi's Constitutive Equation "Viscous" in Nature?

In this section the behavior of the fiber spinning equations derived using Doi's constitutive equation is explored in the absence of gravitational, surface tension and inertial effects. The development of the fiber spinning equations parallels the development with the constitutive equation of Bhave *et al.* described in Section 4.3.1. In the absence of gravity, surface tension and inertia the momentum equation given by Eq. 4.26 reduces to

$$T_{zz} - T_{rr} = -\phi \tag{4.40}$$

Doi's expression for the stress tensor is obtained if the solvent viscosity term and the hydrodynamic drag term in Eq. 3.12 are neglected. The stress tensor equation for the fiber spinning model then reduces to

$$T_{zz} - T_{rr} = -\frac{3}{T}S\left(1 - \frac{N}{3}(2S+1)(1-S)\right) \tag{4.41}$$

Doi's equations for the evolution of the structure tensor are obtained if the time constant λ in Eq. 3.14 is replaced by the following expression

$$\lambda = \lambda_0(1 - \frac{3}{2}(S:S))^2 \tag{4.42}$$

and σ is taken to be unity. The evolution equation for the fiber spinning problem is then given as follows

$$\frac{dS}{d\zeta} = (1-S)(2S+1)\frac{d\ln\phi}{d\zeta} - \frac{S}{\phi(1-S^2)^2 De}\left(1-\frac{N}{3}(1-S)(2S+1)\right) \qquad (4.43)$$

Combining Eqs. 4.40 and 4.41 the following algebraic relation between the velocity and order is obtained.

$$\phi = \frac{3}{T}S\left(1-\frac{N}{3}(2S+1)(1-S)\right) \qquad (4.44)$$

Differentiating Eq. 4.44 and substituting the result in Eq. 4.43 gives the following differential equation for S which depends only on S.

$$\frac{dS}{d\zeta} = -\frac{T}{3De}\frac{S(1-\frac{N}{3}(2S+1)(1-S))}{\left(2S^2-1+\frac{N}{3}(1-S)(1-4S^2)(3S+1)\right)(1-S^2)^2} \qquad (4.45)$$

Equation 4.45 along with the entry condition on the velocity, $\phi = 1/D_R$, expressed in terms of the initial order $S(0)$ through the relation given in Eq. 4.44 constitutes an initial value problem for S in terms of the unknown algebraic parameter T. The parameter T is set by the requirement on the exit velocity, $\phi = 1$.

Neglecting gravity, surface tension and inertial effects it is clear from Eq. 4.28 that it is not possible to obtain an explicit relation between ϕ and S for the Bhave *et al.* constitutive equation unlike the Doi model (cf. Eq. 4.44) due to the velocity gradient term, $d\phi/d\zeta$, that arises from hydrodynamic and solvent contribution to the stress. Thus, $S(0)$ cannot be determined from $\phi(0)$ as with the Doi model. Consequently, to solve the fiber spinning equations derived using the Bhave *et al.* constitutive equation, Eqs. 4.26-4.29, an initial specification on the order is required *in addition* to the initial condition on the velocity. Analogously, with isotropic viscoelastic models such as the White-Metzner model (Fisher and Denn, 1976), an initial stress specification is required *in*

addition to the initial condition on the velocity due to upstream memory effects. For the Doi model, the order S along the spinline, and consequently the stress according to Eq. 4.41, are completely specified without having to supply an *additional* initial condition on the order due to the explicit relation between ϕ and S! In fact, this behavior is analogous to the viscous models such as the Newtonian or power-law models where the spinline stress is completely specified by entry and exit conditions on the velocity alone.

The paradoxical "viscous-like" behavior arises from the absence of a term involving the velocity gradient in the stress tensor. The analysis here exposes a serious limitation with Doi's model in the complex fiber spinning flow. The behavior of Doi's model in other complex flow situations must be examined carefully.

4.4 Linear Stability Analysis

Because the steady-state analysis shows little impact of using the closure approximation and because the closed form of the constitutive equation obtained by using the closure approximation is much more convenient to use than the diffusion equation/stress tensor equation pair, the model of Bhave *et al.* is used to study the stability of the fiber spinning flow. The development of the linear stability equations and boundary conditions is presented in Section 4.4.1. Results from the linear stability analysis are presented and discussed in Section 4.4.2.

4.4.1 Governing Equations and Boundary Conditions

The stability of the steady-state fiber spinning to infinitesimal disturbances is determined by linearizing the system of partial differential equations about the steady-state. The dependent variables are allowed to depend on both time and axial position and are distinguished from their steady-state counterparts by denoting the steady-state solutions with a subscript "0"; for example, the steady-state axial velocity v_z is denoted by $v_{z,0}$. The continuity equation is

$$\frac{\partial A}{\partial t} + \frac{\partial}{\partial z}\left(A v_z\right) = 0 \tag{4.46}$$

and the momentum equation has an additional acceleration term

$$\rho\left(\frac{\partial v_z}{\partial t} + v_z\frac{\partial v_z}{\partial z}\right) = \left[-\frac{\partial}{\partial z}(\tau_{zz}-\tau_{rr}) + (\tau_{zz}-\tau_{rr})\frac{\partial \ln v_z}{\partial z}\right] - \frac{\sigma_s}{2}\sqrt{\frac{\pi}{A}}\frac{\partial \ln v_z}{\partial z} + \rho g \tag{4.47}$$

The time derivative of S, which was dropped in the steady-state analysis must be added to the structure evolution equation.

$$\frac{\partial S}{\partial t} + v_z\frac{\partial S}{\partial z} = (1-S)(2S+1)\frac{\partial v_z}{\partial z} - \frac{\sigma S}{\lambda}\left(1-\frac{N}{3}(1-S)(2S+1)\right) \tag{4.48}$$

Finally, the stress tensor equation is unaffected and is still given by Eq. 4.24.

Again it is convenient to solve the momentum equation for the normal stress difference

$$\tau_{zz}-\tau_{rr} = -\frac{F(t)}{A} + \sigma_s\sqrt{\frac{\pi}{A}}\left[1 - 2\sqrt{\frac{A(0,t)}{A(z,t)}}\right] + \frac{\rho g}{A}\int_0^z A\,ds - \frac{\rho}{A}\left[\int_0^z A\left(v_z\frac{\partial v_z}{\partial s} + \frac{\partial v_z}{\partial t}\right)ds\right] \tag{4.49}$$

The primary variables involved in the linear stability equations are A, v_z, and S. Thus each of them, as well as the force F, are written as a small, time-dependent perturbation about the steady-state

$$\begin{aligned} A(z,t) &= A_0(z)\left(1 + a(z)e^{\delta v_L t/L}\right) \\ v_z(z,t) &= v_{z,0}(z)\left(1 + v(z)e^{\delta v_L t/L}\right) \\ S(z,t) &= S_0(z)\left(1 + s(z)e^{\delta v_L t/L}\right) \\ F(t) &= F_0\left(1 + fe^{\delta v_L t/L}\right) \end{aligned} \tag{4.50}$$

where $|a,v,s,f|\ll 1$. Note that a, v, and s depend on z but that f is a constant. The parameter δ that appears in the exponent is the dimensionless eigenvalue.

The same dimensionless scalings as used in the steady-state analysis are introduced next. Retaining terms linear in the perturbation variables gives

$$\phi_0\frac{da}{d\zeta} = -\phi_0\frac{dv}{d\zeta} - \delta a \tag{4.51}$$

$$\phi_0\frac{dv}{d\zeta} = -\frac{d\phi_0}{d\zeta}v - \frac{4S_0^2}{\left(2S_0^2 + \beta/(1-\beta)\right)}\frac{d\phi_0}{d\zeta}s - \frac{\phi_0 T_0(a-f)}{3De\left(2S_0^2 + \beta/(1-\beta)\right)} - 3S_0\left(1 - \frac{N}{3}\left(1 + 2S_0 - 6S_0^2\right)\right)s + \frac{\beta/(1-\beta)}{3\left(2S_0^2 + \beta/(1-\beta)\right)}\times \left[\frac{1}{2Ca}\phi_0^{1/2}(1-4(\phi_0 D_R)^{1/2})a + Re\,\phi_0\left(\left(\frac{1}{D_R} - \phi_0\right)a + \phi_0 v\right) + \frac{Re}{Fr}\phi_0 I_{1,0}(\zeta)a - \phi_0 I_2(\zeta)\right] \tag{4.52}$$

$$\frac{dI_2}{d\zeta} = \frac{\mathrm{Re}}{\mathrm{Fr}\phi_0}a - \mathrm{Re}\left(\delta v + \frac{d\phi_0}{d\zeta}(a+v)\right) \tag{4.53}$$

$$\phi_0 S_0 \frac{ds}{d\zeta} = -S_0\delta s - \phi_0\frac{dS_0}{d\zeta}(v+s) + \frac{d\phi_0}{d\zeta}H_1(v,s,S_0) + \phi_0(1+S_0-2S_0^2)\frac{dv}{d\zeta} + \frac{H_2(S_0)\sigma}{\mathrm{De}}s \tag{4.54}$$

where

$$H_1(v,s,S_0) = v + S_0(v+s) - 2S_0^2(v+2s)$$
$$H_2(S) = S_0\left(-(1-\frac{N}{3}) + \frac{2NS_0}{3} - 2NS_0^2\right) \tag{4.55}$$

In Eq. 4.52, $I_{1,0}$ refers to the steady-state solution to Eq. 4.27.

The eigenvalue δ and the perturbation variables are allowed to be complex. The set of equations is locally stable for $Re\{\delta\} \leq 0$. Thus, the critical draw ratio, $D_{R,crit}$, at which draw resonance first appears corresponds to $Re\{\delta\} = 0$. For all $D_R > D_{R,crit}$, spinning profiles predicted by the model are unstable.

To solve for the 5 complex unknowns, a, v, s, I_2, and δ, 10 boundary conditions are needed. Equations 4.51-4.55 are developed by assuming that draw resonance is caused by a time-dependent variation in the take-up force at a fixed take-up velocity and a fixed extrusion rate. It is further assumed that the degree of extrudate swell is unaffected by the downstream conditions, in which case the cross sectional area in the extrudate swell region will be constant. These assumptions are the same as those adopted by Fisher and Denn (1976) in their analysis for the White-Metzner model. With these assumptions the boundary conditions for a, v, s, and I_2 are

at $\zeta = 0$,

$$\begin{aligned} Re\{a\},\ Re\{v\},\ Re\{s\},\ Re\{I_2\} &= 0 \\ Im\{a\},\ Im\{v\},\ Im\{s\},\ Im\{I_2\} &= 0 \end{aligned} \tag{4.56}$$

at $\zeta = 1$,

$$Re\{v\},\ Im\{v\} = 0$$

It is worth noting that even though the perturbation variables are zero at $\zeta = 0$, their gradients are not zero, because of the forcing term involving the constant f. The absolute value of the arbitrary magnitude of the disturbance f does not affect the critical draw ratio.

The steady-state and linear stability equations were solved simultaneously to determine the critical draw ratio. As with the steady-state equations, a shooting method in conjunction with the semi-implicit Runge-Kutta stiff ordinary differential equation solver was used to determine the critical draw ratio.

4.4.2 Results and Discussion

As mentioned in the introduction, by using an eigenvalue approach to linear stability Gelder (1971) showed that the Newtonian model is unstable for *all* draw ratios greater than 20.21. Shah and Pearson (1972) in their work with the inelastic, power-law model, show that extension thinning ($n < 1$) and thickening ($n > 1$) predict critical draw ratios less than and greater than 20.21, respectively. Also, the more pronounced the extension thinning, the smaller the critical draw ratio is observed to be. This is consistent with the fact that if the viscosity decreases with increasing extension rate along the fiber length, the ability to dampen fluctuations also decreases, thus lowering the stability. A similar

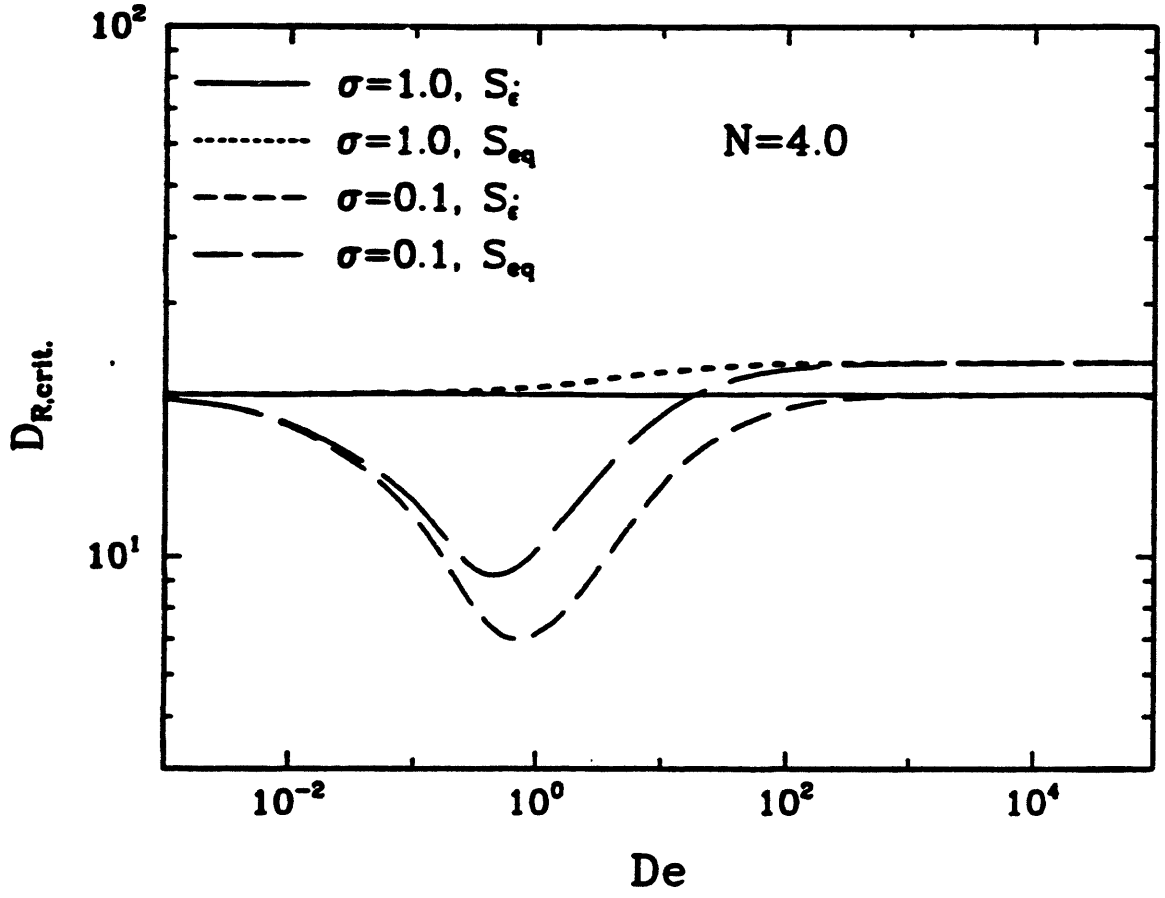

Figure 4.9: Variation of $D_{R,crit}$ with De for N=4.0 and σ=0.1 and 1.0. Results are shown for both $S(0)=S_i$ and S_{eq}.

correlation is observed between $\bar{\eta}_a$ and the stability for the liquid-crystal model.

The dependence of $D_{R,crit}$ on De is shown in Fig. 4.9. First consider the effect of σ on $D_{R,crit}$ for $S(0) = S_\varepsilon$. Recall from Fig. 4.7 that $\sigma = 1.0$ produces a slight extension thickening in the apparent elongational viscosity. Correspondingly, there is very little variation in $D_{R,crit}$ from the Newtonian value as De increases. However, for $\sigma = 0.1$ in the region where $\bar{\eta}_a$ extension thins (note that $\lambda\dot{\varepsilon}_L = De(d\phi/d\zeta)_{\zeta=1}$ varies nearly linearly with De, since $(d\phi/d\zeta)_{\zeta=1}$ does not vary much with De as seen from the velocity profiles in Figs. 4.5a and 4.6a), the critical draw ratio is lower than the Newtonian stability limit of 20.21; and its magnitude depends on the degree of extension thinning. As the apparent elongational viscosity approaches a constant limiting value at large elongation rates, $D_{R,crit}$ increases and finally reaches the Newtonian stability limit. A similar correlation between $\bar{\eta}_a$ and $D_{R,crit}$ is observed for $S(0) = S_{eq}$ except at the high De asymptote where $D_{R,crit}$ is greater than the Newtonian stability limit. The reason for the departure is possibly associated with an increase in the elongational viscosity down the spinline at high De.

Next consider the effects of surface tension, gravity, and inertia on stability. Comparisons with the steady-state experimental data showed that surface tension and gravity are important at least at low De. In addition, inertial effects are probably important at high De. Recall that Shah and Pearson (1974) studied the stability to infinitesimal disturbances in the inlet velocity with the take-up force held constant for a Newtonian fluid. They showed that whereas inertia and gravity are stabilizing, surface tension is destabilizing. Chang *et al.* (1981) also studied the effect of inertia, gravity, and surface tension on the stability of a Newtonian fluid, but to infinitesimal disturbances in

the take-up force in which the inlet and take-up velocities are kept fixed, and obtained the same qualitative trends. However, they demonstrate that the results of Shah and Pearson overpredict the stabilizing effect of gravity and underpredict the destabilizing effect of surface tension, which indicates that the onset of draw resonance is more sensitive to fluctuations in the take-up force than the inlet velocity. The stability of the Newtonian fluid to infinitesimal disturbances in the take-up force was also studied in this analysis in order to obtain a basis of comparison for the stability of the liquid-crystal model at small values of the Deborah number. The results so obtained agree well with those reported by Chang *et al.* (1981).

The stability of the liquid-crystal model for $\sigma = 1.0$, when inertial, gravitational and surface tension effects are taken into account, is shown in Fig. 4.10 for several values of De. Whereas the exit conditions are used to define the dimensionless groups in this analysis, Shah and Pearson (1974) and Chang *et al.* (1981) employ the inlet conditions. Transformation from one basis to the other can be easily made through Eq. 30 and by recognizing that the Weber number, We, is defined as $(\rho v_L^2)/(\sigma_s/2R_L)$. As with the Newtonian model, inertia and gravity are stabilizing, whereas surface tension is destabilizing. The Newtonian limit is reproduced at low De as expected, provided that the zero-elongation-rate elongational viscosity, $\bar{\eta}_0$, is used to define the dimensionless groups Re, Re/Fr and Rc/We. The agreement with the Newtonian results is not quite as good if $3\eta_0$ is used to define these dimensionless groups, as Shah and Pearson (1974) and Chang *et al.* (1981) did in their analyses of the Newtonian model; the underlying reason for this difference is that, whereas the Newtonian elongational viscosity obeys the Trouton

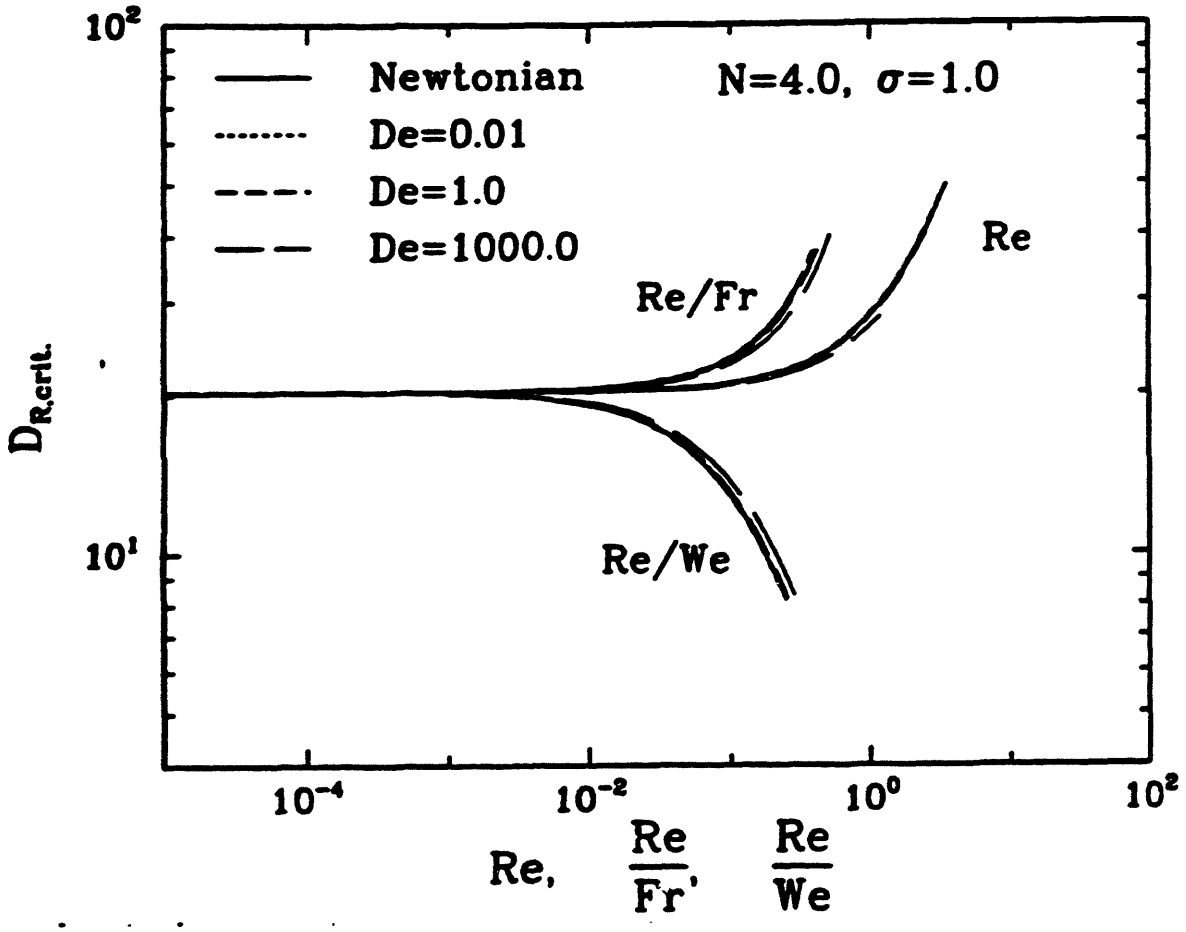

Figure 4.10: Variation of $D_{R,crit}$ with Re, Re/Fr and Re/We for N=4.0, σ=1.0, and De=0.01, 1.0, and 1000. The Newtonian neutral stability curves are shown for comparison. For the liquid-crystal results $S(0)=S_t$.

formula, $\bar{\eta}$ for the liquid-crystal model does not. It is interesting that the stability behavior shown in Fig. 4.10 changes very little with De, which may not be surprising given that the Newtonian stability limit is preserved for all De with σ=1.0, as discussed previously in connection with Fig. 4.9. For other choices of σ, say σ=0.1, the effect of De on a stability diagram such as Fig. 4.10 is certainly tangible. Since the critical draw ratio in the limit of zero Re, Re/Fr and Re/We varies with De for σ = 0.1 (cf. Fig. 4.9), the critical draw ratio for some finite, but equal, value of the dimensionless groups Re, Re/Fr and Re/We would necessarily be different from the Newtonian limit (small De) at least for moderate values of De, because of the predicted extension thinning effect on the stability.

Prilutski (1984) has reported $D_{R,crit}$ values for three different final stretch rates. The data are shown in Fig. 4.11 along with the linear stability prediction of the model. The drop in $D_{R,crit}$ from 18.18 to 4.8 over a narrow range of $\dot{\varepsilon}_L$ is significant. Surface tension might be expected to play a role in the destabilization. However, the dimensionless group Re/We is inversely related to De for fixed R_0. Thus the destabilizing effect of surface tension is insufficient, since Re/We is of order 0.1 for De = 0.01 (cf. Fig. 4.10) encountered in the steady-state experiments; and De $\gg$ 0.01 in the stability experiments (Prilutski, 1991). Consequently the destabilization must be an extension thinning effect. However, in the steady-state experiments very little extension thinning was observed, since high elongation rates were never reached. Since the flow rates and the lengths of the spinline at which the critical draw ratios were determined are not known, a comparison is attempted by considering two different scenarios by which draw resonance can be obtained experimentally: (1) increase the flow rate while keeping the

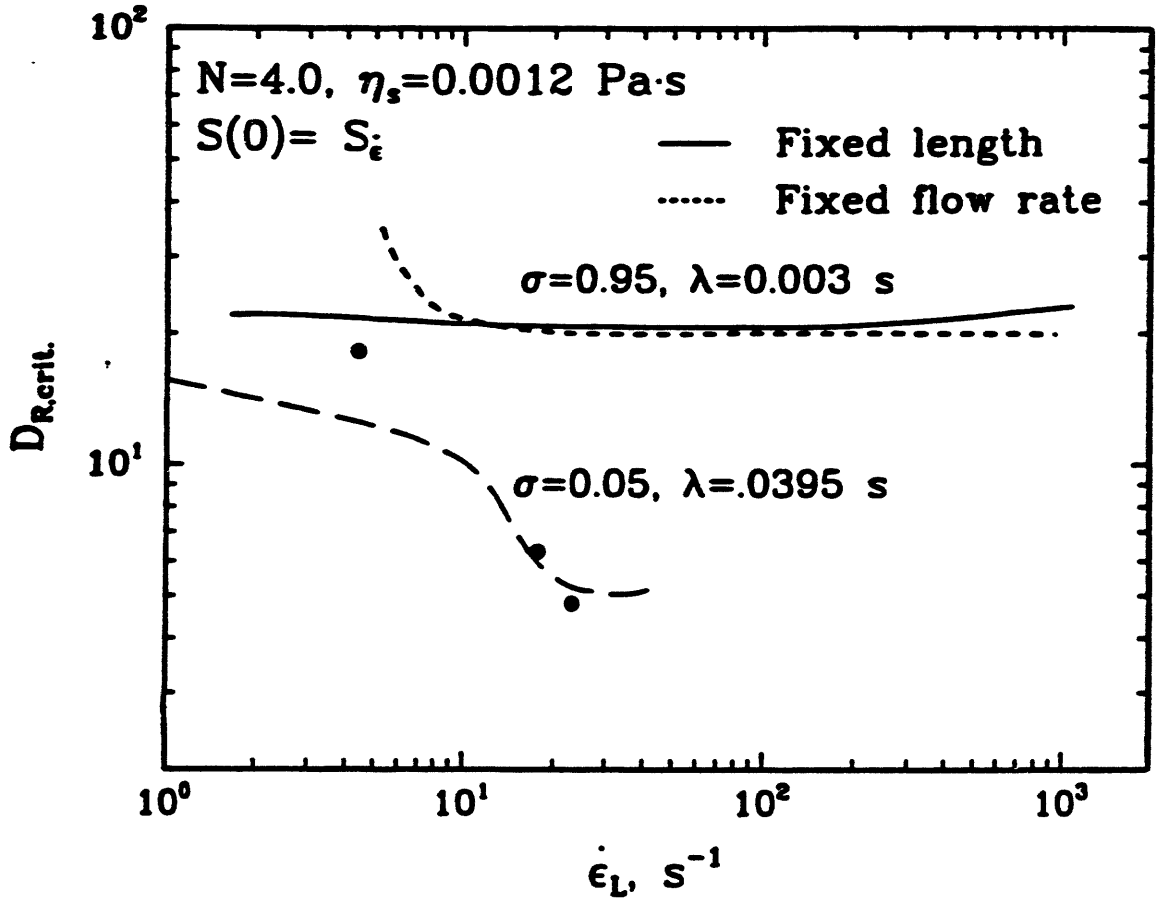

Figure 4.11: Comparison of model predictions for (a) fixed length, L=0.0341 m and (b) fixed flow rate, Q=1.99x10^{-6} m^3/s with the critical draw ratio data of Prilutski (1984) for a hydroxypropyl cellulose solution in acetic acid. Parameter values are N=4.0, σ=0.95 and η_s=0.0012 Pa·s. The initial condition is $S(0)=S_{\dot{\epsilon}}$. Best fit values of σ and λ are shown for comparison.

length fixed and (2) decrease the length while keeping the flow rate fixed. In the first situation the length is assumed to be the same as that in the steady-state experiment with which we have compared our model predictions. In the second situation the flow rate is assumed to be the same as that in the steady-state experimental data. Model parameter values are those determined from the comparison with the steady-state experimental data. Figure 4.11 shows that the comparison with the data is poor for both situations. As evident from Fig. 4.9, a much lower value of σ would be required to predict the observed extension thinning instability. Next an attempt was made to find values of σ and λ for which the comparison with the data is good, provided that the effects of gravity, surface tension, and inertia are ignored. It can be seen that for σ of 0.05 and a λ of 3.95×10^{-2} s the neutral stability curve fits the data well. No attempt was made to determine the neutral stability behavior beyond an elongation rate of 40 s^{-1}, since no data exist in that region. However, the critical draw ratio increases beyond an elongation rate of 30 s^{-1}, and it is expected to approach the Newtonian value at high elongation rates. Prilutski reports good agreement with his draw resonance data by using Doi's constitutive equation. However, in his analysis Prilutski replaces Doi's model with an equivalent generalized Newtonian fluid model with a variable power-law index n where n is determined from the dependence of $\bar{\eta}$ on $\dot{\varepsilon}$. Menon (1990) shows that $\bar{\eta}$ for Doi's model is a constant at small values of $\dot{\varepsilon}$ but extension thins at intermediate and high values of $\dot{\varepsilon}$; in fact, at high values of $\dot{\varepsilon}$, $\bar{\eta}$ extension thins sharply according to Eq. 3.18. Thus, according to the power-law analyses of Shah and Pearson (1972) and Kase (1985), $D_{R,crit}$ is constant at the Newtonian value of 20.21 for small values of $\dot{\varepsilon}$, but decreases sharply to 1.0 for high values of $\dot{\varepsilon}$ when $\bar{\eta}$ extension thins at a power-law index of 0.0 according to Eq. 3.18.

Consequently, good agreement with the data is obtained by Prilutski. Note, however, that Prilutski's analysis does not include memory effects which is important in modeling LCP flows as indicated by the steady state results. In addition, the experimental data at the onset of draw resonance are not well characterized; that is, the flow rate, spinline length and spinline tension at the onset of draw resonance are not known. Well characterized experimental data at the onset of draw resonance is necessary to accurately judge the model predictions. To the best of our knowledge, the stability analysis presented here is the first for the full liquid-crystal constitutive equation.

4.5 Conclusions from Fiber Spinning Analysis

By using the constitutive equation of Bhave *et al.* (1993) for nematic rodlike liquid-crystalline polymer solutions, isothermal fiber spinning models with and without the closure approximation that predict the development of microstructure, velocity, and normal stresses along the spinline were developed, and the effect of two different initial microstructural conditions on the spinning process was examined. A linear stability analysis of the fiber spinning equations was also carried out to predict the onset of instabilities such as draw resonance. The steady-state results show that velocity, structure, and stress profiles are sensitive to the choice of the initial condition. The closure approximation has only a small effect on the velocity and stress profiles and appears to give reasonably accurate results for the prolate, uniaxially symmetric fiber spinning model. Model predictions agree well with the steady-state data of Prilutski (1984) for the hydroxypropylcellulose (HPC)/acetic acid system, but the data are for small De and

consequently do not conclusively support one initial microstructural condition over the other. Linear stability predictions in which the model parameters are determined from the comparison with the steady-state data and values for the unknown length of the spinline (varying the flow rate) or the flow rate (varying the length of the spinline) are assumed, are poor. The critical draw ratio is overpredicted by an order of magnitude at higher elongation rates. Good quantitative agreement is obtained only if the time constant λ is roughly 10 times that in shear flow and the anisotropic drag parameter σ is a factor of 20 smaller than the value that fits the steady-state fiber spinning data. Another interesting result of this study is that the apparent elongational viscosity defined by Eq. 37 compares well with the elongational viscosity $\bar{\eta}$ predicted by the constitutive equation, thereby suggesting that the fiber spinning flow can be used to determine $\bar{\eta}$ for a liquid-crystal polymer solution. In addition, the neutral stability curve constructed from a power-law approximation to the apparent elongational viscosity curve, gives a good estimate of the neutral stability curve determined by solving the full linear stability equations.

In the spinning of liquid-crystalline polymer solutions where the spinline distance over which the polymer solution can be regarded as isothermal or over which the concentration can be regarded as constant is extremely small, the one-dimensional, small slope approximation is questionable. The one-dimensional approximation also assumes cross-sectional homogenity in the order, velocity and stress. Moreover, the one-dimensional simulations presented here suggest that upstream conditions are important. It becomes necessary then to develop a two-dimensional, numerical model for the fiber spinning problem which couples to the upstream spinneret flow. Two-dimensional flow

calculations through the spinneret, which constitutes the upstream portion of the fiber spinning process, are discussed in Chapters 5 and 6.

4.6 Direct Solution of Diffusion Equation: A Comparison of Legendre Polynomial Expansion Technique (LPET) with the Double Lagrangian Method (DLM) of Szeri and Leal

The effect of closure approximation for rigid rod models has been the object of much study lately (for e.g. Advani and Tucker, 1987; Kamal and Mutel, 1989; Altan *et al.*, 1989; Larson and Öttinger, 1991; and Szeri and Leal, 1993). As mentioned in Section 3.2.2 Larson and Öttinger (1991) show that use of the closure approximation results in the evolution equation's not describing physical phenomena such as molecular tumbling at low shear rates in a steady shear flow of a concentrated liquid-crystalline polymer solution. The approximation poses few problems in elongationally dominated flows and does not modify any physical phenomena, at least for prolate molecular orientation about the stretching axis as demonstrated in Sections 4.2 and 4.3. A more serious problem associated with the closure approximation is the appearance of spurious negative values in the distribution function as demonstrated by Szeri and Leal (1993) for a planar Couette flow of a dilute solution of rigid rods. Moreover, a statistically averaged quantity such as the structure tensor S, which is a measure of the variance in the order, could hide significant local information about the distribution density in orientation space if the distribution density is skewed about the maximum value or exhibits other complex phenomena such as secondary local peaks in the distribution. Though the distribution

function provides useful information about the local orientation of the particles, the solution of the diffusion equation could be computationally prohibitive for complex flows especially with standard finite-difference schemes such as the one used by Kamal and Mutel (1989). More sophisticated methods are the double Lagrangian technique of Szeri and Leal (1993) used to solve the planar Couette flow of a dilute suspension of rigid rods and the LPET discussed in Section 4.3.2 in connection with the fiber spinning of concentrated liquid-crystalline polymer solutions. In the ensuing paragraphs the bases behind the two methods are contrasted and their merits and demerits are discussed briefly.

The double Lagrangian method employed by Szeri and Leal is addressed as such since it is Lagrangian in orientation space and physical space. The technique is Lagrangian in orientation space since it tracks a particular particle trajectory in orientation space. It is Lagrangian in the physical space since it tracks the distribution function associated with a fluid element in physical space. In contrast the LPET uses the conventional Eulerian form of the diffusion equation. That is, instead of tracking particle trajectories, it conserves the number of system or material points as they move through a particular region of orientation space. The evolution of the distribution function is also Eulerian in physical space.

Let $\mathbf{u}_0$ be the orientation vector associated with a particle at time t=0. At a future time t, the orientation of the particle, $\hat{\mathbf{u}}(t,\mathbf{u}_0)$, is determined by solving the following partial differential equation for the map between the initial and deformed configurations in orientation space (Szeri and Leal, 1993):

$$\frac{\partial \hat{u}}{\partial t} = \Omega\cdot\hat{u} + G[\dot{\gamma}\cdot\hat{u} - \dot{\gamma}:\hat{u}\hat{u}\hat{u}] - D_0 \det(\nabla_0\hat{u})\nabla\left[\frac{1}{\det(\nabla_0\hat{u})}\right] \tag{4.57}$$

G is a particle shape factor, Ω is the vorticity tensor, and D_0 is the Brownian diffusivity. The distribution function associated with a fluid element in physical space, $f^*(t,\mathbf{u}_0)$ is tracked by the following equation

$$\frac{f^*(t,u_0)}{f^*(0,u_0)} = \frac{1}{\det(\nabla_0\hat{u}(t,u_0))} \tag{4.58}$$

which is a Lagrangian form of the conservation statement for the distribution function. The Eulerian form of the distribution function, $f(t,\mathbf{u})$ and the Lagrangian form of the distribution function $f^*(t,\mathbf{u}_0)$ are related by the definition

$$f^*(t,u_0) = f(t,u)|_{u=\hat{u}(t,u_0)} \tag{4.59}$$

Calculation of the stresses for an initially isotropic orientation ($f^*(0,\mathbf{u}_0)=1/4\pi$) requires integral moment evaluations such as

$$\langle uu\rangle(t) = \int f^*(t,u_0)\,uu\,du = \frac{1}{4\pi}\int \hat{u}(t,u_0)\hat{u}(t,u_0)\,du_0 \tag{4.60}$$

The stresses are coupled to the mass and momentum transport equations in the solution of flow problems.

By simply releasing a set of particles, whose initial distribution of orientations is known, their orientations are allowed to evolve in a natural way according to Eq. 4.57. At a later time, more particles will be concentrated where sharp peaks in the orientation are encountered and few where they are not. In the evaluation of moment integrals, such as Eq. 4.60, a higher resolution will result where the integrand is large numerically and a lower resolution will result where the integrand is small numerically. Thus, the

reformulation of the governing equations in a Lagrangian form allows the double Lagrangian method to determine the discretized form of the coordinate map $\hat{\mathbf{u}}(t,\mathbf{u}_0)$, and hence the moment integrals, in a self-adaptive way. In contrast, the LPET cannot be selective about the number of Legendre polynomials required to depict sharp and non-sharp peaks in the distribution function. If both sharp and non-sharp peaks are encountered many polynomials are wastefully employed in depicting non-sharp or sparsely populated regions. Equations for the evolution of different initial orientations are decoupled in the double Lagrangian method which makes it easy to parallelize the solution of these equations. With LPET the evolution equations for the Legendre coefficients are coupled.

LPET also has its advantages. In flow problems, the solution of the momentum conservation equation is coupled with the difffusion equation through the stress tensor. The stress and other statistical measures of the order require numerical evaluation of the integral moment equations with the double Lagrangian method, whereas, the moment evaluations, though complicated, are expected to be analytical for many flow situations with LPET. In the double Lagrangian method the stress associated with a fluid element is calculated in a way that is Lagrangian in physical space (cf. Eq. 4.60). This information must then be coupled with the macroscopic flow equations which are generally solved in an Eulerian frame of reference. In the planar Couette flow, the fluid elements trace parallel trajectories in the flow direction, say, the x-direction; that is, the flow is transationally invariant. Thus, tracking the fluid elements (and the associated stress) through physical space is not an issue and a grid in the gradient direction, the y-

direction, that gives an adequate numerical representation for the divergence of the stress that appears in the macroscopic momentum equation at time t=0 is expected to be adequate at a later time t. However, most complex flows are not transationally invariant. A situation may arise in a flow where the fluid elements are "close enough" at time t=0 to provide an adequate approximation to the divergence of the stress but are "not close enough" at a later time t to provide an adequate approximation to the divergence of the stress; that is, the discretization in physical space at time t is coarse. It may be necessary, then, to introduce more fluid elements at time t=0 so that a refined enough discretization in physical space can be achieved at time t. This can lead to wasteful discretization where it is not needed; for example at time t=0. Thus, the double Lagrangian method may not be easily amenable to local discretization in the physical domain. In contrast, LPET is amenable to local refinement in the physical domain.

It would be interesting to first make a quantitative evaluation of the two methods by performing a direct calculation of the planar Couette flow using a spherical harmonic expansion since results already exist with the double Lagrangian method. The two methods then need to be compared in more complex flows that are not translationally invariant and where local refinement in the physical domain are expected to improve computational efficiency. The possiblity of using expansion techniques that use wavelets or other basis functions which minimize the number of terms required to capture sharp peaks in the orientation distribution also needs to be explored.

Chapter Five

Two-dimensional Flow Problems

Most processing flows of interest, such as extrusion flows, flows through contracting dies and injection molding flows, are not simple flows, but mixtures of shear and extensional flow components in different proportions. These complex flows, unlike simple shear and extensional flows, are governed by sets of nonlinear partial differential equations, which in general must be solved numerically with techniques such as finite-element methods (FEM) or finite-difference methods. The equation set to be solved for the liquid-crystalline flow problem is composed of the equation of conservation of mass, the equation of conservation of linear momentum, and the constitutive equation which comprises the evolution equation for the structure tensor and the equation for the stress tensor which relates the stress in the fluid to the velocity gradient and the structure tensor.

The numerical solution of similar equation sets for viscoelastic flow problems had met with failure until King *et al.* (1988) showed that the primary cause of these difficulties was associated with using numerical methods not consistent with the mathematical type of the system of equations. They showed that an understanding of the interaction between the mathematical type of the equations and the numerical procedure employed is essential to the development of stable and convergent FEM algorithms. The governing equation set has six characteristics associated with the six canonical variables for the equation set: two imaginary characteristics associated with incompressibility, two

real streamwise characteristics associated with the normal stress components, and two characteristics associated with the components of the momentum equation that may change type from imaginary to real for flows with inertia (Joseph *et al.*, 1985). The Explicitly Elliptic Momentum formulation (EEME) of King *et al.* (1988) respects the mathematical type of the equations. The momentum equation is written in terms of a second-order partial-differential operator that is elliptic when the change of type has not occurred. Using the EEME formulation, King *et al.* (1988) computed stable and accurate solutions for steady viscoelatic flows of an Upper-Convected Maxwell (UCM) model between concentric and eccentric cylinders with the inner cylinder rotating, and for steady flow of a UCM fluid between a stationary inner ellipse and a rotating outer cylinder (King, 1987).

For an Oldroyd-B model, the stress is the sum of a polymer contribution and a solvent contribution. The polymeric contribution is described by the UCM model and the solvent contribution is described by the Newtonian model. Consequently, an Oldroyd-B model reduces to the UCM model in the limit of zero solvent viscosity. Joseph *et al.* (1985) found that the mathematical type of the system of equations governing a two-dimensional flow described by the Oldroyd-B model is qualitatively different than in the limit of zero solvent viscosity. Including the solvent viscosity introduces higher-order derivatives into the equation set, and the seven canonical variables associated with the equation set governing flow are: the pressure, the three components of the velocity gradient tensor and the three components of the polymeric part of the deviatoric stress tensor. The corresponding characteristics are: two imaginary characteristics associated

with incompressibility, two more imaginary characteristics associated with the components of the momentum equation and three real streamwise characteristics associated with the components of the polymer part of the stress tensor. Consequently, the inclusion of a Newtonian solvent contribution changes the mathematical type of the equations governing a two-dimensional flow. Rajagopalan *et al.* (1990) developed the Elastic-Viscous Split Stress (EVSS) formulation that respects the mathematical type of the system of governing equations even for viscoelastic constitutive models with a non-zero Newtonian solvent viscosity. An elliptic operator is constructed for the momentum conservation equation by extracting a viscous contribution from the polymeric part of the stress in addition to the Newtonian viscous contribution from the solvent part of the stress. Using the EVSS formulation Rajagopalan *et al.* (1990) computed stable and convergent solutions for the steady flow of an Oldroyd-B fluid between eccentric cylinders with the inner cylinder rotating and for steady flow through an axisymmetric corrugated tube.

Mixed finite element methods for computation of viscoelastic flows governed by differential constitutive equations vary not only in the formulation but also in the polynomial approximations used for the velocity, pressure and stress fields. Computations of the linear stability of the UCM model in a homogenous, rectilinear shear flow by Brown *et al.* (1993) revealed that the frequently used biquadratic polynomial approximation to the velocity and the stresses and bilinear approximation to the pressure predict a fictitious numerical instability beyond a critical value of De with either the EEME or the EVSS formulation. In fact theoretical results demonstrate that this flow is always stable. Brown *et al.* (1993) developed the EVSS-G formulation for which the

numerical instability disappears; linear stability calculations for the homogenous, rectilinear shear flow are stable to values of De in excess of 50 and converge with mesh size and time step. The EVSS-G formulation differs from the EVSS formulation in that it includes smooth interpolation of the velocity gradient tensor which is compatible with a bilinear approximation to the stress tensor, as opposed to the interpolation of the rate-of-strain tensor and a biquadratic approximation to the stress tensor. The EVSS-G formulation is described in greater detail in Section 5.3.2.

The boundary conditions imposed on the flow domain for a boundary-value problem must also respect the mathematical type of the governing equations. Menon (1990), paralleling the analysis of Joseph *et al.* (1985) for an Oldroyd-B model, studied the mathematical type of the system of PDE's governing two-dimensional flows of liquid-crystalline polymer solutions described by the constitutive equation presented in Section 4. The results from the analysis are discussed in Section 5.1.2.

A description of the flow through a spinneret, which can be represented simplistically by the flow through an axisymmetric contraction (cf. Fig. 5.1), is presented in Section 5.2. Studying such a flow is crucial to the processing of liquid-crystalline polymers. The unique strength of LCP's such as Kevlar, which possess a modulus comparable to steel but at one-fifth the weight, result from the high degree of molecular orientation present in the final product. In a LCP fiber most of the orientation results from the contraction flow through the spinneret and the spinning process that follows. Consequently, it is very important to understand the interplay between the polymer flow and the development of molecular orientation during extrusion and spinning to predict and

control the properties of the final product.

The axisymmetric flow geometry we have chosen, which is shown in Fig. 5.1, has some inherent advantages. The contraction boundaries are smooth and tapered, in contrast with the flow through an abrupt contraction (Yeh *et al.*, 1984, Coates *et al.*, 1992) or a tapered contraction with sharp corners at the junctions upstream and downstream. It is clear from Eq. 3.12 that the asymptotic singular behavior in the stresses near sharp corners must be the same as the velocity gradient, *i.e.* Newtonian-like, since the components of the structure tensor S are bounded. The asymptotic analysis first performed by Dean and Montagnon (1949) and later extended by Moffatt (1964) for an inertialess Newtonian flow near a sharp corner reveals that the asymptotic singular behavior in the stresses and pressure in a tapered contraction with sharp corners is weaker than the singular behavior in the stresses and pressure in an abrupt contraction close to the reentrant corner. However, the local velocity gradient at the reentrant corner is still *infinite* which leads to drastic changes in the solution field around the corner. In fact, due to the high shear rates which exist on the upstream and downstream wall boundaries close to the corner, the polymer molecules are aligned parallel to respective boundaries. Consequently, the components of the structure tensor are degenerate at the sharp corner which makes it difficult to obtain convergent results even for a 2:1 contraction at moderate or high concentrations. Smoothing the corners overcomes this problem and allows the computation of the solution field to higher contraction ratios at all concentrations.

The mathematical type of the equations governing the steady two-dimensional flow

of a LCP solution modeled by the closed form of the constitutive equation presented in Chapter 3 is similar to the mathematical type of the system of equations governing the flows of polymer solutions modeled by the Oldroyd-B or the Giesekus constitutive equations as demonstrated by Menon (1990) (cf. Section 5.1.2). Consequently, a finite element formulation based on the EVSS-G formulation of Brown *et al.* (1993) is used. The important features of the EVSS-G formulation are described in Section 5.3.2. The finite element method used for the liquid-crystalline flow problem is also presented in this section.

5.1 Mathematical Type of Equations Governing LCP Flow

Menon (1990) studied the mathematical type of the system of equations governing the steady two-dimensional flow of a LCP solution modeled by the constitutive equation presented in Chapter 3 in a manner similar to the approach used by Joseph *et al.* (1985) to determine the mathematical type of the equation sets governing the two-dimensional viscoelastic flows modeled by the UCM and Oldroyd-B constitutive equations. The governing equations are first reduced to a system of first-order quasilinear partial differential equations. The characteristic curves which reveal information about the mathematical type of the equation set are then determined by using a standard procedure described in texts by Whitham (1973) or Carrier and Pearson (1988). A brief description of this method is presented in Section 5.1.1. The method assumes that at least some of the characteristics are real *i.e.* the system of equations may all be hyperbolic or of mixed hyperbolic and elliptic character. The method cannot be used directly to determine the

characteristics of a system which is totally elliptic.

5.1.1 Classification of a System of Quasilinear, First-Order, Partial Differential Equations

A general quasilinear first-order system of partial differential equations can be written as

$$\sum_{i=1}^{n} A_i \frac{\partial u}{\partial x_i} = f(x,u) \tag{5.1}$$

where $\mathbf{u} = (u_1, u_2, \ldots u_k)$ is a k-dimensional vector comprising the canonical variables and A_i is a $k \times k$ matrix which like the inhomogenous vector f may depend on the components of x and $\mathbf{u}$. If A_i is independent of $\mathbf{u}$ and f is either linearly dependent or independent of $\mathbf{u}$ then Eq. 5.1 is a linear system.

The characteristics of the equation set 5.1 are defined as curves along which the equations can be transformed to ordinary differential equations in a coordinate system with components parallel and orthogonal to the characteristic curves. The prescription of Cauchy data along a characteristic is insufficient to permit the determination of the solution field in areas adjoining the characteristic (Carrier and Pearson, 1988). Cauchy's theorem of causality governs the well-posedness of an initial value problem. From the definition of a characteristic it follows that data prescribed along the characteristic curve, $\phi(x_1, x_2, \ldots) = \text{constant}$, violate the theorem. Consequently, the characteristic curves for Eq. 5.1 are determined from the converse of the causality theorem, which is written as

$$\det\left(\sum_{i=1}^{n} A_i \frac{\partial \phi}{\partial x_i}(x)\right) = 0 \tag{5.2}$$

The application of the theorem of causality assumes evolutionary character of the equation

set 5.1 and consequently possesses at least one family of real characteristics.

There is a possibility that some or all of the matrices A_i in Eq. 5.1 are singular. This indicates that some of the original coordinate axes are characteristics. Yet in some cases where all matrices A_i are singular, the system of equations are so degenerate that they must be excluded. If the trouble is merely that the original axes coincide with characteristics, a rotation of the axes will lead to nonsingular matrices (Whitham, 1973). This replaces the original matrices A_i by a linear combination of these matrices so that

$$\det(\nu A_i + \mu A_m) \neq 0 \tag{5.3}$$

and the constants ν and μ are both not zero. In most cases where the system of equations are degenerate and Eq. 5.3 cannot be satisfied, the degenerate system of equations are unnecessarily large and can be reduced to smaller systems with coefficient matrices that satisfy Eq. 5.3 (Whitham, 1973).

Because the total derivative $d\phi$ along the characteristic is zero (Carrier and Pearson, 1988), the chain rule of differentiation can be used to give

$$\sum_{i=1}^{n} \frac{\partial \phi}{\partial x_i} dx_i = 0 \tag{5.4}$$

It follows that

$$\frac{\partial \phi}{\partial x_j} = - \sum_{i=1, i \neq j}^{n} \frac{dx_i}{dx_j} \frac{\partial \phi}{\partial x_i} \tag{5.5}$$

Making use of equation 5.5, equation 5.2 is written as

$$\det\left(\sum_{i=1, i \neq j}^{n} \frac{\partial \phi}{\partial x_i} (A_i - A_j \frac{\partial x_i}{\partial x_j}) \right) = 0 \tag{5.6}$$

The slope of the characteristic curves in any pair of directions is found by solving Eq. 5.6 in those coordinate directions.

For a two-dimensional flow with coordinate axes x_1 and x_2, which is of interest in this study, the slope of the characteristics, $\alpha=(dx_2/dx_1)$, is found by solving the equation

$$\det\left(A_2 - \alpha A_1\right) = 0 \tag{5.7}$$

Thus an expression is obtained for α, say $\alpha=a(x_1, x_2, u)$. The characteristic curves are found analytically or by stepwise numerical integration from the relation

$$x_2 = \int a(x_1, x_2, u)\, dx_1 + \text{constant} \tag{5.8}$$

The members of a family of characteristic curves differ only by a constant of integration.

5.1.2 Classification of System of Equations Governing LCP Flow

The equations governing the flow of a LCP solution modeled by the closed form of the constitutive equation presented in Chapter 3 are as follows:

$$(\nabla \cdot \boldsymbol{v}) = 0 \tag{5.9}$$

$$\nabla p + [\nabla \cdot \boldsymbol{\tau}] = \mathbf{0} \tag{5.10}$$

$$\boldsymbol{\tau} = -\eta_s \dot{\gamma} - nkT\left[(1 - \frac{N}{3})\boldsymbol{S} - N(\boldsymbol{S}\cdot\boldsymbol{S}) + N(\boldsymbol{S}:\boldsymbol{S})(\boldsymbol{S} + \frac{\boldsymbol{\delta}}{3}) + 2\lambda(\boldsymbol{\kappa}:\boldsymbol{S})(\boldsymbol{S} + \frac{\boldsymbol{\delta}}{3})\right] \tag{5.11}$$

$$\boldsymbol{S}_{(1)} = \boldsymbol{F}(\boldsymbol{S}) + \boldsymbol{G}(\boldsymbol{\kappa}, \boldsymbol{S}) \tag{5.12}$$

$$\boldsymbol{F}(\boldsymbol{S}) = -\frac{\sigma}{\lambda}\left[(1 - \frac{N}{3})\boldsymbol{S} - N(\boldsymbol{S}\cdot\boldsymbol{S}) + N(\boldsymbol{S}:\boldsymbol{S})(\boldsymbol{S} + \frac{\boldsymbol{\delta}}{3})\right] \tag{5.13}$$

$$\boldsymbol{G}(\boldsymbol{S}, \boldsymbol{\kappa}) = \frac{\dot{\gamma}}{3} - 2(\boldsymbol{\kappa}:\boldsymbol{S})(\boldsymbol{S} + \frac{\boldsymbol{\delta}}{3}) \tag{5.14}$$

Equation 5.9 is the conservation of mass equation for an incompressible fluid and Eq.

5.10 is the momentum conservation equation for inertialess flows, *i.e.* Re=0. Because most polymer processing flows are basically inertialess Menon (1990) analyzed the mathematical type of the foregoing equations only in this limit.

Menon presented a mathematical type analysis of the governing equations 5.9-5.14 for a general two-dimensional flow in Cartesian coordinates. The mathematical type of the governing equations is expected to be independent of the coordinate system. Though not presented, Menon in fact performed a similar analysis for the case of a two-dimensional axisymmetric flow, which has a direct bearing on the problem studied here, and confirmed that results are qualitatively similar to the results obtained in Cartesian coordinates.

In Cartesian coordinates, the equation set 5.9-5.14 is first reduced to a system of quasi-linear first order partial differential equations of the form

$$A_1 u_x + A_2 u_y = f \tag{5.15}$$

The corresponding set of canonical variables are $\mathbf{u}(p, \partial v_x/\partial x, \partial v_y/\partial x, \partial v_x/\partial y, S_{xx}, S_{yx}, S_{yy})$. Using the rules for classification of a system of quasilinear, first-order partial differential equations presented in the previous section, Menon showed that for zero solvent viscosity the characteristics associated with the pressure, velocity derivatives and the structure tensor components are all real, and hence hyperbolic. The hyperbolicity of the structure tensor components means that the microstructural information in the flow is convected hyperbolically along streamlines.

For any non-zero solvent viscosity, the characteristics associated with the seven canonical variables are different. The characteristics associated with the structure tensor

components are still hyperbolic. However, the characteristics associated with the pressure and velocity derivatives are now complex, and hence elliptic. The elliptic behavior of these characteristics result from the dominance of the solvent viscosity operator in determining the mathematical type. Therefore it follows that for non-zero solvent viscosity, the characteristics associated with the equation set 5.9-5.14 are of mixed type.

The mathematical type determined by Menon for the equation set governing the flow of the LCP solutions modeled by the constitutive equation presented in Chapter 3 is similar to that of the corresponding system of equations for a polymer solution modeled by the Oldroyd-B constitutive equation (cf. Joseph *et al.*, 1985). Like Joseph *et al.* (1985), Menon also found that the behavior of the system of equations is qualitatively different in the limit of zero solvent viscosity (UCM model). Therefore, it is important that a numerical algorithm used to solve a two-dimensional flow problem with the liquid-crystal constitutive equation be consistent with the results of the mathematical type analysis obtained by Menon.

5.2 Description of Contraction Flow Problem

The flow of a LCP solution through an axisymmetric contraction geometry is studied. The importance of this flow problem in the processing of LCP's and the advantages of the particular choice of boundary shape have been discussed in the introduction to this Chapter.

5.2.1 Flow Geometry for Contraction Flow

The contraction geometries examined in this study are depicted in Fig. 5.1a-b. The LCP solution flows through a circular tube of radius R_1 and length L_1, which tapers smoothly to a circular tube of radius R_2 and length L_2. The ratio of inlet to outlet radii, R_1/R_2, is the contraction ratio and is denoted by Λ. The small tube is taken to be long enough to allow the velocity components to become fully developed in the small tube.

In Fig. 5.1a, the smooth contraction boundary is modeled by a cubic polynomial $C(R)=aR^3+bR^2+cR+d$ such that $C(R_1)=R_1$, $\partial C(R_1)/\partial r=0$, $C(R_2)=R_2$, and $\partial C(R_2)/\partial r=0$, which completely specify the unknown coefficients a,b,c and d. Note that $R\equiv R(z)$.

In Fig. 5.1b, the smooth, tapered, contraction region is modeled by a conical contraction with rounded corners. The two radii of curvature are presumed to be the same. Shown in Fig. 5.1c are two circles with the same radius, $\Re$, with the internal common tangent of interest to the conical contraction boundary. The upstream and downstream rounded corners blend with the conical part of the contraction at the end points of the internal common tangent *i.e.* (x_1,y_1) and (x_2,y_2) respectively. These coordinates are set by the radii of the two circles and the separation distance between their centers in the x and y directions.

As demonstrated by the geometric construction in Fig. 5.1c, the angle, θ, subtended by the upstream and downstream corners at the center is the same. The angle θ is given by the expression

$$\sin(\theta - t) = \frac{2\Re}{\sqrt{(x_d - x_u)^2 + (y_u - y_d - 2\Re)^2}} \quad \text{where} \quad \tan t = \frac{y_u - y_d - 2\Re}{x_d - x_u} \tag{5.16}$$

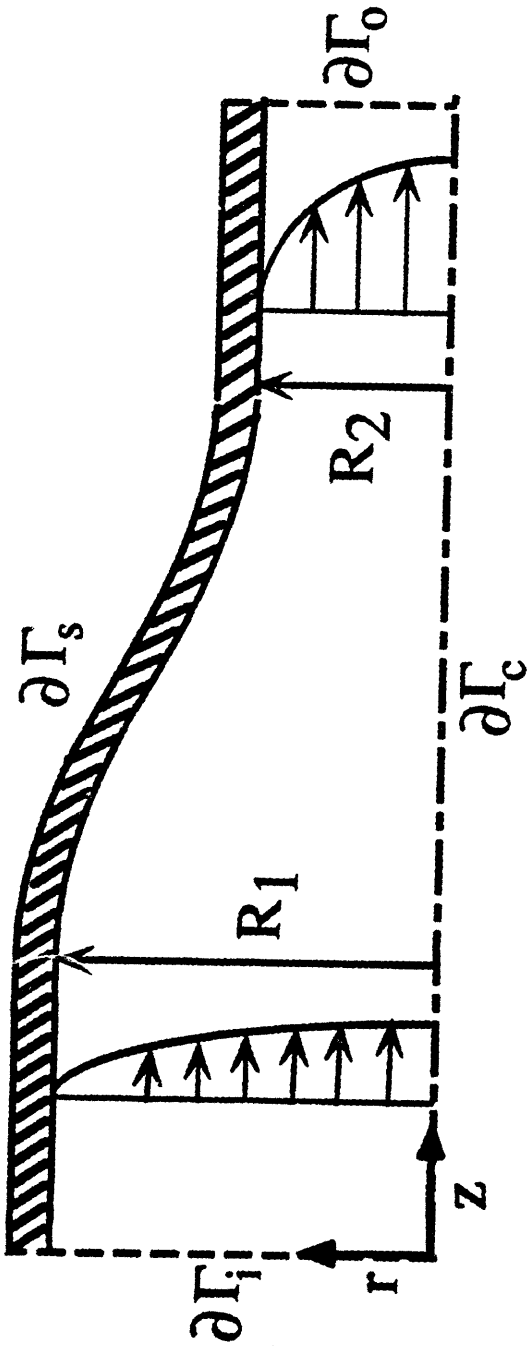

Figure 5.1a: The smooth, cubic contraction geometry.

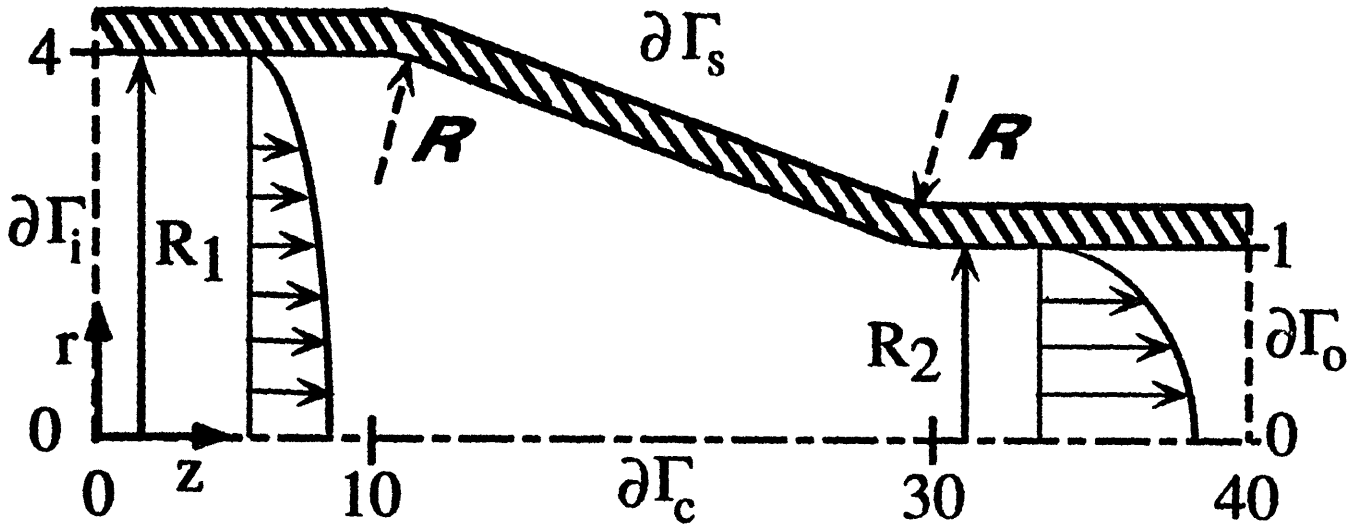

Figure 5.1b: The smooth conical contraction geometry with rounded corners.

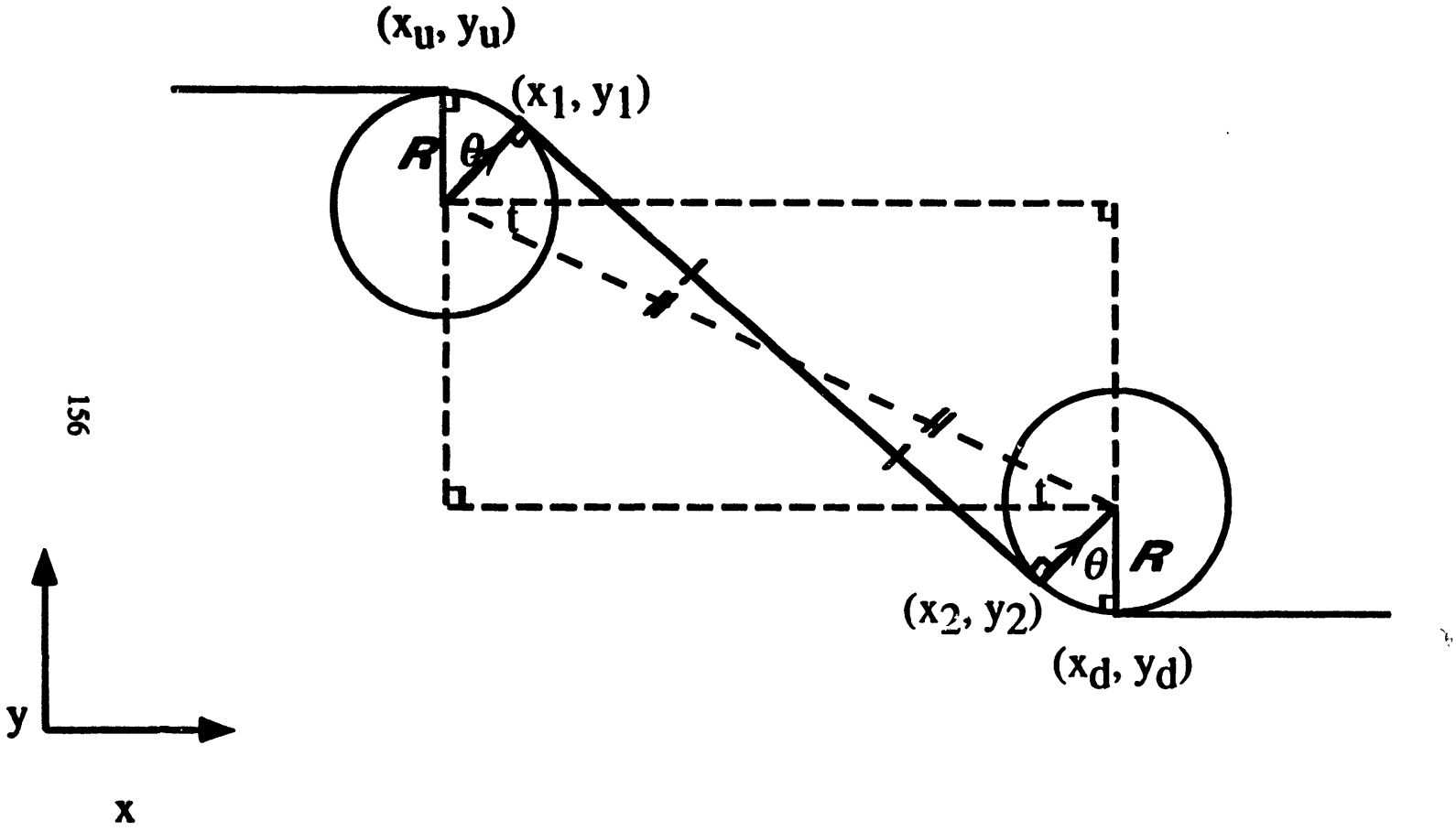

Figure 5.1c: Geometric construction to determine the endpoints of the internal common tangent.

Here, (x_u,y_u) and (x_d,y_d) are the coordinates at the junction of the upstream and downstream tubes with the rounded corners. The angles subtended by rounded corners of different radii are also the same which can be proved easily from basic geometric principles. The angle, however, is now dependent upon the radii of *both* circles and the distance of separation between their centers in the x and y directions. Once θ is known, (x_1,y_1) and (x_2,y_2) are determined as follows

$$\begin{aligned} x_1 &= x_u + \Re\sin\theta\,; \quad y_1 = y_u - \Re(1-\cos\theta) \\ x_2 &= x_d - \Re\sin\theta\,; \quad y_2 = y_d + \Re(1-\cos\theta) \end{aligned} \tag{5.17}$$

Polynomial shape functions are used in the mesh generation package developed by Bornside (1993) to approximate curved boundaries. The next step is to determine the polynomial shape functions that best approximate the rounded corners. A clue to the choice of the appropriate class of polynomial functions is provided by the equation of a circle in Cartesian coordinates

$$y = y_0 \pm \Re\sqrt{1-\left(\frac{x-x_0}{\Re}\right)^2} \tag{5.18}$$

(x_0,y_0) are the coordinates of the center of the circle. The positive sign is used to describe the upper half of the circle and the negative sign the lower half. For small $(x_1-x_0)/\Re = \sin\theta$, only a few terms in the binomial/perturbation expansion in $(x-x_0)/\Re$,

$$y = y_0 \pm \Re\left\{1-\frac{1}{2}\left(\frac{x-x_0}{\Re}\right)^2 - \frac{1}{8}\left(\frac{x-x_0}{\Re}\right)^4 - \ldots.\right\} \tag{5.19}$$

are needed. This perturbation/binomial scheme can be extended easily to depict arcs that subtend even large values of the angle θ at the center (x_0,y_0) by breaking up the arcs into small arcs and representing the small arcs by their respective perturbation expansions.

The choice of the smooth and tapered boundary has an inherent advantage in contrast with the flow through an abrupt contraction (Yeh *et al.*, 1984, Coates *et al.*, 1992) or a tapered contraction with sharp corners at the junctions upstream and downstream. It is clear from Eq. 3.12 that the asymptotic singular behavior in the stresses near sharp corners must be the same as that of the velocity gradient, *i.e.* Newtonian-like, since the components of the structure tensor $\boldsymbol{S}$ are bounded. The asymptotic analysis first performed by Dean and Montagnon (1949) and later extended by Moffatt (1964) for an inertialess Newtonian flow near a sharp corner reveals that the asymptotic singular behavior in the stresses and pressure in a tapered contraction with sharp corners is weaker than the singular behavior in the stresses and pressure in an abrupt contraction close to the reentrant corner. However, the local velocity gradient at the reentrant corner is still *infinite* which leads to drastic changes in the solution field around the corner. In fact, due to the high shear rates which exist on the upstream and downstream wall boundaries close to the corner, the polymer molecules are aligned parallel to respective boundaries as shown in Fig. 5.2. Consequently, the components of the structure tensor are degenerate at the sharp corner which makes it difficult to obtain convergent results even for a 2:1 contraction at moderate or high concentrations. Smoothing the corners overcomes this problem and allows the computation of the solution field to higher contraction ratios at all concentrations.

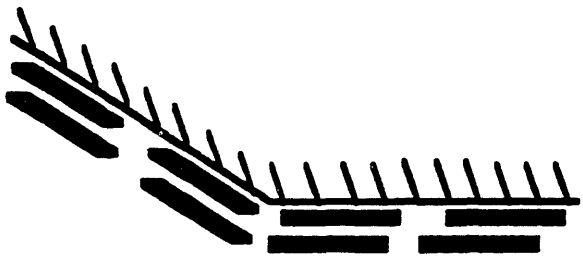

Figure 5.2: Effect of sharp corner on molecular orientation.

5.2.2 Governing Equations and Boundary Conditions

The governing equations for the axisymmetric contraction problem consists of the equation set 5.9-5.14 written in dimensionless form. The scalings used to make the flow variables dimensionless are shown in Fig. 5.1, and are the same as those used by Coates (1992). The lengths are scaled with the downstream tube radius, R_2. The radial and axial velocities are scaled with the average downstream velocity, $V_{2,avg}$. This choice of velocity scaling is appropriate from an experimental point of view: $V_{2,avg}$ depends only on the flow rate through the geometry and not on the choice of the constitutive equation, as other possible velocity scalings, such as the maximum downstream velocity $V_{2,max}$ would. The stresses and pressure are scaled with $\eta_0 V_{2,avg}/R_2$, where η_0 is the solution viscosity defined in Chapter 4.

The Deborah number, De, an important dimensionless group for viscoelastic fluids that arises from the above choice of scalings, is defined as the ratio of a characteristic time of the fluid to a characteristic time for the flow,

$$De \equiv \frac{\lambda_{fluid}}{t_{flow}} = \frac{\lambda_0 V_{2,avg}}{R_2} \tag{5.20}$$

where λ_0 is the relaxation time constant in the limit of zero-shear-rate. The parameter β is the ratio of the solvent viscosity to the solution viscosity and is as defined in Chapter 4. The other parameters in the liquid-crystal constitutive equation (N and σ) are already dimensionless. With these scalings and dimensionless groups the governing equations in dimensionless form are

$$\nabla \boldsymbol{v} = 0 \tag{5.21}$$

$$\mathrm{De}\nabla p + \nabla\cdot\left(-\beta\mathrm{De}\dot{\gamma} - 3(1-\beta)\left[(1-\frac{N}{3})S - N(S\cdot S) + N(S:S)(S+\frac{\delta}{3}) + 2\mathrm{De}(\kappa:S)(S+\frac{\delta}{3})\right]\right) = 0 \tag{5.22}$$

$$\frac{\mathrm{De}}{\sigma}\left(S_{(1)} - \frac{\dot{\gamma}}{3} + 2(\kappa:S)(S+\frac{\delta}{3})\right) + (1-\frac{N}{3})S - N(S\cdot S) + N(S:S)(S+\frac{\delta}{3}) = 0 \tag{5.23}$$

These equations are solved for the velocity, pressure and structure tensor in the flow domain; note that v, p, κ and hence $\dot{\gamma}$ are now dimensionless and different from the quantities appearing in Eqs. 5.9-5.14. The stress tensor is determined subsequently from the structure and velocity gradient by using the dimensionless equation

$$\mathrm{De}\tau = -\beta\mathrm{De}\dot{\gamma} - 3(1-\beta)\left[(1-\frac{N}{3})S - N(S\cdot S) + N(S:S)(S+\frac{\delta}{3}) + 2\mathrm{De}(\kappa:S)(S+\frac{\delta}{3})\right] \tag{5.24}$$

The stream function ψ for an axisymmetric flow is defined as

$$v_r = \frac{1}{r}\frac{\partial\psi}{\partial z}\ ;\quad v_z = -\frac{1}{r}\frac{\partial\psi}{\partial r} \tag{5.25}$$

and is determined from the velocity field by solving the equation

$$\frac{\partial^2\psi}{\partial r^2} - \frac{1}{r}\frac{\partial\psi}{\partial r} + \frac{\partial^2\psi}{\partial z^2} = r\omega_{zr} = r\left(\frac{\partial v_r}{\partial z} - \frac{\partial v_z}{\partial r}\right) \tag{5.26}$$

where ω_{zr} is the zr-component of the vorticity tensor. It is convenient to write Eq. 5.26 in terms of the Laplacian operator to set up the finite-element residual equations. Consequently, Eq. 5.26 is expressed in terms of the Laplacian operator as

$$\nabla^2\psi - \frac{2}{r}\frac{\partial\psi}{\partial r} = r\left(\frac{\partial v_r}{\partial z} - \frac{\partial v_z}{\partial r}\right) \tag{5.27}$$

The boundary conditions used to solve the above governing equations are described in the

following section.

Boundary Conditions

The contraction geometries examined in this study are depicted in Fig. 5.1a-b. The velocity field is assumed to be fully developed at the entrance of the large tube and the small tube is taken to be long enough to allow the velocity to become fully developed and minimize the effect of the axial location of the outflow boundary on the development of the components of the structure tensor in the contraction geometry. The length of the small tube necessary to meet this condition is larger for higher De. In general, the downstream tube length L_2 must be long enough so that

$$\frac{\lambda_{fluid}}{t_{residence\ in\ L_2}} = De \cdot \frac{R_2}{L_2} \ll 1 \tag{5.28}$$

where De is defined by Eq. 5.20, which leads to the general condition

$$\frac{L_2}{R_2} \gg De \tag{5.29}$$

Thus, for De=1.0, $L_2/R_2 \gg 1$. The velocity field is presumed to be axisymmetric throughout the flow and to satisfy the no-slip and no-penetration conditions along the solid boundary. Along the centerline the radial velocity is set to zero. In summary, the velocity boundary conditions are

$$\begin{aligned}
&v = 0 \quad \text{on} \quad \partial\Gamma_s && \text{Essential b.c.} \\
&v_z = v_z(r) \quad \text{on} \quad \partial\Gamma_i && \text{Essential b.c.} \\
&v_r = 0 \quad \text{on} \quad \partial\Gamma_i, \partial\Gamma_o, \partial\Gamma_c && \text{Essential b.c.} \\
&\frac{\partial v_z}{\partial z} = 0 \quad \text{on} \quad \partial\Gamma_o && \text{Natural b.c.}
\end{aligned} \tag{5.30}$$

where the boundaries $\partial\Gamma_i$, $\partial\Gamma_o$, $\partial\Gamma_s$ and $\partial\Gamma_c$ are as indicated in Fig. 5.1. A datum pressure value, p=0, is set on the wall at the exit to completely specify the elliptic saddle

point problem for velocity and pressure.

As discussed in Section 5.1.2, Menon (1990) demonstrated that for a non-zero solvent viscosity, which is studied in this thesis, the components of the structure tensor alone contribute hyperbolic character to the governing equation set. The hyperbolicity demands that boundary conditions be specified only where the characteristics enter the domain (Carrier and Pearson, 1988). Menon's analysis would then require that the boundary conditions for structure components need be specified only at the inlet of the domain, $\partial\Gamma_i$. However, the $\theta\theta$-component of the structure tensor is eliminated from the problem since $\boldsymbol{S}$ is traceless, and does not require a boundary condition specified on it. In summary, in axisymmetric geometries these boundary conditions are

$$\begin{aligned} S_{rr} &= S_{rr}(r) \quad \text{on} \quad \partial\Gamma_i \qquad \text{Essential b.c.} \\ S_{zz} &= S_{zz}(r) \quad \text{on} \quad \partial\Gamma_i \qquad \text{Essential b.c.} \\ S_{rz} &= S_{rz}(r) \quad \text{on} \quad \partial\Gamma_i \qquad \text{Essential b.c.} \end{aligned} \tag{5.31}$$

These boundary conditions along with the equation set 5.21-5.24 presented in the previous section completely determine the velocity, structure, and stress fields in the isothermal flow of a LCP solution through the contraction shown in Fig. 5.1. The nonlinearity of the liquid-crystal constitutive equation, however, requires a numerical solution for these boundary conditions. In dimensionless form, the equations for the fully developed flow through a pipe that govern these boundary conditions are

<u>z-momentum equation</u>

$$\begin{aligned} &-\frac{\Delta p}{2L}R_2 r + \mathrm{De}\left(\frac{\eta_s}{\lambda} + 6nkTS_{rz}^2\right)\frac{dv_z}{dr} + \\ &3nkT\left[\left(1-\frac{N}{3}\right)S_{rz} - N(S_{rr}+S_{zz})S_{rz} + 2N(S_{rr}^2+S_{zz}^2+S_{rz}^2+S_{rr}S_{zz})S_{rz}\right] = 0 \end{aligned} \tag{5.32}$$

Evolution equation

$$(rr\text{-comp}) \quad 2\frac{De}{\sigma}S_{rz}(S_{rr}+\frac{1}{3})\frac{dv_z}{dr} + (1-\frac{N}{3})S_{rr} - N(S_{rr}^2+S_{rz}^2) + 2N(S_{rr}^2+S_{zz}^2+S_{rz}^2+S_{rr}S_{zz})(S_{rr}+\frac{1}{3}) = 0 \tag{5.33}$$

$$(zz\text{-comp}) \quad 2\frac{De}{\sigma}S_{rz}(S_{zz}-\frac{2}{3})\frac{dv_z}{dr} + (1-\frac{N}{3})S_{zz} - N(S_{zz}^2+S_{rz}^2) + 2N(S_{rr}^2+S_{zz}^2+S_{rz}^2+S_{rr}S_{zz})(S_{zz}+\frac{1}{3}) = 0 \tag{5.34}$$

$$(rz\text{-comp}) \quad \frac{De}{\sigma}(2S_{rz}^2-S_{rr}-\frac{1}{3})\frac{dv_z}{dr} + (1-\frac{N}{3})S_{rz} - N(S_{rr}+S_{zz})S_{rz} + 2N(S_{rr}^2+S_{zz}^2+S_{rz}^2+S_{rr}S_{zz})S_{rz} = 0 \tag{5.35}$$

Equations 5.32-5.35 are four equations for the four unknown variables, dv_z/dr, S_{rr}, S_{zz} and S_{rz}. However, the constant pressure gradient $\Delta p/L$ is not known. A volume flow rate constraint is necessary to determine the unknown constant pressure gradient. The volume flow rate constraint is expressed as follows

Volume flow rate constraint

$$1 - 2\int_0^{R_1/R_2} v_z r\,dr = 1 + \int_0^{R_1/R_2} \frac{dv_z}{dr} r^2 dr =$$

$$1 + \int_0^{R_1/R_2} \frac{\frac{\Delta p}{2L}R_2 r - 3nkT\left[(1-\frac{N}{3})S_{rz} - N(S_{rr}+S_{zz})S_{rz} + 2N(S_{rr}^2+S_{zz}^2+S_{rz}^2+S_{rr}S_{zz})S_{rz}\right]}{De(\frac{\eta_s}{\lambda} + 6nkTS_{rz}^2)} r^2 dr = 0 \tag{5.36}$$

The solution to this equation set consists of a cyclic two-step procedure: (1) With an initial guess for the pressure gradient, $\Delta p/L$, corresponding to fully developed flow at the entrance to the large tube, equations 5.32-5.35 are solved for the primary variables dv_z/dr, S_{rr}, S_{zz} and S_{rz} by Newton's method; (2) Newton's method is then employed on the volume constraint equation to obtain a better guess for the pressure gradient. The cyclic

two-step procedure is then repeated until the volume flow rate constraint is satisfied to the specified tolerance.

Once the velocity gradient dv_z/dr is known, the axial velocity field, $v_z(r)$, is constructed by carrying out the integration

$$v_z(r) = - \int_r^{R_1/R_2} \frac{dv_z}{dr} dr \tag{5.37}$$

Equations 5.32-5.37 completely determine the boundary conditions at the entrance to the large tube.

Once the velocity, structure and stress fields are determined for the contraction problem, the stream function is determined from the velocity field by solving the boundary-value problem consisting of Eq. 5.27 along with the boundary conditions

$$\begin{aligned}
\psi &= 0 \quad \text{on} \quad \partial\Gamma_s && \text{Essential b.c.} \\
\psi &= 1 \quad \text{on} \quad \partial\Gamma_c && \text{Essential b.c.} \\
\frac{\partial\psi}{\partial z} &= 0 \quad \text{on} \quad \partial\Gamma_i && \text{Natural b.c.} \\
\frac{\partial\psi}{\partial z} &= 0 \quad \text{on} \quad \partial\Gamma_o && \text{Natural b.c.}
\end{aligned} \tag{5.38}$$

5.3 The FEM Method

The governing equations and boundary conditions for the contraction problem presented in Section 5.2.2 are solved by using a finite element method. Strang and Fix (1973), Carey and Oden (1983) among others discuss the effects of approximations made and the convergence and stability proofs associated with the finite element method. Proofs for existence of solutions with viscoelastic constitutive equations also exist under limiting conditions. By separating the momentum and constitutive equations into explicitly elliptic

and hyperbolic parts, which is similar to the EEME formulation of King *et al.* (1988), Renardy (1985) has established a fixed point iteration with the UCM model to prove existence of solution for small De. The proof requires smoothness in the velocity field up to the second derivative. Using the viscous formulation, discussed by Rajagopalan *et al.* (1990), Renardy *et al.* (1987) have demonstrated the existence of weak solutions with the Oldroyd-B model for small De, again by establishing a fixed point iteration between the elliptic saddle point problem and the hyperbolic constitutive equation. A brief outline of the finite element method follows.

5.3.1 The Method

In finite element methods the domain of interest is divided into a number of non-overlapping subregions called elements. The complete approximating space made up of the union of all the elements is known as the finite element mesh. The accuracy of the method is determined by the characteristic length of the elements, h. The accuracy improves with decrease in h. The solution in each element is approximated by means of piecewise polynomials called basis functions. Lagrangian interpolation polynomials are the most commonly used basis functions and are also the interpolation polynomials of choice in this study. The form of these polynomials and the properties which makes them convenient to use are described in most numerical analysis texts including Burnett (1987). A summary of the two-dimensional Lagrangian polynomials commonly used for viscoelastic flows is given by Crochet, Davies and Walters (1984).

Each element is isoparametrically mapped to a parent element. A pictorial

representation of this non-orthogonal mapping is provided in Fig. 5.3. Over a given element, a variable u is approximated by

$$u = \sum_{k=1}^{N} u^k \psi^k(\xi,\eta) \tag{5.39}$$

where (ξ,η) are the isoparametric coordinates, ψ^k is the basis function for the variable u, and u^k is the expansion coefficient representing the approximation for the variable u at the node *k*. The summation in Eq. 5.39 is taken over the number of nodes in an element at which u is approximated. For a Lagrangian biquadratic approximation N=9, and for a Lagrangian bilinear approximation N=4.

A new idea concerning the Lagrangian finite element approximation for locally refined quadrilateral meshes, particularly important for reentrant free surface and interface shapes and sharp corners, was developed by Tsiveriotis and Brown (1992). The local refinement implemented by Bomside (1993) in a stand-alone mesh generation software package is used in this study.

A brief discussion of the local refinement idea due to Tsiveriotis and Brown (1992) follows. Consider the collection of elements shown in Fig. 5.4 (reproduced from Tsiveriotis and Brown, 1992), where a transition from element e_3 to elements e_1 and e_2 is shown. The boundary of this one-to-two element transition is known as a *transition boundary*. The characteristic of a transition boundary is that it contains two sets of nodes. The first set of nodes are boundary nodes of the coarser element, e_3, on one side of the transition boundary; and the second set consists of the boundary nodes of the two refined elements, e_1 and e_2, on the other side of the transition boundary. The first set of nodes are called *regular nodes* and the second set of nodes are refered to as *pseudonodes*.

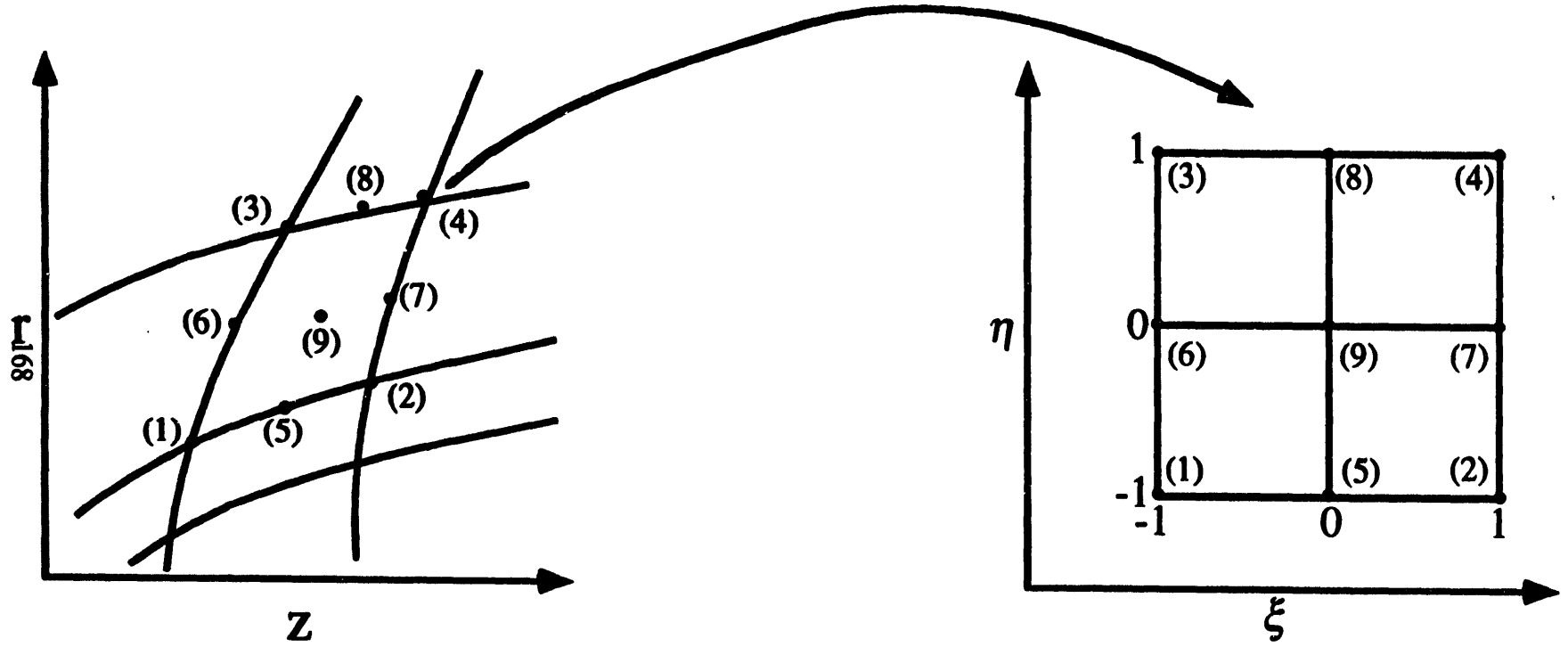

Figure 5.3: Isoparametric transformation used to map an element in (z,r) space onto fixed parent element. () represents the node number.

These nodes are shown in Fig. 5.4 for a Lagrangian bilinear approximation.

Let $\{n_1^i, n_2^i, n_3^i\}$, i=1,...m, be the nodes of the elements e_1, e_2 and e_3 along the boundaries GH, HI and GI, respectively. Then $\{n_1^i, n_2^i\}$ are the pseudonodes and $\{n_3^i\}$ are the regular nodes of the transition boundary GI. Also, let $\{\psi_j^n\}$ be the bilinear basis function corresponding to node n and element e_j. Each basis function ψ_j^n is nonzero at node n and is zero at all other nodes of element e_j.

A continuity problem across the transition boundary arises since the elemental basis functions associated with the regular nodes of the coarse element e_3 cannot be extended to the elemental basis functions associated with the pseudonodes of the finer elements e_1 and e_2. A primary limitation of this discontinuity is that the continuity of the nodal values of the field variables across the transition boundary is not guaranteed. The problem is alleviated by enforcing continuity of the field variables across the transition boundary GI through the essential conditions

$$u_{n_1^i} = \sum_{j=1}^{m} w_{n_3^j}^{n_1^i} u_{n_3^j} \; ; \qquad u_{n_2^i} = \sum_{j=1}^{m} w_{n_3^j}^{n_2^i} u_{n_3^j} \; ; \quad i=1,....,m \tag{5.40}$$

so that the field variable u is now defined at the pseudonodes associated with elements e_1 and e_2. $u_{n_3^j}$ is the value of u at the regular node n_3^j. The weighting functions w_n^l are related to the bilinear basis functions ψ_3^n through the relation

$$w_{n_3^j}^{n_1^i} = \psi_3^{n_3^j}(n_1^i) \; ; \qquad w_{n_3^j}^{n_2^i} = \psi_3^{n_3^j}(n_2^i) \; ; \quad i=1,....,m \;\; j=1,....,m \tag{5.41}$$

Equation 5.40 removes the pseudonodes from the finite element formulation. The regular nodes along the transition boundary are introduced into the finite element formulation

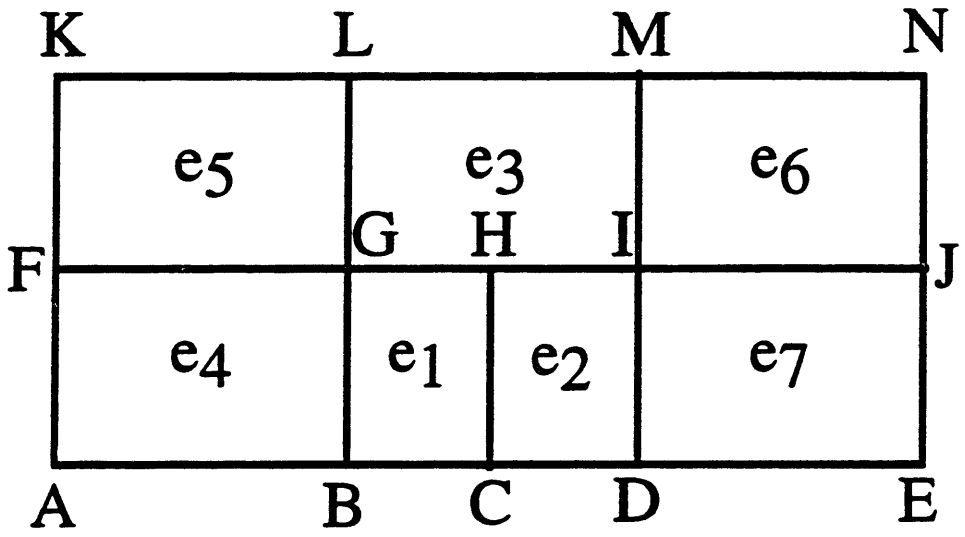

Fig. 5.4: Local refinement of quadrilateral mesh showing one-to-two element transition from element e_3 to elements e_1 and e_2 (reproduced from Tsiveriotis and Brown, 1992).

through new basis functions $\{\Phi_n^j\}$ obtained by patching the elemental basis functions corresponding to the node n_3^j with a weighted combination of the elemental basis functions corresponding to the pseudonodes along the transition boundary. The new basis functions for the example shown in Fig. 5.4 are then given by

$$\Phi_{n_3^i} = \sum_{j=1}^{m} w_{n_3^i}^{n_1^j} \psi_1^{n_1^j} + \sum_{j=1}^{m} w_{n_3^i}^{n_2^j} \psi_2^{n_2^j} + \psi_3^{n_3^i} ; \quad i=2,m-1 \tag{5.42}$$

$$\Phi_{n_3^1} = \sum_{j=1}^{m} w_{n_3^1}^{n_1^j} \psi_1^{n_1^j} + \sum_{j=1}^{m} w_{n_3^1}^{n_2^j} \psi_2^{n_2^j} + \psi_3^{n_3^1} + \psi_4^{n_3^1} + \psi_5^{n_3^1} \tag{5.43}$$

$$\Phi_{n_3^m} = \sum_{j=1}^{m} w_{n_3^m}^{n_1^j} \psi_1^{n_1^j} + \sum_{j=1}^{m} w_{n_3^m}^{n_2^j} \psi_2^{n_2^j} + \psi_3^{n_3^m} + \psi_6^{n_3^m} + \psi_7^{n_3^m} \tag{5.44}$$

where nodes n_3^1 and n_3^m coincide with the points G and I, respectively. These new basis functions guarantee the continuity of the field variables across the transition boundary. The field variable u continues to be defined by Eq. 5.39 at the nodes along the transition boundary but with the original basis function replaced by the new basis function. Based on these definitions local refinement can be introduced into existing finite element formulations with minimal changes. More details on this approach are discussed by Tsiveriotis and Brown (1992).

The dimensionless equations 5.21-5.27 are now put into weighted residual form. The choice of weighting functions used and the formulation of the residual equations is key to the creation of a numerically stable and convergent finite element discretization. If the Lagrangian polynomial basis functions are used as weighting functions the method

is called Galerkin's method (Bathe and Wilson, 1976). For example, the residual equation formed from Eq. 5.23 is written as follows,

$$\int_V \boldsymbol{e}_i\boldsymbol{e}_j : \left[\frac{De}{\sigma}\left(\boldsymbol{S}_{(1)} - \frac{\dot{\gamma}}{3} + 2(\boldsymbol{\kappa}:\boldsymbol{S})(\boldsymbol{S} + \frac{\boldsymbol{\delta}}{3})\right) + (1 - \frac{N}{3})\boldsymbol{S} - N(\boldsymbol{S}\cdot\boldsymbol{S}) + N(\boldsymbol{S}:\boldsymbol{S})(\boldsymbol{S} + \frac{\boldsymbol{\delta}}{3})\right]\phi^{S_{ij}} dV = 0 \tag{5.45}$$

where $\mathbf{e}_i$ and $\mathbf{e}_j$ are unit vectors corresponding to any two coordinate directions and the weighting function used in the above residual equation is ϕ^{Sij} for the variable S_{ij}. Choosing the weighting functions for the field variables and the weighted residual method is vital to the stability and convergence of the numerical algorithm and is not a trivial matter. In the next section some measures used to determine convergence are introduced and stability issues are discussed. Since the equations 5.21-5.27 are of mixed type the rationale behind the weighted residual methods used in this work are discussed in Section 5.3.2.

Convergence and Stability of Finite Element Method

Numerical algorithms that predict solutions which get consistently closer to the exact solution with mesh refinement are convergent. This motivates the need to define an appropriate measure for the magnitude of the error. For the solution to a partial differential equation, the appropriate measure of the magnitude of the error involves an integral of the difference between the approximate solution and the exact solution over the whole domain of the problem.

The L_n norm of an argument u is defined as

$$L_n(u) = \|u\|_{L_n} = \left[\int_V u^n dV\right]^{\frac{1}{n}} \tag{5.46}$$

The L_n operator most often operates on $(u-u^h)$ where u^h is the numerical solution for mesh size h. A measure of the magnitude of the error often used to characterize the error in a finite element method is the L_2 norm which is written for the function u as

$$\|u\|_{L_2} = \left[\int_V u^2 dV\right]^{\frac{1}{2}} \tag{5.47}$$

For convergent finite element methods the L_2 norm of $(u-u^h)$ obeys the relation

$$\|u - u^h\|_{L_2} \leq Ch^m \|u\|_{L_2} \tag{5.48}$$

as $h \rightarrow 0$ where $m>0$ and C is a constant. A positive value for m indicates that the relative error in the approximate solution decreases as h decreases and the numerical algorithm is convergent. Another interpretation of Eq. 5.48 is that as $h \rightarrow 0$ the numerical solution u^h approaches the exact solution u and consequently $L_2(u^h)$ must approach a constant value, $L_2(u)$.

It is also necessary that the numerical algorithm used to solve the system of governing equations be stable. Stability of the numerical approximation of the time-dependent form of the equation set plays a vital role. For time-dependent problems the exact solution evolves in time and frequently reaches a steady-state value. The steady-state may be stable or unstable. Transition from one solution branch to the another occurs at "critical points" in parameter space. It is important for the numerical algorithm to predict these critical points accurately. A description of various types of critical points

and the relationship of the stability of steady state solutions to the eigenvalues of the Jacobian matrix are discussed by Ioss and Joseph (1990). Numerical approximations can lead to inaccurate approximations to the eigenvalues of the Jacobian matrix resulting in the prediction of fictitious critical points (Scheiber and Keller, 1983; Yeh *et al.*, 1984). Stable finite element methods either do not predict fictitious critical points or predict critical points at higher parameter values as the finite element mesh is refined.

Simple Elliptic Problems

Thomasset (1981) considered an elliptic equation of the form

$$\nabla \cdot (\chi \cdot \nabla u) = 0 \tag{5.49}$$

where χ is a positive definite tensor and proved that the Galerkin finite element approximation, u^h, converges to the exact solution u at the rate

$$\| u - u^h \|_{L_2} = O(h^{k+1}) \tag{5.50}$$

where k is the order of the polynomial approximation. Bercovier and Pironneau (1979) have shown that the Stokes flow equations

$$\nabla \cdot v = 0 \tag{5.51}$$

$$\nabla^2 v - \nabla p = 0 \tag{5.52}$$

are strictly elliptic for v with the pressure, p, playing the role of a Lagrange multiplier for satisfying the continuity equation. Thomasset (1981) and Teman (1979) consequently proved that stable and convergent Galerkin finite element methods exist for solving the Stokes flow equations 5.51 and 5.52. Polynomial approximations to the velocity and

pressure must be "compatible" with each other. Brezzi (1972) and Babuska (1977) provide a rigorous criterion for determining admissible choices for the polynomial approximation spaces to the velocity and pressure. Biquadratic approximation functions for the velocity and bilinear functions for the pressure satisfy this criterion. The corresponding convergence estimates are

$$\begin{aligned} \|v - v^h\| &\le Ch^2\|v\| \\ \|p - p^h\| &\le Ch\|p\| \end{aligned} \tag{5.53}$$

First-order Hyperbolic Problems

Strang and Fix (1973) discuss the convergence rates for finite element methods for a simple first-order hyperbolic problem. For solving hyperbolic systems with symmetric and conservative operators and whose solution is smooth, Galerkin's finite element method is proved stable and convergent (Strang and Fix, 1973). These first-order hyperbolic systems can be generally written in the form

$$\frac{\partial u(x,t)}{\partial t} + \nabla \cdot s(x,u,t) + f(x,u,t) = 0 \tag{5.54}$$

where **f** is the forcing term and **s(x,u,t)** is the flux vector such that the first-order matrices

$$A_j = \frac{\partial s}{\partial u_j} \tag{5.55}$$

are symmetric. Johnson *et al.* (1984) studied the conservative first-order linear hyperbolic equation

$$\alpha \cdot \nabla u + \sigma u = f \tag{5.56}$$

where α and σ are O(1), and showed that Galerkin's method converges at the rate given

by

$$\|u - u^h\|_{L_2} \leq O(h^k) \tag{5.57}$$

and is only one power of h away from the optimal estimate for elliptic problems given by Eq. 5.50; k is the order of the polynomial approximation. However, the estimate is based on the assumption that the exact solution to u is perfectly smooth; and in fact the method is unstable to disturbances in the numerical solution and the approximation error can propagate in all directions causing spatial oscillations. For this reason, Galerkin's method is not well suited for solving hyperbolic equations.

The Streamline Upwind Petrov Galerkin (SUPG) technique of Brooks and Hughes (1982) is particularly well-suited to solve hyperbolic systems. If ω^k is the basis function for the variable u, then the weighting function used to construct the residual equation for Eq. 5.56 is given by

$$\phi^k = \omega^k + h(\alpha \cdot \nabla \omega^k) \tag{5.58}$$

For the SUPG method the numerical solution u^h converges to the exact solution u according to

$$\|u - u^h\|_{L_2} + h^{1/2} \|\alpha \cdot \nabla (u - u^h)\|_{L_2} \leq C h^{k+1/2} \|u\|_{L_2} \tag{5.59}$$

As h→0, the error associated with the approximation of the $\alpha \cdot \nabla u$ term goes to zero; and consequently, the approximation error in the derivatives of u are damped and do not cause numerical instabilities as in the case of Galerkin's method.

The residual equations constructed with the chosen weighting functions are integrated numerically over the flow domain by using nine-point Gaussian quadrature.

A description of this and other quadrature formulae can be found in Strang and Fix (1973). The set of partial differential equations is thus reduced to a set of nonlinear algebraic equations. The boundary conditions, as discussed in Section 5.2.2, are applied either as essential boundary conditions, where the residual equation at that boundary node is replaced by the boundary condition, or as natural boundary conditions where the boundary condition is substituted into the residual equation. The algebraic system of equations are solved for the nodal values of the field variables by using a full Newton's method for the particular choice of parameter values in the flow problem.

5.3.2 FEM Formulation for LCP Flow

In this section the development of a finite element formulation is described to solve the equation set 5.21-5.27 along with the boundary conditions 5.32-5.38. A finite element formulation that respects the mixed mathematical type of the equations must be used. The formulation is based on the results of the mathematical type analysis due to Menon, presented in Section 5.1.2, and is similar to the EVSS-G formulation developed by Brown *et al.* (1993).

As discussed in Section 5.1.2, in the presence of a solvent viscosity, *i.e.* $\beta > 0$, the equations governing the flow are of mixed type. The continuity equation 5.9 and the momentum equation 5.10 are associated with elliptic characteristics. Consequently Galerkin's weighted residual method is used for these equations. As mentioned in the introduction to this chapter, King *et al.* (1988) showed that it is vital to the success of the numerical algorithm to rewrite the momentum equation so that it remains elliptic. Their

Explicitly Elliptic Momentum Equation (EEME) formulation involved rewriting the momentum equation in terms of an elliptic second-order operator. Using this formulation they computed stable and accurate solutions for viscoelastic flows for the UCM model. However, the formulation is restricted to low Reynolds number flows and to viscoelastic models with zero solvent viscosity and is not directly applicable to the liquid-crystal constitutive equation.

Rajagopalan *et al.* (1990) extended the idea of writing the momentum equation in terms of a strictly elliptic operator to viscoelastic constitutive models with a Newtonian solvent contribution. For such models the stress is written as the sum of a solvent contribution and a polymer contribution in dimensionless form as follows

$$\tau = \tau_s + \tau_p \tag{5.60}$$

where the Newtonian solvent contribution is given by

$$\tau_s = -\frac{\eta_s}{\eta_0}\dot{\gamma} \tag{5.61}$$

η_0 is the zero-shear-viscosity of the solution and is the sum of the solvent and zero-shear-rate polymer contribution to the viscosity *i.e.*, $\eta_0=\eta_s+\eta_p$. With their formulation, called the Elastic-Viscous-Split-Stress (EVSS) formulation, they obtained numerically stable and convergent results with the Oldroyd-B and Giesekus constitutive equations for the flow between eccentric cylinders and the flow through a corrugated tube. Their formulation involves writing the momentum equation in terms of an elliptic operator composed from the solvent and polymeric contributions to the stress. A viscous contribution is extracted from the polymeric part of the stress by using the formulation of Mendelson *et al.* (1982).

The resulting dimensionless elastic stress is defined as

$$\Sigma = \tau_p + \frac{\eta_p}{\eta_0}\dot{\gamma} \tag{5.62}$$

Substituting Eq. 5.62 into the momentum equation 5.10 gives

$$-\nabla^2 v + \nabla\cdot\Sigma + \nabla p = 0 \tag{5.63}$$

Rajagopalan *et al.* derive the residual equations for the components of the momentum equation by treating the term $\nabla^2 v$ in Eq. 5.63 as the dominant elliptic operator. The term $\nabla\cdot\Sigma$ is considered to be a nonhomogenous forcing function. Galerkin's method is used to discretize the equations from the momentum-continuity pair. The components of the constitutive equation are expressed in terms of the elastic stress and the SUPG method is used to discretize these equations. Rajagopalan *et al.* use bilinear basis functions for the pressure and biquadratic basis functions for the velocity and elastic stress.

Previous viscoelastic simulations (Mendelson *et al.*, 1982; van Schaftingen and Crochet, 1984; Beris *et al.*, 1984) with such a formulation had met with failure due to the presence of spurious oscillations in the stress and velocity fields which become worse with mesh refinement. Writing the constitutive equation in terms of the elastic stress introduces a term $\dot{\gamma}_{(1)}$ that involves second-order velocity derivatives. Interpolating the velocity in terms of a biquadratic polynomial approximation introduces singularities in the approximation to $\dot{\gamma}_{(1)}$. Mendelson *et al.* and others circumvented this problem by integrating this term by parts to obtain a weak form of the constitutive equation. The resulting boundary integral terms are evaluated by using velocity data or computed with the rest of the residual equations. Rajagopalan *et al.* believe that the numerical

instability in these calculations resulted because the treatment of the higher-order velocity derivatives was not consistent with the constitutive equation's being hyperbolic in Σ. They alleviate this problem by a least-squares interpolation of the rate-of-strain tensor $\dot{\gamma}$ thus treating the term $\dot{\gamma}_{(1)}$ as simply nonhomogenous data. Bilinear basis functions are used for this interpolation.

Recent calculations by Brown *et al.* (1993) on the linear stability of a homogenous, rectilinear shear flow with the UCM model show, however, that both the EEME and EVSS formulations predict numerical instabilities beyond a critical value of De, though theoretical results prove that this inertialess flow is always stable. In fact, their calculations clearly show that the energy of the most dangerous disturbance is concentrated near the stationary surface or zero streamline in the base flow irrespective of whether the stationary surface is the top boundary, bottom boundary or the midplane when the two solid boundaries are moving in opposite directions but with the same speed. The origin of this numerical instability is ascribed to the coupling of the polynomial approximations to the variables. With a new mixed finite element formulation called the EVSS-G formulation, in which the finite element approximations are expected to be compatible along the stationary streamline (v=0), Brown *et al.* do not see this numerical instability; linear stability calculations for rectilinear shear flow are stable to values of De in excess of 50 and converge with mesh and time step.

The EVSS-G formulation differs from the EVSS formulation in that it includes smooth interpolation of the velocity gradient tensor which is compatible with a bilinear approximation to the stress tensor, as opposed to the interpolation of the rate-of-strain

tensor and a biquadratic approximation to the stress tensor. The velocity gradient is interpolated instead of the rate-of-strain tensor to provide a continuous approximation to $\Sigma_{(1)}$ (which appears when the constitutive equation is written in terms of Σ) in the limit $\nu=0$ so that a compatible finite element approximation to the entire constitutive equation might be obtained in the limit $\nu=0$. A formulation similar to EVSS-G is used to set up the residual equations for the contraction flow modeled by the liquid-crystal constitutive equation. In this formulation the velocity gradient which is introduced as a new variable is represented by the tensor **G**.

The elastic stress for the liquid-crystal model in dimensionless form is defined as

$$\Sigma = \tau_p + (1-\beta)\dot{\gamma} = \tau + \dot{\gamma} \tag{5.64}$$

Substituting Eq. 5.64 into the momentum equation, Eq. 5.22, and expressing the momentum equation in the EVSS-G form gives

$$\begin{aligned} &\mathrm{De}\nabla p - \mathrm{De}\nabla^2 v + (1-\beta)\nabla\cdot\Big(\mathrm{De}(G+G^{\dagger}) \\ &- 3\Big[(1-\frac{N}{3})S - N(S\cdot S) + N(S:S)(S+\frac{\delta}{3}) + 2\mathrm{De}(G^{\dagger}:S)(S+\frac{\delta}{3})\Big]\Big) = 0 \end{aligned} \tag{5.65}$$

It is important to note that in the limit De=0 this formulation cannot be expected to give stable and accurate results since the elliptic operator drops out of the equation. Equation 5.65 is well defined for all other choices in physical parameter space. The evolution equation for the structure, Eq. 5.23, is written in EVSS-G form as

$$\begin{aligned} &\frac{\mathrm{De}}{\sigma}\left(v\cdot\nabla S - \{S\cdot G\}^{\dagger} - \{S\cdot G\} - \frac{G+G^{\dagger}}{3} + 2(G^{\dagger}:S)(S+\frac{\delta}{3})\right) + \\ &(1-\frac{N}{3})S - N(S\cdot S) + N(S:S)(S+\frac{\delta}{3}) = 0 \end{aligned} \tag{5.66}$$

Equation 5.66 is associated with stream-wise hyperbolic characteristics. Consequently the residuals for this equation are constructed by using SUPG method. In constructing the SUPG weighting function for viscoelastic constitutive equations the term α which appears in Eq. 5.58 would be the velocity v. Since the dimensionless maximum velocity is never very much greater than the Newtonian maximum of two, α, which in this case is v, is not normalized by the norm of the velocity over that element or by the root-mean-square value of the magnitude of the velocity, as done by many researchers including Burdette *et al.* (1989) for the flow of an UCM fluid through a corrugated tube. This is important when simulating flows with recirculation regions or stagnation points, because normalizing this term with the root-mean-square value of the magnitude of the velocity over the element results in large approximation and roundoff errors in areas of vanishing velocity (King, 1988). The residuals for the continuity and momentum equations and the equations that define the velocity gradient tensor **G** are constructed using Galerkin's method. The finite element formulation for the equation set 5.21-5.23 is

$$\int_D (\nabla \cdot v)\phi_j^p dA = 0 \tag{5.67}$$

$$\begin{aligned} -\mathrm{De}\int_{\delta D}\phi_j^V n\cdot(\nabla v)\cdot e_k dl + \mathrm{De}\int_D\left[\nabla\phi_j^V\cdot(\nabla v)\cdot e_k + \phi_j^V(\nabla v)^\dagger:\nabla e_k\right]dA \\ + \int_D \phi_j^V\Big[\mathrm{De}\nabla p + (1-\beta)\nabla\cdot\big(\mathrm{De}(G+G^\dagger) - 3\Big[(1-\frac{N}{3})S - \\ N(S\cdot S) + N(S:S)(S+\frac{\delta}{3}) + 2\mathrm{De}(G^\dagger:S)(S+\frac{\delta}{3})\Big]\Big]\cdot e_k dA = 0\ ;\ k = 1,2 \end{aligned} \tag{5.68}$$

$$\begin{aligned} \int_D\Bigg[\frac{\mathrm{De}}{\sigma}\Big(v\cdot\nabla S - \{S\cdot G\}^\dagger - \{S\cdot G\} - \frac{G+G^\dagger}{3} + 2(G^\dagger:S)(S+\frac{\delta}{3})\Big) + (1-\frac{N}{3})S \\ - N(S\cdot S) + N(S:S)(S+\frac{\delta}{3})\Bigg]:e_m e_n(\phi_j^S + hv\cdot\nabla\phi_j^S)dA = 0\ ;\ \ m,n = 1,2 \end{aligned} \tag{5.69}$$

$$\int_D \phi_j^G[G - \nabla v]:e_m e_n dA = 0 \tag{5.70}$$

The pressure, components of the structure tensor S, and the components of the velocity-gradient tensor G are interpolated with bilinear basis functions. The components of the velocity are interpolated with biquadratic basis functions. The essential boundary conditions for the velocity components are used to replace the corresponding residuals in the momentum equation 5.68. The pressure datum and the inlet boundary conditions for the structure are implemented similarly. The natural boundary conditions on the velocity are implemented through the line integral term in the momentum residual equation 5.68. The numerical integration of the residual equations 5.67-5.70 and the solution of the

discretized equation set for the pressure, velocity, velocity gradient and the structure fields are described in Section 5.3.3.

The solution fields thus obtained are post-processed to determine the stress field and the stream function. The structure tensor matrix is also diagnolized to determine the dominant eigenvalue and the associated eigenvector, also known in liquid-crystal terminology as the nematic director. The invariant of the structure tensor, $S=\{(3/2)(\boldsymbol{S}:\boldsymbol{S})\}^{1/2}$, together with the nematic director determine the degree and the direction of order of the polymer molecules in the flow.

The stress field is calculated from the structure field and the velocity gradient as

$$\begin{aligned} De\boldsymbol{\tau} = -\beta De(\boldsymbol{G} + \boldsymbol{G}^{\dagger}) - 3(1-\beta)\Big[(1-\frac{N}{3})\boldsymbol{S} - N(\boldsymbol{S}\cdot\boldsymbol{S}) + \\ N(\boldsymbol{S}:\boldsymbol{S})(\boldsymbol{S}+\frac{\boldsymbol{\delta}}{3}) + 2De(\boldsymbol{G}^{\dagger}:\boldsymbol{S})(\boldsymbol{S}+\frac{\boldsymbol{\delta}}{3})\Big] \end{aligned} \tag{5.71}$$

The stream function is determined by solving the boundary-value problem consisting of Eq. 5.27 along with the boundary conditions given by Eq. 5.38. A Galerkin finite element method is used for this calculation. The stream function is interpolated using biquadratic basis functions. The weak form of the residual equation is written as

$$\int_{\delta D}(\boldsymbol{n}\cdot\nabla\psi)\phi_j^{SF}\,dl + \int_D\left[-\nabla\phi_j^{SF}\cdot\nabla\psi + \left(-\frac{2}{r}\frac{\partial\psi}{\partial r} - r(\frac{\partial v_r}{\partial z} - \frac{\partial v_z}{\partial r})\right)\phi_j^{SF}\right]dA = 0 \tag{5.72}$$

The essential boundary conditions in Eq. 5.38 replace the line integral term on the boundaries $\partial\Gamma_c$ and $\partial\Gamma_s$. The line integral is zero on the boundaries $\partial\Gamma_i$ and $\partial\Gamma_o$ as dictated by the natural boundary conditions. The treatment here assumes that the equations have elliptic character due to the presence of the dominant elliptic operator $\nabla^2\psi$

and consequently it is appropriate to set conditions at the boundaries of the domain.

Finite Element Meshes

The liquid-crystal polymer flow through the smooth, tapered, contraction geometries shown in Figs. 5.1a and 5.1b was studied for two different contraction ratios, 2:1 and 4:1. Graded mesh sizes were used in the calculations for both contractions. The element size was primarily based on the aspect ratio, R/L, of the geometry in the particular region of the flow. Thus in the upstream section where the flow "sees" a higher aspect ratio the elements are coarse as compared to the downstream section where the aspect ratio is smaller and consequently the elements are fine. Additional refinement is also provided close to the centerline in the contraction region and in the downstream section where a transition from a purely elongational flow at the centerline to a mixture of shear and elongation causes rapid changes in the molecular orientation described by the components of the structure tensor S. The mesh sizes used in this study along with the corresponding number of unknowns and smallest mesh size are listed in Table 5.1. The finest mesh, M2-5, for the 2:1 contraction has 44506 number of unknowns, but most of the results are presented for mesh M2-4 since the L_2-norm of the solution, as we will examine later in Section 6.2.1.2, changes very little with mesh refinement beyond the refinement provided by mesh M2-4. The meshes M4-1 and M4-2 are used for the calculations in the 4:1 contraction with the cubic boundary and the conical boundary with rounded corners respectively. Some sample meshes are shown in Fig. 5.5 including the finest mesh used in this study.

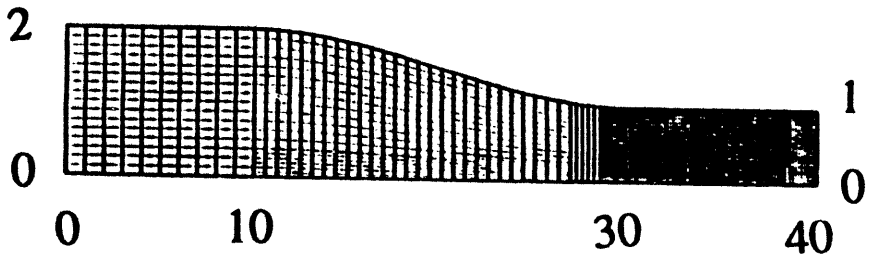

M2-4

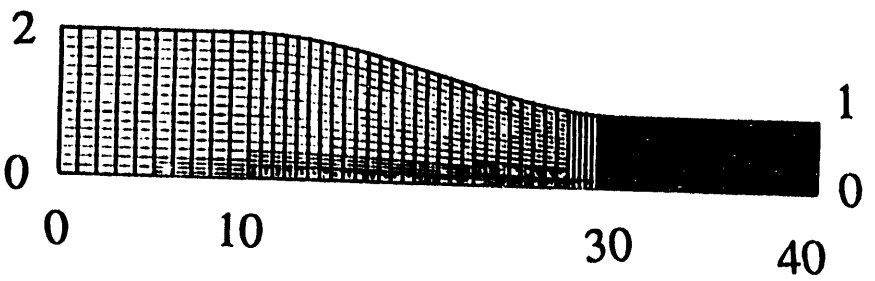

M2-5

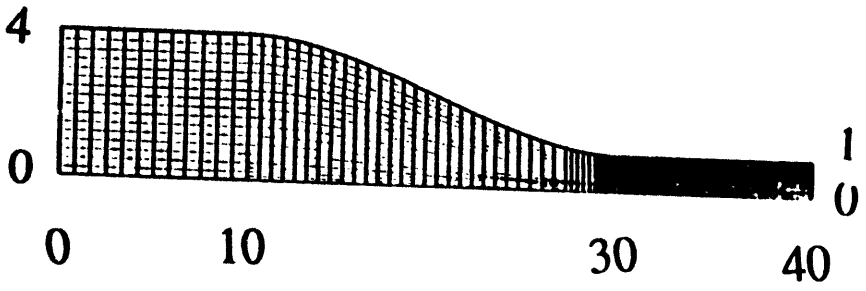

M4-1

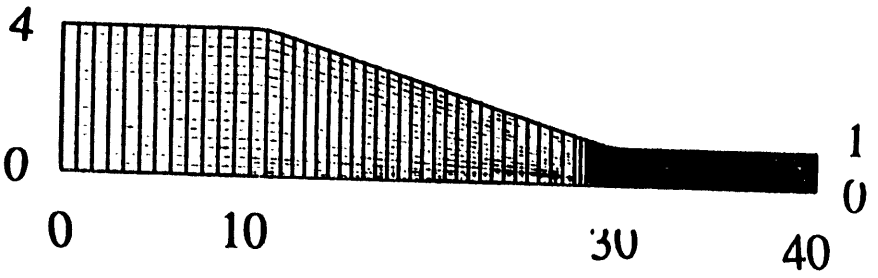

M4-2

Figure 5.5: Sample meshes for 2:1 and 4:1 contractions. The numbers along the mesh borders are dimensionless coordinates scaled by R_2.

Mesh	No. of unknowns	No. of elements	Smallest element size (h_r x h_z)
M2-1	11866	672	1/8 x 5/16
M2-2	22714	1344	1/16 x 5/16
M2-3	31290	1856	1/16 x 5/32
M2-4	37818	2261	1/32 x 5/32
M2-5	44506	2676	1/64 x 5/32
M4-1	37954	2268	1/32 x 5/32
M4-2	38902	2325	1/32 x 4.3/32

Table 5.1: Finite element meshes used in the contraction flow calculations for the LCP solution presented in Chapter 6.

5.3.3 Solution of the Discretized Equation Set

The residual equations 5.67-5.70 are integrated numerically by using nine-point Gauss-Legendre tensor product quadrature, to give a system of nonlinear algebraic equations of the form,

$$R(u^h, De, N) = 0 \tag{5.73}$$

where

$$u^h = \{p^h, S_{rr}^h, S_{zz}^h, S_{rz}^h, G_{rr}^h, G_{zz}^h, G_{rz}^h, G_{zr}^h, v_r^h, v_z^h\} \tag{5.74}$$

is the set of nodal unknowns for a discretization of characteristic size h. This nonlinear algebraic system is solved iteratively by using Newton's method. An initial guess for the approximate solution vector, u_0^h, is given. The solution vector after (j+1) iterations, u_{j+1}^h

is given in terms of the solution vector after j iterations as follows

$$u_{j+1}^{h} = u_{j}^{h} + \delta u_{j+1}^{h} \tag{5.75}$$

where the correction vector is determined by solving

$$\delta u_{j+1}^{h} = -\left[J^{-1}(u_{j}^{h})\right] \cdot R(u_{j}^{h}) \tag{5.76}$$

where $\mathbf{J}^{-1}(\mathbf{u}^{h})$ is the inverse Jacobian matrix. The entries of the Jacobian matrix, defined as $J_{mn}=(\partial R_m/\partial u_n^{h})$, are evaluated analytically. The accuracy of the analytical Jacobian was tested for arbitrary values of the field variables and also for the special case of the contraction flow problem by a comparison with the corresponding numerical Jacobian evaluated by means of a one-sided finite difference scheme described by Burdette *et al.* (1989).

$$J_{mn} = \frac{\partial R_m}{\partial u_n^{h}} = \frac{R_m(u^{h} + \Delta u_n^{h}) - R_m(u^{h})}{\Delta u_n^{h}} \tag{5.77}$$

where the perturbation $\Delta u_n^{h} = 10^{-5}$. The solution for the matrix problem for the correction vector in Eq. 5.76 is carried out with a frontal solver similar to the one introduced by Hood (1976). The determinant of the Jacobian matrix is also evaluated, because a change in the sign of the determinant would indicate a limit point or bifurcation point in the solution family being tracked (Keller, 1977). Newton's method converges quadratically to the solution as long as the initial guess is within the radius of convergence. The Newton iterations are terminated when the L_2 norm of the correction vector is less than a threshold value of 10^{-6}.

In this study only the solutions corresponding to prolate symmetry in the

molecular order in the plane of the flow are tracked. Other solutions where the order possesses prolate symmetry in the direction perpendicular to the plane of the flow (the logrolling state studied by Bhave *et al.*, 1993) can be easily tracked by suitably choosing the appropriate inlet conditions for the order.

Tracking Solution Branches

Realistic polymer processing flows operate at high De. The nematic liquid-crystalline polymer solutions of interest in this thesis are also typically processed at high polymer concentrations. The governing equations, Eqs. 5.21-5.26, are nonlinear under these processing conditions and the Newton iterations typically do not converge to the solution unless the initial guess is close to the actual solution, *i.e.* the radius of convergence is small. It becomes necessary then to devise parameter continuation schemes so that the evolution of the solution in parameter space can be tracked efficiently from a known limit; arc-length continuation is useful when limit points are encountered in parameter space (Fig. 3.6 shows that close to equilibrium, limit points would be encountered in N space). One obvious limit is the Newtonian limit which for the LCP model is captured when N=0, *i.e.* β=1, and De $\rightarrow$ 0. In the Newtonian limit the inertialess governing equations are linear and the Newton iterations must converge to the solution from any initial guess. Another limit, though specific to the contraction flow problem, which in conjunction with parameter continuation and stepping up in contraction ratio is computationally more efficient in computing solutions at high N and De, is the tube flow limit. Though the governing equations are nonlinear in this limit it is easy to provide an initial guess that is the actual solution, *i.e.* the fully developed inflow boundary

conditions.

The evolution of the solution in the Deborah-number space is tracked by using first-order parametric continuation (Kubicek, 1976). Thus, if $\mathbf{u}^h(De_0)$ is the converged solution vector for $De=De_0$, a guess for $De=De_0 + \Delta De$ is estimated as

$$u^h(De_0 + \Delta De) = u^h(De_0) + \left(\frac{\partial u^h}{\partial De}\right)_{De_0} \Delta De \tag{5.78}$$

where

$$\left(\frac{\partial u^h}{\partial De}\right)_{De_0} = -J^{-1}(u^h(De_0)) \cdot \left(\frac{\partial R}{\partial De}\right)_{De_0} \tag{5.79}$$

The Jacobian $\mathbf{J}(\mathbf{u}^h(De_0))$ is the same as that defined in Eq. 5.76 and consequently requires no additional computational effort *i.e.* the LU factorization for the last Newton iteration for the converged solution vector $\mathbf{u}^h$ can be used. The dimension of $(\partial R/\partial De)_{De_0}$ is the same as the residual vector itself and can be easily evaluated along with the residual equations.

The evolution of the solution trajectories in the concentration, N, are also tracked by using first-order continuation and arc-length continuation. The implementation of first-order continuation in N is similar to the implementation in De. Arc-length continuation is implemented in the following manner.

The arc-length Δs along the solution trajectory is defined as

$$\Delta s = |s - s_0| = \sqrt{\|u(s) - u(s_0)\|^2_{L_2} + |N(s) - N(s_0)|^2} \tag{5.80}$$

where $\mathbf{u}(s_0)$ is a known solution at the concentration N_0. In addition to the residual equations 5.67-5.70, a residual equation is constructed for the arc-length as follows:

$$P(u,N,s) = |s-s_0|^2 - \|u(s)-u(s_0)\|^2_{L_2} - |N(s)-N(s_0)|^2 = 0 \qquad (5.81)$$

Then for some specified step-size in the arc-length, $|s\text{-}s_0|$, and initial guesses for the solution vector $\mathbf{u}(s)$ and concentration $N(s)$, a step-size in the concentration δN is determined from the equation

$$\delta N = -\frac{P + \left(\frac{\partial P}{\partial u}\right)^{\dagger} \cdot z}{\frac{\partial P}{\partial N} - \left(\frac{\partial P}{\partial u}\right)^{\dagger} \cdot y} \qquad (5.82)$$

where $\mathbf{y}$ and $\mathbf{z}$ are obtained by solving the equations

$$Jy = \frac{\partial R}{\partial N} \; ; \quad Jz = -R \qquad (5.83)$$

The Jacobian $\mathbf{J}(\mathbf{u}^h(N))$ is the same as that defined in Eq. 5.76 and requires no additional computational effort. As with the first-order continuation, $\partial \mathbf{R}/\partial N$ is evaluated along with the residual equations. More details on the derivation of Eqs. 5.82 and 5.83 are discussed by Keller (1976).

The concentration is then updated by δN for the next Newton iteration, the correction vector given by Eq. 5.76 is evaluated after determining the new residuals and their Jacobians to generate a new guess for the solution vector $\mathbf{u}(s)$, and Eqs. 5.81-5.83 are solved once again to determine δN. The Newton iterations and the concentration updates are repeated until a solution $\mathbf{u}^h(s)$ is obtained that satisfies the residual equations

5.67-5.70 and 5.81. The values chosen for the other parameters in the constitutive equation (β and σ) are indicated in Chapter 6.

Chapter Six

Tube and Axisymmetric Contraction Flows of LCP's

The results of the calculations of liquid-crystal flow through a tube and a smooth, tapered axisymmetric contraction geometry performed by using the finite element method are presented in this Chapter. The calculations are aimed at understanding the variations in the flow field, the molecular order, and the stress fields with Deborah number, concentration and contraction ratio. The solvent viscosity of liquid-crystalline polymer solutions is typically four or more orders-of-magnitude smaller than the scaling for the polymeric contribution to the viscosity $nkT\lambda$. The value $\beta = 1.6\times10^{-5}$ is chosen in all calculations. Rajagopalan *et al.* (1990) have shown that convergent and numerically stable results are obtained for the entire range of viscosity ratios, $0 \leq \beta \leq 1$, with the momentum equation cast in the EVSS formulation. Consequently, the small value of β chosen for these calculations is not expected to pose any numerical difficulties. All calculations are performed with $\sigma=1.0$ which corresponds to isotropic hydrodynamic drag on the polymer molecules as it moves through the solution. As demonstrated in Chapter 3, $\bar{\eta}$ exhibits a small degree of elongation rate thickening for $\sigma=1.0$.

6.1 Flow through Tube Test Problem

Steady-state flow through a circular tube is a non-homogenous shearing motion with the velocity, deformation rate, structure and stress profiles varying only in the radial direction.

Consequently, the solution to the field variables must be the same as the inlet boundary conditions throughout the domain, which makes it easy to test the finite element formulation for different model parameter values. Moreover, the finite element results for the flow through a tube are used as starting guesses for stepping up in contraction ratio which is an added motivation for studying this problem. Results are presented in this section on the effect of De for the concentration N=4.0. This value for the dimensionless concentration is predicted by the liquid-crystal constitutive equation for the 40 wt % hydroxy propyl cellulose in acetic acid liquid-crystalline solution. The dimensionless tube radius and length are: R=1.0 and L=40.0. A 16x32 mesh with 16 elements in the radial direction and 32 elements in the axial direction is used.

Effect of De for N=4.0

Contour plots for the velocity, pressure, structure, velocity gradient, stress and streamlines are shown in Figs. 6.1a-o for De=0.1, 1.0 and 5.0 respectively. Contours for the axial velocity, structure, stress and the rz-component of the velocity gradient tensor are parallel to the z-axis which indicates that there is no axial variation in these variables. The wiggles in the contour plots of radial velocity, rr, zr and zz-components of the velocity gradient result from the numerical approximation to these variables which are zero throughout the domain and is not a manifestion of numerical instabilities in the formulation. Note that the maximum in G_{zz} is located at the inlet (centerline) at moderate and high De whereas it must be zero since the flow is fully developed. Thus the inlet velocity field constructed numerically according to Eq. 5.37 approximates the true fully developed velocity field to the accuracy dictated by the velocity gradient values. Wiggles

De=0.1

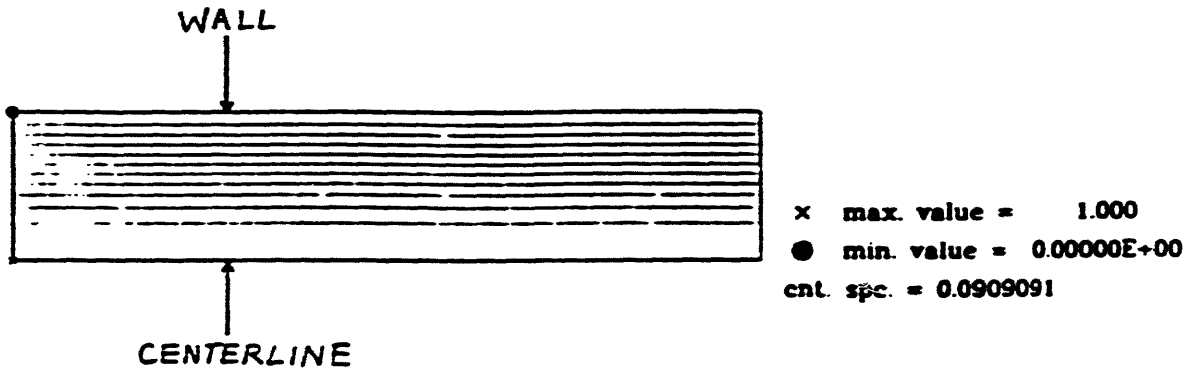

De=1.0

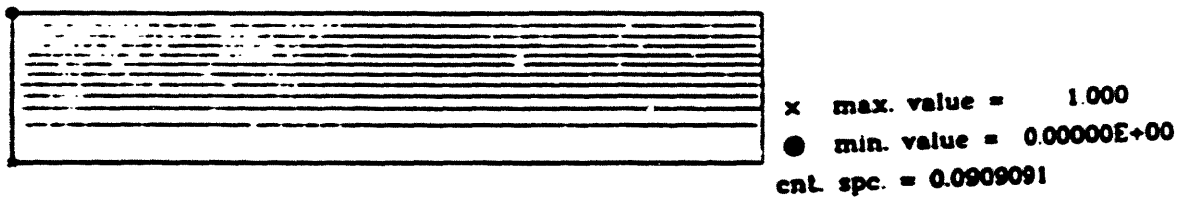

De=5.0

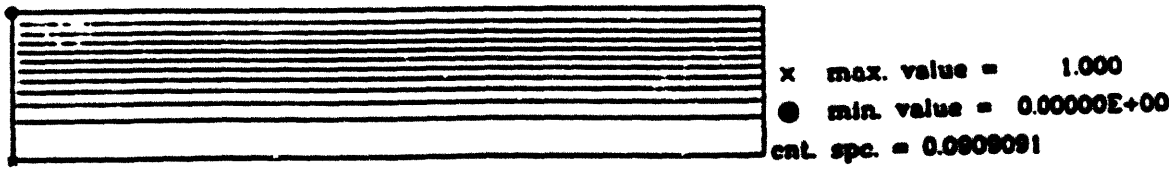

Figure 6.1a Contour plots of streamlines in the flow through a tube for N=4.0, σ=1.0, β=1.6x10^{-5} and De=0.1, 1.0 and 5.0.

De=0.1

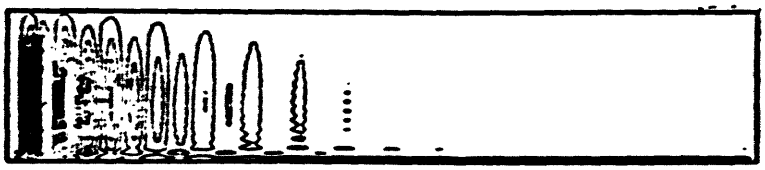

De=1.0

De=5.0

Figure 6.1b Contour plots of radial velocity in the flow through a tube for N=4.0, σ=1.0, β=1.6x10^{-5} and De=0.1, 1.0 and 5.0.

De=0.1

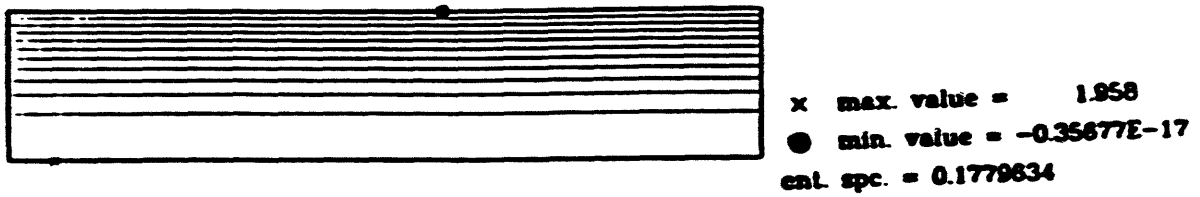

De=1.0

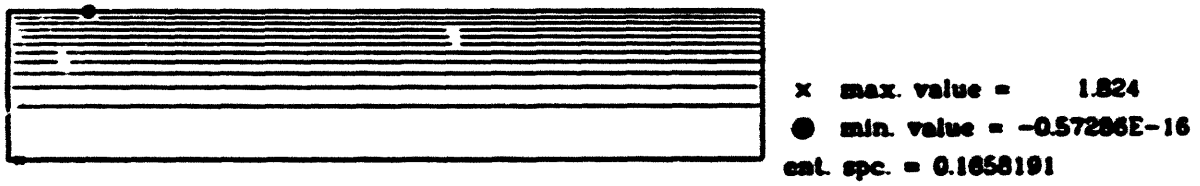

De=5.0

Figure 6.1c Contour plots of axial velocity in the flow through a tube for N=4.0, σ=1.0, β=1.6x10^{-5} and De=0.1, 1.0 and 5.0.

De=0.1

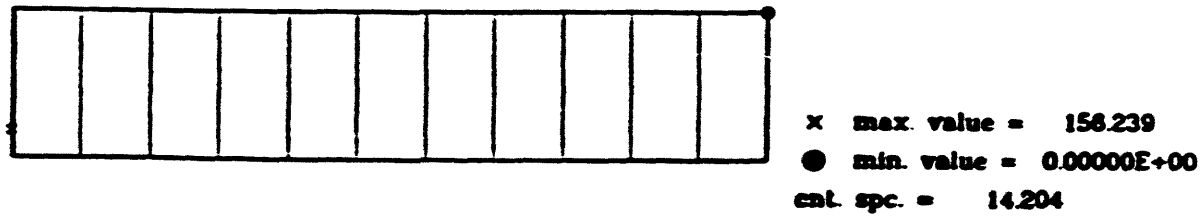

De=1.0

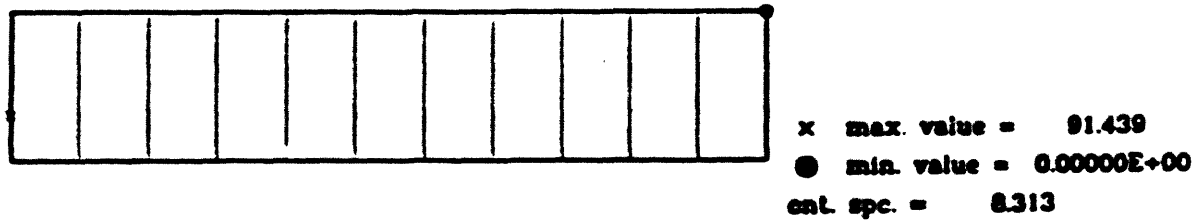

De=5.0

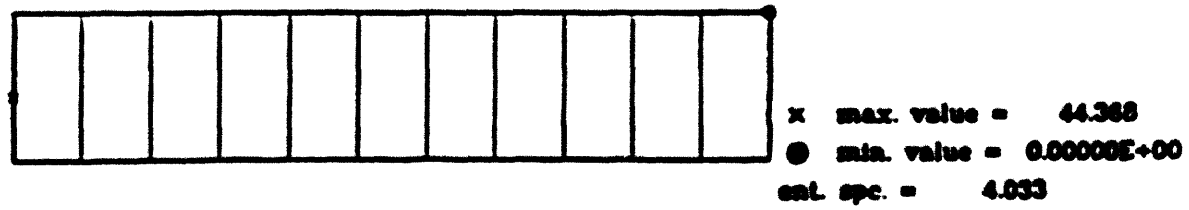

Figure 6.1d Contour plots of pressure in the flow through a tube for N=4.0, σ=1.0, β=1.6x10^{-5} and De=0.1, 1.0 and 5.0.

De=0.1

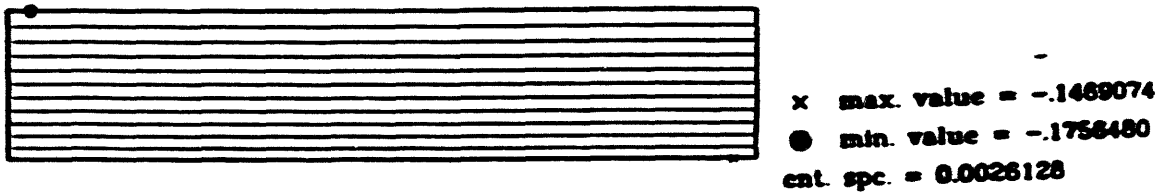

De=1.0

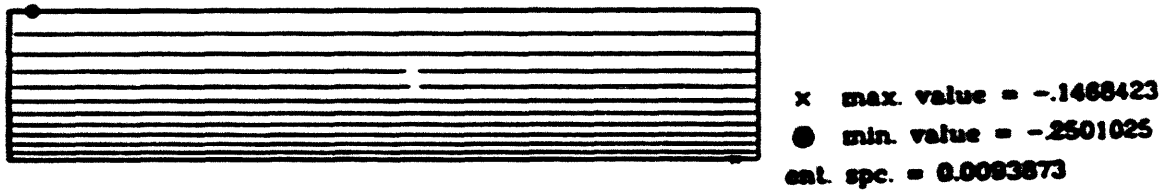

De=5.0

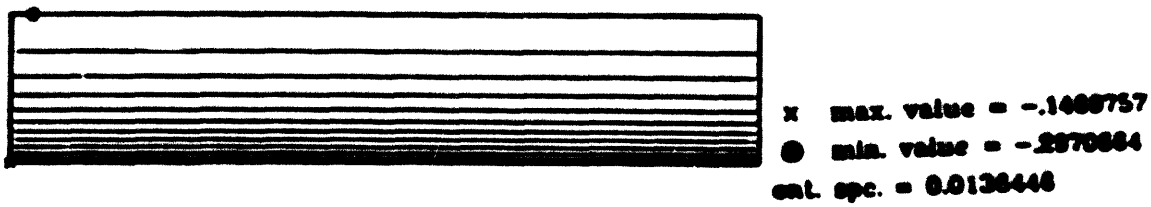

Figure 6.1e Contour plots of S_{rr} in the flow through a tube for N=4.0, σ=1.0, β=1.6x10^{-5} and De=0.1, 1.0 and 5.0.

De=0.1

De=1.0

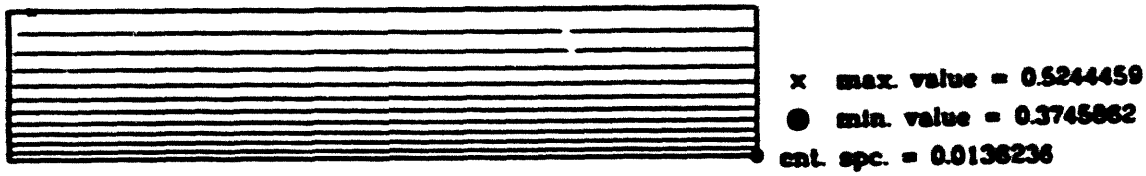

De=5.0

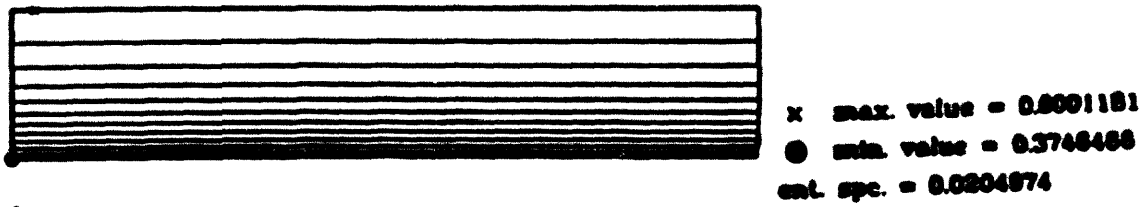

Figure 6.1f Contour plots of S_{zz} in the flow through a tube for N=4.0, α=1.0, β=1.6x10^{-5} and De=0.1, 1.0 and 5.0.

De=0.1

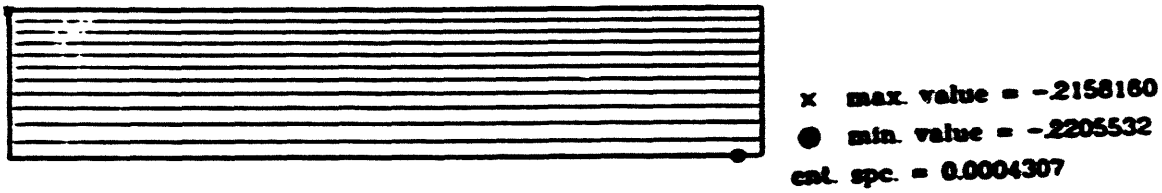

De=1.0

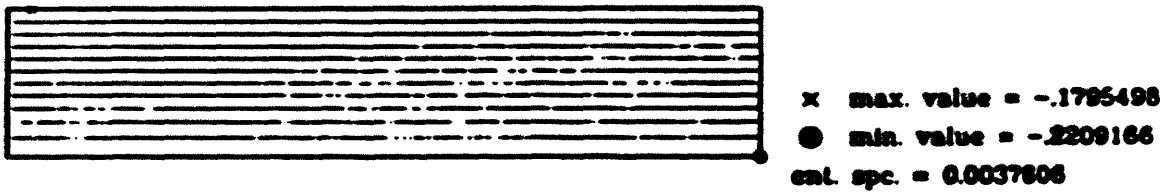

De=5.0

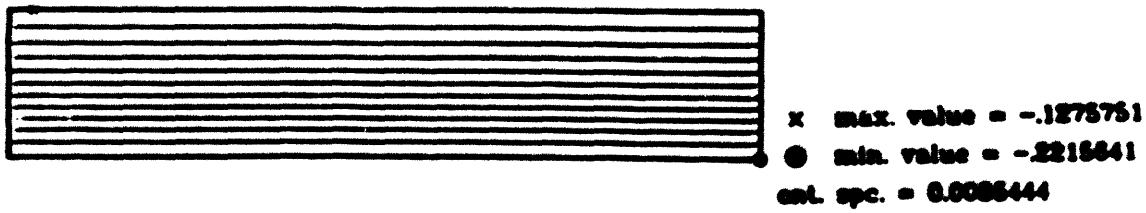

Figure 6.1g Contour plots of S_{rz} in the flow through a tube for N=4.0, α=1.0, β=1.6x10^{-5} and De=0.1, 1.0 and 5.0.

De=0.1

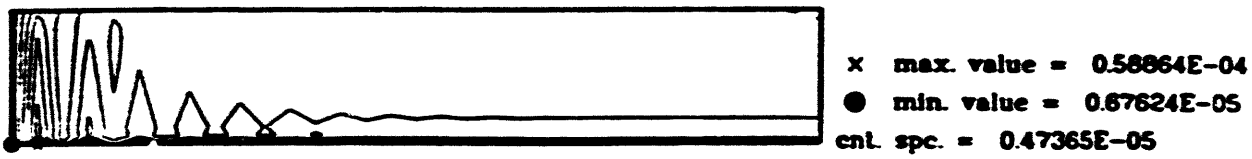

De=1.0

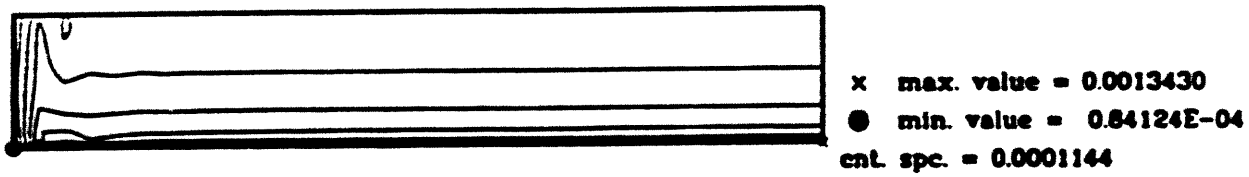

De=5.0

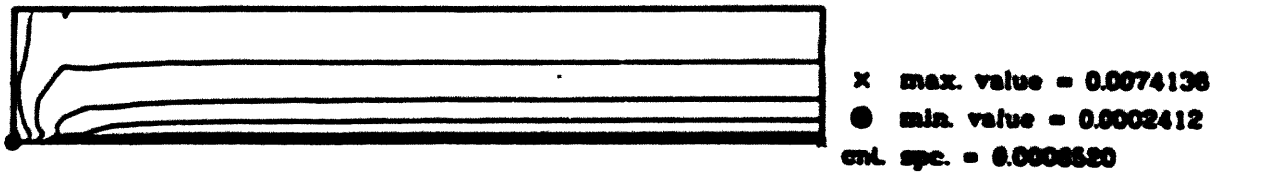

Figure 6.1h Contour plots of De_{π} in the flow through a tube for N=4.0, c=1.0, β=1.6x10^{-5} and De=0.1, 1.0 and 5.0.

De=0.1

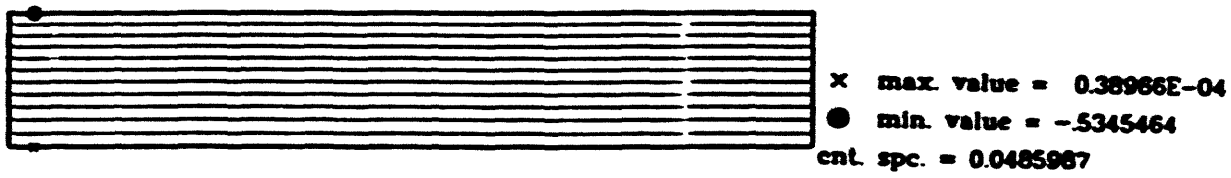

De=1.0

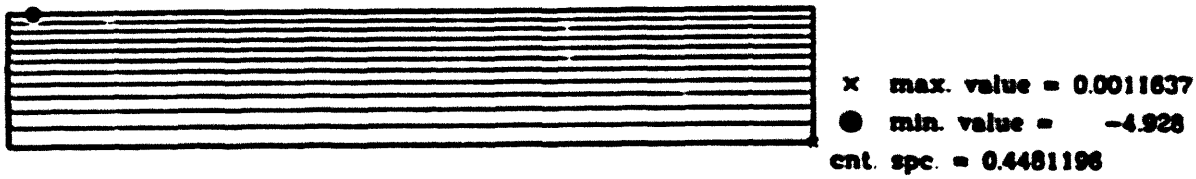

De=5.0

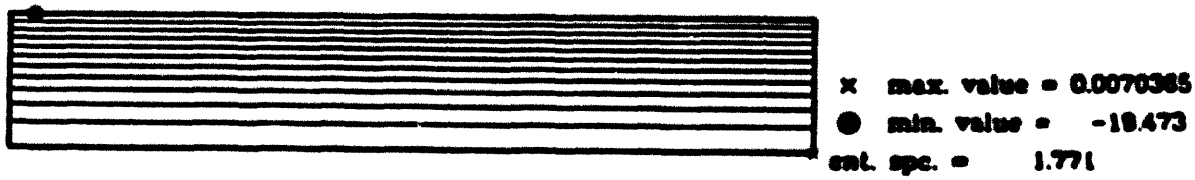

Figure 6.1i Contour plots of Det_{zz} in the flow through a tube for N=4.0, c=1.0, β=1.6x10^{-5} and De=0.1, 1.0 and 5.0.

De=0.1

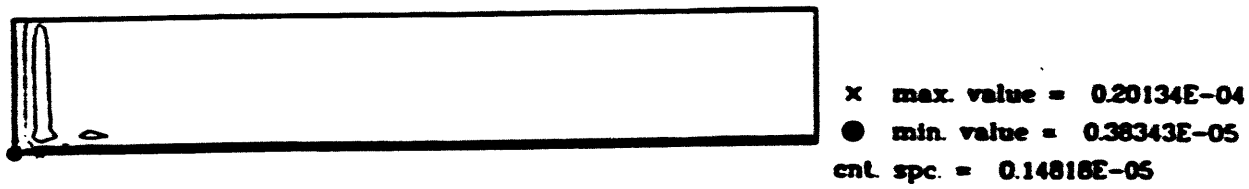

De=1.0

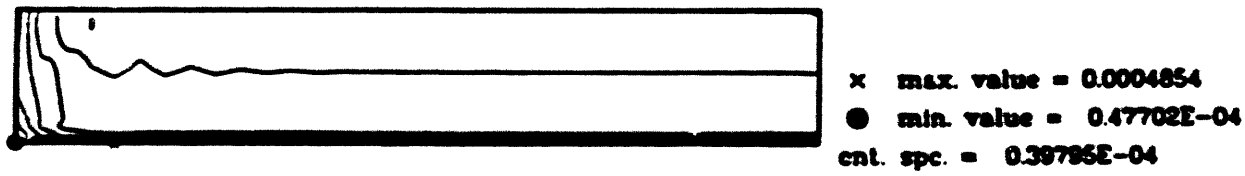

De=5.0

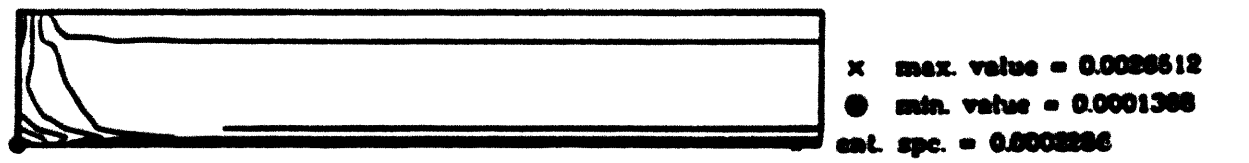

Figure 6.1j Contour plots of De_{gg} in the flow through a tube for N_2=4.0, ϵ=1.0, β=1.6x10^{-3} and De=0.1, 1.0 and 5.0.

De=0.1

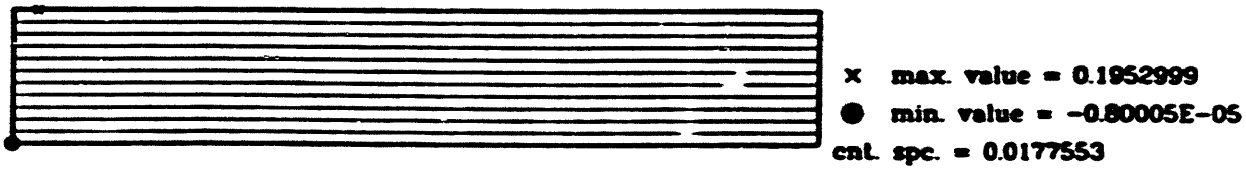

De=1.0

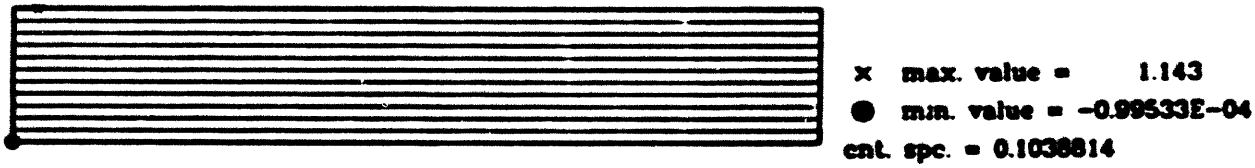

De=5.0

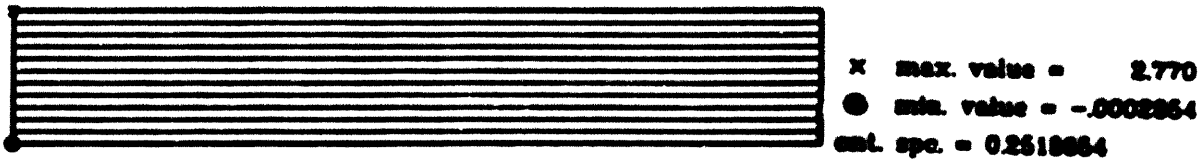

Figure 6.1k Contour plots of Det_{π} in the flow through a tube for N=4.0, c=1.0, β=1.6x10^{-5} and De=0.1, 1.0 and 5.0.

De=0.1

De=1.0

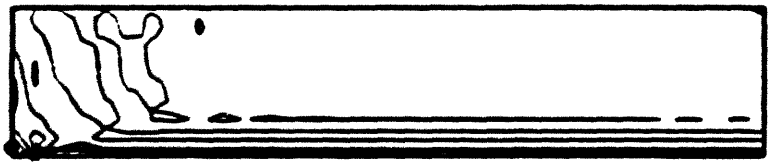

De=5.0

Figure 6.11 Contour plots of G_{rr} in the flow through a tube for N=4.0, σ=1.0, β=1.6x10^{-5} and De=0.1, 1.0 and 5.0.

De=0.1

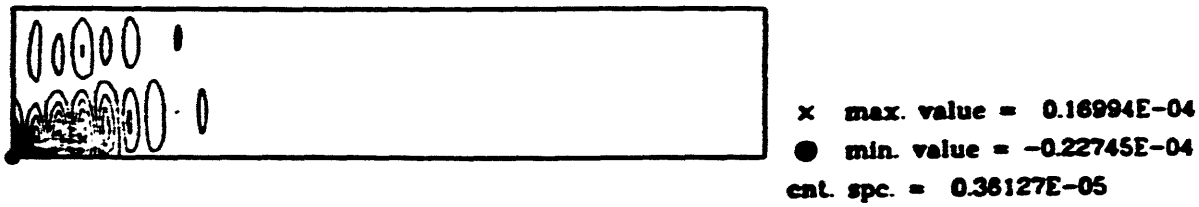

De=1.0

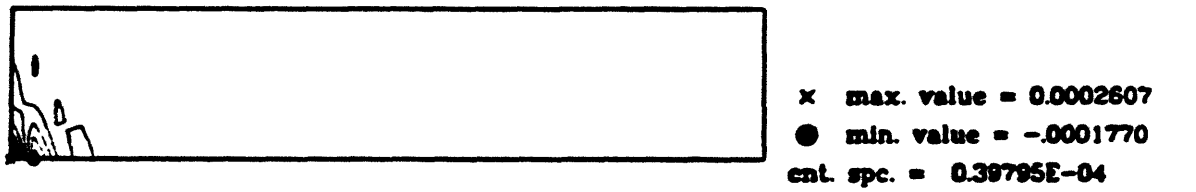

De=5.0

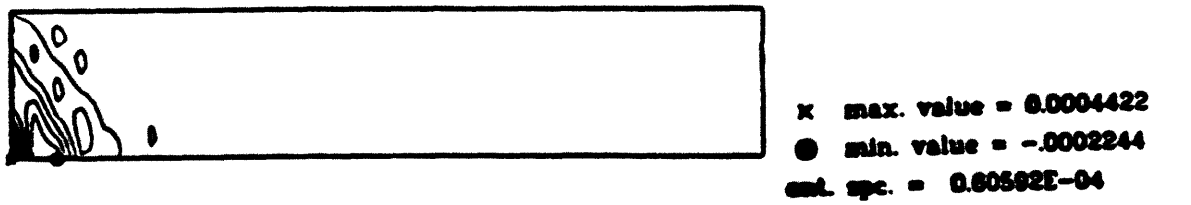

Figure 6.1m Contour plots of G_{zz} in the flow through a tube for N=4.0, σ=1.0, β=1.6x10^{-5} and De=0.1, 1.0 and 5.0.

De=0.1

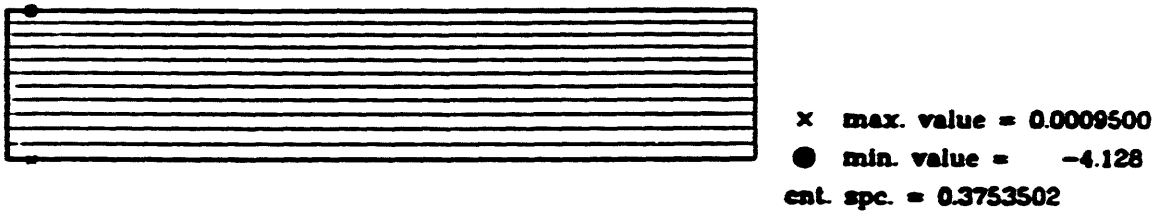

De=1.0

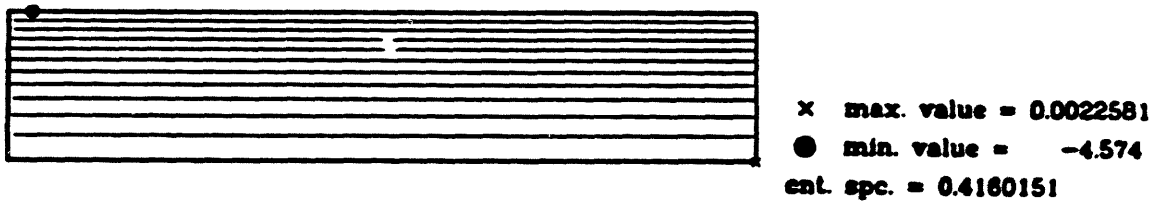

De=5.0

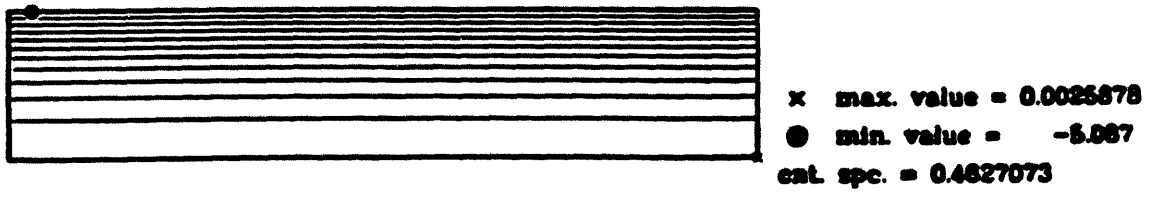

Figure 6.1n Contour plots of G_{rz} in the flow through a tube for N=4.0, σ=1.0, β=1.6x10^{-5} and De=0.1, 1.0 and 5.0.

De=0.1

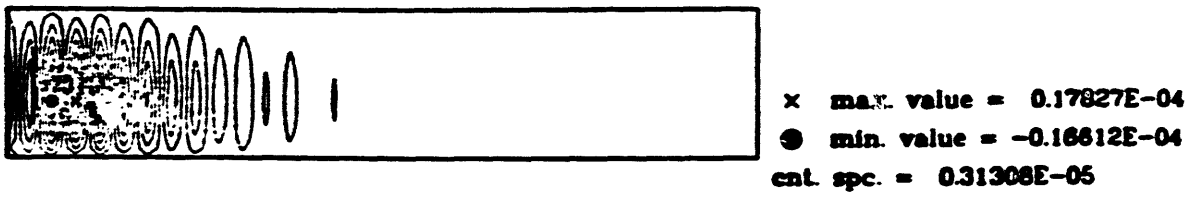

De=1.0

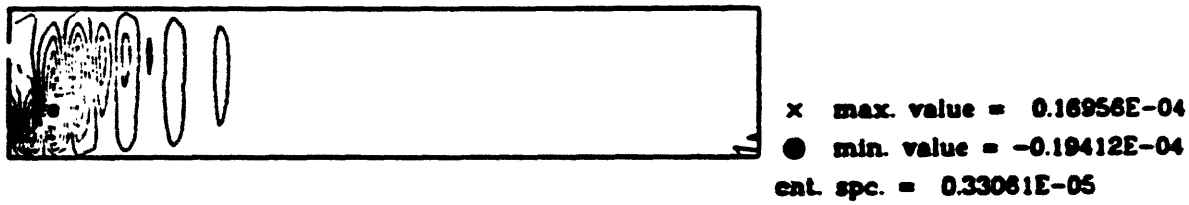

De=5.0

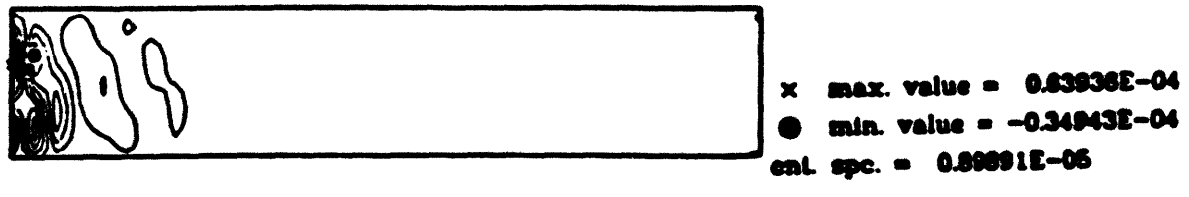

Figure 6.1o Contour plots of G_{zz} in the flow through a tube for N=4.0, σ=1.0, β=1.6x10^{-5} and De=0.1, 1.0 and 5.0.

are also seen in the contour plots for $De\tau_{rr}$ and $De\tau_{\theta\theta}$. Note that for σ=1.0, the stress tensor given by Eq. 3.12 can be expressed in terms of $S_{(1)}$ in dimensionless form as follows

$$\tau = -\beta\dot{\gamma} - 3(1-\beta)\left(\frac{1}{3}\dot{\gamma} - S_{(1)}\right) \tag{6.1}$$

However, for the fully developed tube flow, $\{\dot{\gamma}\}_{rr}$, $\{\dot{\gamma}\}_{\theta\theta}$, $\{S_{(1)}\}_{rr}$ and $\{S_{(1)}\}_{\theta\theta}$ are zero. Thus, τ_{rr} and $\tau_{\theta\theta}$ are zero and the wiggles seen in the contour plots result from the numerical approximation to these variables which are zero throughout the domain. Note that the $De\tau_{rz}$ contours are evenly spaced (linear in r) as expected in a fully developed tube flow.

As mentioned in Section 5.3.2, the most probable prolate molecular orientation angle is given by the eigenvector associated with the dominant eigenvalue of the structure tensor. The eigenvector is also called the nematic director. The eigenvectors associated with the two remaining eigenvalues are perpendicular to the nematic director with one located in the xz-plane and the other perpendicular to the xz-plane. The eigenvectors are mutually orthogonal because S is symmetric. A pictorial representation is provided in Fig. 6.2. The rest of the study concentrates only on the nematic director and all plots showing the prolate molecular orientation angle χ refer to the angle between the director and the axial (z) direction. Radial variations in the invariant of the structure tensor, $S=[3/2(S:S)]^{1/2}$, which quantifies the degree of order, the prolate orientation angle, χ, which locates the nematic director and the axial velocity for the corresponding De's are shown in Figs. 6.3a-c.

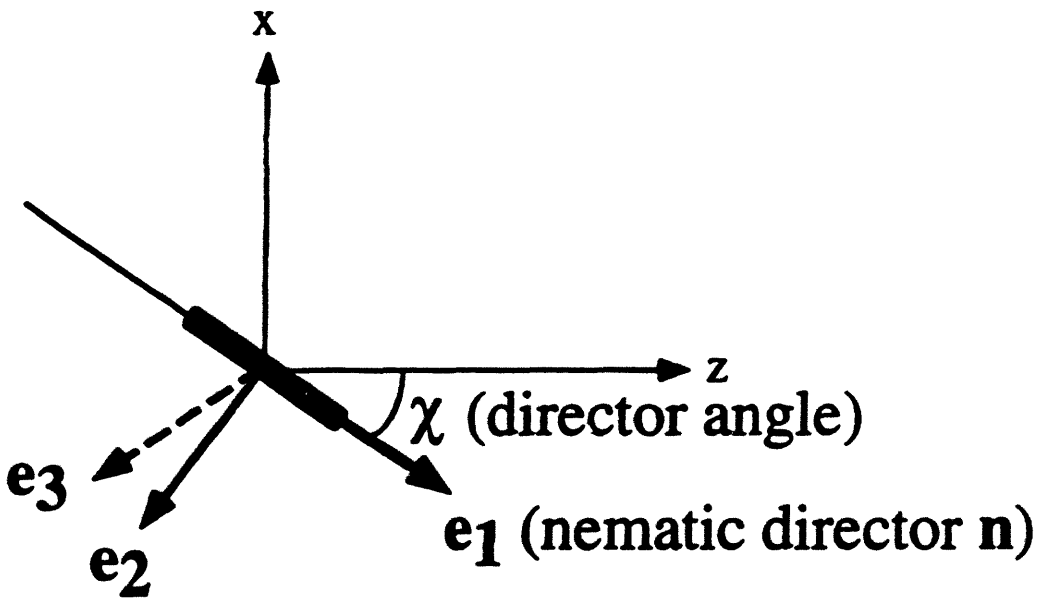

Figure 6.2 Eigenvectors associated with the structure tensor in the flow through a tube and contraction geometries. z is along the axis of the tube and the contraction geometries. The nematic director is indicated by $\mathbf{n}$. $\mathbf{e}_2$ is perpendicular to $\mathbf{n}$ in the xz-plane and $\mathbf{e}_3$ is perpendicular to the xz-plane. χ is shown in degrees in subsequent figures.

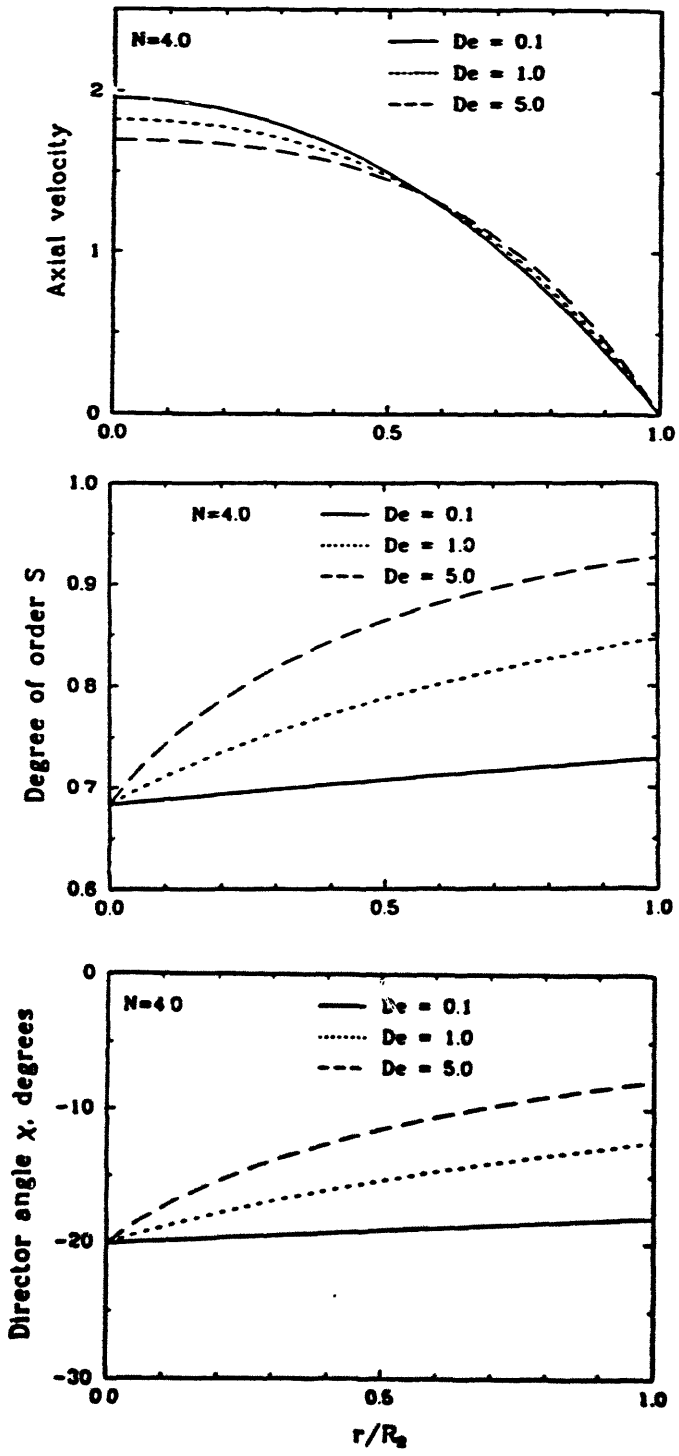

Figure 6.3 Radial variation in (a) the axial velocity v_z, (b) the degree of order S, and (c) the director orientation χ in the flow through a tube for De=0.1, 1.0 and 5.0.

The total dimensionless pressure drop can be written as

$$\frac{\frac{\Delta P}{\eta_0 \langle v \rangle}}{R} = \frac{\pi R^3}{\eta_0}\left(\frac{\Delta P}{Q}\right) = const.\left(\frac{\Delta P}{Q}\right) \tag{6.2}$$

where Q is the volumetric flow rate. It is apparent from Fig. 6.23, then, that the pressure differential required to drive a unit volume flow rate through the tube decreases with De. This is a consequence of shear thinning. The shear thinning is most apparent from Fig. 6.3a. To highlight the shear thinning effect the fully developed Newtonian velocity profile for the flow through a tube given by

$$v_z = 2\left[1-(\frac{r}{R})^2\right] \tag{6.3}$$

is shown. Shear thinning is very small for De=0.1. However, for De=5.0, and to a lesser extent De=1.0, the drop in the maximum centerline velocity as compared to the Newtonian value is testimony to the presence of shear thinning.

Figures 6.3 c and b show that the director alignment with the flow direction and the associated degree of order improve with De. Consequently, the molecular alignment with the flow direction improves which reduces the resistance offered by the molecules to the flow resulting in the observed shear thinning effect. Note that S and χ are radially non-homogenous, especially at high De, since the fully developed flow through the tube is a non-homogenous shearing motion. S is highest at the wall and χ is closest to zero for any De since the shear rate is highest at the wall; that is, the degree of order and the director alignment with the flow direction is best at the wall.

6.2 Flow through Contraction

In Sections 6.2.1 and 6.2.2, the LCP flow through a small contraction (Λ=2) is examined for N=4.0 and 7.0. Issues such as the achievement of a fully developed solution field at the downstream exit, convergence with mesh refinement, effect of De and concentration are discussed. In Section 6.2.3, the effect of increasing the contraction ratio from Λ=2 to 4 is examined. The effect of changing the geometry from a cubic contraction to a conical contraction with rounded corners is examined in Section 6.2.4.

6.2.1 Moderate Concentration; N=4.0

As mentioned in Section 5.2.1, the length of the downstream tube needs to be long enough for the velocity to reach a fully developed profile due to the imposition of a fully developed boundary condition on the velocity field at the exit. Once the velocity profile becomes fully developed, that is the kinematics are fixed, there is still a rate dependent development of S associated with the structure evolution equation; that is, the structure field is not yet fully developed. Let us say, for example, that the velocity field becomes fully developed for a downstream tube length of 10 (z=40 in Fig. 5.5) and there is still a rate dependent development of S; that is, S at z=50 would be different from S at z=40. It is conjectured that the structure development in the contraction geometry when a fully developed velocity boundary condition is imposed at z=40 would be the same as the structure development up to z=40 when a fully developed velocity boundary condition is imposed beyond z=40 due to the hyperbolicity of the structure development. Since the required downstream length increases with De because of the shorter residence time

available to the flow to become fully developed, this conjecture is examined in Section 6.2.1.1 for De=5.0 which is the highest value of De studied in this work. In Section 6.2.1.2, convergence of the solution field with mesh refinement in the L_2-norm is established, and a suitable mesh is chosen for the flow through a 2:1 contraction. In Section 6.2.1.3, the effect of De on the flow field, structure and the stress field (which is postprocessed) is examined. A high degree of order and axial alignment in the director is predicted at De=5.0; also, there is no indication of any qualitative change in the structure development with further increase in De. Hence calculations were not continued beyond De=5.0. No numerical instabilities were observed with increasing De with the EVSS-G formulation and calculations can be continued beyond De=5.0.

6.2.1.1 Effect of Downstream Tube Length

The aim of this section is to first establish a downstream tube length, say $L_{2,0}$, that would be sufficient to predict a fully developed configuration for the velocity at the downstream exit to required accuracy; there must be no radial velocity and the corresponding pressure field should have no radial dependence. Let the corresponding exit boundary be located at $z=z_{exit}=z_0$; note that the entrance to the contraction geometry is located at $z=0$. It is then necessary to test the conjecture proposed in the previous paragraph that the structure development from $z=0$ to $z=z_0$ would not be affected if the downstream length is increased beyond $L_{2,0}$, *i.e.* $z_{exit} > z_0$, even though the structure field at $z=z_0$ is not fully developed. The stress is a dependent variable in this formulation depending on the structure and the velocity gradient and hence is not shown. Information obtained from

the structure tensor is translated into two quantities, the invariant of the structure tensor $S=[3/2(S:S)]^{1/2}$ which quantifies the degree of order and the most probable prolate molecular orientation angle χ which gives the nematic director as described in Section 6.1.

An increase in De can be regarded as a decrease in the residence time available for the flow field to reach a fully developed configuration, which can be compensated only by an increase in the downstream tube length. It is fruitful to test and confirm the conjecture proposed above since increasing the downstream tube length to achieve a fully developed structure field would involve an increase in the computation time associated with the increase in the number of elements with increasing downstream tube length. For this contraction ratio, the downstream tube length was determined for De=5.0, which is the highest value of Deborah number studied, by studying the approach to a fully developed configuration in the exit velocity and by comparing the structure development to that predicted in a contraction geometry with a downstream tube length long enough that S and χ are also fully developed; a downstream tube length that is sufficient for De=5.0 is also expected to be sufficient for smaller values of De.

Figure 6.4a compares the downstream exit profiles in the axial velocity for five different downstream tube lengths at De=5.0. The corresponding radial velocity and pressure profiles are zero everywhere and are not shown. As seen from Fig. 6.4a the axial velocity for a downstream length of 2.5 is far from being fully developed. However, for a downstream length of 10.0 or higher the difference in the centerline velocity is less than one percent of the fully developed value. The velocity profiles are

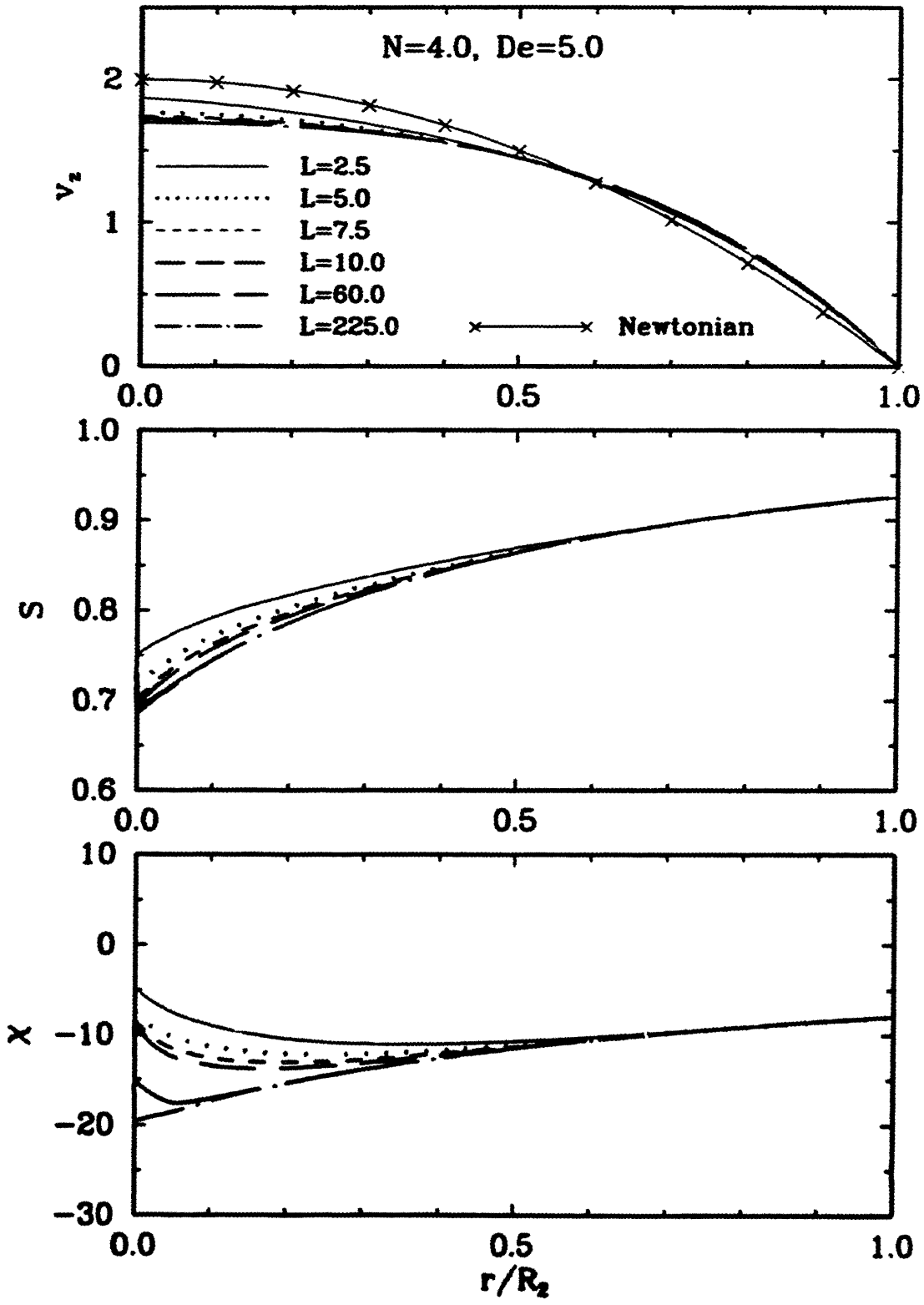

Figure 6.4 Effect of downstream tube length on the radial variation in (a) v_z, (b) S, and (c) χ at the downstream exit in a 2:1 contraction for N=4.0, σ=1.0, β=1.6x10^{-3}, De=5.0 and downstream tube length L=2.5, 5.0, 7.5, 10.0, 60.0 and 225.0.

"plug like" close to the centerline, typical of shear thinning polymer solutions, as opposedto being parabolic with a centerline velocity of two, as observed for Newtonian solutions.

S and χ for the above downstream lengths are shown in Figs. 6.4b and c. It can be seen that S and especially χ require a much longer downstream tube length to achieve a fully developed configuration. The fully developed profiles for a downstream length of 225, as might be expected, compare well with the results presented in Section 6.1 for the non-homogenous shear flow through a tube.

The variation in the order at the centerline with downstream length is shown in Fig. 6.4d. The approach to a fully developed value at the centerline is clear. In fact, a fully developed flow should have no radial and axial velocity gradients at the centerline and consequently the order must correspond to the equilibrium value for N=4.0. As seen from Fig. 6.4d, the deviation from the equilibrium value is only about one percent for a downstream length of 10.0. The variation in the centerline director angle with downstream length is shown in Fig. 6.4e. The zero-shear-rate angle for N=4.0 is also shown for comparison. The approach to a fully developed value in the centerline angle is evident. Unlike the axial velocity or S, χ for a downstream length of 10 is far from the equilibrium value of -20.1 degrees. However, what is of importance is the effect of imposing a fully developed flow field boundary condition at a downstream length of 10 on the structure development in the contraction region and the downstream tube.

Radial profiles of the axial velocity, S and χ at z=30 and 40 are compared for downstream lengths of 10 and 225 in Figs. 6.5a-c. The agreement is excellent except for

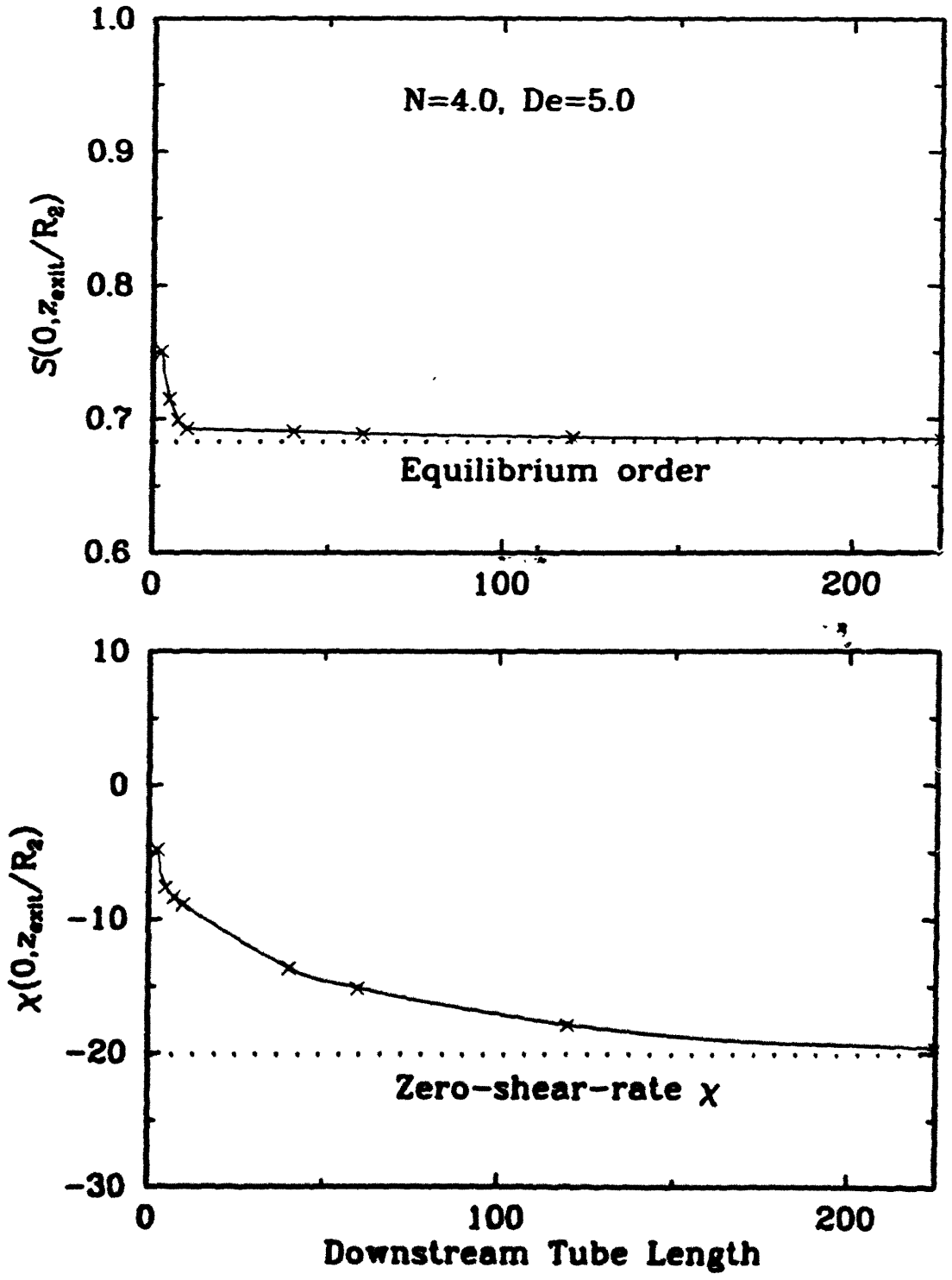

Figure 6.4 Variation in (d) centerline S and (e) centerline χ at the downstream exit with downstream tube length in a 2:1 contraction for N=4.0, σ=1.0, β=1.6x10^{-5} and De=5.0.

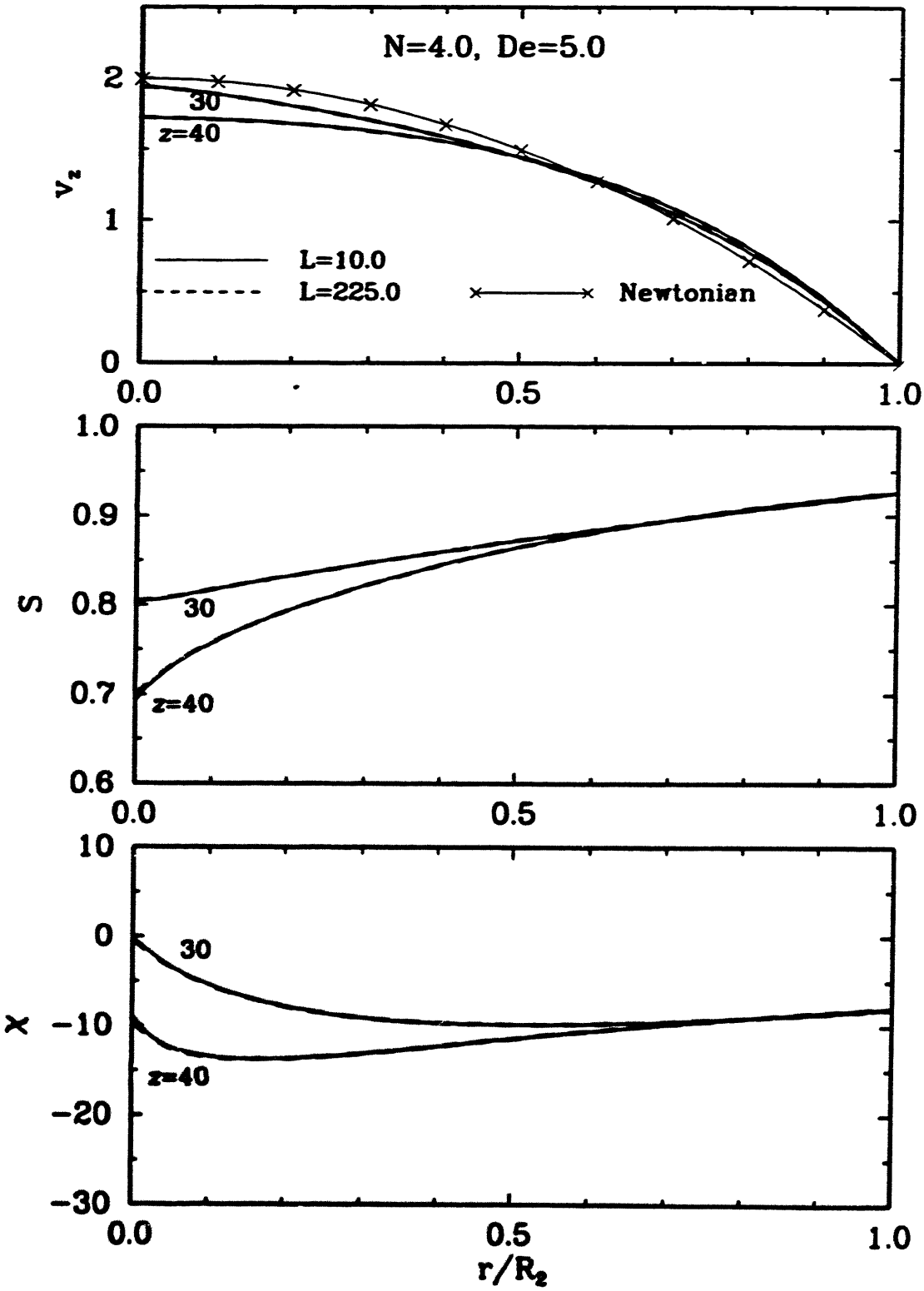

Figure 6.5 Comparison of the radial variation in (a) v_z, (b) S, and (c) χ at $z = 30$ and 40 for downstream tube lengths of 10.0 and 225.0 in a 2:1 contraction for N=4.0, σ=1.0, β=1.6x10^{-5} and De=5.0.

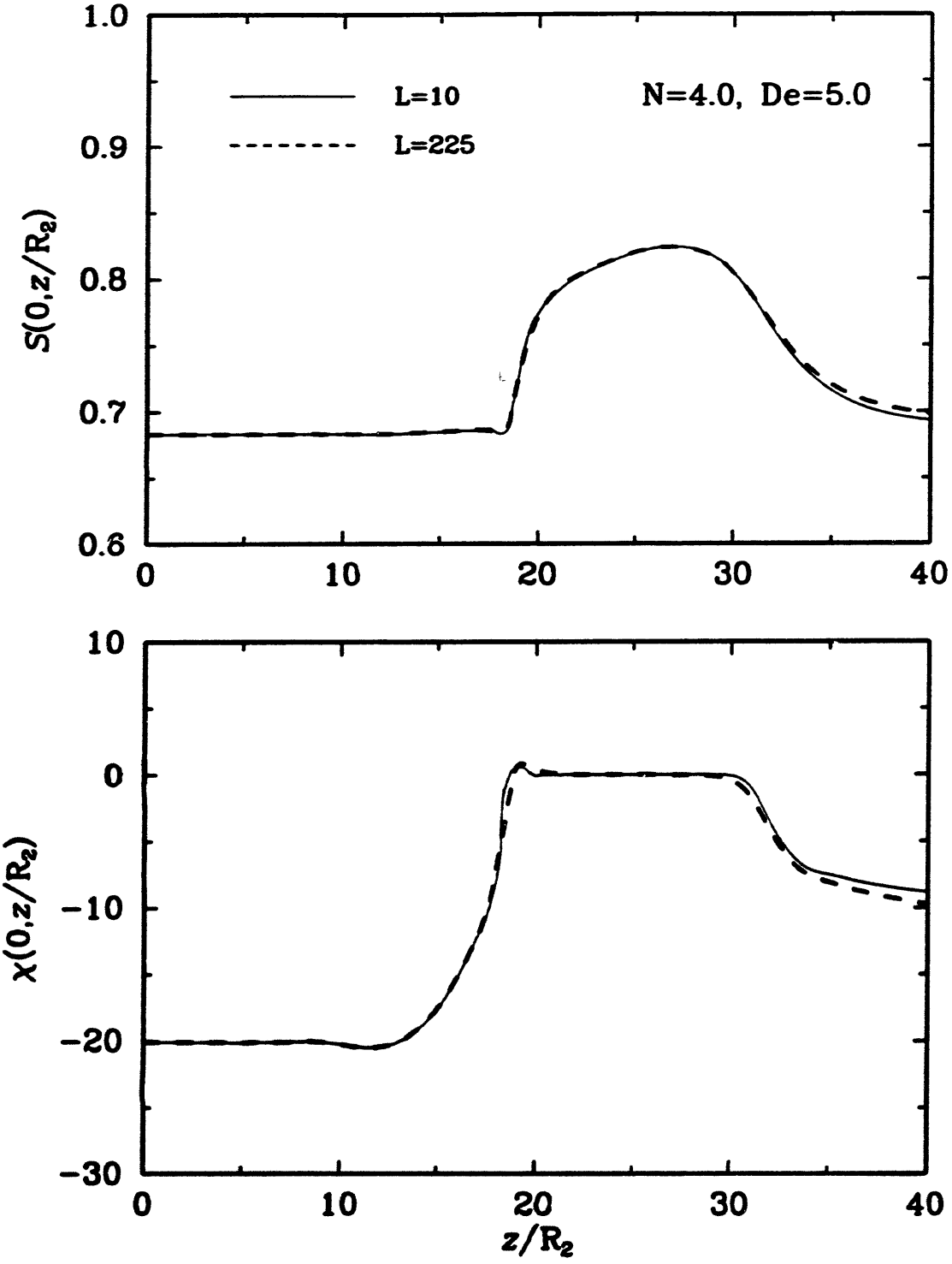

Figure 6.5 Comparison of the variation in (d) centerline S and (e) centerline χ upto z = 40 for downstream tube lengths of 10.0 and 225.0 in a 2:1 contraction for N=4.0, σ=1.0, β=1.6x10^{-5} and De=5.0.

minor deviations in S and χ at the centerline. The centerline order and angle up to z=40 (exit boundary for downstream length of 10) for the two downstream lengths are compared in Figs. 6.5d and e. S and χ near the exit boundary for the downstream length of 10 vary only by one percent from the true value. The results in Figs. 6.5a-e demonstrate that if the velocity at the exit is close to the true fully developed configuration the hyperbolicity in the structure development guarantees that the S and χ solution fields in the contraction geometry would match very well with the true solution field even though S and χ are not fully developed at the exit.

The velocity profile changes only by one percent when the downstream length is increased from 10.0 to 225.0. The S and χ solution fields up to z=40, which defines the exit boundary for a downstream length of 10.0, also show very good agreement with the true fully developed solution field determined with a downstream length of 225. Hence, for the rest of the calculations a downstream length of 10.0 is chosen as a good trade-off between the increase in computation time and the accuracy of the solution for the field variables in the contraction geometry.

6.2.1.2 Convergence with Mesh Refinement

Demonstrating the convergence of the numerical solution to the exact solution with mesh refinement is an important consideration in finite element calculations. One measure of convergence, defined in L_2 space, is given by Eq. 5.48. As a corollary to this equation, $L_2(\mathbf{u}^h)$ must approach $L_2(\mathbf{u})$ in the limit $h \to 0$.

As possibly the most difficult calculation, convergence of solution with mesh

refinement is tested for De=5.0, the highest value of Deborah number studied in this work. The variation in the L_2-norm of the solution field with the number of elements is shown in Fig. 6.6. There is very little change in the solution norm for meshes with 1856, 2261 and 2676 elements. However, the L_2-norm defined as

$$\|u\|_{L_2} = C\left[\int_D \sum_{i=1}^{n} u_i^2 r\,dr\,dz\right]^{\frac{1}{2}} ; \quad n = \text{no. of variables} \tag{6.4}$$

for an axisymmetric problem, fails to test the accuracy of the solution field at the centerline due to the weighting function r. In Figs. 6.7a and b radial profiles for S and χ at the inlet (z=0), downstream exit (z=40) and where the contraction region blends with the downstream tube (z=30) are shown. The radial profiles at the inlet extend up to r/R_2=2, but for the purpose of comparison with the downstream profiles are shown only up to r/R_2=1. Agreement is good everywhere except close to the centerline where some deviations from the predictions for the mesh with 2676 elements are noticed in S and χ for the mesh with 1856 elements. Variation in S and χ along the centerline is shown in Figs. 6.7c and d. S and χ for the meshes with 1856 and 2261 elements show the maximum difference from S and χ for the mesh with 2676 elements near the downstream exit. However, the difference in S and χ between the meshes with 2261 and 2676 elements is very small; S differs by no more than 0.002 and χ differs by no more than half a degree.

From the results shown in Figs. 6.6, 6.7a-d it can be safely inferred that the mesh with 2261 elements is suitable for calculations up to De=5.0 for the 2:1 contraction.

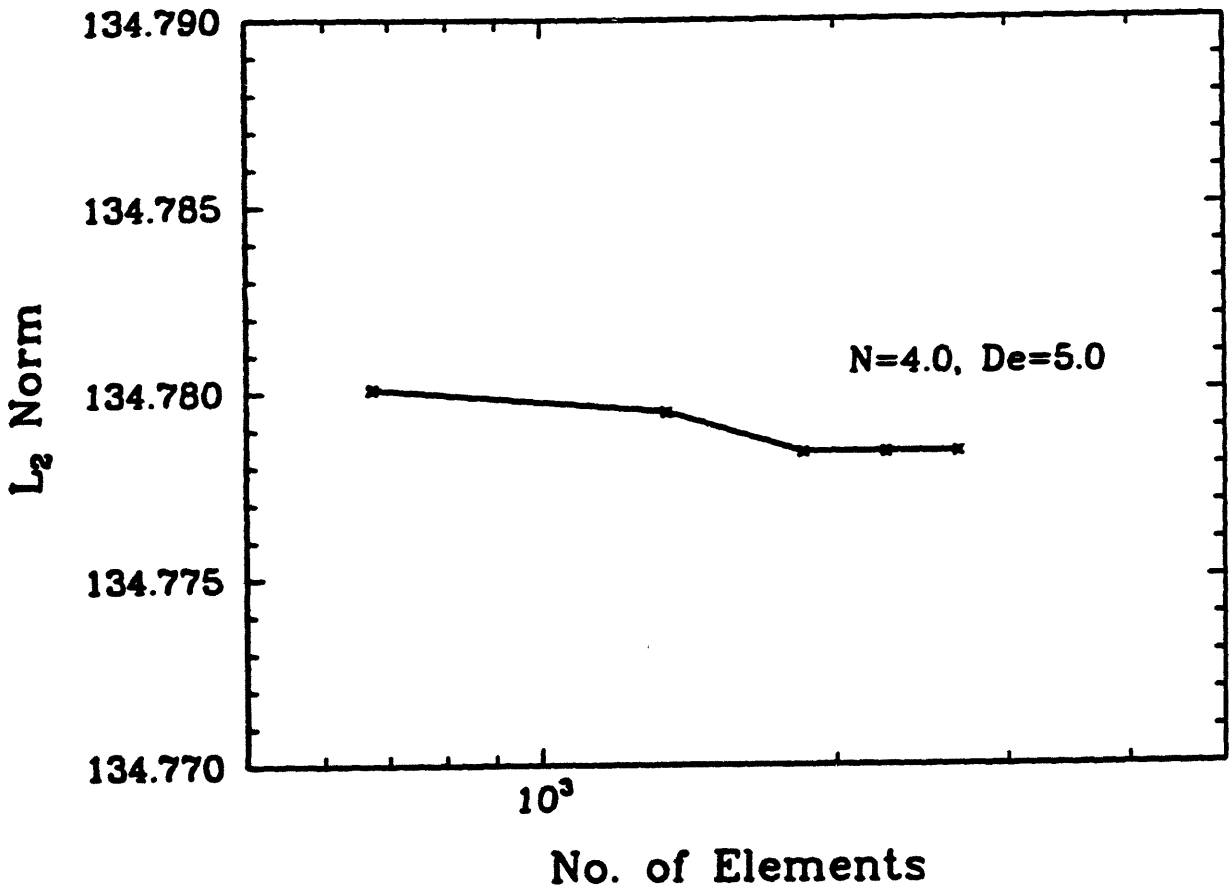

Figure 6.6 Variation in the L_2-norm of the solution field with number of elements in a 2:1 contraction for N=4.0, σ=1.0, β=1.6x10^{-5} and De=5.0.

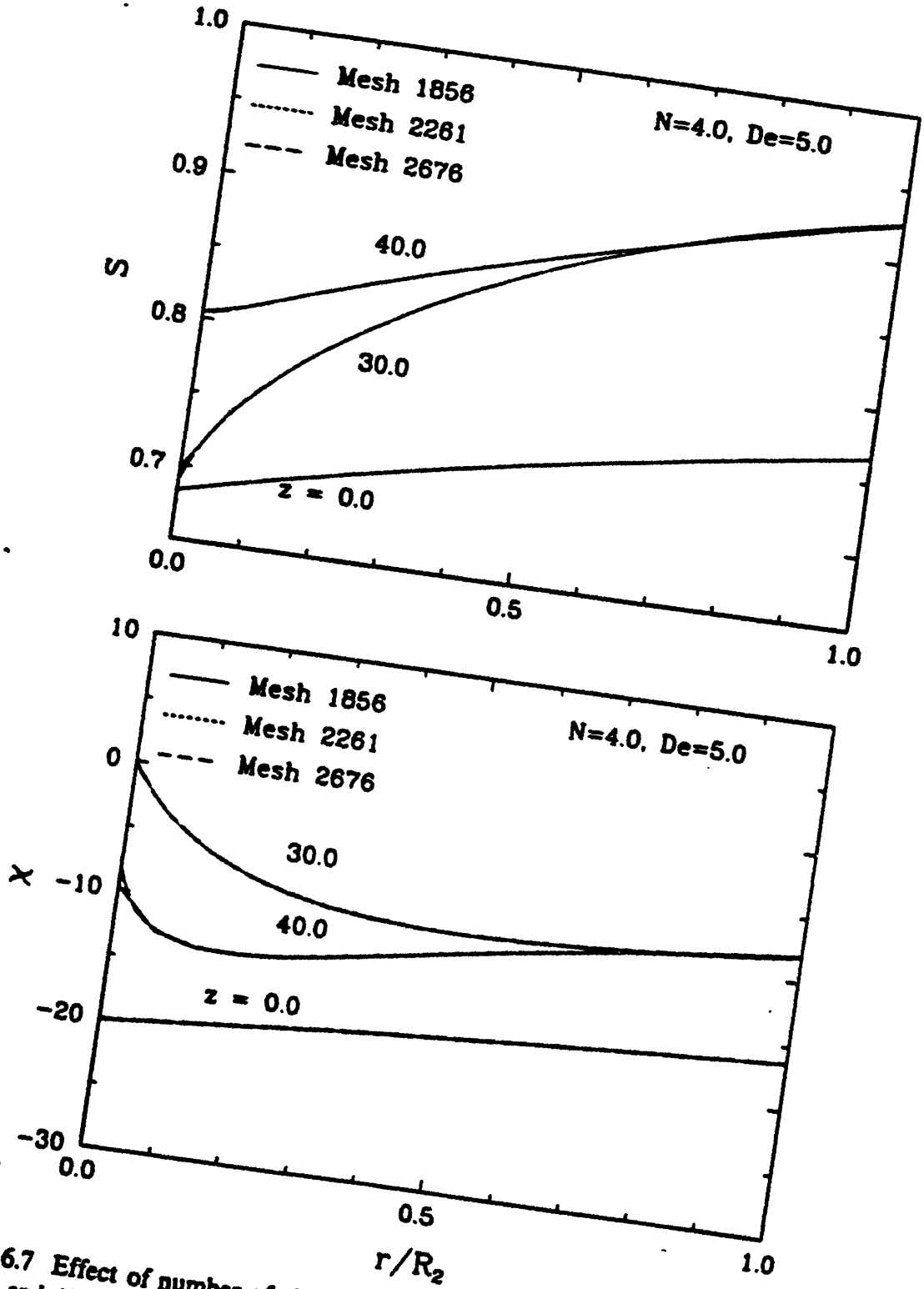

Figure 6.7 Effect of number of elements on the radial variations in (a) S and (b) χ at z=0, 30 and 40 in a 2:1 contraction for N=4.0, σ=1.0, β=1.6x10^{-5} and De=5.0.

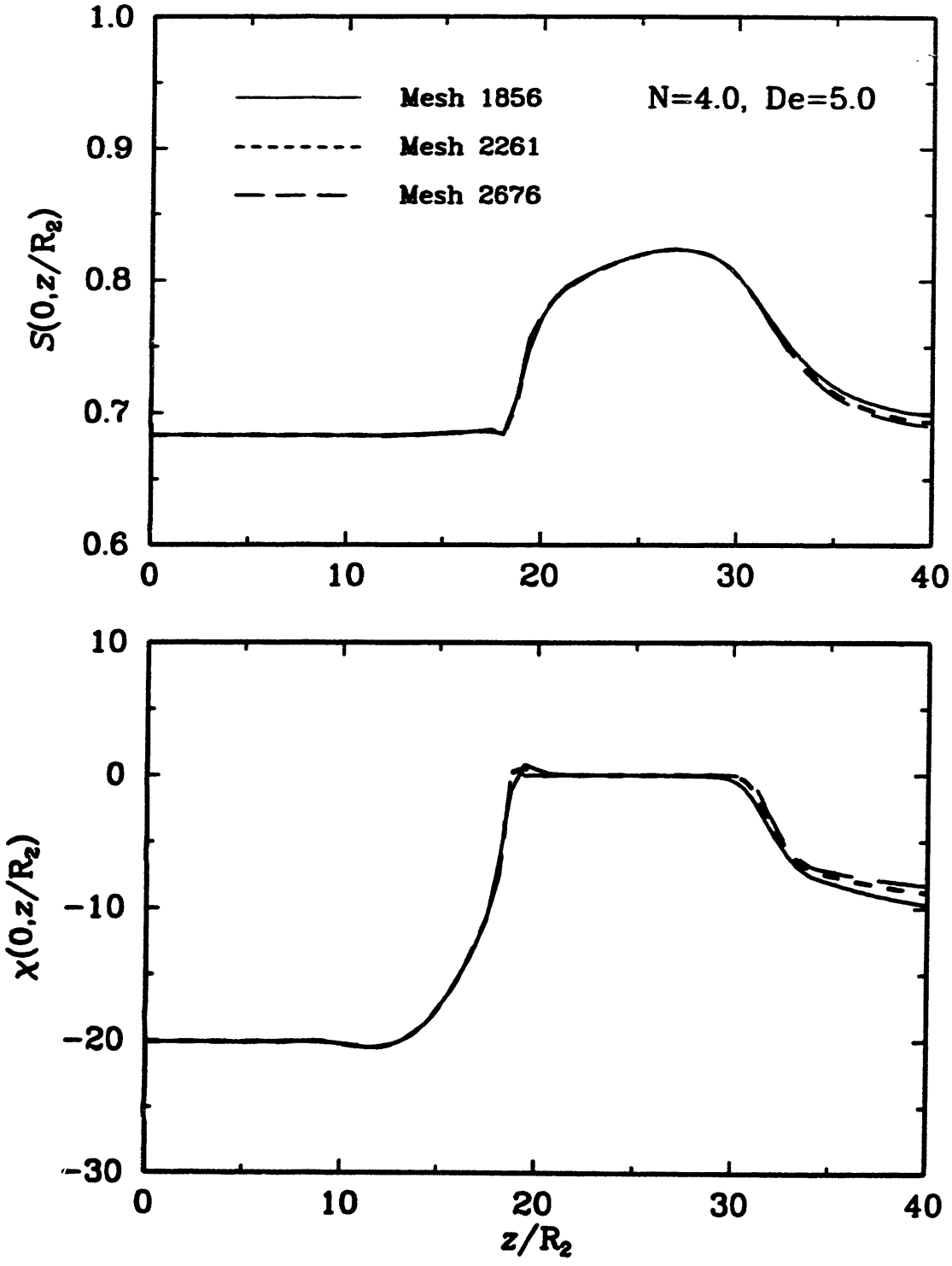

Figure 6.7 Effect of number of elements on the variation in (c) centerline S and (d) centerline χ in a 2:1 contraction for N=4.0, σ=1.0, β=1.6x10^{-5} and De=5.0.

6.2.1.3 Effect of De; De=0.1, 1.0 and 5.0

The aim of this section is to study the effect of small, moderate and reasonably large Deborah numbers on the development of the flow field, the degree of molecular order and the orientation and examine the implications on the assumptions used in the fiber drawing analysis discussed in Chapter 4. The discussion is divided into four sub-sections: (1) effect of De on velocity, (2) effect of De on the degree of order S , (3) effect of De on the director angle χ, and (4) implications for fiber drawing analysis and processing; the validity of the assumptions used in the fiber drawing analysis and design and process conditions to improve the degree and axial homogenity in the molecular orientation are discussed in this sub-section. Contour plots of pressure, components of structure tensor, velocity, components of velocity gradient tensor, components of stress tensor and streamlines are shown in Figs. 6.8a-o for De=0.1, 1.0 and 5.0. Information contained in the contour plots for the components of the structure tensor is transformed into information for S and χ and is shown in Figs. 6.8p-q. To better illustrate the quantitative effect of De on the axial velocity, degree of order and the molecular orientation, as the flow progresses through the contraction geometry shown in Fig. 5.1a, cross-sectional profiles at the inlet, the downstream exit and the axial location where the contraction region blends with the downstream tube are plotted in Figs. 6.9a-c. The radial profiles at the inlet extend up to r/R_2=2 but are shown only upto r/R_2=1 for the purpose of comparison with the downstream profiles. The maximum velocity and the percentage overshoot over the downstream exit velocity are listed in Table 6.1. The effect of De on the development of order and orientation along the centerline and the response to the

De=0.1

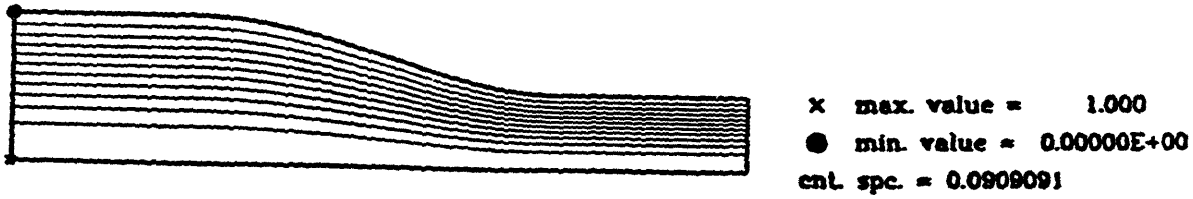

De=1.0

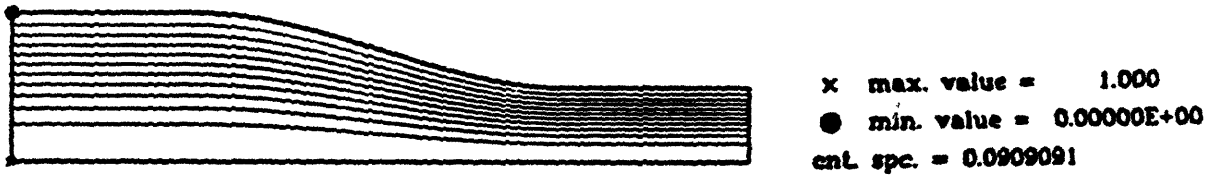

De=5.0

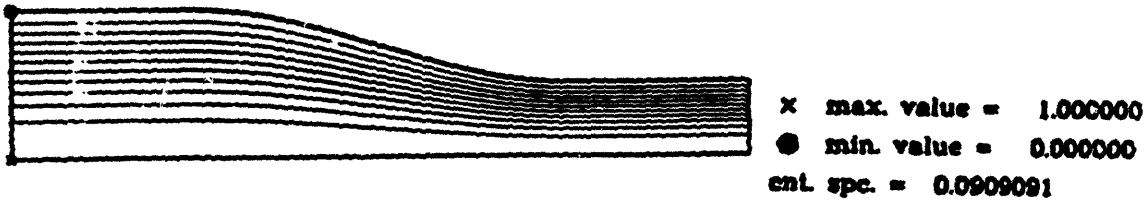

Figure 6.8a Contour plots of streamlines in the flow through a 2:1 contraction for N=4.0, σ=1.0, β=1.6x10^{-5} and De=0.1, 1.0 and 5.0.

De=0.1

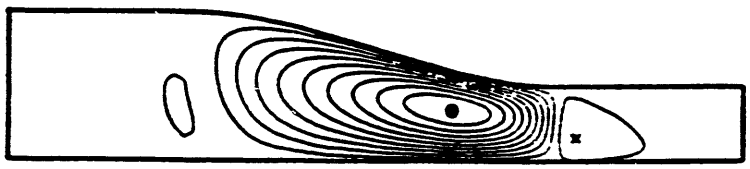

De=1.0

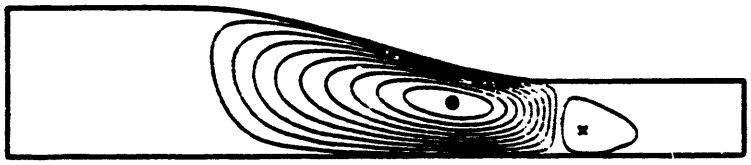

De=5.0

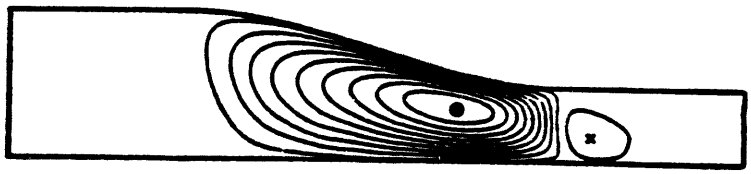

Figure 6.8b Contour plots of radial velocity in the flow through a 2:1 contraction for N=4.0, σ=1.0, β=1.6x10^{-5} and De=0.1, 1.0 and 5.0. Radial velocity is made dimensionless with the average velocity in the downstream tube $V_{2,avg}$.

De=0.1

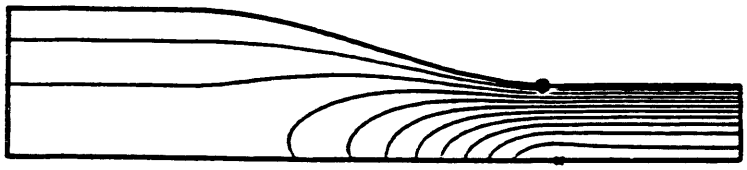

De=1.0

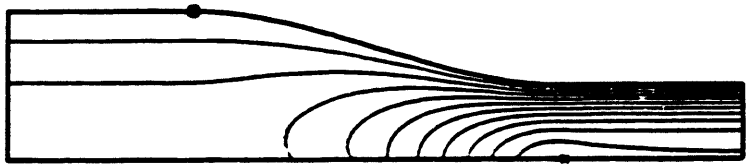

De=5.0

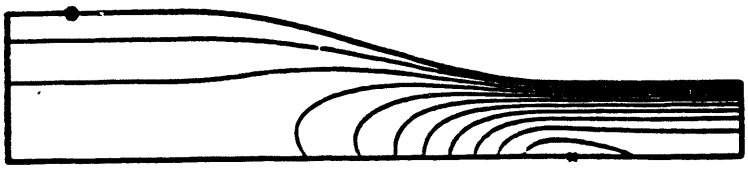

Figure 6.8c Contour plots of axial velocity in the flow through a 2:1 contraction for N=4.0, σ=1.0, β=1.6x10^{-5} and De=0.1, 1.0 and 5.0. The axial velocity is made dimensionless with the average velocity in the downstream tube $V_{2,avg}$.

De=0.1

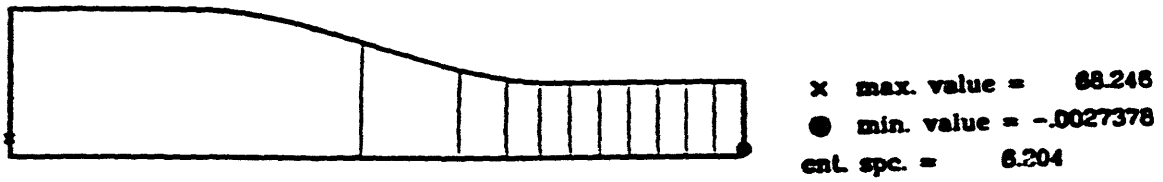

De=1.0

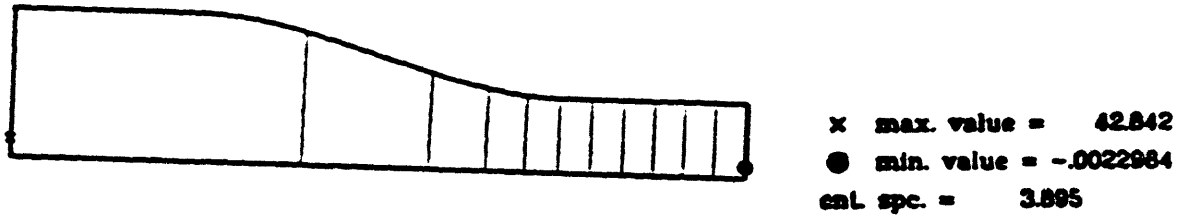

De=5.0

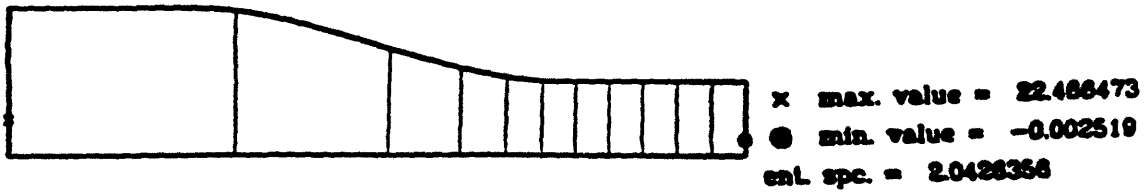

Figure 6.8d Contour plots of pressure in the flow through a 2:1 contraction for N=4.0, σ=1.0, β=1.6x10^{-5} and De=0.1, 1.0 and 5.0.

De=0.1

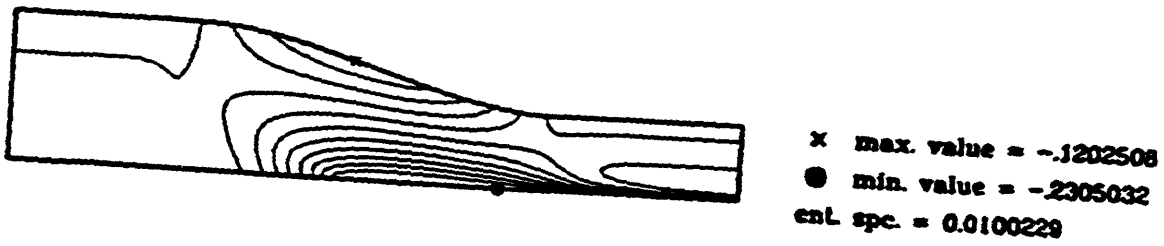

De=1.0

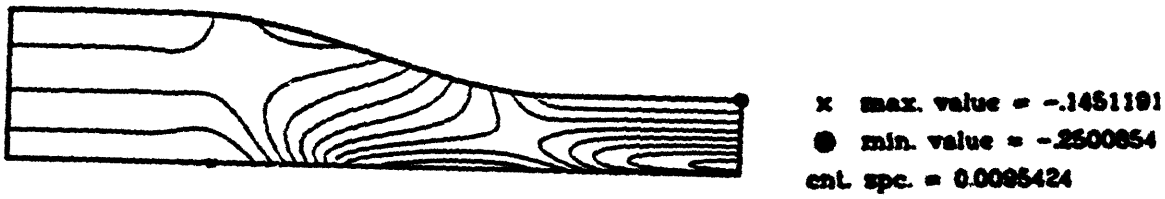

De=5.0

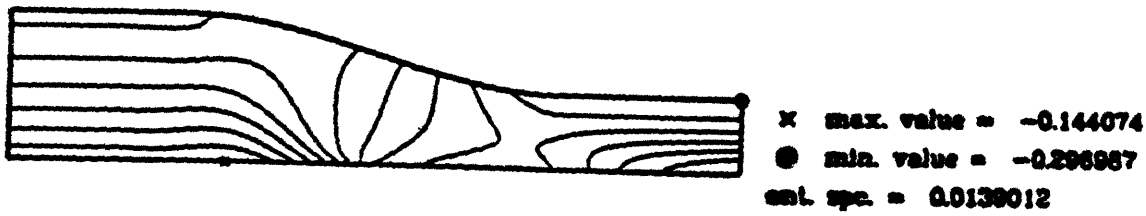

Figure 6.8e Contour plots of S_{rr} in the flow through a 2:1 contraction for N=4.0, α=1.0, β=1.6x10^{-5} and De=0.1, 1.0 and 5.0.

De=0.1

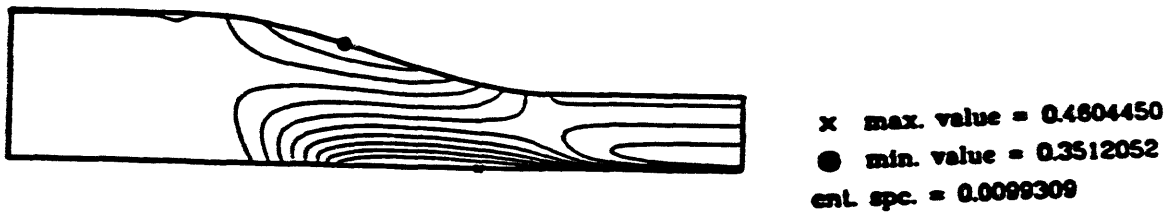

De=1.0

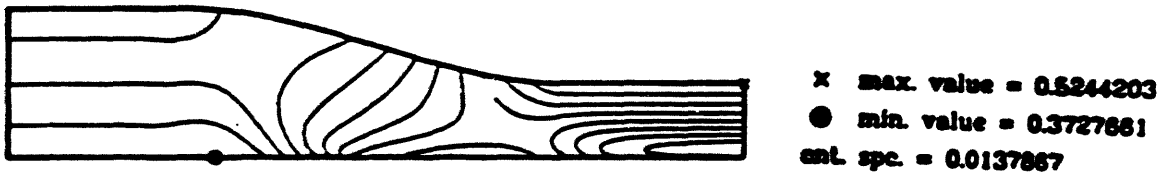

De=5.0

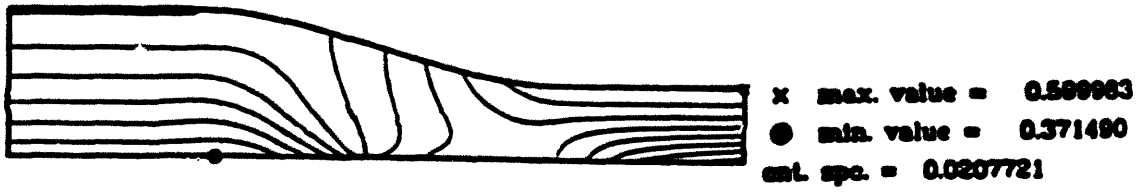

Figure 6.8f Contour plots of S_{zz} in the flow through a 2:1 contraction for N=4.0, σ=1.0, β=1.6x10^{-5} and De=0.1, 1.0 and 5.0.

De=0.1

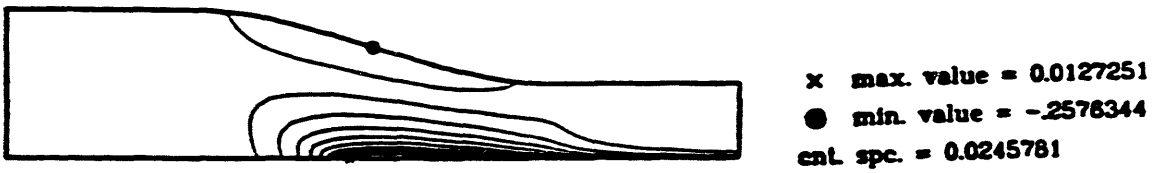

De=1.0

De=5.0

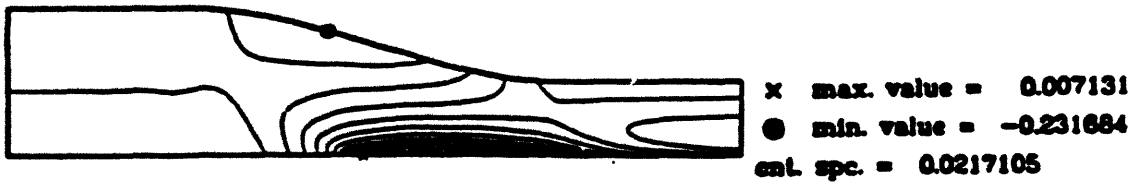

Figure 6.8g Contour plots of S_{rz} in the flow through a 2:1 contraction for N=4.0, σ=1.0, β=1.6x10^{-5} and De=0.1, 1.0 and 5.0.

De=0.1

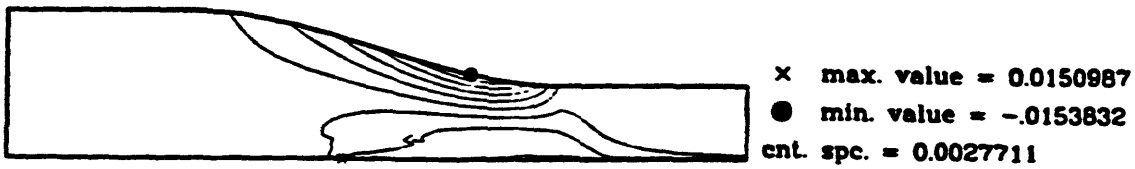

De=1.0

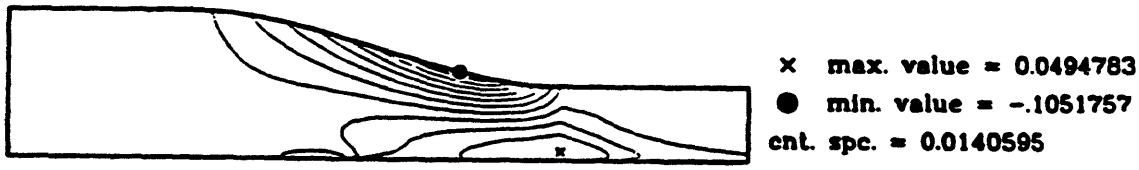

De=5.0

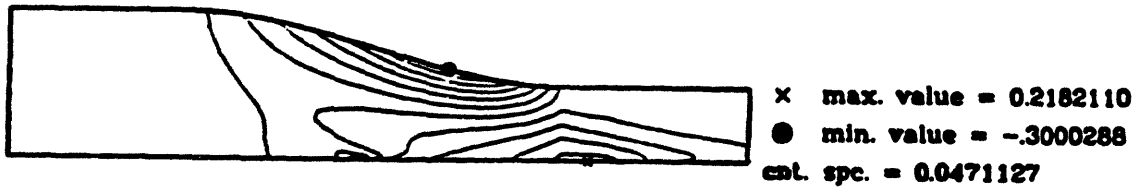

Figure 6.8h Contour plots of $De\tau_{rr}$ in the flow through a 2:1 contraction for N=4.0, σ=1.0, β=1.6x10^{-5} and De=0.1, 1.0 and 5.0.

De=0.1

De=1.0

De=5.0

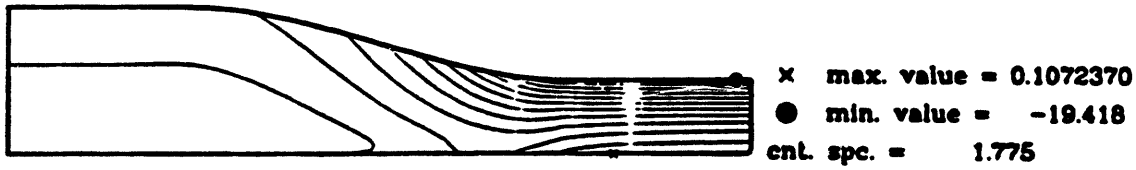

Figure 6.8i Contour plots of $De\tau_{zz}$ in the flow through a 2:1 contraction for N=4.0, σ=1.0, β=1.6x10^{-5} and De=0.1, 1.0 and 5.0.

De=0.1

De=1.0

De=5.0

Figure 6.8j Contour plots of $De\tau_{\theta\theta}$ in the flow through a 2:1 contraction for N=4.0, σ=1.0, β=1.6x10^{-5} and De=0.1,-1.0 and 5.0.

De=0.1

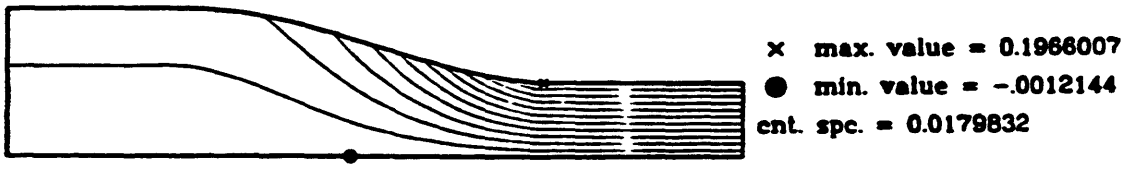

De=1.0

De=5.0

Figure 6.8k Contour plots of $De\tau_{rz}$ in the flow through a 2:1 contraction for N=4.0, σ=1.0, β=1.6x10^{-5} and De=0.1, 1.0 and 5.0.

De=0.1

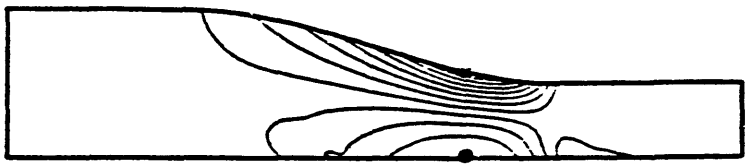

De=1.0

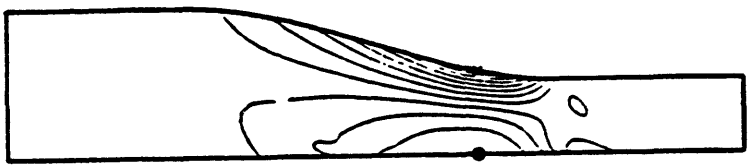

De=5.0

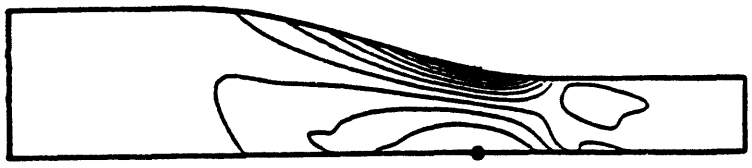

Figure 6.81 Contour plots of G_{rr} in the flow through a 2:1 contraction for N=4.0, σ=1.0, β=1.6x10^{-5} and De=0.1, 1.0 and 5.0.

De=0.1

De=1.0

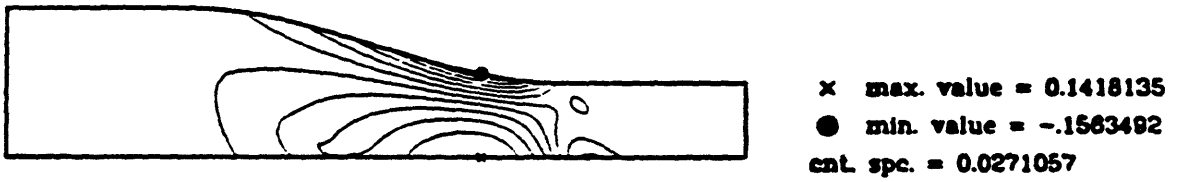

De=5.0

Figure 6.8m Contour plots of G_{zz} in the flow through a 2:1 contraction for N=4.0, σ=1.0, β=1.6x10^{-5} and De=0.1, 1.0 and 5.0.

De=0.1

De=1.0

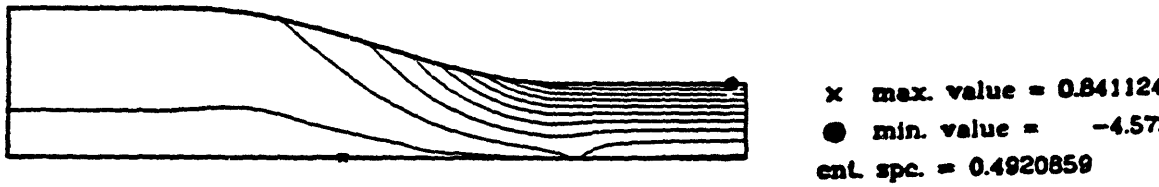

De=5.0

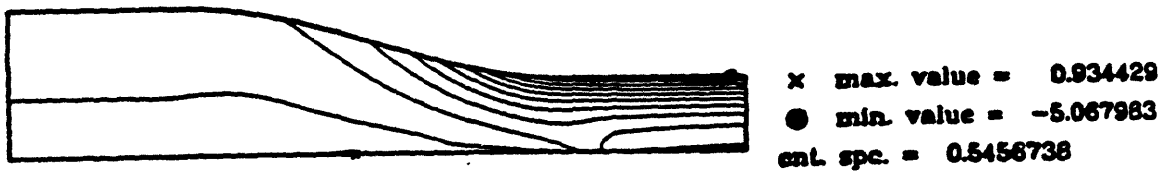

Figure 6.8n Contour plots of G_{rz} in the flow through a 2:1 contraction for N=4.0, σ=1.0, β=1.6x10^{-5} and De=0.1, 1.0 and 5.0.

De=0.1

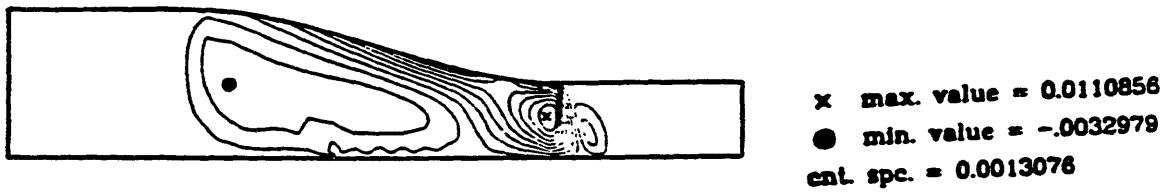

De=1.0

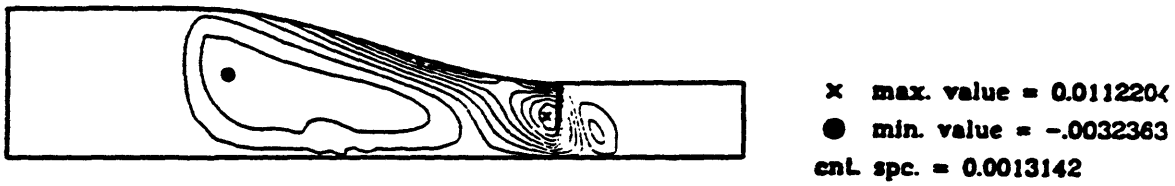

De=5.0

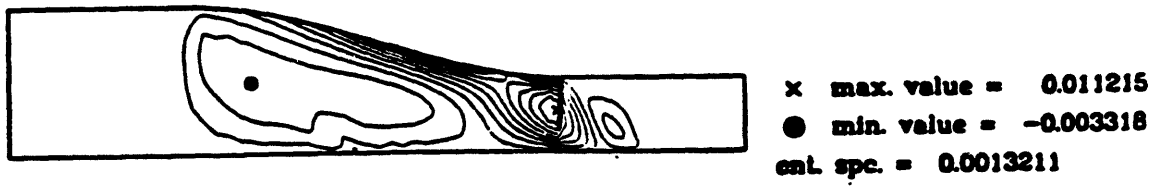

Figure 6.8o Contour plots of G_{zz} in the flow through a 2:1 contraction for N=4.0, σ=1.0, β=1.6x10^{-5} and De=0.1, 1.0 and 5.0.

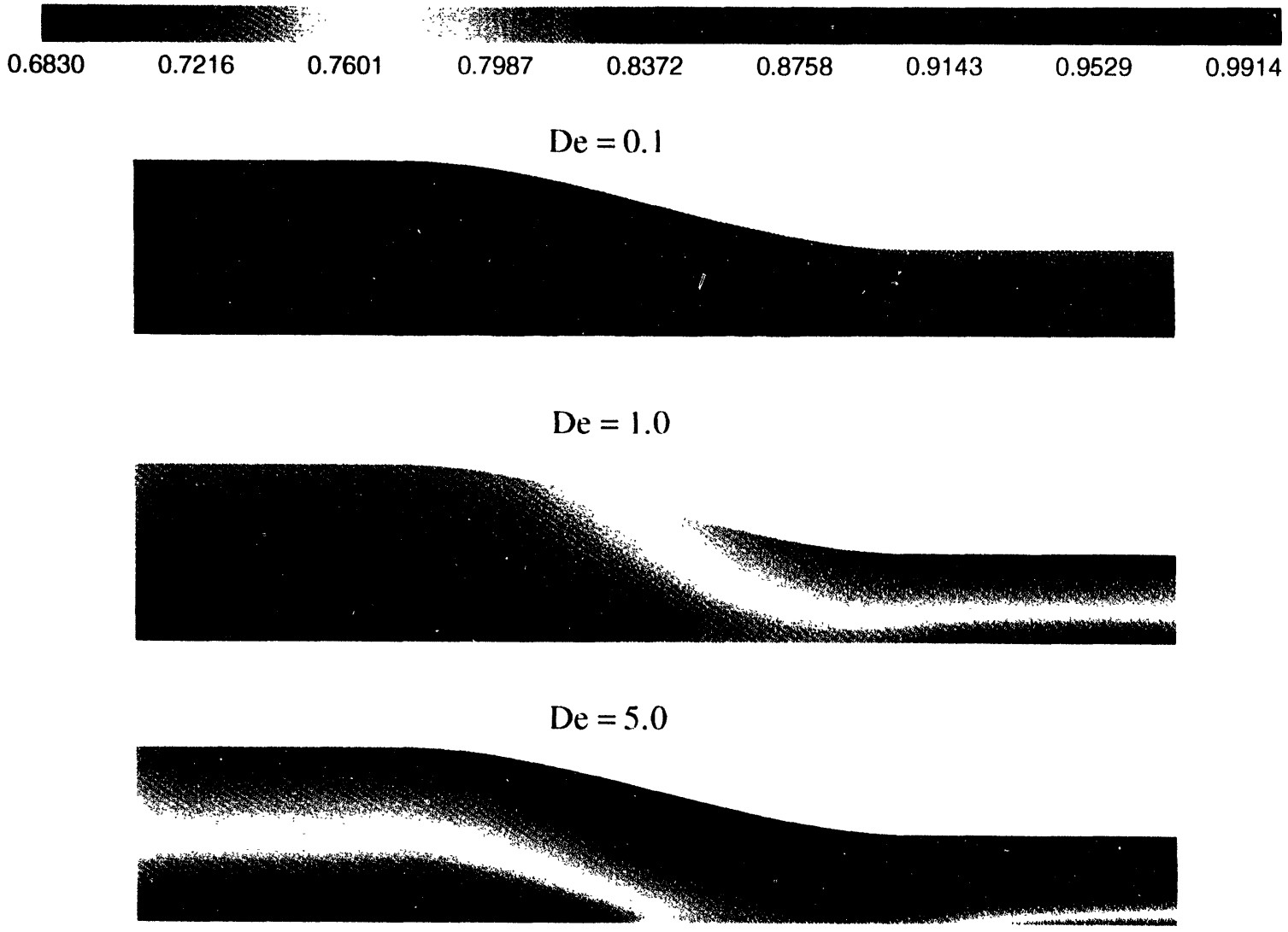

Figure 6.8p: Effect of De on S in a 2:1 contraction for N =4.0, σ=1.0, β= 1.6×10^{-5} and De=0.1, 1.0 and 5.0. S =0.683 is the equilibrium value for N =4.0 and S =1.0 corresponds to perfect order.

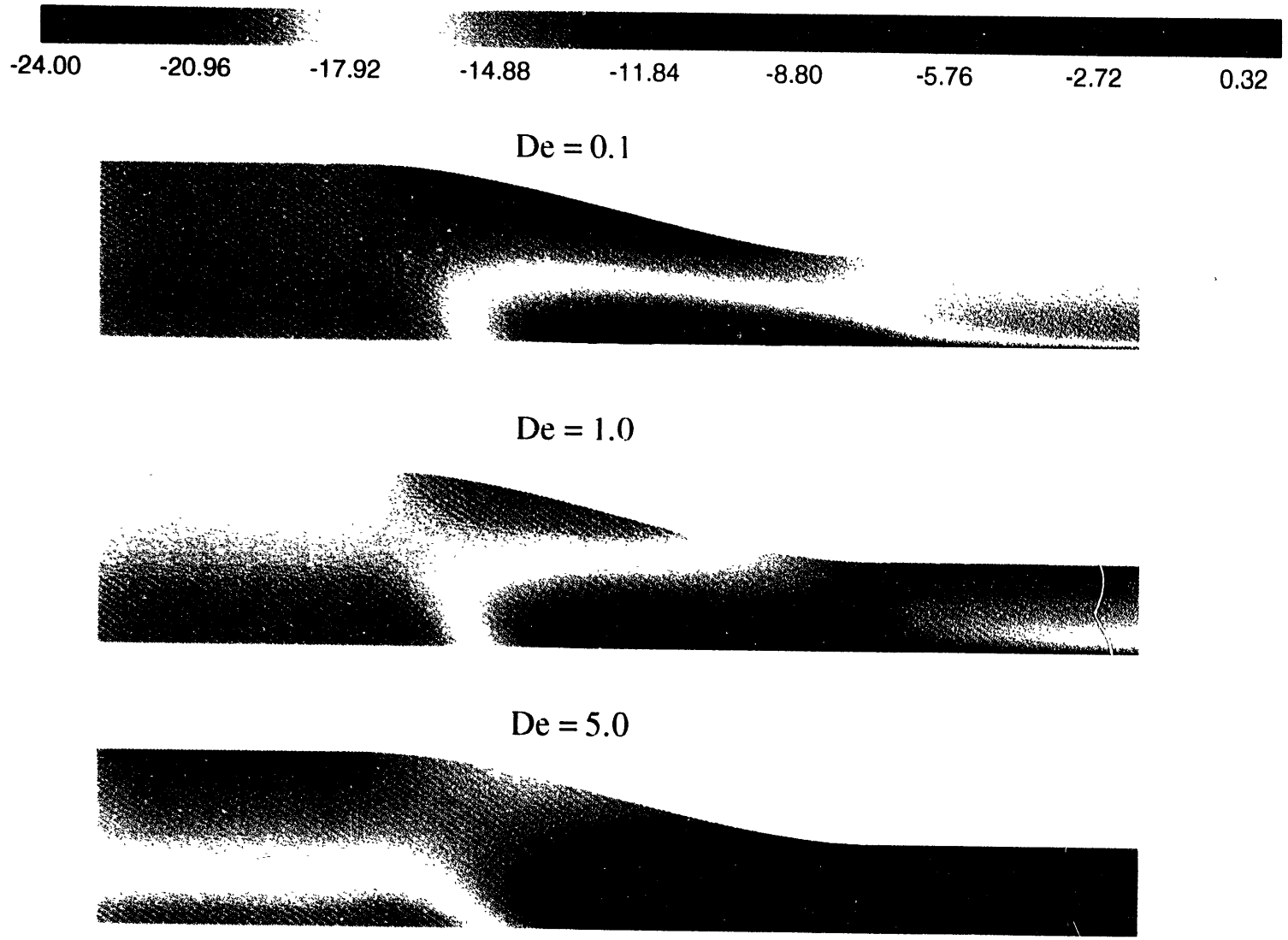

Figure 6.8q: Effect of De on χ in a 2:1 contraction for N =4.0, σ=1.0, β= 1.6×10^{-5} and De=0.1, 1.0 and 5.0. χ=-20.1 degrees is the zero-shear-rate limit. For χ=0, the director is aligned with the die axis.

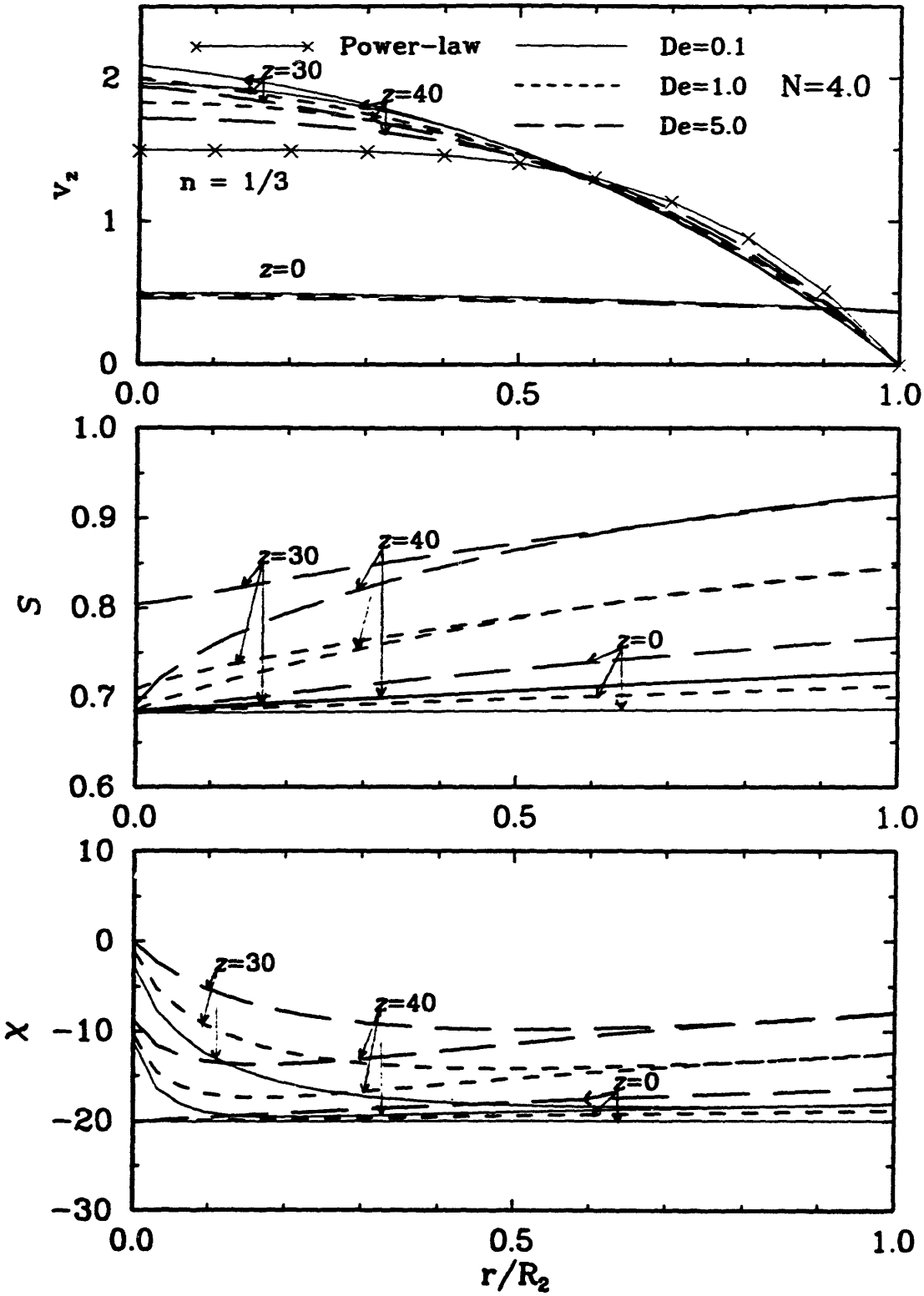

Figure 6.9 Effect of De on the radial variation in (a) v_z, (b) S, and (c) χ at z=0, 30 and 40 in a 2:1 contraction for N=4.0, σ=1.0, β=1.6x10^{-5} and De=0.1, 1.0 and 5.0. The fully developed downstream exit velocity profile for a power-law model with the same shear thinning behavior as the viscosity for the liquid-crystal model is shown for comparison.

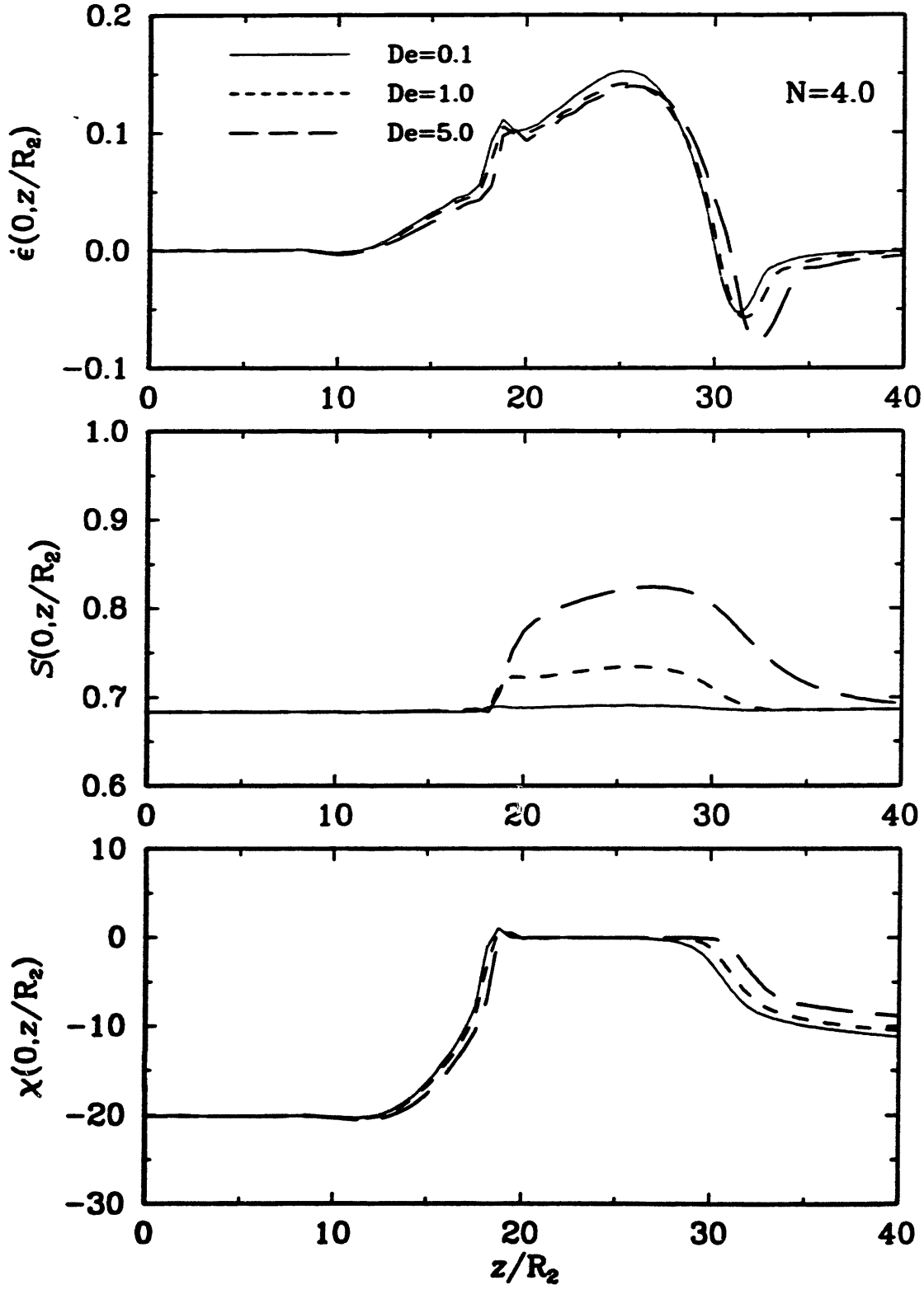

Figure 6.9 Effect of De on the variation in (d) centerline axial velocity gradient $\dot{\epsilon}$, (e) centerline S, and (f) centerline χ in a 2:1 contraction for N=4.0, σ=1.0, β=1.6x10^{-5} and De=0.1, 1.0 and 5.0. $\dot{\epsilon}$ is made dimensionless with $V_{2,avg}/R_2$. The response in S and χ to $\dot{\epsilon}$ is also illustrated.

dimensionless axial velocity gradient $\dot{\varepsilon}(0,z/R_2)$ is illustrated in Figs. 6.9d-f.

Effect of De on Velocity

For a purely Newtonian solution, the fully developed dimensionless velocity profile through the downstream tube of radius R_2 is given by the equation

$$v_z = 2\left[1-(\frac{r}{R_2})^2\right] \tag{6.5}$$

From volume conservation, the velocity through the upstream tube of radius $2R_2$ is then

$$v_z = 0.5\left[1-(\frac{r}{2R_2})^2\right] \tag{6.6}$$

For De=0.1, there is very little shear thinning at the inlet, since the associated shear rates are small, and consequently the velocity profiles are Newtonian. For De=1.0 and 5.0 the maximum centerline velocity is slightly lower than the Newtonian value which is evidence of a small shear thinning effect.

Table 6.1 shows that the maximum velocity decreases with increasing De. The percentage overshoot, however, increases with De due to the effect of shear thinning and the consequent decrease in the downstream velocity. Fig. 6.9d reveals that the maximum velocity (corresponding to $\dot{\varepsilon}(0,z/R_2) = 0$ near the junction of the contraction and the downstream tube) shifts downstream with increasing De. The response in $S(0,z/R_2)$ and $\chi(0,z/R_2)$ to $\dot{\varepsilon}(0,z/R_2)$ is discussed in the following sub-sections. At the junction of the contraction region and the downstream tube, but away from the centerline, the blunt or "plug-like" velocity profiles for De = 1.0 and 5.0 as compared to De = 0.1 (cf. Fig. 6.9a)

De		2:1		4:1 (cubic)	4:1 (rounded)
		N = 4.0	N = 7.0	N = 4.0	N = 4.0
0.1	v_{max}	2.093	2.238	2.250	2.405
	% overshoot	6.61	12.11	14.62	22.58
1.0	v_{max}	2.000	2.172	2.177	2.297
	% overshoot	9.05	13.58	18.71	25.27
5.0	v_{max}	1.960	2.104	2.186	2.281
	% overshoot	13.74	17.05	26.49	31.69

Table 6.1: Effect of contraction ratio, concentration and Deborah number on the maximum velocity and percentage overshoot on the centerline.

indicates an increase in shear thinning with De.

At the downstream exit, the velocity is close to being Newtonian for De=0.1. The centerline velocity is slightly lower than two, which points to a small shear thinning effect. Shear thinning is much more pronounced for De=1.0 and 5.0. The velocity profile predicted for a power-law model with a shear thinning index of -2/3 in the viscosity is shown for comparison since the Bhave *et al.* model predicts a viscosity that has a shear thinning index of -2/3 at high shear rates; note that the Bhave *et al.* model predicts a constant viscosity at low shear rates. However, the fully developed flow field at the downstream exit is non-homogenous in the shear rate, with the shear rate varying

from zero at the centerline to a maximum at the wall. Consequently, the viscosity shear thinning index is not as high as -2/3 near the centerline even for De=5.0, and the corresponding velocity profile is not as blunt or "plug-like" as the velocity profile predicted for the power-law model.

Effect of De on the Degree of Order *S*

A discussion of the effect of De on *S* shown in Figs. 6.8p, 6.9b and e is the object of this sub-section. The effect of De on *S* in the upstream tube is discussed first, which is followed by discussions on the effect of De on *S* in the contraction region and the downstream tube respectively. The effect of De on $S(0,z/R_2)$ and the response in $S(0,z/R_2)$ to $\dot{\varepsilon}(0,z/R_2)$ is also discussed in this connection. *S* takes on values between the equilibrium value of 0.683 (red part of the color spectrum in Fig. 6.8p) and the perfect orientation value of 1.0 (dark blue part of the color spectrum in Fig. 6.8p).

The order at the inlet, as expected, is close to the equilibrium value throughout the range of r/R_2 shown for De=0.1 (cf. Figs. 6.8p and 6.9b). The higher shear rates associated with De=1.0 and 5.0 create a higher degree of order away from the centerline. The centerline value must still be the equilibrium value since the shear rate is zero there.

The higher shear and extension rates in the contraction region are expected to create a higher degree of order than the order present at the inlet. For small De, say De=0.1, however, the order hardly changes from the equilibrium value throughout the contraction region (red everywhere in Fig. 6.8p). The higher elongation rate $\dot{\varepsilon}(0,z/R_2)$ associated with De=5.0, and to a lesser extent De=1.0, leads to a much higher degree of order at the centerline over the equilbrium value as compared to the centerline value for

De=0.1 (cf. Figs. 6.8p and 6.9e). Shear flow, however, seems to dominate the kinematics more than extensional flow in creating order for this tapered contraction geometry, since the order increases monotonically from the centerline to the wall (the color changes monotonically between the red end and the blue end of the spectrum in the contraction region in Fig. 6.8p; Fig. 6.9b also highlights this monotonic increase in the order from the centerline to the wall at the junction of the contraction region and the downstream tube). Once $\dot{\varepsilon}(0,z/R_2)$ starts to increase in the upstream portion of the contraction region, there is a lag of 7-8 downstream tube radii before a sharp increase in $S(0,z/R_2)$ is observed for De = 1.0 and 5.0; the order changes little from the equilibrium value for De = 0.1 (cf. Figs. 6.9d and e). In fact, remarkably, the axial location where $S(0,z/R_2)$ increases sharply coincides with the point where the director becomes aligned with the z-axis. The lag between the maximum in $S(0,z/R_2)$ and $\dot{\varepsilon}(0,z/R_2)$, however, is only of the order of one downstream tube radius for all De.

At the downstream exit, S at the centerline relaxes to the equilibrium value (which is the fully developed value) for all De since the axial velocity gradient decays to zero. As is obvious from Fig. 6.8p and 6.9e, the downstream axial distance over which the centerline order relaxes to equilibrium increases with De. However, the shear dominated kinematics from the contraction region are maintained some distance away from the centerline and there is no decrease in the order in this shear dominated region in the downstream tube.

Effect of De on the Director Angle χ

In this sub-section the effect of De on the director angle χ shown in Figs. 6.8q, 6.9c and 6.9f is discussed. Patterning the discussion after the preceding sub-section the effect of De on χ in the upstream tube is examined first which is followed by an examination of the effect of De on χ in the contraction region and downstream tube respectively. The effect of De on $\chi(0,z/R_2)$ and the response in $\chi(0,z/R_2)$ to $\dot{\varepsilon}(0,z/R_2)$ is also discussed in this connection. Dark blue in the color coding shown in Fig. 6.8q corresponds to perfect alignment of the director with the z-axis and as the color approaches the red part of the spectrum the director becomes increasingly tilted with respect to the axial direction.

At the inlet, the director angle hardly varies from the zero-shear-rate prediction of -20.1 degrees for De=0.1. The higher shear rates associated with De=5.0, and to a lesser extent De=1.0, away from the centerline results in a director orientation that is more closely aligned with the z-axis.

In the contraction region, the pure extension along the centerline aligns the nematic director perfectly with the z-axis for all De (dark blue in Fig. 6.8q). This is consistent with the perturbation analysis presented in Section 4.1 which suggested that even at small elongation rates the director must be aligned with the direction of stretching. However, even if the nematic director is perfectly aligned with the axis at small De, the spread in the distribution function for the orientation about the average or director orientation is still broad since $S(0,z/R_2)$ is not very far from equilibrium. Figures 6.9d and f show that there is no lag in the response of $\chi(0,z/R_2)$ to an increase in $\dot{\varepsilon}(0,z/R_2)$ in the upstream portion of the contraction; for any De, the "dip" in $\dot{\varepsilon}(0,z/R_2)$ near $z/R_2 = 10$ is accompanied by a similar "dip" in $\chi(0,z/R_2)$, and when $\dot{\varepsilon}(0,z/R_2)$ increases to 0.1,

$\chi(0,z/R_2)$ rapidly increases to 0 degrees. Once the director becomes aligned with the z-axis there is no change in the orientation with any further increase in $\dot{\varepsilon}(0,z/R_2)$. $\chi(0,z/R_2)$ does not change until $\dot{\varepsilon}(0,z/R_2)$ approaches zero; though it appears that the director starts to tilt from being oriented with the z-axis when $\dot{\varepsilon}(0,z/R_2) = 0.125$ for De = 0.1, the actual magnitude of the axial velocity gradient, $De\dot{\varepsilon}(0,z/R_2)/\lambda$, (note that $\dot{\varepsilon}(0,z/R_2)$ is defined to be dimensionless) is only of the order of 0.01 s^{-1}. This seems to be consistent with the perturbation analysis which shows that even for very small extension rates the director must be aligned with the flow direction. The downstream shift in the maximum velocity ($\dot{\varepsilon}(0,z/R_2) = 0$) and the corresponding shift in the onset of tilting in the director orientation from the z-axis with increasing De is also clear. In the region away from the centerline, the kinematics is dominated by shear flow. Consequently, the director orientation changes rapidly from the axial orientation predicted at the centerline and is dictated by the shear rates that exist in that region. The maximum change in the director orientation across the contraction is observed for De=0.1; the smallest value of De studied in this thesis. In fact, close to the wall, where only shear flow kinematics exist, the director orientation is worse than the orientation at the entrance to the contraction geometry. This "loss of orientation" is easily explained; in the limit of zero-shear-rate the director is oriented at −20.1 degrees with respect to the flow direction, and since the flow is parallel to the wall, the slope of the wall makes the director orientation with respect to the z-axis worse than −20.1 degrees. In the downstream portion of the contraction region, where the contraction region blends gradually with the downstream tube, the wall slope is no longer a factor and in fact the wall shear makes the director orientation with the z-axis slightly

better than −20.1 degrees (cf. Fig. 6.9c). As expected, for De=1.0 and 5.0, the wall slope makes the director orientation close to the wall in the upstream portion of the contraction region worse than the orientation close to the wall at the entrance to the geometry. In the downstream portion of the contraction region, the radially increasing shear rate for De = 5.0, and to a lesser extent De = 1.0, makes the director oriented much more preferentially with the z-axis than that predicted for De = 0.1 (cf. Figs. 6.8q and 6.9c).

In the downstream tube, the director orientation along the centerline is no longer coaxial with the flow direction due to a relaxation in the extensional flow kinematics (cf. Figs. 6.8q and 6.9f). In fact, as demonstrated in Section 6.2.1.1, for sufficiently long downstream tube lengths (L/R_2 = 225 for De = 5.0) when the director orientation field is fully developed (which match with the tube flow results presented in Section 6.1), the director orientation along the centerline approaches the zero-shear-rate limit; for De = 0.1 and 1.0 the director orientation approaches the zero-shear-rate limit for smaller downstream tube lengths (L/R_2 = 100 for De = 0.1 and L/R_2 = 150 for De = 1.0). However, the shear flow dominated kinematics from the contraction region are maintained some distance away from the centerline and there is very little change in the director orientation in this shear dominated region in the downstream tube.

The increase in $\dot{\varepsilon}(0,z/R_2)$ from zero to $\dot{\varepsilon}_{max}$ may be thought of as an experiment in "startup of steady elongational flow" with time scaling roughly as $(z/R_2)/De$. Similarly the decrease from $\dot{\varepsilon}_{max}$ to 0, albeit non-monotic and going through negative values of $\dot{\varepsilon}(0,z/R_2)$, may be thought of as an experiment in "relaxation following cessation of steady elongation flow" at an elongation rate $\dot{\varepsilon}_{max}$. It is interesting to examine how the response

in $\chi(0,z/R_2)$ differs in "startup of steady elongational flow" and in "relaxation following cessation of steady elongational flow". The response in $\chi(0,z/R_2)$ shown in Fig. 6.9f to the dimensional axial velocity gradient, $De\dot{\varepsilon}(0,z/R_2)/\lambda$ s^{-1}, is illustrated for De=0.1, 1.0 and 5.0 in Fig. 6.10; $\dot{\varepsilon}(0,z/R_2)$ is as shown in Fig. 6.9d. The arrows shown in Fig. 6.10 indicate the direction of flow along the centerline. It is clear that the increase in $\chi(0,z/R_2)$ during "startup of steady elongational flow" traces a different path from the decrease in $\chi(0,z/R_2)$ during "relaxation following cessation of steady elongational flow"; the difference in the χ-response is small for De=0.1 since the axial velocity gradient is small, but becomes magnified with increasing De. Thus, the size of the "hysteresis" exhibited by $\chi(0,z/R_2)$ in the response to $De\dot{\varepsilon}(0,z/R_2)$ increases with De.

Implications for Fiber Drawing Analysis and Processing

To probe rigorously the validity of the one-dimensional assumptions used in the fiber drawing analysis presented in Chapter 4, an integrated finite-element model for the contraction, die swell and fiber drawing region is required. Though such an integrated model is not expected to be computationally limited, it is certainly limited by a lack of complete understanding of the effect of the die swell singularity on the propagation of information of the hyperbolic structure field (equivalently, the stress field in UCM, Oldroyd-B and Giesekus constitutive equations), which is associated with memory effects. In Stokes flow, the singularity does not affect the final die swell since only viscous effects are present and the effect of the singularity is confined to a small region around the die lip as compared to viscoelastic flows where the effect of the singularity is felt much further downstream especially at high De. The die swell singularity issue is

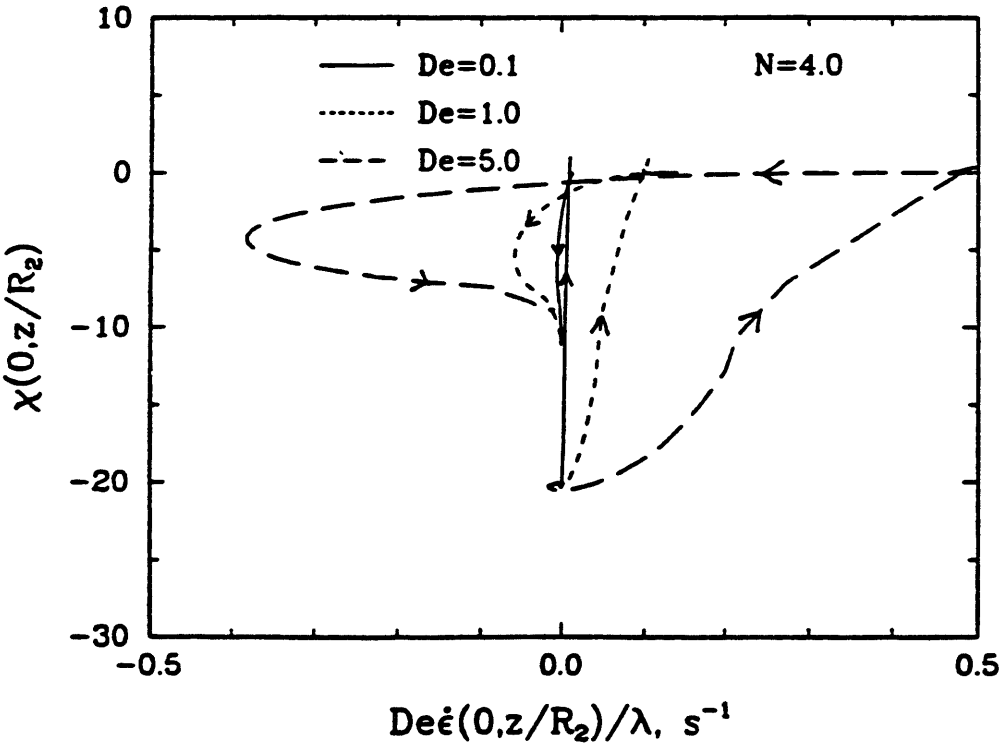

Figure 6.10 Effect of De on the response of χ to startup and relaxation after cessation of steady elongational flow along the centerline in a 2:1 contraction for N=4.0, σ=1.0, β=1.6x10^{-5} and De=0.1, 1.0 and 5.0. De$\dot{\epsilon}/\lambda$ is in s^{-1}.

discussed more elaborately in Appendix A.

Fiber spinning experiments with 40 wt % hydroxy propyl cellulose in acetic acid (Prilutski, 1984) show that the die swell for liquid-crystalline polymers is very small; only 10-15 % even at small tension. It is reasonable to expect then that the deorientation due to die swell is small and that the structure field predicted at the spinneret exit would provide a reasonable estimate of the initial orientation and the homogenity of the orientation in the fiber drawing region. Two key assumptions in the one-dimensional model for the fiber drawing region are (1) S and χ are radially homogenous and (2) the director is oriented with the z-axis with $S_{eq} \leq S(0) \leq S_{\dot{\varepsilon}}$. The spinneret calculations would give a fair idea on the region of validity of the above assumptions in Deborah number space.

Figures 6.8p-q and 6.9b-c show that S and χ will approach radial homogenity for high De when $L/R_2 \rightarrow 0$ (z = 30 plane); in addition the director will be oriented with the z-axis (χ = 0 degrees). The degree of order predicted at the maximum centerline elongation rate $S_{\dot{\varepsilon}}$ would be a good estimate for S across the cross-section. Hence, at high De and $L/R_2 \rightarrow 0$ the assumptions in the fiber drawing model would be valid provided $S(0) = S_{\dot{\varepsilon}}$.

It is apparent from Figs. 6.9b and c that for small De (De = 0.1 is the smallest value studied in this thesis), S is reasonably homogenous about the equilibrium value whereas χ is not; up to a 10 degree variation in the director angle from the centerline to the wall is observed at the downstream exit (L/R_2 = 10 in these calculations). Calculations show that the director orientation is uniform when the χ field is close to

being fully developed (A fully developed configuration is obtained for $L/R_2 = 100$ at De = 0.1). The director orientation itself is close to the zero-shear-rate limit of -20.1 degrees. Hence, at small De and a reasonably long downstream tube length, the one-dimensional fiber drawing model would be valid provided the evolution equation for the structure is modified to account for non-axial prolate symmetry in the director and is solved with the initial condition $S(0) = S_{eq}$, $\chi(0) = \chi_{\text{zero-shear -rate}}$. However, as suggested by the perturbation analysis in Section 4.1 and the contraction flow results at the centerline, it is expected that the purely extensional character of the one-dimensional fiber drawing model would rapidly align the director with the flow direction, though the degree of order would still be close to the equilibrium value at small De. A question arises then as to whether the extensionally dominated flow in the fiber drawing region would wipe out any radial inhomogenity in the director orientation predicted for short downstream tube lengths even at small De. Whether the director orientation becomes radially homogenous and the axial length scale over which the initial inhomogenity disappears can be answered only by a two-dimensional model for the fiber drawing region.

From a processing point of view a high degree of order and axial orientation in the director is important to achieve high tensile strength in the fiber (cf. Fig. 1.1). Only an integrated model would reveal how the spinneret and fiber drawing flows can be optimized fully in creating a high degree of order and axial director orientation in the fiber. However, the isolated spinneret and fiber drawing calculations do highlight what each flow has to offer.

Let us denote the Deborah number in the spinneret and the fiber drawing region

as $De_{spinneret}$ and De_{fiber} respectively. The two are related by the expression

$$\frac{De_{spinneret}}{De_{fiber}} = \frac{L_{fiber}}{R_2}.\frac{1}{D_R} \tag{6.7}$$

where L_{fiber} is the length of the fiber drawing region and D_R is the draw ratio. It is assumed that the velocity at the spinneret exit is not different from the velocity at the origin of the fiber drawing region.

The spinneret calculations show that at high $De_{spinneret}$ and $L/R_2 \rightarrow 0$, S and χ become homogenous. In addition, the director is oriented with the flow direction and the degree of order is high. There are two advantages to creating a high degree of order and axial orientation by operating at high $De_{spinneret}$: (1) the total pressure drop per unit volumetric flow rate decreases dramatically since $L/R_2 \rightarrow 0$, and (2) the pressure drop required to drive a unit volumetric flow rate also decreases due to shear thinning (cf. Fig. 6.23). A limitation may arise, however, in achieving a specific drawdown in the fiber radius in the fiber drawing region; assuming that the dependence of die swell on $De_{spinneret}$ is small (the initial fiber radius in the fiber drawing region would then vary little with $De_{spinneret}$), the calculations in Section 4.3 show that for a high degree of initial order the drawdown tension is 20 % higher than the drawdown tension predicted when the initial order is at equilibrium.

The fiber drawing flow is dominated by extensional flow kinematics. Menon's (1990) results show that if one were to compare the degree of order created in a simple shear flow and a simple elongational flow at the same magnitude of the dimensionless shear rate and elongational rate, the elongational flow creates a higher degree of order as

may be expected intuitively. For example, the degree of order predicted in a simple shear flow and a simple elongational flow at N=4.0 and $\dot{\gamma}=\dot{\varepsilon}$=1.0 are 0.75 and 0.85 respectively. Thus, the extensionally dominated fiber drawing flow, as demonstrated in Chapter 4, creates a high final degree of order even at moderate De_{fiber} for low or high initial order. The calculations in Section 4.3 showed that the final degree of order is slightly higher for moderate and high De_{fiber} if the initial order is high. Consequently, by combining a spinneret flow operated at high $De_{spinneret}$ with a fiber drawing flow operated at moderate De_{fiber} a fiber with a high degree of order can be synthesized. The limitation that arises in drawing down a fiber from high initial order, as mentioned previously, is the higher fiber drawdown tension as compared to the tension required for fiber drawdown from a low initial order.

Unlike the flow through an abrupt contraction studied by Yeh *et al.* (1984) and Coates *et al.* (1992), the smooth and tapered contraction boundary prevents the formation of recirculation regions, at least for the 2:1 and 4:1 contraction ratios and the range of De studied in this thesis, as seen from the streamline contours and should also be an important consideration in the design of spinnerets.

6.2.2 High Concentration; N=7.0

Commercial liquid-crystalline polymers are typically processed from solutions that contain higher polymer concentrations. For example, Kevlar is processed from a liquid-crystalline solution of about 20 wt % PPTA in concentrated H_2SO_4 (Dupont, 1992), which, undergoes a isotropic-nematic phase transition at about 9 wt % PPTA. The dimensionless

concentration, N, for this liquid-crystalline solution is then about 7.0. In Section 6.2.2.1, the effect of De on the flow field, structure and the stress fields is studied for N=7.0. In Section 6.2.2.2, the effect of concentration on the axial velocity, degree of order and orientation is illustrated.

6.2.2.1 Effect of De; De=0.1, 1.0 and 5.0

The aim of this section is to study the effect of small, moderate and reasonably large Deborah numbers on the development of the flow field, the degree of order and director orientation, and the stress field for N = 7.0. Contour plots of pressure, components of structure tensor, velocity, components of velocity gradient tensor, components of stress tensor and streamlines are shown in Figs. 6.11a-o for De=0.1, 1.0 and 5.0. Contour plots of S and χ are shown in Figs. 6.11p-q. The quantitative effect of De on the axial velocity, degree of order and the director orientation, as the flow progresses through the contraction geometry, is better illustrated in Figs. 6.12a-c by plotting the cross sectional profiles at the inlet, the downstream exit and the axial location where the contraction region blends with the downstream tube. The radial profiles at the inlet extend up to r/R_2=2 but are shown only up to r/R_2=1 for the purpose of comparison with the downstream profiles. The effect of De on the development of order and director orientation along the centerline and the response to the dimensionless axial velocity gradient is illustrated in Figs. 6.13d-f.

De=0.1

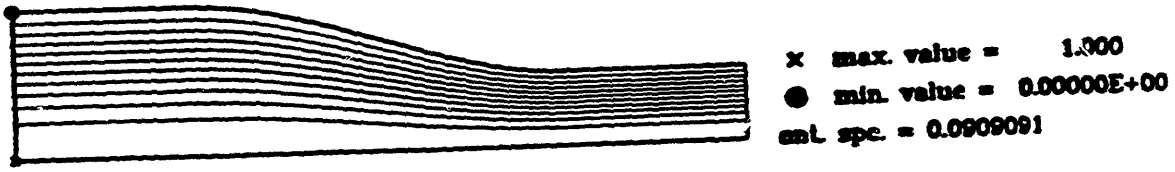

De=1.0

De=5.0

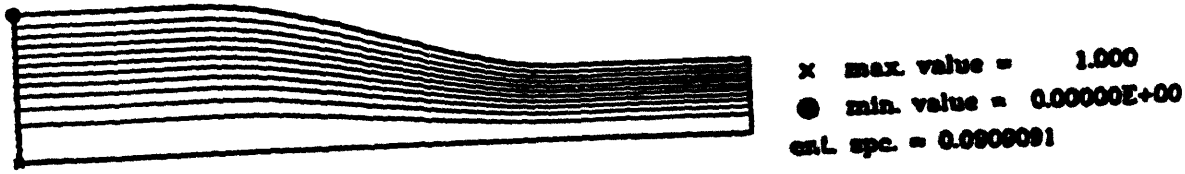

Figure 6.11a Contour plots of streamlines in the flow through a 2:1 contraction for N=7.0, σ=1.0, β=1.6x10^{-5} and De=0.1, 1.0 and 5.0.

De=0.1

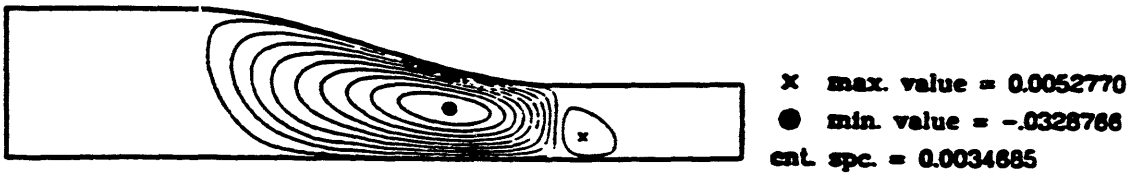

De=1.0

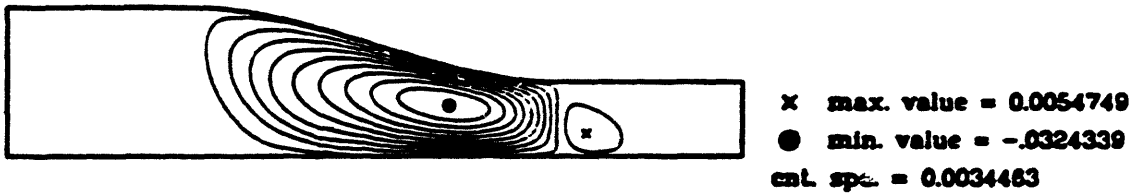

De=5.0

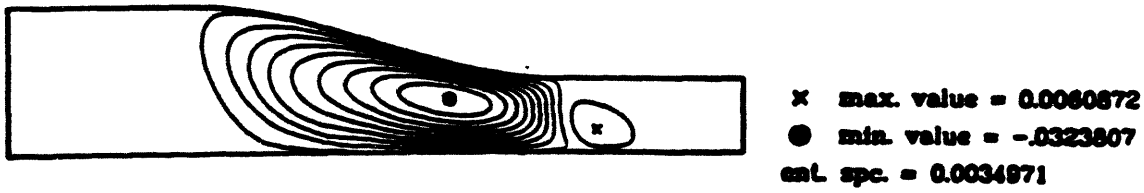

Figure 6.11b Contour plots of radial velocity in the flow through a 2:1 contraction for N=7.0, σ=1.0, β=1.6x10^{-5} and De=0.1, 1.0 and 5.0.

De=0.1

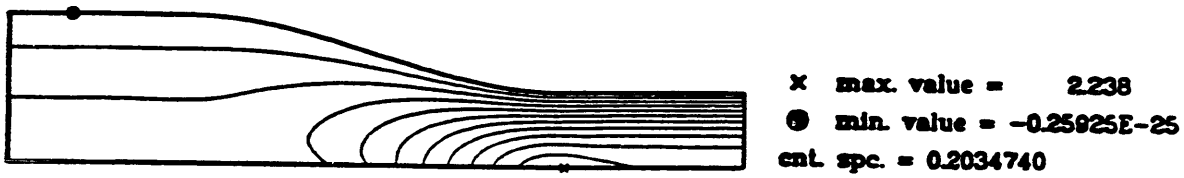

De=1.0

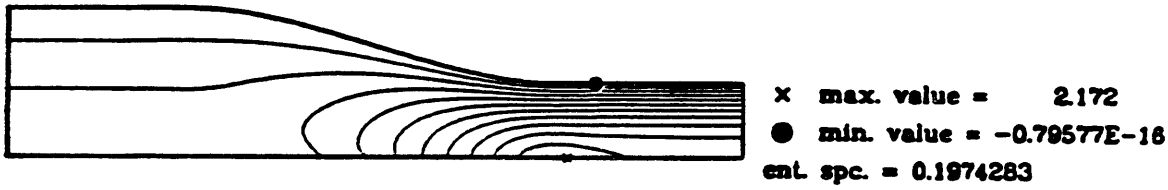

De=5.0

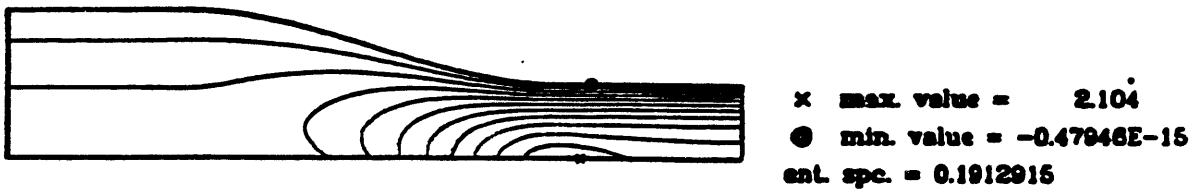

Figure 6.11c Contour plots of axial velocity in the flow through a 2:1 contraction for N=7.0, σ=1.0, β=1.6x10^{-5} and De=0.1, 1.0 and 5.0.

De=0.1

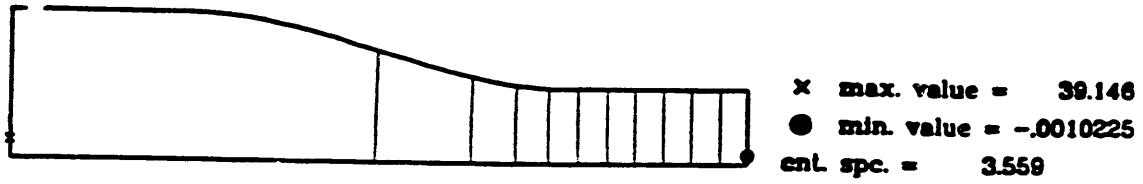

De=1.0

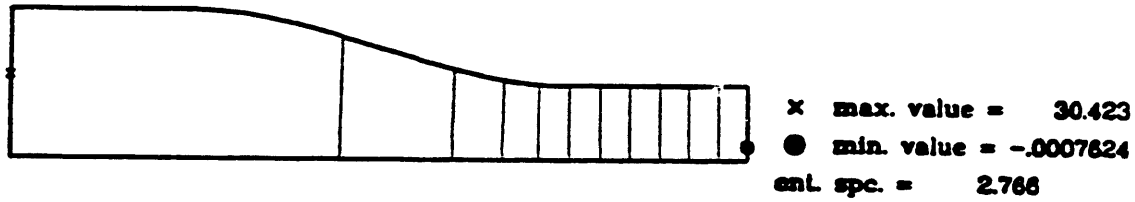

De=5.0

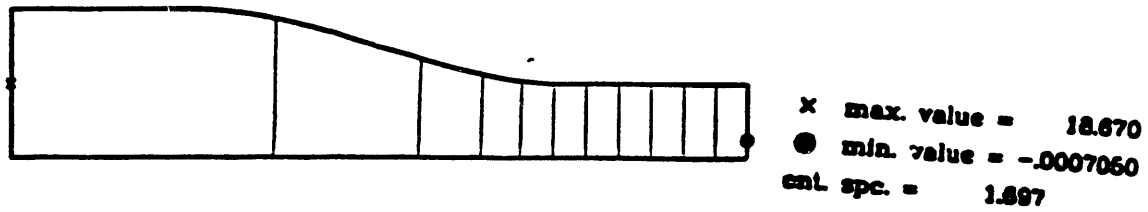

Figure 6.11d Contour plots of pressure in the flow through a 2:1 contraction for N=7.0, σ=1.0, β=1.6x10^{-5} and De=0.1, 1.0 and 5.0.

De=0.1

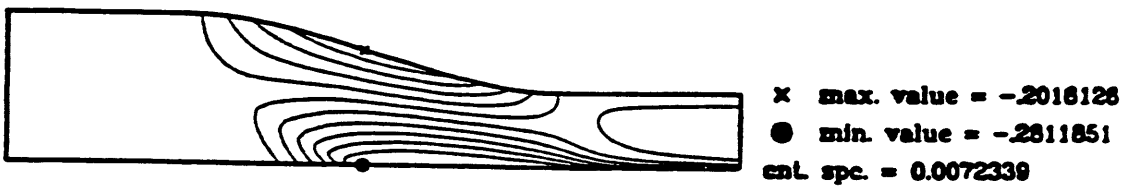

De=1.0

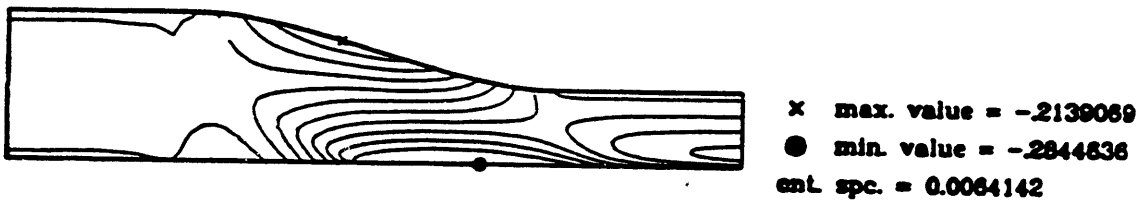

De=5.0

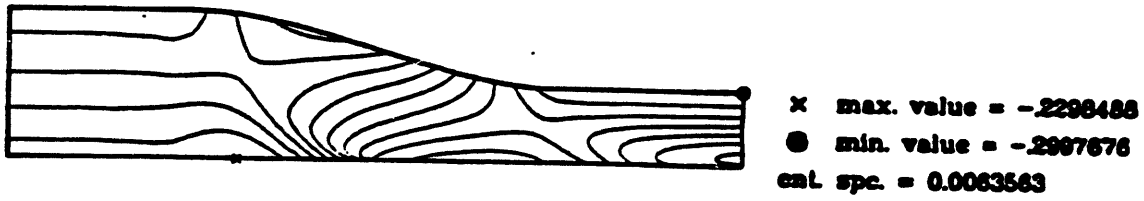

Figure 6.11e Contour plots of S_{rr} in the flow through a 2:1 contraction for N=7.0, σ=1.0, β=1.6x10^{-5} and De=0.1, 1.0 and 5.0.

De=0.1

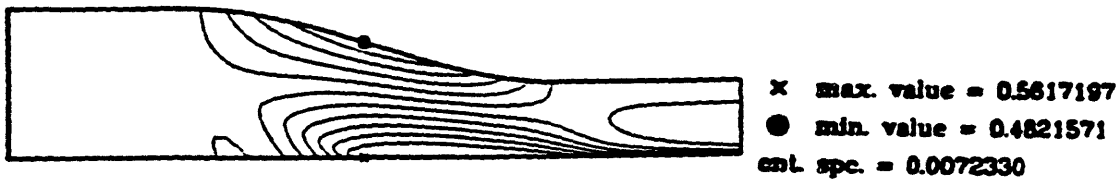

De=1.0

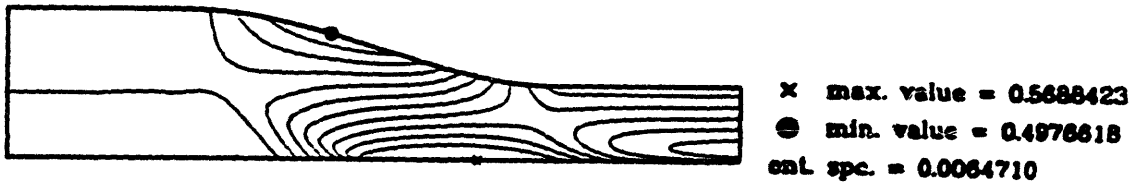

De=5.0

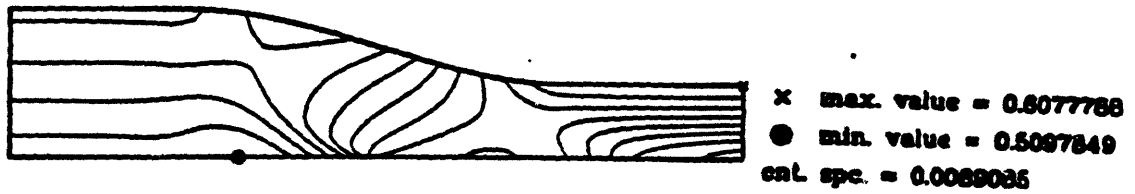

Figure 6.11f Contour plots of S_{zz} in the flow through a 2:1 contraction for N=7.0, σ=1.0, β=1.6x10^{-5} and De=0.1, 1.0 and 5.0.

De=0.1

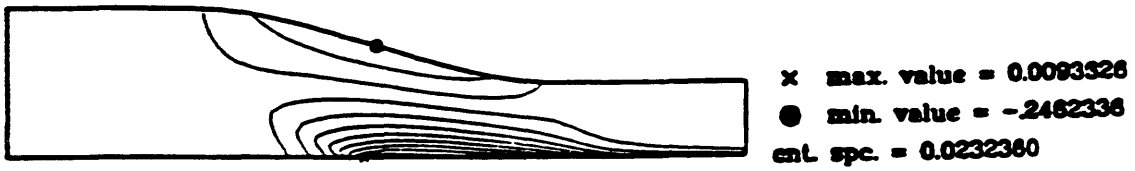

De=1.0

De=5.0

Figure 6.11g Contour plots of S_{rz} in the flow through a 2:1 contraction for N=7.0, σ=1.0, β=1.6x10^{-5} and De=0.1, 1.0 and 5.0.

De=0.1

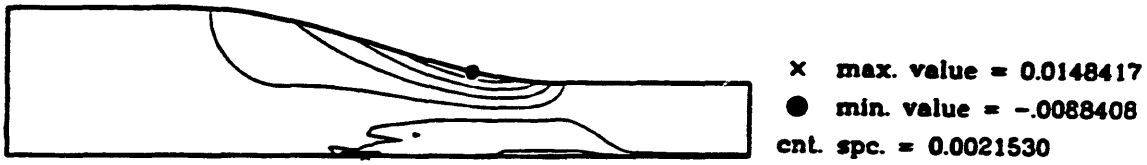

De=1.0

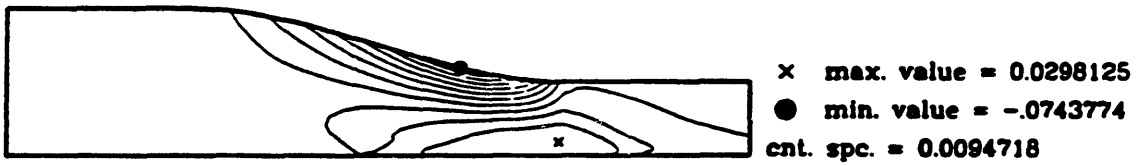

De=5.0

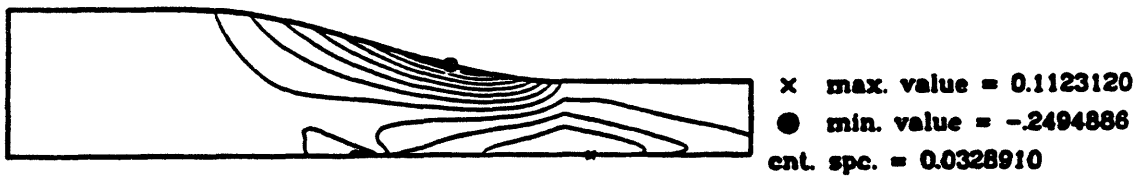

Figure 6.11h Contour plots of $De\tau_{rr}$ in the flow through a 2:1 contraction for N=7.0, σ=1.0, β=1.6x10^{-5} and De=0.1, 1.0 and 5.0.

De=0.1

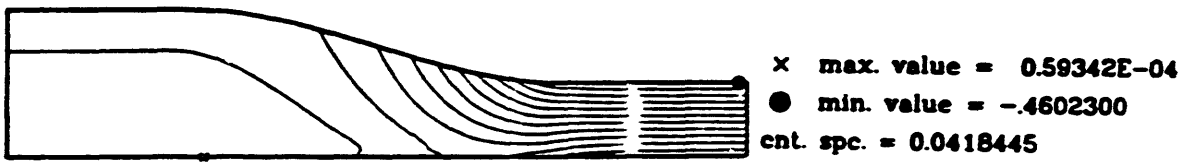

De=1.0

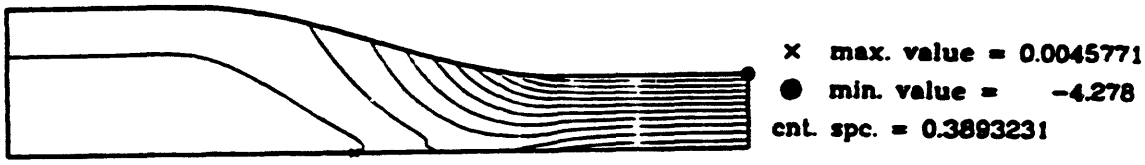

De=5.0

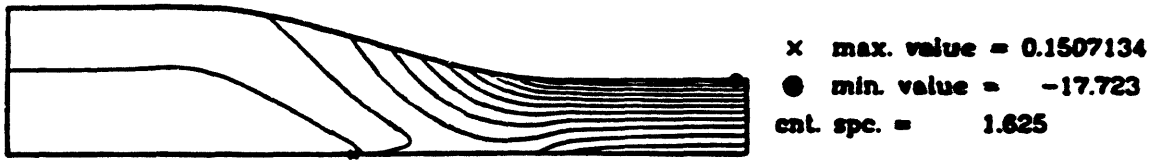

Figure 6.11i Contour plots of $De\tau_{zz}$ in the flow through a 2:1 contraction for N=7.0, σ=1.0, β=1.6x10^{-5} and De=0.1, 1.0 and 5.0.

De=0.1

De=1.0

De=5.0

Figure 6.11j Contour plots of $De\tau_{\theta\theta}$ in the flow through a 2:1 contraction for N=7.0, σ=1.0, β=1.6x10^{-5} and De=0.1, 1.0 and 5.0.

De=0.1

De=1.0

De=5.0

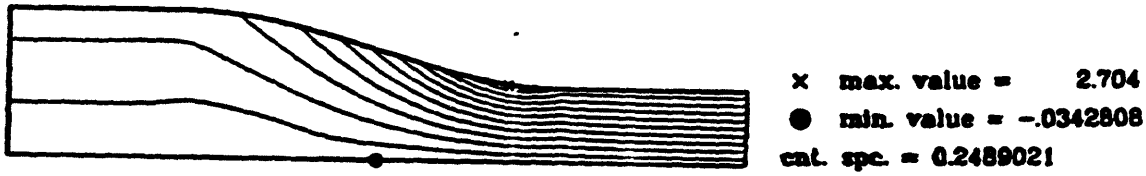

Figure 6.11k Contour plots of $De\tau_{rr}$ in the flow through a 2:1 contraction for N=7.0, α=1.0, β=1.6x10^{-5} and De=0.1, 1.0 and 5.0.

De=0.1

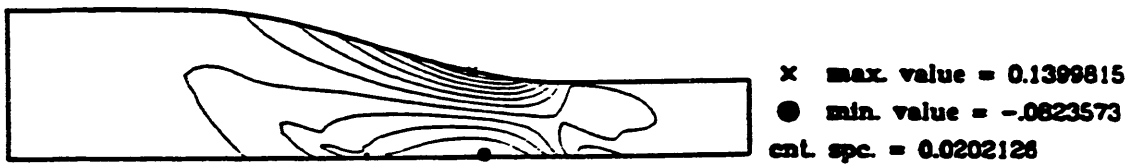

De=1.0

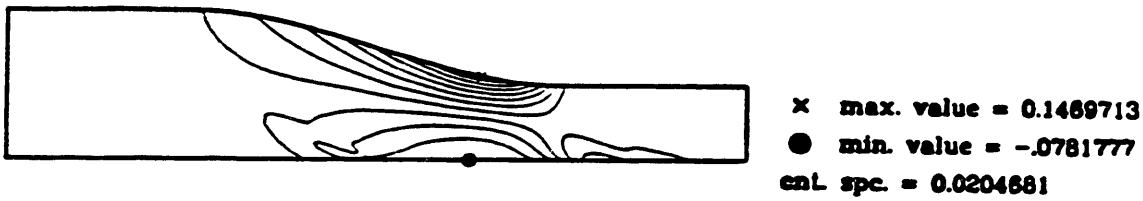

De=5.0

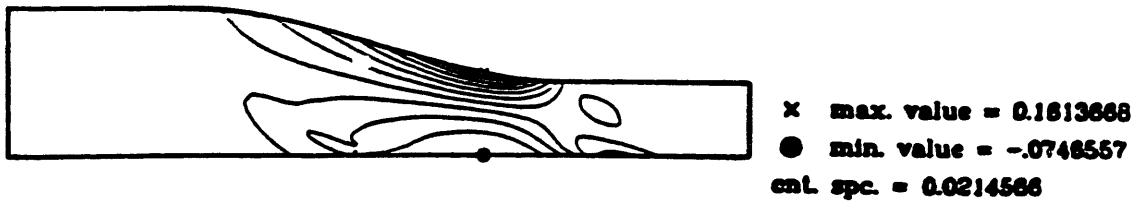

Figure 6.111 Contour plots of G_{π} in the flow through a 2:1 contraction for N=7.0, σ=1.0, β=1.6x10^{-5} and De=0.1, 1.0 and 5.0.

De=0.1

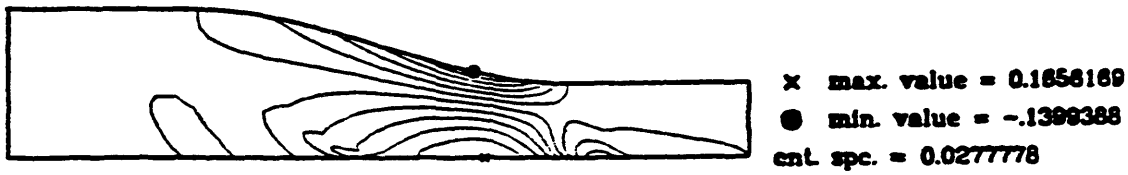

De=1.0

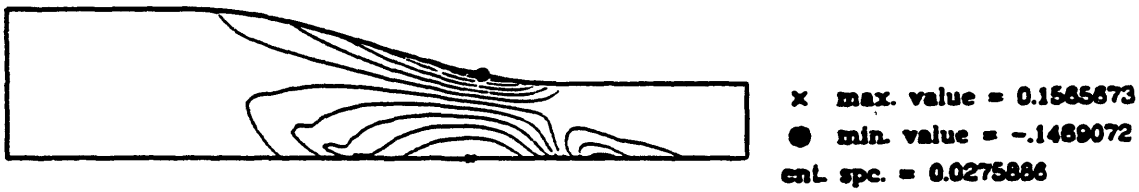

De=5.0

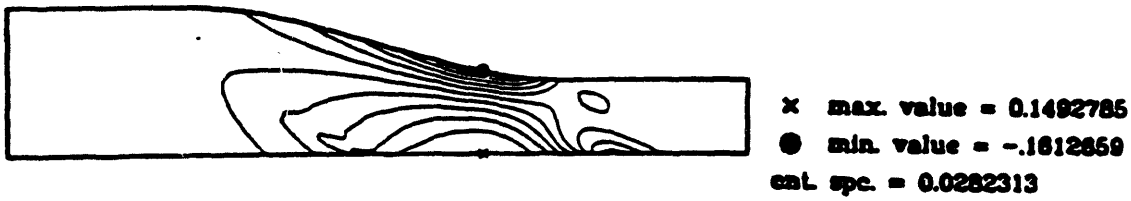

Figure 6.11m Contour plots of G_{zz} in the flow through a 2:1 contraction for N=7.0, σ=1.0, β=1.6x10^{-5} and De=0.1, 1.0 and 5.0.

De=0.1

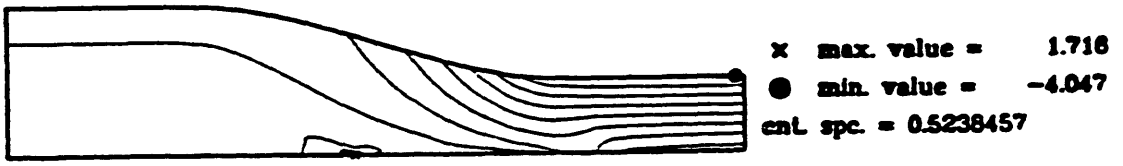

De=1.0

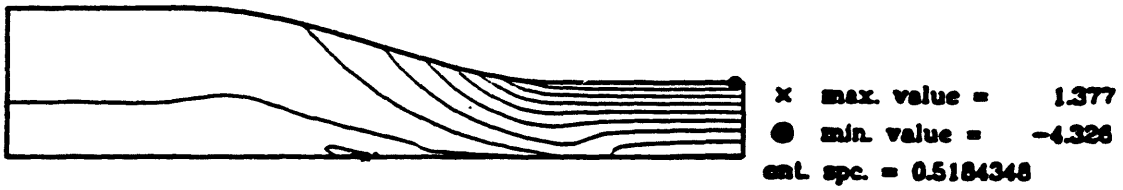

De=5.0

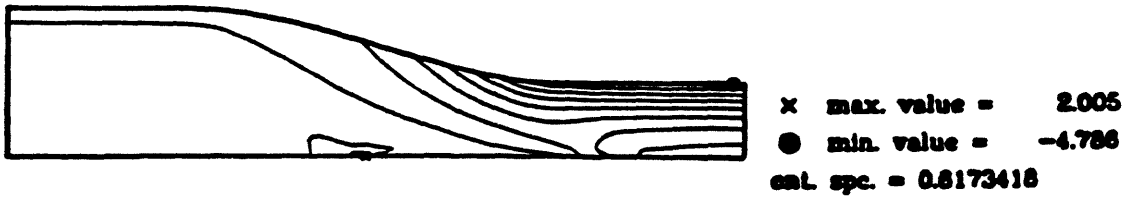

Figure 6.11n Contour plots of G_{rz} in the flow through a 2:1 contraction for N=7.0, σ=1.0, β=1.6x10^{-5} and De=0.1, 1.0 and 5.0.

De=0.1

De=1.0

De=5.0

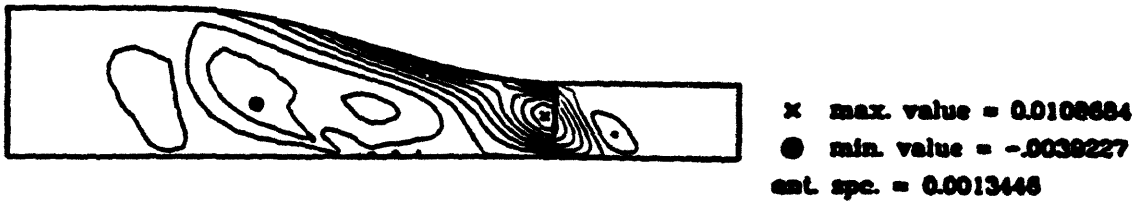

Figure 6.11o Contour plots of G_{xx} in the flow through a 2:1 contraction for N=7.0, σ=1.0, β=1.6x10^{-5} and De=0.1, 1.0 and 5.0.

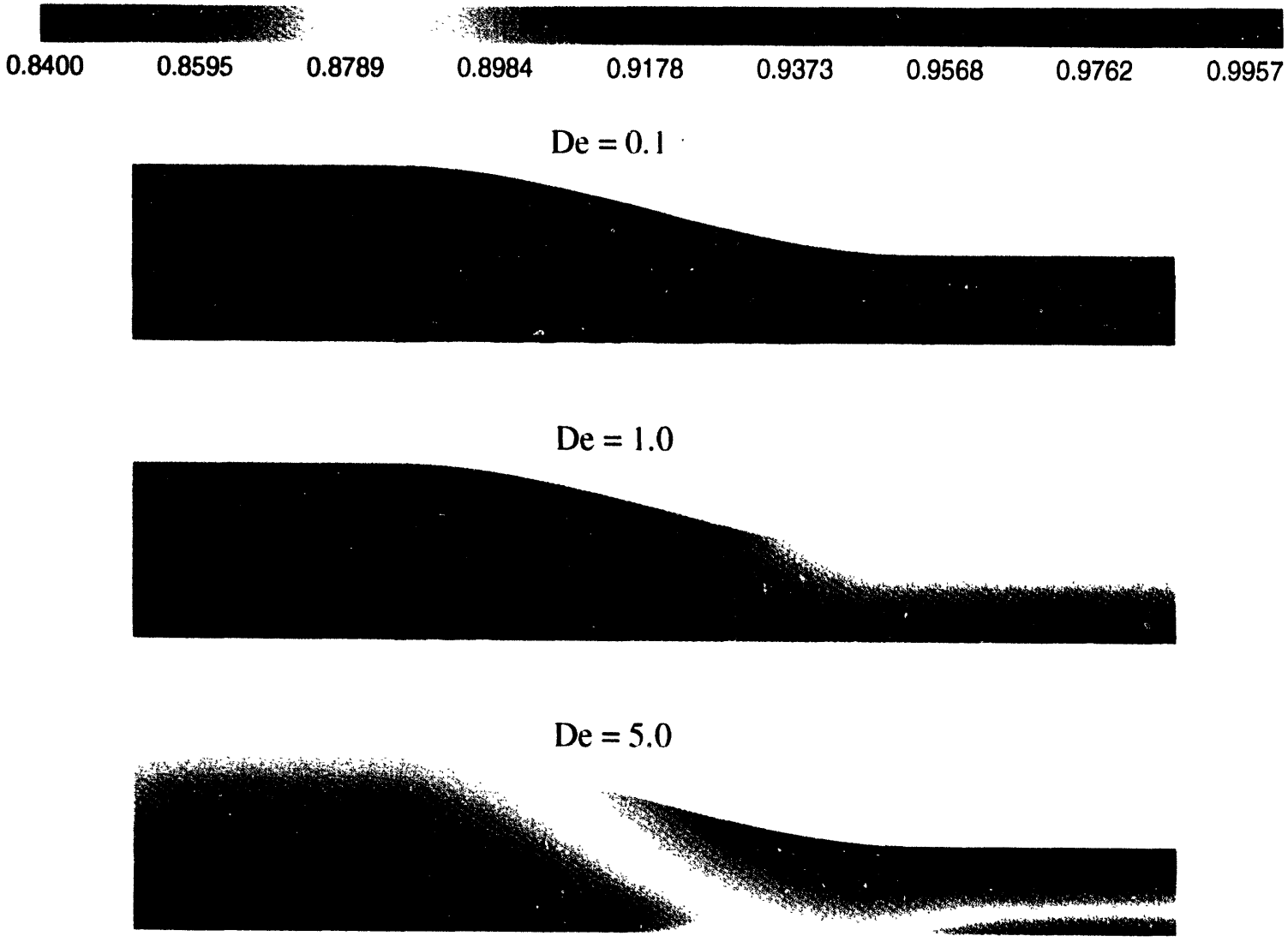

Figure 6.11p: Effect of De on S in a 2:1 contraction for N =7.0, σ=1.0, β=1.6x10^{-5} and De=0.1, 1.0 and 5.0. S =0.840 is the equilibrium value for N =7.0 and S =1.0 corresponds to perfect order.

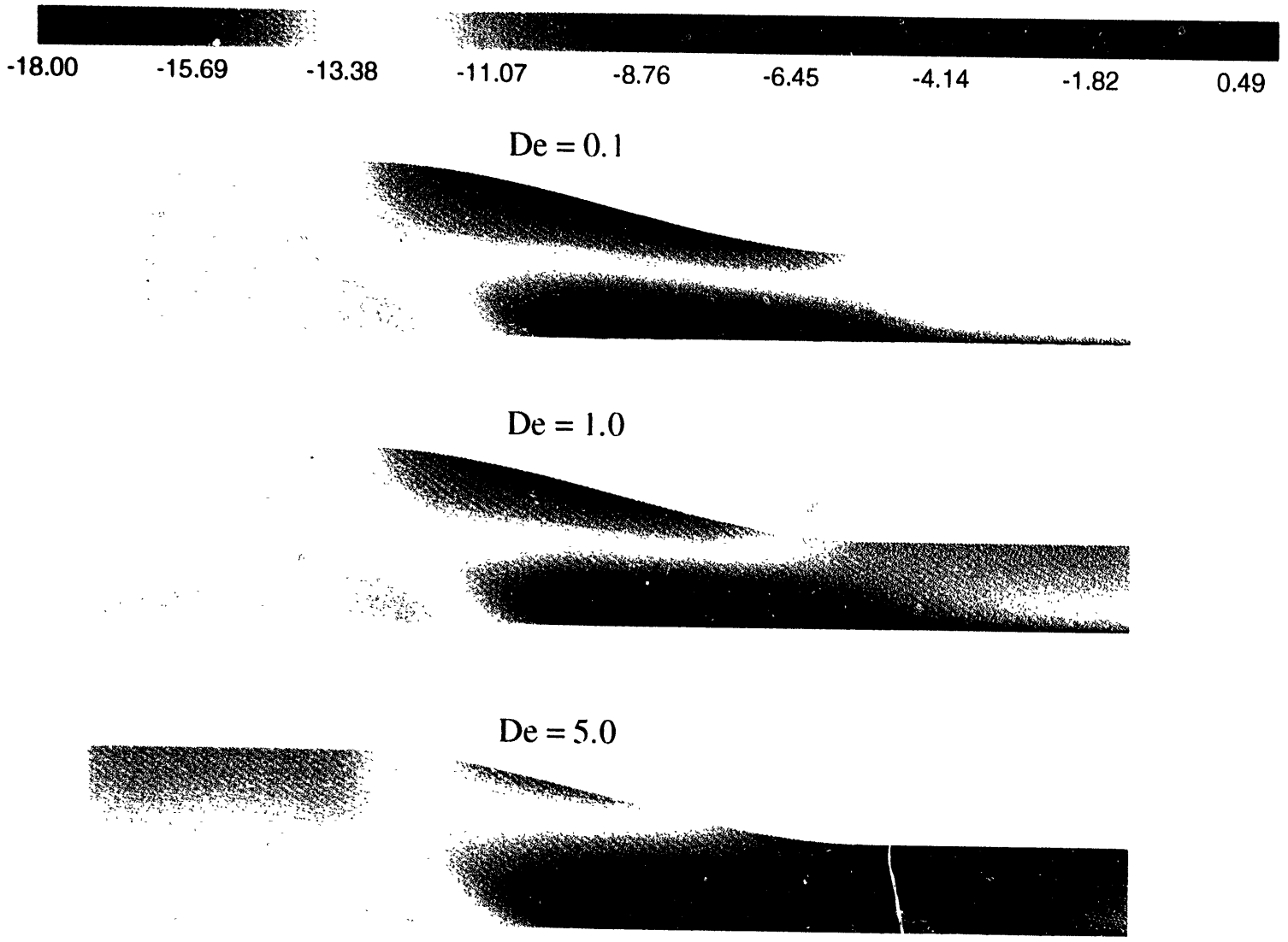

Figure 6.11q: Effect of De on χ in a 2:1 contraction for N =7.0, σ=1.0, β=1.6x10^{-5} and De=0.1, 1.0 and 5.0. χ=-13.7 degrees is the zero-shear-rate limit. For χ=0, the director is aligned with the die axis.

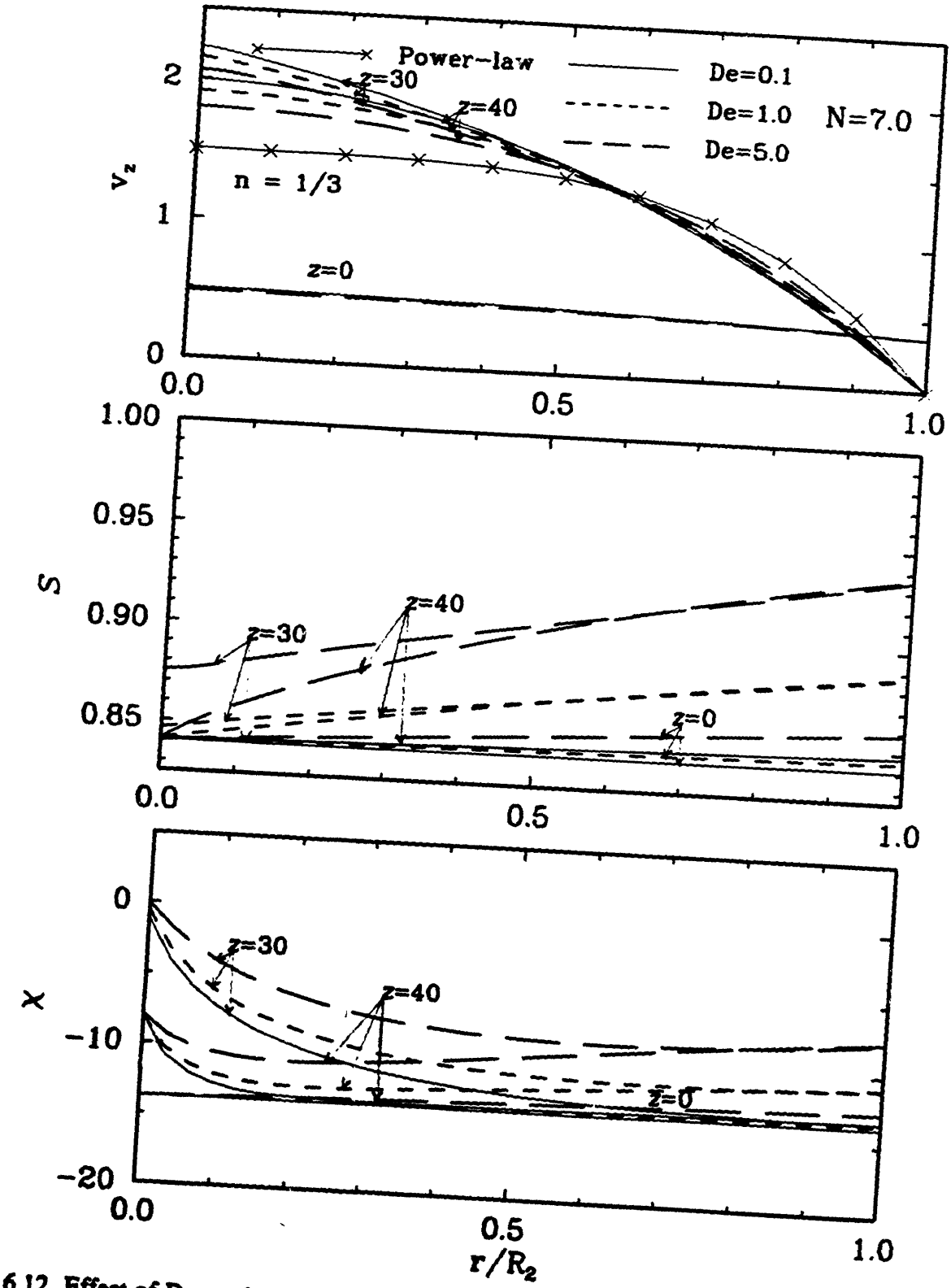

Figure 6.12 Effect of De on the radial variation in (a) v_z, (b) S, and (c) χ at z=0, 30 and 40 in a 2:1 contraction for N=7.0, σ=1.0, β=1.6x10^{-5} and De=0.1, 1.0 and 5.0. The fully developed downstream exit velocity profile for a power-law model with the same shear thinning behavior as the viscosity for the liquid-crystal model is shown for comparison.

Effect of De on Velocity

The qualitative effect of De on the axial velocity is the same as that predicted for $N = 4.0$ (cf. Figs. 6.9a & 6.12a). As discussed in Section 6.2.1.3, the fully developed Newtonian velocity profile through the upstream tube for a 2:1 contraction is given by equation 6.6. For De=0.1, there is very little shear thinning at the inlet since the associated shear rates are small and consequently the velocity profiles are Newtonian. For De=5.0, the maximum centerline velocity is slightly lower than the Newtonian value which is evidence of a small shear thinning effect.

Table 6.1 shows that the maximum velocity decreases with increasing De. The percentage overshoot, however, increases with De due to the effect of shear thinning and the consequent decrease in the downstream velocity. Fig. 6.13d reveals that the maximum velocity (corresponding to $\dot{\varepsilon}(0,z/R_2) = 0$ near the junction of the contraction and the downstream tube) shifts downstream with increasing De. At the junction of the contraction region and the downstream tube, but away from the centerline, the blunt or "plug-like" velocity profiles for De = 1.0 and 5.0 as compared to De = 0.1 (cf. Fig. 6.12a) indicates an increase in shear thinning with De.

At the downstream exit, the velocity profile is Newtonian for De=0.1. For De=1.0 and 5.0 the centerline velocities are lower than the Newtonian value due to shear thinning. The velocity profile predicted for a power-law model with a shear thinning index of -2/3 (n=1/3) in the viscosity is shown for comparison.

Effect of De on *S*

The qualitative effect of De on the degree of order for N=7.0 is the same as that predicted for N=4.0. The order at the inlet, as expected, is close to the equilibrium value across the cross section of the tube for De=0.1. The higher shear rates associated with De=5.0 create a higher degree of order away from the centerline. The order is not very different from the equilibrium value for De=1.0. $S(0,0)$ must be the equilibrium value irrespective of De since the shear rate is zero there.

The higher shear and extension rates in the contraction region are expected to create a higher degree of order than the order present at the inlet. For De=0.1, however, the order hardly changes from the equilibrium value throughout the contraction region (red everywhere in Fig. 6.11p). The higher elongation rate associated with De=5.0, and to a lesser extent De=1.0, leads to a much higher degree of order at the centerline over the equilibrium value as compared to the centerline value for De=0.1 (cf. Figs. 6.11p and 6.13e). Similarly to N = 4.0, a lag is observed between the increase in $\dot{\varepsilon}(0,z/R_2)$ and the response in $S(0,z/R_2)$ for De = 1.0 and 5.0; the order changes little from the equilibrium value for De = 0.1 (cf. Figs. 6.13d and e). The axial location where $S(0,z/R_2)$ increases sharply coincides with the point where the director becomes aligned with the z-axis. The lag between the maximum in $S(0,z/R_2)$ and $\dot{\varepsilon}(0,z/R_2)$, however, is only of the order of one downstream tube radius for all De. Shear flow, however, seems to dominate the kinematics more than extensional flow in creating order for this tapered contraction geometry, since the order increases monotonically from the centerline to the wall; Fig. 6.12b shows this monotonic increase in the order from the centerline to the wall at the

junction of the contraction region and the downstream tube.

At the downstream exit the order at the centerline relaxes to the equilibrium value for all De since there is no axial velocity gradient to create extensional order. However, as observed for N=4.0, the shear flow dominated kinematics from the contraction region are maintained some distance away from the centerline and there is no decrease in the order in this shear dominated region in the downstream tube.

Effect of De on χ

The qualitative effect of De on the director orientation is also similar to the results obtained for N = 4.0. At the inlet, the director angle hardly varies from the zero-shear-rate prediction for De=0.1 and 1.0. The higher shear rates associated with De=5.0, away from the centerline, result in a director orientation that is more preferential with the axial direction.

In the contraction region, the pure extension along the centerline causes the director to be aligned with the z-axis for all De (dark blue in Fig. 6.11q). As explained in Section 6.2.1.3 this is consistent with the perturbation analysis presented in Section 4.1. Though the director is perfectly aligned with the axis even at small De, $S(0,z/R_2)$ is still not very far from equilibrium. Figures 6.13d and f show that there is no lag in the response of the director orientation to an increase in $\dot{\varepsilon}(0,z/R_2)$ in the upstream portion of the contraction; the response in $\chi(0,z/R_2)$ to $\dot{\varepsilon}(0,z/R_2)$ is qualitatively the same as that described in Section 6.2.1.3. The decrease in $\chi(0,z/R_2)$ in the downstream portion of the contraction is also qualitatively similar. In the region away from the centerline, the role played by extensional flow in the kinematics has decayed and shear flow has started to

dominate the kinematics. Consequently, the director orientation changes rapidly from the axial orientation predicted at the centerline and is dictated by the shear rates that exist in that region. The maximum change in the director orientation across the contraction is observed for De=0.1. In fact, close to the wall the director orientation is worse than the orientation at the entrance to the contraction geometry. The reason for the "loss in orientation" was discussed in Section 6.2.1.3. As discussed in Section 6.2.1.3 the wall shear in the downstream portion of the contraction region together with the fact that the wall slope is close to zero makes the director orientation with the z-axis slightly better than the zero-shear-rate limit of -13.7 degrees (cf. Fig. 6.12c). The discussion in Section 6.2.1.3 on the behavior of the director orientation for De = 1.0 and 5.0 also holds for this concentration.

6.2.2.2 Effect of Concentration

The velocity, degree of order and director orientation profiles for N=4.0 and 7.0, as the flow progresses through the contraction, are compared to study the quantitative effect of concentration. As already pointed out in the previous section, qualitatively there is no difference in increasing the concentration from 4.0 to 7.0. Comparisons are presented in Figs. 6.13a-c for De=1.0. The quantitative effect of concentration on the development of $S(0,z/R_2)$ and $\chi(0,z/R_2)$ and their response to $\dot{\varepsilon}(0,z/R_2)$ is illustrated in Figs. 6.13d-f for De = 0.1, 1.0 and 5.0.

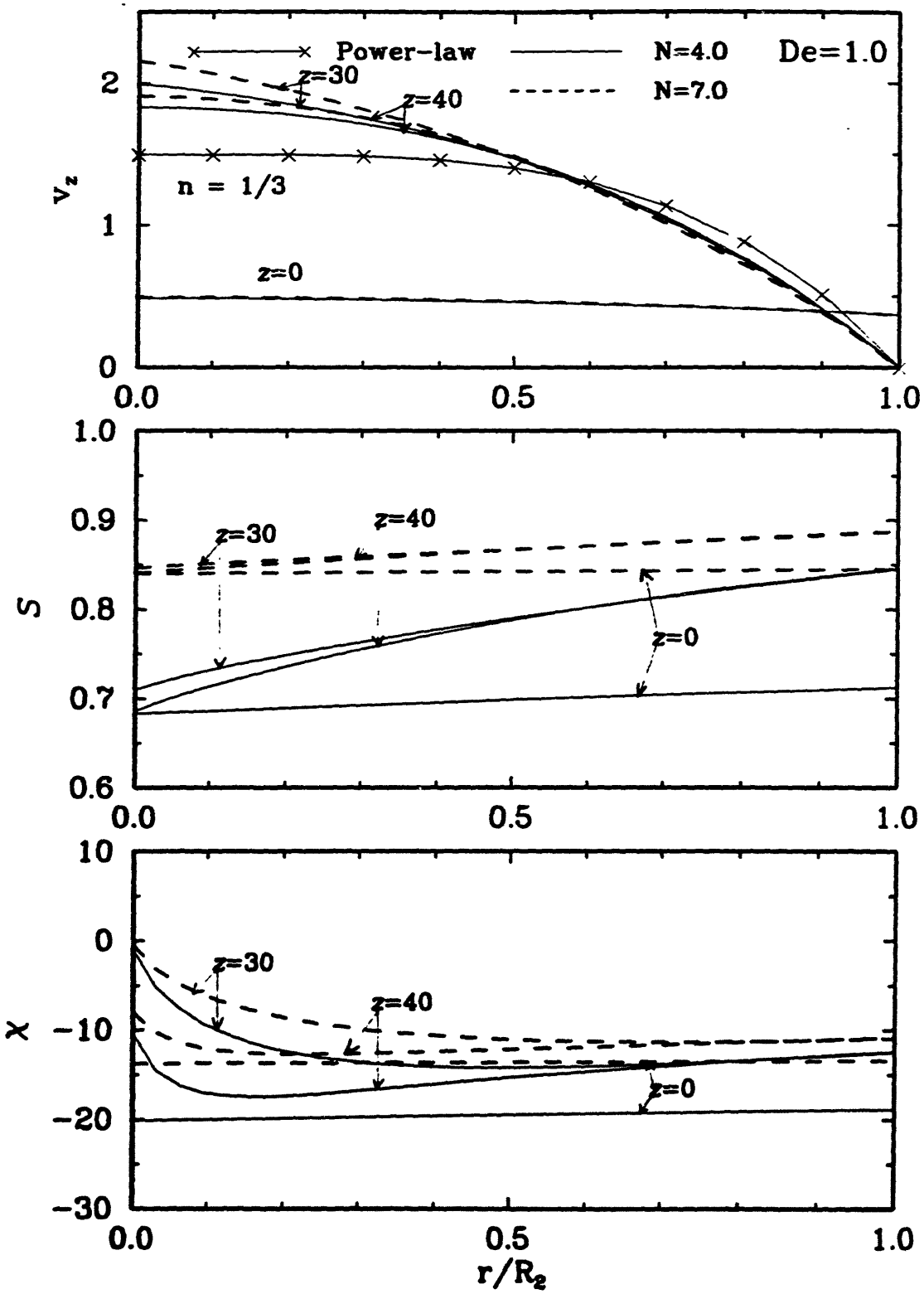

Figure 6.13 Effect of concentration on the radial variation in (a) v_z, (b) S, and (c) χ at z=0, 30 and 40 in a 2:1 contraction for De=1.0, σ=1.0, β=1.6x10^{-5} and N=4.0 and 7.0. The fully developed downstream exit velocity profile for a power-law model with the same shear thinning behavior as the viscosity for the liquid-crystal model is shown for comparison.

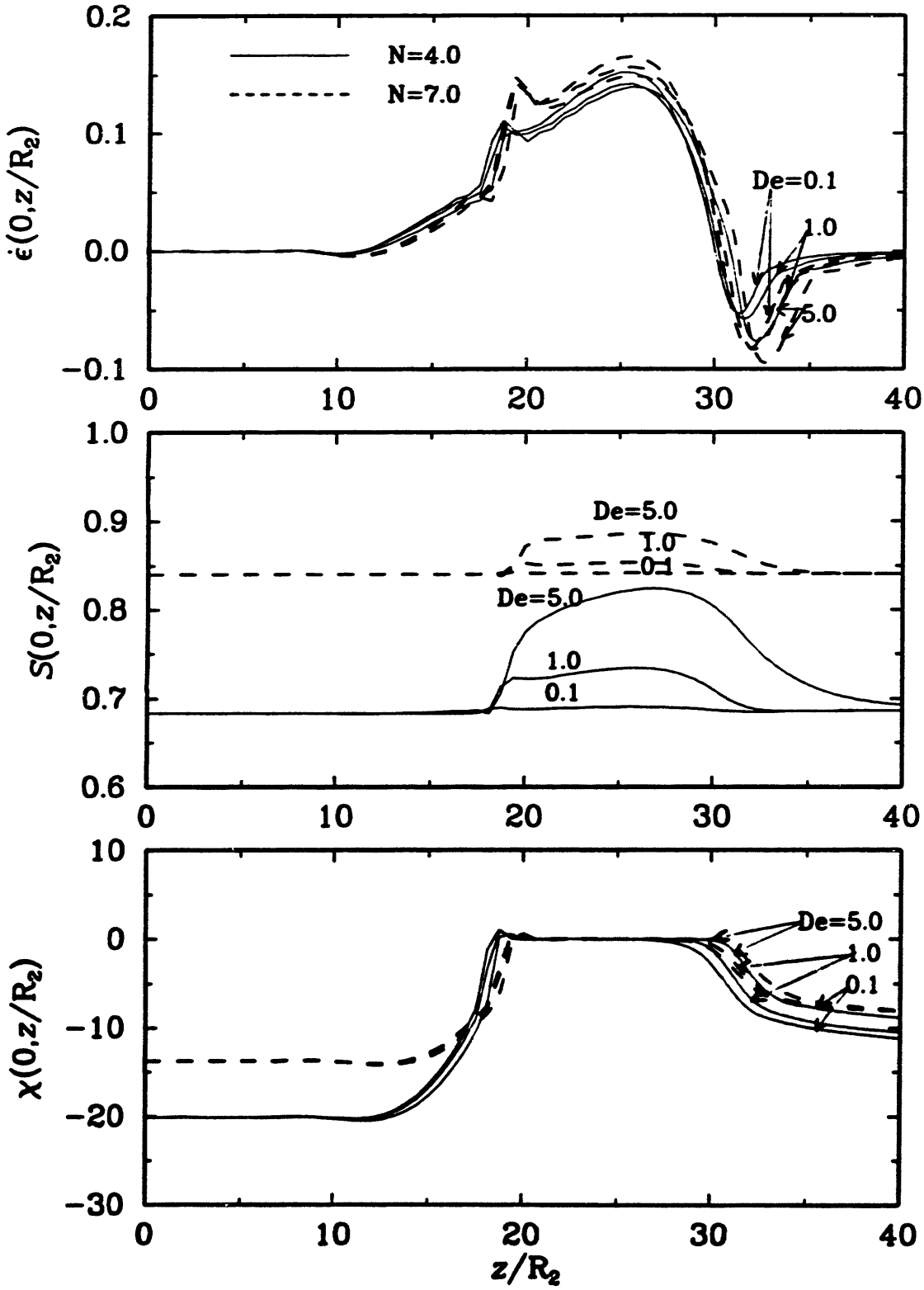

Figure 6.13 Effect of concentration on the centerline variation in (d) $\dot{\epsilon}$, (e) S, and (f) χ in a 2:1 contraction for σ=1.0, β=1.6x10^{-5}, N=4.0 and 7.0 and De=0.1, 1.0 and 5.0.

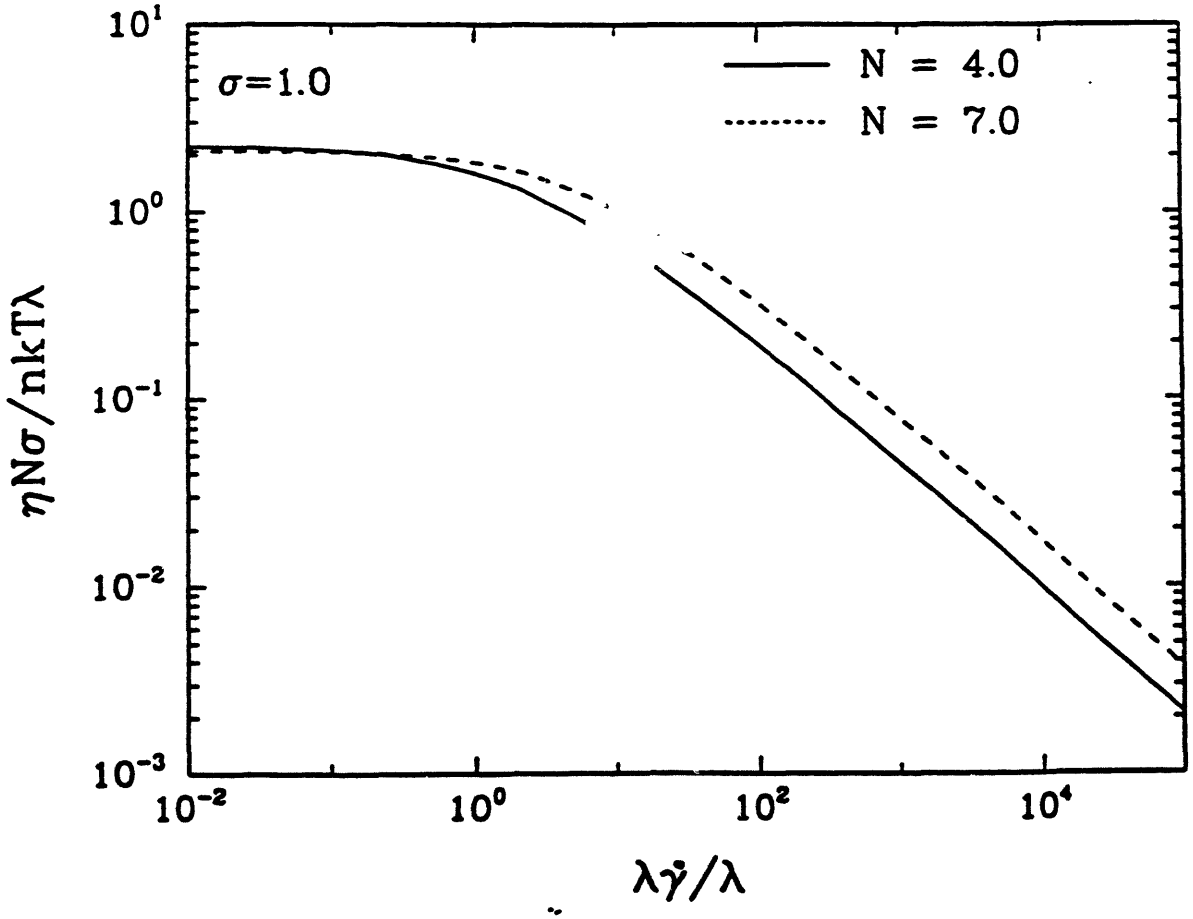

Figure 6.14 Effect of concentration on the dimensionless viscosity for σ=1.0, β=1.6x10^{-5} and N=4.0 and 7.0.

Effect of Concentration on Velocity

Even for De=1.0, shear thinning is small at the inlet since the associated shear rates are small, and consequently the velocity profiles are close to being Newtonian for both concentrations.

Table 6.1 shows that the maximum velocity and the percentage overshoot for N = 7.0 is higher for all De. Fig. 6.13d also reveals that the maximum velocity for N = 7.0 is located further downstream for all De. The higher overshoot is associated purely with the difference in the maximum velocities. In fact, Fig. 6.13a shows that the velocity along the centerline at the downstream exit is higher for N = 7.0 which indicates that shear thinning is less pronounced; this observation also holds for De = 0.1 and 5.0. The reduced shear thinning effect for N = 7.0 could result from a postponement in the onset of shear thinning in the viscosity to higher magnitudes of the rate-of-strain tensor (cf. Fig. 6.14).

Effect of N on S

The order along the centerline at the inlet is different for the two concentrations. The difference arises since the order predicted at equilibrium for N = 4.0 and 7.0 are 0.683 and 0.840 respectively. A comparison of the inlet profiles also reveals that the order increases noticeably towards the wall for N=4.0, whereas it remains close to the equilibrium value for N=7.0 up to the range of r/R_2 shown in Fig. 6.13b. The break-up of the equilibrium phase diagram shown in Fig. 3.6 in shear or extensional flow, studied by Menon (1990) and Bhave *et al.* (1993), demonstrates that the magnitude of the rate-of-strain tensor required to increase the order by a fixed amount, increases with

concentration which explains the above observation.

The higher shear and extension rates in the contraction region create a higher degree of order for both concentrations. Figures 6.8p and 6.11p show that the radial and axial increase in the order is much more substantial for the lower concentration. Fig. 6.13e shows that there is no noticeable effect of concentration on the axial location where the sharp increase in $S(0,z/R_2)$ is observed. Shear flow seems to dominate the kinematics more than extensional flow in creating order for both concentrations for this contraction ratio since the order increases monotonically from the centerline to the wall.

At the downstream exit, the order at the centerline relaxes to the corresponding equilibrium value for both concentrations due to the absence of an axial velocity gradient to create extensional order. However, at De = 5.0, $S(0,z/R_2)$ relaxes to the equilibrium value over a shorter axial distance for $N = 7.0$ which may be due to the smaller difference between the maximum and the equilibrium value.

Effect of N on χ

It is apparent from Fig. 6.13c that $\chi(0,0)$ is different for the two concentrations. In the limit of zero-shear-rate $\chi(0,0)$ for N = 4.0 and 7.0 are -20.1 and -13.7 degrees respectively. The χ profiles at the inlet also show that there is a noticeable decrease in the angle between the director and the z-axis as the radial position increases to $r/R_2=1$ for $N=4.0$, whereas the angle is uniform for $N=7.0$. The break-up of the equilibrium phase diagram in shear or extensional flow indicates that the magnitude of the rate-of-strain tensor required to change the component values of the structure tensor by a fixed amount, increases with concentration which accounts for the different radial dependence of χ for $N = 4.0$ and 7.0.

In the contraction region, the pure extension along the centerline creates perfect axial orientation in the director for both concentrations. However, the director becomes aligned with the z-axis 1-2 downstream tube radii further downstream for $N = 7.0$. In the radial direction, but close to the centerline, χ decreases more rapidly from zero for N=4.0; the maximum difference in χ is about 5-6 degrees. The faster radial decrease in χ for N=4.0 can be explained by the effect of concentration on the break-up of the equilibrium phase diagram. However, away from the upstream portion of the contraction, the radially increasing shear rate does not allow χ to decrease to the zero-shear-rate limit for either concentration. In fact, at z=30 there is a noticeable increase in χ close to the wall for both concentrations; however, the increase in χ is more for N=4.0 due to the more sensitive response to an increase in shear rate as discussed in the preceding paragraph.

In the downstream tube, $\chi(0,z/R_2)$ is no longer zero for either concentration due to a relaxation in the extensional kinematics. The axial location at the onset of decrease in $\chi(0,z/R_2)$ from zero is shifted downstream by 1-2 downstream tube radii for N=7.0. However, $\chi(0,z/R_2)$ shows no dependence on De at the downstream exit for $N = 7.0$. The smaller difference between χ=0 and the zero-shear-rate limit for N=7.0 could explain the observation. The shear flow dominated kinematics that exist from the contraction region are maintained some distance away from the centerline and there is no change in χ in this shear dominated region in the downstream tube. Again, radial changes in χ are more rapid for N=4.0 than N=7.0.

6.2.3 Effect of Contraction Ratio, Λ

In this section, the effect of contraction ratio on the flow field, degree of order, director orientation and stress fields is examined by comparing the results for a 4:1 contraction and the 2:1 contraction studied in sections 6.2.1 and 6.2.2. Comparisons are presented for N=4.0 and De=0.1, 1.0 and 5.0. Contour plots of pressure, structure, velocity, velocity gradient, stress, streamlines, degree of order and director orientation for the respective contraction ratios are shown in Figs. 6.8a-q and 6.15a-q. Note that the dimensionless pressure drop per unit volumetric flow rate defined by Eq. 6.2 and plotted as a function of De in Fig. 6.23 is smaller for the 4:1 contraction for all De due to the larger upstream tube radius. Cross sectional profiles of the axial velocity, degree of order and molecular orientation for the two contraction ratios are compared in Figs. 6.16a-c. The inlet radial profiles extend up to r/R_2=4 for the 4:1 contraction and up to r/R_2=2 for the 2:1 contraction. For comparison with the downstream profiles the inlet profiles are shown only upto r/R_2=1. $S(0,z/R_2)$ and $\chi(0,z/R_2)$ predicted for the two contraction ratios and their responses to $\dot{\varepsilon}(0,z/R_2)$ are compared in Figs. 6.16d-f. The response in the dimensionless normal stress difference is illustrated in Fig. 6.16g.

Effect of Λ on velocity; De=0.1, 1.0 and 5.0

The Newtonian velocity through a tube of radius $4R_2$ is given by the expression

$$v_z = \frac{1}{8}\left[1-\left(\frac{r}{4R_2}\right)^2\right] \tag{6.8}$$

The Newtonian velocity through a tube of radius $2R_2$ is given by Eq. 6.6. It is clear from the comparison with the corresponding Newtonian velocity profiles that the inlet velocity

De=0.1

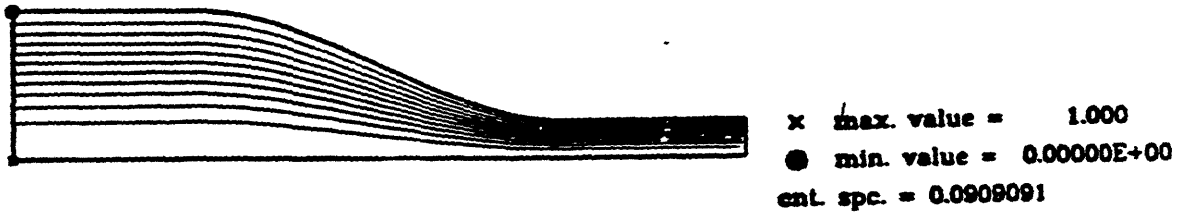

De=1.0

De=5.0

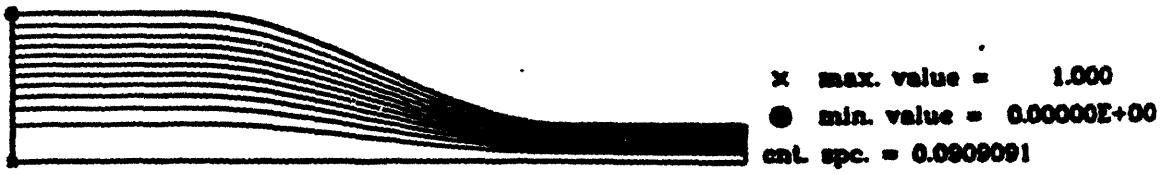

Figure 6.15a Contour plots of streamlines in the flow through a 4:1 contraction for N=4.0, σ=1.0, β=1.6x10^{-5} and De=0.1, 1.0 and 5.0.

De=0.1

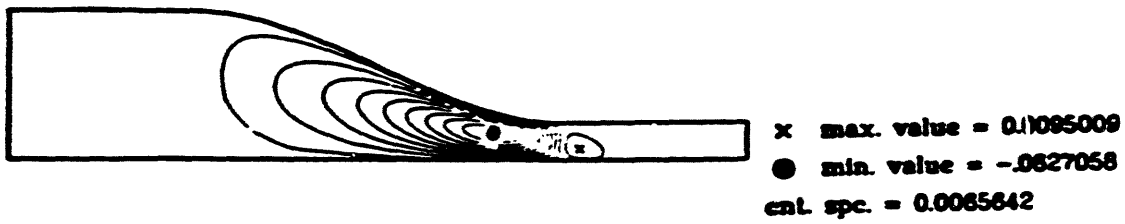

De=1.0

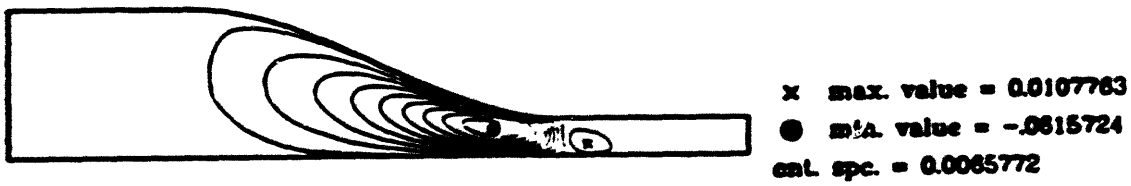

De=5.0

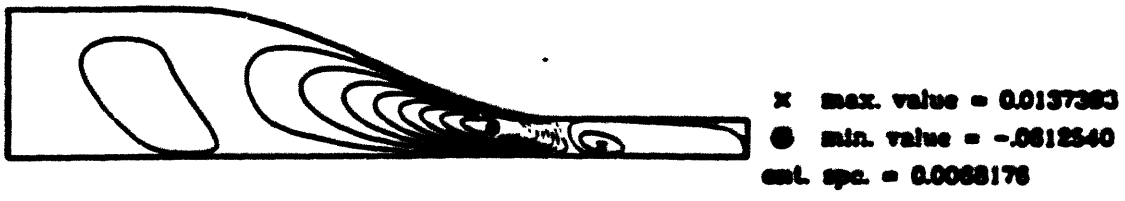

Figure 6.15b Contour plots of radial velocity in the flow through a 4:1 contraction for N=4.0, σ=1.0, β=1.6x10^{-5} and De=0.1, 1.0 and 5.0.

De=0.1

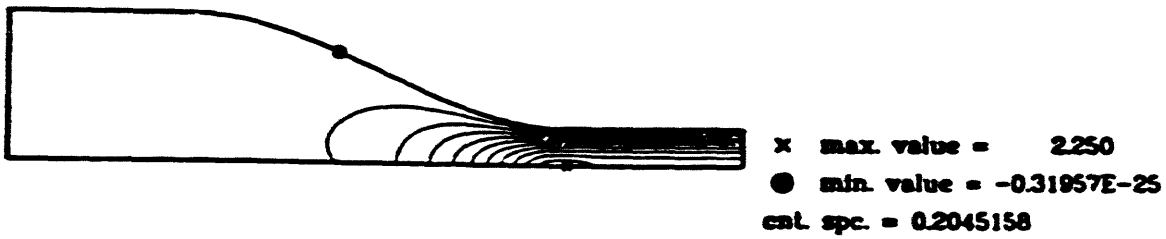

De=1.0

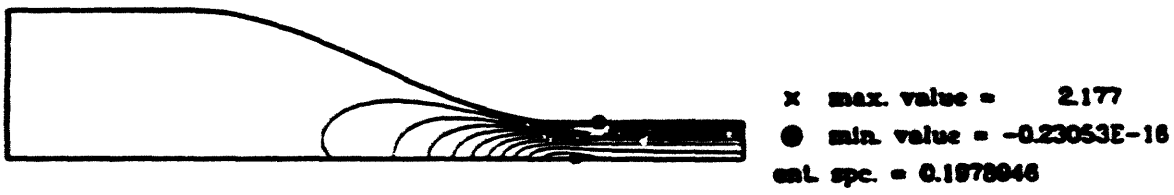

De=5.0

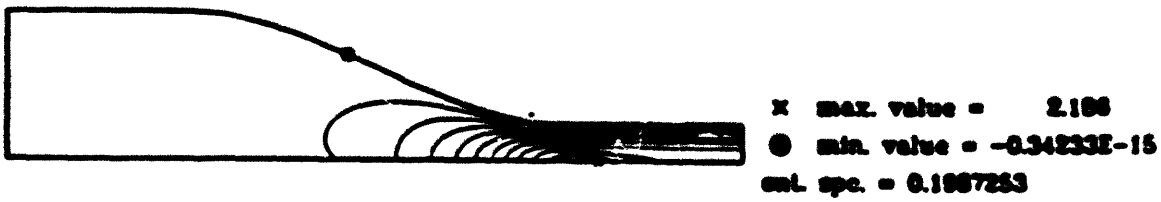

Figure 6.15c Contour plots of axial velocity in the flow through a 4:1 contraction for N=4.0, σ=1.0, β=1.6x10^{-5} and De=0.1, 1.0 and 5.0.

De=0.1

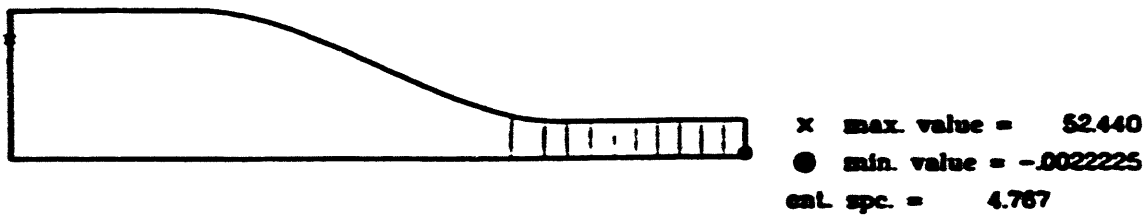

De=1.0

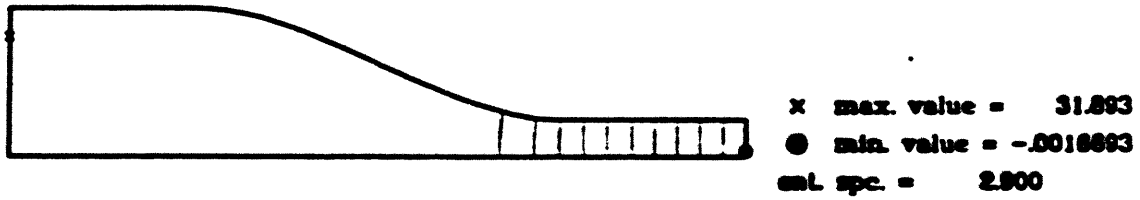

De=5.0

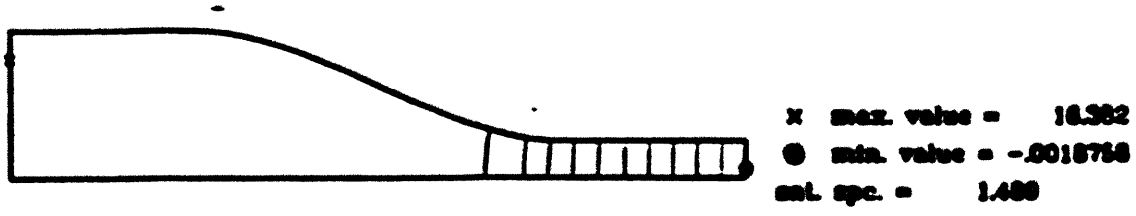

Figure 6.15d Contour plots of pressure in the flow through a 4:1 contraction for N=4.0, σ=1.0, β=1.6x10^{-5} and De=0.1, 1.0 and 5.0.

DE=0.1

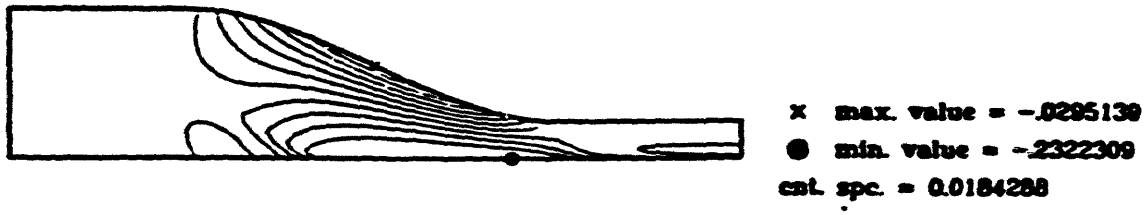

De=1.0

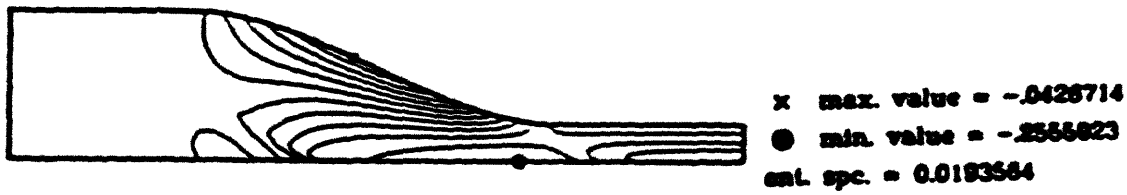

De=5.0

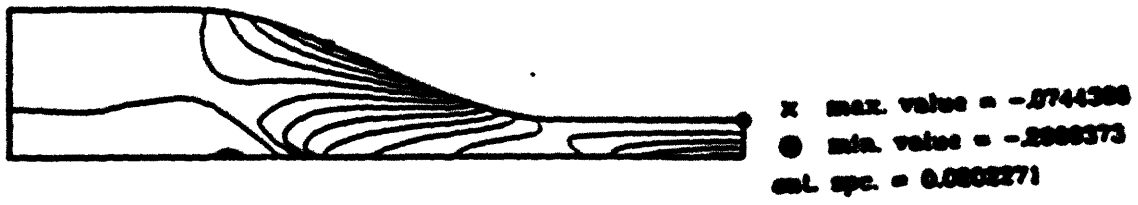

Figure 6.15e Contour plots of S_{rr} in the flow through a 4:1 contraction for N=4.0, σ=1.0, β=1.6x10^{-5} and De=0.1, 1.0 and 5.0.

De=0.1

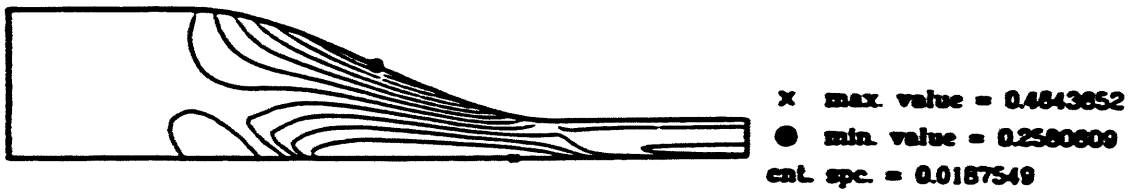

De=1.0

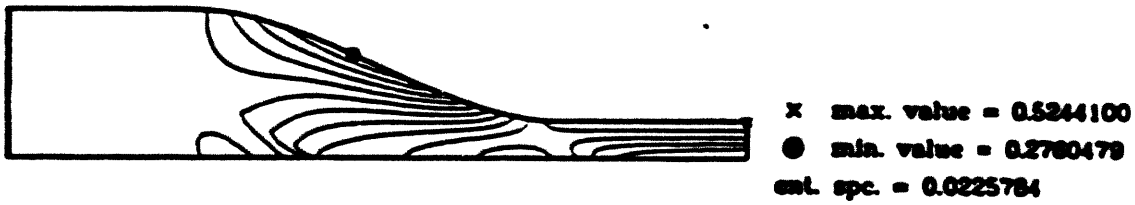

De=5.0

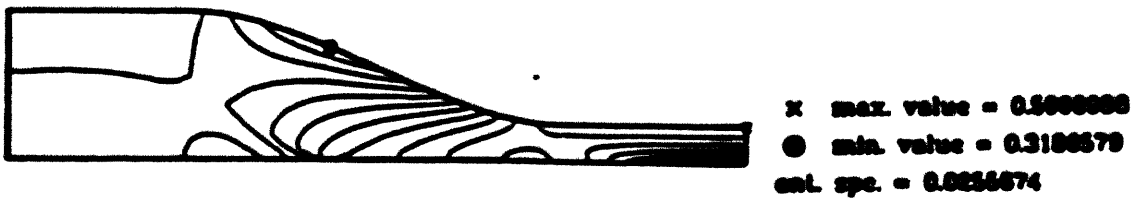

Figure 6.15f Contour plots of S_{zz} in the flow through a 4:1 contraction for N=4.0, σ=1.0, β=1.6x10^{-5} and De=0.1, 1.0 and 5.0.

De=0.1

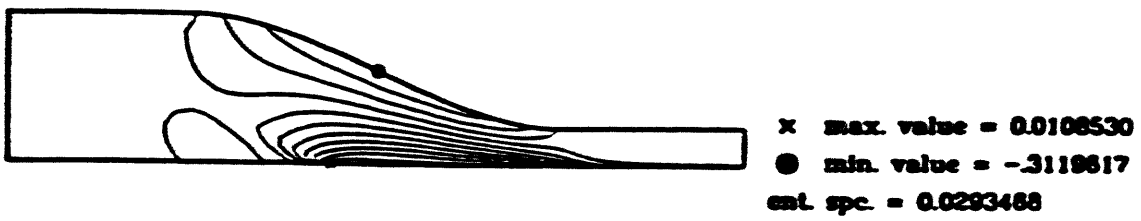

De=1.0

De=5.0

Figure 6.15g Contour plots of S_{rz} in the flow through a 4:1 contraction for N=4.0, σ=1.0, β=1.6x10^{-5} and De=0.1, 1.0 and 5.0.

De=0.1

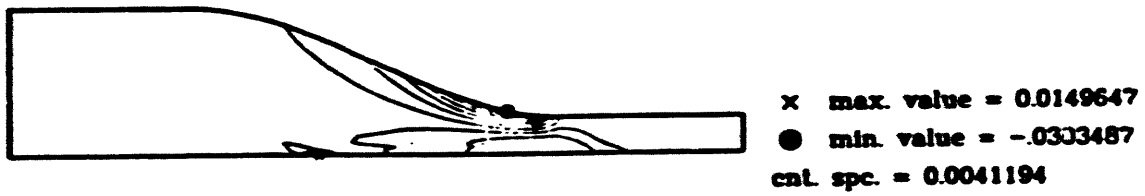

De=1.0

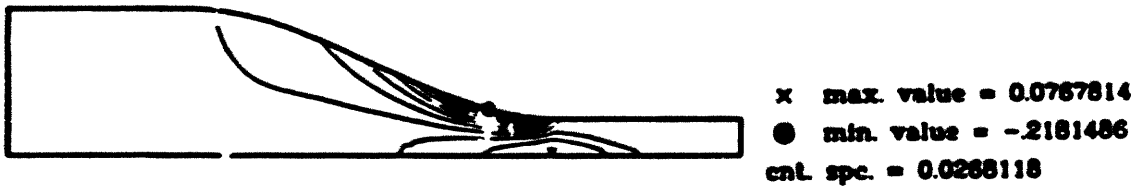

De=5.0

Figure 6.15h Contour plots of Det_{ss} in the flow through a 4:1 contraction for N=4.0, ε=1.0, β=1.6x10^{-5} and De=0.1, 1.0 and 5.0.

De=0.1

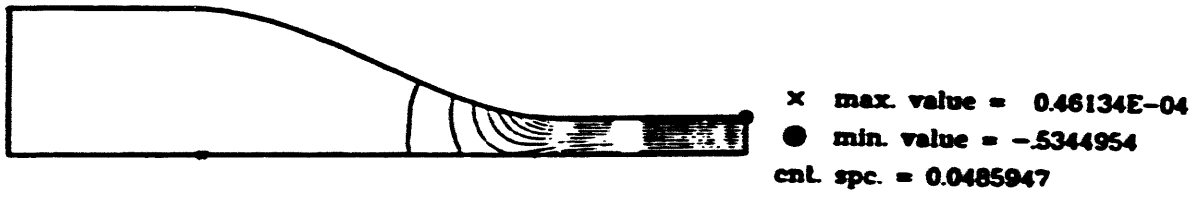

De=1.0

De=5.0

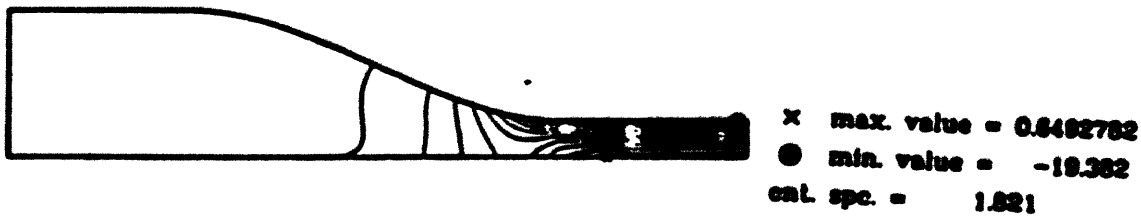

Figure 6.15i Contour plots of Det_{zz} in the flow through a 4:1 contraction for N=4.0, σ=1.0, β=1.6x10^{-5} and De=0.1, 1.0 and 5.0.

De=0.1

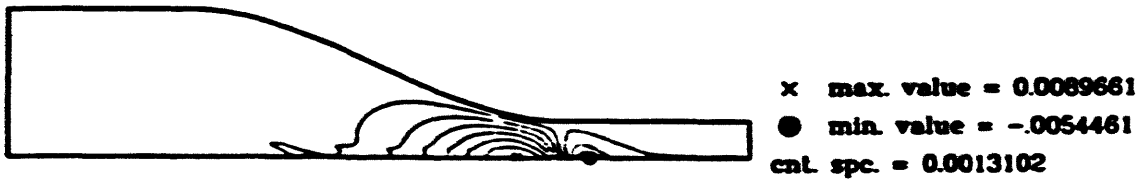

De=1.0

De=5.0

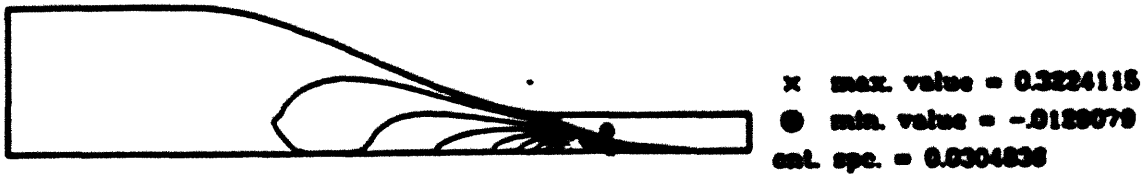

Figure 6.15j Contour plots of $De\tau_{ss}$ in the flow through a 4:1 contraction for N=4.0, ε=1.0, β=1.6x10^{-5} and De=0.1, 1.0 and 5.0.

De=0.1

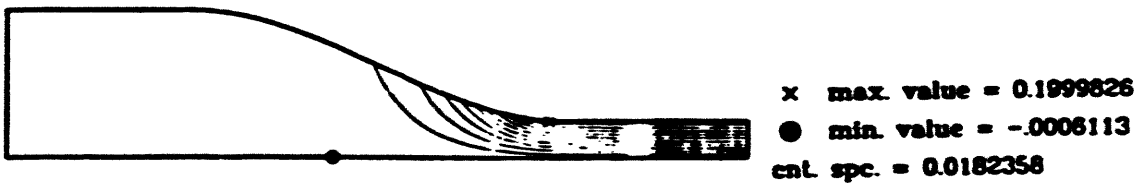

De=1.0

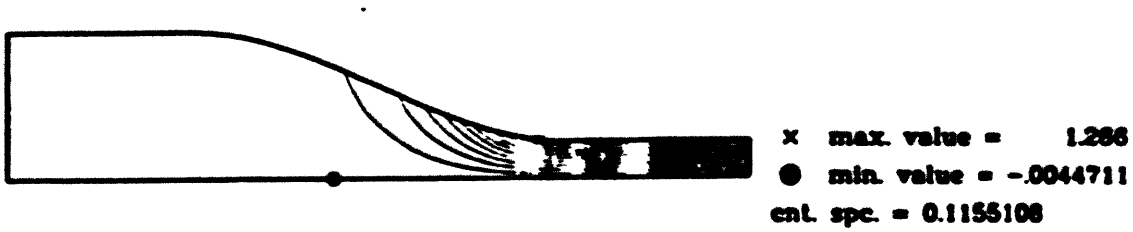

De=5.0

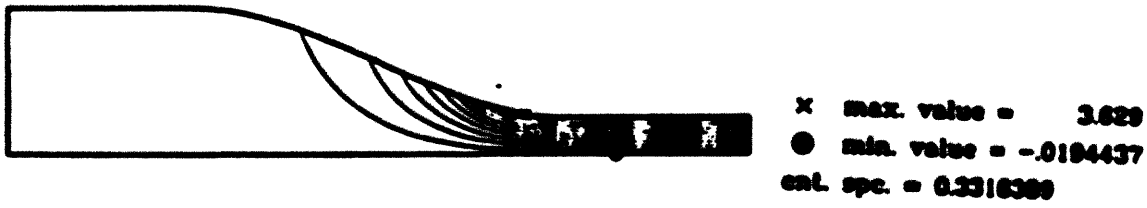

Figure 6.15c Contour plots of $De\tau_{rr}$ in the flow through a 4:1 contraction for N=4.0, σ=1.0, β=1.6x10^{-5} and De=0.1, 1.0 and 5.0.

De=0.1

De=1.0

De=5.0

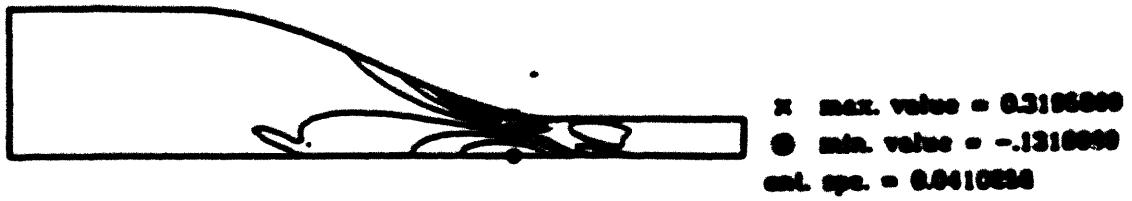

Figure 6.151 Contour plots of G_{11} in the flow through a 4:1 contraction for N=4.0, σ=1.0, β=1.6x10^{-5} and De=0.1, 1.0 and 5.0.

De=0.1

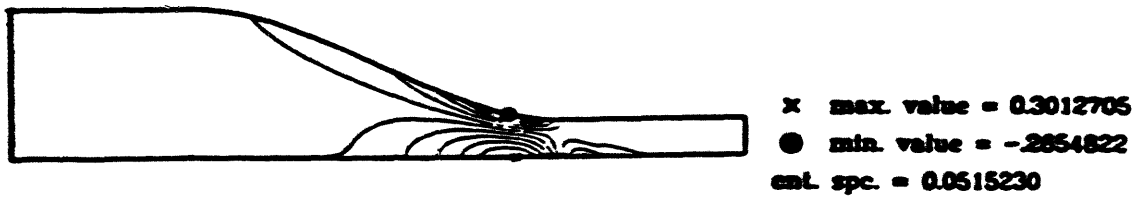

De=1.0

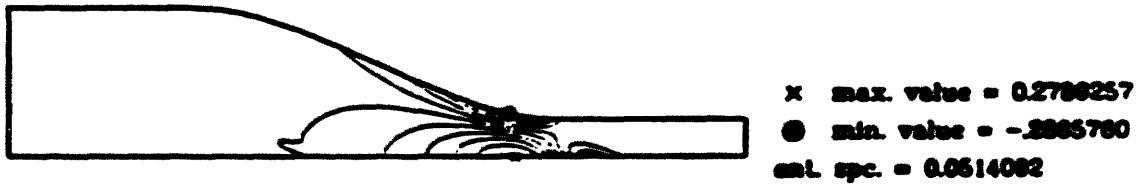

De=5.0

Figure 6.15m Contour plots of G_{xx} in the flow through a 4:1 contraction for N=4.0, α=1.0, β=1.6x10^{-5} and De=0.1, 1.0 and 5.0.

De=0.1

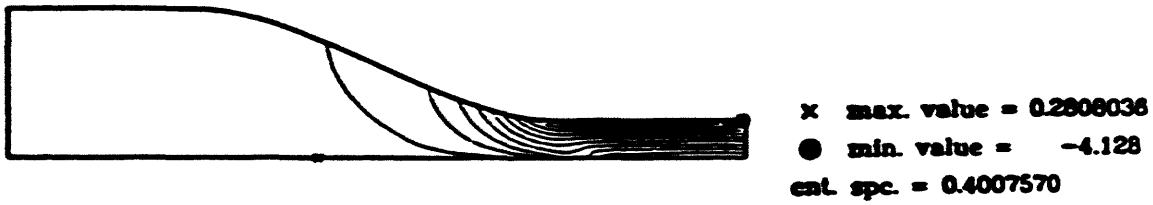

De=1.0

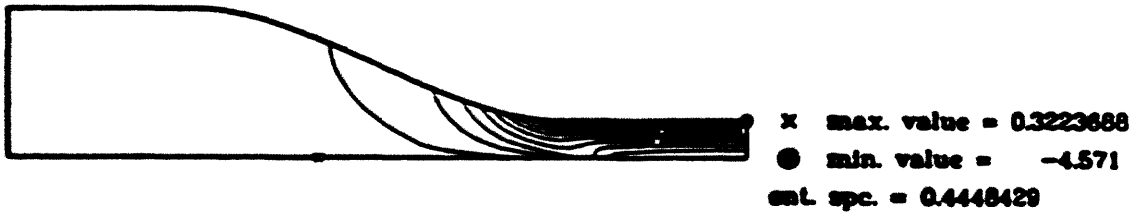

De=5.0

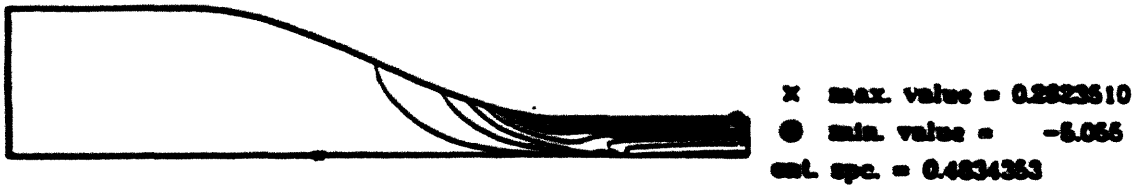

Figure 6.15a Contour plots of G_{rr} in the flow through a 4:1 contraction for N=4.0, σ=1.0, β=1.6x10^{-5} and De=0.1, 1.0 and 5.0.

De=0.1

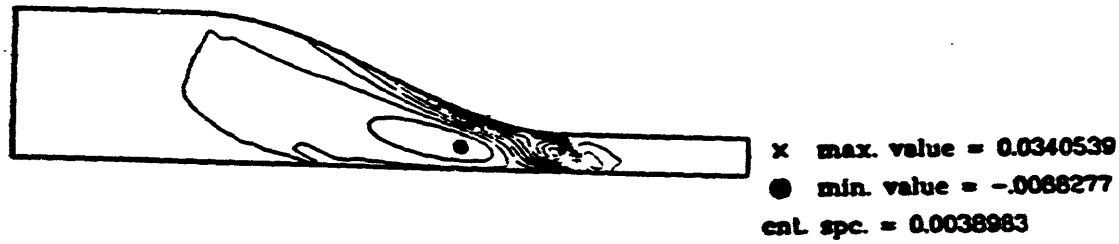

De=1.0

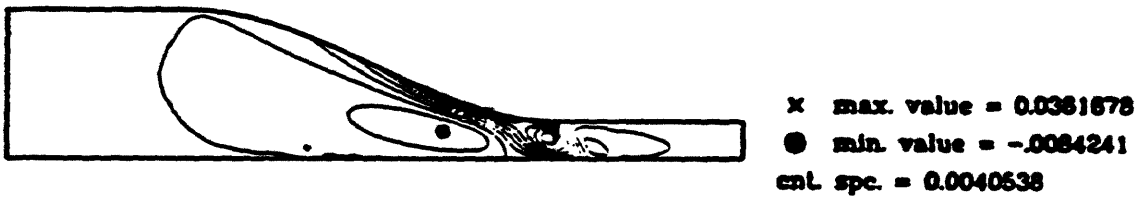

De=5.0

Figure 6.15o Contour plots of G_{zz} in the flow through a 4:1 contraction for N=4.0, σ=1.0, β=1.6x10^{-5} and De=0.1, 1.0 and 5.0.

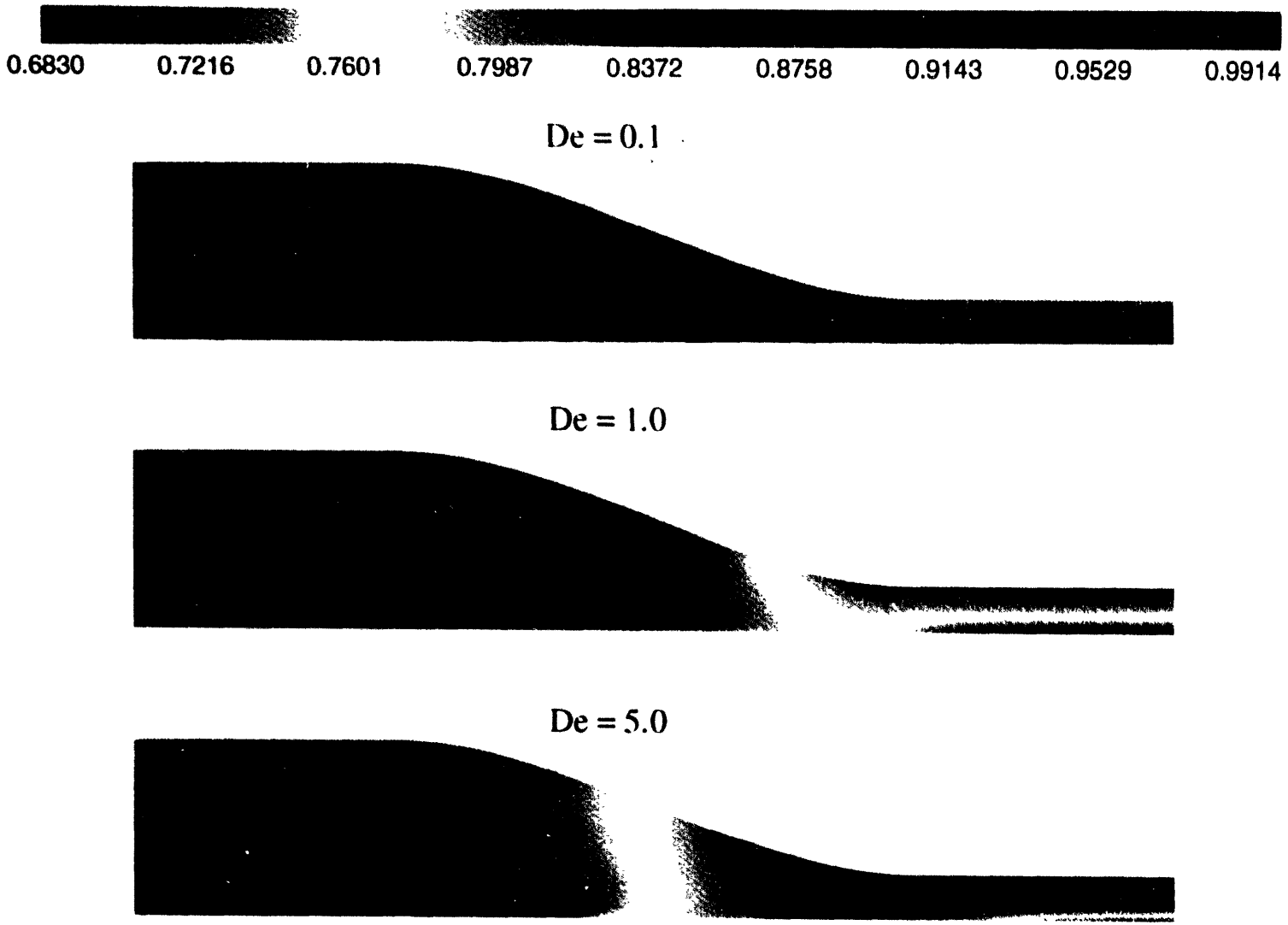

Figure 6.15p: Effect of De on S in a 4:1 contraction for N =4.0, σ=1.0, β=1.6x10^{-5} and De=0.1, 1.0 and 5.0. S =0.683 is the equilibrium value for N =4.0 and S =1.0 corresponds to perfect order.

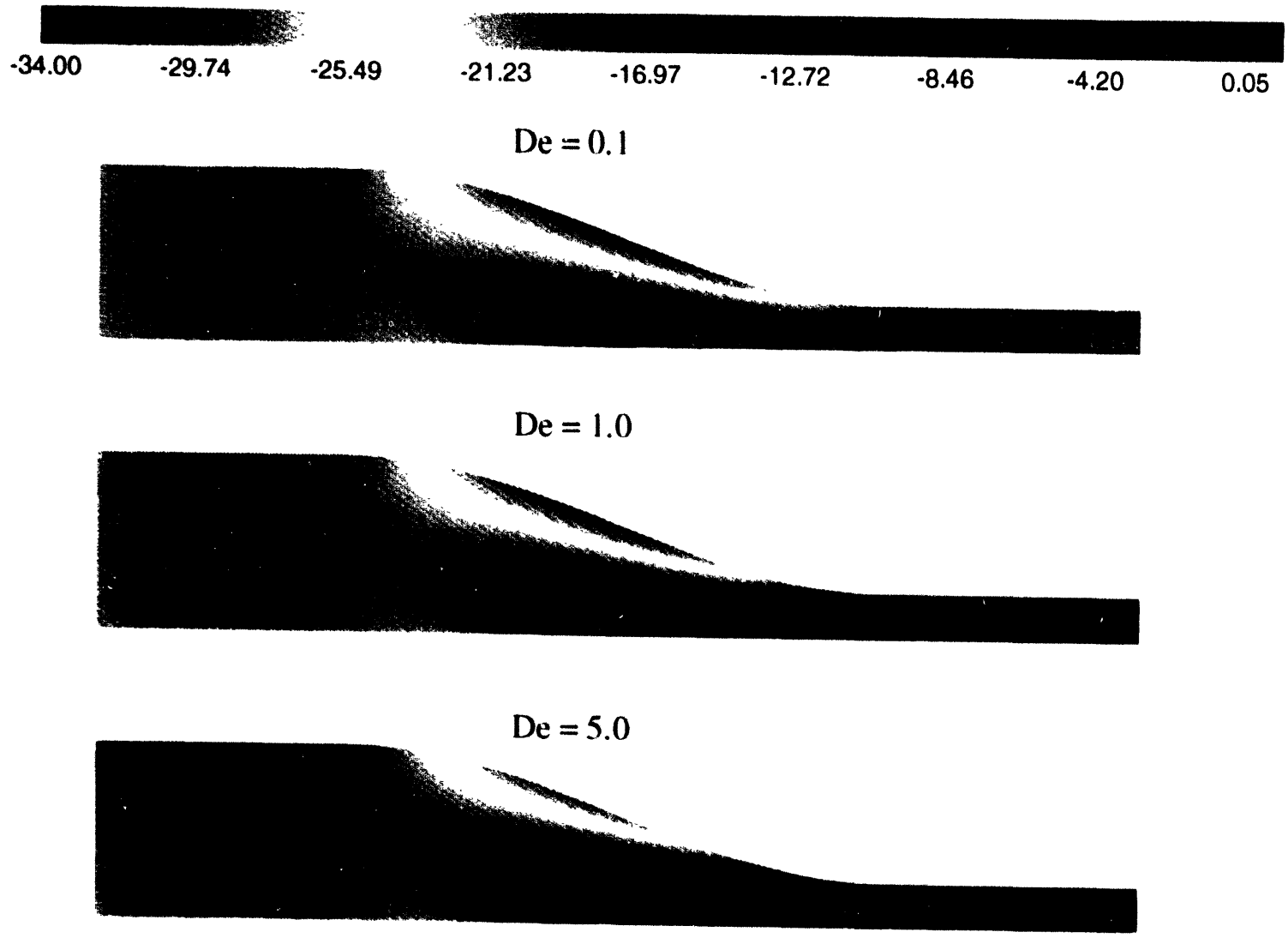

Figure 6.15q: Effect of De on χ in a 4:1 contraction for N =4.0, σ=1.0, β=1.6x10^{-3} and De=0.1, 1.0 and 5.0. χ=-20.1 degrees is the zero-shear-rate limit. For χ=0, the director is aligned with the die axis.

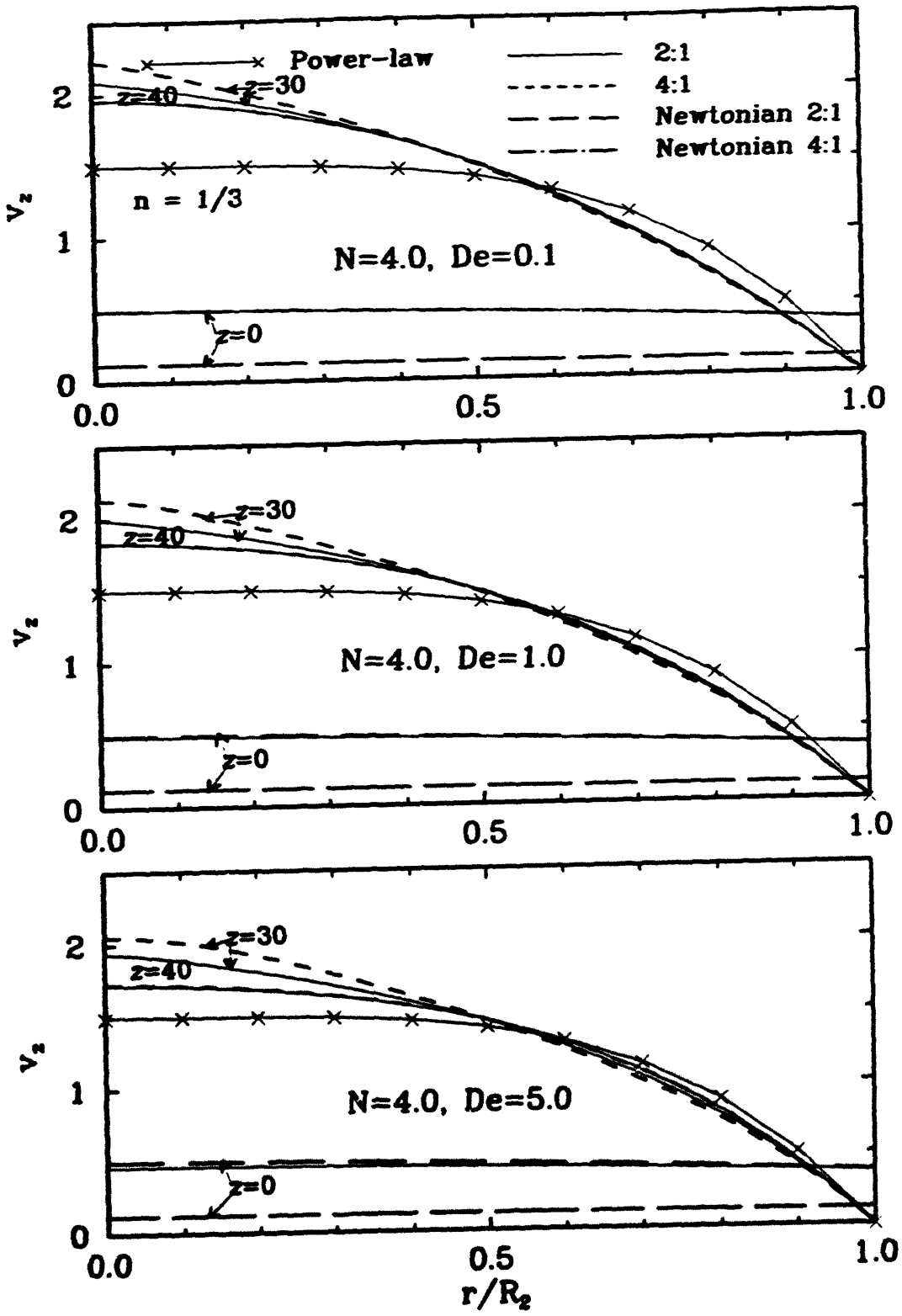

Figure 6.16a Effect of contraction ratio on the radial variation in v_z at z=0, 30 and 40 for N=4.0, σ=1.0, β=1.6x10^{-5}, De=0.1, 1.0 and 5.0 and Λ=2 and 4. The fully developed Newtonian velocity profiles in the respective upstream tubes and the fully developed velocity profile in the downstream tube for a power-law model with an index n=1/3 are shown for comparison. For z=40 the 2:1 and 4:1 results are indistinguishable.

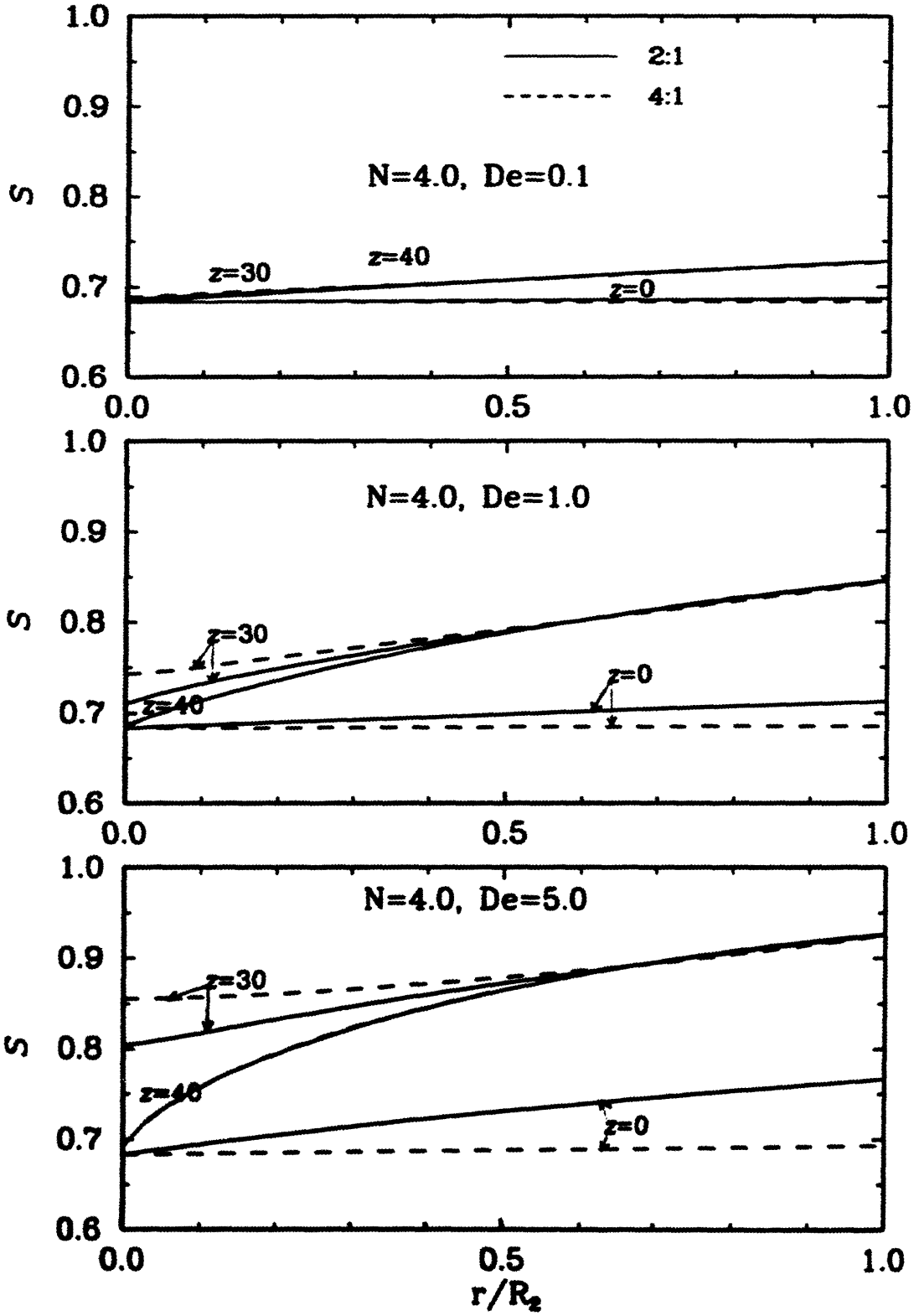

Figure 6.16b Effect of contraction ratio on the radial variation in S at z=0, 30 and 40 for N=4.0, σ=1.0, β=1.6x10^{-5}, De=0.1, 1.0 and 5.0 and Λ=2 and 4. For z=40, the 2:1 and 4:1 results are indistinguishable.

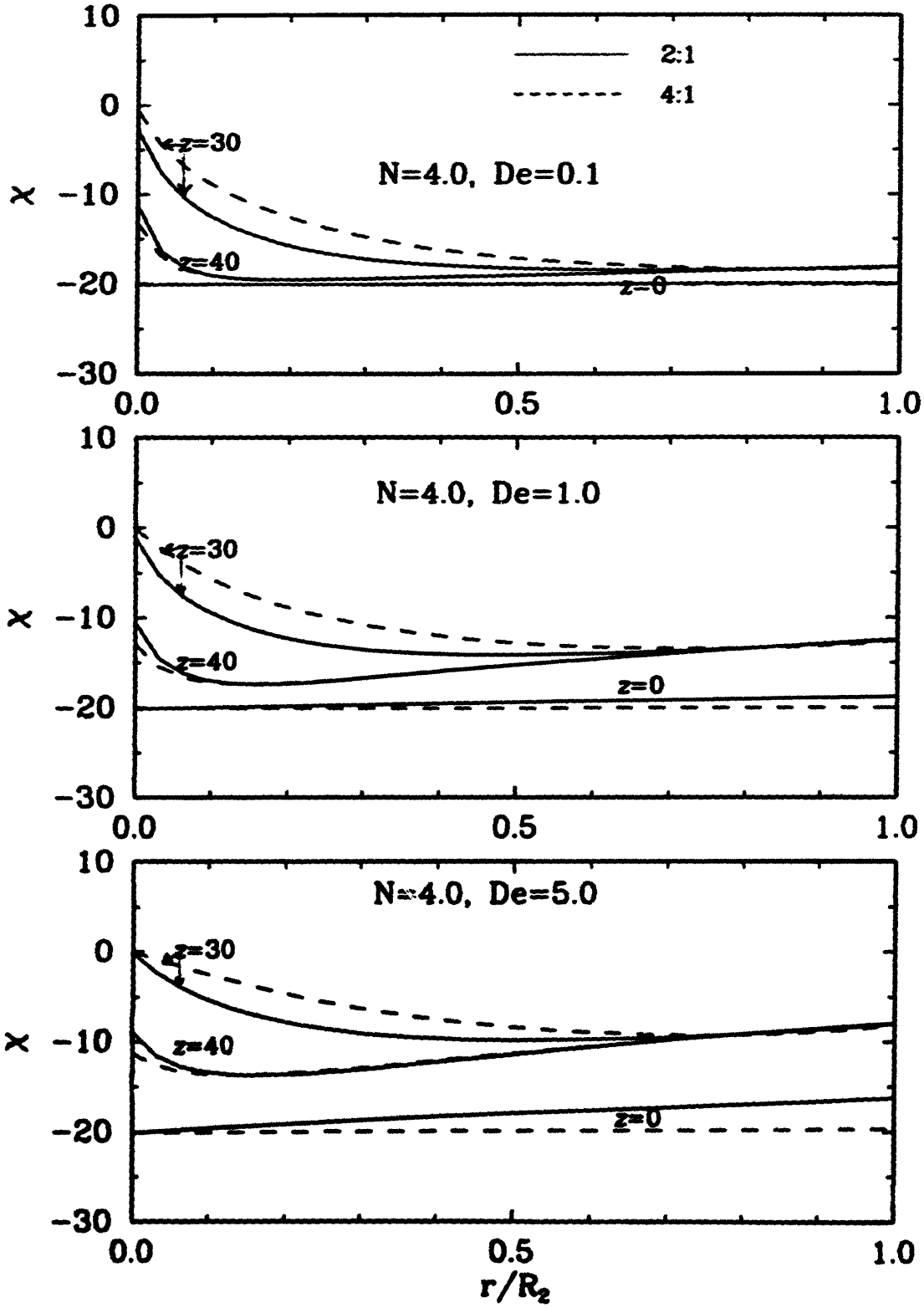

Figure 6.16c Effect of contraction ratio on the radial variation in χ at z=0, 30 and 40 for N=4.0, σ=1.0, β=1.6x10^{-5}, De=0.1, 1.0 and 5.0 and Λ=2 and 4. χ is in degrees.

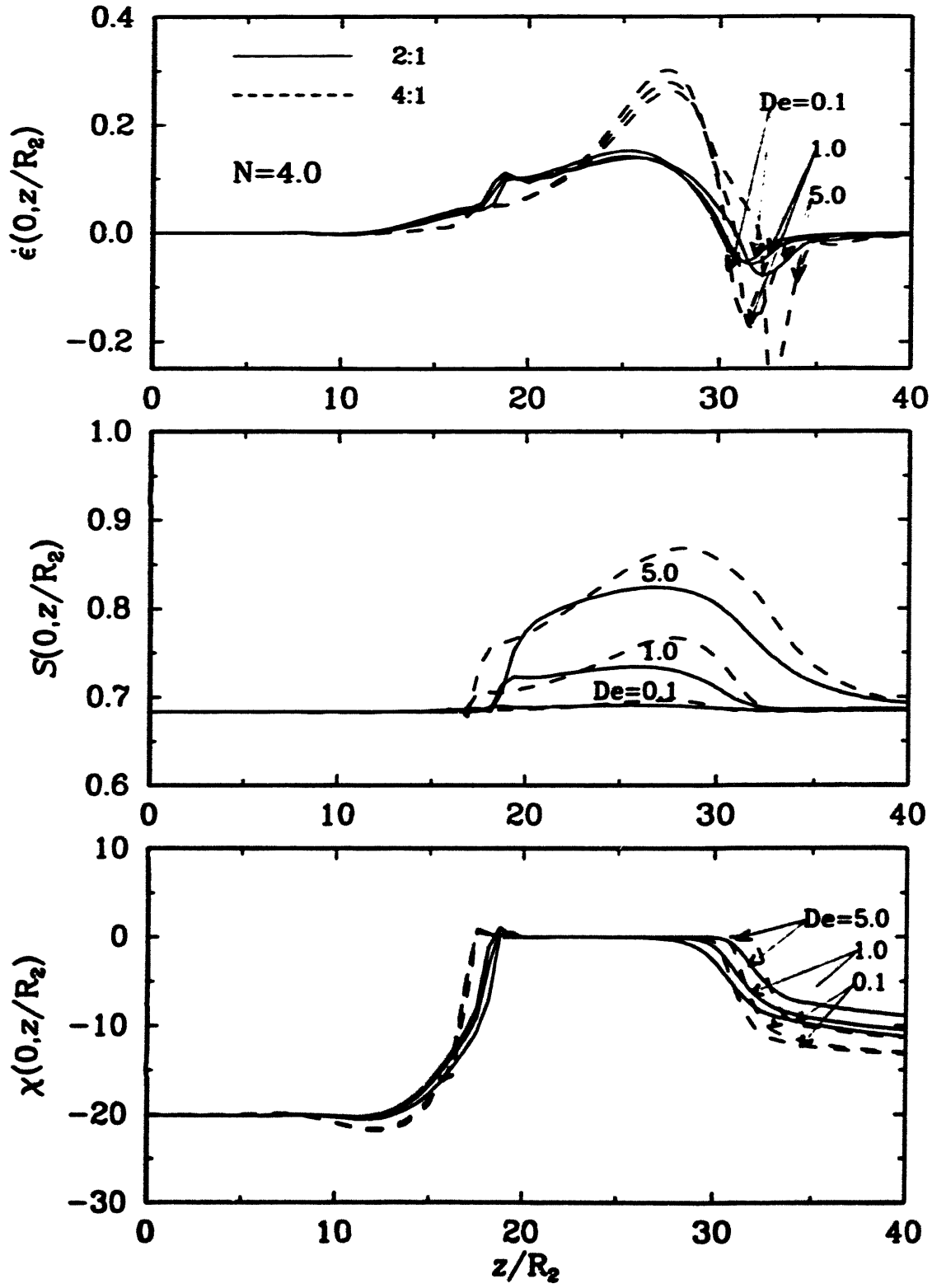

Figure 6.16 Effect of contraction ratio on the centerline variation in (d) $\dot{\epsilon}$, (e) S, and (f) χ for N=4.0, σ=1.0, β=1.6x10^{-5}, De=0.1, 1.0 and 5.0 and Λ=2 and 4.

profiles for the 2:1 and 4:1 contractions are Newtonian for De=0.1. The comparison with the Newtonian velocity profiles at De = 5.0 shows that shear thinning is more evident in the 2:1 contraction. The larger upstream tube radius and the consequent smaller shear rates explain the smaller degree of shear thinning in the 4:1 contraction.

Figure 6.16d shows that in the upstream portion of the contraction region, $\dot{\varepsilon}(0,z/R_2)$ in the 4:1 contraction does not increase as much as in the 2:1 contraction for all De. However, the local peak in $\dot{\varepsilon}(0,z/R_2)$ which coincides with the sharp increase in $S(0,z/R_2)$ is observed 1-2 downstream tube radii earlier in the 4:1 contraction as compared to the 2:1 contraction. Table 6.1 shows that the velocity overshoot is also significantly higher in the 4:1 contraction. In fact, since the velocity profiles at the downstream exit are the same because the downstream tube radius is the same, the higher velocity overshoot results exclusively from the higher maximum velocities. Fig. 6.16d also shows that the axial position of the maximum velocity in the 4:1 contraction for De = 5.0 is shifted downstream relative to its position in the 2:1 contraction by two downstream tube radii. The higher maximum velocities in the 4:1 contraction, in combination with the downstream shift in the maximum velocities, results in a stronger deceleration in the centerline velocity (negative $\dot{\varepsilon}(0,z/R_2)$) to the fully developed downstream value.

Effect of Λ on *S*; De=0.1, 1.0 and 5.0

The shear rates in the upstream tube are roughly smaller by a factor of four for the 4:1 contraction and consequently the order across the tube cross section is closer to the equilibrium value for De=0.1 (cf. Fig. 6.16b). Figures 6.15p and 6.16b also show that the higher shear rates in the 2:1 contraction lead to a higher degree of order for De = 1.0 and

5.0.

Figures 6.8p and 6.15p show that for De = 0.1 there is little difference in S in the upstream portion of the contraction; For De = 1.0 and 5.0, however, the degree of order is much better in the 2:1 contraction. The higher elongation rates and consequently higher extension along the centerline for any De in the downstream portion of the 4:1 contraction region (Fig. 6.16d) results in a higher value of $S(0,z/R_2)$ in this region of the 4:1 contraction (cf. Fig. 6.16e); in fact, the extension rates are higher not only at the centerline but also some distance away from the centerline as reflected in the higher degree of order in the 4:1 contraction at z = 30 in Fig. 6.16b. Figures 6.8p, 6.15p and 6.16b show, however, that there is no difference in the order near the wall for either contraction ratio in the downstream portion of the contraction region for any De. Since the order is dictated by the shear flow kinematics near the wall, it appears that there is little difference between the kinematics in the two contraction ratios in the downstream portion of the contraction region.

Figures 6.16e, 6.16b, 6.8p and 6.15p show that the order at and near the centerline in the initial portion of the downstream tube is higher in the 4:1 contraction due to the higher order created in downstream portion of the contraction region. The rapid decrease in the order, however, wipes out any differences in the order by the time the downstream exit is reached. Figure 6.16b shows that there is no difference in the order at the downstream exit for any De.

Effect of A on χ; De=0.1, 1.0 and 5.0

For De=0.1, the shear rates in the upstream tube are small for both contraction ratios and consequently the director orientation is close to the zero-shear-rate limit (cf. Figs. 6.8q and 6.15q); as with the degree of order, the director orientation with the z-axis is slightly better in the 2:1 contraction (Fig. 6.16c). For De = 1.0 and 5.0, however, the higher shear rates away from the centerline in the 2:1 contraction result in smaller negative values in χ.

In the upstream portion of the contraction region, near the wall, χ is more negative than the zero-shear-limit at De = 0.1 for either contraction ratio (Figs. 6.8q and 6.15q). The greater wall slope, however, results in more negative values of χ in the 4:1 contraction as compared to the 2:1 contraction. When De = 5.0, the higher shear rates in the 2:1 contraction lead to a director orientation that is better than the zero-shear-rate limit, whereas, the orientation remains worse than the zero-shear-rate limit in the 4:1 contraction. A more severe "dip" or loss of orientation is also observed along the centerline in the upstream portion of the 4:1 contraction region (Fig. 6.16f). However, responding to the sharp increase in $\dot{\varepsilon}(0,z/R_2)$, the director in the 4:1 contraction becomes aligned with the z-axis earlier by one downstream tube radius. Once $\chi(0,z/R_2)$ becomes zero there is no change in $\chi(0,z/R_2)$ with any increase in $\dot{\varepsilon}(0,z/R_2)$ for either contraction ratio. Paralleling the downstream shift in the axial location of $\dot{\varepsilon}(0,z/R_2)=0$ in the 4:1 contraction as compared to the 2:1 contraction, the axial location at the onset of decrease in $\chi(0,z/R_2)$ below zero is also shifted downstream by 1-2 downstream tube radii in the 4:1 contraction as compared to the 2:1 contraction. In fact, the downstream shift and the consequent better alignment in the director with the z-axis for a longer axial distance is

apparent not only along the centerline but also away from the centerline for any De in the 4:1 contraction as demonstrated by Fig. 6.16c at $z = 30$.

The stronger deceleration at and near the centerline in the downstream tube of the 4:1 contraction as compared to the 2:1 contraction results in a director orientation that is closer to the zero-shear-rate limit at the downstream exit in the 4:1 contraction for any De (cf. Fig. 6.16c and 6.16f); the difference in $\chi(0,40)$ between the contraction ratios is about 1-2 degrees. Away from the centerline there is no difference in χ between the contraction ratios at the downstream exit. This is not surprising since χ is dictated by the shear flow kinematics, which is identical for the two contraction ratios at the downstream exit.

In addition to the beneficial effects of high De and a very short downstream length from a processing standpoint, as discussed in section 6.2.1.3, a high contraction ratio is also advantageous in creating a higher degree of order near the centerline. The higher order near the centerline also makes the order more homogenous across the cross-section. The director alignment with the spinneret axis is also distinctively better near the centerline in the 4:1 contraction. Note the additional advantage associated with a smaller pressure drop per unit flow rate in the 4:1 contraction.

6.2.4 Effect of Change in Geometry; Conical Contraction with Rounded Corners

In this section the LCP flow through a conical 4:1 contraction shown in Fig. 5.1b is studied. An overlay of the 4:1 cubic and conical contraction geometries used in this study is shown in Fig. 6.17 to illustrate the quantitative difference in the shape of the contraction region. The aim is to examine the effect of the change in the design of the contraction region on the flow field, structure and stress fields.

For the conical contraction geometry shown in Fig. 5.1b, it can be found from Eqs. 5.16 and 5.17 that $(x_1-x_0)/\Re = \sin\theta < 0.2$ up to $\Re=25$ as shown in Fig. 6.18. Thus, only a few terms in the binomial/perturbation expansion given by Eq. 5.19 are necessary to represent the rounded corners. The maximum deviation in the approximation is expected for the value of x farthest from x_0; x_1 and x_2 in this problem. In Fig. 6.19, the absolute magnitudes of the difference y_1-y_{exact} and the derivative of the difference $y_1'-y_{exact}'$ are shown for second and fourth order polynomial approximations for a wide range of $\Re$. The fourth order polynomial is more than sufficient to approximate the rounded corners for this range of $\Re$. As a test, we choose $\Re=10$. All calculations are for $N=4.0$ and $\sigma=1.0$.

The presence of spikes in the pressure field at the junction of the plane of contraction and the polynomial approximation to the rounded reentrant corner in the flow through an abrupt contraction is an issue when a slip boundary condition is used along the walls of the contraction boundary (Nayak, 1993). The spikes are not observed with a no-slip boundary condition. The spikes possibly result from a lack of continuity in the slopes of the plane of contraction and the polynomial approximation to the rounded corner

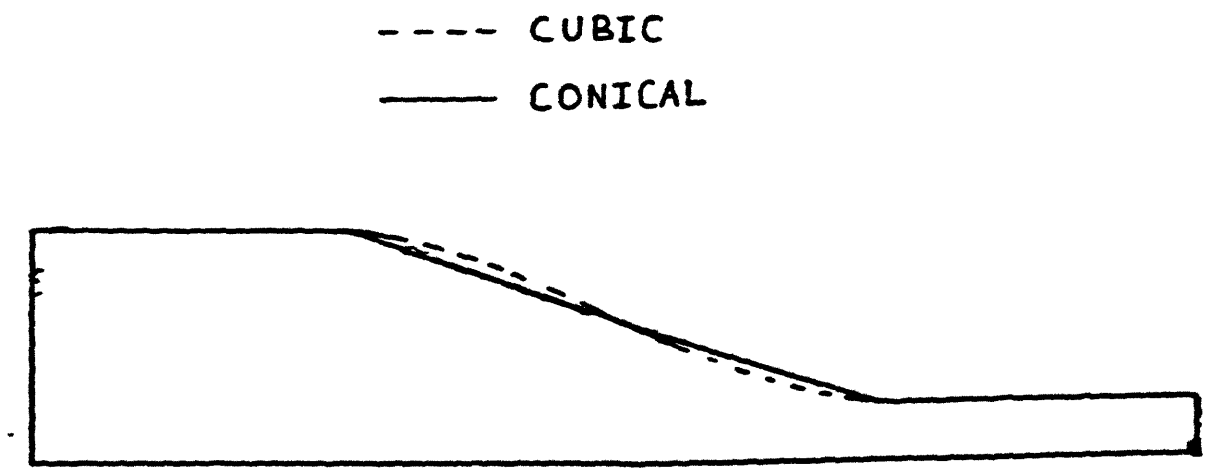

Figure 6.17 Geometric difference between the 4:1 cubic and conical contractions.

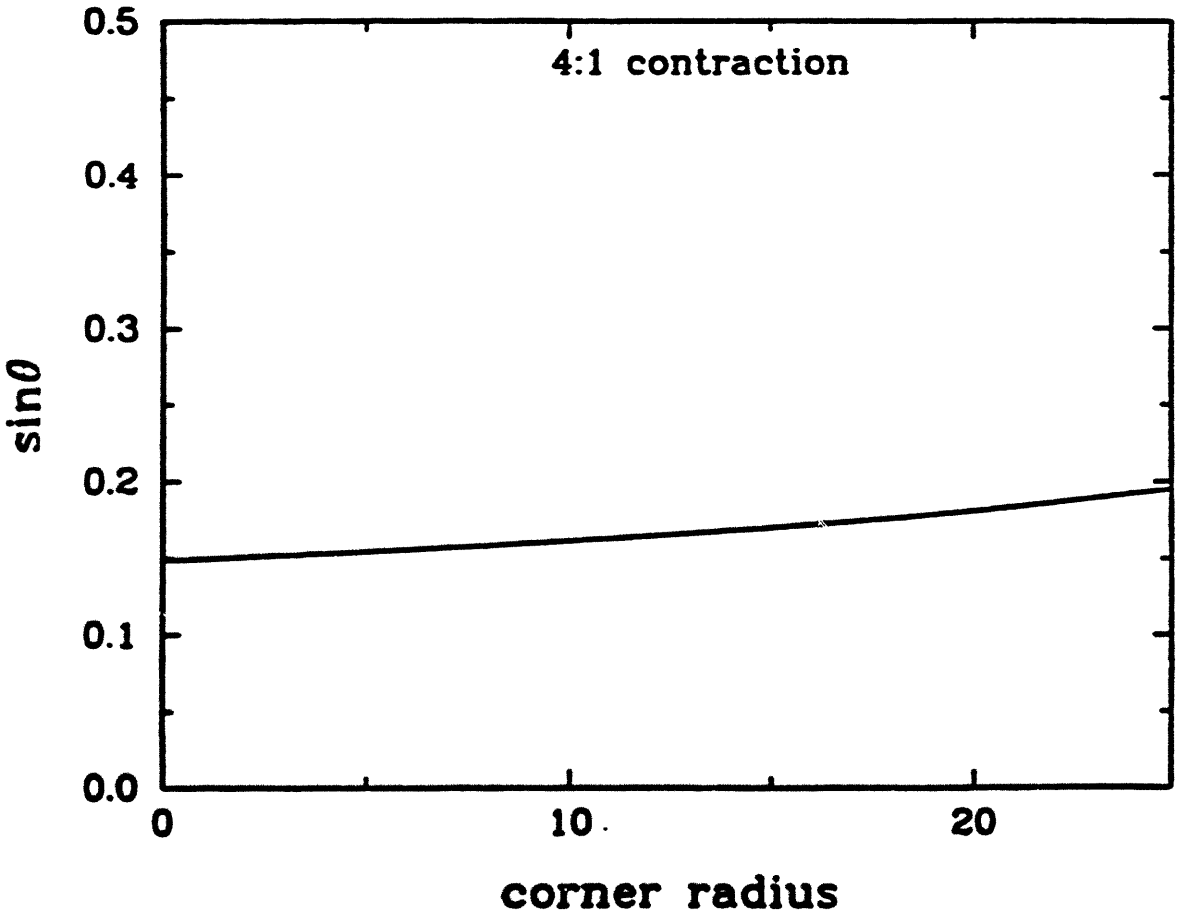

Figure 6.18 Effect of $\Re$ on the perturbation parameter $(x-x_0)/\Re = \sin\theta$.

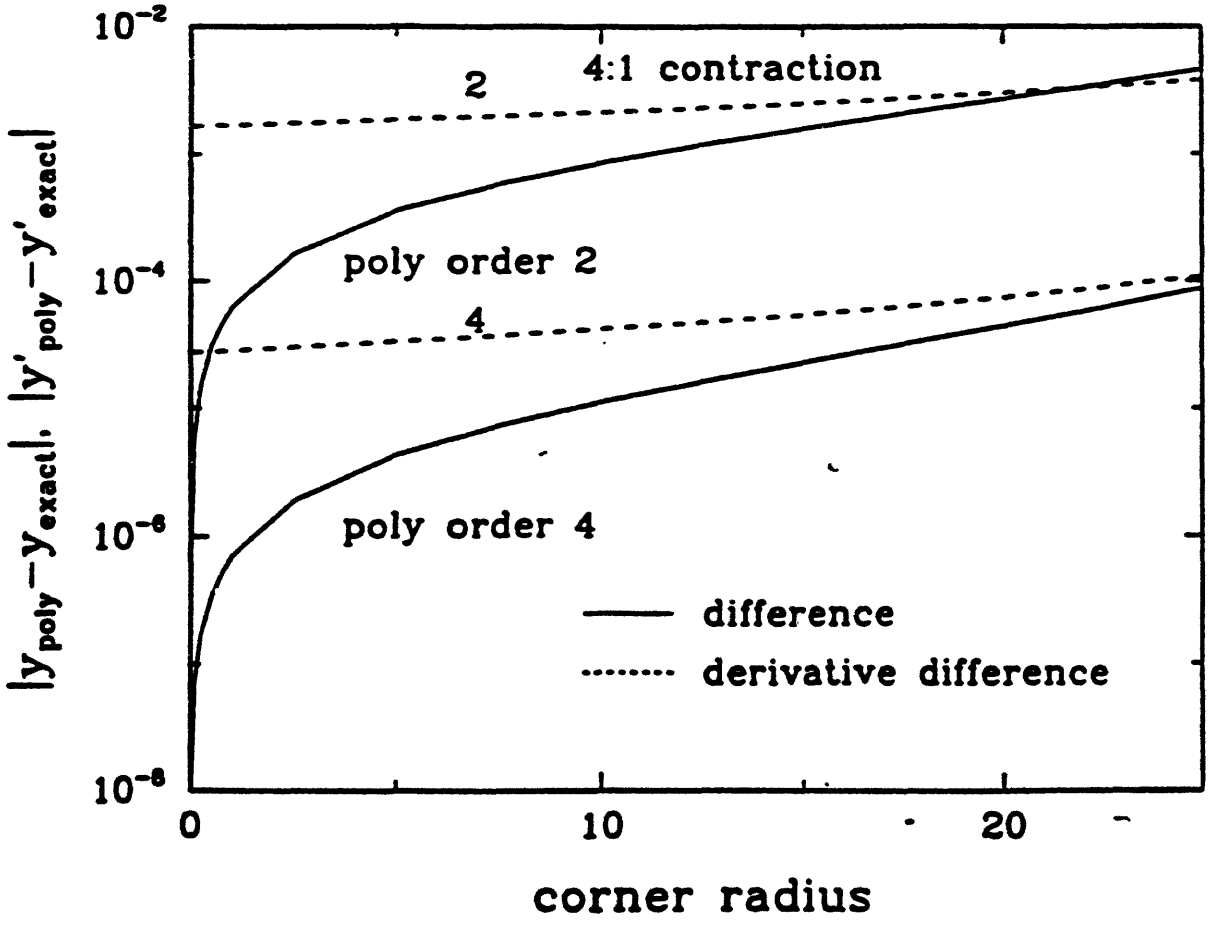

Figure 6.19 Effect of $\mathfrak{R}$ and the number of terms in the perturbation expansion on the accuracy of y_1-y_{exact} and y_1'-y_{exact}'.

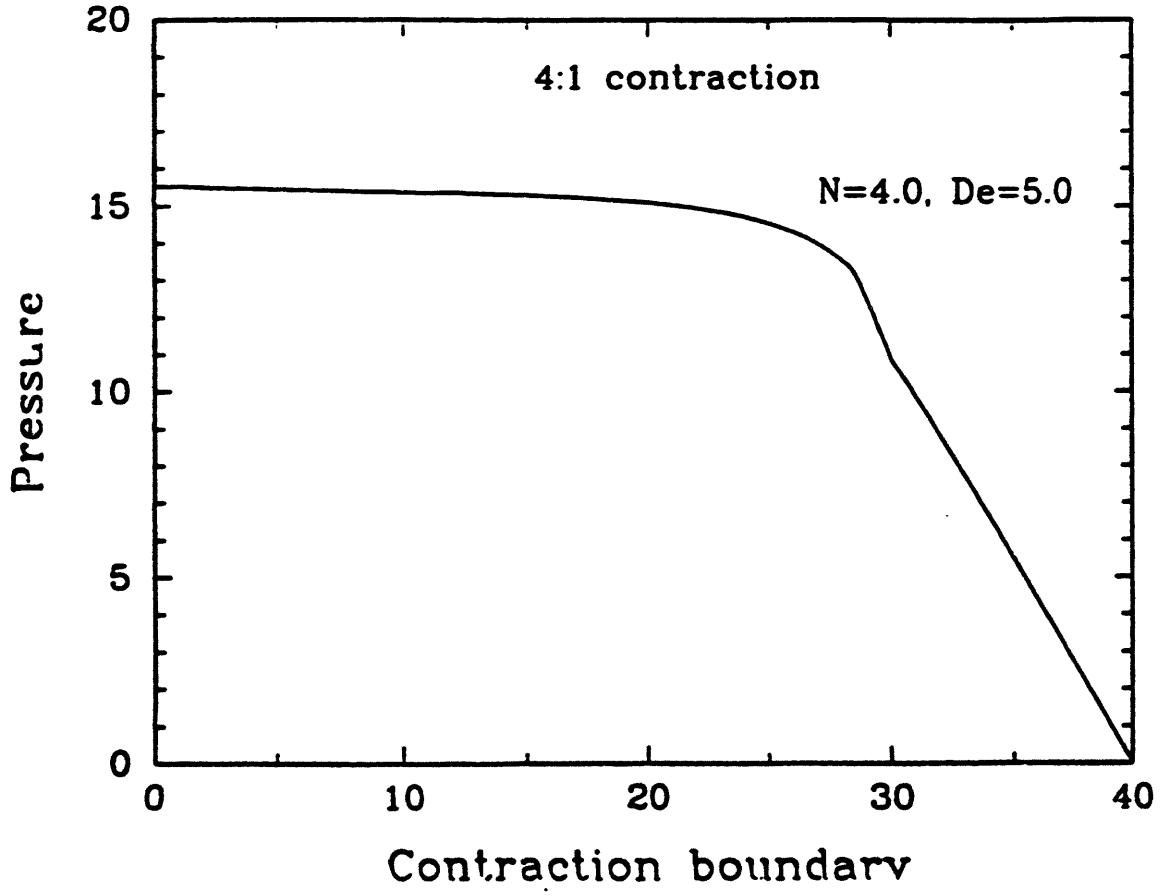

Figure 6.20 Variation in the pressure field along the 4:1 conical contraction boundary with axial distance for N=4.0, σ=1.0, β=1.6x10^{-5}, De=5.0, $\Re$=10 and Λ=4.

or due to an improper choice of the order for the polynomial interpolant to the slip boundary condition (Nayak, 1993). The pressure field along the wall for the conical contraction determined using the perturbation approximation to the rounded corners outlined in equation 5.19 and a no-slip boundary condition does not show these spikes. This is illustrated in Fig. 6.20 for De = 5.0.

The solution to the flow problem through the 4:1 cubic contraction on a mesh with the same number of elements in the r and z directions as used for the 4:1 conical contraction was used as a starting guess to obtain a convergent solution for the 4:1 conical contraction geometry at low De (De=0.1). First order continuation in De was then employed to obtain convergent solution fields at higher values of De.

Contour plots of pressure, flow field, structure, stress fields and streamlines for De=0.1, 1.0 and 5.0 are shown in Figs. 6.21a-o. Contour plots for S and χ are shown in Figs. 6.21p-q. A comparison with the contour plots for the 4:1 cubic contraction in Figs. 6.15a-q shows that qualitatively there is not much difference. The overall pressure drop is higher for the 4:1 cubic contraction since the radius of curvature is higher at the downstream corner and consequently the downstream tube length apparent to the flow is longer. A comparison of the axial velocity, degree of order and molecular orientation, as the flow progresses through the contraction, is shown in Figs. 6.22a-c. $S(0,z/R_2)$ and $\chi(0,z/R_2)$ predicted for the two different contraction geometries and their responses to $\dot{\varepsilon}(0,z/R_2)$ are compared in Figs. 6.22d-f.

De=0.1

De=1.0

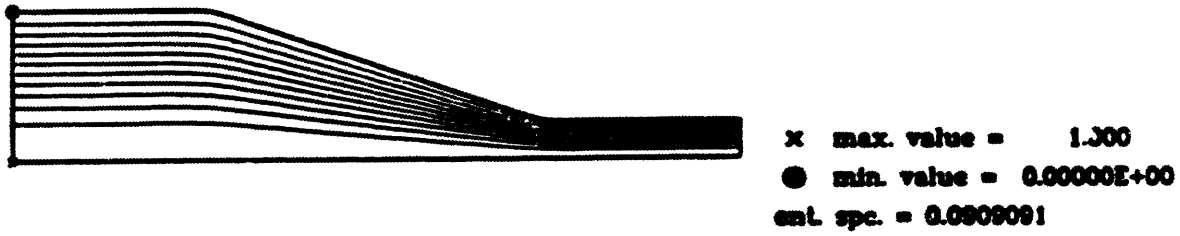

De=5.0

Figure 6.21a Contour plots of streamlines in the flow through a 4:1 conical contraction with rounded corners for N=4.0, σ=1.0, β=1.6x10^{-5} and De=0.1, 1.0 and 5.0.

De=0.1

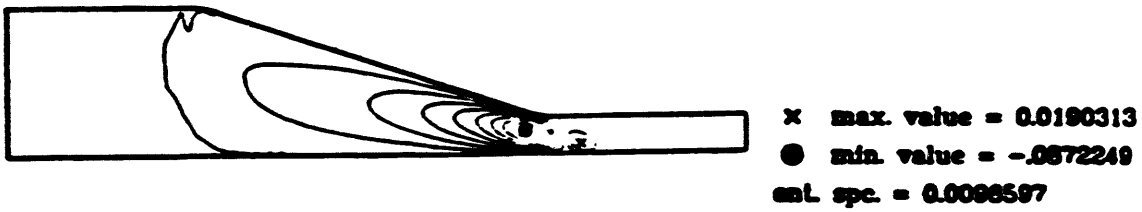

De=1.0

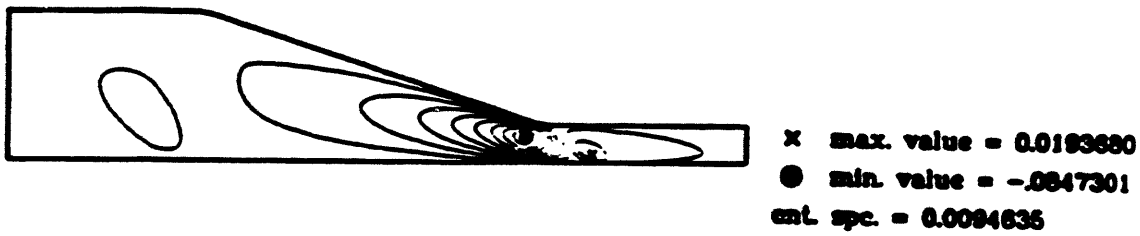

De=5.0

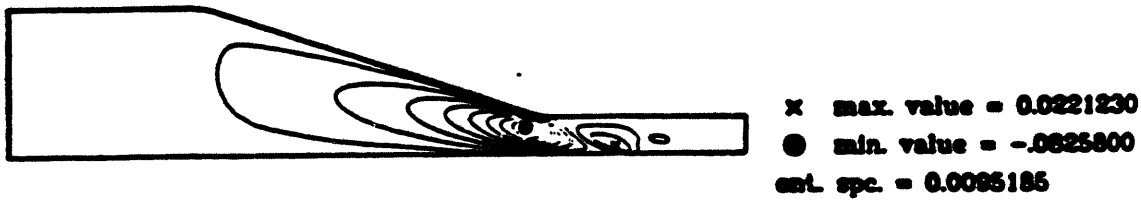

Figure 6.21b Contour plots of radial velocity in the flow through a 4:1 conical contraction with rounded corners for N=4.0, $\overline{\sigma}$=1.0, β=1.6x10^{-5} and De=0.1, 1.0 and 5.0.

De=0.1

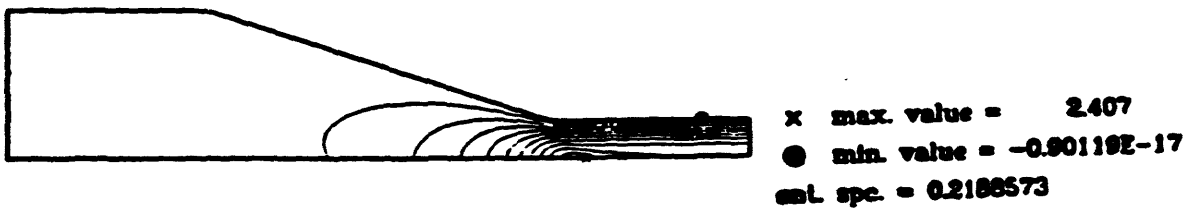

De=1.0

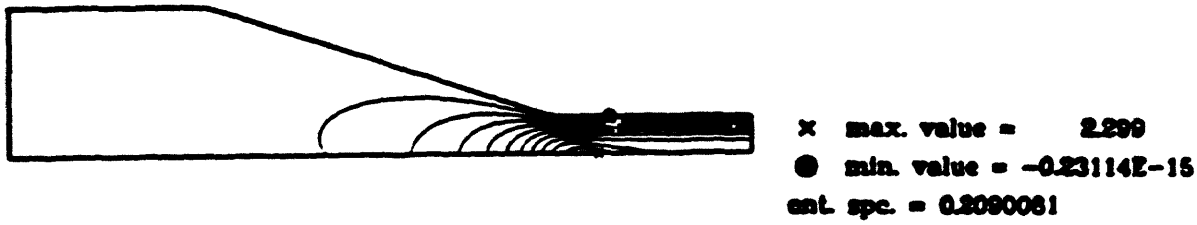

De=5.0

Figure 6.21c Contour plots of axial velocity in the flow through a 4:1 conical contraction with rounded corners for N=4.0, σ=1.0, β=1.6x10^{-5} and De=0.1, 1.0 and 5.0.

De=0.1

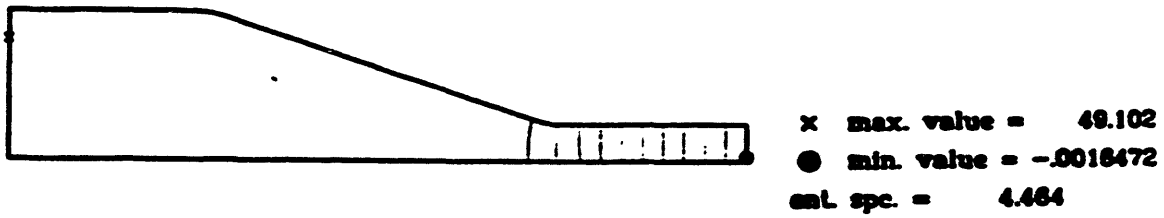

De=1.0

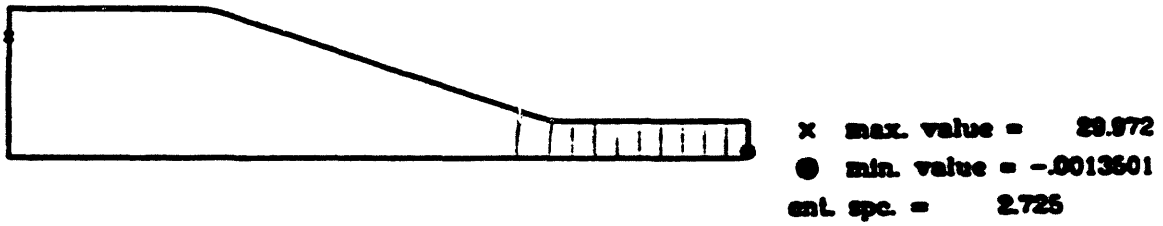

De=5.0

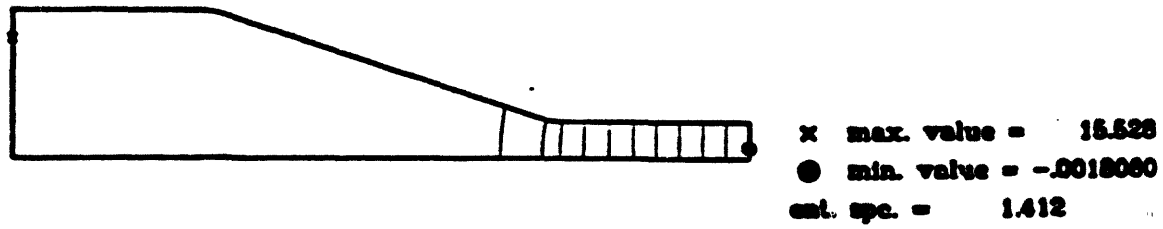

Figure 6.21d Contour plots of pressure in the flow through a 4:1 conical contraction with rounded corners for N=4.0, σ=1.0, β=1.6x10^{-5} and De=0.1, 1.0 and 5.0.

De=0.1

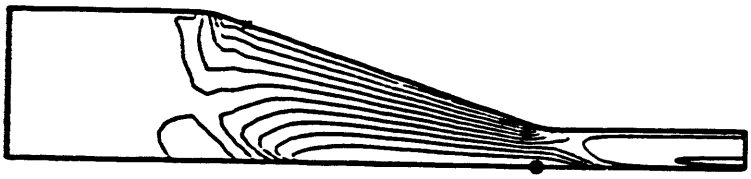

De=1.0

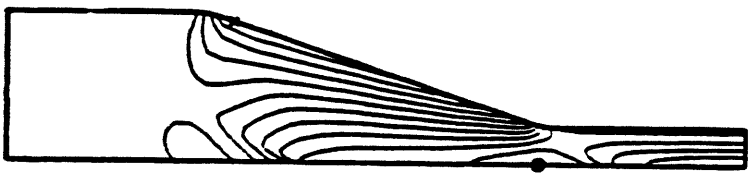

De=5.0

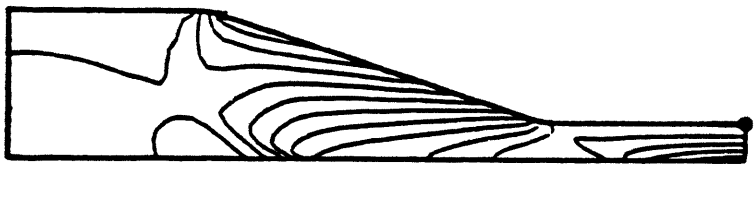

Figure 6.21e Contour plots of S_{rr} in the flow through a 4:1 conical contraction with rounded corners for N=4.0, σ=1.0, β=1.6x10^{-5} and De=0.1, 1.0 and 5.0.

De=0.1

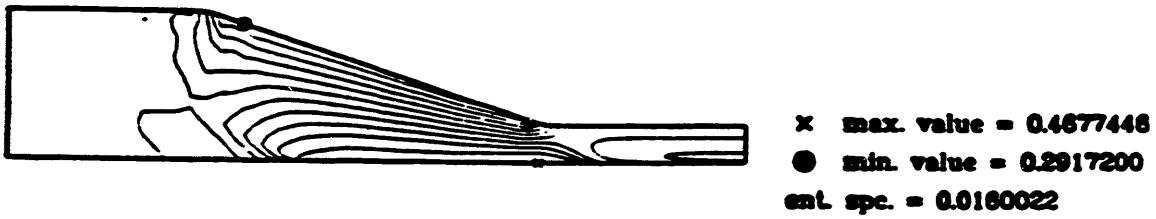

De=1.0

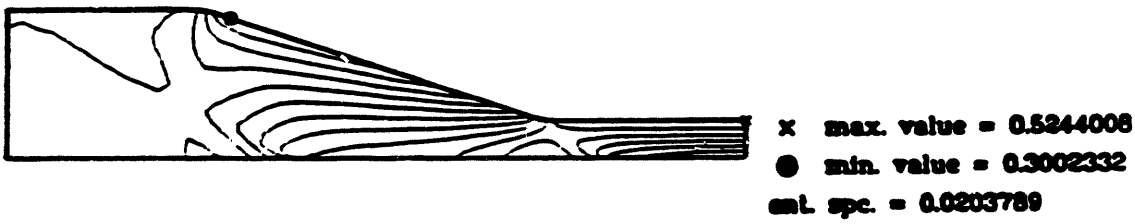

De=5.0

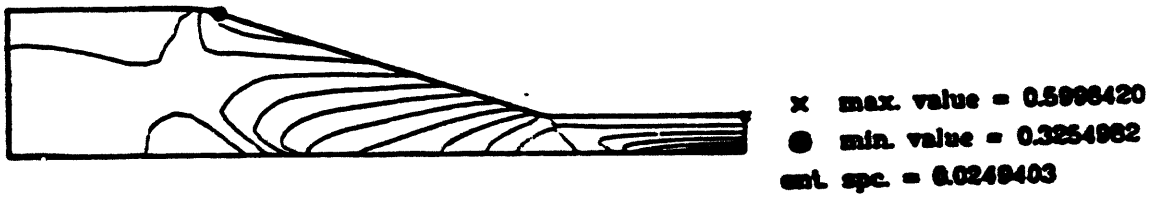

Figure 6.21f Contour plots of S_{zz} in the flow through a 4:1 conical contraction with rounded corners for N=4.0, σ=1.0, β=1.6x10^{-5} and De=0.1, 1.0 and 5.0.

De=0.1

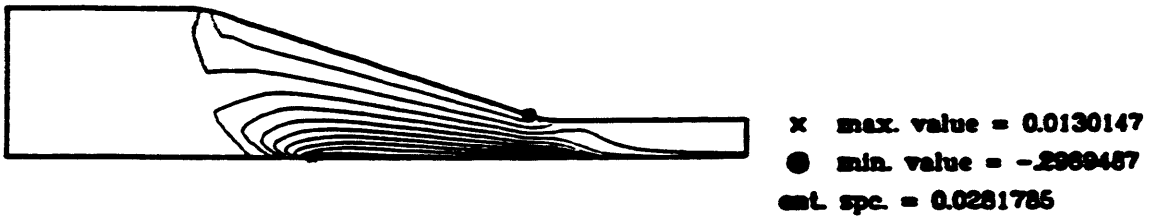

De=1.0

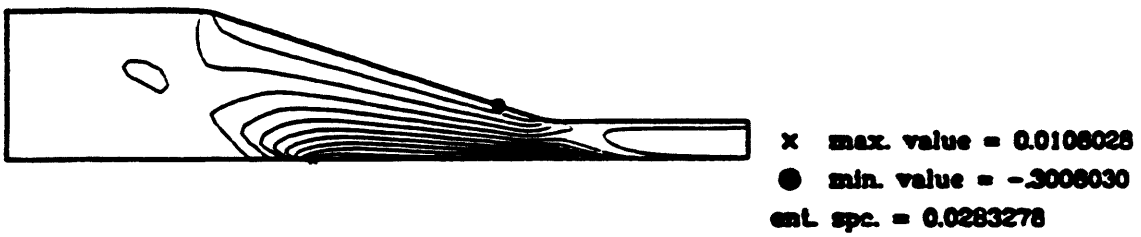

De=5.0

Figure 6.21g Contour plots of S_{rz} in the flow through a 4:1 conical contraction with rounded corners for N=4.0, σ=1.0, β=1.6x10^{-5} and De=0.1, 1.0 and 5.0.

De=0.1

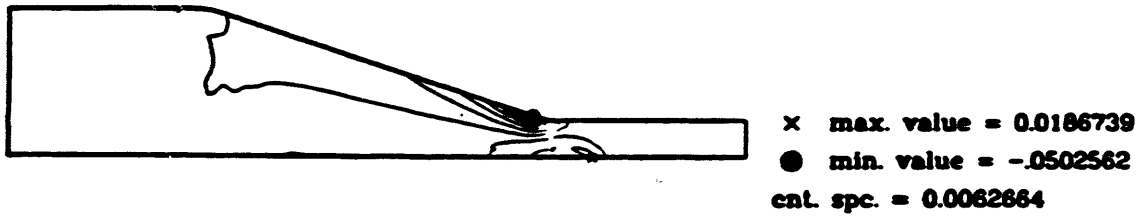

De=1.0

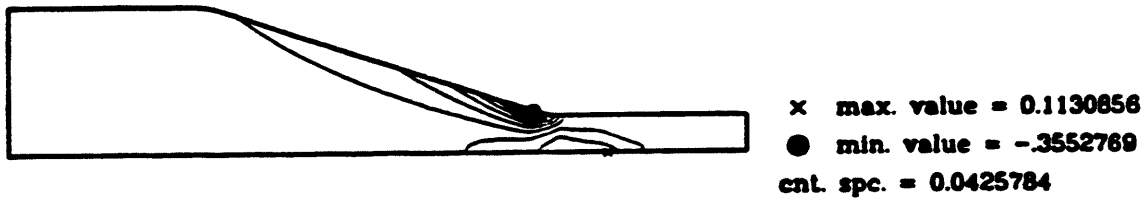

De=5.0

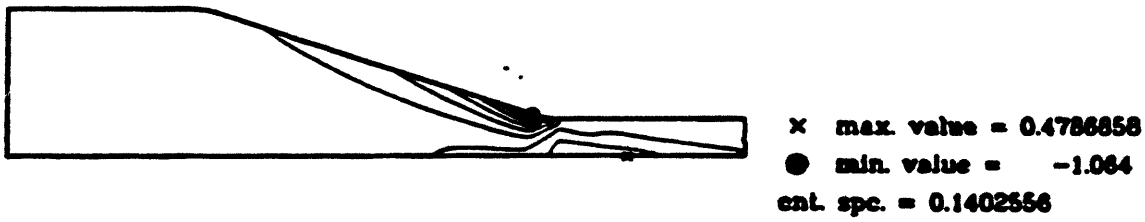

Figure 6.21h Contour plots of $De\tau_{rr}$ in the flow through a 4:1 conical contraction with rounded corners for N=4.0, σ=1.0, β=1.6x10^{-5} and De=0.1, 1.0 and 5.0.

De=0.1

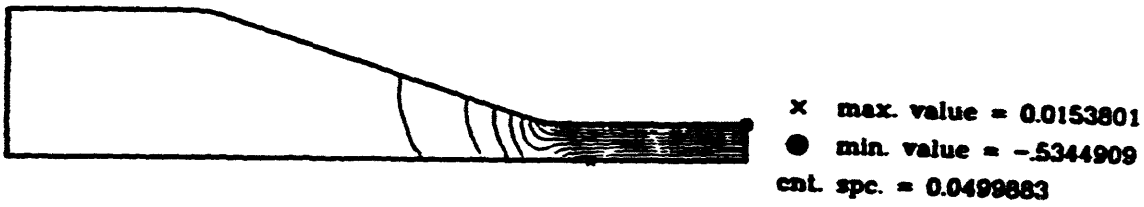

De=1.0

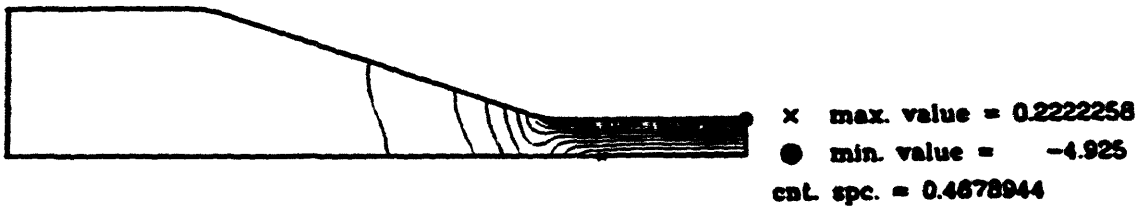

De=5.0

Figure 6.21i Contour plots of $De\tau_{zz}$ in the flow through a 4:1 conical contraction with rounded corners for N=4.0, σ=1.0, β=1.6x10^{-5} and De=0.1, 1.0 and 5.0.

De=0.1

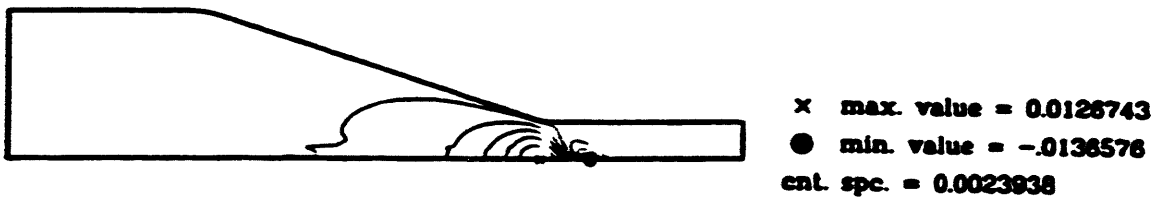

De=1.0

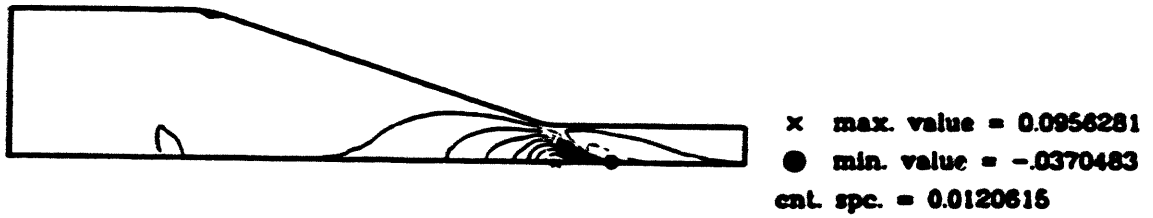

De=5.0

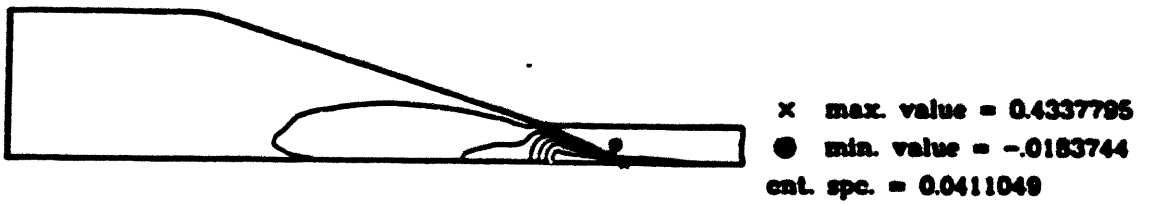

Figure 6.21j Contour plots of $De\tau_{\theta\theta}$ in the flow through a 4:1 conical contraction with rounded corners for N=4.0, σ=1.0, β=1.6x10^{-5} and De=0.1, 1.0 and 5.0.

De=0.1

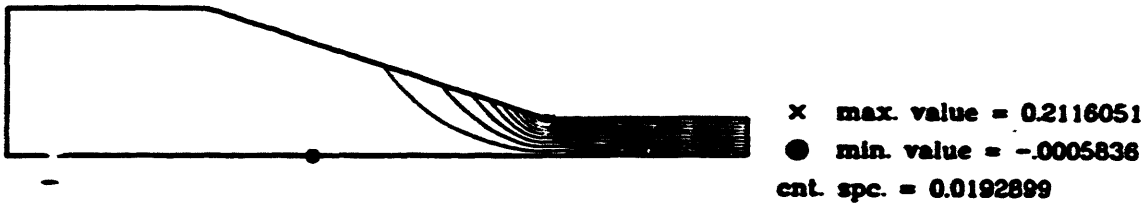

De=1.0

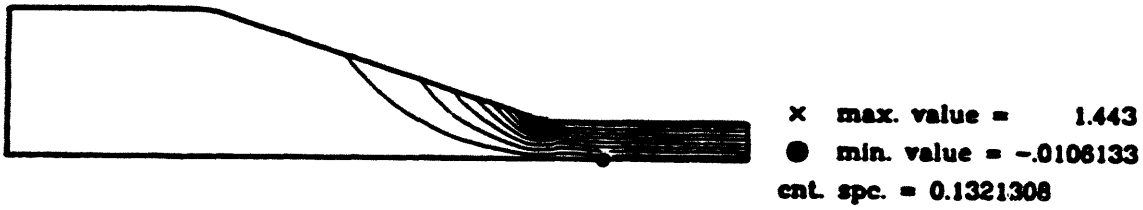

De=5.0

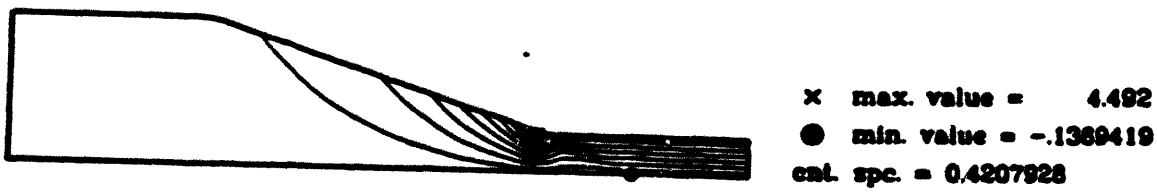

Figure 6.21k Contour plots of Det_{rz} in the flow through a 4:1 conical contraction with rounded corners for N=4.0, α=1.0, β=1.6x10^{-5} and De=0.1, 1.0 and 5.0.

De=0.1

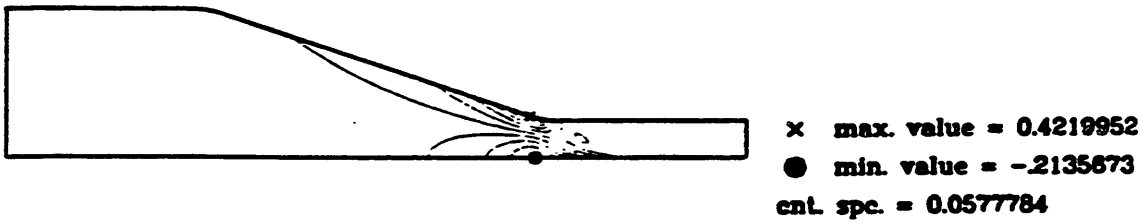

De=1.0

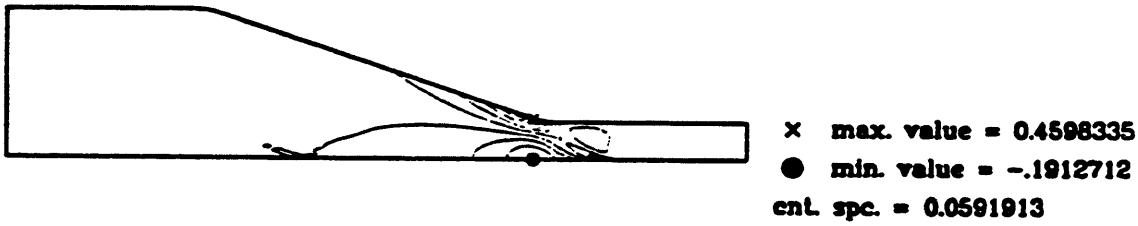

De=5.0

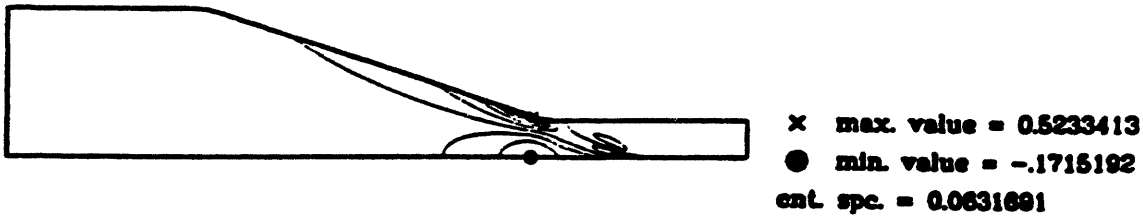

Figure 6.211 Contour plots of G_{rr} in the flow through a 4:1 conical contraction with rounded corners for N=4.0, σ=1.0, β=1.6x10^{-5} and De=0.1, 1.0 and 5.0.

De=0.1

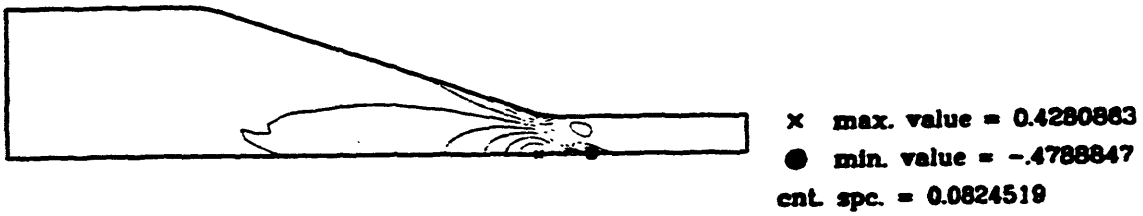

De=1.0

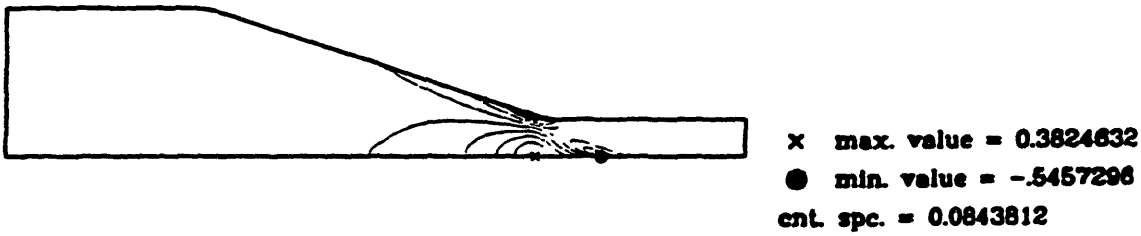

De=5.0

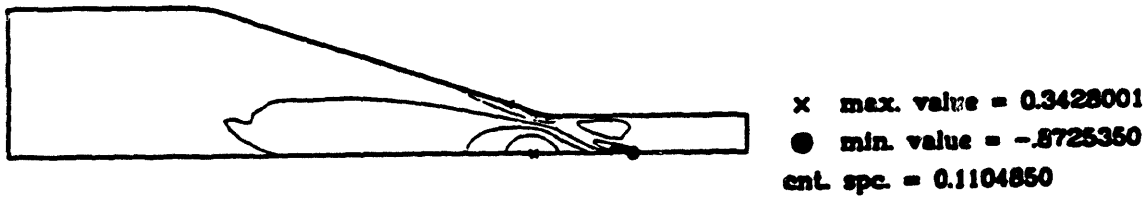

Figure 6.21m Contour plots of G_{zz} in the flow through a 4:1 conical contraction with rounded corners for N=4.0, σ=1.0, β=1.6x10^{-5} and De=0.1, 1.0 and 5.0.

De=0.1

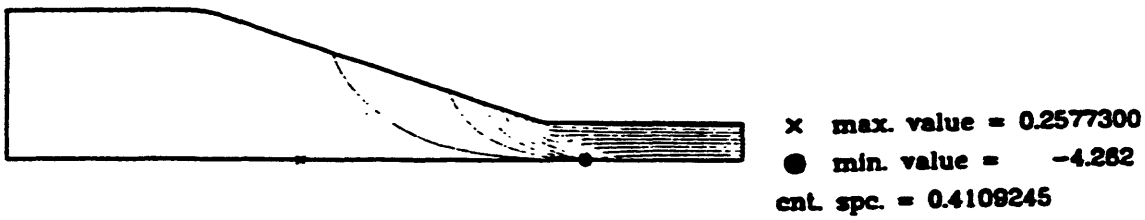

De=1.0

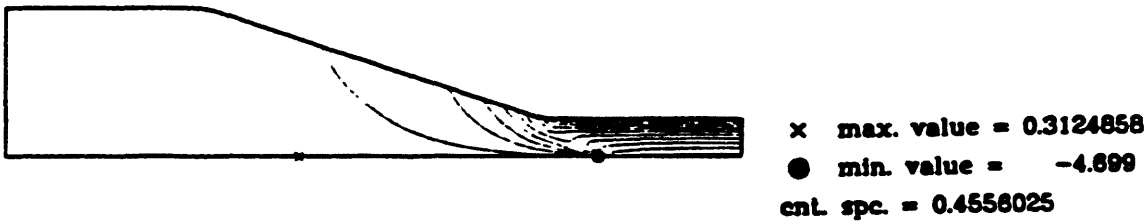

De=5.0

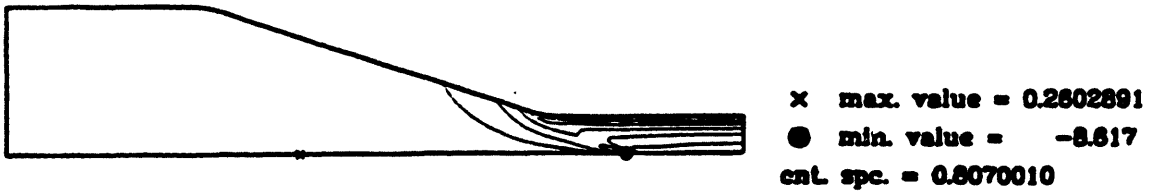

Figure 6.21n Contour plots of G_{rz} in the flow through a 4:1 conical contraction with rounded corners for N=4.0, σ=1.0, β=1.6x10^{-5} and De=0.1, 1.0 and 5.0.

De=0.1

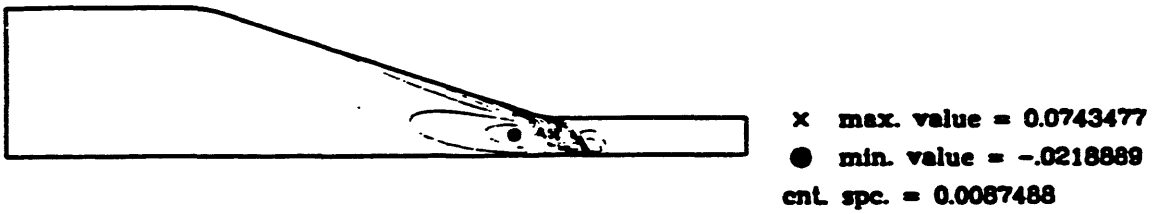

De=1.0

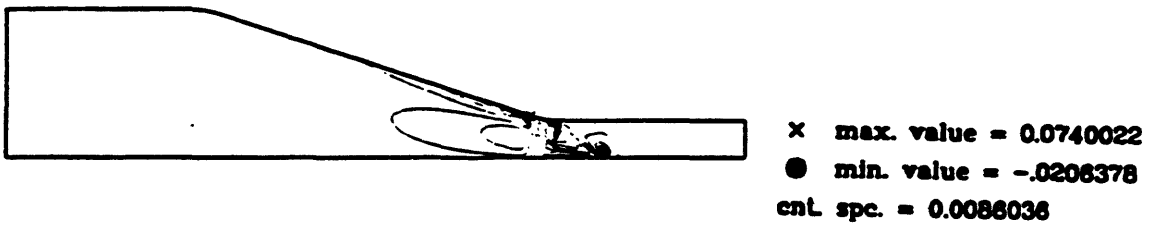

De=5.0

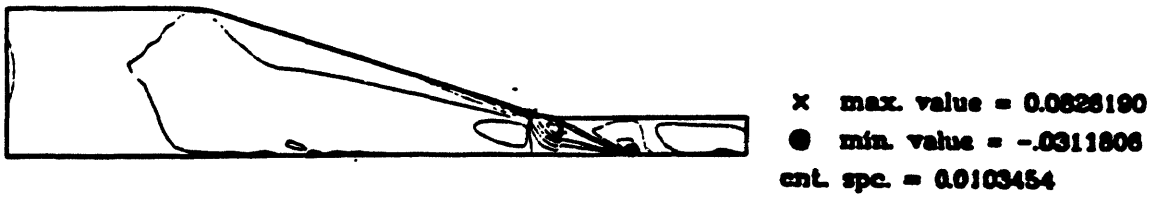

Figure 6.21o Contour plots of G_{zr} in the flow through a 4:1 conical contraction with rounded corners for N=4.0, σ=1.0, β=1.6x10^{-5} and De=0.1, 1.0 and 5.0.

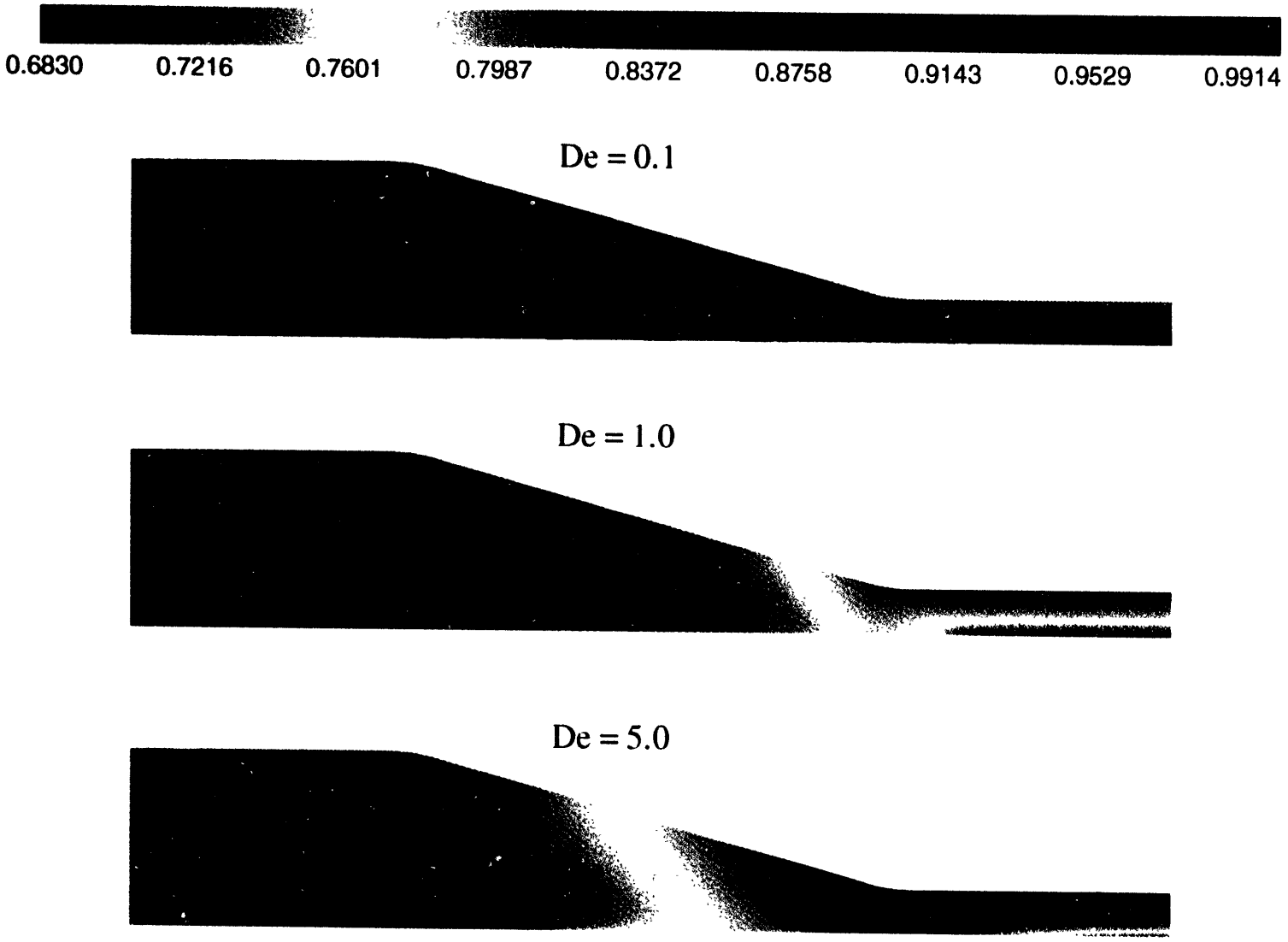

Figure 6.21p: Effect of De on S in a 4:1 rounded corner contraction for N =4.0, σ=1.0, β=1.6x10^{-5} and De=0.1, 1.0 and 5.0. S =0.683 is the equilibrium value for N =4.0 and S =1.0 corresponds to perfect order.

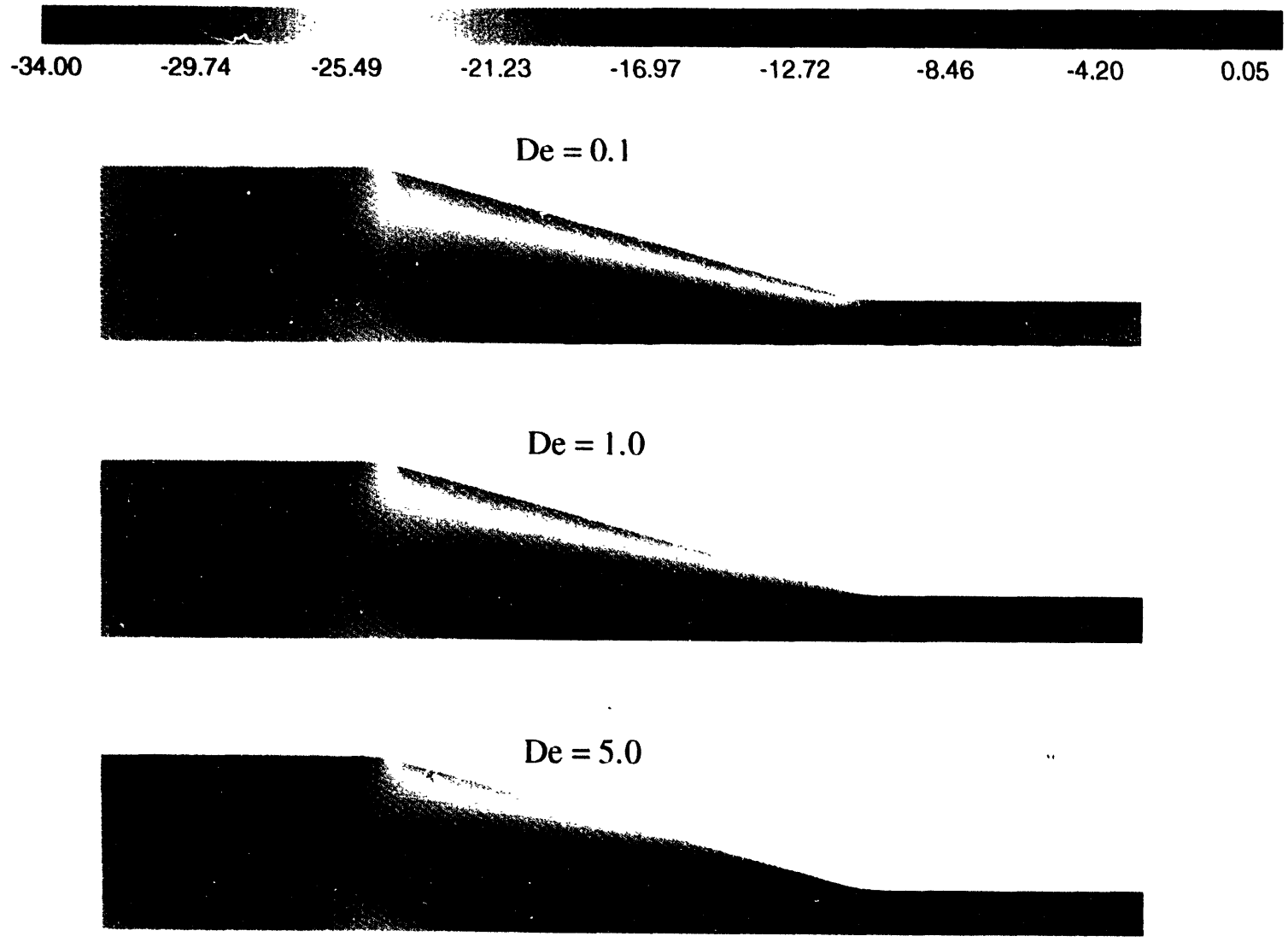

Figure 6.21q: Effect of De on χ in a 4:1 rounded corner contraction for N =4.0, σ=1.0, β=1.6x10^{-5} and De=0.1, 1.0 and 5.0. χ=-20.1 degrees is the zero-shear-rate limit. For χ=0, the director is aligned with the die axis.

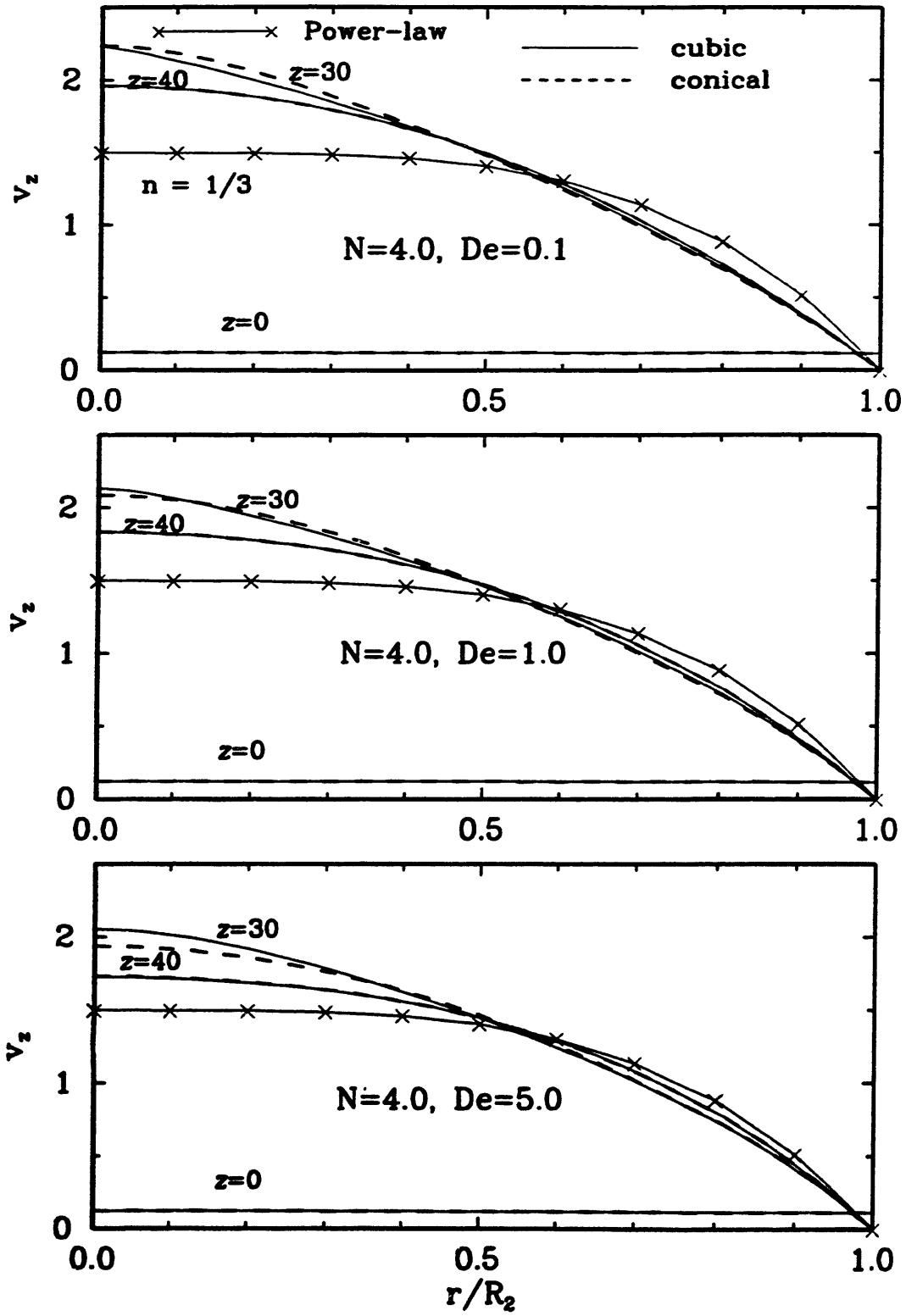

Figure 6.22a Effect of contraction geometry on the axial velocity profiles at z=0, 30 and 40 for N=4.0, σ=1.0, β=1.6x10^{-5}, De=0.1, 1.0 and 5.0 and Λ=4. The fully developed downstream exit velocity profile for a power-law model with the same shear thinning behavior as the viscosity for the liquid-crystal model is shown for comparison.

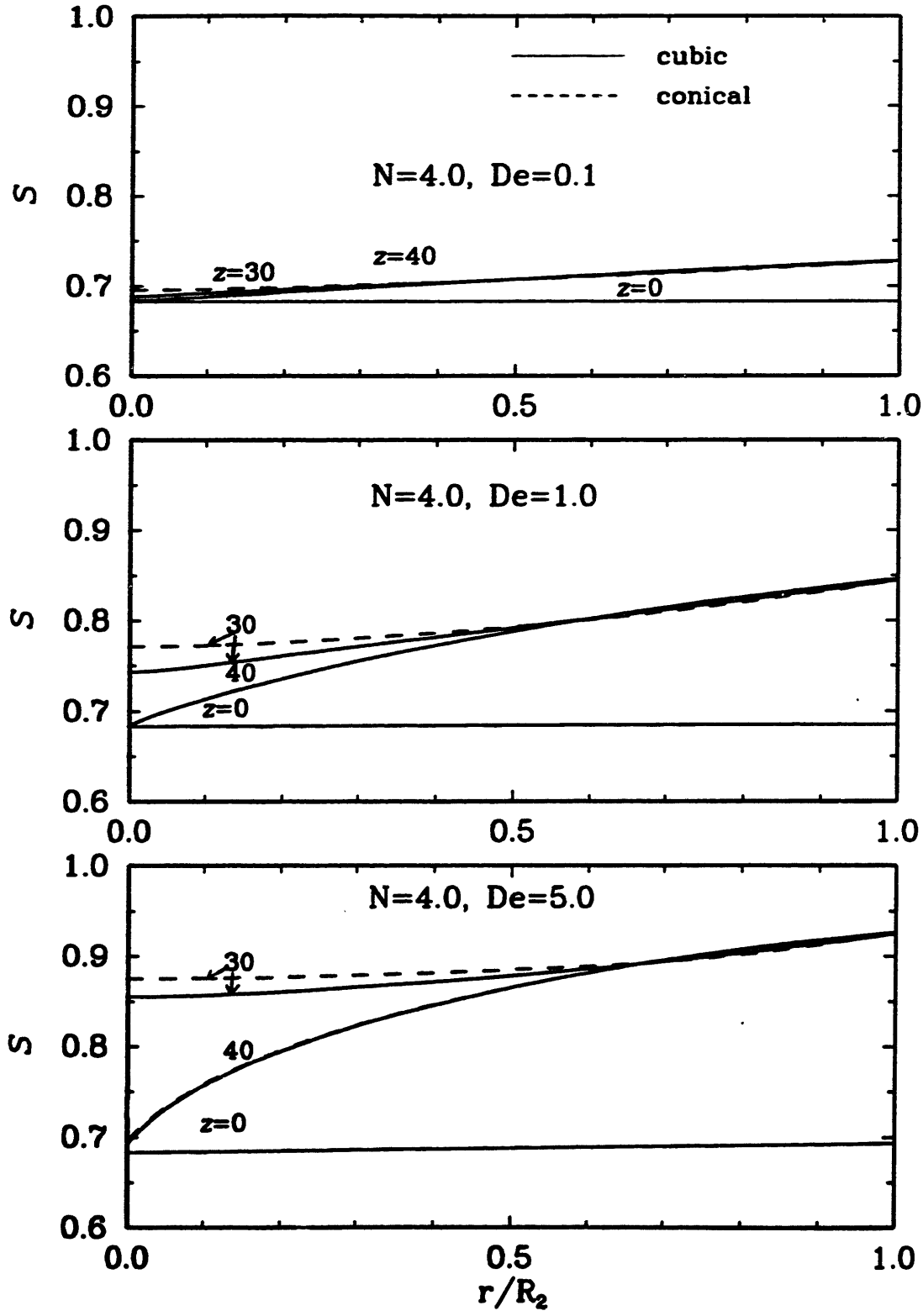

Figure 6.22b Effect of contraction geometry on the degree of order profiles at z=0, 30 and 40 for N=4.0, σ=1.0, β=1.6x10^{-5}, De=0.1, 1.0 and 5.0 and Λ=4.

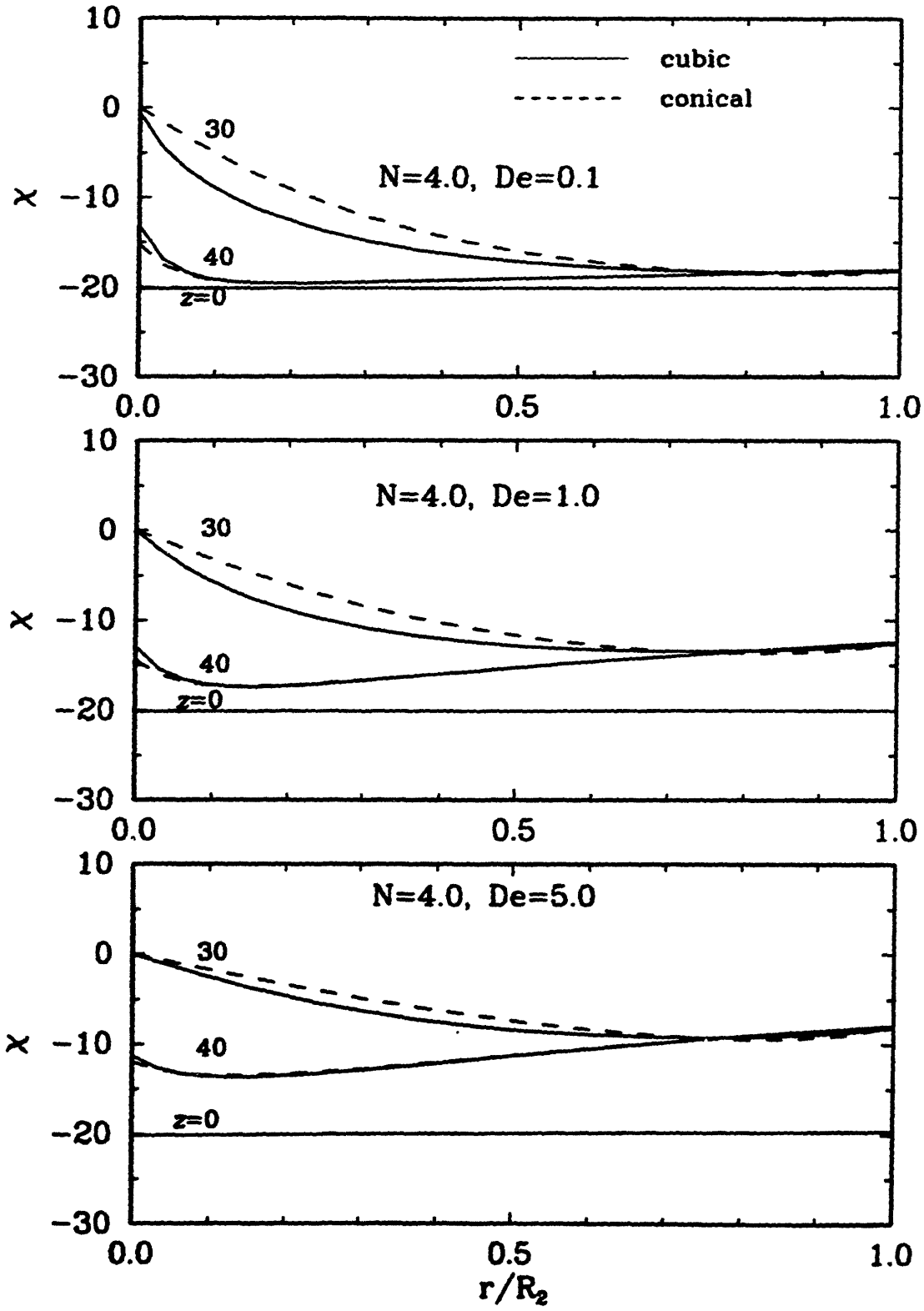

Figure 6.22c Effect of contraction geometry on the director orientation profiles at z=0, 30 and 40 for N=4.0, σ=1.0, β=1.6x10^{-5}, De=0.1, 1.0 and 5.0 and Λ=4.

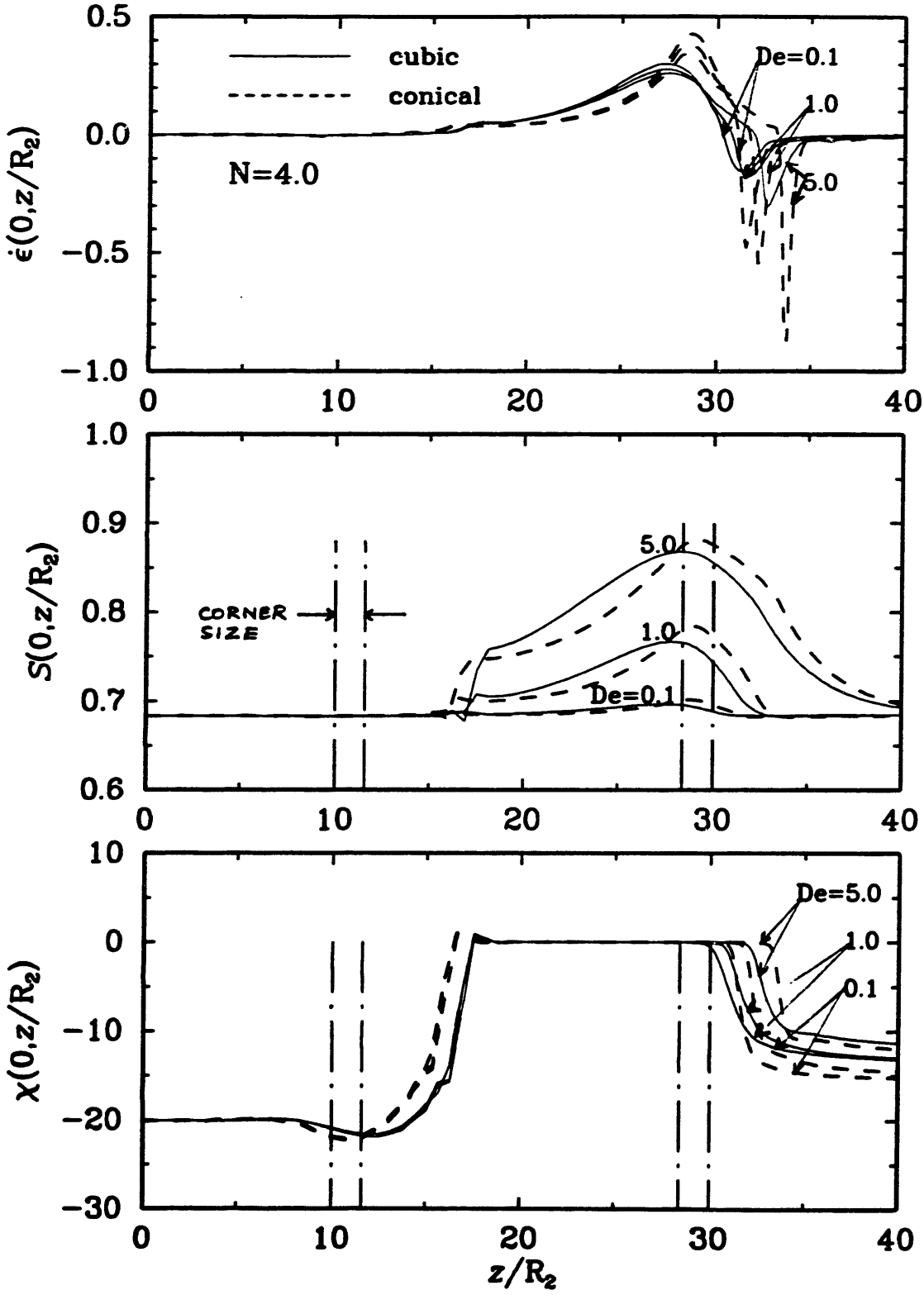

Figure 6.22 Effect of contraction geometry on the centerline variation in (d) $\dot{\epsilon}$, (e) S, and (f) χ for N=4.0, σ=1.0, β=1.6x10^{-3}, De=0.1, 1.0 and 5.0 and Λ=4.

Effect of Geometry on velocity; De=0.1, 1.0 and 5.0

As expected, there is no difference in the upstream and downstream fully developed velocity profiles for any De (cf. Fig. 6.22a). The axial location of the local peak in $\dot{\varepsilon}(0,z/R_2)$ (Fig. 6.22d) in the upstream portion of the 4:1 conical contraction region is 1-2 downstream tube radii ahead of its location in the cubic contraction geometry. Table 6.1 and Fig. 6.22d show that the maximum velocity is higher in the conical contraction and its axial location is also shifted downstream for all De as compared to the cubic contraction geometry; the maximum velocity is reached over a shorter axial distance in the cubic contraction geometry since the radius of curvature of the downstream corner is higher. Since the maximum velocity is higher and there is no difference in the downstream velocity, the percentage overshoot is higher in the conical contraction geometry. As observed in Sections 6.2.1.3 and 6.2.2.1 for the flow through a 2:1 contraction, the percentage overshoot in the centerline velocity in the 4:1 conical contraction also increases with De due to a decrease in the value of the fully developed centerline velocity at the downstream exit with increasing De; in fact the percentage overshoot increases with De though the maximum centerline velocity decreases with De. The decrease in the fully developed centerline velocity at the downstream exit is effected by increased shear thinning in the viscosity with increasing De as noted in Section 6.1. However, high values for the percentage overshoot in the 2:1 and 4:1 contractions even at De=0.1, when shear thinning is insignificant in the downstream fully developed flow. Consequently, the overshoot in the velocity near the junction of the contraction and the downstream tube also results in part from the complex interaction between the kinematics

and the director orientation and the degree of order near the centerline in the downstream portion of the contraction region.

The percentage overshoots are much higher for the LCP flow than that predicted for a shear thinning power-law model; Kim-E (1984) predicts a 1.5% overshoot when the power-law index n=0.2 for which value the shear thinning in the viscosity is significant. The percentage overshoot is also much higher with the LCP constitutive equation as opposed to predictions for the Giesekus, Oldroyd-B and MUCM models reported by Coates (1992) for an abrupt contraction; the smallest overshoot for the LCP model at De = 0.1 is 22.58 % whereas the MUCM model, which seems to predict higher overshoots than either the Oldroyd-B or Giesekus models, predicts an overshoot of 11% at De = 2.0 in the absence of solvent viscosity.

The deceleration in the flow near the centerline in the downstream tube is much higher in the conical contraction geometry. There is very little difference in the velocity profiles close to the wall at z = 30 between the two contraction geometries, which suggests that there is little difference in the kinematics in this shear dominated region for both geometries.

Effect of Geometry on Degree of Order; De=0.1, 1.0 and 5.0

As with the velocity profiles, there is little or no difference in the order at the inlet and downstream exit. In fact, Figs. 6.15p and 6.21p show that there is no difference in the order in the entire upstream tube and close to the downstream exit. A comparison of Figs. 6.15p and 6.21p shows that the degree of order increases more rapidly in the cubic contraction geometry (dark green appears over a shorter axial distance) some distance

prior to the downstream tube due to the higher radius of curvature. However, Figs. 6.22b and 6.22e show that by the time the flow reaches the junction of the contraction and the downstream tube the order is higher at and near the centerline in the conical contraction geometry. This is explained by the higher elongation rates at and near the centerline for all De in the downstream portion of the conical contraction geometry as compared to the cubic contraction geometry. Figs. 6.22b, 6.15p and 6.21p also reveal that there is very little difference in the order close to the wall between the two geometries in the downstream portion of the contraction region and the downstream tube itself, which suggests that there is little difference in the kinematics between the two geometries in this shear dominated region. Figure 6.22g shows that the normal stress difference along the centerline parallels the response in $S(0,z/R_2)$ for both geometries. The maximum normal stress difference is higher in the conical contraction geometry since $\dot{\varepsilon}_{max}$ is higher.

Effect of Geometry on χ; De=0.1, 1.0 and 5.0

As observed with S, χ in the upstream tube is the same for both geometries. Along the centerline, the axial location where $\chi(0,z/R_2)$ becomes zero is located 1-2 downstream tube radii ahead in the conical geometry which happens in response to the appearance of the local peak in $\dot{\varepsilon}(0,z/R_2)$ 1-2 downstream tube radii earlier in the conical geometry as compared to the cubic geometry. However, due to the downstream shift in the axial location of the maximum velocity in the conical geometry, the axial location at the onset of decrease in $\chi(0,z/R_2)$ from zero is also shifted downstream in the conical geometry. Though the axial location at the onset of decrease in $\chi(0,z/R_2)$ from zero is shifted downstream in the conical geometry as compared to the cubic geometry, the stronger

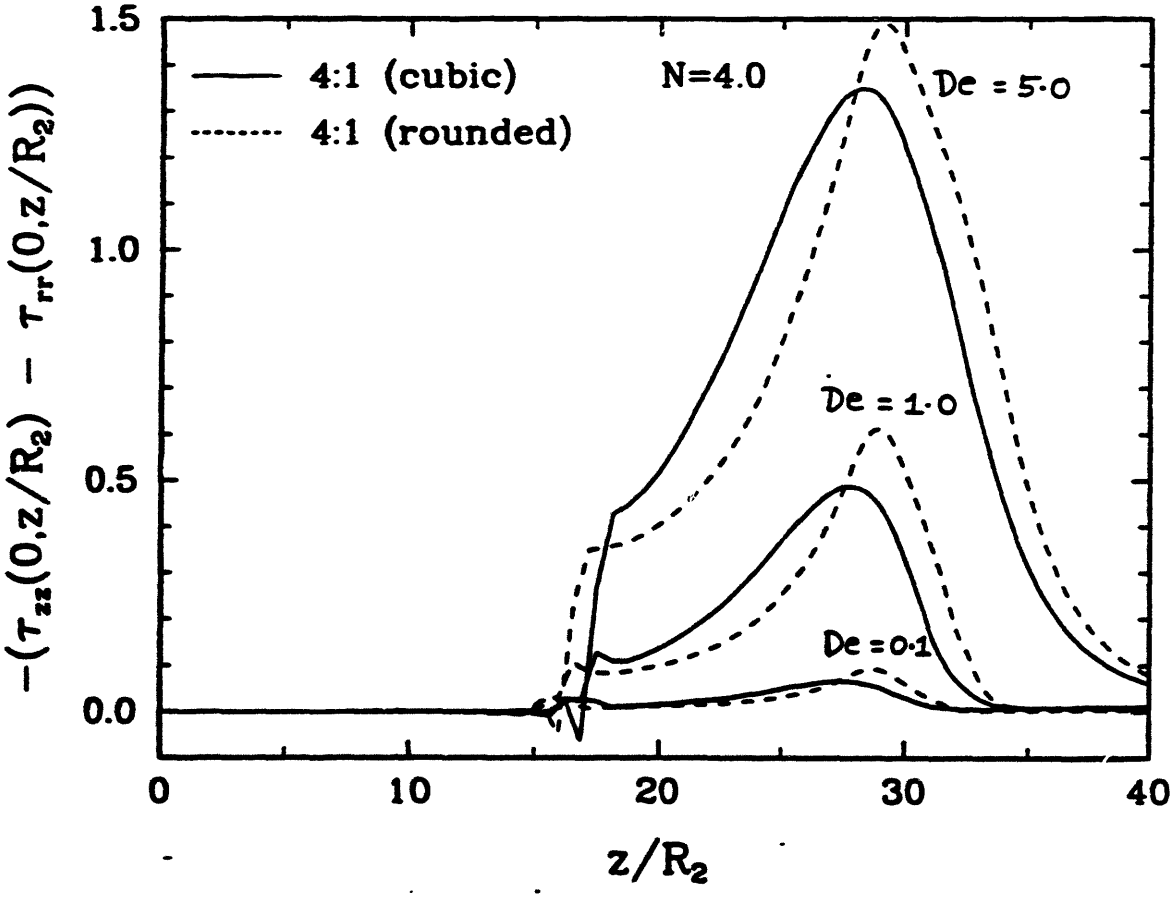

Figure 6.22g Effect of contraction geometry on the centerline response in the dimensionless normal stress difference for N=4.0, σ=1.0, β=1.6x10^{-5}, De=0.1, 1.0 and 5.0 and Λ=4.

deceleration in the velocity field in the downstream tube is associated with a more rapid decrease in $\chi(0,z/R_2)$ in the downstream tube of the conical contraction geometry. In fact, at the downstream exit, $\chi(0,40)$ is closer to the zero-shear-rate limit for any De in the conical contraction geometry; the maximum difference in $\chi(0,40)$ between the two geometries is observed at De = 0.1. Figure 6.22c shows that at z=30, χ is higher by a couple of degrees close to the centerline in the conical contraction due to the higher elongation rates near z=30; close to the wall, χ is slightly higher in the cubic contraction.

From a processing standpoint, the conical contraction geometry with rounded corners and $L/R_2 \rightarrow 0$ creates a higher degree of order near the centerline which leads to a more homogenous cross-sectional order. As shown in Fig. 6.23 the overall pressure drop required to drive a unit volumetric flow rate is slightly smaller for the conical contraction for all De due to the smaller radius of curvature at the reentrant corner which is an advantage of the conical contraction geometry. The effect of other design parameters such as the length of the conical contraction section and the radius of the corners (possibly different radii for the upstream and downstream corners) should be studied more closely.

6.2.5 Couette Correction for Λ = 2 and 4

The Couette correction for the 2:1 and 4:1 contractions computed with the formula

$$C = \frac{\Delta p_{total} - \Delta p_{L_u + L_c/2} - \Delta p_{L_d + L_c/2}}{2\tau_{wd}} \qquad (6.12)$$

is plotted as a function of De in Fig. 6.24. Δp_{total} is the total pressure drop in the

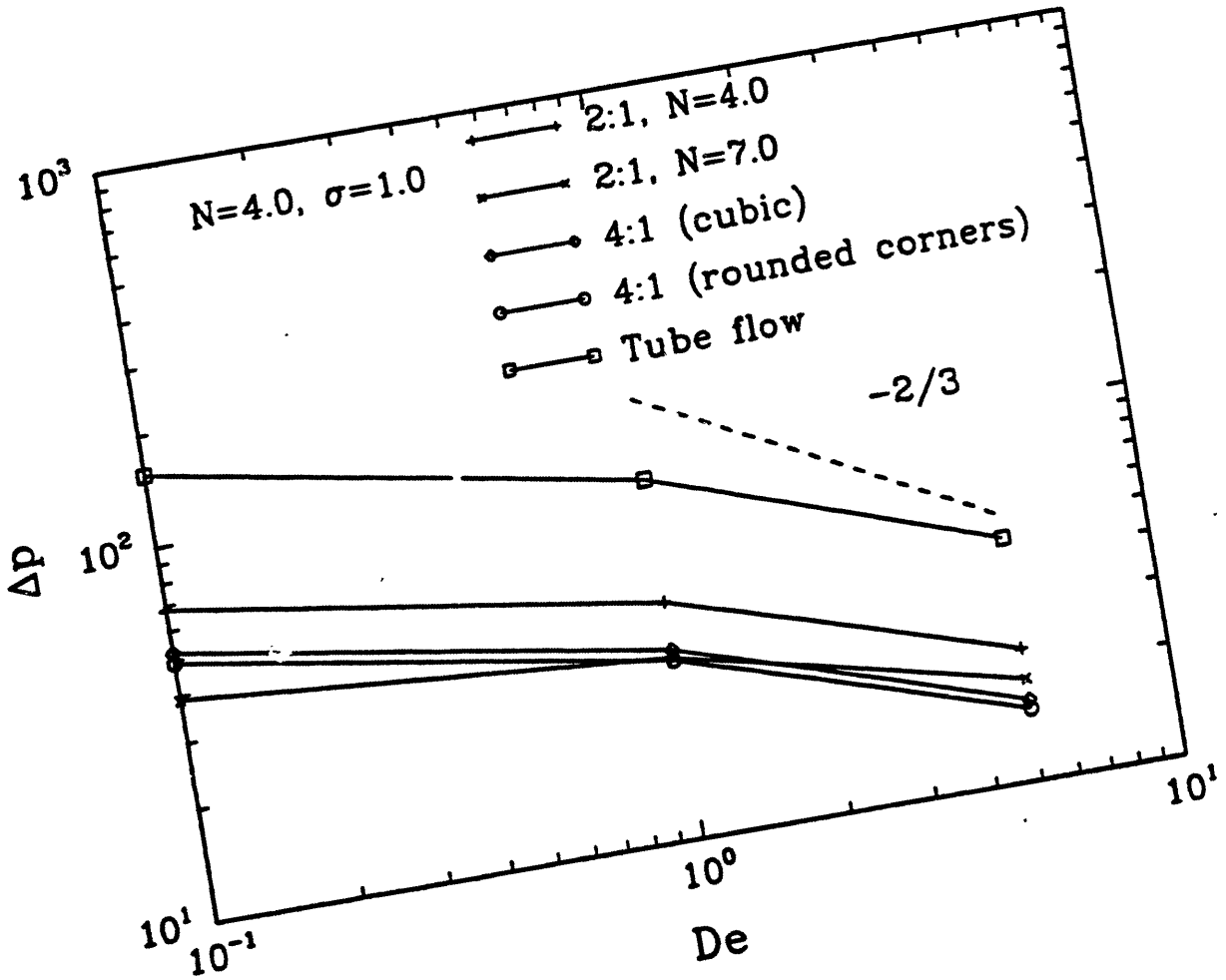

Figure 6.23 Variation in the dimensionless total pressure drop with De for N=4.0 and 7.0, σ=1.0, β=1.6x10^{-5}, and Λ=2 and 4.

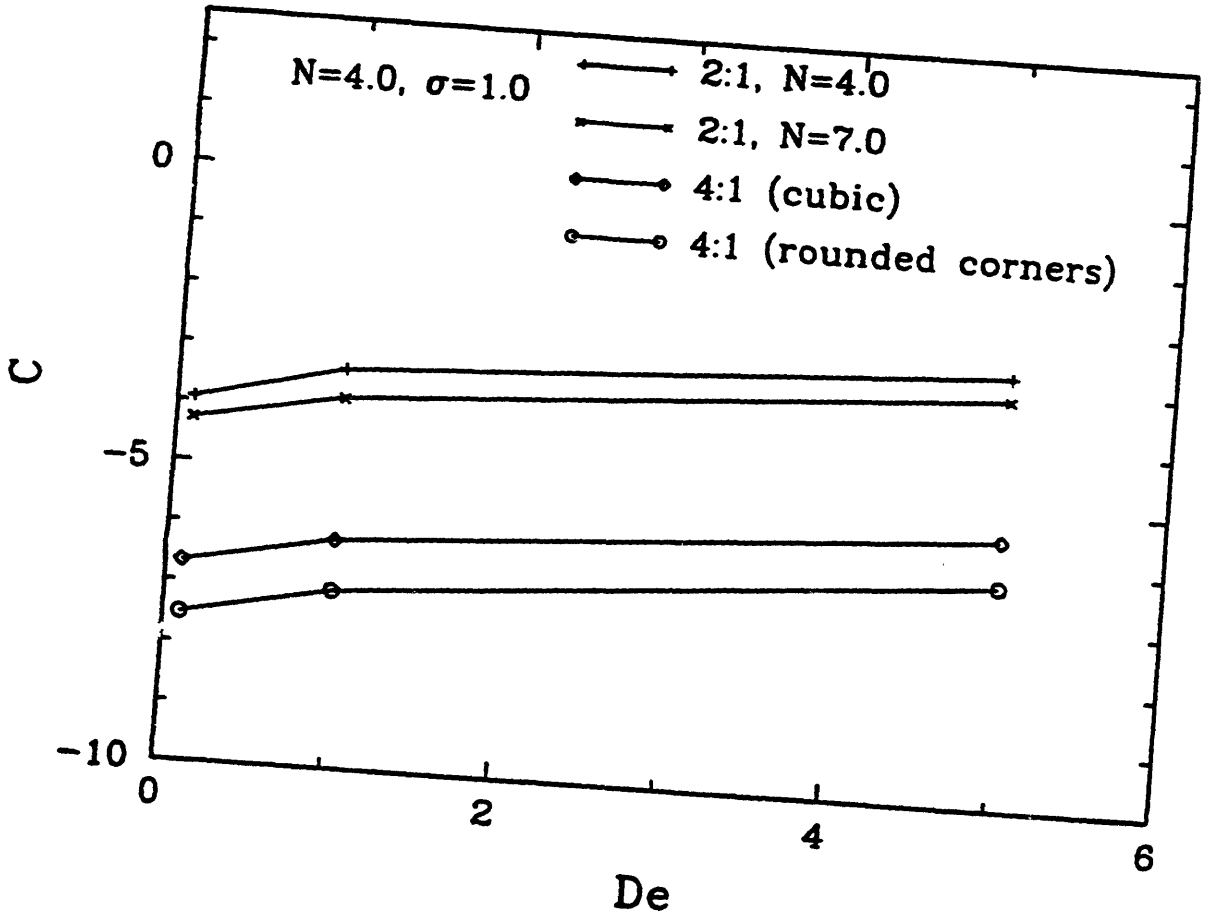

Figure 6.24 Variation in the Couette correction with De for N=4.0 and 7.0, σ=1.0, β=1.6x10^{-5}, and Λ=2 and 4.

contraction geometry. $\Delta p_{L_u+L_c/2}$ is the pressure drop in the flow through a tube with the radius set by the upstream tube in the contraction geometry and the length set by the sum of the length of the upstream tube (L_u) and half the length of the contraction region ($L_c/2$). $\Delta p_{L_d+L_c/2}$ is the pressure drop in a tube of radius R_2 (downstream tube radius) and a length that is the sum of the downstream tube length (L_d) and half the length of the contraction region. The pressure drop is normalized with the fully developed wall shear stress in the downstream tube which is the same for both contraction ratios for a particular value of De and *N*.

The Couette correction in the 4:1 cubic and conical contractions is more negative as compared to the 2:1 cubic contraction due to the smaller overall pressure associated with the larger upstream tube radius. The Couette correction in the cubic 4:1 contraction is slightly less negative than the conical 4:1 contraction due to the higher overall pressure drop associated with the larger radius of curvature at the reentrant corner. The Couette correction shows a slight increase with De for all geometries which is associated with shear thinning in the viscosity. Coates (1992) and Debbaut *et al.* (1988) observed a similar increase in C with the shear thinning Giesekus and PTT constitutive equations respectively. Kim-E (1984) also observed an increase in C with a shear thinning inelastic power-law model. A direct comparison was not made with the results of Coates (1992) due to the difference in the shape of the contraction geometry and the corresponding difference in the definition of the Couette correction.

Unlike the MUCM, Oldroyd-B or Giesekus models studied by Coates (1992),

which capture the Newtonian value of C (C is 0.56 for the abrupt contraction geometry) in the limit of zero De, the results for the LCP model in Fig. 6.24 clearly show that there is no such unique value in the limit of zero De which can be attributed to the anisotropic effect of concentration on the order even at equilibrium in the nematic region. Note the smaller pressure drop predicted at N=7.0 for the range of De studied (cf. Fig. 6.23). The result is not surprising since the higher concentration is associated with a higher degree of molecular order due to stronger intermolecular forces of interaction which reduce the overall pressure drop. Fig. 6.23 also shows that the rate of decrease in the overall pressure drop with increasing De is smaller for N=7.0 due to the reasons discussed in Section 6.2.2.2.

Chapter Seven

Conclusions

Figure 1.2 in the introduction demonstrated the strong dependence of the tensile modulus of a Kevlar® fiber on the molecular orientation with respect to the fiber axis; even small changes in the molecular orientation, when the orientation angle is small, lead to large changes in the tensile modulus. Figure 1.2 also shows that thermal treatment by annealing or other processes does not reduce the molecular orientation angle with respect to the fiber axis, *i.e.* improve the molecular orientation. Besides, thermal treatment processes are expensive. Consequently, it is important to maximize the molecular orientation during the fiber spinning process itself. A model that would relate the development of molecular orientation in the fiber spinning process to the macroscopic properties would be a very useful process design tool in predicting and controlling the product properties, optimizing the product properties, and minimizing production costs. This research contributes to the development of such a design tool.

Four stages were identified in the fiber spinning process shown schematically in Fig. 1.4: (1) spinneret flow which involves flow through a contraction, (2) die swell experienced by the polymer solution as it comes out of the spinneret, (3) fiber drawing which involves extensional stretching of the polymer solution and (4) solidification or coagulation where the solvent is extracted from the polymer solution and the microstructure is frozen in the resultant solid. The solidification issue is not addressed

in this thesis. Conclusions from the analysis of the flow in the remaining three regions are discussed below.

7.1 Conclusions from Fiber Drawing Analysis

A one-dimensional model was developed for the fiber drawing region by using the lubrication approximation and the molecular theory based constitutive equation of Bhave *et al.* (1993) for nematic, rodlike, liquid-crystalline polymer solutions. The aim of the model is to predict the development of microstructure, velocity, and normal stresses along the spinline and examine the effect of the initial microstructural condition on these quantities. Note that the development of the microstructure is described quantitatively by the degree of order S defined in Chapters 3 and 4.

The Bhave *et al.* constitutive equation uses a closure approximation to get a closed form of the constitutive equation which simplifies the flow calculations in complex flows. However, Larson and Ottinger (1991) demonstrated that molecular tumbling is not predicted in simple shear flows when the closure approximation is used. The fiber drawing analysis was therefore carried out by directly solving the distribution function for the molecular orientation to test the effect of the closure approximation in the extensionally dominated fiber drawing flow. The results, presented in Chapter 4, demonstrated the validity of the closure approximation at moderate and high Deborah number (De) in the fiber drawing flow. The technique, based on a Legendre polynomial expansion, is the first such attempt to solve directly for the distribution function in a complex flow and indicates a path for solving other complex flow problems with

molecular models where approximations of uncertain validity must be used to get a closed form constitutive equation.

The sensitivity of the velocity, stress and degree of order (S) profiles in the fiber drawing region to the initial degree of order was examined for two different initial conditions on S that would bracket the range of possible initial values that the spinline might see. These are $S(0)=S_{\dot{\varepsilon}}$, *i.e.* S has the value it would have in a simple elongational flow for the same elongation rate $\dot{\varepsilon}$ as exists at the origin of the fiber drawing region $\zeta=0$, and $S(0)=S_{eq}$, *i.e.* S has its equilibrium value at the polymer concentration N. The fiber drawing model predictions clearly show the sensitivity of the velocity, stress and order profiles to the initial order $S(0)$. The final degree of order predicted for $S(0)=S_{\dot{\varepsilon}}$ is always slightly higher than that predicted for $S(0)=S_{eq}$ at moderate and high De; the corresponding tension required for achieving the same drawdown in the fiber radius is 20 % higher for $S(0)=S_{\dot{\varepsilon}}$. The sensitivity to the initial degree of order $S(0)$ is in contrast to that observed in the modeling with isotropic viscoelastic constitutive equations such as the White-Metzner model studied by Fisher and Denn (1976) where the downstream velocity and stress profiles are found to be insensitive to the choice of the initial condition on the stress.

Another interesting result that emerges from the fiber drawing analysis is that the apparent elongational viscosity $\bar{\eta}_a$ defined by Eq. 4.39 compares well with the elongational viscosity $\bar{\eta}$ predicted by the constitutive equation, thereby suggesting that the fiber spinning flow can be used to determine $\bar{\eta}$ for a liquid-crystal polymer solution provided that the normal stress difference τ_{zz}-τ_{rr} can be measured. This result is in contrast to that observed with models for flexible polymers (Mackay and Petrie, 1989)

where the agreement between $\bar{\eta}_a$ and $\bar{\eta}$ is never good over a wide range of elongation rates.

The only data that has appeared in literature on the fiber drawing of liquid-crystalline polymers is due to Prilutski (1984). Model predictions agree well with the steady-state fiber drawing data of Prilutski (1984) for a 40 wt % hydroxy propyl cellulose (HPC) in acetic acid solution; at equilibrium, the HPC/acetic acid solution undergoes an isotropic-to-nematic phase transition at 30 wt % HPC. However, due to the experimental limitations discussed in Chapter 3, the data are limited to small De. Consequently, even a Newtonian model with a viscosity $\mu = \bar{\eta}_{a,0}/3$, where $\bar{\eta}_{a,0}$ is the zero-elongation-rate apparent elongational viscosity, is able to predict the data well. Data at higher values of De is required to rigorously test the model predictions. In addition, data on the development of molecular order along the spinline is necessary to rigorously test the molecular bases of the model.

An important processing problem in fiber spinning is the appearance of long wavelength (of the order of the spinning length), time periodic oscillations along the length of the fiber beyond a certain drawdown in the fiber radius (known as the critical draw ratio $D_{R,crit}$) even at constant extrusion and take-up speeds that leads to the formation of a fiber of nonuniform thickness which is undesirable. This phenomenon is known as draw resonance. A linear stability analysis of the fiber drawing equations was performed to predict the onset of draw resonance instabilities. The analysis predicts a strong correlation between $D_{R,crit}$ and $\bar{\eta}_a$. Prilutski (1984) also reports critical draw ratio data for different elongation rates at the take-up wheel. However, the flow rate, length

of the spinline and the tension at the onset of draw resonance are not known. Linear stability predictions in which the model parameters are determined from the comparison with the steady-state data, and values for the unknown spinline length (varying the flow rate) or the flow rate (varying the spinline length) are assumed, are poor. The critical draw ratio data is overpredicted by an order of magnitude at higher elongation rates. Good quantitative agreement is obtained only if the time constant λ is roughly 10 times that in shear flow and the anisotropic drag parameter σ is a factor of 20 smaller than the value that fits the steady-state fiber drawing data.

The sensitivity of the fiber drawing model to the initial degree of order $S(0)$ requires two-dimensional calculations that couple to the upstream spinneret flow. The two-dimensional calculations are also necessary to assess the assumption of radial homogenity used in the one-dimensional fiber drawing model. Conclusions on the analysis of the spinneret flow follow.

7.2 Conclusions from Spinneret Calculations

A two-dimensional finite element model based on a slight variation of the EVSS-G formulation proposed by Brown *et al.* (1993) was developed for the liquid-crystalline polymer flow through the spinnerets illustrated schematically in Figs. 5.1a and 5.1b. The response in the degree of order and the average molecular orientation was understood in terms of the flow kinematics. The effect of De on the development of molecular degree of order and orientation was examined for a 2:1 and a 4:1 contraction with cubic contraction boundaries and also a 4:1 conical contraction with rounded corners. The

effect of concentration on the development of order was also examined. The implications of the spinneret calculations on the degree and homogenity of the order in the fiber drawing region and the regions of validity of the one-dimensional fiber drawing model in parameter space was explored. The spinneret calculations were also used to determine what design changes would help maximize the homogenity and the degree of orientation of the molecules with the spinneret axis so that a fiber with a high tensile modulus could be created.

The molecular orientation is described in terms of χ and S; χ is a measure of the average orientation of the molecules with respect to the spinneret axis and S is a measure of the degree of order about the average orientation. The vector that locates the direction of average orientation of the polymer molecules is commonly called the nematic director. Note that χ and S possess radial and axial dependence *i.e.* $\chi \equiv \chi(r/R_2, z/R_2)$ and $S \equiv S(r/R_2, z/R_2)$. The response in χ and S along the centerline and throughout the rest of the domain was understood in terms of the flow kinematics.

The increase in $\chi(0,z/R_2)$ from the zero-shear-rate limit to zero degrees (perfect alignment with spinneret axis) in the upstream portion of the contraction coincided with the increase in $\dot{\epsilon}(0,z/R_2)$ ($\dot{\epsilon}$ is the dimensionless elongation rate). $\chi(0,z/R_2)$ approaches zero earlier by 1-2 downstream tube radii in the 4:1 conical contraction with rounded corners as compared to the 4:1 contraction with the cubic contraction boundary. The approach is faster for either 4:1 contraction geometry as compared to the 2:1 contraction with the cubic boundary. $\chi(0,z/R_2)$ is zero even for small values of the elongation rate in the contraction region as suggested by the perturbation analysis presented in Chapter

4. The axial location at the onset of decrease in $\chi(0,z/R_2)$ from $\chi(0,z/R_2)=0$ was shifted further downstream with increasing De which paralleled the axial shift in $\dot{\varepsilon}(0,z/R_2)=0$. The axial location at the onset of decrease in $\chi(0,z/R_2)$ from zero was shifted furthest downstream for all De in the 4:1 conical contraction with rounded corners. The sharp increase in $S(0,z/R_2)$ from the equilibrium value in the upstream portion of the contraction coincides with $\chi(0,z/R_2)$ becoming zero; the lag between the sharp increase in $S(0,z/R_2)$ and the initial increase in $\dot{\varepsilon}(0,z/R_2)$ is 7-8 downstream tube radii. The lag between the maximum in $S(0,z/R_2)$ and $\dot{\varepsilon}(0,z/R_2)$, however, is only one downstream tube radius.

Close to the wall, it was seen that χ is dictated by the shear rates and the wall slope. For small shear rates, χ is the sum of the wall slope angle and the angle in the limit of zero-shear-rate which makes the director orientation worse than the zero-shear-rate limit. At high shear rates, χ approaches the wall slope angle. S always increases from the centerline towards the wall for all De and for all geometries which suggests that shearing plays a more dominant role in the kinematics in improving the degree of order. The director, however, is best aligned with the spinneret axis ($\chi=0$) on the centerline in the contraction region. χ approaches zero close to the wall at high De in the downstream portion of the contraction where the wall slope is no longer a factor.

The results in Chapter 6 clearly demonstrate that the degree of order and the director orientation with the spinneret axis improve with De in the downstream tube. With increasing De, homogenity in S and χ is much better as $L/R_2 \rightarrow 0$ (L is the downstream tube length which is also called the land length). Close to the wall, there is little change in S and χ between z=30 (the junction of the contraction and the downstream tube) and z=40 (the downstream exit) for any De; the difference in S and χ between the

2:1 and 4:1 contractions is insignificant in this shear dominated region. However, there is a significant decrease near the centerline in χ for all De and also in S at moderate and high De between the axial locations z=30 and z=40. For short land lengths ($L/R_2 \rightarrow 0$), S emerges with a higher value near the centerline in the 4:1 conical contraction geometry as compared to the 2:1 or 4:1 cubic contraction geometries for the range of De studied. Consequently, for short land lengths, the radial homogenity in S is also better in the 4:1 conical contraction for the range of De studied. However, even in the 4:1 conical contraction, the radial homogenity in S is best at high De. χ is also more radially homogenous at high De; the homogenity in χ is better in the 4:1 conical contraction as compared to the 2:1 or 4:1 cubic contraction geometries. At low De, the inhomogenity is primarily in χ. For $L/R_2 \gg 1$, however, χ too becomes homogenous.

Qualitatively, there is no difference in the development of S and χ for the concentrations N = 4.0 and 7.0. Changes in S are smaller for N = 7.0 since the differential between the equilibrium value (S=0.683 for N=4.0 and S=0.840 for N=7.0) and the maximum value (S=1.0 for any concentration) is smaller for N=7.0. Changes in χ are also smaller for N=7.0 since the differential between the zero-shear-rate value (χ=-20.1 degrees for N=4.0 and χ=-13.7 degrees for N=7.0) and the maximum value seen in the 2:1 or 4:1 contraction geometries (χ=0 degrees) is smaller for N=7.0.

Also of interest in processing is the total pressure drop in the geometry. The results demonstrate the effect of De, contraction ratio and the change in the shape of contraction boundary on the pressure drop per unit volumetric flow rate ($\Delta p/Q$). The increase in molecular alignment with the flow direction with increasing De reduces the

viscosity which leads to a decrease in $\Delta p/Q$ with increasing De irrespective of the contraction ratio, shape of the boundary or concentration. The pressure drop, however, is smaller in the 4:1 contraction due to the larger upstream tube radius. The pressure drop in the 4:1 cubic contraction is higher than the 4:1 conical contraction since the flow "sees" the small tube radius for a longer distance due to the larger radius of curvature at the junction of the contraction and the downstream tube. The results also show that $\Delta p/Q$ in the limit of small De is lower for the higher concentration due to better molecular alignment at equilibrium. Unlike the MUCM, PTT, or Giesekus constitutive equations where the Newtonian limit is reached in the limit of small De (Coates, 1992), $\Delta p/Q$ in the limit of $De \rightarrow 0$ is concentration dependent for the liquid-crystal model. A Newtonian limit is encountered only in the isotropic concentration regime. The Couette correction, C, shows a slight increase with De which seems to be typical of shear thinning models (Coates, 1992; Kim-E, 1984; and Debbaut *et al.*, 1988). No recirculation regions were observed for either the 2:1 or 4:1 contractions with the geometric configurations used in this thesis or for the range of De studied.

The results clearly show that De, contraction ratio, shape of geometry, all have an effect on S and χ at the spinneret exit. To maximize S and χ, and to achieve a high degree of radial homogenity in S and χ, it is best to operate at high De with dies designed with short land lengths ($L/R_2 \rightarrow 0$). $\Delta p/Q$ also drops dramatically when the land length is reduced. The 4:1 conical contraction is better than the 2:1 or 4:1 cubic contractions in maximizing and homogenizing S and χ for the same De. The pressure drop per unit volumetric flow rate is also smaller. The effect of higher contraction ratios and smaller contraction lengths (which results in higher taper angles for the same contraction ratio)

on maximizing S and χ needs to be investigated more thoroughly. Increasing the contraction ratio or the taper angle by shortening the contraction length is expected to reduce the pressure drop. However, onset of recirculation regions is also likely, which suggests that there may be an optimal contraction ratio for processing.

It has been experimentally observed that the die swell for liquid-crystalline polymers is small *i.e.* the die swell is comparable to a Newtonian die swell (Prilutski, 1984). It is reasonable then to expect that the molecular deorientation in the die swell region is small and that the spinneret calculations alone, without an integrated fiber spinning model, can provide a good check on the two key assumptions in the one-dimensional fiber drawing analysis; namely, (1) S and χ are radially homogenous and (2) the director is oriented with the z-axis with $S_{eq} \leq S(0) \leq S_{\dot{\varepsilon}}$.

The implications of the spinneret calculations on the one-dimensional fiber drawing analysis was examined in Chapter 6. As already discussed previously, S and χ are radially homogenous at high De and short land lengths ($L/R_2 \rightarrow 0$). It was determined that at high De and short land lengths ($L/R_2 \rightarrow 0$), it is best to use $S(0)=S_{\dot{\varepsilon}}$ in solving the one-dimensional model where $\dot{\varepsilon}$ is the maximum elongation rate on the centerline. The assumption $\chi(0)=0$ in the one-dimensional model is also appropriate and need not be modified. For small De, S is radially homogenous and close to the equilibrium value. χ is inhomogenous near the junction of the contraction and the downstream tube, but becomes homogenous at the zero-shear-rate limit for $L/R_2 \gg 1$. In this limit it appears best to modify the one-dimensional model to allow for non-axial alignment in the director and solve with the initial conditions $S(0)=S_{eq}^{\prime}$ and $\chi(0)=\chi_{zero\text{-}shear}$-

rate. The inhomegenity in χ, however, may not be serious, and $L/R_2 \gg 1$ may not be necessary, since the extensionally dominated fiber drawing flow is expected to align the director with the flow direction even at small elongation rates as suggested by the perturbation analysis in Chapter 4. However, before claiming the validity of a one-dimensional model with $S(0)=S_{eq}$ and $\chi(0)=0$ when De is small, the axial length scale over which the inhomogenity in χ disappears must be clearly established. This requires a two-dimensional model for the fiber drawing region that couples to the upstream spinneret flow.

The study of the spinneret and fiber drawing flows of liquid-crystalline polymers by using a kinetic theory based constitutive equation has revealed important information on the dynamics of orientation of the polymer molecules during the fiber spinning process and its impact on minimizing the production costs and improving the process design so that a fiber with a high tensile modulus can be created. However, in order to fully optimize the fiber spinning process it is necessary to quantitatively understand the orientation dynamics of the polymer molecules in the die swell region. This is possible only with an integrated model for the spinneret, die swell and fiber drawing flows. The primary issue to be tackled in the development of such a model is the singularity in the stress at the die exit which happens due to a sudden change in the boundary data. This singularity is commonly called the die swell singularity. The die swell singularity issue is discussed in the following section.

7.3 Conclusions from Die Swell Singularity Analysis

The die swell singularity, as mentioned in the previous section, happens due to a sudden change in the boundary data, *i.e.* no slip boundary condition on the die or spinneret wall to a shearfree boundary condition on the free surface of the polymer solution. Apelian (1987), Crochet and Keunings (1987) and others report numerical difficulties with Newtonian and viscoelastic models that are associated with the die swell singularity. Therefore, understanding the singularity through analytical means was made one of the aims of the thesis prior to carrying out any numerical calculations in the die swell region. Determination of the nature of the singularity would greatly help in assessing the accuracy of the numerical predictions close to the singularity; the memory effects associated with viscoelastic constitutive equations are expected to convey information about the singularity downstream much more so than viscous models which makes it crucial to understand the singularity for these models.

For constitutive models such as MUCM, shear thinning PTT and the liquid-crystal models, the Newtonian singular behavior is dominant, and consequently, understanding the Newtonian singularity alone should be sufficient to design and evaluate the numerical treament of the singularity; once the singularity is determined it could be incorporated through singular elements into the finite element model.

Singular behavior in the stresses is also predicted in the flow around sharp corners. However, the analytical tractability using the local, self-similar expansion for the stream function postulated by Dean and Montagnon (1949) and Moffat (1964) is greatly simplified due to the absence of curvature effects associated with surface tension. The

curvature of the free surface near the die exit associated with surface tension makes the local analysis difficult even for a Newtonian problem.

The analyses in literature on the die swell singularity are confusing since they do not clearly specify their regions of validity. These analyses are summarized, and their regions of validity detailed, and presented in Appendix A. By introducing an expansion for the free surface height valid close to the singularity, it was demonstrated clearly that when surface tension is not involved in a dominant balance with the total normal stress associated with the fluid, the dominant singular behavior in the stresses is $O(r^{-1/2})$ where r is the radial distance from the singularity; in addition, the free surface exits parallel to the die wall. This result is the same as Michael's (1958) result for a planar free surface and Trogdon and Joseph's (1981) result for linearized free surface boundary conditions. If surface tension is involved in a dominant balance with the total fluid normal stress, an analysis based on the expansion for the free surface height clearly shows that the dominant singular behavior in the stress and the free surface exit angle (α) cannot be determined from the local analysis. However, as suggested, a match with Trogdon and Joseph's eigenfunction expansion results, which are expected to be accurate away from the singularity, would determine the coefficients in the expansion for the free surface height and also α and the dominant singular behavior.

An important question that arises from the die swell singularity analysis is whether or not curvature associated with surface tension involved in a dominant balance with the total fluid normal stress close to the singularity. Calculations with the MUCM model (Apelian, 1987) demonstrate the sensitivity of the downstream swell on the accuracy or magnitude of the stress field close to the die exit (cf. Fig. A.4). Consequently, the

downstream swell in viscoelastic calculations is expected to be sensitive to the particular choice of the dominant balance posed by the above question. Future work must address this question so that an integrated model that models the die swell region accurately can be developed for the fiber spinning process. Future work must also be directed towards experimentally characterizing the molecular orientation dynamics during the fiber spinning process so that the molecular bases of the model for liquid-crystalline polymer solutions can be tested rigorously.

References

Advani, S.G. and C.L. Tucker, "The Use of Tensors to Describe and Predict Fiber Orientation in Short Fiber Composites", *J. Rheol.*, **31**(8), 751-784 (1987).

Altan, M.C., S.G. Advani, S.I. Güceri and R.B. Pipes, "On the Description of the Orientation State for Fiber Suspensions in Homogenous Flows", *J. Rheol.*, **33**(7), 1129-1155 (1989).

Apelian, M.R., "On the Numerical Analysis of Extrusion of Viscoelastic Fluids", Ph.D. Thesis, Massachusetts Institute of Technology, Cambridge (1987).

Babuska, I., "The Finite Element Method with Lagrange Multipliers", *Numer. Math.*, **20**, 179-192 (1973).

Bathe, K.J. and E.L. Wilson, *Numerical Methods in Finite Element Analysis*, Prentice-Hall, New Jersey (1976).

Bechtel, S.E., M.J. Forest, D.D. Holm and K.J. Lin, "One-dimensional Closure models for three-dimensional incompressible viscoelastic free jets: Von-Kármán Flow Geometry and Elliptical Cross-section", *J. Fluid Mech.*, **196**, 241-262 (1988).

Bercovier, M. and O. Pirroneau, "Error Estimates for Finite Element Method Solution of the Stokes Problem in Primitive Variables", *Numer. Meth.*, **33**, 211. (1979).

Beris, A.N., R.C. Armstrong and R.A. Brown, "Finite Element Calculations of Viscoelastic Flow in a Journal Bearing: I. Small Eccentricity", *J. Non-Newtonian Fluid Mech.*, **16**, 141-172 (1984).

Berry, G.C. and C.E. Scroog, "Rigid Chain Polymers: Synthesis and Properties", *J. Polym. Sci. Polym. Symp.*, **65**, (1978).

Bhave, A.V., R.K. Menon, R.C. Armstrong and R.A. Brown, "A Constitutive Equation for Liquid-crystalline Polymer Solutions", *J. Rheol.*, **37**(3), 413-441 (1993).

Bhave, A.V., "Kinetic Theory for Dilute and Concentrated Polymer Solutions: Study of Nonhomogenous Effects", Ph.D. Thesis, Massachusetts Institute of Technology, Cambridge (1992).

Bird, R.B., R.C. Armstrong & O. Hassager, *Dynamics of Polymeric Liquids*, Vol. 1: *Fluid Mechanics*, Wiley, New York (1987), Second Edition.

Bird, R.B., C.F. Curtiss, R.C. Armstrong and O. Hassager, *Dynamics of Polymeric Liquids*, Vol. 2: *Kinetic theory*, Wiley, New York (1987), Second Edition.

Born, M. and H.S. Green, *A General Kinetic Theory of Liquids*, Cambridge University Press (1949).

Bornside, D.A., personal communications (1993).

Brezzi, F., "On the Existence, Uniqueness and Approximation of Saddle-Point Problems Arising from Lagrange Multipliers", *RFAIRO Num. Anal.*, **8**, 129-151 (1974).

Brooks, A.N. and T.J.R. Hughes, "Streamline Upwind/Petrov-Galerkin Formulation for Convection Dominated Flows with Particular Emphasis on the Incompressible Navier-Stokes Equations", *AIChE J.*, **24**(5), 869-879 (1982).

Brown, R.A., M.J. Szady, P.J. Northey and R.C. Armstrong, "On the Numerical Stability of Mixed Finite Element Methods for Viscoelastic Flows Governed by Differential Constitutive Equations", submitted to *Theor. and Comp. Fluid Dynamics* (1993).

Burdette, S.R., P.J. Coates, R.C. Armstrong and R.A. Brown, "Calculations of Viscoelastic Flow through an Axisymmetric Corrugated Tube Using the Explicitly Elliptic Momentum Equation Formulation (EEME)", *J. Non-Newtonian Fluid Mech.*, **33**, 1-23 (1989).

Burnett, S., *Finite Element Analysis*, Addison-Wesley, Massachusetts (1987).

Carey, G.F. and J.T. Oden, *Finite Elements, Vol 2 A Second Course*, Prentice-Hall, Englewood Cliffs, New Jersey (1983).

Carrier, G.F. and C.E. Pearson, *Partial Differential Equations*, Academic Press Inc., London, UK (1988).

Chang, J.C. and M.M. Denn, "An Experimental Study of Isothermal Spinning of a Newtonian and a Viscoelastic Liquid", *J. of Non-Newtonian Fluid Mech.* **5**, 369-385 (1979).

Chang, J.C., M.M. Denn and F.T. Geyling, "Effects of Inertia, Surface Tension, and Gravity on the Stability of Isothermal Drawing of Newtonian Fluids", *Ind. Eng. Chem. Fundamentals*, **20**, 147-149 (1981).

Christensen, R.E., "Extrusion Coating of Polypropylene", *S.P.E.J.*, **18**, 751. (1962).

Cifferi, A. and I.M. Ward, eds., *Ultra-high Modulus Polymers*, Applied Science Publishers, London, (1979).

Coates, P.J., R.C. Armstrong and R.A. Brown, "Calculation of Steady-state Viscoelastic Flow through Axisymmetric Contractions Using EEME Formulation", *J. Non-Newtonian Fluid Mech.*, **42**, 141-188 (1992).

Coates, P.J., "Simulation of the Flow of Viscoelastic Fluids in Contraction Geometries", Ph.D. Thesis, Massachusetts Institute of Technology, Cambridge, Massachusetts (1992).

Crochet, M.J. and R. Keunings, "On Numerical Die Swell Calculation", *J. Non-Newt. Fluid Mech.*, **10**, 85-94 (1982).

Crochet, M.J., A.R. Davies and M.J. Walters, "Introduction to Finite Elements", *Numerical Solutions for the Flow of Viscoelastic Fluids*, Elsevier, Amsterdam (1984).

Cruz-Saenz, G.F., G.J. Donnelly and C. B. Weinberger, "Onset of Draw Resonance during Isothermal Melt Spinning: A Comparison between Measurements and Predictions", *AIChE J.*, **22**, No.3, 441-448 (1976).

Dean, W.R. and P.E. Montagnon, "On the Steady Motion of a Viscous Liquid in a Corner", *Proc. Camb. Phil. Soc.*, **45**, 389-394 (1949).

Debbaut, B., J.M. Marchal and M.J. Crochet, "Numerical Simulation of Highly Viscoelastic Flows through an Abrupt Contraction", *J. Non-Newtonian Fluid Mech.*, **29**, 119-146 (1988).

de Gennes, P.G., *The Physics of Liquid Crystals*, Clarendon, Oxford (1974).

Denn, M.M., C.J.S. Petrie and P. Avenas, "Mechanics of Steady Spinning of a Viscoelastic Liquid", *AIChE J.* **21**, 791-799 (July 1975).

Denn, M.M. and G. Marrucci, "Effect of a Relaxation Time Spectrum on Mechanics of Polymer Melt Spinning", *J. Non-Newtonian Fluid Mech.* **2**, 159-167 (1977).

Denn, M.M., "Continuous Drawing of Liquids to Form Fibers", *Ann. Rev. Fluid Mech.*, **12**, 365. (1980).

Doi, M. and S.F. Edwards, "Dynamics of Rod-like Macromolecules in Concentrated Solution: Part I", *Trans. Farad. Soc. II*, 560. (1977).

Doi, M. and S.F. Edwards, "Dynamics of Rod-like Macromolecules in Concentrated Solution: Part II", *J. Chem. Soc. Farad. II*, **74**, 918. (1978).

Doi, M., "Rheological Properties of Rodlike Polymers in Isotropic and Liquid-crystalline Phases", *Ferroelectrics*, **30**, 247-254 (1980).

Doi, M., "Molecular Dynamics and Rheological Properties of Concentrated Solutions of Rodlike Polymers in Isotropic and Liquid-crystalline Phases", *J. Polym. Sci. Polym. Phys. Ed.*, **19**, 229-243 (1981).

Donnelly, G.J. and C.B. Weinberger, "Stability of Isothermal Fiber Spinning of a Newtonian Fluid", *Ind. Eng. Chem. Fundamentals*, **14**, 334-337 (1975).

Doraiswamy, D. and A.B. Metzner, "The Rheology of Polymeric Liquid-crystals", *Rheol. Acta.*, **25**, 580-587 (1986).

DuPont, personal communications (1992).

Elliot, A. and E.J. Ambrose, *Discuss. Farad. Soc.*, **9**, 246. (1950).

Ericksen, J.L., "Equilibrium Theory of Liquid-Crystals", *Advances in Liquid Crystals*, **2**, 233-298 (1976).

Fisher, R.J. and M.M. Denn, "Finite-Amplitude Stability and Draw Resonance in Isothermal Melt Spinning", *Chem. Eng. Sci.* **30**, 1129. (1975).

Fisher, R.J. and M.M. Denn, "A Theory of Isothermal Melt Spinning and Draw Resonance", *AIChE J.* **22**, 236-245 (1976).

Fisher, R.J. and M.M. Denn, *AIChE J.*, **23**(1), 23. (1977).

Frank, F.C., "On the Theory of Liquid Crystals", *Discuss. Farad. Soc.*, **25**, 19. (1958).

Friedel, G., *Anales Physique*, **18**, 273. (1922).

Gelder, D., "The Stability of Fiber Drawing Processes", *Ind. Eng. Chem. Fundamentals*, **10**, 534-535 (1971).

Grizzuti, N. et al,, "Transient and Steady-State Rheology of a Liquid-Crystalline Hydroxy Propyl Cellulose Solution", *J. Rheol.*, **34**(8), 1293-1310 (1990).

Hermans, P.H. and P. Platzek, *Koll. Z.*, **88**, 68. (1939).

Hood, P., "Frontal Solution Program for Unsymmetric Matrices", *Int. J. Num. Meth. Eng.*, **10**, 379-399 (1976).

Iooss, G. and D.D. Joseph, *Elementary Stability and Bifurcation Theory*, Springer-Verlag, New York (1990).

Ishihara, H. and S. Kase, "Studies on Melt Spinning. V. Draw Resonance as a Limit Cycle", *J. Appl. Polym. Sci.*, **19**, 557-565 (1975).

Ishihara, H. and S. Kase, "Studies on Melt Spinning: VI. Simulation of Draw Resonance using Newtonian and Power-law Viscosities", *J. Appl. Polym. Sci.*, **20**, 169-191 (1976).

Jenkins, J.C. and G.M. Jenkins, "Graphite Produced by Extrusion of Pitch Mesophase", *Carbon*, **25** 473. (1983).

Johnson, C., U. Navert and J. Pitkaranta, "Finite Element Methods for Linear Hyperbolic Problems", *Comp. Meth. Appl. Mech. Eng.*, **45**, 285-312 (1984).

Joseph, D.D., M. Renardy and J.C. Saut, "Hyperbolicity and Change of Type in the Flow of Viscoelastic Fluids", *Arch. Rat. Mech.*, **87**, 213-251 (1985).

Joseph, D.D. and J.C. Saut, *J. Non-Newtonian Fluid Mech.*, **20**, 87. (1986).

Kamal, M.R. and A.T. Mutel, "The Prediction of Flow and Orientation Behavior of Short Fiber Reinforced Melts in Simple Flow Systems", *Polymer Composites*, **10**(5), 337-343 (1989).

Kase, S. and T. Matsuo, "Melt Spinning. I. Fundamental Equations on the Dynamics of Spinning", *J. Polym. Sci.*, part **A**, **3**, 2541-2554 (1965).

Kase, S., T. Matsuo and Y. Yoshimoto, *J. Japan Society of Textile Machinery*, **19**, **3**, T63-T72 (1966), in Japanese.

Kase, S., "Studies on Melt Spinning. III. Velocity Field within the Thread", *J. Appl. Polym. Sci.*, **18**, 3267-3278 (1974).

Kase, S. and J. Katsui, "Analysis of Melt Spinning Transients in Lagrangian Coordinates", *Rheol Acta* **24**(1), 34-43 (1985).

Keller, H.B., "Numerical Solution of Bifurcation and Nonlinear Eigenvalue Problems", *Applications of Bifurcation Theory*, Academic, New York (1977).

Keunings, R., M.J. Crochet and M.M. Denn, "Profile Development in Continuous Drawing of Viscoelastic Fluids", *Ind. Eng. Chem. Fundamentals*, **22**, 347. (1983).

Khagram, M., R.K. Gupta and T. Sridhar, *J. Rheol.*, **29**(2), 191. (1985).

King, R.C., "Stable and Convergent Finite Element Methods for the Calculation of Viscoelastic Flows in Smooth Geometries", Ph.D. Thesis, Massachusetts Institute of Technology, Cambridge, Massachusetts (1987).

King, R.C., M.R. Apelian, R.C. Armstrong and R.A. Brown, "Numerically Stable Finite Element Calculations in Smooth and Singular Geometries", *J. Non-Newtonian Fluid Mech.*, **29**, 147-216 (1988).

Kirkwood, J.G. and P.L. Auer, *J. Chem. Phys.*, **19**, 281. (1951).

Kubicek, M., "Dependence of Solution of Nonlinear Equations on a Parameter", *Ass. Comput. Trans. Math. Software*, **2**, 98. (1976).

Lamb, P., "Analysis of Fabrication Processes", *Advances in Polymer Science and Technology*, SCI monograph 26, 296., SCI, London, England (1967).

Larson, R.G. and H. Ottinger, "Effect of Molecular Elasticity on Out-of-plane Orientations in Shearing Flows of Liquid-crystalline Polymers", *Macromolecules*, **24**, 6270-6282 (1991).

Leslie, F.M., "Theory of Flow Phenomena in Liquid Crystals", *Advances in Liquid Crystals*, **4**, 1-81 (1979).

Mackay, M.E. and C.J.S. Petrie, "Estimates of Apparent Elongational viscosity using the Fiber Spinning and 'Pure' methods", *Rheol. Acta*, **28**, 281-293 (1989).

Maier, W. and A. Saupe, *Z. Naturforsch*, **13a**, 564. (1958); **14a**, 882. (1959).

Marchal, J.M. and Crochet, M.J., "A New Mixed Finite Element Method for Calculating Viscoelastic Flow", *J. Non-Newtonian Fluid Mech.*, **26**, 77-114 (1987).

Marrucci, G., *Trans. Soc. Rheol.*, **16**, 32. (1972).

Marrucci, G., "Rheology of Rodlike Polymers in the Nematic Phase with Tumbling or Shear Orientation", *Macromolecules*, **24**, 4176-4182 (1991).

Matovich, M.A. and J.R.A. Pearson, "Spinning a Molten Threadline: Steady-state Isothermal Viscous Flows", *Ind. Eng. Chem. Fundamentals*, **8**, 512-519 (Aug 1969).

Mendelson, M.A., P.W. Yeh, R.A. Brown and R.C. Armstrong, "Approximation Error in Finite Element Calculations of Viscoelastic Fluid Flows", *J. Non-Newtonian Fluid Mech.*, **10**, 31-54 (1982).

Menon, R.K., "Kinetic theory, Rheology and Complex Flows of Liquid-crystalline Polymers", Ph.D. Thesis, Massachusetts Institute of Technology, Cambridge (1990).

Metzner, A.B. and G.M. Prilutski, "Rheological Properties of Polymeric Liquid-crystals", *J. Rheol.*, **30**, 661-691 (1986).

Meyer, R.B., F. Lonberg, V. Taratuta, S. Fraden, S. Lee and A.J. Hurd, "Measurements of the Anisotropic Viscous and Elastic Properties of Lyotropic Polymer Nematics," *Farad. Discuss. Chem. Soc.*, **79**, 125. (1985).

Michael, D.H., "The Separation of a Viscous Liquid at a Straight Edge", *Mathematika*,

5, 82. (1958).

Moffatt, H.K., "Viscous and Resistive Eddies near Sharp Corners", *J. Fluid Mech.*, **18**, 1-18 (1964).

Moldenaers et al., "Flow-induced Anisotropy and its Decay in Polymeric Liquid Crystals", *J. Rheol.*, **35**(8), 1681-1699 (1991).

Nayak, R., personal communications (1993).

Nickell, R.E., R.I. Tanner and B. Caswell, *J. Fluid Mech.*, **65**, 189. (1974).

Onogi, Y., J.L. White and J.F. Fellers, "Rheology and Rheo-optics of Polymer Liquid Crystals", *J. Non-Newtonian Fluid Mech.*, **7**, 121-151 (1980).

Onsager, L., "Effects of Shape on the Interaction of Colloidal Particles", *Ann. N.Y. Acad. Sci.*, **51**, 627. (1949).

Parodi, O., "Stress Tensor for Nematic Liquid-Crystals", *J. Phys.* (Paris), **31**, 581. (1970).

Pearson, J.R.A. and M.A. Matovich, "Spinning a Molten Threadline: Stability", *Ind. Eng. Chem. Fundamentals*, **8**, 605-609 (1969).

Pearson, J.R.A., *Mechanics of Polymer Processing*, Elsevier Applied Science Publishers, London (1985).

Pearson, J.R.A., Y.T. Shah and R.D. Mhaskar,"On the Stability of Fiber Spinning of Freezing Liquids", *Ind. Eng. Chem. Fundamentals*, **15**, 31. (1976).

Petrie, C.J.S. and M.M. Denn, "Instabilities in Polymer Processing", *AIChE J.*, **22**(2), 209. (1976).

Phan-Thien, N., "A Nonlinear Network Viscoelastic Model", *J. Rheol.*, **22**, 259-283 (1978).

Picken, S.J., J. Aerts, R. Visser, and M.C. Northolt, "Structure and Rheology of Aramid Solutions: X-ray Scattering Measurements", *Macromolecules*, **23**, 3849-3854 (1990).

Press, W.H., B.P. Flannery, S.A. Teukolsky and W.T. Vetterling, *Numerical Recipes: The Art of Scientific Computing*, Cambridge University Press, Cambridge (1986).

Press, W.H. and S.A. Teukolsky, "Integrating Stiff Ordinary Differential Equations", *Computers in Physics*, 88-91 (May/Jun 1989).

Prilutski, G.M., "The Rheology of Polymeric Liquid-crystals", Ph.D. Thesis, University of Delaware, Newark (1984).

Prilutski, G.M., personal communications (1991).

Quinzani, L.M., "Birefringence Studies of Entry Flows of Concentrated Polymer Solutions", Ph.D. Thesis, Massachusetts Institute of Technology, Cambridge, Massachusetts (1991).

Rajagopalan, D., R.C. Armstrong and R.A. Brown, "Finite Element Methods for Calculation of Steady, Viscoelastic Flow Using Constitutive Equations with a Newtonian Viscosity", *J. Non-Newtonian Fluid Mech.*, **36**, 159-192 (1990).

Ramalingam, S., "On the Fiber Spinning of Liquid-crystalline Polymers", Ph.D. Thesis Proposal, Massachusetts Institute of Technology, Cambridge, Massachusetts (1990).

Renardy, M., "Existence of Slow Steady Flows of Viscoelastic Fluids with Differential Constitutive Laws", *Z. Angnew. Math. u. Mech.*, **65**, 449-451 (1985).

Renardy, M., W.J. Hrusa and J.A. Nohel, *Mathematical Problems in Viscoelasticity*, John Wiley and Sons, Inc., New York (1987).

Richardson, S., "A 'Stick-Slip' Problem Related to the Motion of a Free Jet at Low Reynolds Number", *Proc. Camb. Phil. Soc.*, **67**, 477-489 (1970).

Rutledge, G.C., "The Solid State Structure and Properties of Stiff Chain Aramids", Ph.D. Thesis, Massachusetts Institute of Technology, Cambridge, Massachusetts (1990).

Samulski, E.T. and D.B. Du Pre, "Polymeric Liquid Crystals", *Advances in Liquid Crystals*, **4**, G.H. Brown, Academic, NY (1979).

Samulski, E.T., "Molecular Structure and Liquid Crystallinity", *Farad. Discuss. Chem. Soc.*, **79**, 7. (1985).

Schreiber, R. and H.B. Keller, "Spurious Solutions in Driven Cavity Calculations", *J. Comp. Phys.*, **49**, 165. (1983).

See, H., M. Doi and R.G. Larson, "The Effect of Steady Flow Fields on the Isotropic-nematic Phase Transition of Rigid Rod-Like Polymers", *J. Chem. Phys.*, **92**, 792-800 (1990).

Shah, Y.T. and J.R.A. Pearson, "Stability of Fiber Spinning of Power-law Fluids", *Poly. Eng. Sci.* **12**, 219-223 (1972).

Shah, Y.T. and J.R.A. Pearson, "On the Stability of Non-isothermal Fiber Spinning-General Case", *Ind. Eng. Chem. Fundamentals.*, **11**, 150-153 (1972).

Shah, Y.T. and J.R.A. Pearson, "On the Stability of Isothermal and Nonisothermal Fiber Spinning of Power-law Fluids", *Ind. Eng. Chem. Fundamentals.*, **13**, 134-138 (1974).

Spearot, J.A. and A.B. Metzner, "Isothermal Spinning of Molten Polyethylenes", *Trans. Soc. Rheol.* **16**, 495-518 (1972).

Sridhar, T., Gupta, R.K. and J. Puszynksi, "Steady Spinning of the Oldroyd Fluid B: I. Theory", *J. Non-Newtonian Fluid Mech.*, **21**, 99. (1986).

Sridhar, T., R.K. Gupta, D.V. Boger and R. Binnington, "Steady Spinning of the Oldroyd Fluid B. II. Experimental Results", *J. Non-Newtonian Fluid Mech.*, **21**, 115-126 (1986).

Strang, G. and G.J. Fix, *An Analysis of the Finite Element Method*, Prentice-Hall, New Jersey (1973).

Sturges, L.D., "Die Swell: The Separation of the Free Surface", *J. Non-Newtonian Fluid Mech.*, **6**, 155-159 (1979).

Suto, S., H. Gotoh, W. Nishibori, and M. Karasawa, "Rheology of Liquid-crystalline Solutions of Hydroxypropyl Cellulose in m-Cresol", *J. Appl. Polym. Sci.*, **37**, 1147-1151 (1989).

Szeri, A.G. and L.G. Leal, "A New Computational Method for the Solution of Flow Problems of Microstructured Fluids: Part II. Inhomogenous Shear Flow of a Suspension", submitted *J. Fluid Mech.* (1993).

Teman, R., *Navier-Stokes Equations*, North Holland, New York (1979).

Thomasset, F., *Implementation of Finite Element Methods for Navier-Stokes Equations*, Springer-Verlag, New York (1981).

Trogdon, S.A. and D.D. Joseph, "The Stick-Slip Problem for a Round Jet: II. Small Surface Tension", *Rheologica Acta*, **20**(1), 1-13 (1981).

Tsou, J. and D.C. Bogue, *J. Non-Newtonian Fluid Mech.*, **17**, 331. (1985).

Tsiveriotis K. and R.A. Brown, "Solution of Free Boundary Problems Using Finite-Element/Newton Methods and Locally Refined Grids: Application and Analysis of Solidification Microstructure", *Int. J. Num. Meth. Fluids*, (1992).

van Shaftingen, J.J. and M.J. Crochet, *Int. J. Num. Meth. Fluids*, **4**, 1065. (1984).

Vassilatos, G., "On the Stability of Drawdown of Polymer Melts", presented at 68th Annual Meeting *AIChE*, Los Angeles, California (1975).

White, J.L. and J.F. Fellers, "Macromolecular Liquid-crystals and their Application to High-Modulus and Tensile-Strength Fibers", *J. Appl. Polym. Sci.: Appl. Polym. Symp.*, **33**, 137. (1978).

White, J.L., *Polymer Engineering Reviews*, **I**(4), 299. (1981).

Whitham, G.B., *Linear and Nonlinear Waves*, John Wiley and Sons (1973).

Wissbrun, K.F., "Rheology of Rod-like Polymers in the Liquid-crystalline State", *J. Rheol.*, **25**, 616. (1981).

Yang, H.H., *Kevlar Aramid Fiber*, Wiley, New York (1993).

Yeh, P.W., Kim-E, R.C. Armstrong and R.A. Brown, "Mutiple Solutions in the Calculation of Axisymmetric Contraction Flow of an Upper-Convected Maxwell Fluid", *J. Non-Newtonian Fluid Mech.*, **16**, 173-194 (1984).

Zeichner, G.R., "Spinnability of Viscoelastic Fluids", M.Ch.E. Thesis, University of Delaware, Newark (1973).

Ziabicki, A., *Fundamentals of Fiber Formation*, Wiley, New York (1976).

Ziabicki, A. and K. Kedzierska, "Mechanical Aspects of Fiber Spinning Process in Molten Polymers I. Stream Diameter and Velocity Distribution Along the Spinning Way", *Koll. Z.*, **171**, 51. (1960).

Appendix A

Die Swell Singularity Analysis for a Newtonian Fluid

Many mathematical models for viscoelastic flows of commercial interest contain regions where the local velocity gradients and stresses become large and in some cases infinite due to the presence of sharp corners or abrupt changes in the boundary data. These flow singularities complicate both the mathematical and numerical analysis of a given flow configuration. One such singularity is encountered at the die exit. Figure A.1 shows the flow through a channel and the subsequent die swell flow of the free jet. The flow singularity occurs due to an abrupt change in the boundary condition from no-slip on the channel wall to shear free on the extrudate free surface.

It is believed that the computational difficulties in calculating extrusion flows of Newtonian and viscoelastic liquids are caused by this flow singularity (Apelian, 1987; Crochet and Keunings, 1980; and Crochet and Keunings, 1982). Figures A.2 and A.3 show the stress contours from the calculations of Apelian (1987) and Crochet and Keunings (1980) for the planar die swell of a Newtonian and a UCM fluid respectively, close to the singularity. The Newtonian stress fields, which are in the limit of zero surface tension, contain oscillations near the singularity that propagate downstream. The oscillations are most severe in the shear stress along the free surface. Figure A.3 illustrates the oscillations in the pressure, shear stress and longitudinal stress at De=0 (the Newtonian model is recovered in this limit) and De=0.5 for the UCM model. The

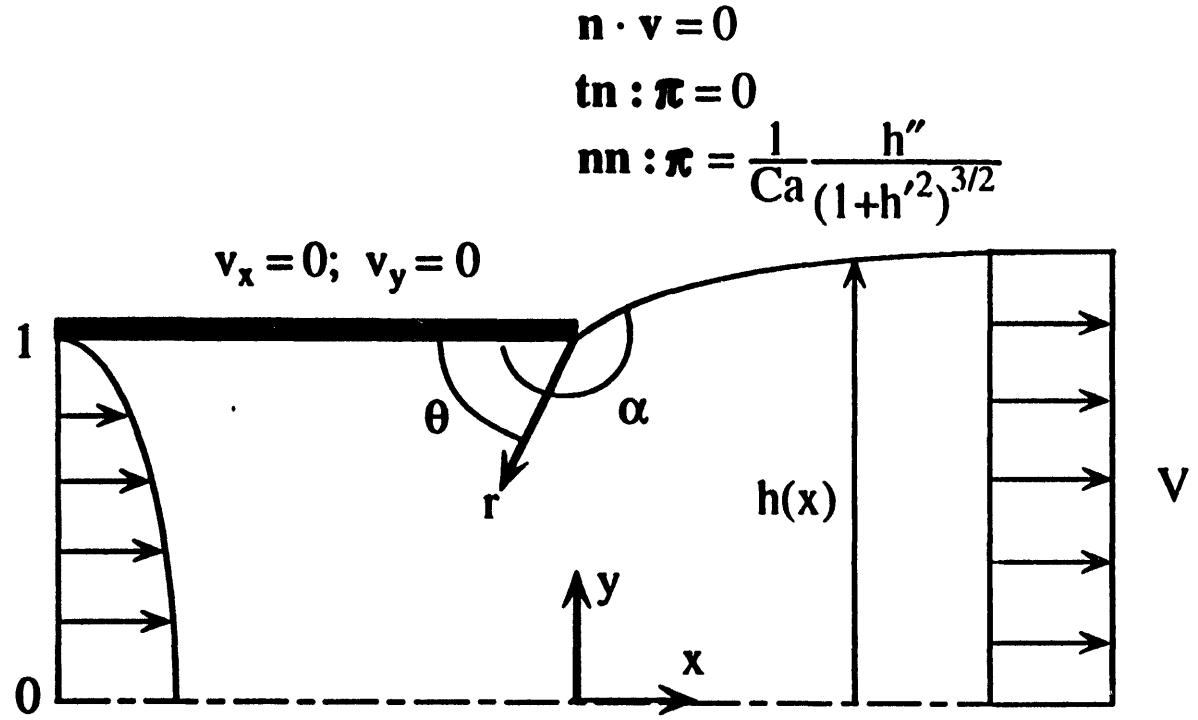

Figure A.1: Planar die swell with the boundary conditions of interest to the local singularity analysis are shown. The free surface height h(x) and the free surface exit angle α are also indicated. The downstream fully developed velocity is V.

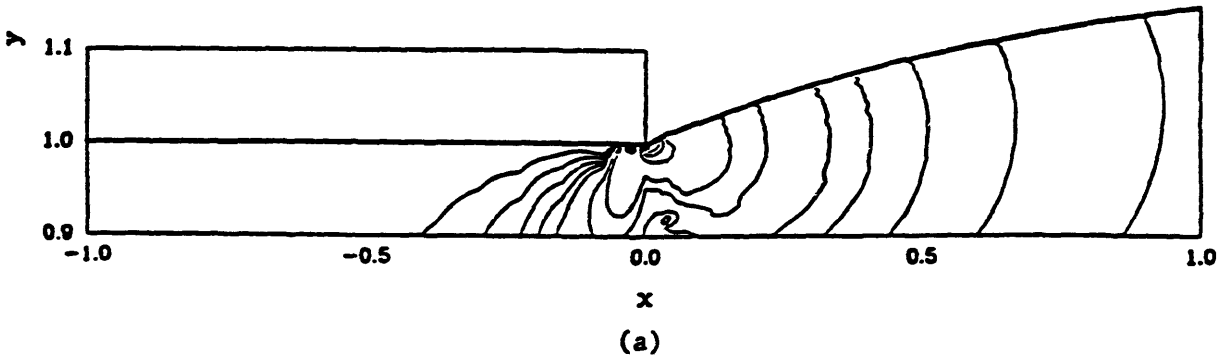

(a)

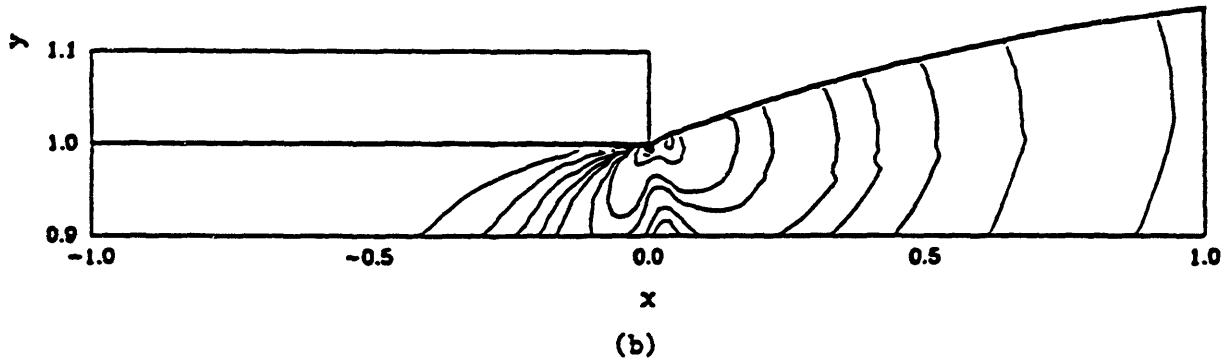

(b)

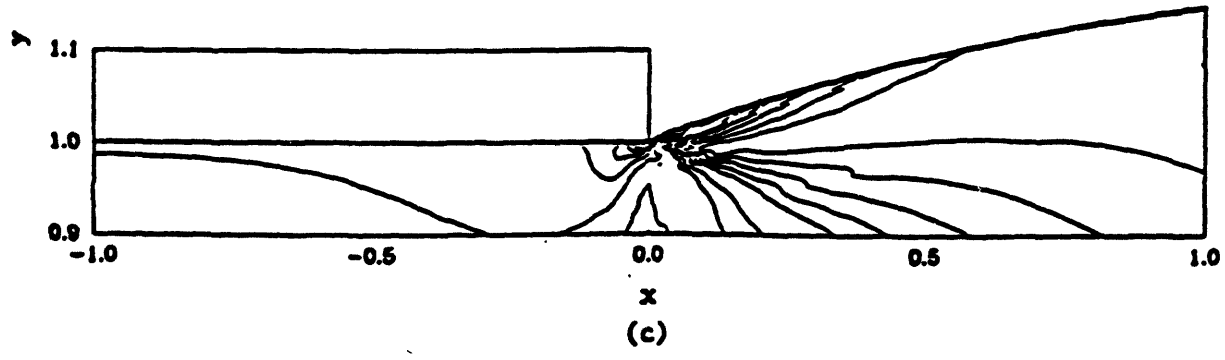

(c)

Figure A.2: Contours of (a) τ_{xx}, (b) τ_{yy} and (c) τ_{yx} for the planar die swell of a Newtonian fluid close to the singularity. Results are in the limit of zero surface tension (reproduced from Apelian, 1987).

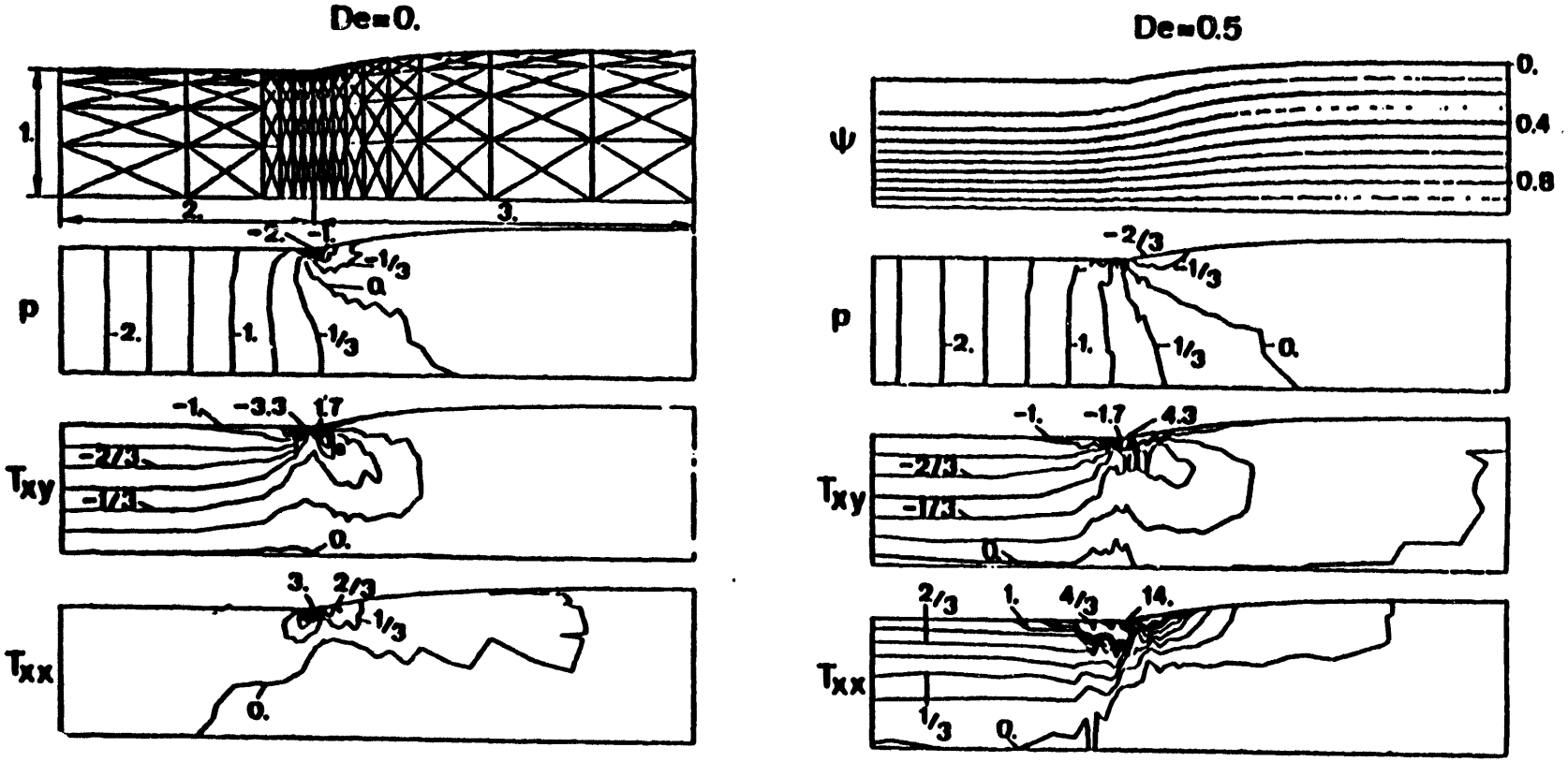

Figure A.3: Contour plots of (a) pressure, (b) τ_{yx} and (c) τ_{xx} for the planar die swell of a UCM fluid close to the singularity. Results are shown for De=0.0 (Newtonian limit) and De=0.5. The finite element mesh and streamlines for De=0.5 are also shown (reproduced from Crochet and Keunings, 1980).

oscillations worsen as De is increased to 0.5 and also propagate further downstream as compared to the Newtonian limit. As mentioned in Chapter 6, it is the lack of understanding of this singular behavior that is the outstanding issue in carrying out two-dimensional finite element calculations for the entire fiber spinning process in which the upstream spinneret flow and the downstream fiber drawing flow are coupled through the die swell.

Apelian (1987) reports a final swell ratio, $h(x=\infty)$ (according to the notation in Fig. A.1), of 1.19 for a Newtonian fluid in the limit of zero surface tension on a mesh whose smallest element size near the die exit is 0.01. Crochet and Keunings (1982) and Silliman and Scriven (1979) report the same final swell ratio on meshes whose element sizes are much coarser near the die exit. Thus, the final die swell appears to be insensitive to the propagation of information from the die swell singularity; this result is not surprising since the Newtonian fluid in the absence of inertia is associated with purely viscous effects which are dissipated in a small region close to the singularity. The final swell ratio computed for the viscoelastic MUCM model by Apelian (1987) as a function of De and for different meshes is shown in Figure A.4; the capillary number Ca=0.015 used in these calculations corresponds to a large surface tension effect. The smallest element sizes close to the singularity for meshes M4 and M5 used by Apelian are 0.01 and 0.005 respectively; mesh M6 has twice the discretization in the x-direction as mesh M5 close to the singularity. The results in Fig. A.4 demonstrate the sensitivity of the final swell ratio to the mesh refinement close to the singularity as De increases; that is, the downstream flow is affected by the propagation of information from the singularity for

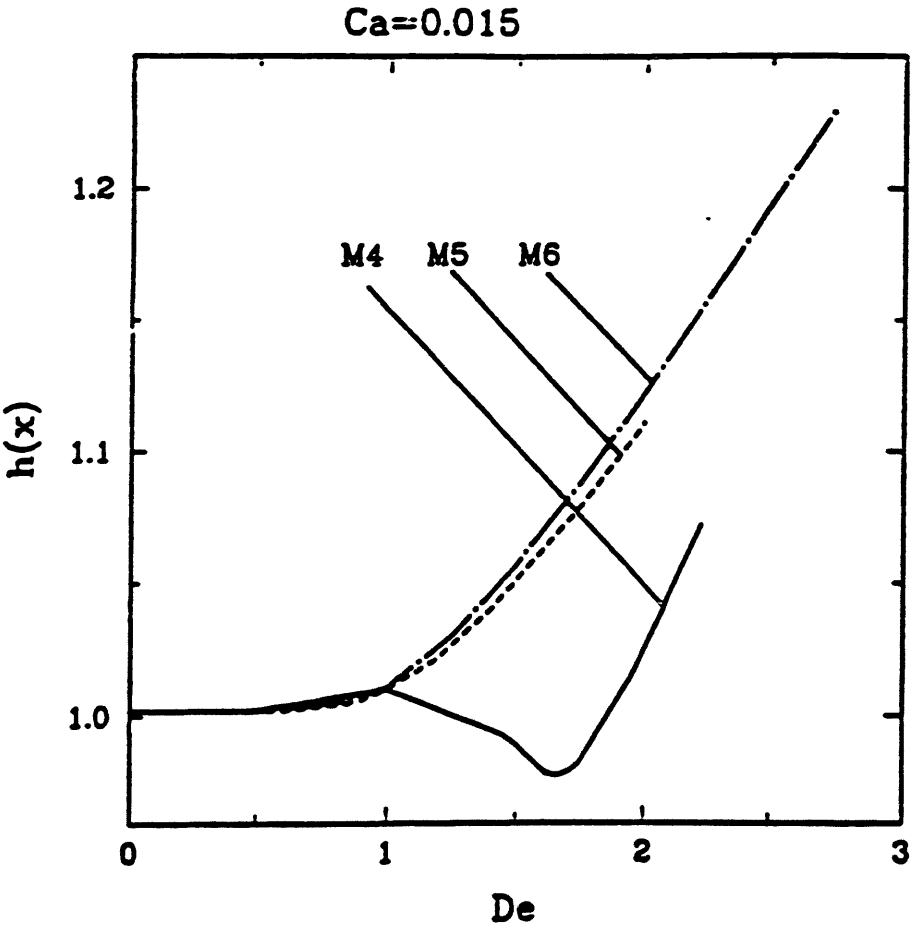

Figure A.4: The effect of mesh refinement close to the singularity and De on the final swell ratio, h(x=∞), for the planar die swell of a MUCM fluid. The capillary number Ca=0.015 in these calculations. The smallest element size close to the singularity for meshes M4 and M5 are 0.01 and 0.005 respectively; mesh M6 has twice the discretization as mesh M5 in the x-direction close to the singularity (reproduced from Apelian, 1987).

the viscoelastic MUCM model. Consequently, accurate treatment of the singularity is necessary in modeling viscoelastic die swell flows.

The analyses by Dean and Montagnon (1949) and Moffat (1964) elucidate the singularity associated with a Newtonian flow past a sharp corner. Experimental data for the 5.0% PIB in C14 (Quinzani, 1991) near the reentrant corner in a planar contraction flow shows excellent agreement with the predictions of the Newtonian model (Coates, 1992) which leads one to hypothesize that the Newtonian singular behavior is dominant in polymer solutions even at the die exit. Asymptotic analyses for constitutive equations such as the MUCM, PTT and the liquid-crystal model discussed in this thesis, also suggest that the Newtonian singular behavior should be dominant at the die exit for these models. However, the dominant Newtonian singular behavior itself is not known for the die swell problem except under limiting conditions. One such limit is the stick-slip or the infinite surface tension limit. In fact, in the stick-slip limit, the finite element calculations of Apelian (1987) show that the MUCM model exhibits a dominant Newtonian singular behavior close to the die exit which confirms the predictions of the asymptotic analysis. For all these reasons, understanding the Newtonian die swell singularity would definitely result in more effective treatment of the singularity in viscoelastic flow calculations.

The aim of this section is to define the governing equations and boundary conditions associated with the Newtonian die swell singularity problem, summarize the work on the understanding of the die swell singularity, examine their regions of validity and finally present an analysis that is possibly more general in scope than the analyses

to date.

A.1 Die swell Problem Description

The fiber spinning flow discussed in this thesis is cylindrically symmetric, *i.e.* axisymmetric. However, the die swell singularity analyses in the literature are confined to a flow that is planar perpendicular to the page due to the analytical tractability using a separable expansion for the stream function of the form proposed by Dean and Montagnon (1949). The singular behavior in the stresses predicted by these analyses, however, is not expected to be different for axisymmetric flow since these are local analyses and close from any point on the circular die orifice the flow is expected to appear locally planar. Hence, the discussion in this section is restricted to planar die swell. A planar two-dimensional die swell is illustrated in Fig. A.1. A more restrictive assumption used in some of the singularity analyses is neglect of curvature in the plane of the page, whence, surface tension forces do not play a role in the normal force balance on the free surface. All the analyses also assume that inertial effects are unimportant near the singularity.

The x and y coordinates in Fig. A.1 have been nondimensionalized with half the channel width. The dimensionless free surface height is given by $h(x)$. Both velocity components are made dimensionless with the fully developed plug flow velocity, V, at the exit. The governing equation and boundary conditions relevant to the local singularity analysis are then

Governing equation

No slip and no penentration

$$v_x = -\frac{\partial \psi}{\partial y} = 0; \quad v_y = \frac{\partial \psi}{\partial x} = 0 \quad \text{on } y = 1, x \le 0 \tag{A.2}$$

By noting that the normal and tangent unit vectors to the free surface are given by

$$n = \frac{1}{(1+(\frac{dh}{dx})^2)^{\frac{1}{2}}}[-\frac{dh}{dx}e_x + e_y]; \quad t = \frac{1}{(1+(\frac{dh}{dx})^2)^{\frac{1}{2}}}[e_x + \frac{dh}{dx}e_y] \tag{A.3}$$

the boundary conditions on the free surface can be written as

Kinematic constraint

$$v_x - \frac{dh}{dx}v_y = 0 \text{ or } \frac{\partial \psi}{\partial x} + \frac{dh}{dx}\frac{\partial \psi}{\partial y} = 0; \text{ on } y = h(x), x \ge 0 \tag{A.4}$$

Zero shear stress

$$4\frac{\partial v_y}{\partial y}\frac{dh}{dx} + (\frac{\partial v_y}{\partial x} + \frac{\partial v_x}{\partial y})(1-(\frac{dh}{dx})^2) = 0$$

or (A.5)

$$4\frac{\partial^2 \psi}{\partial x \partial y}\frac{dh}{dx} + (\frac{\partial^2 \psi}{\partial x^2} - \frac{\partial^2 \psi}{\partial y^2})(1-(\frac{dh}{dx})^2) = 0 \text{ on } y = h(x),\ x \ge 0$$

Normal stress balance

$$\frac{1}{Ca}\frac{\frac{d^2h}{dx^2}}{(1+(\frac{dh}{dx})^2)^{\frac{3}{2}}} = p - 2\frac{\frac{\partial v_y}{\partial y}(1-(\frac{dh}{dx})^2) - (\frac{\partial v_y}{\partial x} + \frac{\partial v_x}{\partial y})\frac{dh}{dx}}{1+(\frac{dh}{dx})^2} \text{ on } y = h(x), x \ge 0$$

or

$$\frac{1}{Ca}\frac{\frac{d^2h}{dx^2}}{(1+(\frac{dh}{dx})^2)^{\frac{3}{2}}} = p - 2\frac{\frac{\partial^2\psi}{\partial x\partial y}(1-(\frac{dh}{dx})^2)-(\frac{\partial^2\psi}{\partial x^2}-\frac{\partial^2\psi}{\partial y^2})\frac{dh}{dx}}{1+(\frac{dh}{dx})^2} \text{ on } y = h(x), x\geq 0 \quad \text{(A.6)}$$

where Ca = ($\mu V/\sigma_s$). Here, μ is the viscosity, V is the fully developed downstream velocity and σ_s is surface tension. It is common to determine the singular behavior in the stresses in the polar (r,θ) coordinate system indicated in Fig. A.1. The change from (x,y) to (r,θ) is achieved through the transformation $x = -r\cos\theta$ and $y = 1 - r\sin\theta$. The partial differential operators are related as follows

$$\frac{\partial}{\partial x} = \cos\theta\frac{\partial}{\partial r} - \frac{\sin\theta}{r}\frac{\partial}{\partial\theta}; \quad \frac{\partial}{\partial y} = \sin\theta\frac{\partial}{\partial r} + \frac{\cos\theta}{r}\frac{\partial}{\partial\theta} \quad \text{(A.7)}$$

A.2 Overview of Singularity Analyses in Literature

A.2.1 Michael's (1958) Analysis without Surface Tension

Michael postulated that the intersection of the free surface and the plane of the page is a straight line close to the die exit, and he implicitly discounts surface tension in the normal force balance. The free surface emerges at an unknown angle α (Fig. A.1) which is to be determined from the governing equation, Eq. A.1, and the boundary conditions, Eqs. A.2, A.4, A.5 and A.6, cast in polar coordinates. The biharmonic governing equation for the stream function admits solutions of the form

$$\psi = \sum_{n=1}^{\infty} r^{\lambda_n + 1} f_n(\theta) \tag{A.8}$$

where

$f_n(\theta) = [A_n \sin(\lambda_n + 1)\theta + B_n \cos(\lambda_n + 1)\theta + C_n \sin(\lambda_n - 1)\theta + D_n \cos(\lambda_n - 1)\theta]$

and λ_n is the eigenvalue associated with the index n such that $0<\lambda_1<\lambda_2<\cdots<\lambda_n<\cdots$ and A_n, B_n, C_n and D_n are arbitrary constants. Michael showed that for the above solution to satisfy the boundary conditions non trivially, $\sin\alpha = 0$. For $\alpha = \pi$, which is the mode of practical significance in this problem, the dominant eigenvalue λ_1 is 1/2. The corresponding dominant asymptotic behavior in the stresses is $\tau \sim T(\theta)\, r^{-1/2})$ as $\frac{r}{r} \rightarrow 0$. The force per unit width of the boundary into the plane of the page is given by $\int_0 \tau_{ij} dr$.

Thus, the $r^{-1/2}$ behavior in the stresses results in a finite force at the singularity.

A.2.2 Richardson's (1970) Analysis - Stick-slip Problem (Ca → 0)

The problem described in Section A.1 reduces to the stick-slip problem in the limit of infinite surface tension (Ca → 0). In the stick-slip limit (Fig. A.5) the normal stress balance on the free surface given by Eq. A.6 is not considered. By using the separable expansion for ψ given by Eq. A.8, enforcing the no-slip and no-penetration conditions at $\theta=0$, and requiring the kinematic constraint and the zero shear stress condition at $\theta=\pi$, Richardson demonstrated that the dominant term in the neighborhood of the singularity is $O(r^{-1/2})$. Solutions with a more singular behavior e.g., $O(r^{-3/2})$, are theoretically possible but are excluded on physical grounds since they involve a infinite force at the singularity.

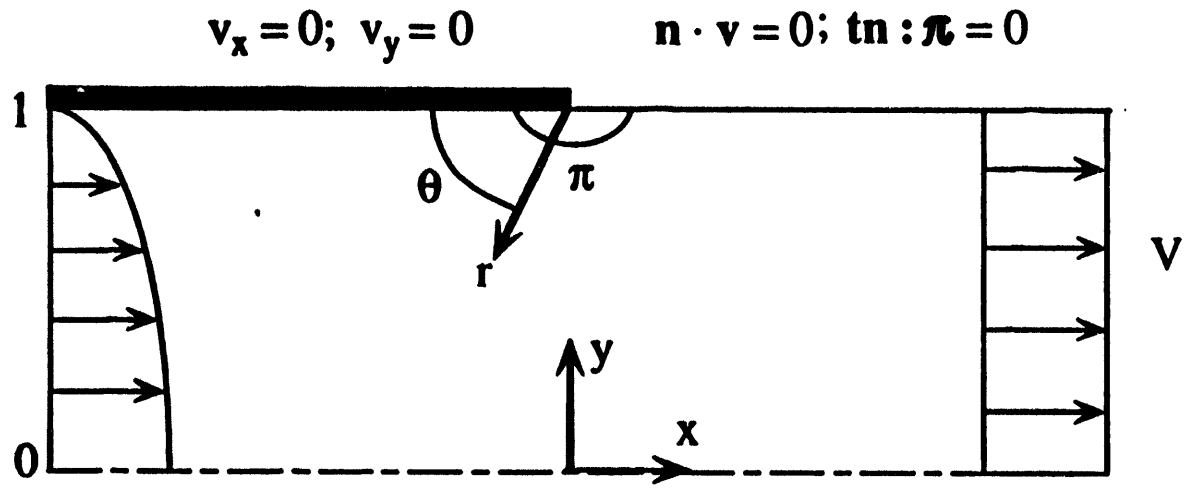

Figure A.5: The stick-slip problem with the boundary conditions of interest to the local singularity analysis are shown. The downstream fully developed velocity is V.

A.2.3 Sturges's (1979) Analysis - Any Surface Tension

Michael's analysis presumes that the free surface is planar in which case the curvature is not a factor in the normal stress balance. Sturges argues that the planar free surface assumption may not be valid, however, for the die swell problem. Sturges postulates that with the curvature unrestricted, instead of using Eq. A.6 as a boundary condition in the local analysis it could be used to determine the free surface shape once ψ is found. Based on this postulate and the fact that the kinematic constraint and the zero shear stress condition on the free surface can be applied on the tangent plane $\theta=\alpha$ for small r, he obtains the following eigenvalue equation for λ

$$\lambda_n \sin 2\alpha - \sin 2\alpha \lambda_n = 0 \text{ where } n = 1,2,\cdots \qquad \text{(A.9)}$$

on using the separable expansion for ψ given by Eq. A.8 and also enforcing the no slip and no penetration conditions on the wall. The angle α is as indicated in Fig. A.1. Sturges claims that since it is not possible to determine α or the constants in the expansion for ψ without additional boundary conditions, the quantities must be determined from the global flow geometry. Thus Sturges's analysis suggests that the local analysis is insufficient to determine α when curvature is included. Eq. A.9 predicts the worst singularity ($O(r^{-2/3})$) for $\alpha = 3\pi/2$. Michael's result ($O(r^{-1/2})$) is obtained at $\alpha=\pi$. Though Sturges's observation that the die swell free surface need not be plane is accurate, it is not clear why α cannot be determined by a local analysis if the normal stress balance is included as a boundary condition as in the analysis of Michael. This aspect is examined in Section A.4.

A.2.4 Trogdon and Joseph (1981) Analysis - Arbitrary Surface Tension

Trogdon and Joseph (1981) use a different approach from Sturges to deal with the die swell free surface curvature. Exploiting the fact that the Newtonian die swell is small, 12-13 % of the channel width, they postulate a Taylor series expansion for the field variables (generally denoted by V_j) on the free surface which takes the following form

$$V_j(x,h(x)) = V_j(x,1) + (h(x)-1)\frac{\partial V_j}{\partial y}(x,1) + O((h(x)-1)^2) \tag{A.10}$$

Note that near the singularity the Taylor series must be demonstrated to be convergent since the expansion would be singular due to the velocity gradient and higher order derivatives growing to infinity. They then introduce the following new variables

$$\begin{aligned} \hat{\psi} &= \psi - \psi_0 \\ \hat{p} &= p - p_0 \\ \hat{v}_x &= v_x - v_{x,0} \\ \hat{v}_y &= v_y \end{aligned} \tag{A.11}$$

where $(\cdot)_0$ refers to the downstream fully developed solution. They also apply the free surface boundary conditions at y=1 since $h(x)-1<<1$. The governing equations and the linearized boundary conditions derived by Trogdon and Joseph in terms of these new variables are

Governing Equation

$$\nabla^4\hat{\psi} = 0 \tag{A.12}$$

No slip and no penetration

$$\frac{\partial\hat{\psi}}{\partial y} = \frac{\partial\hat{\psi}}{\partial x} = 0 \quad \text{on } y = 1, \ x\leq 0 \tag{A.13}$$

Kinematic constraint

$$\frac{\partial \hat{\psi}}{\partial x} - \frac{dh}{dx} v_{x,0} = 0 \quad \text{on } y = 1, \ x \geq 0 \tag{A.14}$$

The above equation assumes that $v_x = v_{x,0}$ even for $x \rightarrow 0$ which is invalid since the continuity in the velocity at the die exit would require $v_x = 0$.

Zero shear stress condition

$$\frac{\partial^2 \hat{\psi}}{\partial x^2} - \frac{\partial^2 \hat{\psi}}{\partial y^2} = 0 \quad \text{on } y = 1, \ x \geq 0 \tag{A.15}$$

Eq. A.15 assumes that $dh/dx \ll 1$.

Normal stress balance

$$\frac{1}{Ca v_{x,0}} \frac{\partial^2 \hat{\psi}}{\partial x^2} = p - 2 \frac{\partial^2 \hat{\psi}}{\partial x \partial y} \quad \text{on} \quad y = 1, \ x \geq 0 \tag{A.16}$$

The kinematic constraint has been used to express d^2h/dx^2 in terms of the modified stream function. Eq. A.16 also assumes that $dh/dx \ll 1$. After making the transformation to polar coordinates, as discussed in Section A.1, Trogdon and Joseph arrive at the conclusion that the dominant singular behavior in the stress is $O(r^{-1/2})$ for any surface tension. Applying the free surface boundary conditions on $y=1$ or $\theta=\pi$ along with the *a priori* assumption $dh/dx \ll 1$ leads to $\alpha=\pi$ (Fig. A.1 notation). As mentioned earlier, the expansion in Eq. A.10 is singular when velocity derivatives are involved and it is necessary to demonstrate that the series expansion is convergent, *i.e.* since the series would be in powers of r, for small r, close to the singularity it is sufficient to show that terms involving higher order derivatives are negligible compared to terms involving lower order derivatives. Trogdon and Joseph do not address this issue. However, the final result they obtain, as will be shown in Section A.3, does lead to a convergent expansion.

Employing the linearization implied by the expansion in Eq. A.10, Trogdon and

Joseph have solved the die swell problem over the entire domain by using an eigenfunction expansion for the axisymmetric problem; the eigenfunction expansions are expressed in terms of Bessel functions in the radial direction and exponentially decaying functions in the axial direction. From this analysis they conclude that the shear stress on the boundary of the pipe is insensitive to changes in the surface tension parameter as the exit plane is approached and that the singular behavior is not inconsistent with the predictions of the local analysis. Their eigenfunction expansion also indicates that the free surface slope goes to zero as $x \rightarrow 0$ for any surface tension which is consisent with the local analysis.

A.3 A Linearized Analysis of the Die swell Singularity

It is clear that the assumptions leading to Eqs. A.14, A.15 and A.16 in Trogdon and Joseph's analysis are questionable near the singularity. The axial velocity v_x must approach zero as $x \rightarrow 0$. Also, $(h(x)-1) \ll 1$ can be satisfied without requiring that $dh/dx \ll 1$ close to the die exit. We carry out an analysis paralleling Trogdon and Joseph but without requiring the above assumptions and without introducing the new variables given by Eq. A.11. A power series expansion for $h(x)-1$ or $h(r)-1$ (since variables are linearized about $\theta=\pi$) in r

$$h(r)-1 = h_0 r^{p_0+1} + h_1 r^{p_1+1} + O(r^{p_2+1}) \quad \text{where } p_2>p_1>0 \qquad \text{(A.17)}$$

for small r is arbitrarily introduced to account for curvature effects. The constants $\{h_i\}$ and exponents $\{p_i\}$ are to be determined from the kinematic constraint and the normal stress balance.

A discussion of the linearized approach without the restricting assumptions of Trogdon and Joseph follows. By employing the separable expansion in Eq. A.8 and the no slip and no penetration conditions which are independent of the linearization, the components of the velocity are found to be

$$\begin{aligned} v_y(x,1) &= 2C_1 r^{\lambda_1}\sin\lambda_1\pi + 2C_2 r^{\lambda_2}\sin\lambda_2\pi + \cdots \\ v_x(x,1) &= 2B_1 r^{\lambda_1}\sin\lambda_1\pi + 2B_2 r^{\lambda_2}\sin\lambda_2\pi + \cdots \end{aligned} \tag{A.18}$$

Substituting Eq. A.17 into the kinematic constraint then yields

$$\begin{aligned} O(r^{\lambda_1}): &\quad h_0 = \frac{C_1}{B_1}; \quad p_0 = 0 \\ O(r^{\lambda_2}): &\quad h_1 = \left(\frac{C_2}{B_1(p_1+1)} - \frac{C_1 B_2}{B_1^{\,2}}\right)\frac{\sin\lambda_2\pi}{\sin\lambda_1\pi}; \quad p_1 = \lambda_2 - \lambda_1 \end{aligned} \tag{A.19}$$

It can verified that other choices for p_0 and p_1 cannot be more dominant. The constants and the eigenvalues are yet to be determined. Since this is an eigenvalue problem there will be an arbitrary constant *i.e.* a constant such as B_1 cannot be determined (see Eqs. 1C.3-6 and 1C.3-8 in Bird *et al.* (Vol. 1), 1987 for example). The zero shear stress condition at dominant order gives

$$O(r^{\lambda_1 - 1}): \quad 2\lambda_1 C_1 \sin\lambda_1\pi - \lambda_1 B_1\left(1 - \frac{C_1^{\,2}}{B_1^{\,2}}\right)\cos\lambda_1\pi = 0 \tag{A.20}$$

It is clear that since p_0=0 the dominant term in the expansion for h(x)-1, given by Eq. A.17, does not contribute to the d^2h/dx^2 appearing in the curvature term associated with the normal force due to surface tension. The dominant orders at which the total normal stress associated with the fluid and the surface tension appear are

$$O(r^{\lambda_1-1}): \quad \frac{4}{B_1}\left(1+\frac{C_1^2}{B_1^2}\right)^{-1}\left(2\lambda_1 C_1 \sin\lambda_1\pi - \lambda_1 B_1\left(1-\frac{C_1^2}{B_1^2}\right)\cos\lambda_1\pi\right)$$

$$O(r^{p_1-1}): \quad \frac{1}{Ca}\frac{p_1(p_1+1)h_1}{\left(1+\frac{C_1^2}{B_1^2}\right)^{3/2}} \qquad \text{(A.21a,b)}$$

It is clear that the zero-shear-stress requirement also leads to zero total normal stress associated with the fluid which arises due to the linearization and the subsequent application of the free surface boundary conditions at $\theta=\pi$. It is also clear that the surface tension cannot be involved then in a dominant balance with the total normal fluid stress at $O(r^{\lambda_1-1})$. Now $p_1-1 \le \lambda_i-1$ or $p_1-1 \ge \lambda_1-1$. Note that p_1-1 can never match with the next order in the total normal stress which is $O(r^{\lambda_2-1})$ *i.e.* $p_1-1 = \lambda_2-\lambda_1-1 < \lambda_2-1$ always. Consequently the surface tension is unable to match with the total normal stress associated with the fluid at $O(r^{\lambda_2-\lambda_1-1})$ and Eq. A.21b must be zero *i.e.* $h_1=0$.

Let us next examine the validity of the singular expansion given by Eq. A.10. The expansions for the velocity components are as follows

$$v_y = v_y(x,1) + (h(x)-1)\frac{\partial v_y}{\partial y}(x,1) + (h(x)-1)^2\frac{\partial^2 v_y}{\partial y^2}(x,1) + \cdots \qquad \text{(A.22)}$$

which gives

$$v_y = \underline{2C_1 r^{\lambda_1}\sin\lambda_1\pi} + 2C_2 r^{\lambda_2}\sin\lambda_2\pi + \cdots$$
$$+ \frac{C_1}{B_1}\left(\underline{2B_1\lambda_1 r^{\lambda_1}\sin\lambda_1\pi} + \cdots\right) + \frac{C_1^2}{B_1^2}\left(\underline{O(r^{\lambda_1})} + \cdots\right) + \cdots \qquad \text{(A.23)}$$

$$v_x = v_x(x,1) + (h(x)-1)\frac{\partial v_x}{\partial y}(x,1) + (h(x)-1)^2\frac{\partial^2 v_x}{\partial y^2}(x,1) + \cdots \tag{A.24}$$

which gives

$$v_x = \underline{2B_1 r^{\lambda_1}\sin\lambda_1\pi} + 2B_2 r^{\lambda_2}\sin\lambda_2\pi + \cdots + \frac{C_1}{B_1}(\underline{(-2C_1\lambda_1\sin\lambda_1\pi + 4\lambda_1 B_1\cos\lambda_1\pi)r^{\lambda_1}} + \cdots) + \frac{C_1^2}{B_1^2}(\underline{O(r^{\lambda_1})} + \cdots) + \cdots \tag{A.25}$$

The second, third and other underlined terms in the expansion that are $O(r^{\lambda_1})$ must be neglected compared to the first underlined term if the singular expansion is to be valid at $O(r^{\lambda_1})$. It can be verified that $C_1=0$ leads to $\cos\lambda_1\pi=0$ from the zero-shear-stress condition. $C_1=0$ and the requirement that $h_1=0$ also leads to

$$h(r) - 1 = O(r^{p_2+1}) \quad \text{where } p_2 > \lambda_2 - \lambda_1 \tag{A.26}$$

which might be expected to validate the singular expansions given by Eqs.A.22 and A.24 at $O(r^{\lambda_1})$. However $h_1=0$ also leads to $v_y(x,1)=0$ at $O(r^{\lambda_1})$ from Eq. A.19.

Finally, the validity of the singular expansion must be verified at this order. Continuing the above procedure it can be shown that for the singular expansions to be convergent, $C_n=0$ for all n and consequently $h(r)-1$ must be zero through all orders in r. Other choices besides $C_n=0$ do not appear to satisfy simultaneously the singular expansions for both velocity components.

Thus, a valid linearized set of free surface boundary conditions applied at $\theta=\pi$ leads to the following conclusions: (1) Surface tension cannot be involved in a dominant balance with the total normal stress associated with the fluid. This leads to Michael's result that the dominant behavior in the stress is $O(r^{-1/2})$, (2) The free surface has to emerge parallel to the wall since C_1 is zero. In fact the free surface has zero curvature

since $h(r)$-1 is zero through all orders in r in order for the singular expansion to be valid.

A.4 A Die swell Singularity Analysis without Linearization

The analysis by Sturges shows that if curvature is involved in a dominant balance with the fluid normal stress, the dominant singular behavior varies with α. However, he does not consider the boundary condition on the normal stress in the local analysis and consequently concludes that α and the unknown constants in the stream function expansion can be determined only from the global flow geometry, which is different than the analysis of Michael without curvature, where consideration of the normal stress boundary condition in the local analysis determined α. The aim of this analysis is to determine if a local analysis determines α when curvature is involved in a dominant balance with the total normal stress associated with the fluid, and if not, to propose a scheme that allows α to be determined from the global solution.

The analysis in Section A.3 shows that linearization about $\theta=\pi$ leads to a zero total normal stress associated with the fluid. This decouples surface tension from a dominant balance with the fluid normal stress and leads to the determination of constants $\{h_i\}$ in the series expansion for h(r)-1 in r for small r. When the series expansion given by Eq. A.17 is expanded about the tangent plane $\theta=\alpha$, *i.e.* $h_0=-\sin\alpha$ and $p_0=0$, and is introduced into the kinematic constraint after the no penetration and no slip boundary conditions have been used to eliminate the constants A_i and D_i, we get

$$O(r^{\lambda_1}): \qquad f_1(\alpha) = 0 \tag{A.27}$$

and the constants and exponents in the expansion for $h(r)$-1 are given by

$$O(r^{\lambda_1}): \quad h_0 = -\sin\alpha; \quad p_0 = 0$$
$$O(r^{\lambda_2}): \quad h_1 = \frac{f_2(\alpha)(\lambda_2+1)}{\cos\alpha(p_1+1)f_1'(\alpha)}; \quad p_1 = \lambda_2 - \lambda_1 \tag{A.28}$$

where $f_n(\alpha)$ and $f_n'(\alpha)$ *i.e.* $df_n(\alpha)/d\theta$ are given by

$$f_n(\alpha) = B_n[\cos(\lambda_n+1)\alpha - \cos(\lambda_n-1)\alpha] + C_n[\sin(\lambda_n-1)\alpha - \frac{(\lambda_n-1)}{(\lambda_n+1)}\sin(\lambda+1)\alpha]$$
$$f_n'(\alpha) = B_n[(\lambda_n-1)\sin(\lambda_n-1)\alpha - (\lambda_n+1)\sin(\lambda_n+1)\alpha] + C_n(\lambda_n-1)[\cos(\lambda_n-1)\alpha - \cos(\lambda_n+1)\alpha] \tag{A.29}$$

The zero shear stress condition on the $\theta=\alpha$ plane at dominant order gives

$$O(r^{\lambda_1-1}): \quad f_1''(\alpha) = 0 \tag{A.30}$$

where $f_n''(\alpha)$ is $d^2f_n(\alpha)/d\theta^2$. Equations A.27 and A.30 give the eigenvalue equation

$$\lambda_1\sin2\alpha - \sin2\alpha\lambda_1 = 0 \tag{A.31}$$

which is the same as Eq. A.9 obtained by Sturges but for the dominant eigenvalue.

Evaluating the total normal stress at the free surface associated with the Newtonian fluid at $\theta=\alpha$ gives

$$O(r^{\lambda_1-1}): \quad \frac{4B_1\lambda_1^2(\lambda_1+1)\sin\alpha}{(\lambda_1-1)\sin\lambda_1\alpha} \tag{A.32}$$

which shows that unlike the result obtained with linearization about $\theta=\pi$, the fluid normal stress need not be zero. Surface tension is not decoupled in this case and can be involved in a dominant balance with the fluid normal stress *i.e.* $p_1-1=\lambda_1-1=\lambda_2-\lambda_1-1$. The dominant balance gives

$$O(r^{\lambda_1-1}): \quad \frac{h_1}{B_1} = \frac{4\lambda_1\tan\alpha}{(\lambda_1-1)\sin\lambda_1\alpha}\mathrm{Ca} \tag{A.33}$$

If surface tension is not involved in the dominant balance, then the fluid normal stress must be zero, *i.e.* $\sin\alpha=0$, and Michael's result is obtained. There are only two equations,

Eqs. A.31 and A.33, for four unknowns λ_1, α, B_1 and h_1; Eq. A.28 only relates the coefficients associated with $f_2(\alpha)$ to the coefficients associated with $f_1(\alpha)$. External information is required to determine h_1, α, B_1 and λ_1. The eigenfunction expansion method used by Trogdon and Joseph to solve the die swell problem with the linearization assumption is expected to be satisfactory away from the singularity since the linearized expansions would not be singular and the assumption they use in the kinematic constraint discussed in Section A.2.4 would be acceptable. If h_1 and B_1 are determined from a match with the eigenfunction expansion in the limit of small r, the dominant singular behavior $O(r^{\lambda_1-1})$ and α can be determined from Eqs. A.31 and A.33. Note the appearance of the Ca scaling in Eq. A.33. If the series expansion

$$h(r) - 1 = -\sin\alpha\, r + h_1 r^{\lambda_1+1} + O(r^{p+1}) \quad \text{where } p>\lambda_1 \tag{A.34}$$

is to be valid for small r it is clear that the matching region must shrink to smaller values of r with increasing Ca. That is, $|h_1 r^{\lambda_1+1}| \ll |-r\sin\alpha|$ leads to the condition

$$r^{\lambda_1} \ll \left| \frac{(\lambda_1 - 1)\sin\lambda_1\alpha\cos\alpha}{4\lambda_1 B_1 \mathrm{Ca}} \right| \tag{A.35}$$

The analysis indicates that α (the free surface exit angle) and the dominant singular behavior ($O(r^{\lambda_1-1})$) are different depending on whether or not curvature is involved in a dominant balance with the fluid normal stress. If curvature is not involved in the dominant balance, then the local analysis decides α and λ_1 *i.e.* $\alpha=\pi$ and $\lambda_1=1/2$. If curvature is involved in the dominant balance, then α and λ_1 cannot be decided independently by the local analysis. As suggested, a match with the eigenfunction expansion results of Trogdon and Joseph is a possible way to determine α and λ_1.

An important question that arises from the die swell singularity analysis is whether or not curvature associated with surface tension involved in a dominant balance with the total fluid normal stress close to the singularity. Viscoelastic calculations with the MUCM model (Apelian, 1987), which has a dominant Newtonian singularity, clearly demonstrated the sensitivity of the downstream swell on the accuracy of the stress field close to the die exit (cf. Fig. A.4). Since the dominant Newtonian singular behavior in the stress is different depending on whether or not curvature is involved in a dominant balance with the total fluid normal stress, the above question is expected to have an effect on the downstream swell in viscoelastic calculations. Future work must address this question so that an integrated model that models the die swell region accurately can be developed for the fiber spinning process.

Appendix B

Fiber Drawing Analysis for Liquid-Crystalline Polymers Using Doi's Reptation Time Constant

In Chapter 3, the constitutive equation developed from a kinetic theory framework by Bhave *et al.* (1993) for liquid-crystalline polymers was presented and its viscosity predictions were compared with the predictions of the Doi (1981) model. It was demonstrated that the viscosity predictions of the Bhave *et al.* model was much better than the viscosity predictions of the Doi model; in fact, the Doi model predicts a viscosity that is aphysical at high shear rates. In the original version of the Bhave *et al.* constitutive equation, Menon (1990) retained two choices for the time constant λ; these choices are given by Eq. 3.16. In the current version only the time constant $\lambda=\lambda_0$ is used since the viscosity predictions for this choice of time constant compare better with experimental data than the viscosity predictions with $\lambda=\lambda_0(1-S^2)^2$. Besides, elongational viscosity data obtained by Prilutski (1984) from fiber spinning experiments are limited to small elongation rates and consequently cannot be used to decide which choice of time constant is appropriate in an extensional flow. For these reasons, the fiber drawing calculations and spinneret calculations presented in Chapters 4, 5 and 6 were restricted to the time constant $\lambda=\lambda_0$.

The order dependent time constant $\lambda=\lambda_0(1-S^2)^2$ was first derived by Doi (1981) using reptation arguments for concentrated solutions. This assumes that the rotation of

a rod-like molecule in such a solution is hindered by the presence of other rod-like molecules and that the rod moves by translating in a tube-like region about its axis.

In this section, a fiber drawing analysis for liquid-crystalline polymers is presented by using the constitutive equation given by Eqs. 3.12-3.14 and choosing λ to be $\lambda_0(1-S^2)^2$. In Sections B.1 and B.2 the steady-state and linear stability models and their predictions are discussed.

B.1 Steady-State Fiber Spinning Model

In Section B.1.1, the spinning equations that predict the velocity, normal stress and degree of order profiles in the filament for $\lambda=\lambda_0(1-S^2)^2$ are presented. In Section B.1.2, model predictions of the spinline velocity, stress and degree of order are discussed and the effect of initial degree of order on the development of these profiles is examined. Comparisons are also made with the predictions of the fiber drawing model presented in Chapter 4 which used $\lambda=\lambda_0$.

B.1.1 Steady-State Spinning Equations

The assumptions used in the derivation of the spinning equations with $\lambda=\lambda_0(1-S^2)^2$ are the same as those used in Chapter 4 in the derivation of the spinning equations with $\lambda=\lambda_0$. The dimensionless variables are still given by Eq. 4.25. The dimensionless groups are defined by Eq. 4.30 with λ replaced by λ_0 in the definition of De. The momentum equation, Eq. 4.26-4.27, remains unchanged. The stress tensor equation, Eq. 4.28 and the evolution equation for the structure tensor, Eq. 4.29, must be modified for $\lambda=\lambda_0(1-S^2)^2$:

the modified equations are as follows

Stress tensor equation

$$De\frac{d\phi}{d\zeta} = \left[\frac{\frac{-(T_{zz}-T_{rr})T}{3} - S\left(1-\frac{N}{3}(2S+1)(1-S)\right)}{\frac{\beta}{1-\beta} + 2S^2(1-S^2)^2}\right] \qquad (B.1)$$

Evolution equation for the structure tensor

$$\frac{dS}{d\zeta} = (1-S)(2S+1)\frac{d\ln\phi}{d\zeta} - \frac{\sigma S}{\phi De(1-S^2)^2}\left(1-\frac{N}{3}(1-S)(2S+1)\right) \qquad (B.2)$$

The boundary conditions are the same as those listed in Eq. 4.31. Note, however, that $S(0)=S_\epsilon$ can be different for the two choices of λ; $S(0)=S_{eq}$ is independent of the choice of λ.

B.1.2 Results and Discussion

Figure B.1 shows the axial velocity and orientation distribution for various De's for N=4.0, (which is in the nematic-phase region at equilibrium, as seen from Fig. 3.6) and isotropic hydrodynamic drag (σ = 1.0). The draw ratio (D_R=3.0) used in these calculations and in Chapter 4 are the same. Inertia, gravity, and surface tension are neglected. Variation of dimensionless final elongation rate, $\dot{\epsilon}_L$, with De is shown in Fig. B.2a.

For a Newtonian fluid the final elongation rate $\dot{\epsilon}_L$ is given by $ln D_R$, which for a D_R of 3.0 is roughly 1.10. For De→0, the velocity profile is expected to be Newtonian since the stress becomes linear in the velocity gradient close to equilibrium as seen from

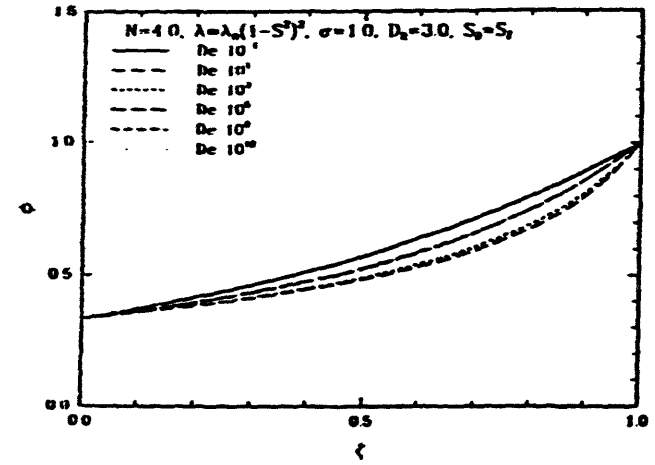

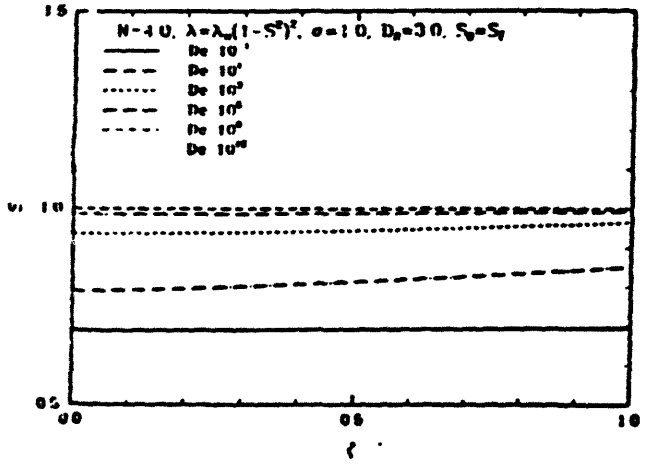

Figure B.1: Variation of (a) velocity ϕ, and (b) order parameter S with distance ζ down the threadline for N=4.0, σ=1.0, D_R=3.0 and De=10^{-1}, 10, 10^3, 10^5, 10^8 and 10^{12}. The initial condition for the microstructure is $S(0)=S_e$ and the time constant $\lambda=\lambda_0(1-S^2)^2$. Velocity profiles for De=10^{-1} and 10^{12} are indistinguishable.

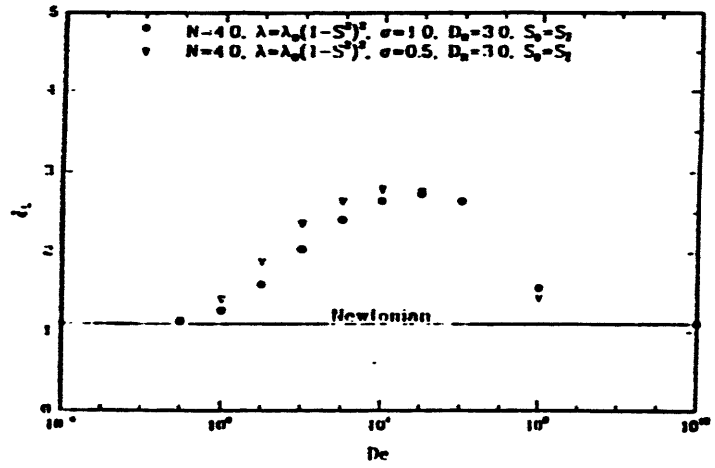

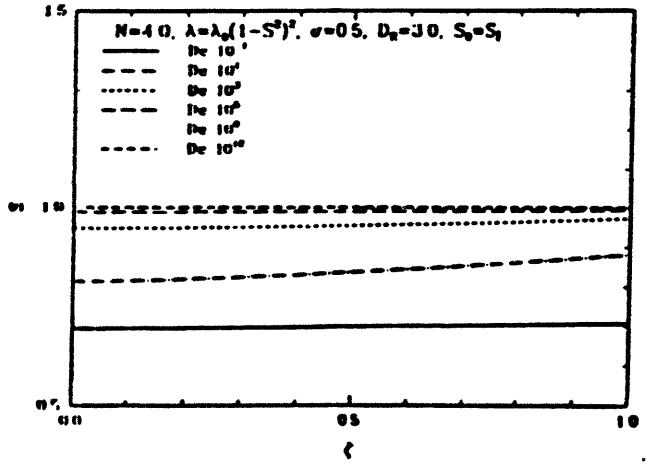

Figure B.2: Variation of (a) the dimensionless final elongation rate $\dot{\varepsilon}_L$ with De for σ=0.5 and σ=1.0, and (b) order parameter S with distance ζ down the threadline for σ=0.5 and De=10^{-1}, 10, 10^3, 10^5, 10^8 and 10^{12}. The other model parameter values are N=4.0 and D_R=3.0. The initial condition for the microstructure is $S(0)=S_\varepsilon$ and the time constant $\lambda=\lambda_0(1-S^2)^2$.

Eq. 3.12. But apparent elongational viscosity $\bar{\eta}_a$ defined by Eq. 4.39, is much bigger than the Trouton elongational viscosity $\bar{\eta}=3\eta_s$ for Newtonian fluids in the limit $\dot{\varepsilon}_L \to 0$ as seen from Fig. B.7, which implies a significant polymer contribution to the stress.

At a De of 10^{-1} the velocity profile is very close to Newtonian behavior since the degree of order S hardly varies with position and is very close to the equilibrium value for N=4.0 determined from Fig. 3.6. As De increases, the profiles become more and more concave, with $\dot{\varepsilon}_L$ becoming maximum close to a De of 10^5. For De's higher than 10^5, the profiles decrease in concavity and become "Newtonian" once again. The behavior at high De's can be explained by rewriting Eq. B.1 for the normal stress difference.

$$T_{zz} - T_{rr} = \frac{3De\beta}{T(1-\beta)}\frac{d\phi}{d\zeta} + \frac{3}{T}\left[S\left(1-\frac{N}{3}(2S+1)(1-S)\right) + 2De(1-S^2)^2S^2\frac{d\phi}{d\zeta}\right] \quad \text{(B.3)}$$

Solvent	Brownian motion	Intermolecular potential	Hydrodynamic drag

The physical origin of the various terms is marked below the equation. For high De's, S is extremely close to 1.0 (Fig. B.1b). Thus the intermolecular force contribution becomes negligible. The Brownian motion term is negligible compared to the solvent term. The hydrodynamic term also becomes small compared to the viscous term, in spite of the high velocity gradient, because $(1\text{-}S^2)^2 \to 0$. So, its not surprising that the velocity becomes Newtonian at very high De's. Infact the apparent elongation viscosity $\bar{\eta}_a$ equals the Trouton viscosity of the Newtonian solvent as seen from Fig B.7, due to the predominance of viscous forces.

The effect of anisotropic drag is illustrated in Fig. B.2. $\dot{\varepsilon}_L$ reaches a maximum at a lower De, and also drops faster to the Newtonian value. So the effect of anisotropy

in the drag is to quicken the response to increasing De by increasing the degree of orientation for the same De, as seen by comparing Figs. B.1b and B.2b.

The effect of concentration on the velocity and degree of order is shown in Fig. B.3. The concentration N=1.0 is in the isotropic region at equilibrium. Once again velocity and ε_L respond more quickly with increasing De as compared to the response for N=4.0 shown in Fig. B.1a and B.2a. The equilibrium order for N=1.0 is zero as compared to 0.683 for N=4.0. It can be seen by comparing Figs. B.1b and B.3b that S changes much more rapidly with increasing De for the lower concentration which results in the quicker response observed in velocity and ε_L with increasing De for N=1.0.

Simulations carried out with $\lambda=\lambda_0$, which predicts viscosity data better as discussed in Chapter 3, are shown in Figs. B.4 for comparison. The velocity profiles deviate very little from the Newtonian limit for σ=1.0. A closer examination of Eqs. 4.28 and B.3 explains why this is so. Since λ_0 is not multiplied by $(1-S^2)^2$, the combination of hydrodynamic and viscous terms swamp the intermolecular potential term and the Brownian motion term. Thus, for reasonably large De's, the dimensionless normal stress difference can be approximated as

$$T_{zz} - T_{rr} \approx \frac{3De}{T}\left(\frac{\beta}{1-\beta} + 2S^2\right)\frac{d\phi}{d\zeta} \qquad \text{(B.4)}$$

with an effective dimensionless viscosity given by $(3De/T)(\beta/(1-\beta) + 2S^2)$ where S is relatively independent of axial position as seen from Fig. B.4b. This results in the normal stress difference being linear in the velocity gradient.

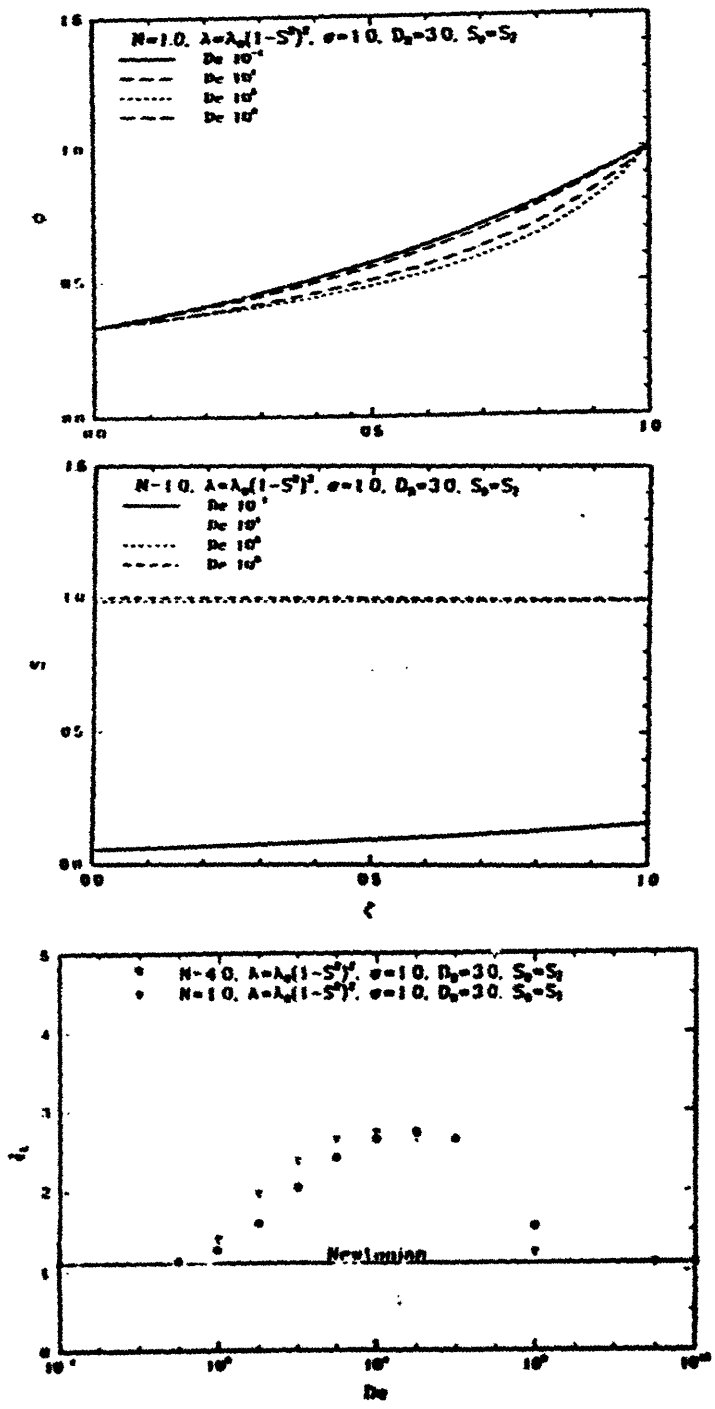

Figure B.3: Variation of (a) velocity ϕ and (b) order parameter S with distance ζ down the threadline for N=1.0, σ=1.0, D_R=3.0 and De=10^{-1}, 10, 10^3, 10^5, 10^8 and 10^{12}. The initial condition for the microstructure is $S(0)=S_e$ and the time constant $\lambda=\lambda_0(1-S^2)^2$. Effect of N on (c) the variation of the dimensionless final elongation rate $\dot{\varepsilon}_L$ with De is also illustrated.

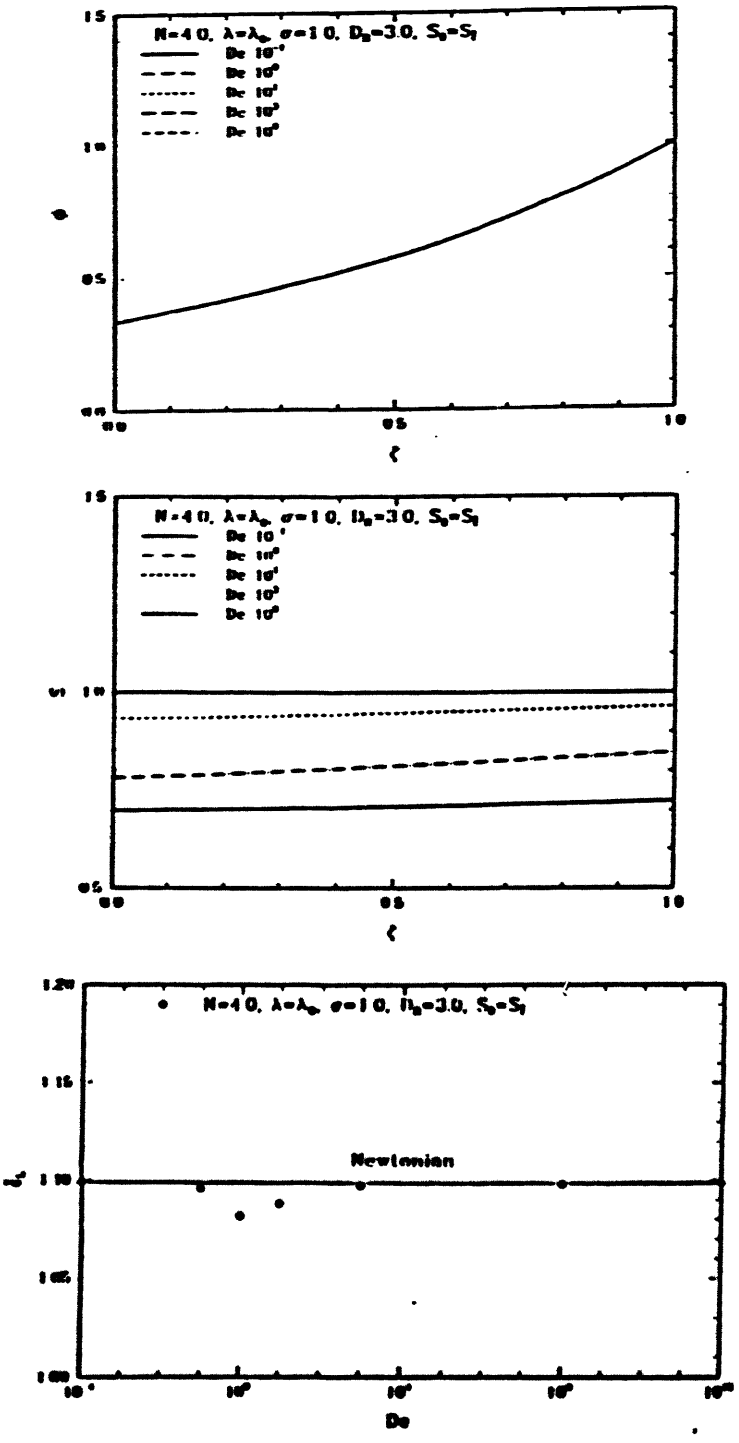

Figure B.4: Variation of (a) velocity ϕ and (b) order parameter S with distance ζ down the threadline for N=4.0, σ=1.0, D_R=3.0 and De=10^{-1}, 1, 10, 10^3, and 10^8. The initial condition for the microstructure is $S(0)=S_\ell$ and the time constant $\lambda=\lambda_0$. Variation of (c) the dimensionless final elongation rate $\dot{\epsilon}_L$ with De is also illustrated.

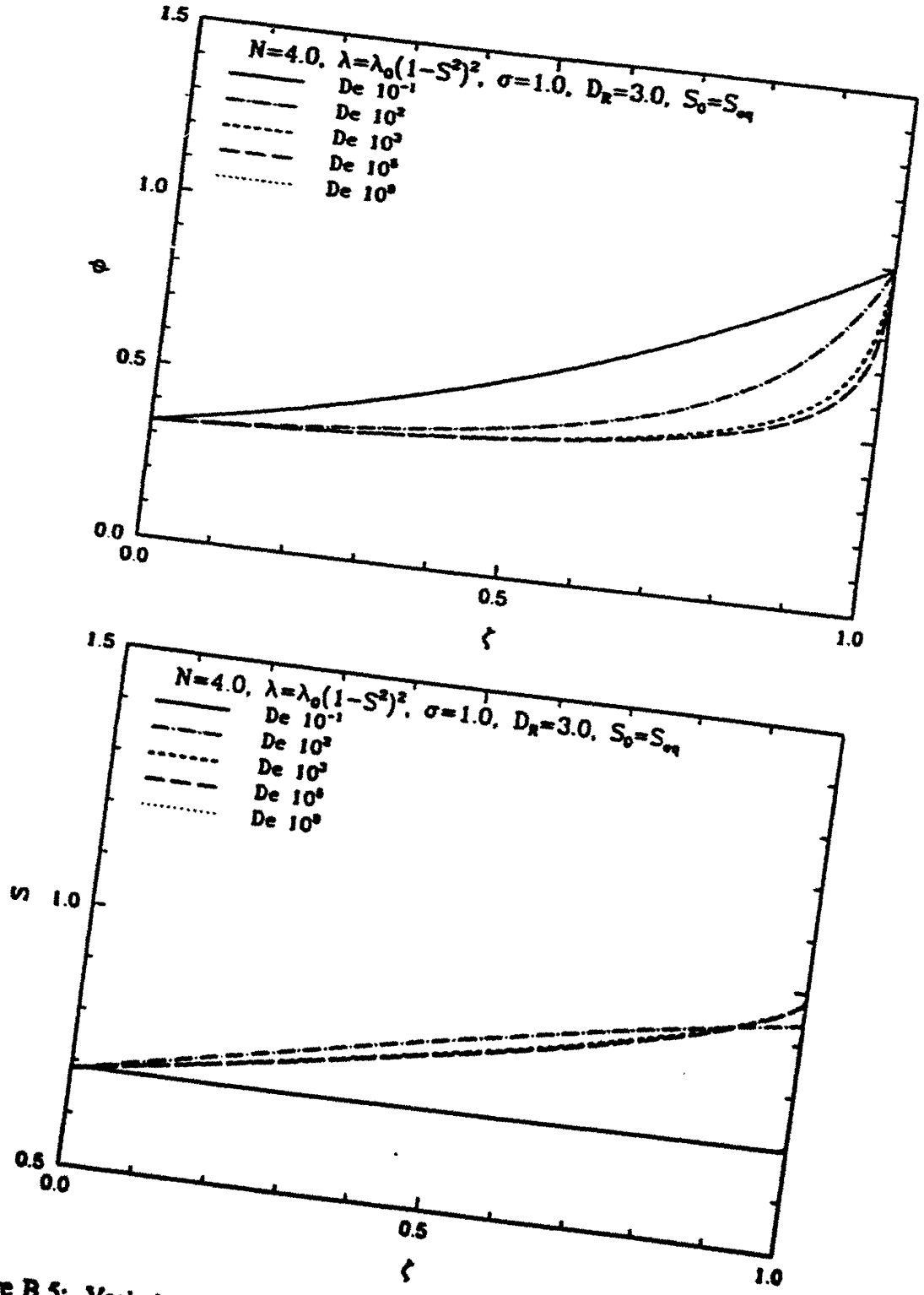

Figure B.5: Variation of (a) velocity ϕ and (b) order parameter S with distance ζ down the threadline for N=4.0, σ=1.0, D_R=3.0 and De=10^{-1}, 10^2, 10^3, 10^5 and 10^8. The initial condition for the microstructure is $S(0)=S_{eq}$ and the time constant $\lambda=\lambda_0(1-S^2)^2$.

Figure B.5 shows the effect of $S(0)=S_{eq}$ on the velocity and orientation profiles for N=4.0 and $\lambda=\lambda_0(1-S^2)^2$, at the same draw ratio. The velocity profiles become increasingly concave as De increases until there seems to be no observable change beyond a De of 10^5. Unlike the case where $S(0)=S_e$, the velocity profiles do not become Newtonian at high De. This is not surprising since the value of $\lambda=\lambda_0(1-S^2)^2$ is higher for the equilibrium initial condition, and the viscous term does not dominate the hydrodynamic term as much. The normal stress difference can be approximated for large De as follows

$$T_{zz} - T_{rr} \approx \frac{3De}{T}\left(\frac{\beta}{1-\beta} + 2(1 - S^2)^2S^2\right)\frac{d\phi}{d\zeta} \qquad \text{(B.5)}$$

The normal stress difference is no longer linear in the velocity gradient since S varies much more along the spinline for the equilibrium initial condition. Consequently, the non-Newtonian like velocity profiles for large De's are to be expected.

The effect of the equilibrium initial condition on the velocity and orientation profiles for $\lambda=\lambda_0$, are shown in Fig. B.6 for comparison. Some degree of "elasticity" is exhibited, since the velocity profiles become less concave than the Newtonian profile. The velocity profile is linear for the perfectly elastic case, and can be obtained as a limiting case with the Maxwell model (Denn, 1976). Once again, there is hardly any change with De, at high De's, either in the velocity or the orientation. The velocity profile is not Newtonian for large De's since S is not constant and has to increase from the equilibrium value to a value close to 1.0 resulting in a non-linear relationship between the stress and the velocity gradient as seen from Eq. B.4. For both choices of λ it can

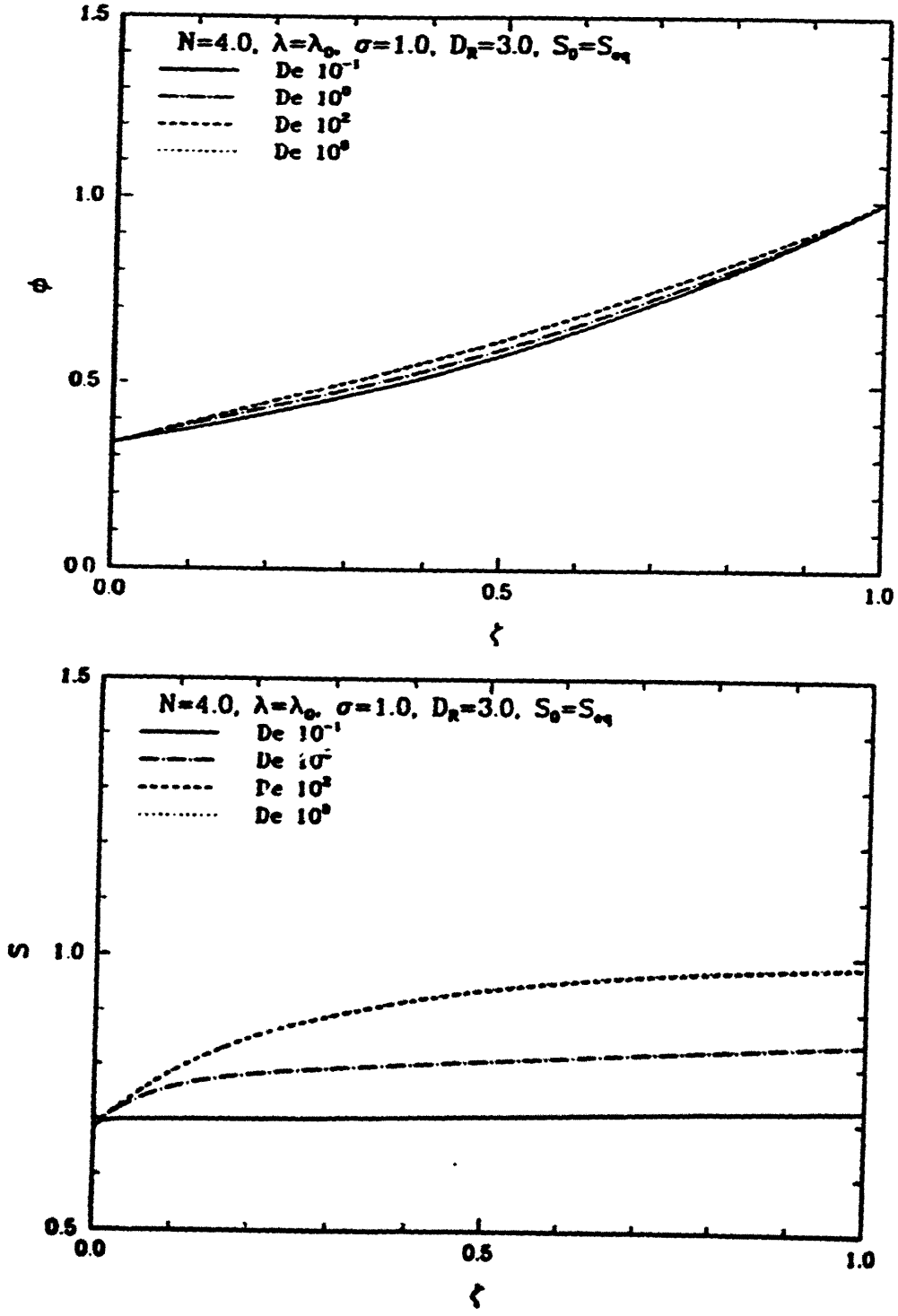

Figure B.6: Variation of (a) velocity ϕ and (b) order parameter S with distance ζ down the threadline for N=4.0, σ=1.0, D_R=3.0 and De=10^{-1}, 1, 10^2 and 10^8. The initial condition for the microstructure is $S(0)=S_{eq}$ and the time constant $\lambda=\lambda_0$.

be seen that the velocity and orientation profiles are sensitive to the choice of the initial condition $S(0)$.

The apparent elongational viscosity $\bar{\eta}_a$ for $\lambda=\lambda_0(1-S^2)^2$ and $\lambda=\lambda_0$ are shown in Fig. B.7; the initial condition is $S(0)=S_\varepsilon$. The simple elongational viscosity $\bar{\eta}$ for the respective λ's are shown for comparison. There is very little difference between $\bar{\eta}_a$ and $\bar{\eta}$ for the entire range of $\dot{\varepsilon}_L$ for both choices of λ which suggests that solving the one-dimensional fiber spinning equations with the initial condition $S(0)=S_\varepsilon$ would directly give us $\bar{\eta}$ for any $\dot{\varepsilon}$. Therefore, if the fiber spinning experiments are designed such that the one-dimensional lubrication approximation equations are valid (which implies the existence of elongational flow alone), $\bar{\eta}_a$ obtained from the experiment is expected to give a good estimate of $\bar{\eta}$ for the elongation rate $\dot{\varepsilon}_L$. However, the validity of the lubrication approximation itself is questionable at high De's which can only be resolved by carrying out two-dimensional FEM simulations back into spinneret.

Figure B.8 illustrates the effect of concentration, σ, and initial condition on $\bar{\eta}_a$ for $\lambda=\lambda_0(1-S^2)^2$. The effect of initial condition on $\bar{\eta}_a$ for $\lambda=\lambda_0$ is also shown for comparison. For small $\dot{\varepsilon}_L$, $\bar{\eta}_a$ is constant and is numerically equal to the zero-elongation-rate viscosity, η_o. η_o is obviously different for the two different concentrations. In the extension thinning region, $\bar{\eta}_a$ has a slope close to -2/3 for $S(0)=S_\varepsilon$, which agrees with the asymptotic limit predicted for $\bar{\eta}$ by Menon (1990). For high $\dot{\varepsilon}_L$, $\bar{\eta}_a$ is bounded from below by the Trouton viscosity, $3\eta_s$. For $S(0)=S_{eq}$, $\bar{\eta}_a$ has a slope slightly greater than -2/3 in the extension thinning region for this draw ratio. The lower bound for $\bar{\eta}_a$ is also much higher than the Trouton viscosity for the equilibrium initial condition. The apparent

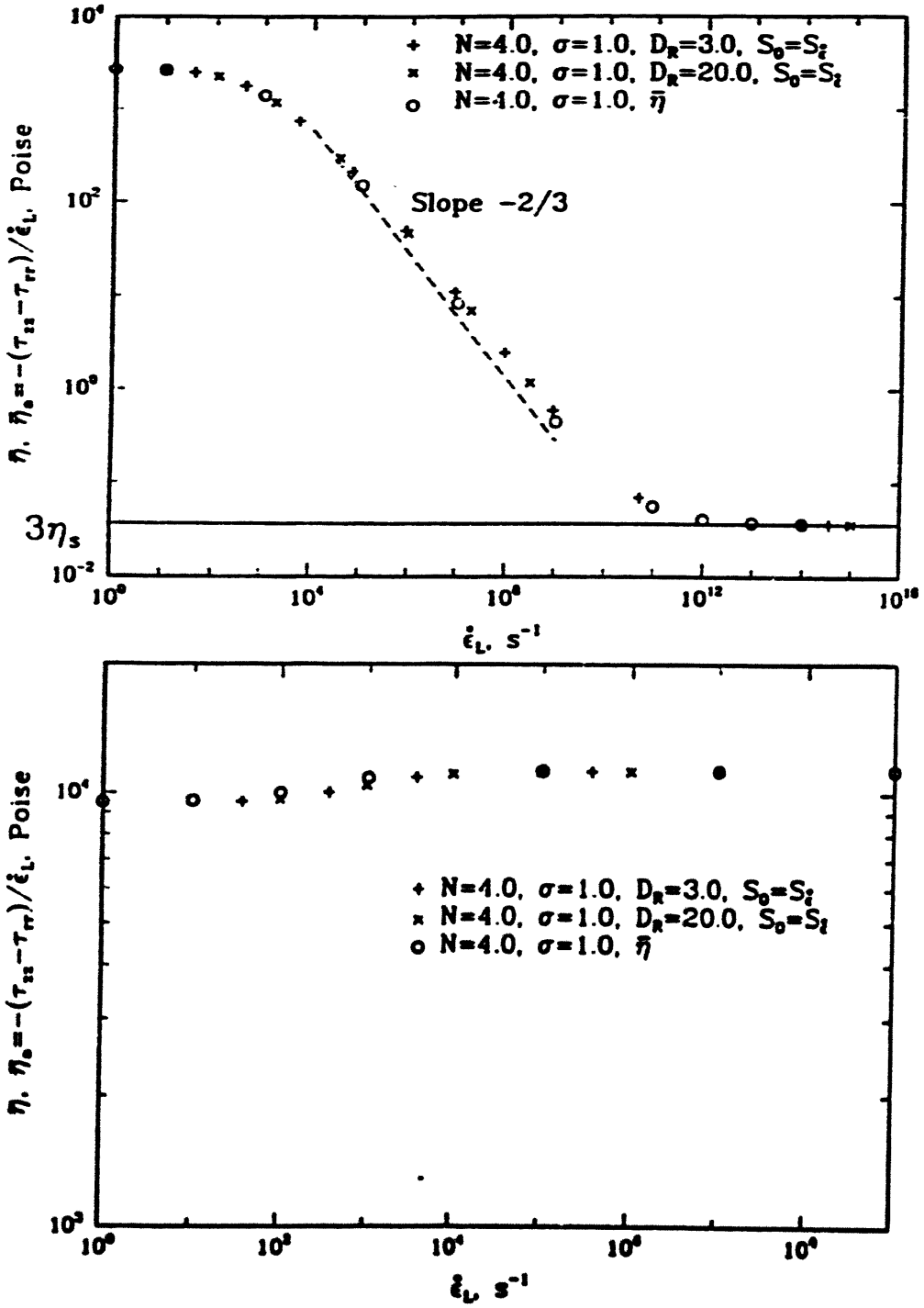

Figure B.7: Effect of draw ratio on the apparent elongational viscosity $\bar{\eta}_a$ for N=4.0, σ=1.0 and the two different time constants (a) $\lambda=\lambda_0(1-S^2)^2$ and (b) $\lambda=\lambda_0$. The initial microstructural condition is $S(0)=S_\xi$. The true elongational viscosity $\bar{\eta}$ for the respective time constants are also shown for comparison.

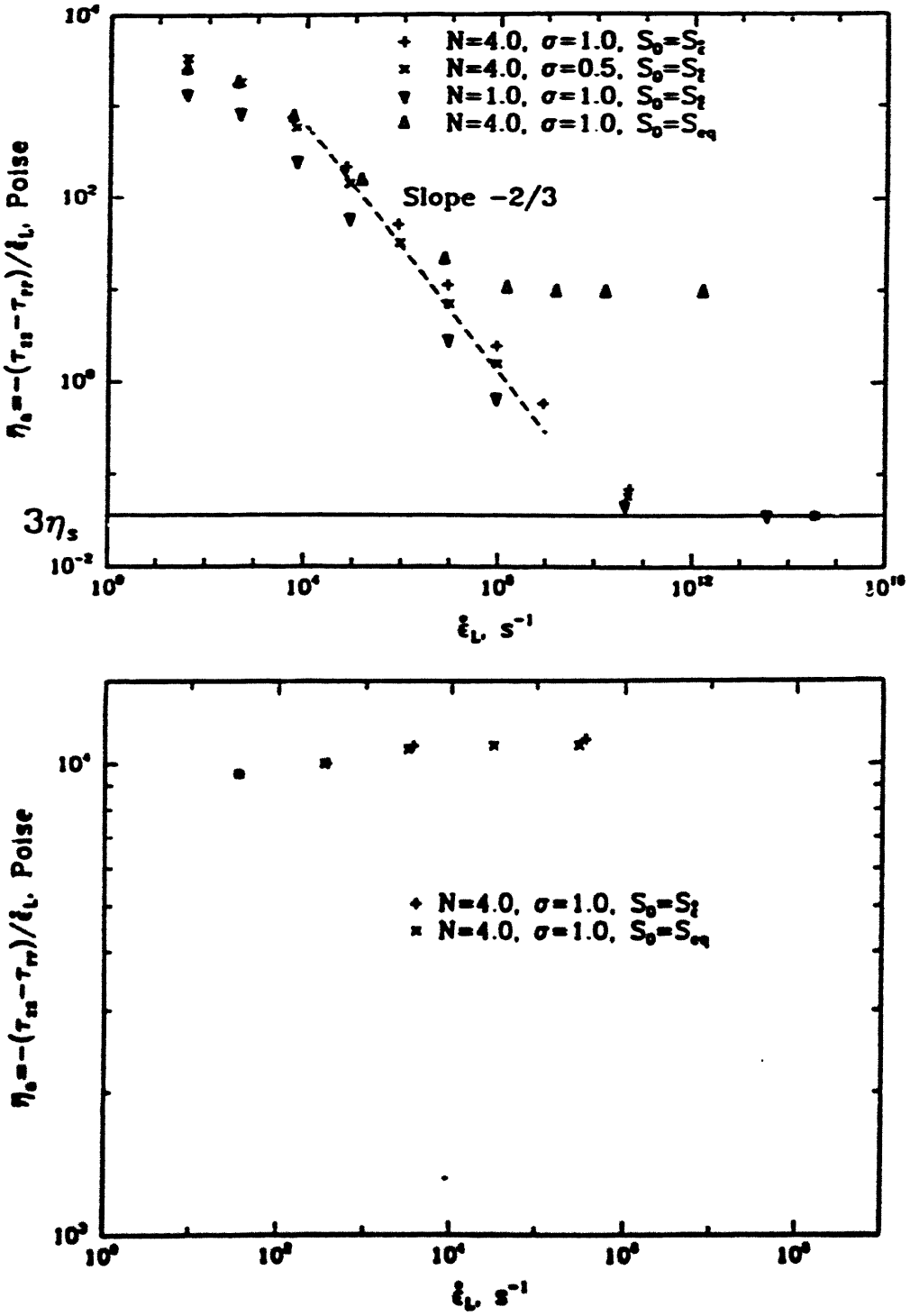

Figure B.8: Effect of N, σ and $S(0)$ on (a) the apparent elongational viscosity $\bar{\eta}_e$ for $\lambda=\lambda_0(1-S^2)^2$. The effect of $S(0)$ on (b) the apparent elongational viscosity $\bar{\eta}_e$ for $\lambda=\lambda_0$ is also shown.

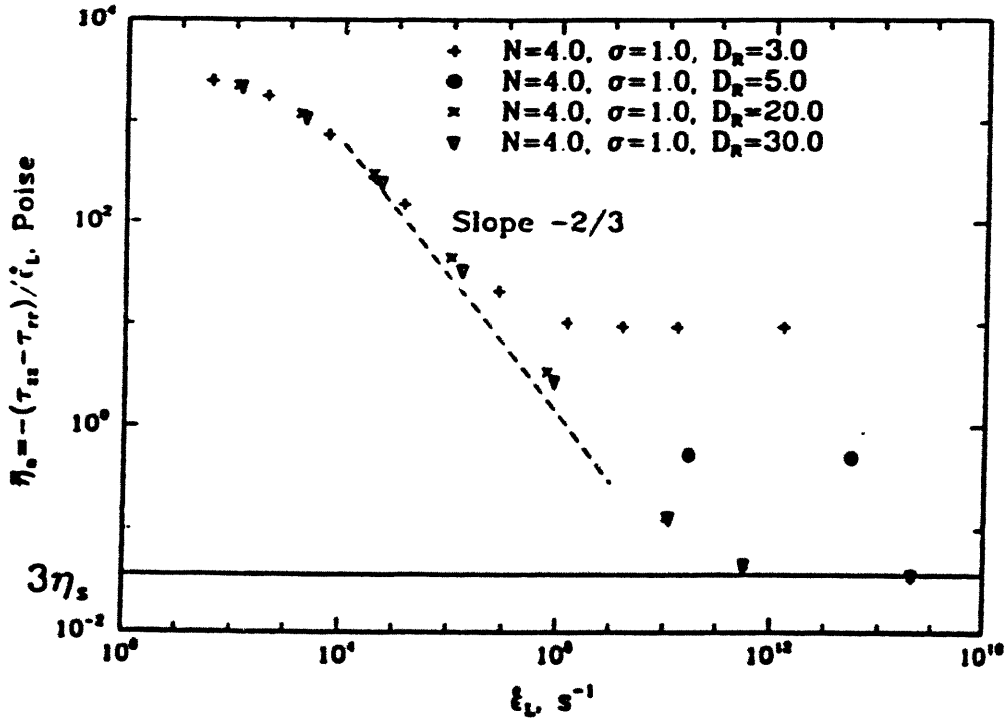

Figure B.9: Effect of draw ratio on the apparent elongational viscosity $\bar{\eta}_a$ for N=4.0, σ=1.0 and D_R=3.0, 5.0, 20.0 and 30.0. The initial microstructural condition and time constant are $S(0)=S_{eq}$ and $\lambda=\lambda_0(1-S^2)^2$ respectively.

elongational viscosity behavior for $\lambda=\lambda_0$ was discussed in Chapter 4. The initial condition has very little effect on $\bar{\eta}_a$ for this model.

Figures B.7 and B.9 show the effect of draw ratio on $\bar{\eta}_a$ for the two different initial conditions. For $S(0)=S_\epsilon$, there is very little difference in the $\bar{\eta}_a$ profiles, except that $\bar{\eta}_a$ is always lower for the higher draw ratio in the extensional thinning region, due to the higher values for the final elongation rate. In fact, for every value of the elongation rate, there is a unique value of the power-law index n. This result is of significance to the stability analysis discussed in Section B.2, since analytical and numerical (Kase, 1985; Shah and Pearson, 1972) stability results exist already for power-law models. We might anticipate that the critical draw ratio predicted by the liquid-crystal model at each and every elongation rate $\dot{\epsilon}_L$ would be comparable to the power-law result where n is determined from the $\bar{\eta}_a(\dot{\epsilon}_L)$ plot. As already discussed in Chapter 4, the comparison with the stability results for the power-law model is favorable for $\lambda=\lambda_0$.

Increasing the draw ratio, affects the apparent elongational viscosity predictions in the extension thinning region and also the lower bound values when the initial condition is $S(0)=S_{eq}$, as seen from Fig. B.9. So, $\dot{\epsilon}_L$ is no longer unique in n, which invalidates the power-law interpretation of stability for this choice of the initial condition. However, the asymptotic slope is never smaller than -2/3, and the value of n for each $\dot{\epsilon}_L$ with $S(0)=S_\epsilon$ appears to be the lower limiting value for the initial condition $S(0)=S_{eq}$.

Model predictions of the experimental data obtained by Prilutski (1984) for $N=2.3$ (isotropic at equilibrium) and $N=4.0$, are shown in Figs. B.10-B.12 for both choices of λ. For N=2.3, the computed values of De and D_R are 7.84×10^{-3} and 7.89 respectively. The

model predictions of the normal stress difference are much better when gravity and surface tension are included in the momentum balance. For this extremely small De, the choice of λ does not matter as seen from Figs. B.10 and B.11. Initial condition also has little effect on the model predictions since De is very small.

For N=4.0, De and D_R have been computed to be 7.63×10^{-3} and 3.63 respectively. There seems to be some improvement in the predictions without the effects of gravity and surface tension as compared to the case where N=2.3, as seen from Figs. B.10 and B.12; model predictions for N=4.0 and $\lambda=\lambda_0$ were shown in Chapter 4. The higher concentration requires a larger tension for roughly the same De, resulting in the diminished effect of gravity and surface tension. This is confirmed by the normal stresses observed for N=4.0. However, inclusion of gravity and surface tension once again improves the normal stress prediction for both choices of λ.

Though the model predicts available experimental data really well, it should be kept in mind that all data are at very low De's, due to the experimental limitations discussed in Chapter 3. Therefore in all experiments the elongational viscosity hardly varies from the zero-elongation-rate elongational viscosity $\bar{\eta}_0$ and the elongation thinning or thickening stage is never reached. So the particular choice of the initial condition or λ is not resolved by available experimental data. For a rigorous test of the model, data at higher De's are required.

B.2 Linear Stability Analysis

In Section B.2.1, the linear stability equations that predict the onset of draw resonance

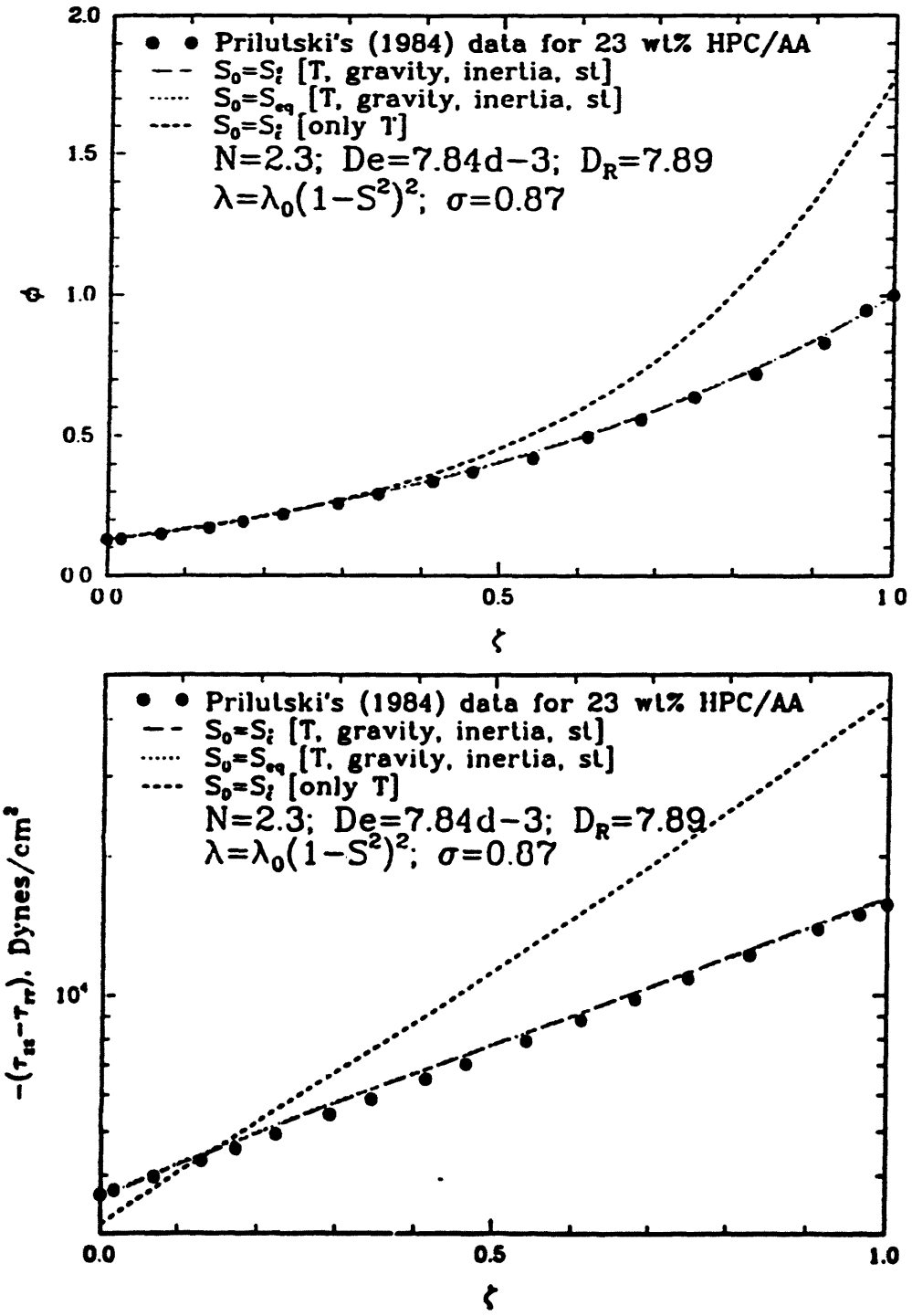

Figure B.10: Comparison of model predictions with the data of Prilutski (1984) for a hydroxy propyl cellulose solution in acetic acid with N=2.3, D_R=7.89, η_s=0.012 Poise, De=7.84×10^{-3}, σ=0.87, $\lambda=\lambda_0(1-S^2)^2$ and $S(0)=S_\xi$ and S_{eq}: (a) velocity and (b) normal stress difference. The prediction obtained without including gravity and surface tension is shown for comparison with $S(0)=S_\xi$.

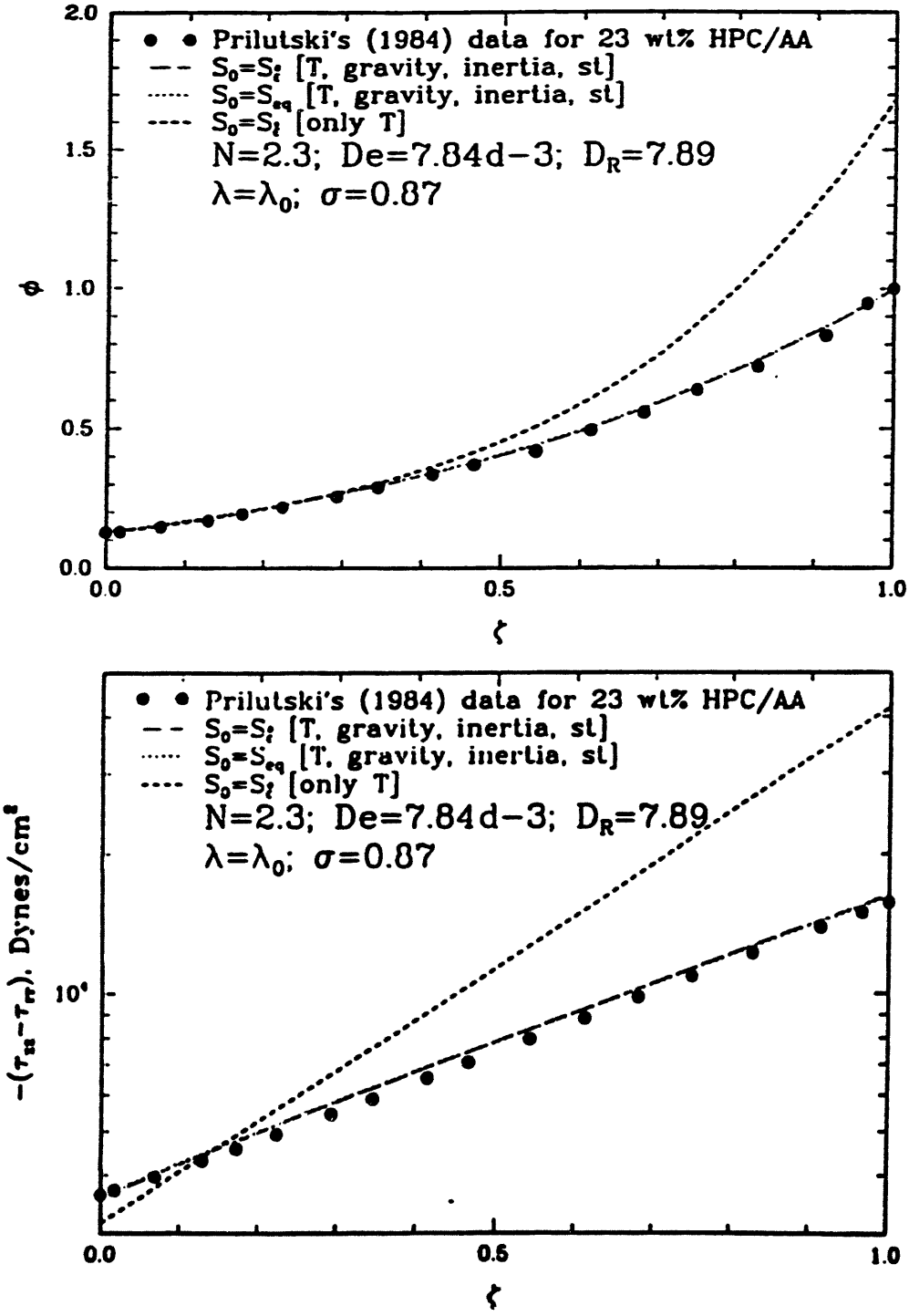

Figure B.11: Comparison of model predictions with the data of Prilutski (1984) for a hydroxy propyl cellulose solution in acetic acid with N=2.3, D_R=7.89, η_s=0.012 Poise, De=7.84×10^{-3}, σ=0.87, $\lambda=\lambda_0$ and $S(0)=S_t$ and S_{eq}: (a) velocity and (b) normal stress difference. The prediction obtained without including gravity and surface tension is shown for comparison with $S(0)=S_t$.

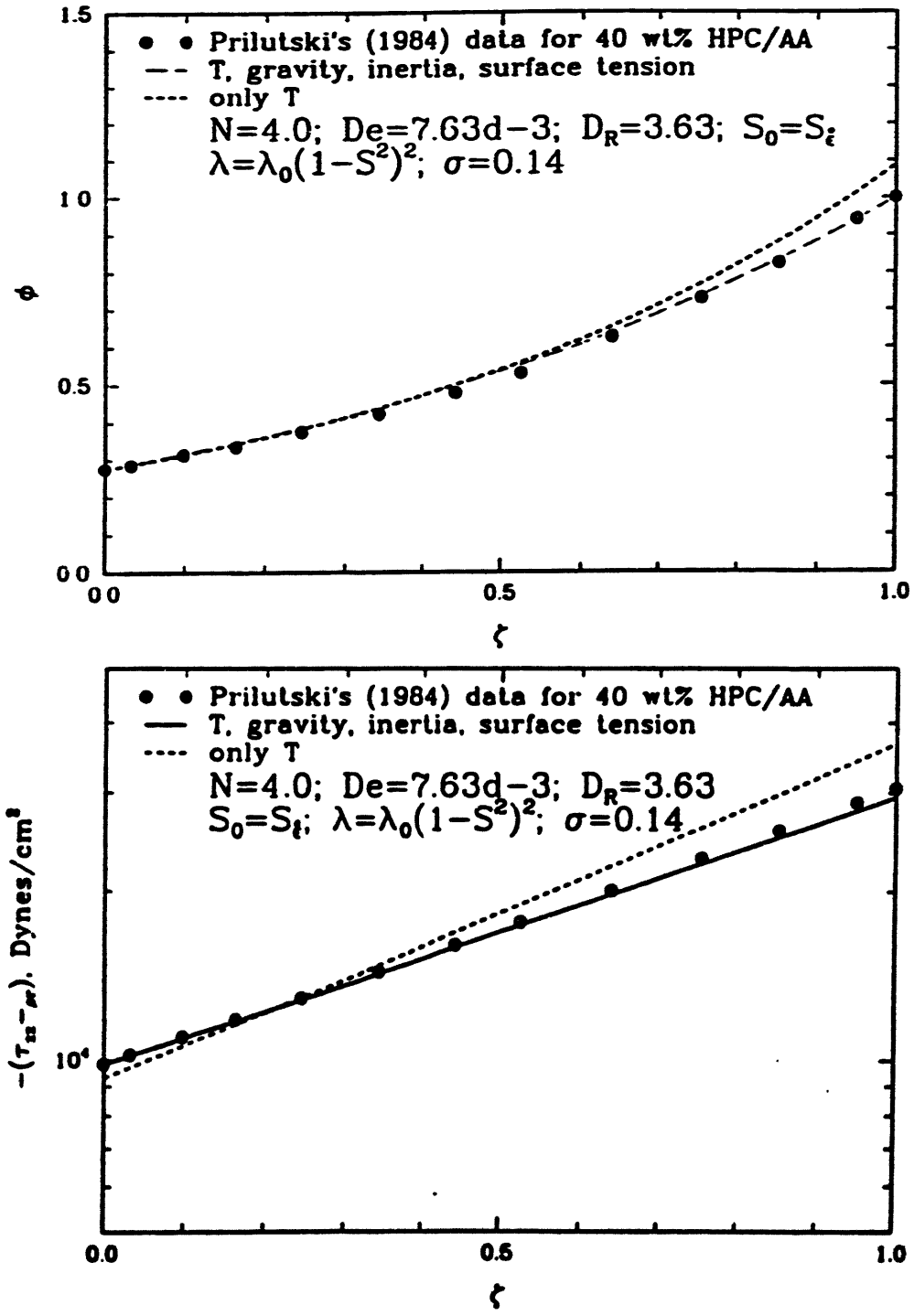

Figure B.12: Comparison of model predictions with the data of Prilutski (1984) for a hydroxy propyl cellulose solution in acetic acid with N=4.0, D_R=3.63, η_s=0.012 Poise, De=7.63×10^{-3}, σ=0.14, $\lambda=\lambda_0(1-S^2)^2$ and $S(0)=S_\ell$: (a) velocity and (b) normal stress difference. The prediction obtained without including gravity and surface tension is shown for comparison.

instabilities are presented for $\lambda=\lambda_0(1-S^2)^2$. In Section B.2.2, the linear stability predictions are discussed and some comparisons are made with the linear stability predictions presented in Chapter 4 which used $\lambda=\lambda_0$.

B.2.1 Linear Stability Equations

The assumptions used in the derivation of the linear stability equations with $\lambda=\lambda_0(1-S^2)^2$ are the same as those used in Chapter 4 in the derivation of the linear stability equations with $\lambda=\lambda_0$. The linear stability equations for $\lambda=\lambda_0$ were given by Eqs. 4.51-4.55. Equations 4.51, 4.53 and 4.54 remain unchanged for $\lambda=\lambda_0(1-S^2)^2$. In addition, the algebraic relation for $H_1(v,s,S_0)$ in Eq. 4.55 remains unchaged. Equation 4.52 and the algebraic relation for $H_2(S_0)$ in Eq. 4.55 are modified as follows for $\lambda=\lambda_0(1-S^2)^2$

$$\phi_0\frac{dv}{d\zeta} = -\frac{d\phi_0}{d\zeta}v - \frac{4S_0^2(1-3S_0^2)(1-S_0^2)}{\left(2S_0^2(1-S_0^2)^2+\beta/(1-\beta)\right)}\frac{d\phi_0}{d\zeta}s - \frac{\phi_0 T_0(a-f)}{3De\left(2S_0^2(1-S_0^2)^2+\beta/(1-\beta)\right)} - 3S_0\left(1-\frac{N}{3}\left(1+2S_0-6S_0^2\right)\right)s + \frac{\beta/(1-\beta)}{3\left(2S_0^2(1-S_0^2)^2+\beta/(1-\beta)\right)}\times \left[\frac{1}{2Ca}\phi_0^{1/2}(1-4(\phi_0 D_R)^{1/2})a + Re\,\phi_0\left(\left(\frac{1}{D_R}-\phi_0\right)a+\phi_0 v\right)+\frac{Re}{Fr}\phi_0 I_{1,0}(\zeta)a-\phi_0 I_2(\zeta)\right] \tag{B.6}$$

$$H_2(S_0) = \frac{S_0}{(1-S_0^2)^3}\left(-(1-\frac{N}{3})(1+3S_0^2)+\frac{2NS_0}{3}(1+S_0^2)-2NS_0^2(1+\frac{S_0^2}{3})\right) \tag{B.7}$$

The boundary conditions are those listed in Eq. 4.56.

B.2.2 Results and Discussion

Stability plots ($D_{R,crit}$ vs. De) have been obtained for N=1.0 and N=4.0. The effect of σ and the initial condition $S(0)$ have also been investigated for N=4.0. Stability plots for $\lambda=\lambda_0$ are also shown for comparison.

Stability curves for N=1.0 and N=4.0 are shown in Figure B.13. For $\lambda=\lambda_0$, $D_{R,crit}$ is close to the Newtonian critical draw ratio of 20.21 for all De as was observed for N=4.0 in Chapter 4 and replotted in Fig. B.13b. As discussed in Section B.1.2, $\bar{\eta}_a$ is constant at low and high values of elongation rate or De for $\lambda=\lambda_0(1-S^2)^2$. Consequently, $D_{R,crit}$ approaches the Newtonian limit of 20.21 at low and high De. For intermediate values of De the combination of the intermolecular potential and Brownian motion terms on the one hand and the hydrodynamic drag term on the other have a marked effect on stability, and $D_{R,crit}$ decreases to about 3.5, before it rises again to the Newtonian value. The same behavior is not observed with the $\lambda=\lambda_0$ model since for intermediate values of De the hydrodynamic drag contribution dominates, and the normal stress difference looks like Eq. B.4 without the solvent contribution. Since S is relatively constant (a high degree of order, S=0.98, is achieved for De=100) the normal stress difference is "Newtonian" resulting in a critical draw ratio close to 20.21. Since the hydrodynamic drag term is bigger for the $\lambda=\lambda_0$ model, a comparison between the stability plots for the two λ models indicates that an increase in the hydrodynamic term would increase stability.

Stability results for N=4.0, are shown in Fig. B.13b. Figure B.14a illustrates the quantitative effect of concentration on stability. For N=1.0, S=0 at equilibrium, whereas S=0.683 for N=4.0. So the Brownian motion, intermoleular potential and hydrodynamic

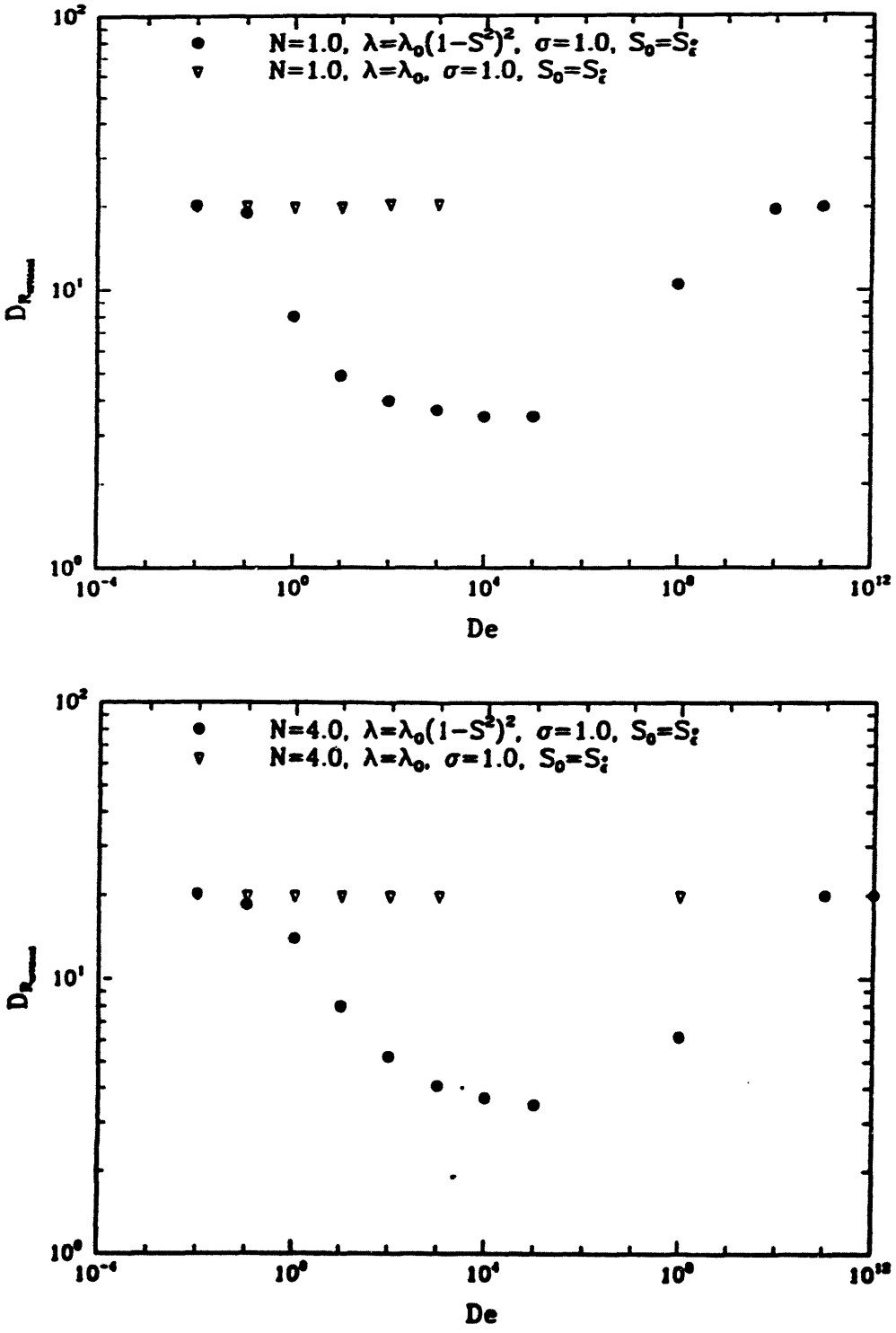

Figure B.13: Variation of $D_{R,crit}$ with De for (a) N=1.0 and (b) N=4.0 and σ=1.0, $S(l)=S_e$ and both choices of λ.

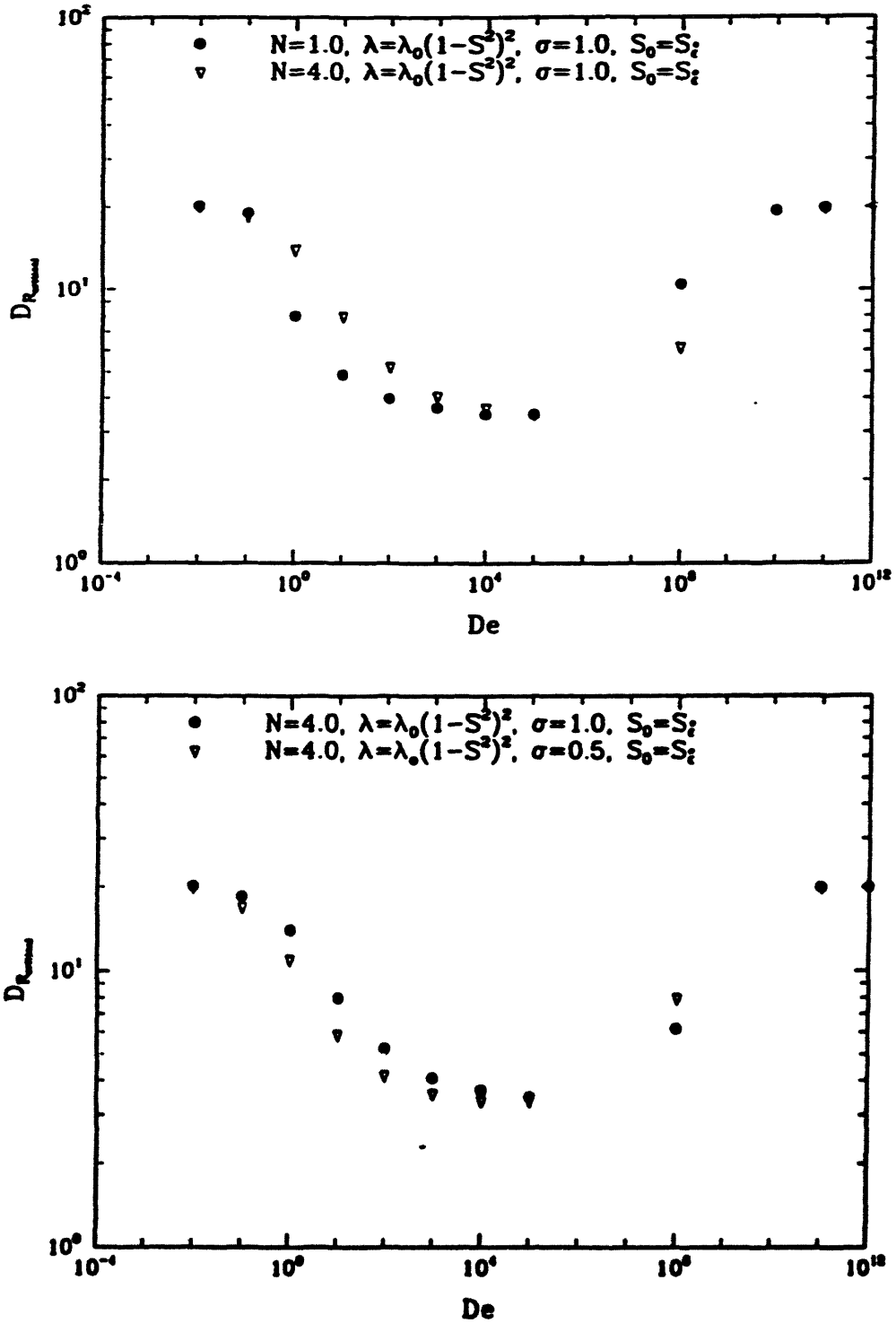

Figure B.14: Effect of (a) N and (b) σ on the variation of $D_{R,crit}$ with De. Results are shown for $\lambda=\lambda_0(1-S^2)^2$ and $S(0)=S_e$.

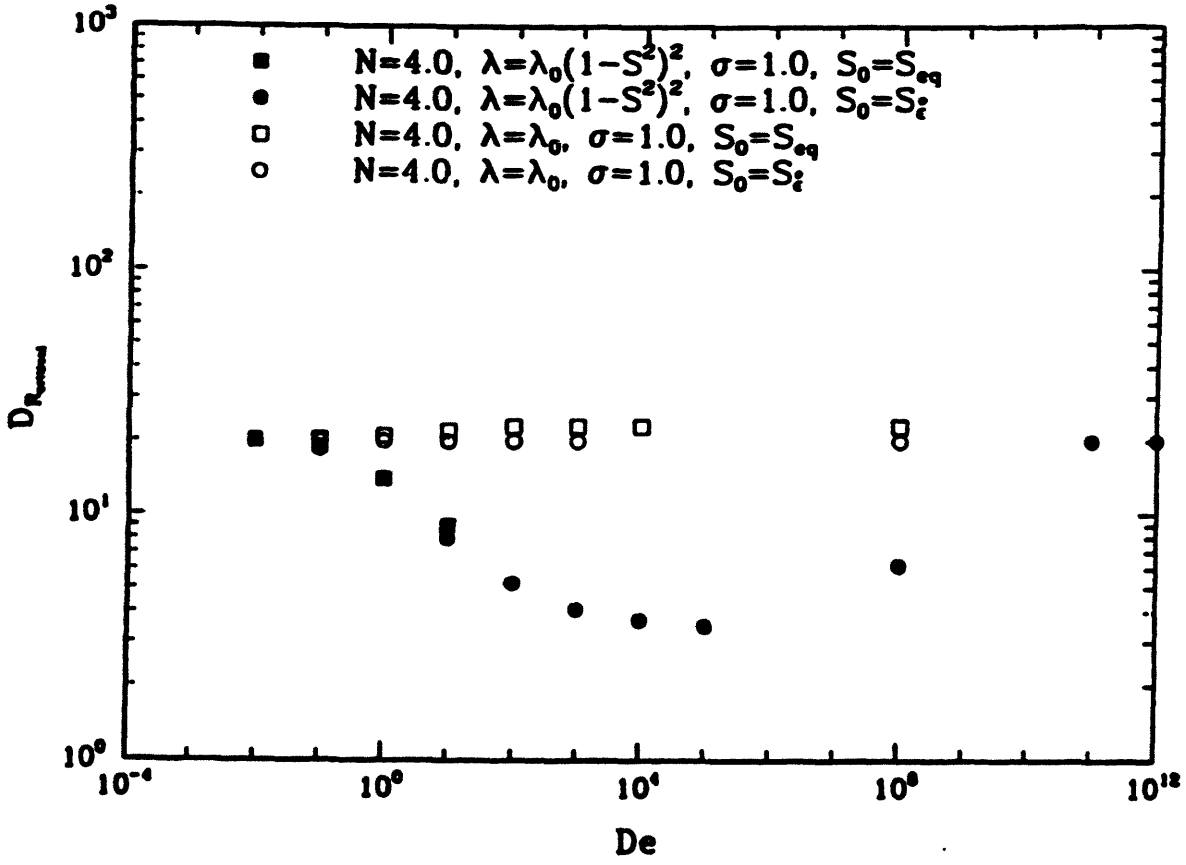

Figure B.15: Effect of initial condition $S(0)$ on the variation of $D_{R,crit}$ with De. Results are shown for N=4.0, σ=1.0 and $\lambda=\lambda_0(1-S^2)^2$ and λ_0.

drag terms change more rapidly with De for N=1.0 resulting in the earlier response observed. As already seen in Section B.1.2, increasing anisotropy quickens the response to increasing De. This is confirmed by Fig. B.14b.

The effect of the initial condition $S(0)=S_{eq}$ on stability, is shown in Fig. B.15. The corresponding stability curves for $S(0)=S_{\xi}$, are shown for comparison. The effect of initial condition is negligible for the $\lambda=\lambda_0$ model as already seen in Chapter 4. For $\lambda=\lambda_0(1-S^2)^2$, for small De, when S is reasonably close to the equilibrium value, the stability curves overlap. Beyond a De of 10.0, the stability behavior is unclear. A more thorough analysis is required to determine the stability response at high De's.

The stability results seem to correlate well with the apparent elongational viscosity plots shown in Figs. B.7 and B.8. It is seen from Fig. B.7 that draw ratio has very little qualitative effect on the $\bar{\eta}_a$ profile. In fact, as discussed in Section B.1.2, the stability predictions of a power-law model with variable index n, where n is determined from the apparent elongational viscosity plot seem to compare well with the stability results of the liquid-crystal model for $S(0)=S_{\xi}$. In Fig. B.7a the asymptotic slope of -2/3 (n=1/3) is reached around a De of 10^5. The critical draw ratio for n=1/3 is around 3, which compares well with the stability predictions of the liquid-crystal model. In addition, the apparent elongational viscosity is constant for low and high De's. So the stability must be Newtonian for these limits, which is predicted by the linear stability analysis.